

Jeff Jones

From Pattern Formation to Material Computation

Multi-agent Modelling of *Physarum Polycephalum*

Emergence, Complexity and Computation

Volume 15

Series editors

Ivan Zelinka, Technical University of Ostrava, Ostrava, Czech Republic
e-mail: ivan.zelinka@vsb.cz

Andrew Adamatzky, University of the West of England, Bristol, United Kingdom
e-mail: adamatzky@gmail.com

Guanrong Chen, City University of Hong Kong, Hong Kong
e-mail: eegchen@cityu.edu.hk

Editorial Board

Ajith Abraham, MirLabs, USA

Ana Lucia C. Bazzan, Universidade Federal do Rio Grande do Sul, Porto Alegre
RS Brasil

Juan C. Burguillo, University of Vigo, Spain

Sergej Čelikovský, Academy of Sciences of the Czech Republic, Czech Republic

Mohammed Chadli, University of Jules Verne, France

Emilio Corchado, University of Salamanca, Spain

Donald Davendra, Technical University of Ostrava, Czech Republic

Andrew Ilachinski, Center for Naval Analyses, USA

Jouni Lampinen, University of Vaasa, Finland

Martin Middendorf, University of Leipzig, Germany

Edward Ott, University of Maryland, USA

Linqiang Pan, Huazhong University of Science and Technology, Wuhan, China

Gheorghe Păun, Romanian Academy, Bucharest, Romania

Hendrik Richter, HTWK Leipzig University of Applied Sciences, Germany

Juan A. Rodriguez-Aguilar, IIIA-CSIC, Spain

Otto Rössler, Institute of Physical and Theoretical Chemistry, Tübingen, Germany

Vaclav Snasel, Technical University of Ostrava, Czech Republic

Ivo Vondrák, Technical University of Ostrava, Czech Republic

Hector Zenil, Karolinska Institute, Sweden

About this Series

The Emergence, Complexity and Computation (ECC) series publishes new developments, advancements and selected topics in the fields of complexity, computation and emergence. The series focuses on all aspects of reality-based computation approaches from an interdisciplinary point of view especially from applied sciences, biology, physics, or Chemistry. It presents new ideas and interdisciplinary insight on the mutual intersection of subareas of computation, complexity and emergence and its impact and limits to any computing based on physical limits (thermodynamic and quantum limits, Bremermann's limit, Seth Lloyd limits...) as well as algorithmic limits (Gödel's proof and its impact on calculation, algorithmic complexity, the Chaitin's Omega number and Kolmogorov complexity, non-traditional calculations like Turing machine process and its consequences,...) and limitations arising in artificial intelligence field. The topics are (but not limited to) membrane computing, DNA computing, immune computing, quantum computing, swarm computing, analogic computing, chaos computing and computing on the edge of chaos, computational aspects of dynamics of complex systems (systems with self-organization, multiagent systems, cellular automata, artificial life,...), emergence of complex systems and its computational aspects, and agent based computation. The main aim of this series is to discuss the above mentioned topics from an interdisciplinary point of view and present new ideas coming from mutual intersection of classical as well as modern methods of computation. Within the scope of the series are monographs, lecture notes, selected contributions from specialized conferences and workshops, special contribution from international experts. More information about this series at

<http://www.springer.com/series/10624>

Jeff Jones

From Pattern Formation to Material Computation

Multi-agent Modelling of Physarum
Polycephalum



Springer

Jeff Jones
Unconventional Computing Centre
University of the West of England
Bristol
United Kingdom

ISSN 2194-7287 ISSN 2194-7295 (electronic)
Emergence, Complexity and Computation
ISBN 978-3-319-16822-7 ISBN 978-3-319-16823-4 (eBook)
DOI 10.1007/978-3-319-16823-4

Library of Congress Control Number: 2015937729

Springer Cham Heidelberg New York Dordrecht London
© Springer International Publishing Switzerland 2015

This work is subject to copyright. All rights are reserved by the Publisher, whether the whole or part of the material is concerned, specifically the rights of translation, reprinting, reuse of illustrations, recitation, broadcasting, reproduction on microfilms or in any other physical way, and transmission or information storage and retrieval, electronic adaptation, computer software, or by similar or dissimilar methodology now known or hereafter developed.

The use of general descriptive names, registered names, trademarks, service marks, etc. in this publication does not imply, even in the absence of a specific statement, that such names are exempt from the relevant protective laws and regulations and therefore free for general use.

The publisher, the authors and the editors are safe to assume that the advice and information in this book are believed to be true and accurate at the date of publication. Neither the publisher nor the authors or the editors give a warranty, express or implied, with respect to the material contained herein or for any errors or omissions that may have been made.

Printed on acid-free paper

Springer International Publishing AG Switzerland is part of Springer Science+Business Media
(www.springer.com)

For Wendy

Preface

This book describes simple multi-agent mechanisms which model the behaviour of an extraordinary creature, the true slime mould *Physarum Polycephalum*. This giant (up to square metre sized) single-celled organism was once known only for its curious biological properties and behaviour. Since the start of this 21st Century, however, it has been the subject of a wide range of studies into its computational abilities. *Physarum* is both fascinating and puzzling because it can perform such complex biological and computational feats without a brain, or indeed any specialised nervous tissue. It has since become the subject of intensive research in both classical and unconventional computing and robotics research.

To model the behaviour of slime mould in this book, we describe and explore the complex pattern formation that emerges from interactions within a population of very simple mobile agents. The agents themselves are so simple and generic that they may be regarded as particles, yet their interactions yield surprisingly complex emergent patterns. An evaluation of the pattern formation produced by these particle interactions is described, along with the effects of key model parameters. We show that these patterns exhibit second-order behaviours which approximate phenomena observed in physical systems, including self-organised network assembly and network minimisation. We use these emergent and quasi-physical pattern formation mechanisms as the basis of a simple bottom-up model of *Physarum* slime mould. We reproduce its biological behaviour, demonstrating how *Physarum* may offload some computation to the environment in a parsimonious two-way mechanism of sensing — and subsequently modifying — spatial diffusion gradients.

We then show how this virtual slime mould (as with real slime mould) can be considered as a material-based, spatially represented, unconventional computing substrate, approximating a wide range of computing problems by propagation through space and morphological adaptation; including path planning, proximity graph formation and minimisation, convex hulls, concave hulls, internal skeletons, Voronoi diagrams, combinatorial optimisation (both feedback

controlled and simple ‘blind’ methods), data smoothing, spline curves, simple geometric and numerical statistical analysis, and noisy estimation.

The model can also reproduce the spontaneous and self-organised emergence of oscillations within the ‘material’ of which it is composed. We demonstrate how the emergence and synchronisation of oscillations within the plasmodium can also occur in the model, replicating the typical oscillation patterns of the *Physarum* plasmodium. We subsequently demonstrate how these oscillations can be harnessed to generate distributed collective transport mechanisms and controllable soft-bodied amoeboid movement.

We conclude by considering how the multi-agent approach can be extended beyond modelling *Physarum* into the realm of modelling other dynamical systems including repulsive particles, mixed material types, phase separation phenomena, patterning in growing materials, phyllotaxis-type patterns and 3D transport networks.

The results in this book demonstrate the power and range of harnessing emergent phenomena arising in simple multi-agent systems for biological modelling, computation and soft-robotics applications. With the aid of rich explanatory images, video recordings and interactive simulations the reader can explore the power of bottom-up multi-agent models and will hopefully be motivated to explore and develop their own experiments with these simple yet powerful systems.

November 2014
Bristol

Jeff Jones

Acknowledgements

I would like to thank:

- Andrew Adamatzky for his experimental ‘wet’ slime mould contributions to Chapters 9, 10, 12 and 13. And also for his designs of composite logic gates that were implemented in Chapter 7. But most importantly for his relentless support, insights, motivation and encouragement. A finer mentor could not be had.
- Soichiro Tsuda for his help and experimental contribution to *Physarum* oscillatory synchronisation in Chapter 15.
- Larry Bull for his advice and positive support.
- A number of people who have helped me in informal, but constructive and motivational, support, including Ben De Lacy Costello, Susan Stepney and Yukio-Pegio Gunji.
- Thomas Ditzinger, Engineering Editorial, Springer-Verlag, for his support and help.
- Mr. G Senthilkumar, ECC Processing Team, Scientific Publishing Services, for his proofing assistance.

I am grateful for the funding support of the University of the West of England Department of Computer Science and the award of a UWE SPUR Early Career Research grant, the award of Leverhulme Trust Research Fellow, and the funding provided by the EU research programme FP7 ICT Ref 316366.

Contents

Part I Slime Mould *Physarum Polycephalum*

1	Introduction and Overview	3
1.1	Introduction and Overview	3
1.2	Objectives	4
1.3	Methodology	4
1.4	Structure of the Book	5
2	Slime Mould <i>Physarum Polycephalum</i>	13
2.1	Introduction	13
2.2	<i>Physarum Polycephalum</i>	13
2.3	Generation of Contractile Force and Oscillation Rhythm	15
2.4	Formation and Adaptation of the Plasmodial Tube Network	16
2.5	Oscillatory Synchronisation within the Plasmodium	17
2.6	Computational Behaviour of <i>Physarum Polycephalum</i>	19
2.7	<i>Physarum Polycephalum</i> and Robotics	23
2.8	Computational Models of <i>Physarum Polycephalum</i>	25
2.9	<i>Physarum</i> as a Dynamical LALI Mechanism of Pattern Formation	27
2.10	Requisite Properties for <i>Physarum Polycephalum</i> Models	28

Part II Modelling *Physarum Polycephalum*

3	A Multi-agent Model of <i>Physarum</i>	33
3.1	Introduction	33
3.2	Motivations for Model Choice	33
3.3	A Multi-agent Virtual Material Approach	35
3.4	Growth and Adaptation of the Virtual Plasmodium	40

3.5	Representing the Agent Population Environment Habitat	41
3.6	Self-Assembly of Emergent Transport Networks	44
3.7	Factors Affecting Network Dynamics	47
3.8	From Pattern Formation to Network Adaptation	53
3.9	Factors Affecting Network Adaptation.....	55
3.10	Observation of von Neumann's Law and Plateau Angles ...	58
3.11	Summary — A Virtual Plasmodium	59
4	Modelling the Biological Behaviour of <i>Physarum</i>	61
4.1	Introduction	61
4.2	Initial Network Formation from Solid Plasmoidal Sheet....	61
4.3	Morphological Adaptation of Pre-existing Plasmodia	62
4.4	Growth and Adaptation of Plasmoidal Networks.....	64
4.5	Avoidance of Light Hazards and Repellents	70
4.6	Connectivity of Virtual Plasmodium Networks	71
4.7	Environmental Factors Affecting Growth and Adaptation	75
4.8	Summary: Environmental Mediation of Behavioural Complexity	86
5	Implementing Neural Phenomena in Unorganised Non-neural Substrates	91
5.1	Introduction	91
5.2	Computing Without Neurons ins Slime Mould	91
5.3	Model Parameters and Problem Representation	92
5.4	Lateral Inhibition Phenomena via Attractant Stimuli	94
5.5	Lateral Activation Phenomena via Adverse Stimuli	94
5.6	Towards Unorganised Collective Perception	97
5.7	Summary: Unorganised Material Analogues of Neural Phenomena	105
Part III Material Computation in a Multi-agent Model of <i>Physarum Polycephalum</i>: Mechanisms and Applications		
6	Modelling Computational Behaviour of <i>Physarum</i>	109
6.1	Introduction	109
6.2	Maze Solution by Morphological Adaptation	109
6.3	Natural Network Formation and Minimisation in <i>Physarum</i>	112
6.4	Spanning Trees	112
6.5	Construction and Minimisation of Proximity Graphs	113
6.6	From Area to Distance, Exploration to Exploitation	120
6.7	Summary: Innate Material Approximation of Network Computation	123

7 Approximating Classical Computing Devices with the Multi-agent Model	125
7.1 Introduction	125
7.2 <i>Physarum</i> Gates	125
7.3 Asynchronism	129
7.4 Outcomes of Reversing Gradients of Chemoattractants	130
7.5 Computational Modelling of <i>Physarum</i> Gate Behaviours	131
7.6 Modelling the Half Adder	135
7.7 Summary: <i>Physarum</i> -Based Logic Gates — A Square Peg in a Round Hole?	139
8 Dynamical Reconfiguration of Transport Networks Using Feedback Control.....	141
8.1 Introduction	141
8.2 Dynamical Reconfiguration of Transport Networks	143
8.3 Network Feedback Mechanism	147
8.4 Results	149
8.5 Characteristics, Limitations and Interpretations of Results	156
8.6 Summary: Dynamical Networks — Direct Control or Guided Influence?	158
9 Material Approximation of Combinatorial Optimisation	161
9.1 Introduction	161
9.2 Can Slime Mould Directly Compute the TSP?	162
9.3 Material Approximation of the TSP by a Shrinking Blob	164
9.4 Results	167
9.5 Summary	177
10 Voronoi Diagrams and Their Variants with Attractant and Repulsion Fields	181
10.1 Introduction	181
10.2 Approximation of Voronoi Diagram by <i>Physarum Polycephalum</i>	182
10.3 Computational Perspectives on Slime Mould Computation	183
10.4 Model Parameters and Problem Representation	184
10.5 Results	185
10.6 Summary: Environmentally Mediated Plane Division and Minimisation	196

11 Material Representation of Area and Shape: Convex Hull, Concave Hull and Skeleton	199
11.1 Introduction	199
11.2 Convex Hull by Material Shrinkage around Attractants	200
11.3 Convex Hull by Material Shrinkage around Repellents	200
11.4 Convex Hull by Self-organisation	200
11.5 Representing the Shape of a Set of Points	202
11.6 Approximation of the Concave Hull by Shrinkage	203
11.7 Approximating the Concave Hull by Growth	205
11.8 Transformation between Convex and Concave Hull	207
11.9 Internal Representation of a Shape - Skeletonisation	207
11.10 Summary: Representing Area and Shape	211
12 Material Computation of Data Smoothing and Spline Curves	213
12.1 Computational Limitations of Slime Mould	213
12.2 Towards Modelling Morphological Adaptation in Slime Mould	214
12.3 Overview of Morphological Adaptation Approach	215
12.4 Data Smoothing and Filtering	215
12.5 Approximating Spline Curves by Morphological Adaptation	218
12.6 Properties and Limitations of Material-Based Spline Curves	220
12.7 Interpolating Spline Curves	225
12.8 Summary: Exploiting Material Relaxation Phenomena for Data Smoothing	231
13 Tracking Statistical Properties and Changing Data via Morphological Adaptation	233
13.1 Sclerotinisation as an Inspiration for Centroid Computation	233
13.2 Approximating Arithmetic Statistics by Morphological Adaptation	240
13.3 Spatial Approximation of Data Tracking	243
13.4 Mechanisms of Data Tracking by Morphological Adaptation	246
13.5 Summary: Towards Harnessing Material Relaxation for Statistics	251
14 Morphological Adaptation Approaches to Path Planning	253
14.1 Path Planning: Unconventional Computing Approaches	253
14.2 Morphological Adaptation in the Model Slime Mould	254
14.3 Summary: Shaping a Material to Find a Path	264

Part IV From Emergent Oscillations to Collective Transport and Amoeboid Movement

15 Emergence and Transitions of Spatio-temporal Oscillations	269
15.1 Introduction	269
15.2 Oscillatory Behavior in the <i>Physarum</i> Plasmodium	269
15.3 Experimental Results	272
15.4 Oscillatory Behaviour in the Particle Model	277
15.5 Summary: The Emergence of Synchronous Oscillations	285
16 Modelling Collective Transport and Amoeboid Movement	289
16.1 Collective Transport — Introduction	289
16.2 Results	290
16.3 Amoeboid Movement — Introduction	298
16.4 Emergence of Collective Amoeboid Movement	299
16.5 Persistent Movement in a Small Blob Fragment	300
16.6 External Control of Collective Amoeboid Movement	302
16.7 Cleavage and Fusion of the Collective	304
16.8 Morphological Adaptation of the Collective	305
16.9 Summary: Towards Distributed Soft-Bodied Robotics	307
Part V Conclusions and Beyond <i>Physarum</i> Models	
17 Summary of the Approach and Modelling beyond <i>Physarum</i>	313
17.1 Overview	313
17.2 Main Research Findings	313
17.3 Contribution, Limitations and Scope for Further Work	322
17.4 Extending and Generalising Multi-agent Pattern Formation	324
Appendix: Supplementary Material.....	349
References.....	351
Index	367

Part I
Slime Mould *Physarum Polycephalum*

Chapter 1

Introduction and Overview

“I came in from the wilderness, a creature void of form.”

(Bob Dylan, 1974.)

1.1 Introduction and Overview

This book concerns the computational approximation of the behaviour of the true slime mould *Physarum Polycephalum*, using a multi-agent approach. The giant single-celled organism has long been of biological interest, primarily due to its large size, complex internal streaming, and sensory-motor behaviour. In the last decade, however, it has been the subject of intense research into the complex computational properties it exhibits during its foraging, growth and adaptation. During the plasmodium, or vegetative, stage of its life cycle, *P. Polycephalum* can efficiently locate, migrate towards, and engulf nutrient sources whilst simultaneously avoiding hazardous threats in its environment. It is then able to dynamically adapt its amorphous body to form efficient protoplasmic transport networks connecting the nutrient sources.

The computational interest in *P. Polycephalum* coincides with two other current research themes in computer science and biology. The first is the topic of ‘Artificial Life’, which, in the definition we use here, seeks to find out how interactions between simple non-living components can produce some of the emergent complexity seen in living systems [1]. *P. Polycephalum* is of particular interest to Artificial Life research because its component parts are, relatively speaking, very simple — in its plasmodium stage it is a single massive and amorphous multinucleate cell with no specialised nervous tissue. Yet *P. Polycephalum* displays complex behaviour which belies, perhaps even appearing to transcend, its simple parts and, because it is composed of such simple cellular components, can be considered as a minimal example for the study of complex behaviour.

The second theme, termed unconventional, or non-classical, computation, seeks to explore alternative computational paradigms to the dominant theoretical construct of Turing machines, which are typically embodied in von Neumann's architecture of stored-program computers. *P. Polycephalum* is again well suited to this theme since it is a living example of material computation where the material properties and microscopic interactions within a substance may be harnessed for macroscopic computational behaviours [2]. Furthermore it is an example of a spatially implemented computational system in which certain computational problems and their solutions are not required to be specified symbolically as a set of sequential instructions (as in the classical paradigm), but instead may be presented in their 'natural' form of spatial patterns (representing the initial problem configuration), executed by the natural and intrinsic physical properties of the substrate, and whose results are also represented by the final patterned state of the system (although in living systems such as *P. Polycephalum* the classical notion of a 'final' result may actually be an equilibrium state or dynamic transitions around such states).

1.2 Objectives

The aims of the book are twofold. Firstly, to model and reproduce the complex biological and computational behaviour of *P. Polycephalum* which is manifested in its complex foraging, growth, pattern formation, network adaptation, oscillatory transport, and amoeboid movement. Secondly, we aim to reproduce these complex phenomena using methods which are also inspired by the plasmodium itself. That is, by using only very simple component parts and local microscopic interactions to generate the complex macroscopic behaviours in an emergent, bottom-up, manner.

Why is this second aim so important to us? *P. Polycephalum* (along with many other natural systems) is attractive to science because it suggests that it is the interactions between simple components, rather than any 'special' properties of individual components, which are responsible for the emergence of complex behaviour [3]. Indeed the plasmodium may be the extreme case of the problem of how the functional and structural loci of apparently intelligent behaviour are laid bare: its amorphous body plan, the lack of specialised tissues, the fault tolerance and redundancy of the plasmodium. All of these properties conspire to render analytical explanations for the seat of plasmodial complexity impossible.

1.3 Methodology

By developing a computational approximation of *P. Polycephalum* using a similarly fine-grained approach (aimed to model at the material level) and limiting ourselves to only simple component parts and local interactions, we

limit the reliance on higher level ‘black-box’ explanations as much as possible. This allows us the freedom to adopt a synthetic (constructive) approach in which to explore the role of self-organisation and emergent behaviour and attempt to answer the questions regarding the plasmodium’s complex behaviour which may simply be phrased as: “How can the plasmodium achieve so much, with so little?”.

The results presented herein using the fine-grained multi-agent approach capture the wide range of behaviours that we are concerned with in this book. They suggest that the simple material interactions within the plasmodium are indeed sufficient to generate and explain its complex behaviour. They also suggest that the plasmodium may efficiently implement a strategy of sensing, exploiting, and subsequently modifying (via engulfment) environmentally mediated information via nutrient diffusion gradients.

From a computing perspective we can then employ the model as a spatially represented unconventional computing substrate — a virtual material which can be externally influenced to perform computational tasks. We describe a wide range of computational and robotics problems that can be tackled using the complex emergent behaviour embedded and distributed within the model. We hope that the wide range of biological and computational behaviours reproduced in the model will stimulate the interest of the reader to further develop their own ‘varieties’ of the model for novel uses.

1.4 Structure of the Book

1.4.1 Chapter 2: Overview and Previous Research

We review the biological properties and behaviour of the organism and give a history of the research into the complex biological phenomena which it exhibits. We then give a brief overview of the concepts of classical and unconventional computation which are relevant to this research. The recent research which explores the computational behaviour of *P. Polycephalum* (hereafter shortened to *Physarum* for simplicity) is then described. We summarise the computational properties of *Physarum*, how these are thought to emerge from simple local material interactions, and how these differ from classical computing architectures, specifically in how these properties are spatially represented, decentralised, redundant, fault tolerant and emergent.

We conclude by suggesting how we may implement complex *Physarum*-like behaviour using non-classical paradigms which satisfy two aims: Firstly to model and reproduce the complex biological and computational behaviour of *Physarum* so that we may perhaps glean some clues as to how its complex phenomena (foraging, growth, adaptation, movement) emerge from simple internal parts and interactions. Secondly, that we can implement the distributed computations exhibited by *Physarum* (specifically network growth

and adaptation and collective movement) in a manner which is naturalistic and complements the simplicity and desirable properties of the organism itself.

In order to judge the success of the modelling approach we must explicitly state the phenomena that must be reproduced in order to successfully model the behaviour of *Physarum*. Each aspect of the plasmodium's behaviour, and its reproduction by the model, is described in subsequent chapters.

1.4.2 Chapter 3: A Multi-agent Material-Based Model of *Physarum Polycephalum*

The research which initially highlighted the computational properties of *Physarum* was the complex dynamical pattern formation demonstrated by the formation and adaptation of nutrient transport networks between nutrient sources. The plasmodium has been described as a living and adaptive membrane bound reaction-diffusion pattern formation mechanism [4]. In order to reproduce its morphological repertoire we must utilise an approach which is equally flexible.

The basis of the model is a virtual material approach where spontaneous and dynamical pattern formation phenomena emerge from simple and local interactions within a multi-agent mobile particle population. The dynamical network patterns are formed by, and composed of, the collective positions and movement of the particle population. The motivation for the modelling approach is given and we describe the base model behaviour, exploring a parametric evaluation of the model and its behaviour. The virtual material approach is the core structure upon which the subsequent modelling of the complex behaviours of foraging, growth, adaptation, oscillatory phenomena, collective transport, and collective movement are based.

1.4.3 Chapter 4: Modelling Biological Behaviour of *Physarum Polycephalum*

This chapter reproduces the pattern formation, foraging and growth behaviour of the plasmodium in response to a complex environment. The initial formation of the transport network from a homogeneous material is assessed and the collective response of the network to the presence or absence of nutrients is demonstrated. Foraging, growth and adaptation of the virtual plasmodium is assessed under a range of environmental conditions, including low nutrient concentration, high nutrient concentration and noisy environments (i.e. environments which present uncertain sensory stimuli to the organism). The static and dynamic connectivity of the virtual plasmodium networks is explored. We describe how the amorphous body plan of the virtual plasmodium responds to differences in environmental stimuli. We use a simple mechanism by which the behaviour of the virtual plasmodium is influenced

by the environment. This mechanism is a *two-way* interaction based on the diffusion of nutrient gradients in the environment, the engulfment of nutrients, and eradication of the gradients by the plasmodium. We demonstrate that the interactions of the virtual plasmodium with the environment provide a simple and plausible explanation of the apparent ‘intelligence’ observed in *Physarum*.

1.4.4 Chapter 5: Implementing Neural Phenomena in Unorganised Non-neural Substrates

Simple organisms such as slime mould possess no neural tissue yet, despite this, are known to exhibit complex computational behaviour. Could simple organisms such as slime mould approximate neural phenomena without recourse to neural tissue? We describe a model whereby LI can emerge without explicit inhibitory wiring, using only bulk transport effects. Lateral Inhibition (LI) occurs in a wide range of neural sensory modalities, but is most famously described in the visual system of humans and other animals. The mechanism generates an increase in contrast between spatial environmental stimuli. We use material flux within the multi-agent model to reproduce the characteristic edge contrast amplification effects of LI using excitation via attractant based stimuli, and explore a counterpart behaviour, Lateral Activation, where stimulated regions are inhibited and lateral regions are excited, using simulated light irradiation. In addition to the enhancement of local edge contrast, long-term changes in population density distribution correspond to a collective response to the global brightness of 2D image stimuli, including the scalloped intensity profile of the Chevreul staircase and perceived brightness differences in the Simultaneous Brightness Contrast (SBC) effect. The model approximates LI contrast enhancement phenomena and global brightness perception in collective unorganised systems without fixed neural architectures, suggesting novel mechanisms to generate collective perception of contrast and brightness in distributed computing and robotic devices.

1.4.5 Chapter 6: Modelling Computational Behaviour of *Physarum Polycephalum*

This chapter reproduces the computational behaviour of the *Physarum* plasmodium which has been shown to be capable of approximating a wide range of computational problems. We use the virtual plasmodium to reproduce the behaviour of *Physarum* in maze problems and to approximate network based geometric computations, including spanning trees and proximity graphs. We examine how the transformation of *Physarum* from an area representation (covering its environment) to a distance representation (connecting the nutrients in the environment) may be reproduced in the model plasmodium.

1.4.6 Chapter 7: Approximating Classical Computing Devices with the Multi-agent Model

In this Chapter we examine the suitability of the model plasmodium for implementing classical computing devices. We extended previous work on the development of *Physarum* based individual logic gates and simulated more complex designs of logic gates and combinations of gates to form half adder circuits. Although the results show that these circuits are possible, we demonstrate that the difficulties in timing and sensory control would make practical and reliable operation of such gates unlikely.

1.4.7 Chapter 8: Dynamical Reconfiguration of Transport Networks Using Feedback Control

External control of embedded material behaviour by the application of external fields is a long term goal of non-classical computation. In this chapter we investigate a method of dynamically controlling the evolution of transport networks formed by the multi-agent model. To achieve this we use a real-time network analysis method to build an emergent ‘picture’ of current network connectivity. Based on this connectivity we feed back information via local increases or decreases in node concentration. The method exhibits very complex network evolution with particular transition motifs and longer term metastable states. We are able to guide the evolution of transport networks towards solutions of simple instances of the Travelling Salesman Problem (TSP), suggesting that the goal of external control of material evolution via application of external field stimuli is possible.

1.4.8 Chapter 9: Material Approximation of Combinatorial Optimisation

Building on the previous chapter of feedback control of material computation to approximate the TSP, we considered whether a more simple, and innately embedded material computation, method could approximate this challenging problem. In this approach a ‘blob’ of this material was placed over a set of data points projected into the lattice, representing TSP city locations, and the blob was reduced in size over time. As the blob shrunk it morphologically adapted to the configuration of the cities, halting when the blob no longer completely covered all cities. By manually tracing the perimeter of the blob a path between cities was elicited corresponding to a TSP tour. Despite the simplicity, and single instance ‘blind’ searching of the problem, the method produced good results in comparison with numerical brute force approaches. We discuss similarities between this method and previously suggested models of human performance on the TSP and suggest possibilities for further improvement.

1.4.9 Chapter 10: Voronoi Diagrams and Their Variants with Attractant and Repulsion Fields

Voronoi diagrams are canonical examples of unconventional computing, harnessing the propagation of information in space to partition the plane. It has previously been separately demonstrated that *Physarum* can approximate the Voronoi diagram by means of attractant stimuli and also by means of repellent stimuli. In this chapter we use the model to reproduce computation of Voronoi diagrams using both approaches. We build upon the earlier research by exploring simultaneous presentation of attractant and repellent fields and the effect of varying the concentrations of both. Using this method we can approximate weighted Voronoi diagrams and the growth of so-called ‘cellular’ Voronoi diagrams from seed points. We find that, by varying the relative concentration of attractants and repellents, we can smoothly transform the plane partitioning patterns of classical Voronoi diagrams into hybrid structures which contain features of plane division and internal path minimisation.

1.4.10 Chapter 11: Material Representation of Area and Shape: Convex Hull, Concave Hull and Skeleton

A representation of the shape of an image are classical problems in computational geometry and image analysis. The Convex Hull and Concave Hull are both representations of the area occupied by a set of points. However, whilst the Convex Hull is relatively simple to precisely define, the Concave Hull is not, and many variations exist (often biased depending on which field in which they are utilised). The skeleton of an image is an *internal* representation of its overall shape widely used in image analysis. In this Chapter we examine different approaches to representing shape with the multi-agent model. We approximate Convex Hulls and Concave Hull using the morphological adaptation behaviour of the multi-agent model. We examine whether it is possible to approximate these structures by growth, fusion, envelopment and shrinkage. We also examine possible mechanisms to induce transformations between the two structures. We approximate the internal skeleton of a shape by shrinking down the model plasmodium when it is patterned as a binary shape which projects a repulsive field. We find that the minimising behaviour of the model is useful for avoiding spurring artifacts often seen in classical skeletonisation approaches.

1.4.11 Chapter 12: Material Computation of Data Smoothing and Spline Curves

In *Physarum* predictable morphological adaptation is prevented by its adhesion to the underlying substrate. We investigated what possible computations could be achieved if these limitations were removed and the organism

was free to completely adapt its morphology in response to changing stimuli. We demonstrated how a material computation by the model could be used to transform and summarise properties of spatially represented datasets. We found that the virtual material relaxed more strongly to high-frequency changes in data which was be used for the smoothing (or filtering) of data by approximating moving average and low-pass filters in 1D datasets. The relaxation and minimisation properties of the model enabled the spatial computation of B-spline curves (approximating splines) in 2D datasets. Both clamped and unclamped spline curves, of open and closed shapes, were represented and the degree of spline curvature corresponded to the relaxation time of the material. Interpolating splines could not directly be approximated due to the formation and evolution of Steiner points at narrow vertices, but were approximated after rectilinear pre-processing of the source data. This pre-processing was further simplified by transforming the original data to contain the material inside the polyline.

1.4.12 Chapter 13: Tracking Statistical Properties and Changing Data via Morphological Adaptation

The properties of networks constructed by slime mould are known to be influenced by the local distribution of stimuli within its environment. But can the morphological adaptation of slime mould yield any information about the *global* statistical properties of its environment? We explored this possibility using the multi-agent model. We demonstrated how morphological adaptation in blobs of virtual slime mould, mimicking the sclerotinisation phenomenon, could be used as a simple computational mechanism to approximate the geometric centroid of 2D shapes. We extended this approach to simple numerical datasets for the approximation of the arithmetic mean from spatially represented sorted and unsorted data distributions, and the estimation and dynamical tracking of moving object position in the presence of noise contaminated input stimuli. The results suggest that it is indeed possible to utilise collectives of very simple components with limited individual computational ability (for example swarms of simple robotic devices) to extract statistical features from complex datasets by means of material adaptation and sensorial fusion.

1.4.13 Chapter 14: Morphological Adaptation Approaches to Path Planning

Path planning is a classical problem in computer science and robotics which has recently been implemented in unconventional computing substrates such as chemical reaction-diffusion computers. These novel computing schemes

utilise the parallel spatial propagation of information and often use a two-stage method involving diffusive propagation to discover all paths and a second stage to highlight or visualise the path between two particular points in the arena. Using the multi-agent model we demonstrate how path planning may be performed directly by morphological adaptation. We initially demonstrate simple path planning by a shrinking blob of virtual plasmodium between two attractant sources within a polygonal arena. We examine cases where multiple paths are required and the subsequent selection of a single path from multiple options. Collision-free paths are implemented via repulsion from the borders of the arena. Finally, obstacle avoidance is implemented by repulsion from obstacles as they are uncovered by the shrinking blob. These examples show proof-of-concept results of path planning by morphological adaptation which complement existing research on path planning in novel computing substrates.

1.4.14 Chapter 15: Emergence and Transitions of Spatio-temporal Oscillations

A complex range of oscillatory phenomena are observed in *Physarum*. Previous computational approaches to the generation of oscillatory phenomena utilised the interactions between pre-existing oscillatory components which rather sidesteps the issue of the emergence of oscillatory behaviour itself. In this chapter we demonstrate how a simple change to the motor behaviour of the particle population can generate *de novo* oscillatory phenomena from non-oscillatory components. The change alters the smooth particle flux to one which displays temporary interruptions caused by local blocking of occupancy. Using this approach the complex internal oscillation patterns seen in the plasmodium are reproduced, as are the transitions between the oscillation pattern types. Using the results of the model coupled with experimental findings we suggest a mechanism for the cause of the transition of the complex internal oscillation patterns observed in the *Physarum* plasmodium itself and in protoplasmic droplets extracted from veins of the *Physarum* protoplasmic network.

1.4.15 Chapter 16: Modelling Collective Transport and Amoeboïd Movement

The oscillatory phenomena of *Physarum* are used for transport of nutrients throughout the protoplasmic network by means of shuttle streaming and the movement of the plasmodium itself. In chapter 16 we utilise the generation of oscillatory behaviour described in chapter 15 to investigate mechanisms of collective transport. We demonstrate that in a constrained collective the oscillatory behaviours result in the emergence of travelling waves which can be

utilised to accomplish collective transport. We show that unconstrained particle collectives utilise the emergent travelling wave phenomena to generate collective amoeboid movement to shift the position of the collective in space. We describe simple mechanisms by which the movement and position of the collective can be influenced by external stimulation by attractants and hazards and its potential application to robotics. We conclude by demonstrating the flexibility and redundancy of the collective by cleaving the material into functional and separately controllable parts which may later be re-fused to reform a single unit.

1.4.16 Chapter 17: Summary of the Approach and Modelling Beyond Physarum

We summarise the findings of the individual modelling tasks and integrate the individual features of the model as a whole. We describe the successes of the modelling approach which can be attributed to its adherence to the simple and local material approach and discuss some limitations of the model. One of the notable characteristics of the multi-agent particle approach used is the bottom-up generation of complex quasi-physical phenomena from simple component parts. We discuss how the virtual material approach may potentially be useful in other modelling tasks, including the modelling of cell migration, angiogenesis sprouting, soap film evolution, and lipid membrane dynamics. In particular we discuss the role of bottom-up self-assembly and dynamical behaviour in the modelling of complex phenomena and suggest that these interactions may be able to capture some behaviours missed in conventional modelling approaches. We present preliminary examples of material patterning in interfacial systems (phase separation, interfacial mixing), phyllotaxis-type patterning and three Dimensional transport networks.

1.4.17 Chapter A: Appendix — Supplementary Material

Due to the dynamical behaviour of the virtual plasmodium model the complex evolution of the pattern formation by emergent transport networks cannot be easily ascertained by static visualisations alone. Supplementary video recordings are included showing the formation and adaptation of the networks, computation by the virtual plasmodium, oscillatory phenomena and collective transport and amoeboid movement, showing examples relating to the results in each chapter. We also enclose the source code scripts of the base model behaviour using the Processing language. The supplementary material can be viewed online at: <http://uncomp.uwe.ac.uk/jeff/book/material.htm>.

Chapter 2

Slime Mould *Physarum Polycephalum*

“We’re not computers, Sebastian, we’re physical.”

(Roy Batty, 1982.)

2.1 Introduction

This chapter introduces *Physarum*, describing the organism, its composition, habitat, behaviour and the biological basis of its network adaptation and oscillatory phenomena. We examine how *Physarum* approximates computational and robotic behaviour, relating it to classical and non-classical computing approaches. We explore previous modelling approaches to *Physarum*, framing its computational behaviour as a type of membrane-bound reaction-diffusion computation. Finally, we set out a list of requisite behaviours which must be reproduced when modelling the organism.

2.2 *Physarum Polycephalum*

Physarum Polycephalum, the true, or many-headed, slime mould, is a member of the Physaridae family of slime moulds. It belongs to the order Physarida of the Myxogastria class, part of the Myxomycete phylum of the kingdom Amoebozoa [5]. *Physarum* is an acellular slime mould (not to be confused with the cellular slime mould *Dictyostelium discoideum*) and has a complex life cycle with a combination of haploid and diploid phases.

The complexity and re-entrant nature of the cycle reflect a complex response to environmental challenges. Sporulation by cellular differentiation occurs in response to worsening environmental conditions including thermal, illumination and pH extremes. Haploid nuclei are released after meiosis as spores from fruiting bodies which, if landing in suitable conditions, germinate to form amoebae cells. Unfavourable conditions result in encasement

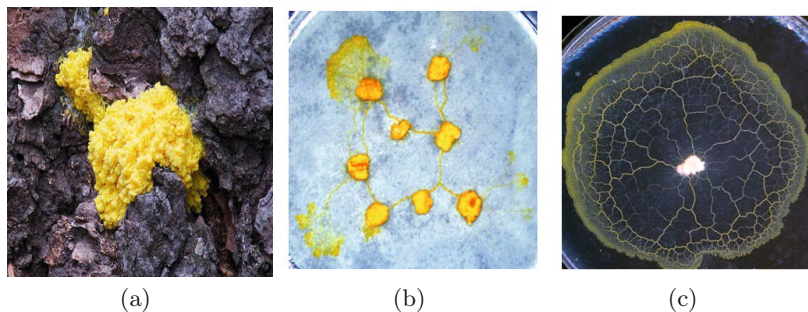


Fig. 2.1 Plasmodium of *P. Polycephalum*. (a) Wild growth pattern (Image: Jerry Kirkhart), (b) Growth by pseudopodium extension at low nutrient concentration on damp filter paper to engulf oatmeal flake nutrients, (c) Radial growth pattern at high nutrient concentration (plasmodium initially inoculated on oatmeal flake in the centre of the image. Image from [4], courtesy of Andrew Adamatzky).

of the amoebae to form cysts to protect the cells until environment conditions improve. Extremely favourable conditions (usually artificially induced) result in highly mobile flagellated swarm cells. Fusion of amoebae cells results in diploid unicellular plasmodia and repeated nuclear division yields a syncytium, a single multinucleate membrane bound cell. Under certain laboratory conditions small microplasmodia may be generated by fragmenting the culture in a liquid medium and further preserved by inducing a spherule phase. However, under normal conditions the small plasmodia from stage 11 become the main vegetative and foraging stage, the plasmodium.

The plasmodium, stage is a giant single cell, usually visible to the naked eye. It is a syncytium, formed by repeated division of diploid nuclei, which may grow to over a square metre in size. It grows in cool, damp regions, migrating across its habitat, engulfing and feeding on bacteria and fungi which grow on decaying vegetative matter. When dried and starved a dormant phase, the sclerotium, is formed. The plasmodium may be regenerated from a sclerotium by reintroducing moisture and nutrients. The growing plasmodium extends outwards as it forages for nutrients, streaming forwards with a characteristic pulsatile progression. In the wild the plasmodium is usually yellow coloured (other *Physarum* species exist with different colouring) and amorphous (Fig. 2.1a). Under controlled conditions the growth patterns are strongly affected by nutrient concentration. At low concentrations (for example damp filter paper or non-nutrient agar) plasmodium grows by extending pseudopodium-like processes which project towards the nutrients (Fig. 2.1b). At high nutrient concentrations (for example oatmeal agar) the plasmodium grows outwards in a radial pattern from the inoculation site (Fig. 2.1c).

The net rate of forward movement is up to 1cm/h [6]. The pulsatile motion is caused by contractile oscillations within the plasmodium with a period of approximately 1-2 minutes [7]. The oscillatory activity results in a to-and-fro

transport of protoplasm within the plasmodium, known as shuttle streaming, at a velocity of up to 1.3 mm/s [8] and protoplasm is transported to the leading edge of the growth front. Behind the leading edge of growth a network of protoplasmic tubes is spontaneously assembled (Fig. 2.2a). The tube network is used to transport microscopic nutrient fragments embedded within the endoplasm between different parts of the plasmodium. The network is highly ramified near the growth front, becoming sparse and more coarse at the initial inoculation site.

The geometry of the tube network is highly dynamic and assembly and disassembly of the network is observed in response to changing environmental conditions. When nutrient sources are placed within a large plasmodium the organism adapts its morphology via adaptation of the tube network to form efficient paths between the nutrient sources, dependent on the distribution and size of the nutrients. [9, 10, 11]. The *quality* of nutrients also affects the behaviour of the plasmodium. Latty and Beekman found that higher quality nutrients resulted in a longer time spent at nutrient sources with a densely patterned local search (thus fully ‘mining’ a rich local source of nutrients), whereas plasmodia located near poor quality nutrients spent less time within the region and displayed less dense foraging patterns, departing the area sooner [12]. The foraging behaviour was also influenced by an apparent assessment of ‘risk’ presented by nutrients located within light irradiated regions hazardous to the plasmodium [13]. Dussatour et al. discovered a more subtle nutrient choice, finding that the plasmodium is able to distribute its body plan to engulf a selection of complementary macro-nutrients (proteins and carbohydrates) to ensure an optimal intake of nutrients [14].

2.3 Generation of Contractile Force and Oscillation Rhythm

A cross-section of a protoplasmic tube is shown in Fig. 2.2b, indicating its constituent parts and the directions of shuttle streaming within the tube. The protoplasmic tube is comprised of an external membrane, the plasmalemma, surrounding concentric layers of outer gel-like ectoplasm (Gel) and an inner watery, or sol-like, inner endoplasm core (Sol) [15]. The ectoplasm contains fibrils composed of actin and myosin complexes. Unlike actomyosin in human muscle tissue, which is ordered into regular striated arrangements and bundles, the arrangement of actomyosin complexes in the plasmodium are initially disorganised. After formation of the tube network, however, the fibrils in the ectoplasm become arranged primarily longitudinally (Fig. 2.2b, ‘L’) and circumferentially (Fig. 2.2b, ‘C’), adhering to invaginations in the plasmalemma. The tube lies on a slimy polysaccharide capsule (Capsule) which adheres it to the growth substrate. Internal metabolic processes and external stimulation (for example, chemoattractants, chemorepellents, temperature) [16, 17] cause fluctuations in the concentration of intracellular compounds

(including ATP, ADP, Ca^{++} , $c\text{AMP}$, $c\text{GMP}$, NADH, H^+) [18, 19, 20, 21]. The persistence of contractile forces after replacing endoplasmic sol with artificial media established the location of the origin of contractile force within the gel ectoplasm [22].

Actomyosin complexes within the ectoplasm contract and relax in response to changing concentrations of intracellular compounds, shortening the length of the fibrils and compressing the inner endoplasm core [23, 24]. Protoplasmic veins contract both radially and longitudinally [25, 26] and hydrostatic pressure induced by the contractions passively transports the endoplasmic sol along the protoplasmic tube network [27].

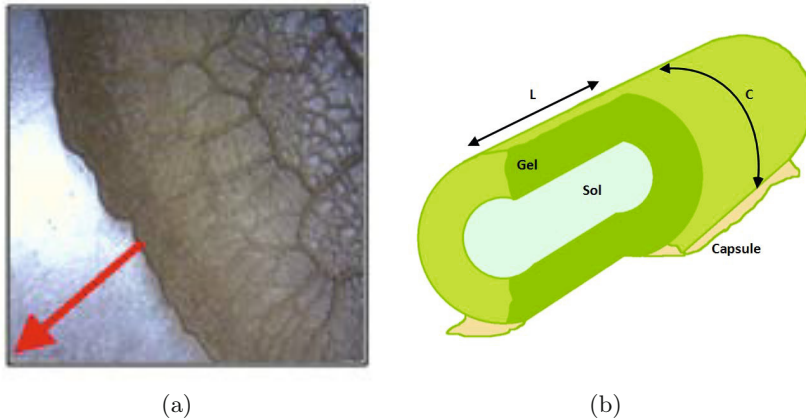


Fig. 2.2 Composition of *P. Polycephalum* protoplasmic tube network. (a) Tube network forming behind growth front (growth direction arrowed, Image courtesy of Andrew Adamatzky), (b) Schematic illustration of protoplasmic tube vein section indicating Gel and Sol regions, polysaccharide slime capsule and the orientation of longitudinal ('L') and circumferential ('C') fibrils.

2.4 Formation and Adaptation of the Plasmodial Tube Network

To form the tube network from a solid mass of cellular material a pattern formation mechanism is required, in order to break the isotropic symmetry of the material. The force responsible for the initial formation of the tube network is the spontaneous, and initially disorganised, contraction of actomyosin complexes within the plasmodium. The generation of contractile forces from internal metabolic processes and external stimuli results in a distributed pattern of oscillations in thickness of the plasmodium. Regions under contraction pressure have endoplasmic sol pumped away whereas regions undergoing relaxation accept incoming material. Interactions between small independent

domains of oscillatory activity soon begins to show regular rhythms. Small droplets of plasmodium material can spontaneously form regular oscillatory rhythms within 20 minutes [28]. Clues to the nature of this mechanism can be observed experimentally. In an existing plasmodium network, veins which become disconnected from nutrient sources wither and collapse. Conversely, veins with a direct connection to nutrients become thicker and wider. If two veins connect to the same nutrient source, the shorter vein will typically persist [9]. This suggests that the flux of material through the plasmodium may be an integral component of the mechanism in terms of both providing a force and providing an information flow to be amplified. Similar plausible mechanisms based on mechanical influences and material flux have been suggested for pattern formation in plants, for example venation patterns as formed from visco-elastic interactions [29], and the flux canalisation hypothesis [30, 31]. One possible mechanism for the enhancement of tubes with high flux is the phenomenon of stretch activation in which it was observed that the actomyosin fibres within longitudinally stretched protoplasmic tubes align with the direction of the tension force [32, 33]. Tube network adaptation in *Physarum* is further enhanced by the polymerisation and depolymerisation of actin fibres which results in solation of actin which is then transported through the endoplasmic channels and redistributed towards the active growth front of the plasmodium. The redistribution of plasmodium material via the protoplasmic tube network not only affects tube network adaptation, but is also used to shift the mass of the plasmodium itself to enable motility during its foraging, avoidance of environmental hazards, and morphological adaptation of the plasmodium.

2.5 Oscillatory Synchronisation within the Plasmodium

Initial studies into the oscillatory phenomena of *Physarum* were concerned with its physical properties. More recently, research has investigated the computational synchronisation properties endowed by the oscillatory mechanisms. Synchronisation phenomena can be observed in biological oscillators, such as circadian rhythms [34] and central pattern generators [35]. Synchronisation enhances adaptation, provoking a robust response to external/internal noise by dynamically modulating the oscillation rhythm [36]. Like other biological oscillators, the *Physarum* plasmodium is also able to modulate the oscillation rhythm to behave adaptively to environmental changes. The oscillation rhythm at a local site of the cell is modulated by nutrient, chemical, optical and thermal stimuli. Local changes in oscillation frequency are propagated to other unaffected parts of the cell through protoplasmic streaming, eventually forming a phase gradient within the cell through mutual entrainment [37, 38]. The phase gradient determines the direction of cell migration

(i.e. moving towards/from the stimulus) and the plasmodium is thus able to adapt to environmental change without any hierarchical central control system.

An externally perturbed plasmodium tries to reorganize and synchronise the oscillation rhythms between local parts of the cell. This process is crucial in order to maintain its body plan as one single cell. If a piece of *Physarum* plasmodium is removed from a large culture, it spontaneously regenerates a synchronised oscillation within the cell. Takagi and Ueda observed that a small plasmodium cell shows various dynamic transitions between spatio-temporal oscillation patterns in the course of body restructuring [28]. The oscillatory behaviour of the plasmodium is also known to be size-invariant [39].

Oscillations within a single strand of plasmodium from a plasmodium network (for example, as described in [7]) have been shown to exhibit complex entrainment [40]. By carefully controlling the habitat of *Physarum* within a micro-fabricated structure, the dynamics of oscillatory activity can be optically recorded. Takamatsu et al. performed a series of studies in which small wells of plasmodium, wide enough to contain a single oscillator, were linked by straight connecting passages to mechanically couple the oscillatory behaviour [41, 42, 43]. Beginning with simple dumbbell shaped structures, the oscillation patterns were optically recorded (interpreted as being inversely proportional to the thickness of the plasmodium) and a pattern of in-phase and anti-phase oscillations were observed. As one chamber contracted, material was transported through the mechanical coupling between the two wells. The interaction strength between the two oscillators was dependent upon the amount of material transferred between the two oscillators and a reciprocal relationship was observed between the thickness of both wells. In more complex cyclic rings of three, four and five well structures, regular patterns of spatio-temporal oscillation modes were observed [44, 45]. The spatio-temporal patterns corresponded to those predicted by the theoretical models used to suggest plausible mechanisms of motor control and transitions of animal gait patterns [46]. Oscillatory interactions in the two-dimensional behaviour of *Physarum* were studied in [47] who found independent spiral oscillatory foci during the initial growth of a plasmodium, later becoming associated with phase differences at different locations within the organism. The interactions between external environmental stimuli and coupled oscillators within the plasmodium may be responsible for the propagation of information about the environment [48, 17], and indeed the distributed control of its complex behaviour [49], movement [50], and even endow the organism with a primitive form of memory [51]. Takagi and Ueda investigated how low-level stimuli (for example carefully timed optical pulses) may be used to affect spatio-temporal oscillation patterns [52], potentially directing the patterns into different phases [53], or away from regimes known to be harmful to the survival of tissues dependent on self-organised oscillatory activity [54, 55].

2.6 Computational Behaviour of *Physarum Polycephalum*

Physarum may be interpreted as a complex mechanism of dynamical pattern formation based upon two survival requirements: efficiency of foraging behaviour (searching of a maximal area) and efficiency of nutrient transport (minimal transport distance and fault tolerance) [9]. The behaviours used to fulfil these requirements are growth, movement and area reduction, utilising oscillatory interactions which are emergent from low-level contractile activity. The complex biological behaviour observed in *Physarum*, combined with the relative simplicity of its cell, and the distributed nature of its control system, make *Physarum* a suitable subject for research into non-classical, or *unconventional*, computation substrates. The term ‘unconventional’ is misleading if one considers that the vast majority of computation in living systems is non-classical [2] and a brief overview of the two concepts is required.

The current dominant model of computing, classical computation, is based on silicon embodiments of Turing’s notion of a Universal Machine. The success of the approach is due to the concept of the stored program computer, whose behaviour is governed by a sequence of simple logical and arithmetic symbolic instructions. Problem data, and their solutions, must be transformed into a representation which allows the solution by the machine instructions. The individual instructions are very simple indeed but, when executed, (subject to iteration and conditional branching to different parts of the instruction stream) they transform the input data to yield output data containing the problem solution. Both instructions (program) and data may be represented in the same medium and the behaviour of the computer may be changed by simply changing the contents of the instructions and data storage. Thus a single mechanism may be driven by its program and data to ‘become’ any other machine, as long as the desired behaviour is known and completely specifiable. The success of the classical approach is partly due to this flexibility of its architecture and partly due to the vast speed at which modern digital computing devices operate.

Unconventional computation is an approach whereby the natural properties and processes of physical or living materials are harnessed to provide useful computational functions. The motivation for the study of unconventional computation is threefold. Firstly, many natural systems exhibit properties which are not found in classical computing devices, such as being composed of simple and plentiful components, having redundant parts (i.e. not being dependent on highly complex units), and showing resilient or ‘fault tolerant’ behaviour. Secondly, non-classical computation is often observed in systems which show emergent behaviour. Although the definition of emergence is difficult to define precisely and the subject of debate [56, 57] it may be summarised as being novel behaviour which emerges from the interactions between simple component parts, and which — critically — cannot be described in terms of the lower level component interactions. Emergent behaviour is characterised by

systems with many simple, local interactions and which display self-organisation, i.e. the spontaneous appearance of complexity or order from low-level interactions. Many of the attractive features of non-classical computing devices (redundancy, fault tolerance) are thought to be based on the mechanisms of self-organisation and emergence, and the study of these properties is useful not only from a computational perspective, but also from a biological viewpoint – since much of the complexity in living systems appears to be built upon these principles.

The third reason for interest in non-classical computing is because, for a number of applications at least, utilising the natural properties of physical systems for computation is a much more efficient means of computation. Non-classical computation can take advantage of parallel propagation of information through a medium (for example in the chemical approximation of Voronoi diagrams [58], or the parallel exploration of potential path choices in path problems using microfluidic gas discharge plasmas [59, 60].

Non-classical computing is not without its disadvantages, some of which are mainly theoretical. It may be difficult to represent certain computational problems in a way which can harness the physical behaviour of the non-classical substrate. Non-classical substrates may be ‘one-shot’ computing entities, not capable of reconfiguration or re-use (although some authors contend that this is an advantage, [61]). Certain problems which are suited to symbolic or logical transformation may be difficult to translate into spatial and propagative formats. This difficulty manifests itself in terms of how to represent data input and also how to ‘read’ the problem solution. This problem is exacerbated when considering how to interface non-classical computers to traditional computers to exploit the latter’s storage, archival and search abilities. The issue of when to stop the computation also arises since natural systems tend not to halt when a problem is solved, but often tend to adopt a dynamic equilibrium among different states. This difficulty in halting is because the ‘computation’ performed by the natural system is merely due to our *interpretation* of the natural behaviour in that system as computation when, in fact the system, and components of that system, neither know nor care about the externally applied computational task.

More practical problems also arise from non-classical approaches. They may be made from exotic materials or at challenging scales (such as DNA [62, 63], enzymes [64], plasmas [59, 65]) and as such may be expensive and difficult to fabricate. Alternately they may simply be impractical, relatively slow, or ill suited to performing certain operations, which would be more efficiently computed by classical approaches. However this limitation may be due to the lack of complete understanding of the mechanics of particular systems. A wider knowledge of the parameters affecting the behaviour of such systems may render them more suitable for exploitation computationally.

One alternative to utilising the actual physical or living system to perform non-classical computation is to try to abstract the most salient features of the system in question and encode these behaviours within classical (or at least

symbolically encoded) algorithms. A notable example is evolutionary computation, where population variation mediated by mutation and recombination is incorporated into a population of ‘chromosomes’ representing program parameters [66] or the programs themselves [67]. A further abstraction — of the environment and population in this instance — is seen in the method of Particle Swarm Optimisation (PSO), in which a population of candidate solutions moves about a ‘landscape’ (search space), guided by shared information about the current optimal solutions [68]. Even more relevant to the research in this book is the example of Ant Colony Optimisation, a family of meta-heuristic approaches where the phenomena of pheromone sensing and deposition by ant colonies is abstracted and used to enforce a cost to different paths in combinatorial optimisation problems [69]. In all of these examples, however, the complex spatial and physical interactions of the source systems are lost during the abstraction to a classical encoding. The abstracted models are thus biased towards the assumptions as to which physical features are responsible for the complex computation and risks losing a rich potential well of computational power freely available in the physical system.

Adamatzky suggested that *Physarum* is an ideal candidate for research into non-classical computing devices because it is inexpensive, relatively simple to cultivate, configurable and amenable to external influence and control [4]. In the last decade there has been intense research into its computational abilities, prompted by Nakagaki, Yamada and Toth, who reported the ability of the *Physarum* plasmodium to solve a simple maze problem. The authors placed plasmodium fragments on an agar substrate patterned to form a maze (walls of the maze were represented by dry plastic regions which the plasmodium tends to avoid). The fragments merged to form a single plasmodium and nutrient oat flakes were placed at the start and exit points of the maze, initiating oscillatory contractions at these sites.

Over a period of 8 hours the plasmodium adopted its body plan and the protoplasmic tube network shrank away from locations not connected to the nutrients, such as dead ends. In a series of 19 experimental runs the authors found that the remaining plasmodium reproduced the shortest path from start to exit in 5 runs and combinations of other possible paths in the majority of the remaining runs [70].

The fact that such a simple single-celled organism without any nervous tissue could solve what was previously considered to be a complex problem generated much publicity and raised interesting questions regarding the nature of, and minimum requisites for, intelligent behaviour. In their paper the authors suggested that: “This remarkable process of cellular computation implies that cellular materials can show a primitive intelligence” [70].

Solving a maze does not, in itself, require intelligence, as was recently demonstrated effectively in a simple system in which an oil droplet (exploiting convection currents and surface tension effects) migrated along a pH gradient formed within a maze to track the shortest path through the maze [71]. In fact, the starting configuration of the plasmodium in the Nakagaki et al.

maze actually included all paths. The adaptation of the plasmodium essentially removed all the redundant paths. The maze configuration solved by the slime mould was the same as that used by Steinbock et al., who utilised the propagation of a chemical wave from the start of the maze to the exit, to find the shortest path through the maze [72]. In the Steinbock et al. approach [72], to elicit the actual path required a separate computation backwards along a time-lapsed vector field indicating the propagation of the wave. A swarm computation approach to the same problem was also described, in which a particle population (initialised at the start) followed the gradient of the propagating wave as it propagated through the maze [73]. It has recently been demonstrated that the *Physarum* plasmodium can also solve mazes in this same direct manner, i.e. in a single pass by tracking the source of a chemoattractant [74].

The publicity surrounding the initial findings of Nakagaki et al. prompted subsequent research into the range of computational abilities of slime mould. It has been demonstrated that the plasmodium successfully approximates spatial representations of various graph problems. In [9] the authors examined the connectivity of the tube network when the plasmodium was presented with multiple sources of nutrients. They found that the plasmodium constructed networks that combined features of minimum path length (approximating the Steiner tree) and cyclic connectivity (giving resilience to random disconnection of a path). It has subsequently been demonstrated that the *Physarum* plasmodium successfully approximates spatial representations of various graph problems including generation of Voronoi diagrams and collision-free path planning [75], Delaunay triangulation [76], spanning trees [77, 78, 79], proximity graphs [80], convex hulls and concave hulls [81]. These research examples all used the spatial foraging behaviour of the plasmodium to approximate graph problems which are conventionally solved using algorithmic approaches. Methods to control the propagation of the plasmodium using attractants, repellents and light irradiation were investigated by Adamatzky in [82, 83, 84].

The oscillatory phenomena and avoidance of light irradiation were exploited by Aono and colleagues for combinatorial optimisation problems [85, 86, 87], specifically small instances of the Travelling Salesman Problem, and found that the chaotic behaviour of the internal oscillations helped the plasmodium avoid deadlock situations, preventing the organism from becoming trapped in local minima – behaviour which is useful in terms of computational and biological search strategies. The behaviour of *Physarum* in response to strong long-distance attractant stimuli combined with short-distance repulsive stimuli was found to follow attractor cycles around simple stimuli and limit-cycle motion with more complex stimuli arrangements [88].

It is somewhat traditional in unconventional computing to validate the computational equivalence of a particular computing substrate with the components of classical computing devices [89, 90, 91]. It should be stressed that such research is motivated by exploring theoretical computational *potential*, rather than suitability. In [92], the authors demonstrated how a foraging plasmodium

of *Physarum* could be used to construct simple logic gates. A similar approach based on the ballistic computing model was implemented using *Physarum* in [93]. The likelihood of extending the *Physarum* approach for more complex adding circuits was explored in simulation in [94] who found that foraging errors were compounded by small delays in signal timing at junctions, rendering the approach unfeasible for larger adding circuits. An alternative approach based on harnessing the more natural propagative behaviour of the organism to construct spatially represented universal machines (Kolmorogov-Uspensky Machines, or KUM) was studied in [95, 96] in which the basic operations of the KUM were replicated experimentally and in simulation.

Physarum utilises its self-made protoplasmic network to transport nutrients within its cell body. The transport phenomena correspond to transportation networks formed by collectives in other living systems including fungi [97, 98], ants [99] and humans [100]. Since the plasmodial network is a single cell, constructed from ‘bottom-up’ principles, how does the structure of the plasmodium networks compare to other artificial transport networks which are typically constructed from hierarchical ‘top-down’ methodologies? The task is somewhat difficult as *Physarum* is only concerned with survival, rather than solving externally applied problems, however early research into the topic of nature-inspired transport networks using *Physarum* was performed by Adamatzky and Jones who found that *Physarum* networks closely approximated the major motorway network connecting the most populous UK urban areas [101]. The authors also found that the plasmodium effected an efficient response to simulated disastrous contamination of individual urban areas, implemented by diffusion of salts within the region. The plasmodium migrated away from contaminated regions to relatively unpopulated areas before re-establishing network connectivity when the damaged areas were contamination-free. This study was recently extended to include the major motorway networks in different countries [102], and an intriguing similarity between the historical evolution of human networks (for example cattle droving trails, iron age trails, roman roads, modern arterial routes) can be mirrored in the evolution of early stage fine-grained *Physarum* networks to later networks with thicker and more sparse connectivity [103]. The connectivity of *Physarum* networks was also compared with the regional rail system surrounding Tokyo by Tero et al. who, using a novel approach to represent environmental hazards using light irradiation, also found a similar correspondence between the human and plasmodial networks, in terms of distance and connectivity [104].

2.7 *Physarum Polycephalum* and Robotics

Classical robotics approaches typically connect separate sensory, control, and locomotion systems, using complex parts with little redundancy. Nature inspired robotics takes inspiration from aggregate populations, collective transport, segmentation of component parts, and soft-bodied motion in liv-

ing systems. Swarm approaches to nature inspired computing seek to elucidate the sensory mechanisms and individual interactions which generate the complexity patterning and movement seen at very different scales in natural systems including car traffic dynamics [105], human walking patterns [100], flocking and schooling [106], collective insect movement [107], and bacterial patterning [108]. In all these examples there is a population of entities in space, coupled by sensory information. Sensory coupling mechanisms between individuals has also been abstracted at a minimal level of self-propelled particles to find common mechanisms [109].

Progress in biologically inspired robotics has also been made by considering the use of even simpler structures which straddle the boundary of non-living physical materials and living organisms including those acting as biological fibres and membranes [110], lipid self assembly in terms of networks [111], pseudopodium-like membrane extension [112] and even those exhibiting simple chemotaxis responses [71]. Some engineering and biological insights have already been gained by studying the structure and function of what might be termed ‘semi-biological’ materials and the complex behaviour seen in such minimal examples raises questions about the lower bounds necessary for the emergence of apparently intelligent behaviour.

An ideal hypothetical candidate for a biological machine would be an organism which is capable of the complex sensory integration, movement and adaptation of a living organism, yet which is also composed of a relatively simple material that is amenable to simple understanding and control of its properties. *Physarum* may be a suitable candidate organism which meets both criteria; i.e. it is a complex organism, but which is composed of relatively simple materials. From a robotics perspective it was shown that by its adaptation to changing conditions within its environment, the plasmodium may be considered as a prototype micro-mechanical manipulation system, capable of simple and programmable robotic actions including the manipulation (pushing and pulling) of small scale objects [113], transport and mixing of substances [83] and as a guidance mechanism in a biological-mechanical hybrid approach where the response of the plasmodium to light irradiation was used to provide motor and feedback control to a robotic system [53]. A *Physarum* inspired approach to amoeboid robotics was demonstrated by Umedachi et al. [114] in which an external ring of coupled oscillators, each connected to passive and tuneable springs was coupled to an inner fluid-filled bladder. The selective compression of the peripheral springs mimicked the contraction of the gel phase of the plasmodium, and the hydrostatic transmission of water pressure within the bladder represented the the flux of sol within the plasmodium. The transmission of the oscillating motion deflected the peripheral shape of the robot and the resulting movement exhibited flexible behaviour and amoeboid movement.

2.8 Computational Models of *Physarum Polycephalum*

Early models of *Physarum* were focused on individual biological aspects of its behaviour, most notably the generation, coupling, and phase interactions between oscillators within the plasmodium. More recently, the overall behaviour of the organism has been modelled in attempts to discover more about its distributed computation abilities.

2.8.1 Computational Models of *Physarum* Oscillatory Phenomena

Oscillatory phenomena in *Physarum* have been studied using numerical models to represent the interactions between oscillators in one dimensional systems [115, 49, 51], typically modelling the contractions generating protoplasmic streaming phenomena and temporal phase interactions arising from the coupling of the chemical oscillators to mechanical material flux. The model used in [51] was used to explain the primitive memory effect observed in *Physarum*, although an alternative explanation based upon memristive effects was suggested in [116]. Methods of approximating the alignment of actomyosin fibres within the plasmodium were presented in [117] and, more generally, oscillatory phenomena within cytogels were modelled in [33]. Numerical models have also been utilised in two dimensions to approximate interactions between pattern transitions [118], spatial response to environmental changes [48] and amoeboid movement [119].

2.8.2 Computational Models of *Physarum* Pattern Formation and Adaptation

The topology of the *Physarum* protoplasmic tube network is influenced by nutrient concentration and distribution, and evolves to achieve a compromise between minimal transport costs and fault tolerance [9]. Since the plasmodium obviously cannot have any global knowledge about the initial or optimal topology, the network must evolve by physical forces acting locally on the protoplasmic transport.

Tero et al. have suggested that protoplasmic flux through the network veins may be the physical basis for evolution of the transport network: given flux through two paths, the shorter path will receive more sol flux. By generating an autocatalytic mechanism to reward veins with greater flux (by thickening/widening them) and to apply a cost to veins with less flux (the veins become thinner), shorter veins begin to predominate as the network evolves. This approach was used for the mathematical model of *Physarum* network behaviour to solve path planning problems [120, 121]. This method indirectly supports the reaction-diffusion inspired notions of local activation (enhancement of shorter tube paths) and lateral inhibition (weakening of longer tube

paths). The starting point for the model of Tero et al. is a randomly connected protoplasmic tube network, surrounding a number of nutrient sources (network nodes) which act as sources and sinks of flux. By beginning with a complete network the Tero model, although successful in generating impressive solutions to network problems, sidesteps the issues and mechanisms of initial network formation, plasmodium growth, foraging, and adaptation to a changing nutrient environment.

Gunji et al. introduced a cellular automaton (CA) model which considered both plasmodial growth and amoeboid movement [122]. The model placed importance on the transformation of hardness/softness at the membrane and the internal transport of ‘vacant particles’ from outside the membrane resulting in deformation of the original morphology, movement and network adaptation. The model was also able to approximate instances of maze path planning and coarse approximations of the Steiner tree problem and a recent version has been developed to incorporate network growth and adaptation [123]. A hexagonal CA was used by [124] to approximate the growth patterns displayed under differing nutrient concentrations and substrate hardness. The patterns reflected experimental results well but did not exhibit morphological adaptation of the tube network. A recently introduced automata model by Sawa et al. deforms the initial shape of the cell array by exchanging material between cells provided that the difference between two adjacent cells does not exceed a threshold d and the total amount of plasmodium does not exceed another threshold u . The model combines features of the Gunji group approach (deformation of an initial mass of plasmodium) with the simple parametric tuning of the Takamatsu approach but as yet does not incorporate response to nutrient sources or growth and shrinkage of the plasmodium [125].

Hickey and Noriega adapted a classical ant colony optimisation algorithm to modify a decision tree in their representation of *Physarum* behaviour in a simple path planning problem [126]. Their algorithm (as with many implementations of ant algorithms) transformed the spatial representation into a graph representation and provided broadly similar results to path optimisation by *Physarum*.

Adamatzky has noted that the *Physarum* plasmodium is computationally equivalent, and indeed exceeds the performance of, current prototypes of reaction-diffusion computers [78, 79]. According to Adamatzky the plasmodium “can be considered as a reaction-diffusion, or an excitable medium encapsulated in an elastic growing membrane.” [4]. The wave propagation of information within plasmodium in response to a complex environment corresponds to a particular type of chemical processor operating in a sub-excitable mode, where the propagation of travelling waves within the plasmodium is influenced by the presence of local nutrient stimuli.

2.9 *Physarum* as a Dynamical LALI Mechanism of Pattern Formation

The question of how regular spatial patterns may arise within a material from a homogeneous initial state was first formally addressed by Turing who considered the interactions of two hypothetical chemicals [127]. Turing's model relied on the auto-catalytic production of an activator chemical which enhanced the production of a second chemical which, in turn, inhibited the formation of the activator chemical. Critically, the inhibitor diffused more quickly than the activator and a pattern of local activation and lateral inhibition was produced. Variations in the parameters of the differential equations describing the interactions of the chemicals (which Turing called morphogens) enhanced differences between random instabilities in the concentration profiles of the reactants. By visually interpreting the concentration of the two chemicals (for example, as different colours) characteristic patterns of spots or stripes are formed. The reaction-diffusion approach has been the dominant theoretical model of pattern formation and the mechanisms have been used for explanations of both gross body plan and specialised organ development [128, 129], and the coat and skin patterns of organisms [130]. Many variations of Turing's original two morphogen method have been developed in attempts to develop more complex patterning. These include the effects of different boundary conditions and extra sources and sinks of chemical stimuli [131], and the coupling of different reaction-diffusion processes. For example the output of one patterning process 'P-A', may be used as the input pattern (concentration profile) for a separate process, 'P-B'. The combination of different simple patterning processes generates more complex patterning such as reticulate or polygonal patterns [132, 133].

Although chemical based reaction-diffusion (RD) approaches can produce complex patterning there are questions as to their role in pattern formation in living systems. It is only relatively recently that Turing-like RD patterns have been observed in chemical systems [134, 135]. It is also well known that a number of other mechanisms are able to generate complex patterning. Mechanical models have been suggested as pattern formation mechanisms. In these systems the substrate is deformed in some way (for example by traction forces exerted by cells on their substrate as they move) so as to provide local autocatalytic stimuli to attract local cells and initiate patterning [136]. Alternatively cellular models exist that utilise purely chemotaxis stimuli to allow cells to migrate towards concentration gradients and initiate patterning [137, 138]. More recently, a combination of these methods have been used, the mechano-chemical approaches [139, 140].

It is possible to classify all of the above mechanisms of pattern formation as lateral inhibition based. In this classification all of the previously mentioned methods are generalised as a phenomenon of Local Attraction and Long-range Inhibition (LALI) [129, 141, 142]. Although the local activation mechanisms all utilise some form of auto-catalytic behaviour, the inhibition can take very

different forms: There may be direct lateral inhibition (for example by neural inhibition, [143], direct inhibition by a diffusing inhibitor chemical (as in Turing-type RD), or indirect inhibition via substrate depletion or a movement away from a local ‘zone of influence’.

The above approaches are inspired by fine-grained chemical, substrate and cellular interactions and most commonly modelled by continuum-based mathematical models. Bonabeau suggested that agent based modelling may be more suitable for modelling systems where low-level interaction produce emergent global behaviours [144]. Pattern formation mechanisms in nature are usually composed of very large populations of discrete, relatively independent, entities and can be seen in both living and non-living systems at very different spatial and temporal scales. In non-living physical systems Turing-like patterning has been observed in vertically oscillated granular media [145] and, at larger spatial and time scales, complex patterning has been observed in sorted patterned ground at climatic regions where freeze-thaw cycles regularly occur [146].

In living systems complex patterning is observed in many instances where large colonies of individuals exist, including growth patterns in bacterial colonies [147, 148], social insect movement patterns [149] and nest structures [150]. Complex patterning continues as the size of the individual increases: flocking patterns of birds [106], pedestrian movement [151] and traffic flow [105] are all well studied examples. Some of these pattern formation mechanisms have certain features in common: The patterning is an emergent phenomenon, qualitatively different from, and not specified by, the individual behaviours. The patterns are often composed of the ‘actors’ themselves [144] from the ‘bottom-up’ and the patterns formed may be used for transport of substances within the organism structure [97, 152]. Finally the patterns formed are often dynamic, adaptable in response to changing environmental conditions (such as nutrient availability) and are resilient to external damage. It is notable that *Physarum* shares many of these features.

2.10 Requisite Properties for *Physarum Polycephalum* Models

Previous models of *Physarum* have concentrated on single aspects of the organism’s behaviour, namely network adaptation, branching patterns, oscillatory synchronisation, internal wave transport, and plasmodium movement. An ideal model would encompass all of these behaviours in a single model yet also allow the separate study of each behaviour in isolation. Another aspect of the plasmodium which would be desirable in a model is the replication of the distributed control of the plasmodium. It is this behaviour which allows growth of the plasmodium, adaptation in response to changing environmental conditions and the survivability of the organism in response to excision of part of the plasmodium, or fusion of two separate plasmodia. To be biologically relevant, the mechanism for network adaptation must also approximate

the auto-catalytic nature of the plasmodium (flux through shorter tubes is amplified, flux through longer tubes is diminished). The simple nature of the constituent material parts of the plasmodium strongly suggest that emergent behaviour from simple component parts and interactions should play an important role in such a model. In the following chapter we present a multi-agent approach to modelling *Physarum* utilising a LALI mechanism of reaction-diffusion pattern formation which exhibits the aforementioned properties distributed within a virtual material.

Part II

Modelling *Physarum Polycephalum*

Chapter 3

A Multi-agent Model of *Physarum*

“...but a drop or bubble may realise in an instant the whole apparatus of curves.... bearing witness to the fact that one common law is obeyed by every point or particle of the system. Where the underlying equations are unknown to us, as happens in so many natural configurations, we may still rest assured that kindred mathematical laws are being automatically followed, and rigorously obeyed, and sometime half-revealed.”

(D’arcy Wentworth Thompson, 1917)

3.1 Introduction

This chapter describes the multi-agent model of *Physarum*, which is a particle based reaction-diffusion pattern mechanism behaving as a collective virtual material. The base model behaviour is described and its pattern formation properties explored in an evaluation of model parameters.

3.2 Motivations for Model Choice

We wish to approximate the biological patterning behaviour and computational behaviour of the *Physarum* plasmodium. Furthermore we wish to reproduce certain features of the plasmodium: simple components, distributed behaviour (and computation), oscillatory phenomena, and morphological adaptation. In this section we describe the motivation for a fine-grained, spatially implemented, material-based approach.

3.2.1 Granularity

When deciding on a modelling strategy we must choose a level of detail, or granularity, at which to simulate the desired process. We must choose a level

which captures the desired behaviour, does not make too many experimental assumptions, yet which does not model irrelevant details. Whilst we seek simplicity we must bear in mind the words of caution (attributed to Einstein), that models should be: "...as simple as possible (but no simpler)". For spatially implemented models the granularity choice is particularly important since it impacts directly on factors such as the lattice representation and the base behaviour encoded in the model. For example, for a biological organism, we might consider the following possible grain levels for *Physarum*: *atomic-molecular-chemical-actomyosin-plasmalemma-plasmodium*.

We wish to implement the self-organisation phenomena which result in the distributed, de-centralised and emergent behaviour of the plasmodium. Choosing a high-level approach would force us to make too many modelling assumptions about the causal factors generating these phenomena. We must therefore choose a granularity which is fine enough to show emergent properties, which is extensible and is computationally tractable. A similar difficulty occurs at the simpler fine-grained levels; the genetic and biochemical interactions which occur in *Physarum*, although well studied, are not yet completely understood, nor computationally tractable. Although lower levels of grain appear conceptually simpler to implement (since the individual behavioural steps are smaller and simpler), it is not possible to directly specify the higher level observed phenomena, such as the foraging and adaptation behaviour of *Physarum*, in terms of lower granularity since a complex behaviour pattern such as "migrate towards stimulus" is beyond the scope of such a simple instruction set.

3.2.2 A Continuum of Material Patterning

By exploiting 'material properties' we mean the behaviour that a material *collectively* demonstrates under certain environmental conditions, as opposed to the behaviour of its individual constituent parts. Many materials exhibit complex patterning in response to environmental stresses, including fracture patterns in ceramics [153], drying materials [154], and dielectric breakdown [155]. However this patterning is typically non-mutable. To model adaptive patterning in *Physarum* the chosen mechanism must be capable of adjusting its pattern over time, i.e. the patterning must be more flexible. We can consider patterning as a continuum where, at one extreme, there is rigid 'one shot' patterning to relieve stresses in the material. Moving further along the continuum we observe greater flexibility or adaptability in the patterning, as observed in leaf venation where Couder et al. argue that part of the mechanism must exhibit visco-elastic properties to form and maintain patterning [29]. Even more flexibility results in patterning as seen in gels [156], lipid networks [111] and soaps and froths [157, 158]. At the extreme end of this scale there are materials which maintain cohesion but little patterning, such as oils and water. We can use this continuum of material patterning as an

inspiration to devise a mechanism which allows mobility, complex patterning, adaptability, shows cohesion, and is stable over time.

3.2.3 Material-Like Properties in Collectives

In some instances, loose aggregates of materials or individuals can also demonstrate material-like patterning, for example in agitated granular media [145], crowd behaviour in emergencies [159], liquid-like flows in ant colonies [160], or flocking patterns of birds ([106]). In such examples the physical forces responsible for cohesion in real materials are replaced by indirect coupling of individuals provided by direct contact, visual information, or chemotactic cues. This suggests that by incorporating such a coupling method we can gain material-like properties within loose collectives.

3.2.4 Spatial Implementation

As prototype non-classical computing devices utilise physical properties of their substrates, the choice of a spatial representation for the *Physarum* model using a non-classical approach is logical. However, this also requires that the mechanisms used in the model must also be incorporated spatially, as opposed to abstracted numerically. For our approach we utilise a 2D lattice based model to represent the structure of the plasmodium and an isomorphic diffusive lattice to represent the flux within the plasmodium as described below.

3.3 A Multi-agent Virtual Material Approach

The model used to approximate the behaviour of *Physarum* is based on the multi-agent approach. A population of very simple particle-like mobile software agents interact within a 2D diffusive lattice comprising their environment. The approach used is in the tradition of fine-grained and ‘bottom-up’ models, where macroscopic phenomena emerge from the interactions between simpler components at the microscopic scale.

The level of granularity chosen corresponds to the movement interactions within the plasmodium gel/sol matrix. By choosing this level we are removing the complexity of sub-atomic, atomic and molecular details. It is important to note that we are also removing the ‘layer’ of chemical interactions within the plasmodium. It is these interactions which generate the motive force for the protoplasmic streaming within the plasmodium. We remove this layer partially because it is not yet fully understood biologically or energetically, and partially because it has already been demonstrated that this layer may be approximated by conceptualising the plasmodium as a membrane bound sub-excitable reaction diffusion system [4]. Therefore we assume that the

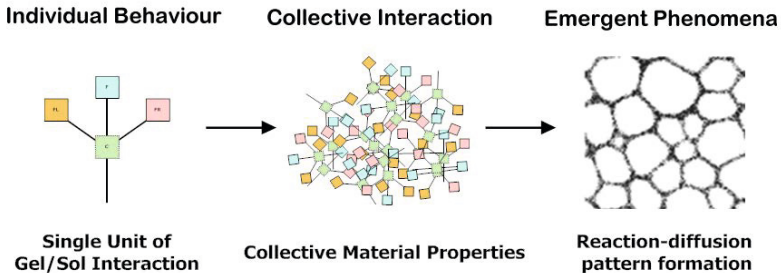


Fig. 3.1 Multi-agent based approach approximates gel / sol plasmodium interactions. left) single agent particle, middle) collective mass of agents, right) complex pattern formation.

chemical transformations, over the surface of, and within the plasmodium provide a contractile force acting upon individual hypothetical units of gel/sol comprising the actomyosin network of the plasmodium. It is the coupling and flux within the gel/sol matrix which we explicitly model in this report and which, we will show, is sufficient to explain the complex behaviour of the *Physarum* plasmodium. The approach is summarised in Fig. 3.1.

3.3.1 Model Overview

The model specifically addresses the generation of network formation and adaptation, oscillatory phenomena and transport phenomena exhibited by *Physarum*. We divide the model into three parts, beginning with the base ‘material’ behaviour of network formation and adaptation. The material properties of the model must be emergent, distributed within the material and utilise a mechanism of self-organised dynamical pattern formation. The base behaviour of the model is then expanded to reproduce growth and adaptation of the *Physarum* plasmodium. This allows the exploration of how foraging and adaptation is influenced by nutrients within the environment. The third part of the model is the addition of oscillatory behaviour. As with the base model behaviour, oscillatory phenomena in the model must be an emergent property and thus arise from the interactions within the material. The addition of subsequent behaviours to the base model behaviour must not impinge upon previous behaviours, which are subsumed within the new additions. Results pertaining to each are included in separate chapters for clarity.

Firstly we must reproduce the basic material properties of the plasmodium, i.e. a virtual material which is capable of complex dynamical pattern formation and adaptation from the particle collective. The material properties must be distributed within the collective and emerge from the interactions between the simple components, requiring no special component parts. In this chapter we summarise the behaviour and parametric evaluation of the

base material and its response to simple analogues of environmental stimuli by the formation of transport networks between the stimuli.

3.3.2 The Building-Block of a Virtual Plasmodium

The model framework is a particle representation of reaction-diffusion (RD) processes. Unlike classical RD models, which are composed of the interactions of at least two simulated activator/inhibitor reactants in a diffusive environment, there is only a single representative reactant: a mobile particle which senses and deposits simulated chemoattractant as it moves within a diffusive environment. The combined sensing and deposition of chemoattractant represent an active mode of RD computation — the particle both senses and modifies the diffusion field. This is an alternative to a passive mode where the computation is achieved purely by wavefront propagation and in which the particles only follow the diffusion field [73]. In general terms the framework belongs to the LALI (Local Activation and Long range Inhibition) approaches which encompasses RD methods [141], and specifically agent based approaches into LALI patterning [144].

The virtual plasmodium is comprised of a population of agent particles, whose population size is given by p (or, as a percentage of lattice area, $\%p$). The diffusive lattice is represented by a discrete two-dimensional floating point array. Agent particle positions are stored on a coupled discrete lattice (isomorphic to the diffusive lattice) but, in an attempt to overcome the limitations of movement of the discrete representation, the particles also store an internal floating point positional and angular representation which is rounded to a discrete value to compute movement updates and sensory inputs. A single particle, and an aggregation of particles, is related to the *Physarum* plasmodium in the following way: The plasmodium syncytium is conceptualised as an aggregate of identical components. Each particle represents a hypothetical unit of gel/sol interaction. Gel refers to the relatively stiff sponge-like matrix composed of actin-myosin fibres and sol refers to the protoplasmic solution which flows within the matrix.

The structure of the protoplasmic network is indicated by the collective pattern of particle *positions* and the flow of sol is represented by the collective *movement* of the particles. The resistance of the gel matrix to protoplasmic flux of sol is generated by particle-particle movement collisions. As an analogy one can imagine a tightly crowded population within a room, the confined space generating collisions and thus resistance to movement. Local amplification of flux is provided by particle – particle sensory coupling. An analogical description of the coupling can be understood if the population in the room were coupled by linking hands with close neighbours, thus when one neighbour moves it creates a local increase in flow (and a temporary vacant space) which attracts nearby particles.

3.3.3 Agent Particle Sensory Behaviour

A single agent represents a hypothetical particle of *Physarum* plasmodium gel/sol structure. When a particle moves, the movement can be said to represent the protoplasmic flux of sol. When a particle is not able to move it can be said to represent the immobile gel matrix. The general morphology of an agent and its basic underlying algorithm is illustrated in Fig. 3.2. Each agent is typically initialised at a randomly chosen unoccupied and habitable location and with a random orientation (from zero to 360° , freeing the agent from the restrictive rectangular architecture of the underlying lattice). The agent receives chemotactic sensory stimuli from its environment (chemoattractant levels stored in the diffusive lattice) via three forward sensors (Fig. 3.2a) and the agent responds to differences in the local environment chemoattractant levels by altering its orientation angle to face the locally strongest concentration by rotating left or right about its current position (Fig. 3.2b). The sensor offset distance (in pixels) is represented by the *SO* parameter and it can be considered as a scaling parameter. The agent is forward biased, i.e. only the sensors directly in front of the agent's current position are used to influence its behaviour, thus ensuring a continuous movement-based dynamic.

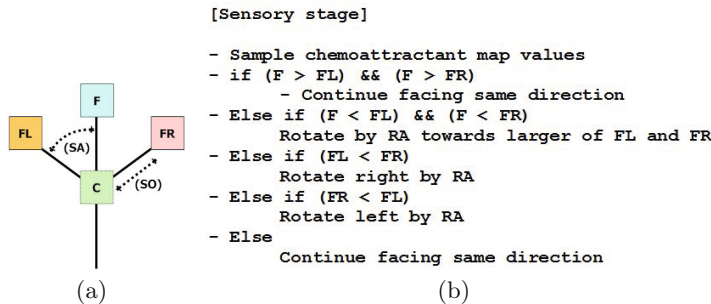


Fig. 3.2 Base agent particle morphology and sensory stage algorithm. (a) Illustration of single agent, showing location ‘C’, offset sensors ‘FL’, ‘F’, ‘FR’, Sensor Angle ‘SA’ and Sensor Offset ‘SO’, (b) simplified sensory algorithm.

3.3.4 Agent Particle Motor Behaviour

The motor behaviour of the particles represents the flux of material within the plasmodium. The motor behaviour operates in either non-oscillatory or oscillatory modes (Fig. 3.3). The non-oscillatory mode represents an idealised movement with no build up of forces within the plasmodium due to obstruction. As will be demonstrated, this mode generates smooth evolution of network structure with no obstruction and hence no emergence of oscillatory phenomena. This mode is used to assess the network evolution under ideal conditions and is described below.

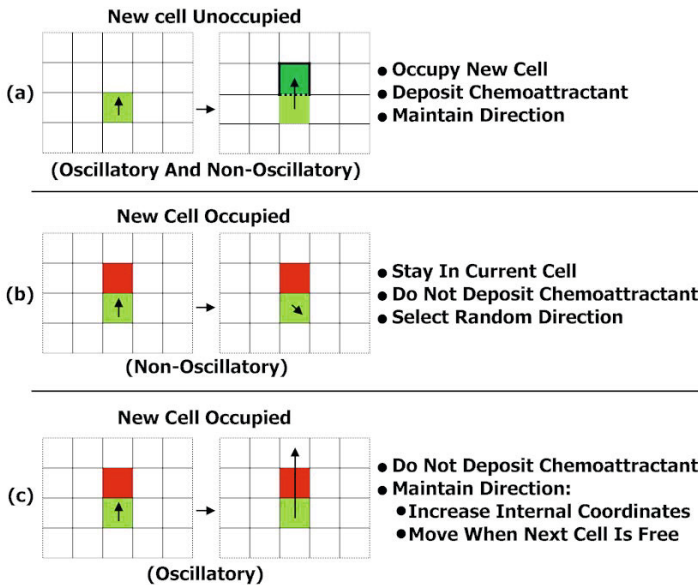


Fig. 3.3 Agent particle motor behaviour under non-oscillatory and oscillatory conditions. (Top) movement to vacant site, (Middle) behaviour if site is occupied (non-oscillatory), (Bottom) behaviour if site is occupied (oscillatory).

At each execution step of the scheduler every agent attempts to move forward in the lattice by the value SS (default value of 1) in the current direction. After every agent has attempted its move, the entire population executes its sensory behaviour. If the movement is successful (i.e. if the next site is not occupied) the agent moves to the new site and deposits a constant chemoattractant value into the diffusive lattice, given by the value $Dept$, with a default value of 5 units (Fig. 3.3a). In the default, non-oscillatory condition, if the movement is not successful the agent remains in its current position, no chemoattractant is deposited, and a new orientation is randomly selected (Fig. 3.3b). The selection of a new direction if the agent is blocked prevents deadlock in the lattice and clustering of agents.

In the oscillatory motor condition, however, we wish to approximate the build up of resistance within the plasmodium. If a chosen site is occupied the agent remains in the current cell and increments an internal coordinate counter facing the same direction. When a site becomes free the agent occupies the new site, moving past the blocked site (Fig. 3.3c). This simple mechanism results in temporary blockages until the particles are able to ‘push past’ each other and results in the emergence of surging movement which is described in more detail in chapter 15.

3.4 Growth and Adaptation of the Virtual Plasmodium

Growth and adaptation of the particle model population is implemented using a simple method based upon local measures of space availability (growth) and overcrowding (adaptation by population reduction). This is undoubtedly a gross simplification of the complex factors involved in growth and adaptation of the real organism (such as metabolic influences, nutrient concentration, waste concentration, slime capsule coverage, bacterial contamination etc.). However the simplification renders the population growth and adaptation more computationally tractable and the specific parameters governing growth and shrinkage are at least loosely based upon real environmental constraints. Growth and shrinkage states are iterated separately for each particle and the results for each particle are indicated by tagging Boolean values to the particles. Any particles tagged for growth/shrinkage are considered by the framework scheduler at regular intervals of periods given by G_f and S_f , the growth/shrinkage frequency (default value, every 3 scheduler steps). The growth and shrinkage rules for each particle are given below, with default values indicated in brackets:

Let n be the number of particles within local window radius G_w (9) centred around the current particle position (x, y) . Let $rand$ be the random number generated between 0 and 1 with uniform distribution. $Gmin$ (0) and $Gmax$ (10) are the local crowding size, outside which growth cannot occur. $pDiv$ (1) is a probability that a particle will multiply if the conditions are suitable.

```

if ( $n > Gmin$  AND  $n \leq Gmax$ ) AND ( $rand < pDiv$ )
divideparticle = True
Else
divideparticle = False

```

At each scheduler division step any particles tagged with the *divideparticle* flag attempt to multiply by executing the following pseudocode:

```

If (divideparticle)
Choose random cell in window radius 1 around current particle position,
if available.
Create new particle in this cell.

```

The shrinkage rules for each particle are given as:

Let n be the number of particles within local window radius S_w (5) centred around current particle position (x, y) . Let $Smin$ (0) and $Smax$ (24) be the local crowding size outside which the particle will be removed.

```

if ( $n > S_{min}$  AND  $n \leq S_{max}$ )
    shrinkparticle = False
Else
    shrinkparticle = True

```

At each scheduled shrinkage step, any particles tagged with ‘shrink’ are removed.

3.5 Representing the Agent Population Environment Habitat

The environment is implemented spatially using a discrete 2D lattice. Each addressable site (x, y) on the lattice refers to a unique location which may store a single agent particle. Each (x, y) address may also address values in isomorphic lattices representing flux within the plasmodium and the locations of nutrients, hazards and toxins. The flux of sol within the plasmodium is represented by a floating point value in a diffusive lattice and referred to as generic ‘chemoattractant’.

3.5.1 Habitat Configuration

To represent the experimental environment the lattice is configured by supplying the scheduler with a 2D greyscale image. The image represents a configuration map for the experiment. A coding system is used to denote particular environmental features with particular greyscale levels, including habitable background regions, experimental borders, inhabitable regions, hazardous regions, nutrient stimuli locations, and specific inoculation sites. An initial population of agent particles, representing a small fragment of plasmodium, is created (size p , where p is the initial number of particles) and initialised with random orientations at either background regions or specific inoculation sites.

3.5.2 Representation of Nutrient Chemoattractants

Simulated chemoattractant nutrient source stimuli whose position and concentration are stored in the configuration map are projected to the diffusive lattice at every step of the scheduler. The concentration of the chemoattractant stimuli (in arbitrary units) is given by the greyscale intensity at the lattice site. The concentration can be adjusted by multiplication with a global weighting parameter $Proj_d$.

3.5.3 Representation of Nutrient Chemorepellents

Physarum is known to migrate away from certain compounds [161, 82]. To reproduce the effect of chemorepellent stimuli at specific sites, negatively weighted values, Rep_d , are used to project features in the environment at these locations. Because the agent particle behaviour is to orient towards stronger concentration regions, particles will move away from the chemorepellent regions. Under growth and adaptation conditions, an agent particle is not able to divide if it is within a repellent region.

3.5.4 Representation of Response to Illumination

Physarum plasmodium tends to avoid areas under illumination [162]. This phenomenon has been used to affect the structure of the plasmodium transport network and the directional migration of plasmodia [163, 84]. To implement this phenomenon in the model we include a specific hazard value in the lattice. Illuminated areas in the environment are tagged with the hazard value. If an agent is located within an illuminated region, denoted by a window L_w centred about the agent (default value 5), the value of sensed chemoattractant in the sensor is reduced by multiplying it by a weighting factor L_d , whose value may be between zero and 1. Lower values of L_d reduce the value of sensed chemoattractant in the illuminated region and the collective is thus less attracted to the illuminated region. Under growth and adaptation conditions, an agent particle is not able to divide if it is within an illuminated region.

3.5.5 Diffusion Mechanism

The chemoattractant stimuli are diffused by means of a simple mean filter kernel of size D_w , (typically 3×3). The diffusion operator is applied to all cells simultaneously via pseudo-parallelism methods. The diffusing chemoattractant values may be damped by the value D_d (typically 0.1) to adjust the concentration of the diffusion gradient away from the nutrient source. (mean of D_w , multiplied by $(1 - D_d)$, smaller values of D_d resulting in less damping of diffusion). The persistence of the diffusion gradient corresponds to the quality of the nutrient substrate of the plasmodium's environment (for example the different growth patterns seen in damp filter paper and nutrient-rich agar substrates). Differences in the stimulus concentration (greyscale value in the configuration map) and stimulus area (the size of nutrient source), affect both the steepness, and propagation distance of the diffusion gradient and affect the growth patterns of the synthetic plasmodium.

If the movement of agent particles represents the flux within the tube network, the frequency of diffusion, given by the parameter D_f , represents the persistence of the tube network itself. Typically the value is 1, i.e. diffusion

is carried out after every scheduler step, and results in faster adaptation of the tube network. A larger value of D_f will result in less frequent diffusion and greater persistence of the tube network.

3.5.6 Gradient Suppression and Nutrient Consumption

Suppression of the production of nutrient gradients when nutrients are engulfed by the model plasmodium is achieved by a simple method. At each iteration of the scheduler the local neighbourhood E_w (default value 5), centred around every position in the lattice, is checked to see if it is occupied by a particle and, if so, the projection of nutrient to the diffusive map is reduced by multiplying by a damping factor E_d , between 0 and 1.

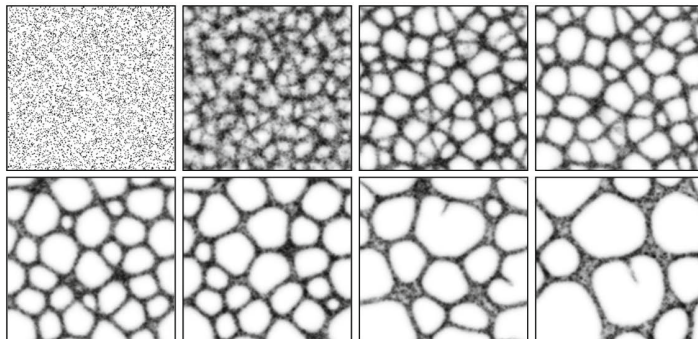


Fig. 3.4 Spontaneous formation and evolution of transport networks. Lattice 200×200 , $\%p15$, $SA\ 22.5^\circ$, $RA\ 45^\circ$, $SO\ 9$, Images taken at: 2, 22, 99, 175, 367, 512, 1740 and 4151 scheduler steps.

Consumption of nutrients is achieved in a similar way: At each iteration of the scheduler the local neighbourhood C_w (default value 5), centred around every position in the lattice, is checked to see if it is occupied by a particle. If any consumable nutrients are within this area the nutrient level is decremented by a value C_d (larger values of C_d result in faster consumption). Decrementing the nutrient level reduces the concentration of chemoattractant projected onto the diffusive lattice. When the nutrient level at a particular part of the lattice reaches zero no further projection occurs at this point. For experiments on simulated nutrient-rich substrates which simulate an agar substrate rich in nutrients (for example cornmeal agar), it is also possible to specify higher concentrations of nutrients (relating to oat flake positions) which are not consumed as quickly as the background substrate.

3.6 Self-Assembly of Emergent Transport Networks

We begin the examination of the behaviour of the particle population by studying fixed population sizes and the initiation of network formation. This allows us to explore and evaluate the base behaviour of the model and explore its parameters. After initialisation at random locations and orientations, the randomly distributed agent population spontaneously forms network trails (see Fig. 3.4, and supplementary video recordings for this chapter).

The spatial patterns are formed by, and composed of, the bi-directional flow of agents (see supplementary recording of ‘naked’ particles with visible sensors). The network forms because agents are attracted to the strongest local source of chemoattractant. Individual agents secrete chemoattractant when they move forwards successfully. The chemoattractant diffuses into the lattice, ensuring that nearby agents are attracted to the area and a positive feedback (Local Activation) loop is formed. Lateral inhibition is not explicitly encoded and is generated by the local depletion of the substrate: Particles within low concentration regions are attracted to nearby regions of high concentration and the number of agents in the low concentration regions further diminishes, thus further reducing attraction of such regions to the particles. Because the agent particles only deposit chemoattractant after successful movement, and because the agents have a forward biased sensory apparatus, static clustering of agents is avoided and a dynamic network is formed.

3.6.1 Network Motifs

The dynamical nature of the network exhibits complex emergent properties. Smaller cyclic areas of the network gradually contract and disappear. As the smaller cyclic areas disappear, larger lacunae predominate and grow as the smaller regions shrink. Occasionally, however, a bifurcation will appear in one of the network edges and a new path ‘sprout’ will branch out across the dividing space of a single lacuna. When the gap is breached there is a surge of movement as the two moving flows are connected. This surge includes an outflow from the far edge to the moving sprout as agents within the trail at the far edge are attracted to the chemoattractant flow of the sprout.

The result is a dynamical network whose shape is constantly changing but whose composite parts remain the same in number. For the default sensor parameters ($SA 22.5^\circ$, $RA 45^\circ$) the network never stabilises completely (although temporarily stable regimes have been observed, see supplementary recordings). The complexity of the network evolution is also affected by changes in network structure. For example, the collapse of a cyclic structure by contraction, redistributes agents into different parts of the network. This affects network flow in local areas, further changing the configuration. A simple relationship is thus formed: The change in network structure (e.g. branching, closing) affects local agent flux which, in turn, affects the network structure ... and so on. The dynamical evolution of the network with the

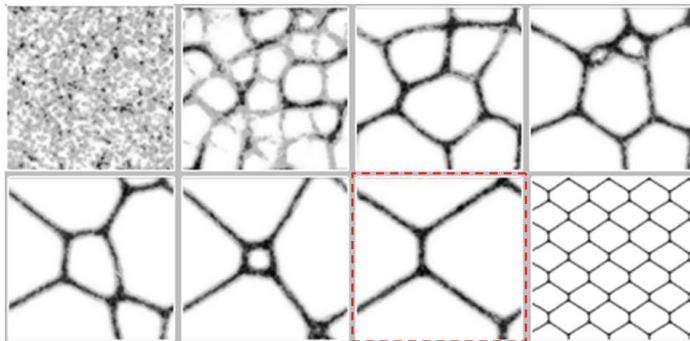


Fig. 3.5 Stable minimising network approximates hexagonal tiling. Final image shows approximate hexagonal tiling of stable state image 7 (dashed).

default parameters is because the rotation angle is significantly greater than the sensor angle. The wide rotation angle places the sensors away from the main gradient stream after a rotation. If this is coupled with random changes in direction (due to agent-agent collisions) a new bifurcation can become stabilised and reinforced by agent flow.

When both SA and RA are 45° the same initial complex network evolution is observed but the bifurcation and sprouting of new trails does not persist. In this case the lacunae gradually become larger as the smaller cycles are closed. Eventually a simple network is formed which, when tiled, approximates a regular hexagonal tiling (Fig. 3.5).

The networks evolve without any pre-patterning of the environment and different configurations appear at each run. The shape of the network is influenced by the random initial distribution of agents and the random initial orientation of the agents. The chemoattractant trails that emerge when the agents move quickly break symmetry when, for example, one area by chance accrues more chemoattractant than another. Once agents aggregate in trails, unoccupied areas become more devoid of chemoattractant (as the trails diffuse away), further amplifying the disparity (and attraction for) the areas. Like classical approaches to reaction-diffusion pattern formation, there is a reaction component (the deposition of chemoattractant by agents and the orientation towards stronger concentration). There is also a diffusion component (the diffusion of the chemoattractant from the deposition sites). However, unlike classical morphogen based models of Turing-type pattern formation, there is no explicit inhibition mechanism present. Note that without the presence of a diffusion mechanism, the patterning would be dependent to a large extent on the initial distribution and orientation of the agents.

3.6.2 Bi-directional Transport — Shuttle Streaming

The mass behaviour of the agent population shows collective network formation. When observing a single agent's movement, however, the movement does not follow the smooth flow that might be expected. The movement is hesitant and moves backwards and forwards as it progresses along a particular path. To investigate the characteristics of single agent movement the movement of a single particle was recorded. The network was a single path with periodic boundary conditions and the particle position was recorded over the course of 4000 scheduler steps and the result is shown in Fig. 3.6. The movement trend to the right side is punctuated by direction changes, indicative of shuttle-streaming. Example of such movement can be seen in the supplementary recordings. Due to the lack of resistance in particle flow under the non-oscillatory motor behaviour condition of the model, to-and-fro oscillations in particle flow tend not to accumulate. Under oscillatory conditions, however, interruption in particle flow can aggregate, resulting in stronger shuttle-streaming phenomena (see chapter 16, section 16.2.2).

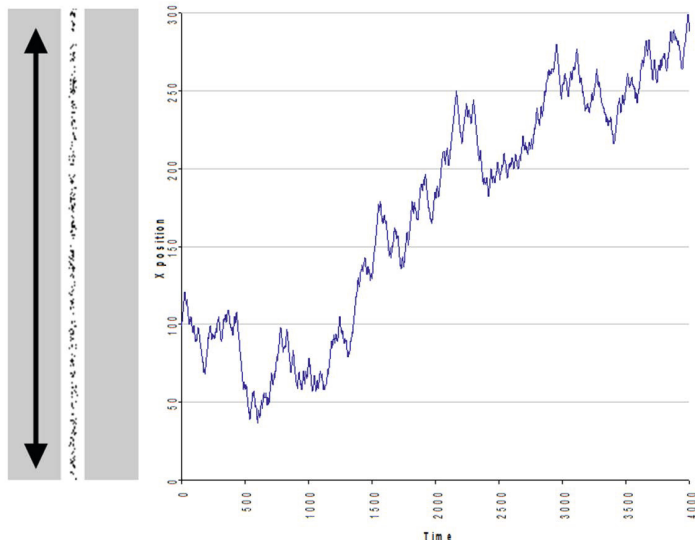


Fig. 3.6 Tracking of single particle shows characteristic shuttle streaming movement pattern. (Left) Particles confined in single path with periodic boundary, (Right) Plot of single particle X coordinate position over 4000 scheduler steps. $P=300$, $SA\ 45^\circ$, $RA\ 45^\circ$, $SO\ 9$.

3.6.3 Formation of Planar Sheet-Like Structures

It is also possible for the emergent agent networks to form uniform sheet-like structures. Fig. 3.7 shows the evolution of the stable $SA 45^\circ$, $RA 45^\circ$ network without periodic boundary conditions. The agents again coalesce into network trails and the contraction behaviour condenses the network until all interior space is removed and a sheet-like mass remains. This sheet configuration also exhibits unusual properties: the sheet itself forms a minimal surface shape and ripple-like activity can be seen to propagate through the sheet (see supplementary recordings). The sheet also shows relatively stable dissipative ‘islands’ of greater trail flow. The islands reflect areas where a temporary vacancy of agents exists. The number and size of the islands is related to the sensor offset distance (SO) of the agents. When the SO parameter increases, the number of vacancy islands decreases and the spacing between them increases (Fig. 3.7). This suggests that the vacancy islands self-assemble based upon SO , agent positions and orientation and represent transient regions of free movement. The $SA 22.5^\circ$, $RA 45^\circ$ networks also condense when boundary conditions are fixed, but no solid sheet-like mass is formed: the branching activity preventing network condensation into a complete sheet structure.

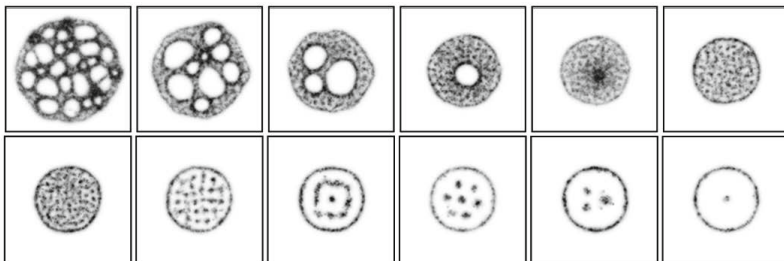


Fig. 3.7 Formation of sheet-like structures and the emergence of dissipative vacancy ‘islands’. Top row (left to right) Network evolution over time: $\%p = 20$ agent trails, $SA 45^\circ$, $RA 45^\circ$. Bottom row (left to right) Dissipative vacancy island patterns at $SO: 9, 13, 19, 23, 28, 38$.

3.7 Factors Affecting Network Dynamics

There are a number of factors which affect the patterning and evolution of the emergent transport networks, which are discussed below.

3.7.1 Sensory Scale and Pattern Formation

The SO parameter (the distance in pixels between the agent position on the lattice and its three forward sensors) acts as a scaling factor. An example of how the SO parameter affects network formation can be seen in Fig. 3.8 for

SO distances of 3, 9, 15 and 25 pixels. The SO parameter affects the scaling of the patterns because the distance from the agent location to the position of the sensors reflects an indirect coupling between separate agents. When SO is small the agent receives sensory input from the chemical cues of only nearby agents and the coupling is weak. With large SO values the increased distance represents a strong coupling between distant agents. The stronger coupling results in coarser patterns with correspondingly large network structures and path thickness. In general terms very small sensor offset distances (SO 3 – 7) result in fine-grained network formation and evolution whilst larger offsets result in coarse-grained networks. As the network scale increases, so does the speed of network evolution. As the network paths are composed of agent particles, network paths formed by agents with larger SO have greater flux than those with smaller SO .

3.7.2 Population Density

The sensor scale may also affect the type of pattern formed, due to interplay with population density. At high population densities, there is less possibility of free agent movement (recall that agents only deposit chemoattractant when a move forwards is successful) and, as the sensor offset scale increases, there is a shift from network / lacunae pattern formation towards striped and spotted pattern formation (Fig. 3.9). The shift in pattern type at high population densities and large sensor scales is due to the fact that the agents free movement is restricted. The pattern of spots seen below (for example, at $\%p$ 90 and SO 27) is actually produced by the formation of vacancy domains — small regions of vacant space surrounded by areas solidly packed with immobile agent particles. At low $\%p$ the patterning is associated with areas of high agent occupancy (and movement) whereas at high $\%p$ the patterning is actually associated with areas of relatively low occupancy (but relatively free movement).

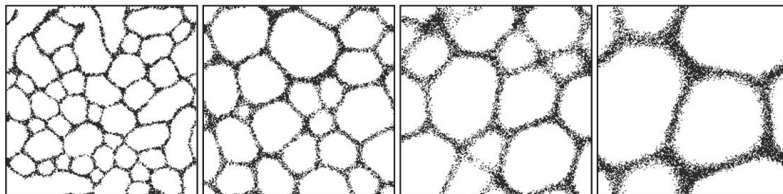


Fig. 3.8 Effect of Sensor Offset distance on pattern scale and granularity. Left to Right: Patterning produced with SO of 3, 9, 15, 25 pixels, Lattice 200×200 . For all experiments: $\%p=15$, $SA 45^\circ$, $RA 45^\circ$, Evolution stopped at 500 steps.

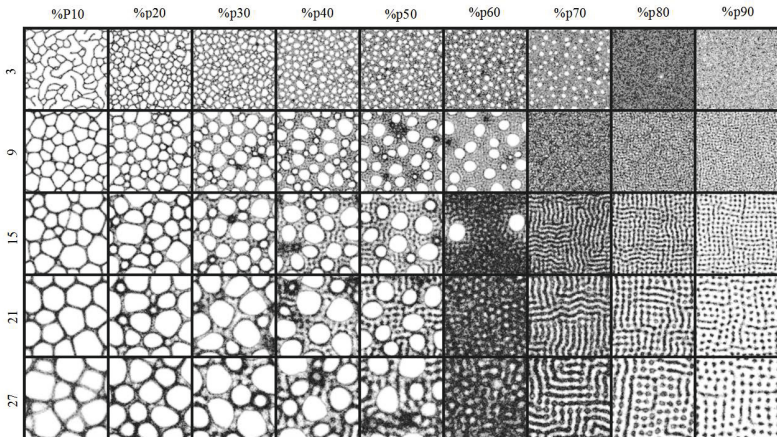


Fig. 3.9 Interaction between population size and sensory scale. Columns: $\%p$, Rows: SO distance, Lattice 300×300 , $SA 45^\circ$, $RA 45^\circ$, Each experiment run for 500 steps.

3.7.3 Diffusion Properties

The pattern formation and evolution is also affected by the parameters which affect the diffusion of chemoattractant within the diffusion map, in terms of concentration, diffusion distance and gradient. Decreasing the damping factor D_d increases the concentration of chemoattractant in the diffusion map, as shown in Fig. 3.10. The increased concentration results in greater attraction of particles over a larger distance (bottom row). At low concentration the particle networks (top row) are more uniform in thickness, at high concentration the networks differ in thickness as clumps of particles aggregate together.

A decrease in D_d results in an increase in overall chemoattractant concentration and chemoattractant path width (Fig. 3.11a). The width of the diffusion kernel D_w also affected the peak height and width of the chemoattractant gradient. Larger kernels distributed the chemoattractant over a wider area, with a lower peak in concentration (Fig. 3.11b).

The diffusion damping parameter D_d affects the cohesion of the particle population. When a plasmodial sheet (a large mass of particles) is formed, the sheet is held together by the mutual attraction of particles to the chemoattractant flux produced by their own movement. The cohesion force minimises the approximate shape of the sheet to a circular form. This cohesion is also affected by the coupling provided by the SO parameter. The results in Fig. 3.12 demonstrate the effect of the damping parameter on the behaviour of a plasmodial sheet. Initially the sheet of particles has a D_d value of 0.05 (i) which results in strong cohesion. When D_d is increased to 0.1

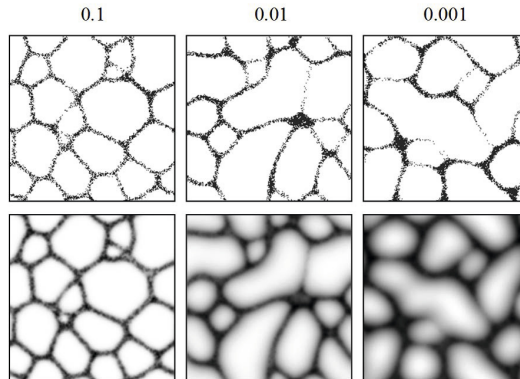


Fig. 3.10 Effect of chemoattractant concentration on network evolution. Top row: Transport networks composed of particle positions, Bottom row: Chemoattractant gradient concentration profile, $\%p$ 10, SA 45° , RA 45° , SO 9, D_d 0.1, 0.01 and 0.001. All experiments run for 500 steps.

(ii) the level of chemoattractant flux falls (see cross-section), as does the cohesion between the particles (visualised by the larger number of gaps between particles) but the cohesion is still strong enough to hold the sheet together. When D_d is increased to 0.5 (iii) the cross-section indicates that there are transient regions within the sheet where no flux is present. The breakdown in flux also occurs at the periphery of the sheet. Because there are regions where no cohesive force exists between the particles, and thus no difference in concentration between unoccupied regions of the environment and some parts of the plasmodial sheet, the approximately circular periphery of the sheet deforms and small pseudopodium-like filaments emerge (iv). These filaments extend and grow outwards from the main mass of particles. Decreasing the D_d parameter back to 0.1 restores the flux density above the zero level and restores cohesion to the mass of particles (v). The pseudopodium filaments begin to retract back into the mass of particles. Decreasing D_d to 0.05 increases the cohesion further (vi) until the plasmodial sheet regains its previous morphology.

The adaptation of the particle population to changing diffusion parameters mirrors the response of the *Physarum* plasmodium to changing environmental conditions. When nutrient conditions are poor the plasmodium extends pseudopodia into the nearby environment in an attempt to locate nutrients [124]. Conversely, when a plasmodium already occupies a rich source of nutrients, energy is conserved by remaining at that site until the nutrients are depleted [12]. The change in dynamical pattern formation by the model population suggests how the changes in the environment may play a direct role in the behaviour of an organism. This suggestion will be further explored in chapter 4.

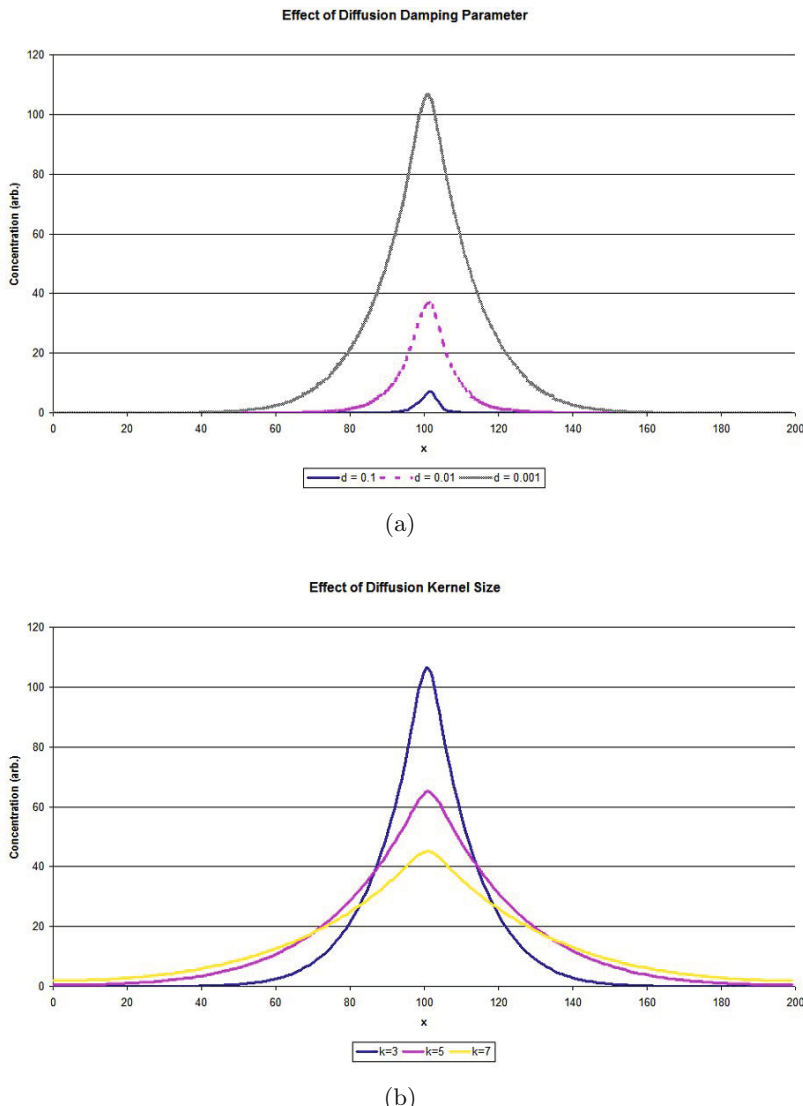


Fig. 3.11 Effect of diffusion damping and kernel size on chemoattractant distribution. (a) Decreased diffusion damping results in increased peak value and chemoattractant path width, (b) Decreased kernel size results in increased peak value and decreasing path width. $p=500$, $SA\ 45^\circ$, $RA\ 45^\circ$, $SO\ 9$, $Dep_t\ 5$, single vertical line of particles with periodic boundary.

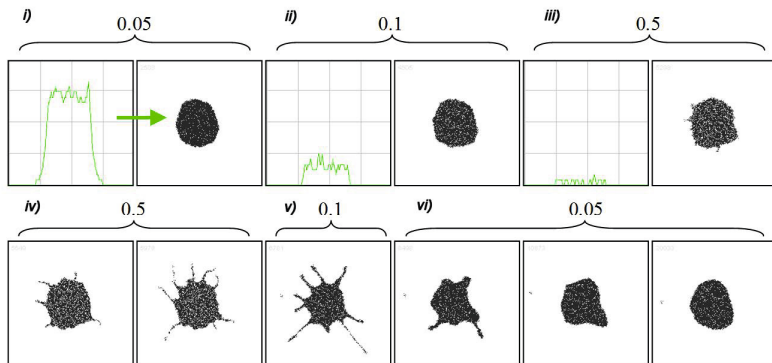


Fig. 3.12 Changes in cohesion result in pseudopodium extension and retraction. (Top row) Plot indicates chemoattractant concentration across arrowed line, (Bottom row) Extension and retraction of pseudopodia due to changes in cohesion (above).

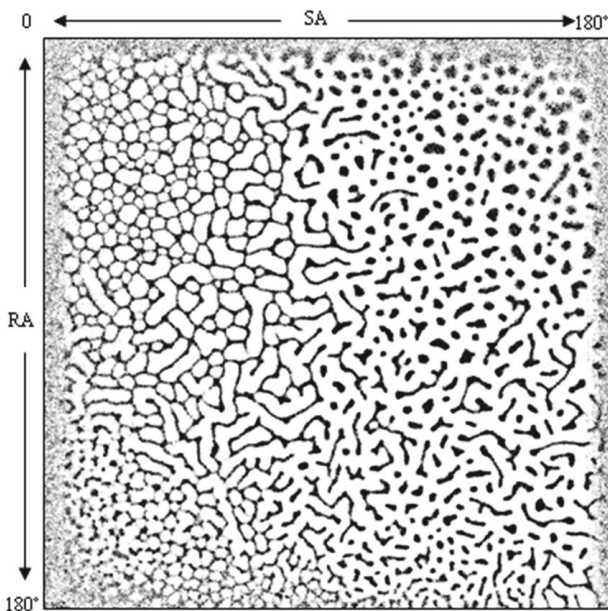


Fig. 3.13 Parametric mapping of *SA* and *RA* sensory parameters. $\%p=20$, *SO* 5, after 400 scheduler steps, *SS* 0.25 per step.

3.7.4 Sensor Angle and Rotation Angle

By adjusting the RA/SA parameters characteristic Turing-type patterns are generated. Fig. 3.13 illustrates the range of patterning when both RA and SA vary from zero to 180° on a fixed population size. A wide range of reaction-diffusion patterning including reticular, labyrinthine and spotted can be observed. The parameter ranges, particularly the sensor angle (SA), affects the cohesiveness of the population. At low SA (e.g. 22.5°) values there are dynamical branching reticular patterns. Increasing SA to 45° results in minimising reticular patterns. Further increases in SA result in labyrinthine and island patterns.

The emergent patterns invoked by the SA parameter are similar, at least superficially, to different pattern types observed in *Physarum* (reticulated networks, pseudopod-like extensions, sclerotium formation) under differing environmental conditions, such as those seen in [124]. This suggests that environmental variations such as substrate hardness, humidity and desiccation may affect the patterning mechanism within *Physarum* in a similar way Fig. 3.14.

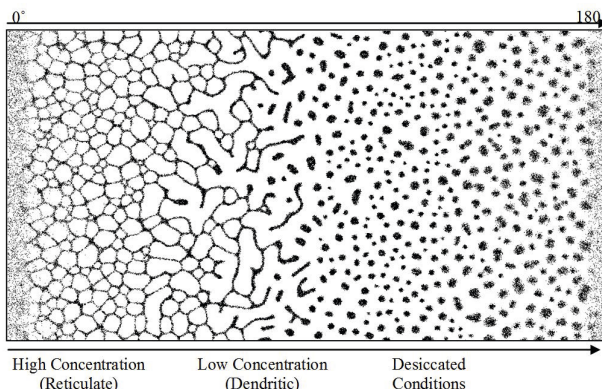


Fig. 3.14 SA parameter reproduces environmental conditions on plasmodium patterning. $SA: 0\text{--}180^\circ$, $RA 45^\circ$.

3.8 From Pattern Formation to Network Adaptation

The default behaviour of the emergent transport networks is a complex and dynamical pattern formation and evolution. Since it is possible to generate complex patterns without pre-existing cues, the presence of externally presented stimuli (pre-existing patterning cues) may be expected to guide, or modulate in some way, the underlying pattern formation process. Results of the particle population response to external (simulated nutrient) stimuli are

presented below. The nutrient stimuli are represented by sources of chemoattractant. The exact location of the source is represented by pixel locations in the agent environment lattice. The concentration of the stimulus is related to the pixel intensity of the stimulus, multiplied by the projection weight $Proj_d$. At each scheduler step locations that are marked by stimulus pixels were projected to the diffusive lattice. The projected stimuli are thus subject to the same diffusion process that applies to the agent produced chemoattractant. The weighting of the pre-pattern stimuli affects both the steepness and the area of the local concentration gradient (Fig. 3.15).

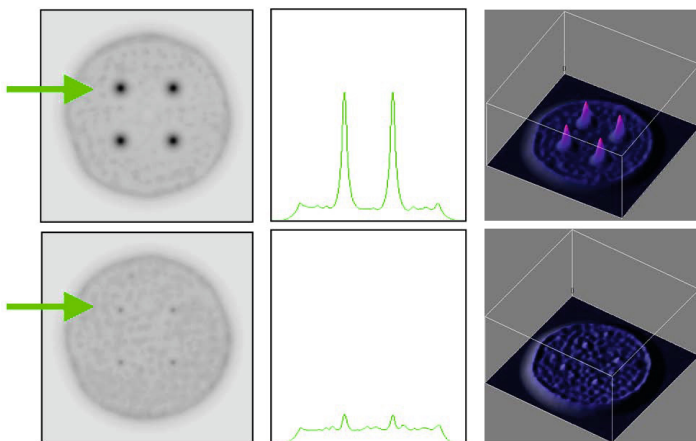


Fig. 3.15 Visualising external nutrient stimuli and the effect of stimuli weighting. (Left to right) Chemoattractant levels of a circular ‘sheet’ of agents with pre-pattern stimuli cues arranged as the four corners of a square, cross-section plot (indicated by arrow), 3D visualisation of chemoattractant concentration Pre-pattern projection weighting $Proj_d$: Top row = 0.06, bottom row = 0.01.

Because the projection stimuli are projected to the chemoattractant flux map, the stimuli act as sources of attractant to the agent population. An example of the effect of simple pre-pattern stimuli is shown in Fig. 3.16. When initialised with a small population size, the network initially emerges in the same way as previous examples. The network soon condenses around the strong chemotaxis stimuli presented by the two stimuli points in a similar effect to that seen by pins constraining soap film evolution [158], and the phenomenon of Zener pinning where dispersed particles affect the evolution of grain growth boundaries [164]. Using these points as an anchor, the network evolves until redundant paths are removed and the shortest path is left. When the number of stimulus sources is increased, the network evolution exhibits minimisation behaviour characteristic of minimum Steiner tree formation (for a given set of points, the Steiner tree represents the shortest amount of connecting material when all points are connected). The tree is

formed when redundant network paths are shortened and closed by the emergent minimisation effects (Fig. 3.17). The supplementary recordings illustrate that the network converges on the final tree shape, despite often following very different dynamic graph trajectories.

3.9 Factors Affecting Network Adaptation

To examine the factors affecting evolution we assessed the simplest case of a three node network where a central node is surrounded by two outer nodes at equal distance and equal angles. A small population (100) was initialised on a horizontal line spanning the three nodes (see scheme in Fig 3.18a).

Initially the angle between the two outer nodes was 180° and this angle was systematically decreased at regular intervals (one degree every 200 scheduler steps), pivoting the outer nodes around the central nodes. When a critical angle was reached the two outer network paths touched near the vicinity of the central node and merged. The mutual attraction of the flows pulled the network away from the central node and the direct connection to the central node was broken by the characteristic ‘zipping’ motif. The zipping behaviour continued until the three competing network flows stabilised at a Steiner point. The critical angle was measured at different nutrient $Proj_d$ of 0.005, 0.05, 0.5 and 5, and at different SO scales of 5, 9 and 13 pixels. A summary of the results is shown in Fig 3.18b.

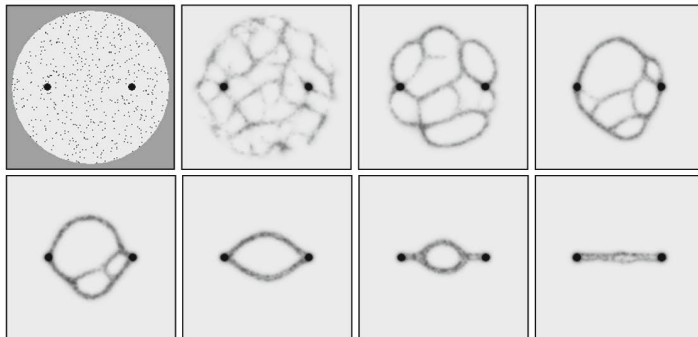


Fig. 3.16 Pattern formation and evolution under the influence of nutrient stimuli. 200×200 lattice, $\%p$ 2, SA 45° , RA 45° , SO 9, (Top Left) Environment shows: pre-pattern cues (dark spots), initial agent positions (small grey flecks) and boundary of the environment (uniform grey), Remaining images (left to right): Evolution of network formation as the network becomes ‘snagged’. Minimisation of the network continues until the shortest path between the stimuli remains.

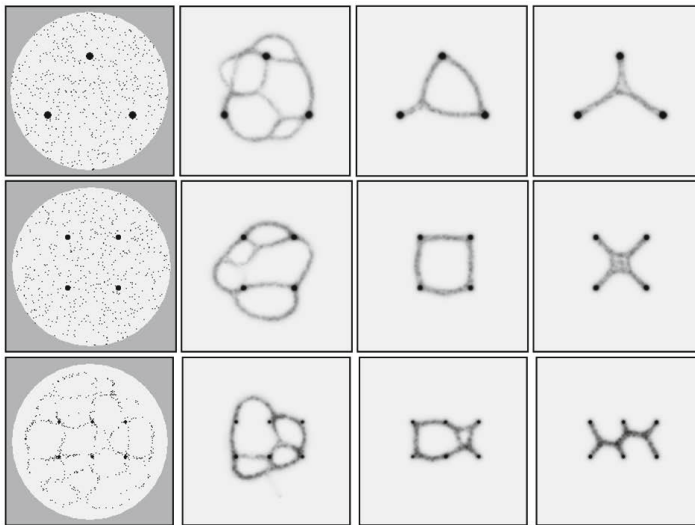


Fig. 3.17 Approximation of Steiner minimum trees in simple nutrient stimuli arrangements. Lattice 200×200 , $SA 45^\circ$, $RA 45^\circ$, $SO 9$, $\%p=2$ (except bottom row, $\%p=1.25$).

The results summarised in the chart indicate that both $Proj_d$ and SO affect the size of the critical angle. Increasing SO distance resulted in the critical angle occurring at larger angles than with smaller SO . This is because a larger sensor offset distance results in thicker network paths and these paths come into proximity with each other at relatively larger network angles. The effect of nutrient concentration, via $Proj_d$ is more pronounced. Smaller weights do not exert as great an influence on the network paths as do larger weights (indeed at $SO 5$ and $Proj_d 0.005$ the attraction of the nodes was not strong enough to constrain the paths reliably, resulting in serpentine foraging network paths, and no information on the critical angle could be obtained). At high projection weights the influence of the nodes resulted in a much smaller critical angle and also a wider region of influence on nearby network paths. Very high concentration could even ‘unzip’ nearby Steiner points, returning the connections to the node itself. The wide region of influence at high concentration is analogous to the influence of different peg diameters in soap film minimisation schemes [165]. High concentration stimuli take the form of a circular area of relatively large diameter which separates the two outer paths connecting to the circle, thus the critical angle can be reduced to a smaller value before the paths contact and merge. Low concentration stimuli result in a smaller stimulus area which is not able to separate the two outer paths to the node, resulting in a larger critical angle before the paths merge.

Although the findings illustrate the critical angle for evolution around a single node of the network it should be emphasised that changes to a single

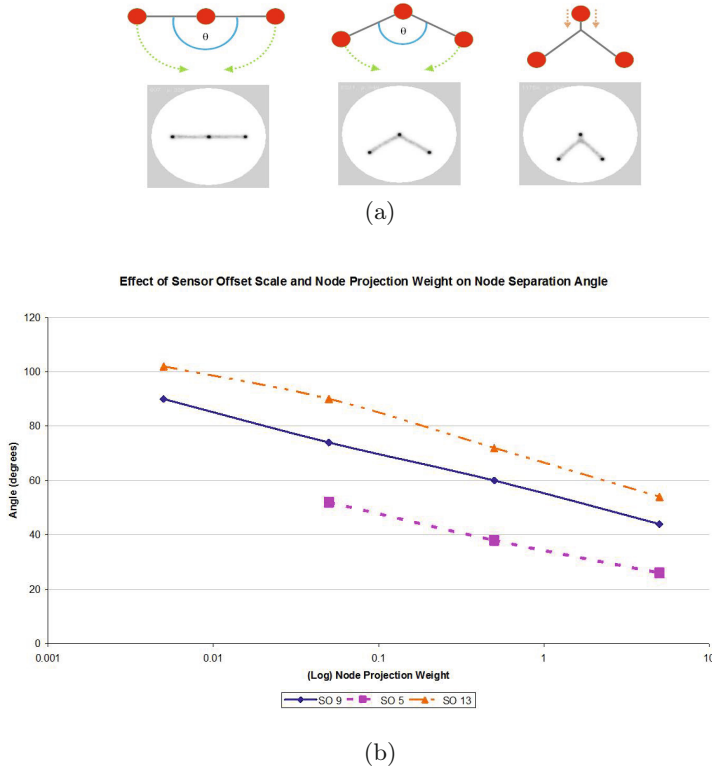


Fig. 3.18 Node detachment angle influenced by sensor scale and nutrient node concentration. (a) Schematic illustration of experimental evolution (top), and experimental snapshots (bottom). Rightmost image shows example just after critical angle has been exceeded and unzipping starts. (b) Plot of critical sensor angle thresholds at different node concentration and sensor offset distances.

node position can have a significant impact on the evolution of the entire network. This is because when the network configuration changes (by zipping away from a node when a critical angle between two outer nodes is reached) this reconfiguration subsequently affects the node angles at other locations in the network. The effects are compounded when one takes into consideration that the network evolution is continuing at all parts of the network simultaneously. The final configuration (if indeed the word final can be used, since the configuration consists of dynamical network flows) only occurs when the flows in the entire network are balanced.

3.10 Observation of von Neumann's Law and Plateau Angles

The evolution of contractile networks shows characteristic evolution dynamics which approximate those observed in soap films, froths and grain growth [157], and lipid nanotube networks [111]. The global dynamics are composed of individual transformations between cells (of lacunae) in the network. A topological reconfiguration known as a *T2* relaxation process is observed when a lacuna surrounded by three paths shrinks (Fig. 3.19, top row). When the lacuna has completely closed the resulting Steiner point stabilises between the three nodes at a typical angle of 120° , demonstrating Plateau angles (a more complete analysis of angle distributions is given in chapter 4). *T1* topological processes are observed when the four or more paths merge (Fig. 3.19, second row). The four way junction is not stable and the paths separate, forming a new edge whose extension continues until the network approximates the Steiner minimum tree.

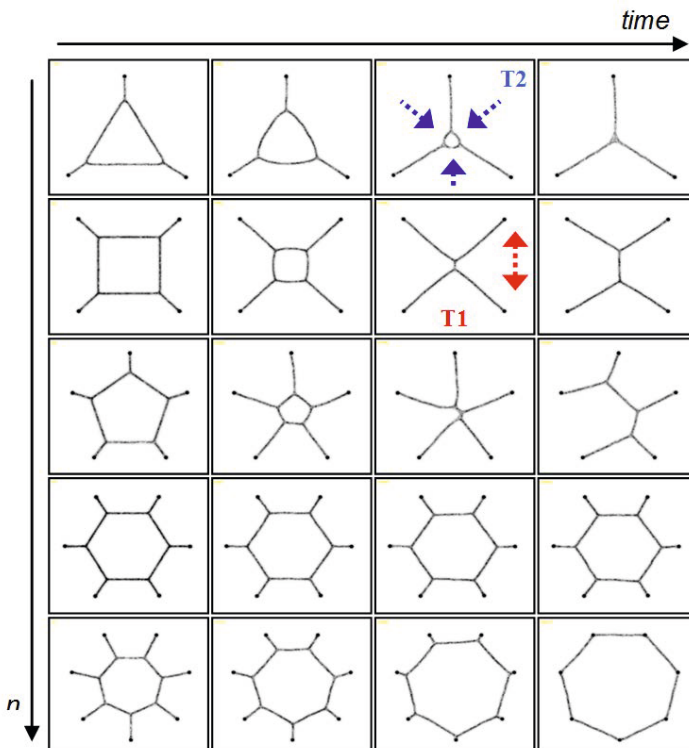


Fig. 3.19 *T2* and *T1* relaxation processes, Plateau phenomena, and von Neumann's law. n represents number of nodes and edges (For explanation of *T2* and *T1* evolution see text).

When the number of nodes increases, network evolution is a complex combination of T_2 and T_1 processes (for example in Fig. 3.19, third row there is a T_2 process relaxation which results in the expansion of two separate T_1 processes). For regular configurations the network evolution observes von Neumann’s law where cells with sides $n < 6$ shrink, cells with $n > 6$ six sides grow in size, and cells where $n = 6$ maintain the same shape.

3.11 Summary — A Virtual Plasmodium

We approximate *Physarum* using a fine-grained bottom-up approach as the coupled interaction of components within the actomyosin matrix. We do not consider the complex chemical and energetic transformations responsible for the individual contractile forces within the plasmodium. However we do consider the local coupling mechanisms by which the individual contractile forces interact. We thus assume that the complex and dynamical patterning of the *Physarum* plasmodium is an emergent property caused by the gel/sol interactions.

We use a multi-agent method in which we couple a population of simple mobile agents to a diffusive chemoattractant lattice. Individual hypothetical units of gel and sol interaction are represented by a single agent particle. Collectively, the combined position and pattern of the population represents the entire plasmodium. The position of the particle represents the presence of plasmodium at a location and the movement of a particle represents protoplasmic flux at a location. The concentration of chemoattractant at individual lattice sites represent the level of protoplasmic flux at each site in the lattice.

The particle population collectively exhibits complex, emergent and dynamical pattern formation by self-organised interactions. The pattern formation behaviour corresponds to the spontaneous pattern formation seen in the *Physarum* plasmodium and, from a broader perspective, approximates a wide range of Turing-like patterning. We found that the emergent transport networks formed by the model exhibited quasi-physical second order properties during their complex evolution, showing complex network adaptation and minimisation and specific motifs within the complex evolution of the networks. These motifs included network branching, network path anastomoses, zipping/unzipping of paths and bi-directional movement approximating shuttle streaming. A comprehensive parametric evaluation characterised the behaviour of the model under a variety of sensory parameter combinations, demonstrating different pattern types and changes in pattern scale. The effect of environmental conditions was explored, including crowding effects in large populations and the effect of diffusion parameters on population cohesion. We examined the effect of nutrient placement, critical angles between nutrients, and nutrient concentration on network adaptation. The quasi-physical behaviours were found to observe Plateau’s phenomena of 120° angles at Steiner junctions and the emergence of network relaxation processes adhered to von Neumann’s law.

The base collective behaviour of the model is that of a virtual material which, by virtue of its complex *Physarum*-like patterning and network adaptation, we may term a ‘Virtual Plasmodium’. In the next chapter we show how the base model behaviour may be used to reproduce the complex biological behaviour seen in *Physarum* under a range of environmental conditions.

Chapter 4

Modelling the Biological Behaviour of *Physarum*

“Then, suddenly, something happened to it. It did not explode. Nor was there any sound. Rather, it seemed to slit open, as if it had been burst into instantaneous bloom by a vast number of white cilia which rayed out in all directions. The instinctive reaction was to jump back from the window away from it. We did.”

(John Wyndham, 1953)

4.1 Introduction

This chapter presents results reproducing a range of biological patterning observed in *Physarum* using the virtual plasmodium model. We demonstrate the initial formation of protoplasmic networks, and the growth and adaptation under differing nutrient concentration and substrate conditions. We conclude by suggesting how the model may provide clues as to the generation of apparently ‘intelligent’ behaviour of the plasmodium.

4.2 Initial Network Formation from Solid Plasmodial Sheet

In an environment with high nutrient concentration an explant of *Physarum* grows outwards radially to form a uniform sheet-like plasmodium behind the growth front. As the growth front moves forwards there is a breaking of symmetry as protoplasm is transported to different regions of the plasmodium, forming a protoplasmic network which becomes sparse over time (Fig. 4.1).

In the virtual plasmodium the mutual attraction between the particles and the chemoattractant they deposit on forward movement results in cohesion of the collective. The uniform structure of the virtual sheet is preserved, despite this uniform pattern being composed of dynamically moving particles. To demonstrate the formation of transport networks from a uniform sheet we

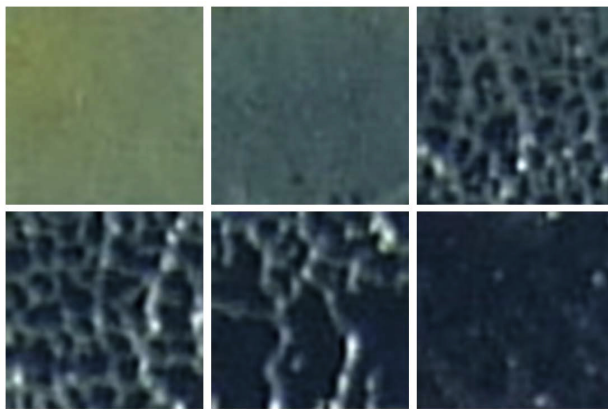


Fig. 4.1 Symmetry breaking in *Physarum* plasmodium to form protoplasmic network (Images courtesy of Andrew Adamatzky)

begin with the simplest case of an idealised hypothetical sheet, a square patch of particles with periodic boundary conditions. When randomly selected particles were removed from the sheet lacunae began to form and grow and the remaining particles self-assembled into networks (Fig. 4.2). When using larger sensor scales the sheet proved more resilient to breakup and the lacunae were more scarce and grew more slowly over time. Smaller sensor scales resulted in less cohesion and a much more rapid breakdown of symmetry was observed with greater initial fragmentation of the sheet.

4.3 Morphological Adaptation of Pre-existing Plasmodia

Initial research into the network adaptation of *Physarum* concentrated on the morphological adaptation of fully grown plasmodia to the placement of nutrients within the environment. When the plasmodium occupies a T shaped piece of agar in which only two branches contain nutrient sources, the protoplasmic network in the branch without nutrients eventually collapses, leaving only the connection between the nutrients. The virtual plasmodium also removes redundant paths, by withdrawing pseudopodia from dead-ends. In Fig. 4.3 a, the virtual plasmodium is initialised in the same configuration as the real plasmodium. The smaller branches in the tube network collapse (Fig. 4.3 b-c) and a pseudopodium retracts from the region without nutrients to leave only the connection between the two nutrient sources intact (Fig. 4.3 d-e).

The selection of a shorter path is also reproduced in the virtual plasmodium. In Fig. 4.4a the virtual plasmodium is inoculated to cover an arena with two nutrient sources, at the top and bottom of the arena, linked by two possible paths. Adaptation of the model population is implemented in this

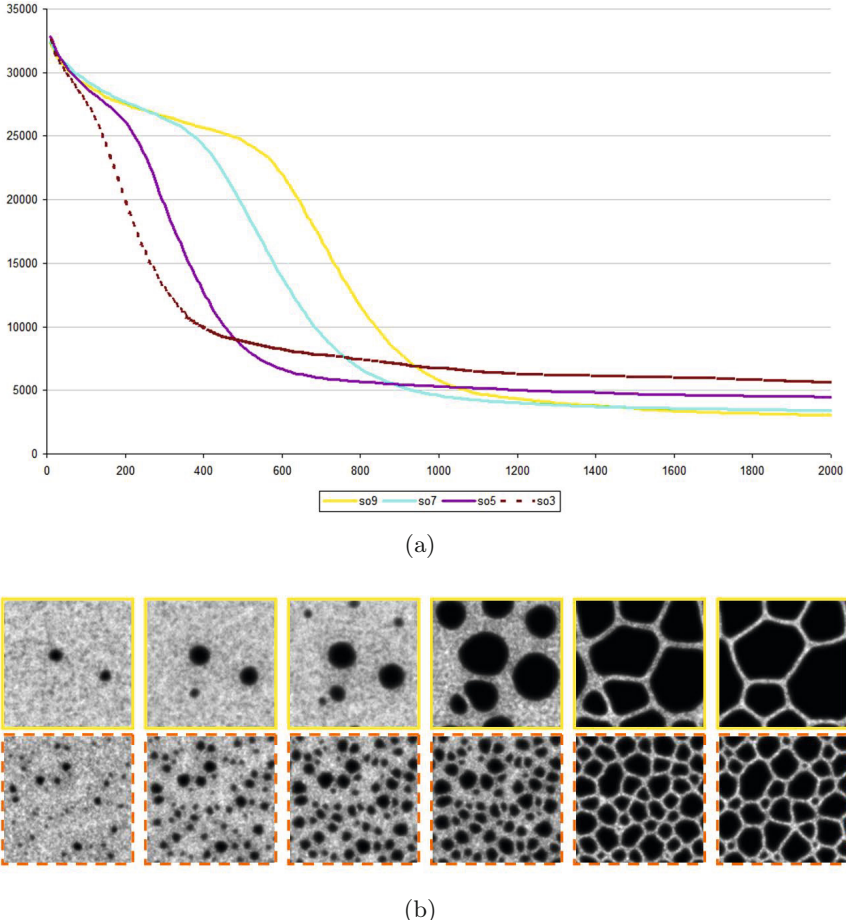


Fig. 4.2 Breakdown of model uniform plasmodial sheet to form transport network. (a) Plot of population size at different SO , (b) (top) At SO 9, time: 400, 450, 500, 700, 1000 and 2000 steps, (bottom) At SO 3, time: 100, 150, 200, 250, 1000 and 2000 steps.

case by randomly removing particles with $p=0.0001$, beginning after 2500 steps. As adaptation progresses the collective shrinks during its adaptation, resulting in the selection of the shorter left path and elimination of flux from the longer right path. The flux of particles through each path, and reduction in size of the plasmodium, is shown in Fig. 4.4b and the selection of the shorter path is indicated by the sudden fall in flux through the right channel after 25000 steps. The graph shows three distinct regions of behaviour during the adaptation, as indicated on the graph. Between approximately 2500 and 10500 steps (Stage I) the flux through both regions is roughly equal.

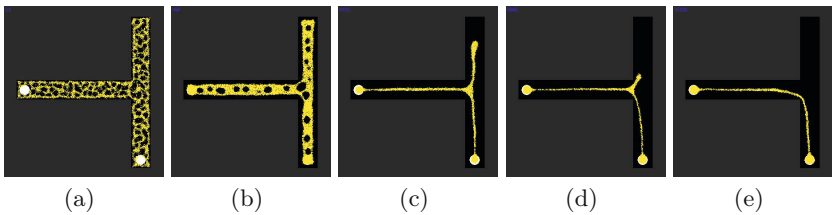


Fig. 4.3 Dead-end removal by the model plasmodium. (a) Virtual plasmodium (particle positions shown) is inoculated in T shape with two nutrient sources (white discs) and initial network forms, (b-e) Network adaptation removes smaller channels and withdraws pseudopodium leaving only nutrient sources connected.

The sharp fall in flux during this time is due to the thickness of the plasmodium in the channels being reduced and flux is equal during this time because the thickness of the plasmodium acts as a buffer or reservoir of particles to reinforce the flux of both channels. During stage II (10500 to 25000 steps) this reservoir of extra material is exhausted and alternation of the levels of flux in the left and right paths is observed as the two paths compete for flux. The shorter left path receives a greater flux of particles as the distance to be traversed is shorter and the bidirectional flux of particles thus reinforces the shorter path. In stage III the flux through the right channel is eliminated as agent particles switch to the left channel.

The selection of a shorter path by path reinforcement reproduces the flux canalisation of the plasmodium tube network. The collective behaviour of the agent population can be interpreted as a auto-catalytic LALI mechanism as it also approximates the foraging behaviour seen in ants [166] which in turn inspired meta-heuristics such as the Ant Colony Optimisation system [69]. Unlike the Ant Colony Optimisation method (which calculates presumed flux based upon path length, in a conventional algorithm), the agent population actually implements the spatial deposition of chemoattractant in the arena.

4.4 Growth and Adaptation of Plasmodial Networks

4.4.1 Dendritic Foraging Growth on Nutrient-Poor Substrates

The foraging and minimisation behaviour of the model closely approximates the behaviour of the plasmodium. In Fig. 4.5 we inoculated a *Physarum* plasmodium (cultivated in plastic containers, on paper kitchen towels sprinkled with distilled water and maintained in darkness at temperature 22–25°C, except for observation and image recording) by placing it on the circled nutrient oat flake (Asda Smart Price Porridge Oats). Periodically the plasmodium was photographed using Nikon S510 digital camera. After covering the nutrient

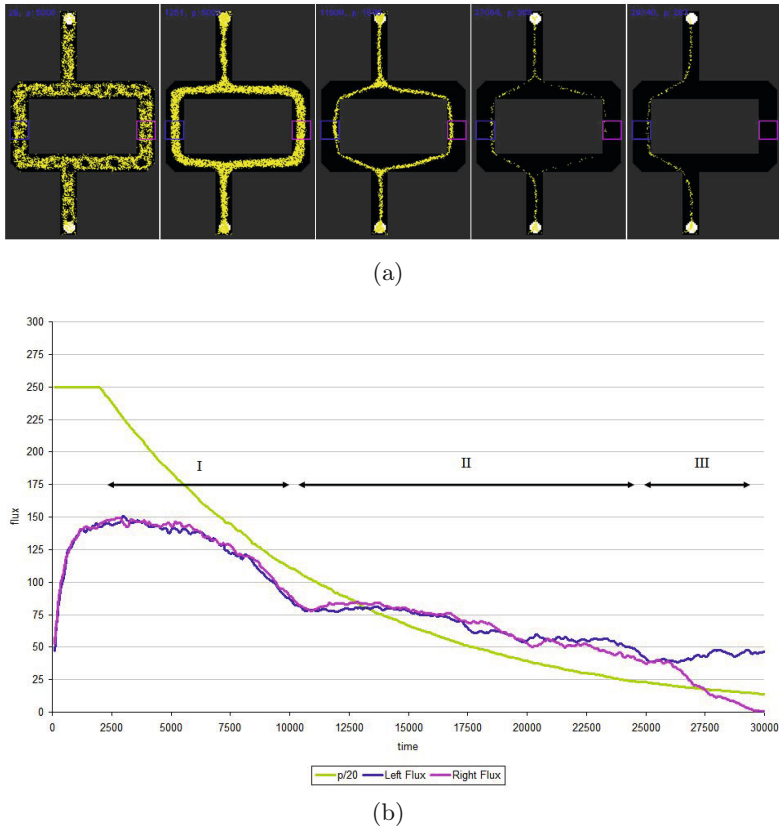


Fig. 4.4 Selection of shorter path by virtual plasmodium (a) Virtual plasmodium (particle positions shown) is inoculated in arena with two nutrient sources (white discs) connected by two paths. Flux is measured in the two path options (square regions) and composite image shows evolution at 29, 1251, 11908, 27064 and 29740 steps. (b) Graph showing flux in both path options (jagged lines) as the virtual plasmodium shrinks (smooth curve).

source the growth front migrates by streaming to nearby flakes, eventually forming a plasmodial network spanning the nutrients.

The virtual plasmodium reproduces the network growth behaviour when inoculated at a single nutrient source (Fig. 4.6). The growing particle collective surges towards nearby nutrient sources with pseudopod-like growth, engulfs them (thus suppressing the diffusion of nutrients from that node), and constructs a transport network which approximates the Steiner tree. When the experiment was reproduced without the condition of suppressing diffusion from nodes when engulfed, full network connectivity was not achieved. The population traversed nearby nodes to the inoculation site but did not explore to contact the remaining nodes (see supplementary recording).

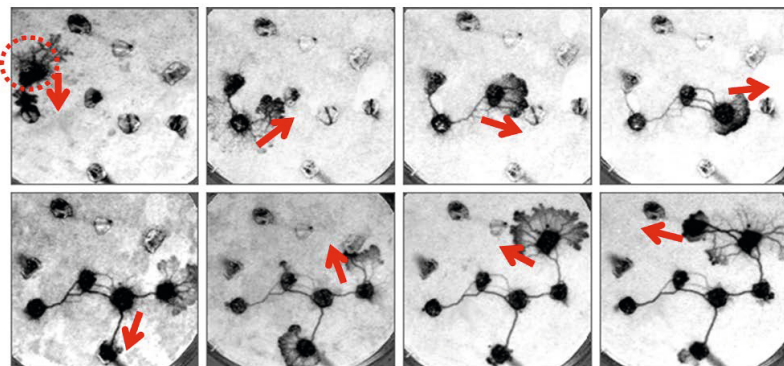


Fig. 4.5 Approximation of spanning tree by *Physarum* in nutrient-poor conditions. Plasmodium is initialised on circled oat flake. Pseudopodia extend from original source towards nearby oat flakes and a protoplasmic tube network connects the nutrient sources. Arrows show current active growth front for clarity.

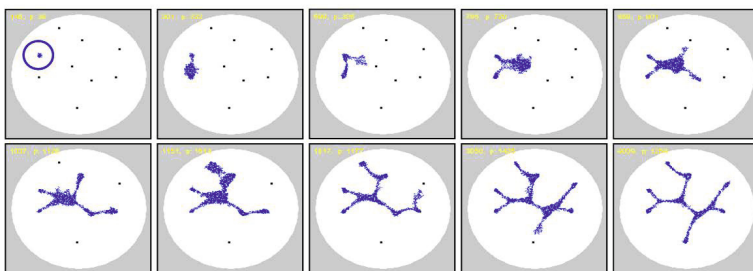


Fig. 4.6 Construction and minimisation of model transport network by pseudopod extension. Nutrient nodes indicated as dots inside circular arena approximating shape of Petri dish. Particles shown as mass of dots. Virtual plasmodium inoculated on left side (circled node). Images show foraging and engulfment of nodes projecting diffusing chemoattractant gradients. Final network configuration approximates the Steiner tree.

4.4.2 Expansive Radial Growth on Nutrient-Rich Substrates

The microscopic self-assembly of the particle networks also show effects in the macroscopic patterns and behaviours of the particle population. Fig. 4.7a shows the growth of *Physarum* from an inoculation seed (oat flake) on a nutrient-rich oatmeal agar substrate. The growth approximates circular wave-front propagation with a thick growth front and radial spoke-like veins connecting the source. By tracking outwards from a single vein from the source flake a hierarchical branching pattern can be observed.

Using the growth behaviours in the particle model, a small population was initiated at a central point on a circular source of nutrients. The nutrient-rich substrate was approximated by projecting diffusive stimuli to the environment. The particles moved outwards towards the chemoattractant, consuming the ‘nutrients’ upon contact. The outward movement provided suitable growth stimuli (space availability) and the particle population increased. As the population grew the particle population adapted its size. Overcrowded particles were removed, mimicking decay of the plasmodium and the patterns were morphologically similar to those of *Physarum* (Fig. 4.7). Adjusting the division probability parameter $pDiv$ maintained the hierarchical branching but altered the density of the particle network.

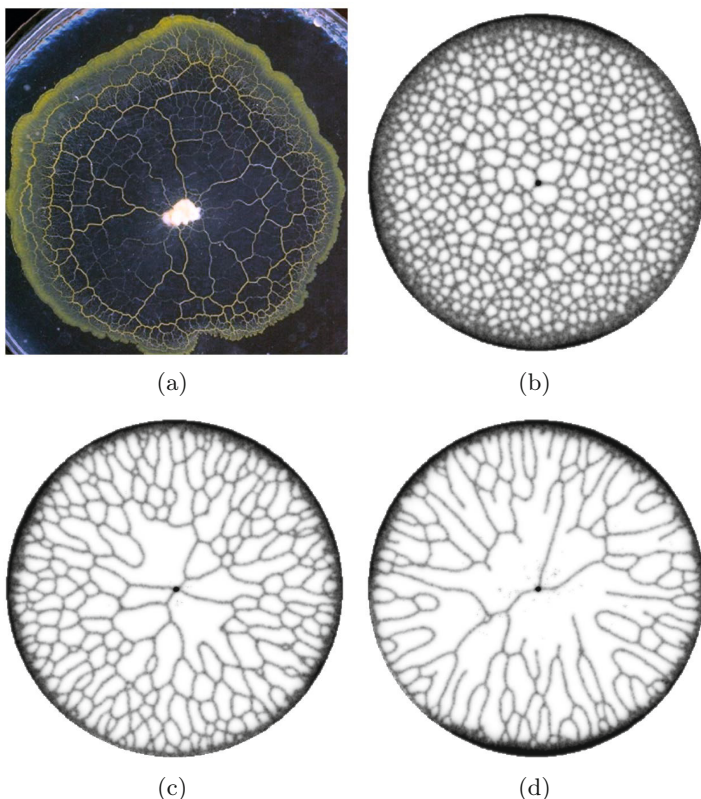


Fig. 4.7 Radial growth of *Physarum* and model on nutrient-rich substrate. (a) Plasmodium of *Physarum* inoculated at oat flake on oatmeal agar (image from [4], courtesy of Andrew Adamatzky). (b-d) Population inoculated at centre of circle. Framework halted when particles encounter border of arena. (b) Growth at $pDiv$ 0.2, (c) 0.08, (d) 0.06.

The emergent transport networks formed by the microscopic interactions of the particle population with their environment reflect not only static pattern morphologies adopted by the *Physarum* plasmodium, but also the long term network adaptation seen in the organism. *Physarum* morphology, evolution and behaviours are strongly affected by the availability, location and concentration of nutrients. The organism appears to behave in a manner which initially optimises (maximises) area exploration and which later adapts its network by optimising (minimising) network distance and network resiliency to damage [9]. The growth and adaptation morphology of *Physarum* strongly depends on the nutrient concentration — high concentration environments generate radial expansive growth whereas low concentration environments result in dendritic growth. Although attempting to characterise the behaviour of such different growth types runs the risk of anthropomorphism, the wave-like (nutrient-rich) behaviours appear more aggressive in terms of the apparent speed of growth and rapid area coverage (see supplementary recordings). The dendritic (nutrient-poor) behaviours appear almost tentative in terms of growth speed and area coverage.

The same morphological and apparent behavioural effects were observed in the particle model when background environmental conditions were modified. Fig. 4.8 and Fig. 4.9 show the effects of high and low concentrations of nutrient substrates on the morphology and collective behaviours of the particle population. The environment is represented by discrete oat flakes (white circles) and nutrient-rich oatmeal agar medium background (grey background). In both experiments identical geometric configurations were used in the environment (i.e. the placement of simulated oat flakes were identical), but the concentrations of the background substrate were different. In both cases the population grows as the environment is searched for nutrients. After the search is complete both conditions spontaneously undergo network contraction and minimisation until minimal network configurations are achieved. In the high concentration condition (Fig. 4.8) the growth is wave-like and expansive and the final network configuration resembles a relative neighbourhood graph with a number of cycles in the network. The growth in low concentration background conditions (Fig. 4.9) shows dendritic growth patterns and the search of the environment is slower. The final network configuration is also more tree-like with only a small inner cycle.

The cause of the differences in growth and adaptation patterns is the background nutrient concentration. In the high concentration condition, the background presents a stronger stimulus to the periphery of the virtual plasmodium and the ‘pull’ of the environment causes expansive movement outwards and provides space for growth. As nutrients are depleted by the outwardly moving population, the background stimulus moves further outward from the edge of the collective and the outer regions of the population move further towards the nutrients. In the low concentration condition the lower background concentration does not provoke such a strong attraction to the population because the nutrient gradients are approximately the same

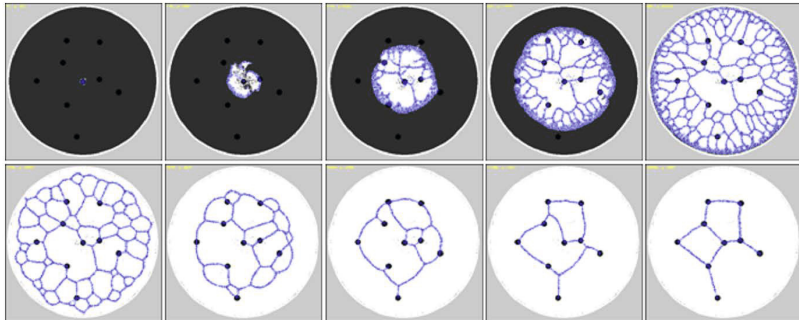


Fig. 4.8 Radial growth and adaptation at high background nutrient concentration. Background nutrient concentration $Proj_d$ 0.01, Population initialised at central node. Images sampled at 11, 110, 213, 327, 487, 1476, 4576, 7004, 11240 and 25000 scheduler steps. Consumed nutrient indicated by white areas.

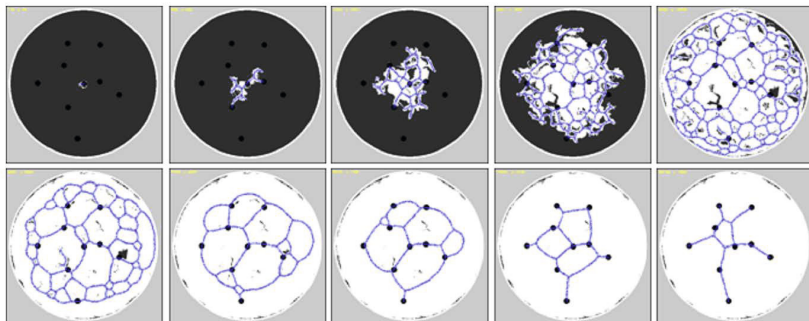


Fig. 4.9 Dendritic growth and adaptation with lower background nutrient concentration. Background nutrient concentration $Proj_d$ 0.001 Consumed nutrient indicated by white areas. Population initialised at central node. Images sampled at 116, 566, 1262, 2361, 3636, 4880, 7448, 9640, 17620 and 36708 scheduler steps.

as the background level of chemoattractant flux. Growth of the population does gradually occur outwards but this is only when significant differences in concentration are created by the local consumption of nutrients by foraging particles. The effect of nutrient concentration on the particle population size can be observed in Fig. 4.10 which indicates the rapid expansion in population size under high concentration conditions (the environmental search is completed at a maximum population size of 21258 at 470 scheduler steps) followed by a rapid initial collapse in population size as network adaptation continues. The low concentration condition shows a slower rise in population size (maximum population of 13574 with search completed in 3440 steps)

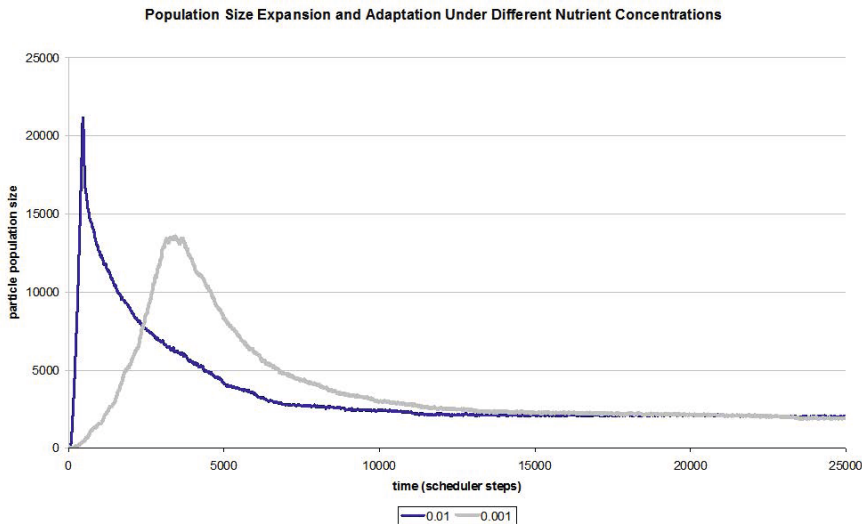


Fig. 4.10 Model population growth and adaptation at different nutrient concentration. Concentration 0.01 indicated by sharp peak in population size, 0.001 indicated by lighter shade and lower peak in population size.

with a slower initial rate of network adaptation. The population sizes of both conditions converge within 15,000 steps although the final network size of the low concentration condition is slightly smaller than the high concentration condition due to the reduced number of cyclic regions in the configuration.

4.4.3 Growth Patterns on Substrates with Varying Nutrient Concentrations

When *Physarum* is inoculated in the middle of an agar dish where one half of the dish is plain agar and the other half is nutrient-rich oatmeal agar, the plasmodium shows preferential growth towards the nutrient-rich side (Fig. 4.11a,b). The growth pattern on the nutrient-rich side is florid and radial, whereas the growth pattern on the plain agar is much smaller and shows a dendritic pattern. The model plasmodium behaves similarly when inoculated in an arena with high concentration nutrient projection on the left and low concentration on the right (Fig. 4.11c), showing much stronger radial growth on the high concentration side and weak growth on the low concentration side.

4.5 Avoidance of Light Hazards and Repellents

Avoidance of light irradiation and chemorepellents was implemented in the model by decreasing the agent sensor values by multiplying by a weighting

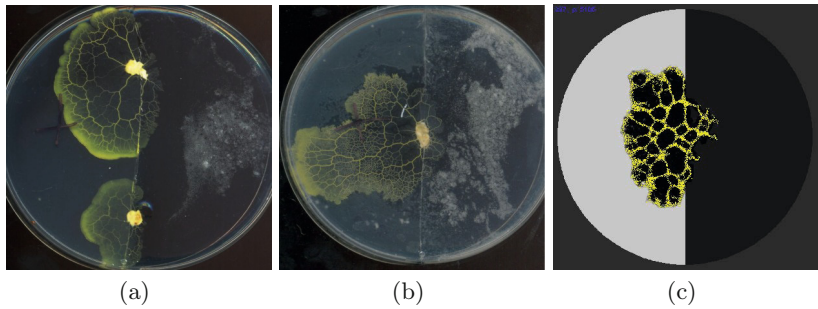


Fig. 4.11 Combination of radial and dendritic growth on dual-concentration substrates. (a) and (b) Plasmodium inoculated at centre line of dish with left side composed of nutrient-rich oatmeal agar and right side plain agar (images courtesy of Andrew Adamatzky), (c) Model plasmodium (particle positions shown) inoculated at centre of dish with left side high concentration and right side low concentration.

factor in areas of the arena exposed to values corresponding to light (L_d , weight factor from 0 to 1, default of 0.2) and repellents (R_d , weight factor from 0 to -1 , default -0.2) respectively. Fig. 4.12 illustrates the response of both fixed and adaptive population sizes to simulated light hazards, in this case vertically placed bars obstructing a straight path between two nutrient sources. For fixed populations the population shifts the bulk of its shape away from illuminated regions (Fig. 4.12, left). In adaptive populations the virtual plasmodium curves around the light obstacles to connect the two nutrient sources at opposite sides of the arena (Fig. 4.12, right), thus reproducing the collision-free path planning by *Physarum* reported in [75].

When growing in an environment containing both nutrients and repellents the *Physarum* growth front extends towards nutrients whilst moving away from repellents. This behaviour was reproduced in the model which avoided the repellent regions (Fig. 4.13, light squares) whilst growing towards and consuming nutrients (dark squares) in the arena.

4.6 Connectivity of Virtual Plasmodium Networks

Baumgarten and Hauser performed image analysis to extract and describe the structure and topology of *Physarum* transport networks [167]. They found that the nodes (junctions) within the plasmodium network had, almost exclusively, degree of connectivity equal to 3. To examine the connectivity of virtual plasmodium networks we adopted a similar approach to that of Baumgarten and Hauser. Transport networks formed by a radially growing virtual plasmodium within a simulated nutrient-rich substrate (Fig. 4.14a) were skeletonised (reduced to single pixel thickness, Fig. 4.14b) using the ImageJ image analysis software [168]. We extended the skeletonisation analysis method of

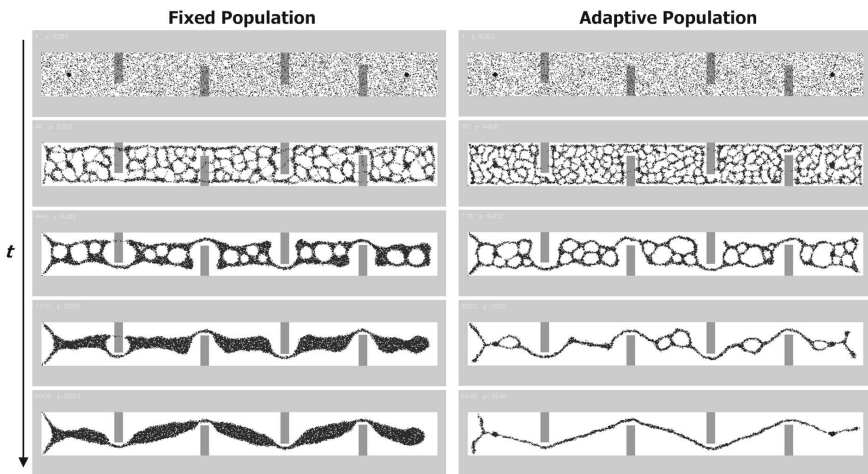


Fig. 4.12 Avoidance of simulated light hazards in fixed and adaptive populations. Population (particle positions shown) is initialised in arena with two nutrient sources at either end interrupted by vertical bars of projected light. Population adapts to avoid migrating onto exposed areas. (left) fixed population, (right) adaptive population.

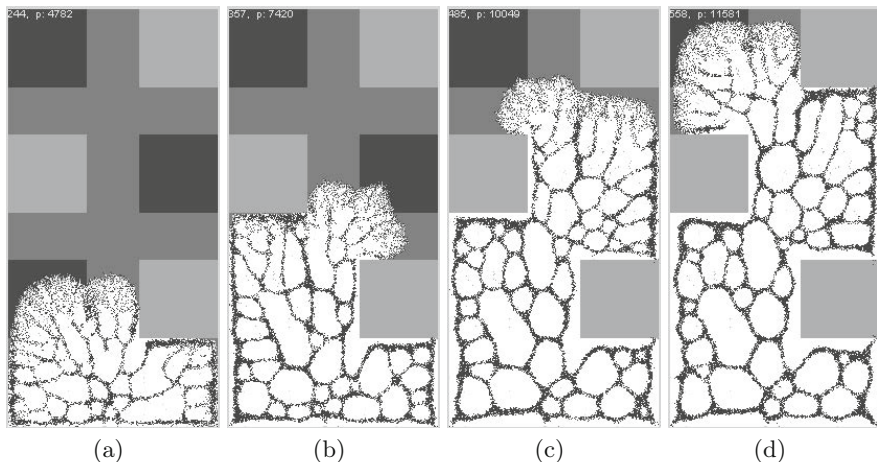


Fig. 4.13 Growth towards attractants and avoidance of repellents in model plasmodium. a-d) Growth of model plasmodium (particle positions shown) on simulated nutrient-rich substrate with high concentration regions indicated by dark grey squares and repellents by light grey squares.

Arganda-Carreras et al. [169] in order to calculate the connectivity information from the skeletonised image data (Fig. 4.14c and d). Analysis of virtual transport networks found that the degree of connectivity matched that found by Baumgarten and Hauser (specifically, a mean degree of 3.02 in a sample of 2069 junctions). The vast majority of junctions were of degree 3 (Fig. 4.15a) and the distribution of angles about these junctions showed that the most common angle was 120° (Fig. 4.15b).

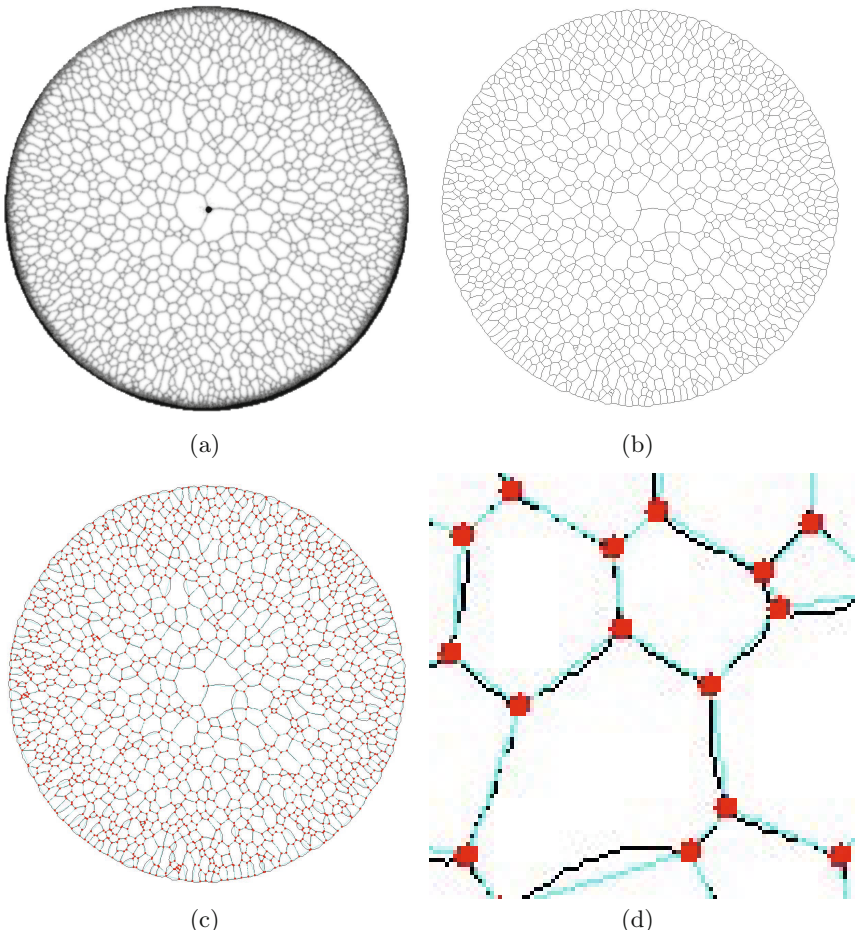


Fig. 4.14 Extraction of junction data from virtual plasmodium network. (a) Emergent transport network formed by growing virtual plasmodium on simulated nutrient-rich substrate, (b) Skeleton extracted from (a), (c) ‘logical’ junction connectivity calculated from (b), (d) Enlarged section from (c) showing junctions (solid discs), original network paths (dark lines) and ‘logical’ paths (pale lines).

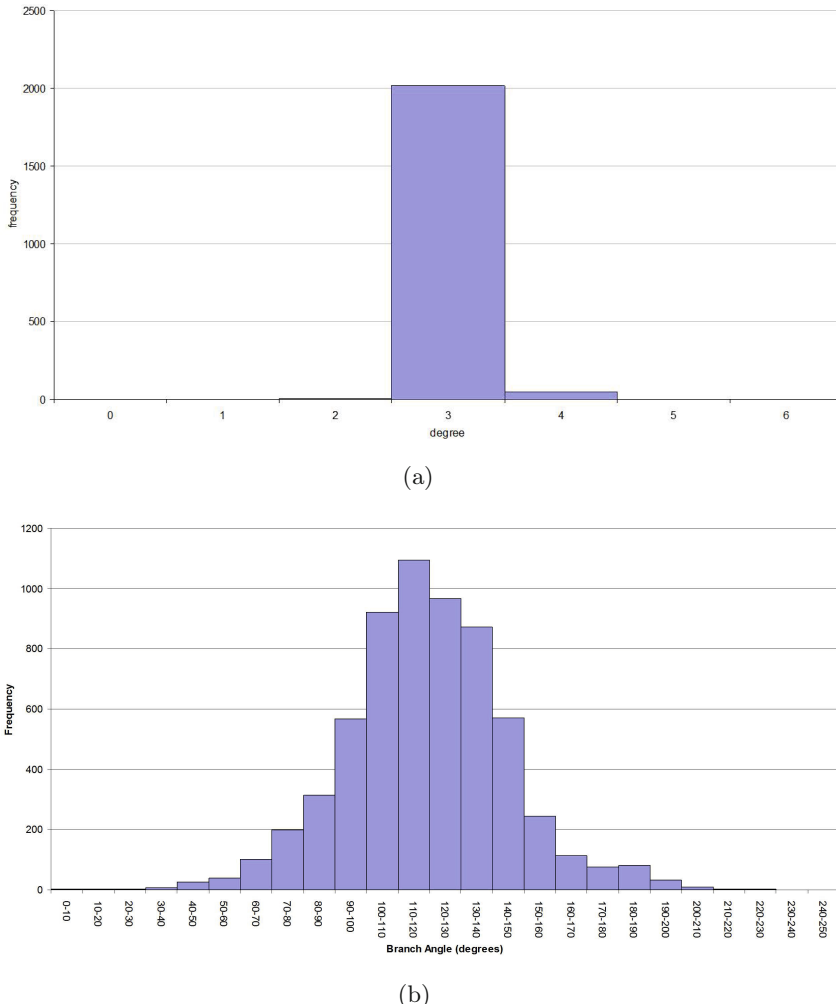


Fig. 4.15 Distribution of degree and angle distribution in virtual plasmodium network. (a) Histogram of junction degree calculated from Fig. 4.14. Number of junctions was 2069 and mean degree was 3.02, (b) Plot of histogram distribution of junction angles showing the most frequent angle of 120°.

4.6.1 Dynamical Evolution of Network Connectivity

Analysis of static snapshots of virtual transport networks does not illustrate the complex evolution of their formation, evolution and minimisation. We developed methods to dynamically track the evolution of connectivity of the networks. A typical example is shown in Fig. 4.16a,b, where a virtual plasmodium is represented by a population of 9600 particles initialised at random

locations in a circular arena containing 100 nutrient nodes. Transport networks spontaneously formed within the ‘plasmodium’. The network became smaller as competing paths merged. The minimisation process was affected by attraction to the nodes which served to constrain the evolution of the network. The majority of the minimisation occurred in the first 2500 steps in both high and low concentration conditions. When high node concentration was used (Fig. 4.16a, projection weight 0.1) the closure of network lacunae was restricted by the attraction of the network to the nodes. At low concentration (Fig. 4.16b, projection weight 0.01) there was less constraining of network adaptation which persisted for a longer time resulting in a shorter overall network (Fig. 4.17a) and larger lacunae (Fig. 4.17b).

To analyse the dynamical changes in connectivity as the network evolution progressed, we analysed the networks every 50 scheduler steps. The network trail images (as per examples in Fig. 4.16a-b) were skeletonised and each skeleton junction point was analysed to assess its degree of connectivity. We implemented the fast skeletonisation method described by Mukundan ([170], and personal communication) to enable the dynamical tracking of junction points (specifically the moving Steiner junction points). The changes in connectivity degree at low and high concentration are shown in Fig. 4.18.

In both conditions there is a steep initial decline in the number of junctions of degree 3, reflecting the initial shrinkage of the transport networks (see supplementary video recordings for a visual illustration). In the high weight condition the evolution is mostly stabilised after 5000 steps with the majority of junctions being of either degree 2 or 3. In the low concentration condition the minimisation (closure of network cycles) continues after 5000 steps with a fall in degree 3 connectivity and a corresponding increase in degrees 1 and 2. The increase in degrees 1 and 2 is visualised pictorially (Fig. 4.16b) as more isolated nodes (degree 1) and the organisation of networks into longer chains of nodes (degree 2) when compared to the high concentration condition (Fig. 4.16a).

4.7 Environmental Factors Affecting Growth and Adaptation

Growth of *Physarum* is dependent on the availability, concentration and placement of nutrient sources in the environment. The plasmodium membrane is sensitive to diffusion gradients and preferentially grows towards nearby sources of nutrients by extending pseudopodia towards the nutrients. Adamatzky found that on nutrient-poor conditions (damp filter paper and oat flake nutrient nodes) the plasmodium initially constructs a spanning tree when inoculated at a single site and constructs networks relating to the upper ranges of the Toussaint hierarchy of proximity graphs when inoculated at multiple sites [80].

To assess the effect of chemoattractant diffusion, nutrient concentration and nutrient placement on the growth in the particle model we inoculated a

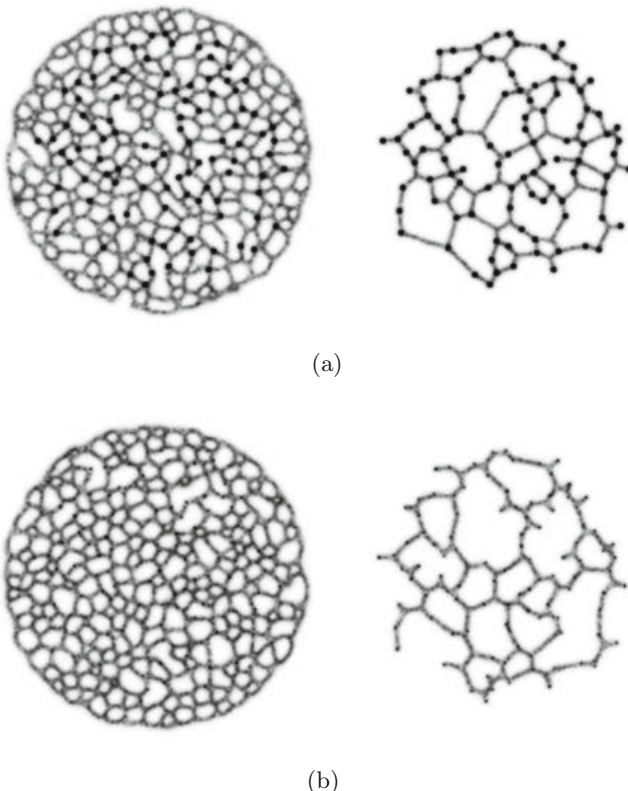


Fig. 4.16 Effect of nutrient concentration on transport network structure in a 100 node network. (a) Initial transport network (left, 102 steps) and final network configuration (right, 14994 steps) at high nutrient concentration. (b) Evolution of network at low nutrient concentration.

small population at a simulated nutrient source. We assumed (as in [80]) that any nutrients covered by the virtual plasmodium would suppress the diffusion of chemoattractant from that source. Fig. 4.19 shows the effects of placing nutrients near the plasmodium. When the diffusing chemoattractant gradient reaches the initial site of population initialisation, the particles closest to the gradient are attracted towards the gradient and move towards it. The movement of the population stimulates flow from the periphery of the collective and a pseudopod-like process emerges and moves towards the source of the gradient. The width of the pseudopodium active region is dependent on the size of the chemoattractant gradient. When the nutrient source is reached the engulfment by the particles suppresses the diffusion from the node and the connection is stabilised and minimised. The adaptation also occurs when stimuli are removed from the environment by retracting the pseudopodium

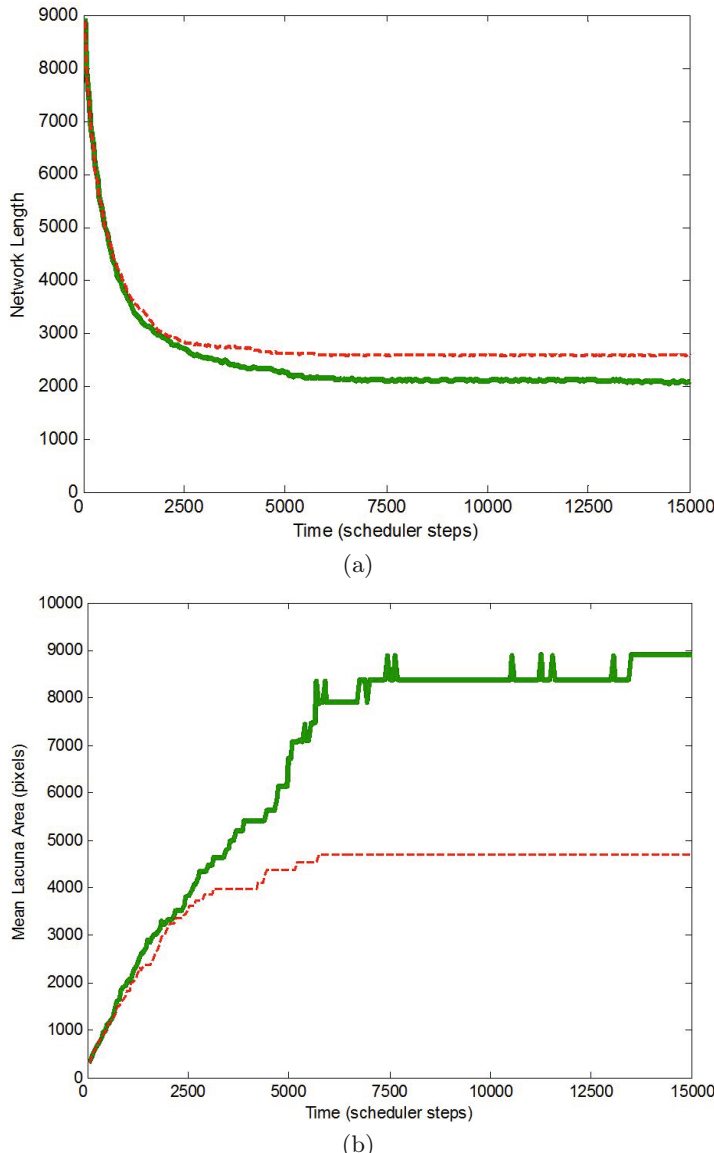


Fig. 4.17 Effect of nutrient concentration on transport network connectivity in a 100 node network. (a) Evolution of transport network length at nutrient concentration 0.1 (dashed) and 0.01 (solid), (b) Evolution of mean lacuna size at nutrient weights 0.1 (dashed) and 0.01 (solid).

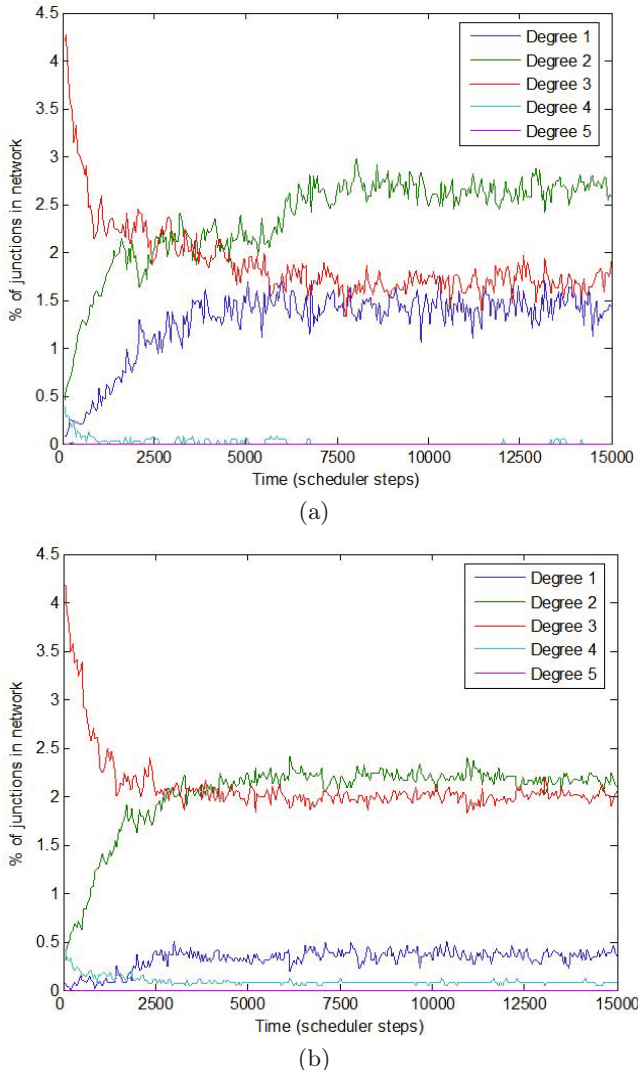


Fig. 4.18 Dynamical evolution of junction degree connectivity at different nutrient concentrations. Plot of the percentage of junction connectivity in the network showing changes in each degree of connectivity as network minimisation progressed.
 (a) Evolution at nutrient weight 0.01, (b) Evolution at weight 0.1.

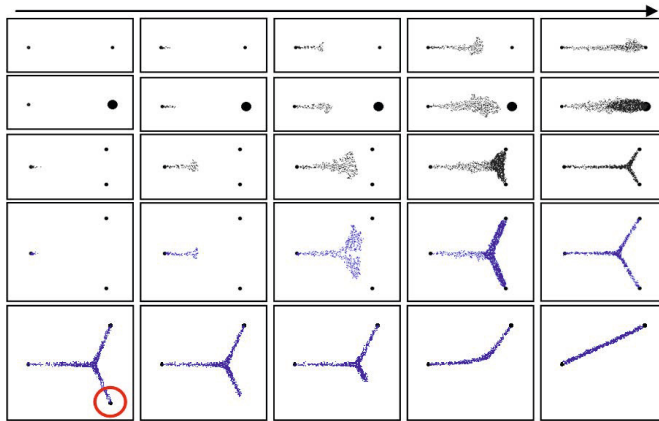


Fig. 4.19 Pseudopodium extension and evolution in model plasmodium: Discovery, pseudopod extension, tube network formation, pseudopod retraction and network adaptation in particle model. Population initialised on left, time progresses in arrowed direction. Nutrient source on right projects chemoattractant into the diffusing gradient field. Pseudopod extension observed as particles multiply. Network minimisation continues once all nodes have been located.

from the deleted source and adapting the network shape in response (bottom row, deleted node is circled).

4.7.1 Nutrient Distance

As the growing population discovers new nutrient sources the transport network automatically adapts its shape in response to the new nutrient sources. Fig. 4.20 shows the network adaptation as information about the nutrient locations arrives at different times due to their increasing distance. The network adapts in response to the changing environment and minimises the distance when all the nutrients are located.

The example in Fig. 4.20 illustrates one mechanism of how stimuli from the environment (diffusion of chemoattractants and differences in the gradient arrival time at the plasmodium) can shape the behaviour of the particle collective. The effect of the environmental conditions on *Physarum* itself was studied by Nakagaki who found that the plasmodium adapted its size and tube network to favour both larger nutrient sources (in terms of surface area) and nutrient sources of higher nutrient concentration [11]. Latty and Beekman demonstrated the effect of nutrient quality on search strategy in *Physarum* when foraging for nutrients and exploiting a nutrient patch [12]. They found that the plasmodium persisted longer at high quality patches of nutrients in

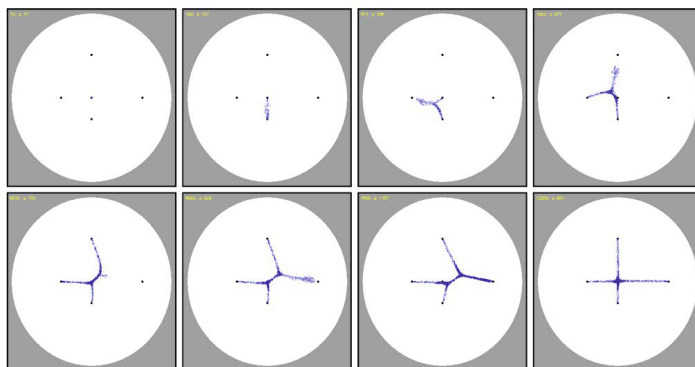


Fig. 4.20 The effect of distance on nutrient discovery and network adaptation. Inoculation of particle population at central node. Closest nutrient source is 50 pixels away. Distances to other nodes are 75, 100 and 125 pixels. Transport network shape adapts as new nutrient sources are discovered. Final image shows optimised transport network when foraging is complete.

order to ‘mine’ the high quality nutrients (an intensive search of the area near the nutrient patch). Lower quality patches resulted in shorter time spent in the region and a more extensive foraging of the environment.

4.7.2 Nutrient Size and Concentration

The effect of nutrient size was studied by inoculating a small population at the centre of a circular arena surrounded by four nutrient sources at identical distances (Fig. 4.21). Each image in the figure shows the concentration gradients (left side of each image) and the particle positions (right side). When nutrient sources were the same size and concentration the particle collective grew by extending pseudopodia towards the nutrients at the same time (Fig. 4.21, left column). When the pseudopodia reached the nutrients the engulfment suppressed the projection of nutrients into the arena and reduced the concentration gradients. When the nutrients were at different concentrations the pseudopodia were preferentially extended in the direction of the strongest nutrients first (Fig. 4.21, middle column). Pseudopodia were only extended to the remaining nutrients (in decreasing order of concentration) when the gradient of the previous nutrient block was suppressed by engulfment. When all sources had been located network adaptation took place (Fig. 4.21, middle column). When the nutrients varied in size only, the concentration gradients from the larger nutrient blocks were larger and pseudopodia were extended to the larger nutrients first. After all nutrients had been discovered the network adapted again to cover the regions of the nutrients but the mass of the population was shifted towards the position of the largest nutrient block (Fig. 4.21, right column, bottom image).

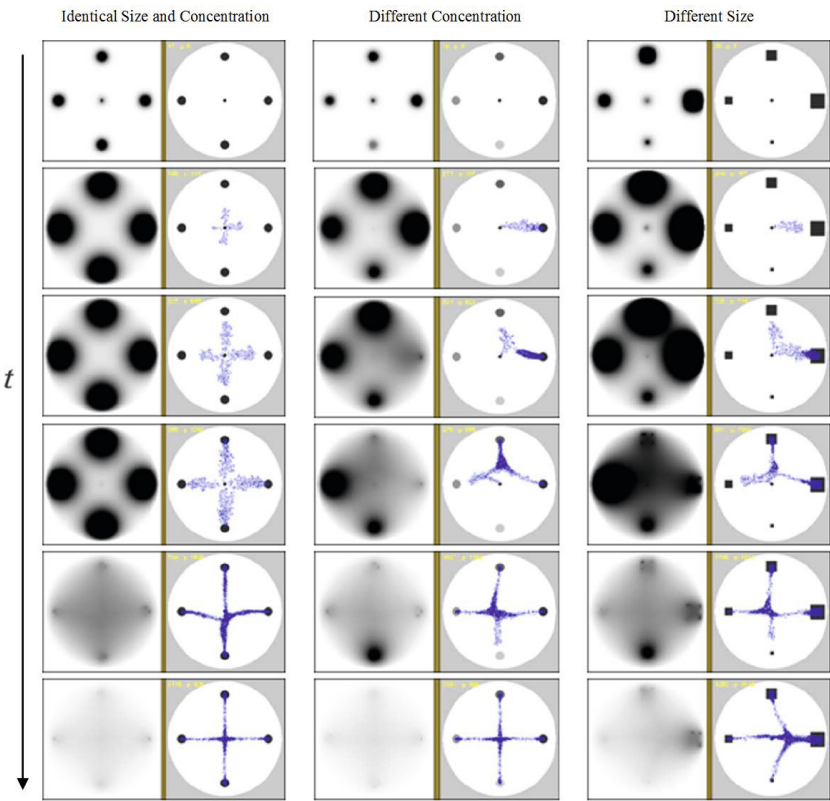


Fig. 4.21 The effect of nutrient size and concentration on network foraging behaviour. Evolution proceeds from top to bottom. Left of each image shows diffusion gradients, right side shows nutrients and particle positions, Left: All nutrients are of equal size and concentration, Middle: Nutrients are of equal size but different concentration, Right: Nutrients are of equal concentration but different size.

4.7.3 Effects of Environmental Noise on Network Adaptation

Plasmodia of *Physarum* live in complex, noisy environments. To assess the response of the virtual plasmodium to noise a noisy environment was implemented by modulating the configuration of an experimental arena with increasing levels of Gaussian noise (Fig. 4.22a-c). The noise contamination presented an extra source of information to the agent particles in addition to the nutrient stimuli nodes. A fixed population was initialised in the arena and formed minimising networks for 20,000 steps. A record of occupancy for every cell in the arena was incremented every time a cell became newly occupied. In the noise free arena the population minimised to a spanning tree structure

(Fig. 4.23a). At increasing noise levels the networks structure contained more cyclic connections (Fig. 4.23c,e) as the noise stimuli caused the population to continue to explore the arena. The plots of cumulative distribution frequencies of occupancy levels indicate that when noise was not present the majority of cells in the lattice were occupied less frequently (during the initial period of network formation and minimisation, Fig. 4.23b). As noise increased the increase in foraging resulted in greater occupancy in more of the lattice sites (indicated by a less steep curve, Fig. 4.23d,f).

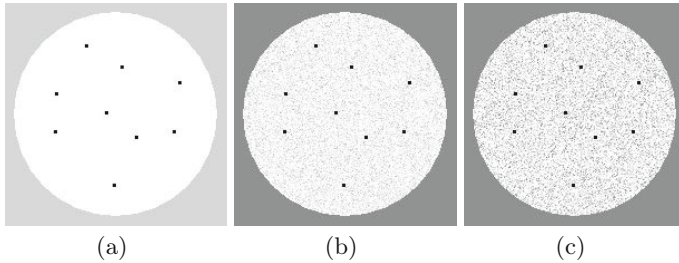


Fig. 4.22 Representation of noise contamination on environment arena. (a) Source data points, (b) Contamination with Gaussian noise $\sigma = 10$, (c) Contamination with $\sigma = 20$ (b and c enhanced by gamma correction for visibility).

4.7.4 Consumption of Nutrients

The suppression of nutrient concentration gradients represents a complex non-linear and dynamical environment as the nutrient gradients are in constant flux. In real world systems the complexity is compounded by the consumption of nutrients. The effects of such complex interactions between spatial position, concentration and consumption are shown in Fig. 4.24. The examples show an initial inoculation site at the bottom centre of a circular arena. Above the inoculation site are three nutrient sources of identical size but potentially different concentration (pixel intensity 255 or 50). In Fig. 4.24i all three nutrients are identical and the pseudopodium grows towards the closest source and extends further pseudopodia as the middle nutrient is consumed and gradients from the outer nutrients reach the collective. A similar situation occurs in Fig. 4.24ii but the migration from the central nutrient is delayed because the nutrient is of higher concentration than the outer nodes and its consumption takes longer. In Fig. 4.24iii both outer nutrients are of higher concentration and, although the collective initially grows towards the closer central node, the mass of the collective extends towards the outer nodes as the gradient is stronger. In example Fig. 4.24iv the growth of the collective towards the central nutrient node is waylaid by the stronger attraction towards the left node. Extension towards the rightmost node only occurs after the majority of the left node has been consumed. Finally, in Fig. 4.24v the

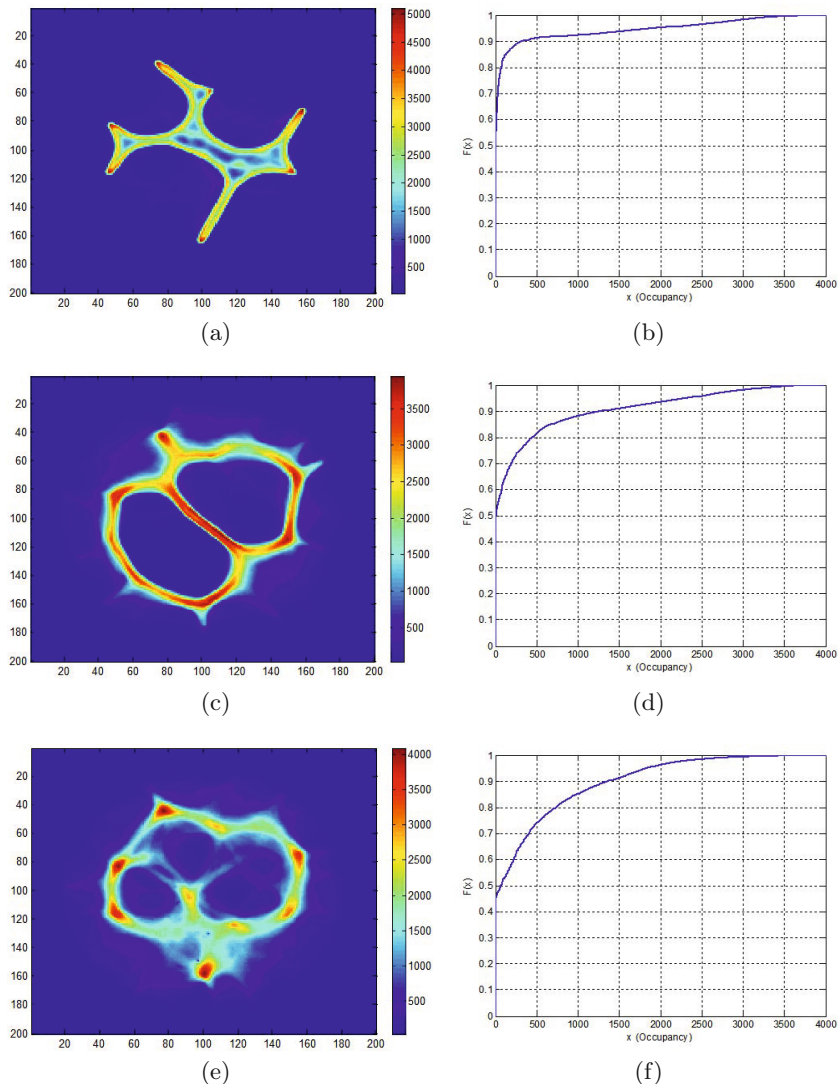


Fig. 4.23 Effect of environmental noise on network adaptation. (a,c,e) Plot of occupancy frequency over 20,000 scheduler steps, (b,d,f) Plot of cumulative distribution frequency indicating occupancy of sites on image at different noise contamination levels.

collective grows towards the (closest) central node and then to the leftmost node which is equal in concentration. Growth towards the node on the right only occurs when the other nodes are mostly depleted.

4.7.5 Effect of Physical Substrate Properties on Growth Patterns

Growth patterns in collective organisms may be affected by the physical properties of the growth substrate. In bacterial colonies the hardness of the growth medium affects the locomotion of individuals and the resulting colony patterns with bacteria, in general, favouring less rigid growth media [108]. *Physarum* also exhibits different locomotion behaviours depending on the properties of the substrate. Takamatsu found that *Physarum* propagates a longer distance and with straighter protoplasmic tubes when the medium hardness increases [124]. Qualitative physical differences in substrates also affect foraging behaviours, possibly by affecting the adhesion of the plasmodium and its slime capsule to the substrate as it moves. Fig. 4.25 illustrates the effect of different substrate medium types on foraging behaviours. Growth on crushed oat flakes on damp filter paper results in aggressive non-uniform growth (Fig. 4.25a), possibly because the uneven surface presents an irregular interface at the periphery of the plasmodium. A relatively smooth nutrient-rich agar medium results in more uniform wave-like expansive growth (Fig. 4.25b).

A similar effect can be elicited in the particle model by a difference in growth behaviour. Non-uniform conditions may be simulated by having new particles select random directions from the particle which spawned them. This results in characteristically ‘aggressive’ foraging behaviours (Fig. 4.26a) with the random direction of new particles creating a writing growth margin. The periphery of the collective shows travelling waves of activity as particles are created and destroyed. The aggressive foraging activity continues long after the nutrients have been consumed and the collective finally shrinks to its minimum size.

Uniform media may be simulated by providing newly created particles with the same direction as the particles which spawned them (supported by the observation that *Physarum* plasmodia often exhibit a characteristic directional persistence to their movement). This results in uniform expansive growth behaviour (Fig. 4.26b). The lack of foraging activity at the growth margin results in a more cohesive population which shrinks when the majority of nutrients have been consumed. A side-effect of the cohesive behaviours is the fact that the shrunken population migrates towards small residues of unconsumed nutrients and extends outwards to engulf and consume them.

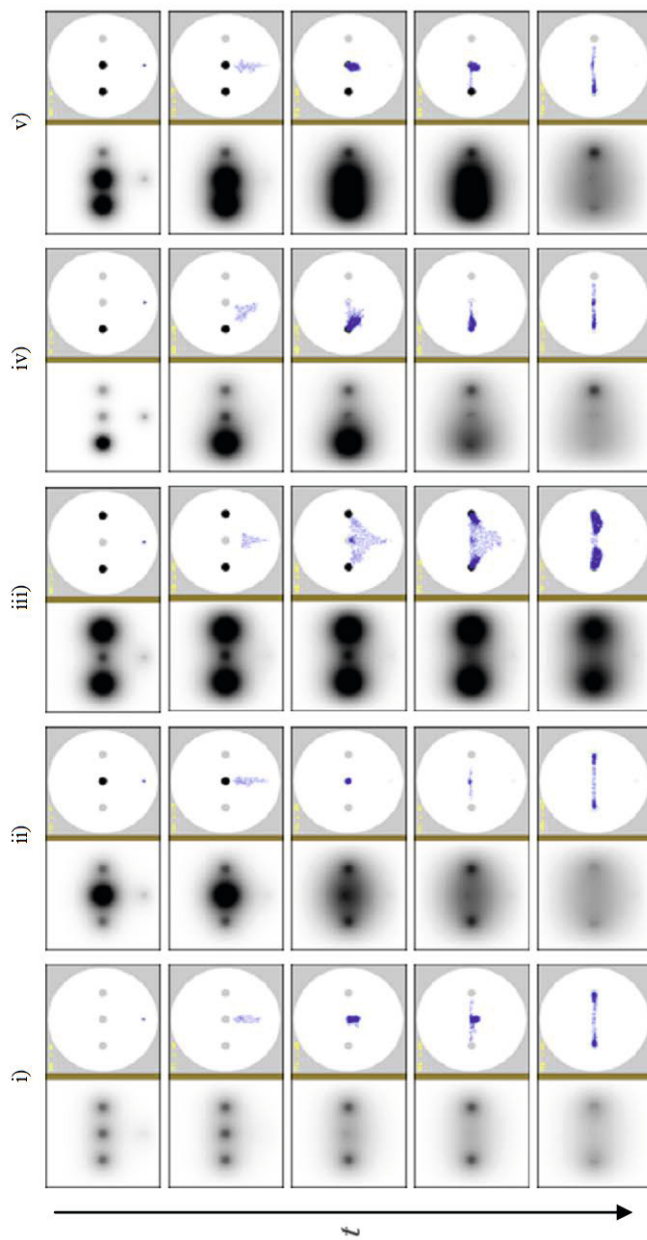


Fig. 4.24 Effect of nutrient concentration and consumption on foraging behaviour. Time evolution proceeds left to right in direction of arrowed t . Left of each image shows diffusion gradients, right side shows nutrients and particle positions.

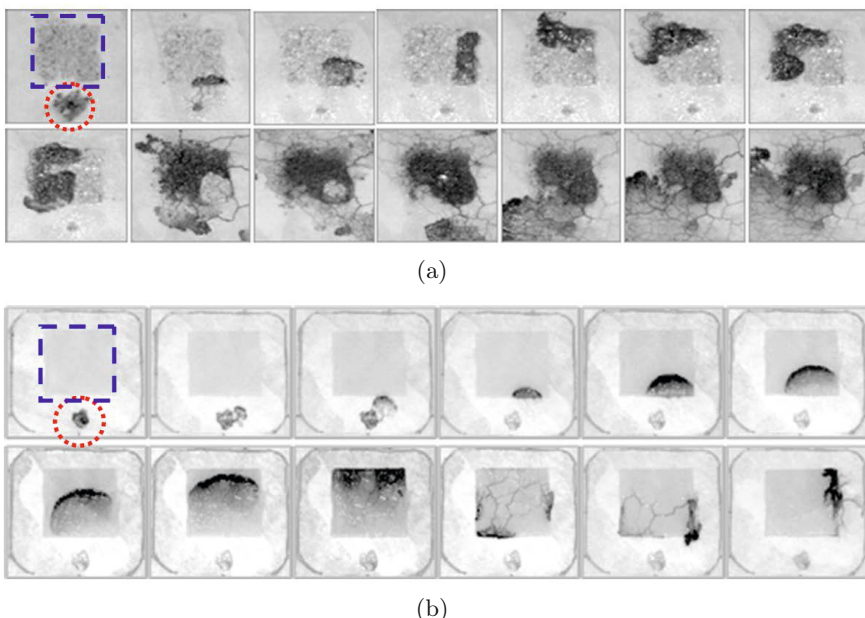


Fig. 4.25 Growth patterns of *Physarum* on different substrates. (a) *Physarum* (dashed circle) inoculated on oat flake at the bottom of the arena migrates towards square area (dashed square) composed of crushed oat flakes. Exploration of environment and consumption of nutrients continues in an ‘aggressive’ manner. (b) *Physarum* (dashed circle) inoculated on oat flake at the bottom of the arena migrates towards square area (dashed square) composed of nutrient-rich oatmeal agar. Exploration of environment and consumption of nutrients continues as a progressive wave-like expansion.

4.8 Summary: Environmental Mediation of Behavioural Complexity

We have reproduced some of the biological pattern formation behaviours of *Physarum* using the virtual plasmodium model. The model demonstrates the formation of transport networks from a solid ‘sheet’ of material, network adaptation of pre-existing plasmodia, selection of shortest path, hazard and repellent avoidance, and network adaptation. A complex foraging ability is observed, capable of distinguishing between the closest, strongest, and largest sources of nutrients in uniform and noisy environments.

It must be stressed that the computational model is an idealised representation of the relationship between the organism and its environment. In real-life the environmental conditions, and thus the gradients, would be far less stable and this may be partially responsible for the relative unpredictability of the behaviour of the plasmodium. The adaptation response (changes in

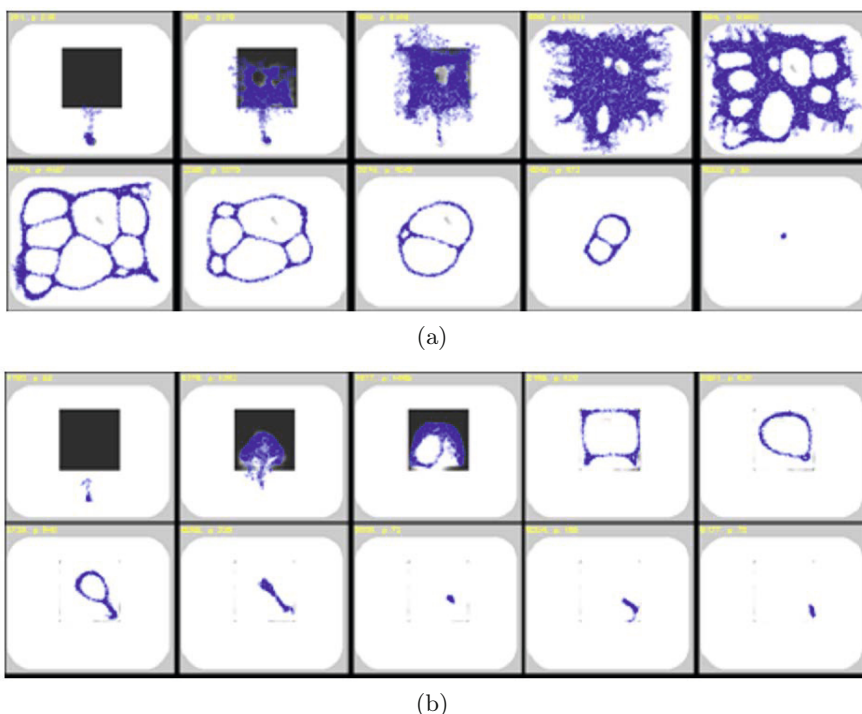


Fig. 4.26 Variations of growth patterns in model via differing growth parameters. (a) Model growth behaviour with random directional selection shows ‘aggressive’ foraging growth. Foraging continues for some time after nutrients have been consumed, (b) Model growth behaviour with identical directional selection (new particle takes direction of previous particle) shows expansive growth and rapid minimisation after majority of nutrients have been consumed. Note that the shrunken collective moves about the arena and consumes remaining nutrients.

morphology) of the particle transport networks in response to environmental changes is also much greater than observed in *Physarum*. This is because the adhesion of the plasmodium to the substrate by the slime capsule (and remnants of old protoplasmic tubes) is not seen in the model transport networks which thus adopts a more idealised minimisation of network length than seen in the organism. The mechanism for population growth and adaptation is also obviously a great simplification of what must occur in the organism, yet is still implemented using constraints which must apply to the organism, i.e. under local, distributed conditions. Despite the idealised relationship between the model, organism and environment the model captures essential emergent behaviours of the plasmodium using only very simple, local and distributed sensory and motor interactions, which is also the case with *Physarum* itself.

Although we have presented a general scheme of an environmentally mediated mechanism for complex morphological behaviours, such a mechanism obviously requires a cellular basis which is not represented in this simulated approximation and is thus out of scope for this model. The cellular mechanism must provide a means of responding to environmental stimuli which come into contact with the plasmodium (sensory behaviours) and a means of generating and directing movement towards (or away from, in hazardous cases) the stimuli. In the particle approximation forward biased movement is intrinsic to the particle specification and the question of how it is generated is not considered.

Nakagaki's seminal experiment exploring complex behaviours in *Physarum* by its ability to solve maze problems [70] provokes questions about the nature of intelligence because *Physarum* does not possess any conventional nervous system or specialised tissue deemed to be necessary for intelligent behaviours to emerge. One possible response is to dismiss the tasks and state that some problems do not actually require intelligence in the first instance. Indeed it is actually possible to perform similar path planning tasks using only physical systems such as chemical reaction-diffusion media [72, 171], or chemotactic oil droplets [71]. However, merely dismissing the task as not requiring intelligence in some way appears to 'move the goalposts' of the definition of intelligence. Would these tasks still be deemed to require intelligence had it not been demonstrated that such a simple organism could solve them?

If we cannot look to the components of *Physarum* itself for clues about its complex behaviours, perhaps some of its abilities can be explained by its complex interactions with the environment. Stigmergic communication has been suggested as a mechanism to encode information about previous actions by individuals in a population [172] and the environment may be considered as an external storage medium. The location and quantity of such stimuli (for example ant corpses or pheromone trails) may be subject to alteration by physical forces such as evaporation or diffusion. In the above examples of maze solving using physical systems, the schemes also make use of the pre-processing of the system by physical forces in the environment, typically diffusion processes. The 'solutions' to the maze are actually methods of displaying the shortest path which has already been computed (in effect, back-tracking to the origin of the gradient).

In the results demonstrated in this chapter, the role of the environment, in particular the diffusion of simulated nutrient gradients, is also critical in invoking an adaptive response from the particle collective. The complex response of the collective is a dynamic interplay between the effect of nutrient gradients at the periphery of the collective (stimulating movement towards the gradient and thus multiplication of the particles) and the changes in gradient concentration caused by engulfment and consumption of the nutrients by the collective. We have shown that such a simple interaction can generate a complex range of *Physarum*-like patterning and foraging behaviours under different environmental conditions.

Optimality in foraging is critical to the survival of organisms and a balance must be found between the cost of searching for new nutrients and the exploitation of the nutrients at the current location. From the results obtained in this chapter we suggest that two-way interactions between the organism and the environment, mediated by the dynamic adjustment of concentration gradients, may provide a suitable mechanism for the complexity of foraging, growth and adaptation behaviours observed in *Physarum*. The mechanism may also provide insights into the apparent intelligence of this simple organism. How can the plasmodium find the optimal (closest, strongest, largest) nutrient sources and exploit and connect nutrient patches efficiently when it does not have the nervous system which would allow it to make informed decisions about such tasks? In higher organisms the foraging behaviour is selected by the organism itself. That is, the organism decides upon, or computes, the foraging choice, which is then executed. In simpler organisms which do not have a nervous system, such as *Physarum*, the environment may be responsible for a greater part of this computation, i.e. for inducing the behaviour in the organism.

Note, however, that *Physarum* is not merely a passive substance reacting to pre-processing by external conditions, nor indeed is there a final static problem solution; the organism morphology reflects, and contributes towards, a continuing adaptive response to current environmental conditions. The modification of nutrient concentration gradients by their engulfment and consumption is in itself a complex modulation of the ‘signal’ which encodes information about the environment.

If *Physarum* does utilise the complex processing of concentration gradients by the environment does this support the view that the organism is not intelligent? Or is the opposite true: perhaps it could instead be viewed as a highly efficient outsourcing of processing which enables a computationally ‘lean’ organism to contribute towards and exploit a highly desirable and efficient search strategy? The adoption of such a mechanism which could exploit natural processing in the environment would prove highly desirable in artificial computing schemes such as distributed robotics which are necessarily limited in computational abilities and power consumption. Examples of how the multi-agent virtual material approach may be used to reproduce the computational abilities of *Physarum* are described in the following chapters.

Chapter 5

Implementing Neural Phenomena in Unorganised Non-neural Substrates

“Blind man running through the light of the night with an answer in his hand.
Come on down to the river of sight and you can really understand.”

(Neil Young, 1970)

5.1 Introduction

Living organisms perceive their environment with a wide variety of special sensory modalities. Enhancing the contrast in the stream of information from these senses allows organisms to discriminate between small changes in signal level, potentially enhancing survivability. Lateral Inhibition (LI) is a neural mechanism which enhances the activity of neurons directly exposed to excitatory stimuli whilst suppressing the activity of their near neighbours (see Fig. 5.1 for a schematic illustration). LI phenomena have been described in auditory [173], somatosensory [174] and olfactory senses [175], but are most famously described in the visual systems of a wide range of animals, including humans [176, 177, 178].

5.2 Computing Without Neurons in Slime Mould

LI phenomena, and the mechanisms which generate them, result in an effective and efficient means of enhancing environmental perception in organisms containing nervous systems ranging from the most complex to the most primitive. But can such mechanisms occur in organisms which do not possess any nervous system? As we know slime mould does not possess any neural tissue which could be used to enhance environmental perception. Furthermore, the organisation of the plasmodium ‘material’ is unorganised and constantly changing its morphology. Nevertheless, we also know that the plasmodium

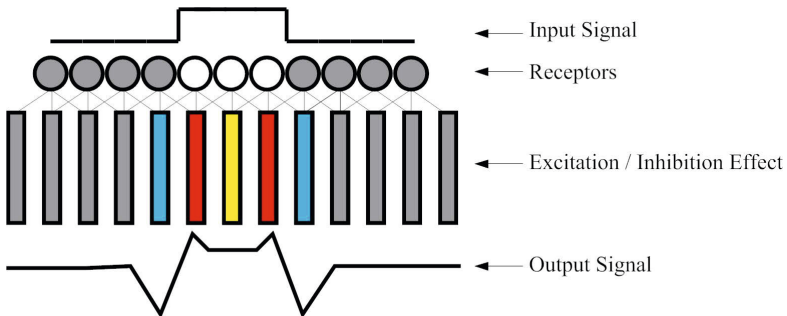


Fig. 5.1 Schematic illustration of Lateral Inhibition response. Original stimulus (top) activates neurons (circled) whose local inhibitory wiring results in excitation and inhibition effects in neighbouring neurons (bars), resulting in the enhanced output signal (bottom).

can forage towards nearby sources of attraction (and away from local repellents). Is it possible that the plasmodium possesses unorganised mechanisms which are analogous to LI phenomena?

In this chapter we take inspiration from very simple organisms, such as slime mould, without neural tissue which nevertheless exhibit very complex behaviours. We describe collective mechanisms by which sensory contrast enhancement phenomena analogous to LI phenomena can emerge in disorganized non-neural systems. We use the multi-agent particle based model to demonstrate and elucidate the low-level behaviours which generate these collective phenomena. In Section 5.3 we describe the parameters used for the experiments in this chapter. In Section 5.4 we examine the emergence of LI phenomena in the model in response to presentation with attractant stimuli. The opposite response — Lateral Activation — is described in response to presentation with adverse stimuli (simulated light irradiation) in Section 5.5. In Section 5.6 we show how a *global* collective representation of an environment (in this case an approximation of overall brightness) can be generated by bulk drift of population density in response to greyscale spatial patterns presented as attractant stimuli. We conclude in Section 5.7 by summarising the results, the main contributions of this chapter, and examining potential applications of these collective phenomena for computing and robotics applications.

5.3 Model Parameters and Problem Representation

It was shown in [179] (see Fig. 3.7) that large SO values result in regular self-organised domains ('vacancy islands') of small vacant regions in the material. This would not be desirable in these experiments as we gauge the response of the material by measuring population distribution density (which would

be affected by the presence of these domains), so we randomly selected the *SO* parameter for each particle, at each scheduler step, from the range of 1 – 20 pixels. This maintained the cohesion of the material whilst avoiding the formation of these vacancy domains. Variations in both *SA* and *RA* parameters have been shown to generate a wide range of reaction-diffusion patterns [179] and for these experiments we used *SA* 60° and *RA* 60°.

The presentation of simple uniform attractant stimuli to the virtual plasmodium was achieved by incrementing attractant values by 1.275 units at stimulated regions every scheduler step. The presentation of Adverse stimuli (simulated light irradiation) to the model was achieved by reducing the sensitivity of the particle sensors in illuminated regions by 80% and reducing particle chemoattractant deposition in the same regions by 80%.

Representation of more complex stimuli with difference brightness levels (Section 5.6) was achieved by incrementing attractant values by the corresponding stimuli image pixel brightness at each location on the lattice and scaling this value downwards by multiplying by 0.01. The reduction in attractant concentration by scaling reduces the attractant stimuli concentration towards the baseline flux generated by the particle movement and maintains the integrity of the virtual plasmodium (stronger stimuli would cause the material to tear). Diffusion within in the lattice was implemented at each scheduler step and at every site in the lattice via a simple mean filter of kernel size 5×5 . Damping of the diffusion distance, which limits the distance of chemoattractant gradient diffusion, was achieved by multiplying the mean kernel value by 0.95 per scheduler step.

5.3.1 Interpretation of Neuronal Responses in Non-neural Mechanisms

To explore mechanisms corresponding to LI in non-neural systems we must translate the relevant neuroscience terminology into terms which can be represented in the model system. Input stimuli (such as light to the human visual system) can be represented in the model by spatial projection of simulated chemoattractants. These stimuli attract the particles comprising the virtual plasmodium. We may say that the projection of chemoattractants results in an excitatory response. Conversely we can generate an inhibitory response by the spatial projection of repellents or other adverse stimuli. Slime mould is known to avoid illumination with certain wavelengths of visible light and we can use this feature to generate an inhibitory response in the model.

The basic responses of excitation (by chemoattraction) and inhibition (by repulsion or irradiation) are short term approximations of the neural response. To approximate long-term neural responses (changes in spatio-temporal patterns of neural activity) we must utilise the changing spatial density distribution of the particles comprising the model material, in response to the projected stimuli, i.e. changes in the population density correspond to regions of increased / decreased neural activity. The model must

also respond to the withdrawal of stimuli. In neural systems this would result in a reversion to baseline activity. In the model this must be represented by the restoration of uniform population density on withdrawal of the stimuli.

5.4 Lateral Inhibition Phenomena via Attractant Stimuli

We initialised the virtual plasmodium comprising 8000 particles within a 300×100 pixel tube-like horizontal arena bordered by inhabitable areas on the top and bottom and open ended left and right edges. Periodic boundary conditions were enforced. We measured population density across the arena by counting the number of particles in the Y-axis for each X-axis position. We recorded population density every 10 scheduler steps. After initialisation the population, constrained by the architecture of the arena, formed a single tube with relatively uniform population density (Fig. 5.2,a and density plot in b).

An attractant stimulus was presented to the virtual plasmodium after 500 scheduler steps by projecting chemoattractant into the middle-third habitable section of the arena (white region in Fig. 5.2,c). The attractant stimulus caused increased flux of particles into the stimulus area, an increase in population density in this area, and a corresponding decrease in density outside the stimulus region (Fig. 5.2,e and plot in f). Upon removal of the stimulus after 4000 steps the population was no longer attracted to the central region and the tube adapted its shape in response to the uniform chemoattractant profile (Fig. 5.2,g and plot in h). The population density eventually returned to uniform density across the arena (Fig. 5.2,i and plot in j).

A space-time plot of the population density indicates how the changes in population density are initiated at the stimulus boundaries and propagate outwards from these regions (Fig. 5.3). Regions inside the attractant stimulus area correspond to excitation areas and regions outside correspond to inhibited activity. The presentation of attractant stimuli, and the response of the particle population, causes an increase in signal contrast (measured in terms of population density) between stimulated and non-stimulated areas (Fig. 5.4).

5.5 Lateral Activation Phenomena via Adverse Stimuli

To examine the collective response to Adverse Stimuli (simulated exposure to illumination, which the *Physarum* plasmodium avoids), we used the same arena with the virtual plasmodium inoculated as a horizontal strip with approximately uniform density (Fig. 5.5, a and density profile in b). The stimulus pattern was again in the central third of the arena, but the attractant region was replaced with a region of simulated illumination. Particles at the border of exposed areas preferentially moved to unexposed regions and the

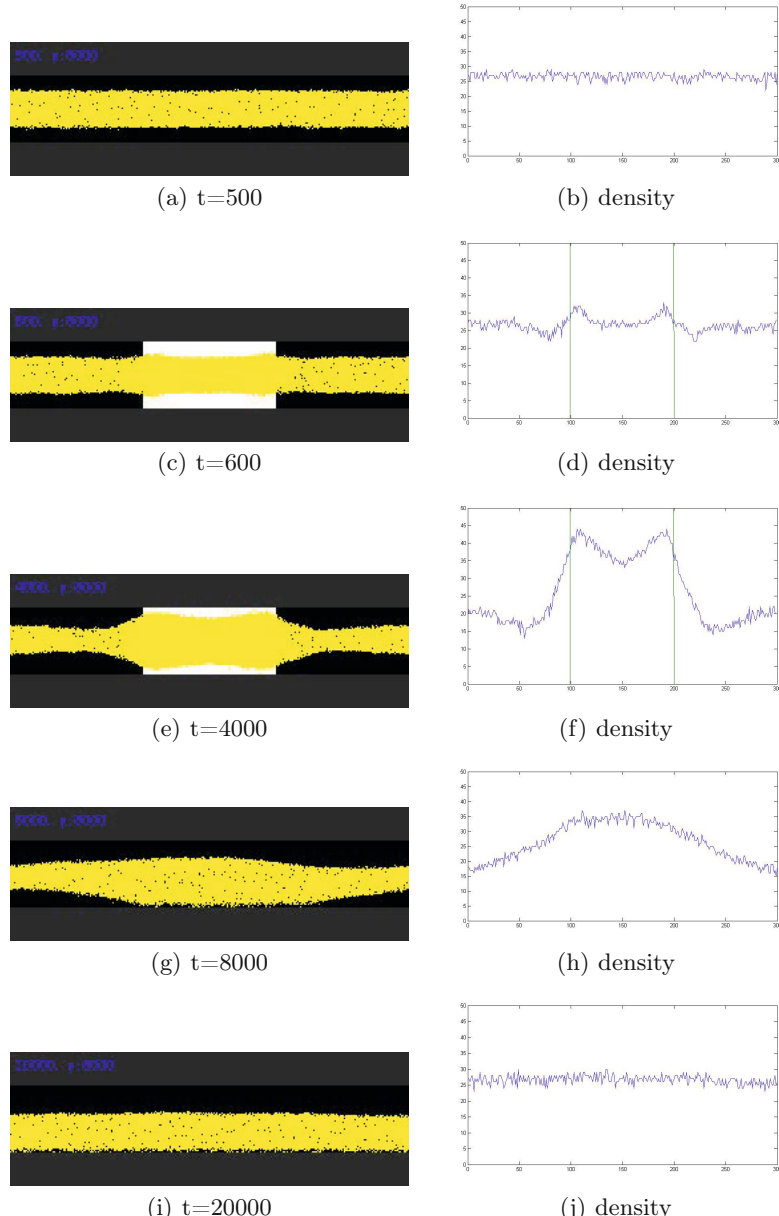


Fig. 5.2 Response of virtual plasmodium flux to attractant stimulus. a) population initialised within horizontal arena forms single tube, c) presentation of attractant stimulus bar (light area) results in flux towards stimulus area, e) population density is increased at stimulus region and reduced at unstimulated region, g) removal of stimulus results in adaptation to uniform attractant profile, i) uniform density is restored, b,d,f,h,j) cross-section plots of population density across the arena.

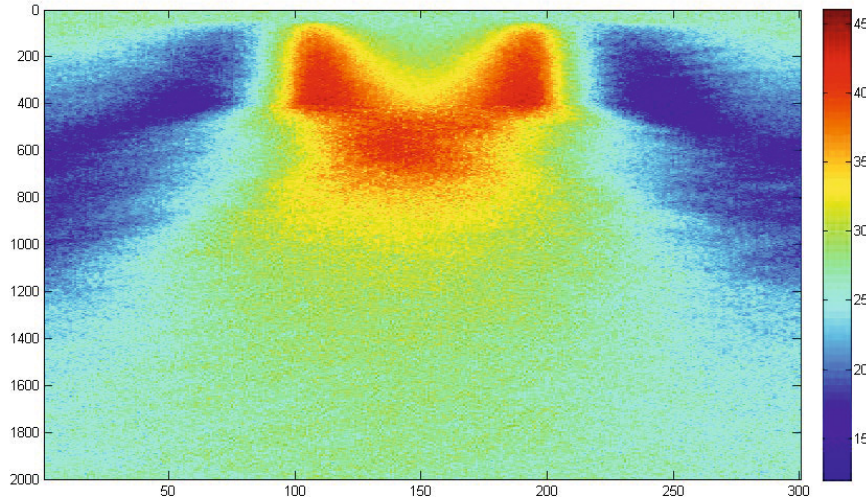


Fig. 5.3 Space-time plot of population density flux under attractant stimuli conditions, time proceeds downwards. Note that changes in density are initiated at borders of the stimulus boundary.

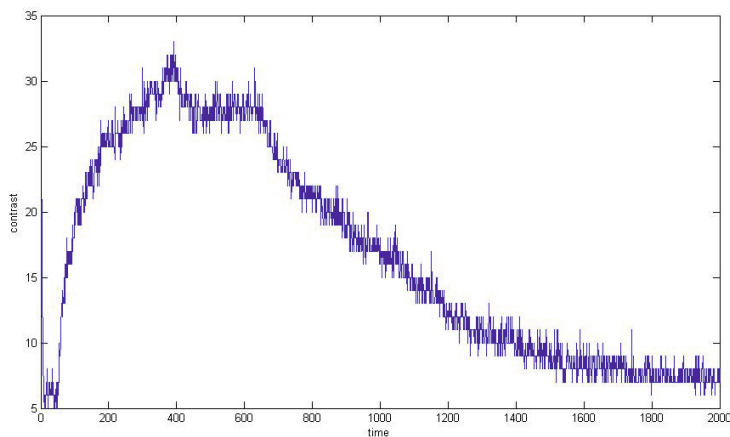


Fig. 5.4 Presentation of attractant stimuli and its effect on population density, interpreted as signal contrast enhancement. Stimulus presented after 50 samples ($t=500$), stimulus removed after 400 samples ($t=4000$) causing gradual reversion to baseline activity.

local coupling of particles resulted in collective flux away from the stimulus area (Fig. 5.5, c and e). The resulting density profile (Fig. 5.5, d and f) demonstrates the inhibition effect within the illuminated region whilst the un-exposed neighbouring regions show an increase in population density. When the adverse stimulus was removed from the central region the population density re-normalised to a uniform level within 15000 steps (Fig. 5.5, g and i and corresponding density profiles in h and j respectively). The space-time plot of changing population density shows the inhibition effect in the central region and the lateral propagation of increased density (Fig. 5.6). Areas inside the adverse stimulus correspond to an inhibition response and areas outside correspond to excited activity. As in the attractant stimuli case, the presentation of adverse stimuli increases the signal contrast (population density) between illuminated and non-illuminated regions (Fig. 5.7).

5.6 Towards Unorganised Collective Perception

The changes in population density over time in response to patterns of attractant and adverse stimuli correspond to unorganised Lateral Inhibition and Lateral Activation mechanisms respectively. How do these mechanisms respond to more complex arrangements of stimuli? We examine the response of the virtual plasmodium to attractant stimuli in the pattern of the Chevreul staircase illusion (Fig. 5.8a). The Chevreul staircase is a sequence of identical width uniform vertical bars. Each bar is lighter in intensity than its leftmost neighbour (see cross-section intensity plot in Fig. 5.8e). Although each bar is uniform in intensity the image is typically perceived as having a scalloped profile across each bar, i.e. the left side of each bar (when adjacent to a darker bar) is perceived as being lighter, and the right side of each bar (when adjacent to a lighter bar) is perceived as being darker. The mechanisms underlying this illusory percept are considered to be mediated by activity at the retinal and cortical levels [180], [181].

We initialised the virtual plasmodium (comprising 169,402 particles) on an arena patterned with the Chevreul staircase image (692×288 pixels). Each vertical bar corresponded to increasing concentration stimuli. Periodic boundary conditions were used and two bordering bars offering no stimuli were placed at the left and right of the image. The initially uniform distribution of particles (Fig. 5.8b) was affected by the attractant stimuli and particles migrated to regions of higher concentration. The flux of particles changed the population density, with higher occupancy emerging in regions which corresponded to lighter areas of the original image (Fig. 5.8c). Note that within each bar the density is greater towards the left side of the bar. This is caused by influx from the darker bar to the left and efflux towards lighter bars to the right. A plot of the population density at 400 scheduler steps demonstrates both the scalloped response to each bar junction and the global increase in density towards the lighter bars (corresponding to

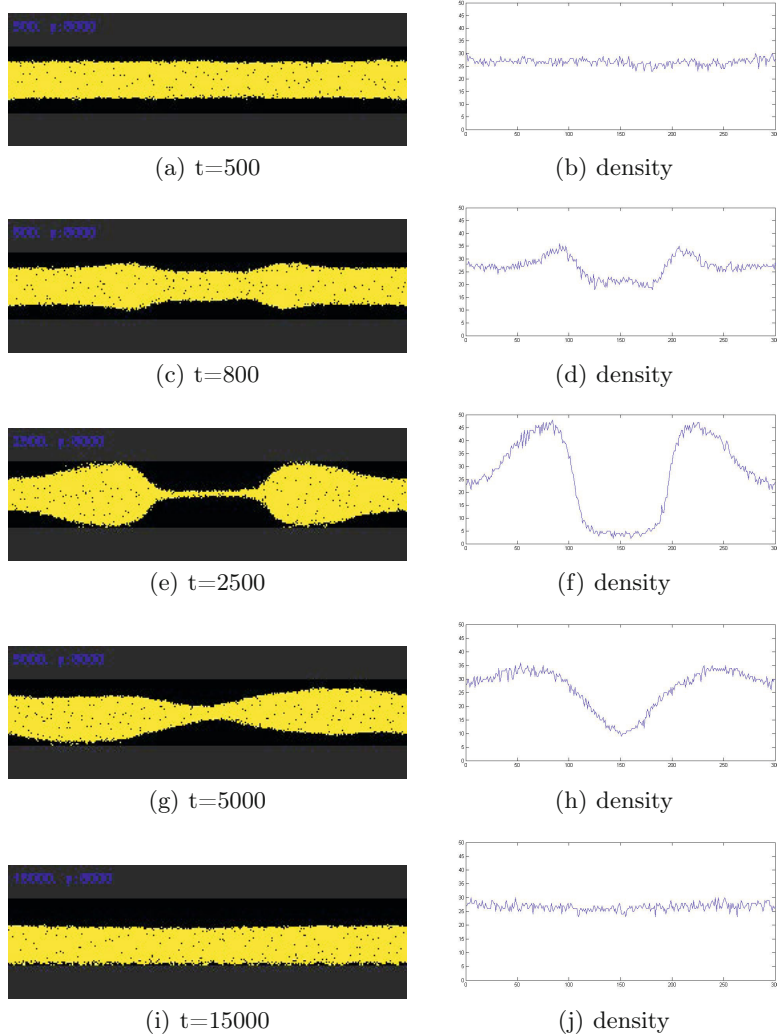


Fig. 5.5 Response of virtual plasmodium flux to simulated light irradiation. a) population initialised within horizontal arena forms single tube, c) presentation of simulated light irradiation (centre, not shown) results in flux away from irradiated area, e) population density is decreased at irradiated region and increased at un-exposed region, g) removal of adverse stimulus results in increased flux to inner region, i) uniform density is restored, b,d,f,h,j) cross-section plots of population density across the arena.

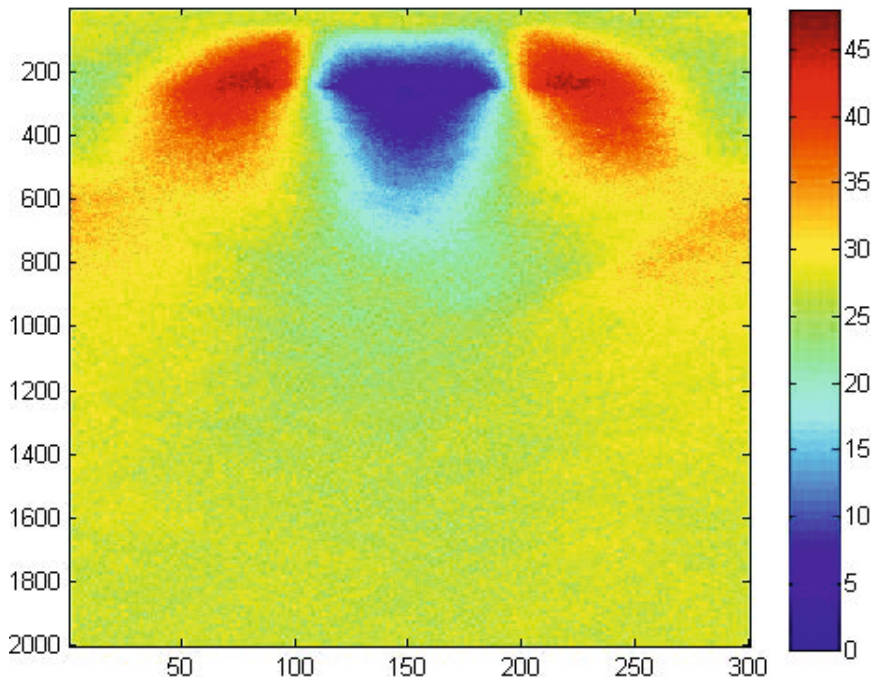


Fig. 5.6 Space-time plot of population density flux under adverse stimuli condition, time proceeds downwards. Note that changes in density are initiated at borders of stimulus boundary.

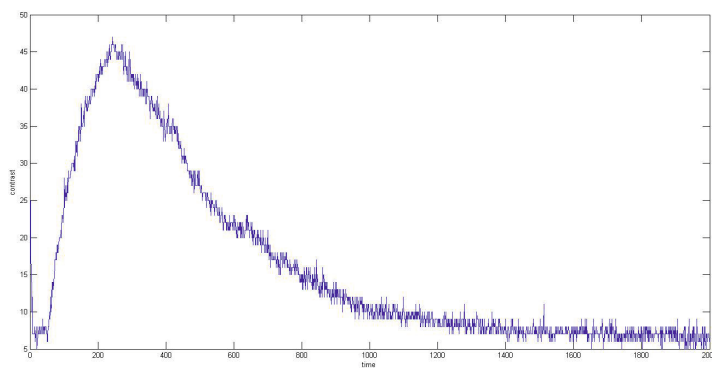


Fig. 5.7 Presentation of adverse stimuli (simulated light irradiation) and its effect on population density, interpreted as signal contrast enhancement. Adverse stimulus presented after 50 samples ($t=500$), stimulus removed after 250 samples ($t=2500$) causing gradual reversion to baseline activity

the perceived lightness of the global image, Fig. 5.8e). A space-time plot of the evolution of population density indicates that the scalloped effect occurs immediately after presentation with the stimuli (Fig. 5.9). The differences in density between the bars also starts immediately after presentation but the full increase in ‘brightness’ between each bar occurs much later, due to the time taken for particles to migrate towards higher concentration areas (Fig. 5.8e, note the gradual increase in density in each bar over time). The increase in contrast of the global (entire arena) population density over time can be seen in Fig. 5.10. This contrast is caused by the relatively slow flux of particles across the entire arena and corresponds to a coarse representation of the image brightness.

The Chevreul staircase consists of contiguous regions of gradually increasing lightness. Another illusory perception of lightness occurs in regions with non-contiguous increases in lightness. This is known as the Simultaneous Brightness Contrast (SBC) effect.¹

A simple example of SBC is shown in Fig. 5.11a. The image consists of two large squares, the left-most square in dark grey and the right-most square in a lighter grey. Overlaying the centre of each square is a vertical band of grey (intermediate in lightness between the left and right squares). Although the vertical grey bands are of equal lightness (see cross-section in 5.11d), their lightness is perceived differently: the band on the left is typically perceived as lighter than the band on the right. As with the Chevreul staircase the explanatory mechanisms for this illusion have been suggested as LI at the retinal and cortical level. How does the virtual plasmodium respond when presented with this stimuli?

We initialised the model on a 600×300 lattice with 153,000 particles (approximately the same density as used in the Chevreul staircase experiments) with uniform initial distribution (5.11b) and periodic boundary conditions. The lightness differences of the SBC image areas were represented as differing attractant concentration profiles. The population response is to migrate from areas of low concentration (brightness) towards areas of high concentration. This flux is mobilised at the junctions between light and dark regions and a global difference in population density is produced (5.11c). Because the vertical grey band in the darker square is surrounded by a darker region, it receives influx from the darker square. The vertical band within the lighter square is surrounded by a lighter region and there is an efflux of particles to the lighter square. Simultaneously there is transport of particles at the centre of the image (the border between the two large squares) towards the lighter side, and also at the left and right edges of the image (due to periodic boundary conditions). The resulting population density plot (5.11e) shows that the vertical band in the left square is perceived as ‘brighter’ than the band in the right square (although the stimuli concentration presented was identical).

¹ Note that the terms *lightness* (SLC) and *brightness* (SBC) are both used in the literature to describe the same perceptual effect, though their actual definitions are somewhat different, depending on the particular presentation of the stimuli.

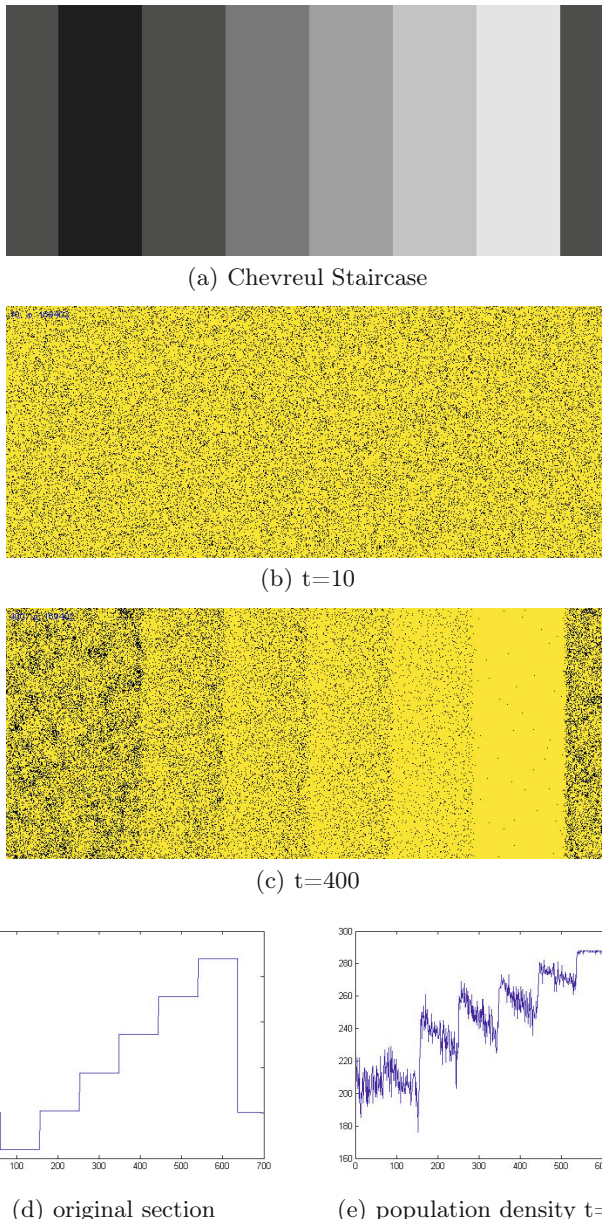


Fig. 5.8 Collective representation of the Chevreul staircase illusion. a) Original greyscale Image of uniform bars of increasing lightness (surrounded by left and right borders), b) initial uniform population distribution of particle population, c) population distribution after 4000 scheduler steps showing increased population density at lighter (greater attractant concentration) regions, d) cross-section profile of original image stimulus, e) cross-section of population density at $t=400$ showing scalloped borders and increasing contrast.

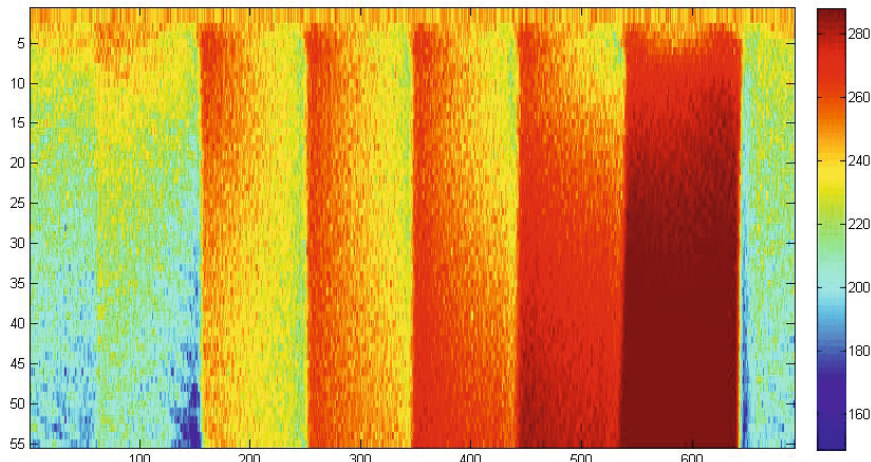


Fig. 5.9 Space-time plot of population density flux under Chevreul illusory stimulus, time proceeds downwards

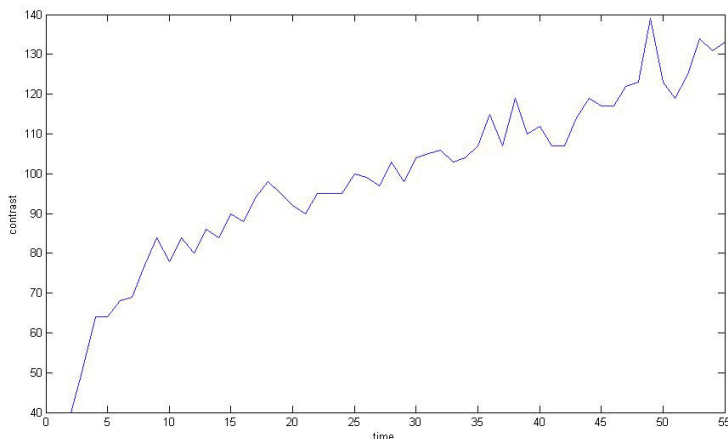


Fig. 5.10 Plot of the emergence of global contrast by particle flux in response to the Chevreul staircase stimulus (difference in population density range, from an initially random density distribution, to halting at 550 scheduler steps)

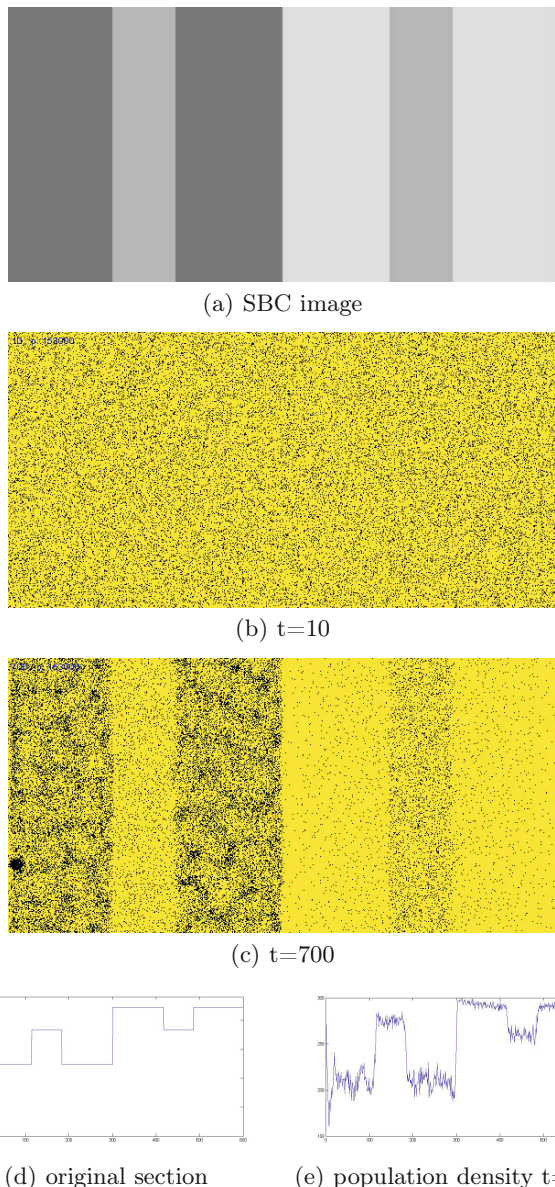


Fig. 5.11 Collective representation of the Simultaneous Brightness Contrast (SBC) illusion. a) Original greyscale Image of two large squares, each with a central band of identically light grey, b) initial uniform population distribution of particle population, c) population distribution after 700 scheduler steps showing increased population density at lighter (greater attractant concentration) regions and greater density in the left central grey strip, d) cross-section profile of original image stimulus, e) cross-section of population density at $t=700$ showing illusory percept of the left central grey strip as brighter than the right central grey strip

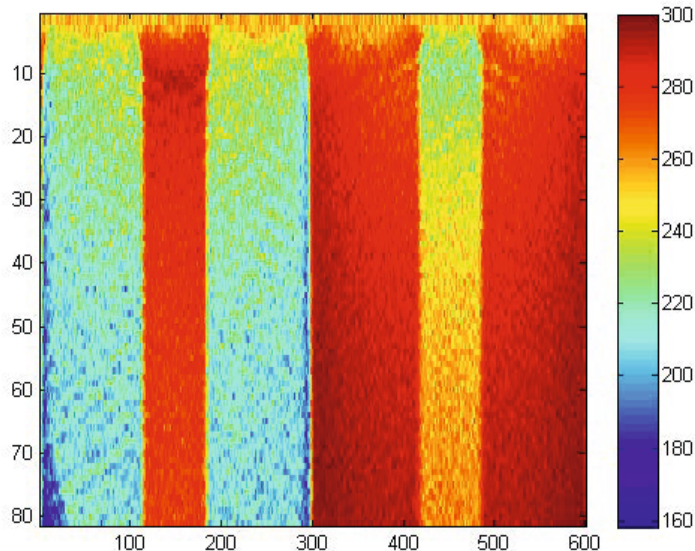


Fig. 5.12 Space-time plot of population density flux under Simultaneous Brightness Contrast stimulus, time proceeds downwards

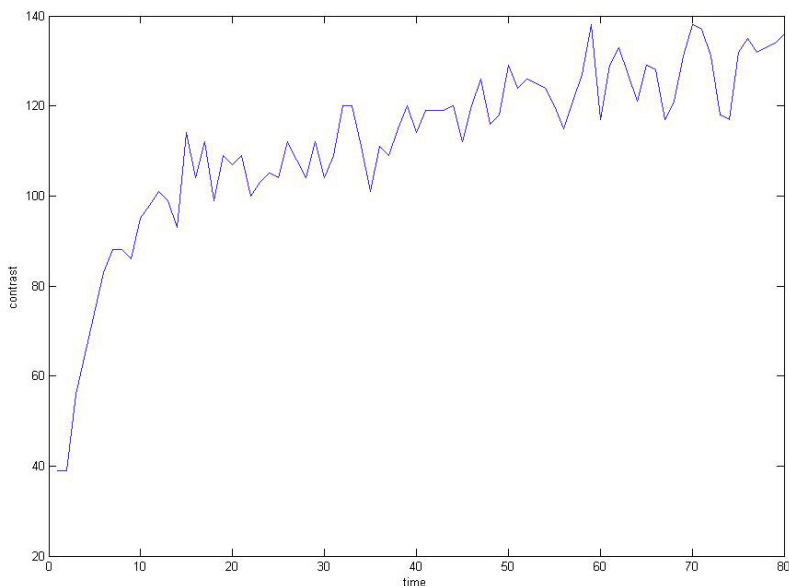


Fig. 5.13 Plot of the emergence of global contrast over time by particle flux in response to the SBC stimulus (difference in population density range, from an initially random density distribution, to halting at 800 scheduler steps)

This illusory percept matches that of human subjects when presented with the same stimulus type [182].

A space-time plot of the evolution of population density demonstrates the differences in population density emerging as the experiment progresses. As with the Chevreul staircase, the local response to adjacent stimuli in the SBC image is instantaneous, whereas the global response to overall brightness changes in the image takes significantly longer, (also seen in the contrast plot in Fig. 5.13), again caused by the relatively slow movement of particles across the image areas.

5.7 Summary: Unorganised Material Analogues of Neural Phenomena

We have demonstrated the results of modelling experiments into the generation of spatial contrast enhancement analogous to Lateral Inhibition in unorganised non-neural systems using a multi-agent model of slime mould *Physarum polycephalum*. The results show the classic LI contrast enhancement in response to attractant stimuli and its opposite counterpart behaviour (Lateral Activation) in response to adverse stimuli (simulated light irradiation). These effects does not require pre-existing inhibitory connectivity and are generated by bulk transport of the particles comprising the virtual material, initiated at the borders of stimuli projection. Restoration of uniform baseline activity (population density distribution) is established when stimuli are removed. In addition to the local edge contrast enhancement we observed long-term changes in population density distribution when the population was presented with a more complex attractant stimulus pattern. This was caused by the flux of particles towards brighter regions of the image and corresponds to a (rather crude) collective response to the global brightness of the original image stimuli, including the scalloped intensity profile of the Chevreul staircase and the perceived difference of two identically bright patches in the Simultaneous Brightness Contrast (SBC) effect. Interestingly, this simple mechanism reproduces the illusory human percepts in both the Chevreul staircase and SBC figures.

The most notable feature of this approach is that LI phenomena can be approximated without explicit fixed inhibitory connections. This suggests possible mechanisms by which simple organisms without neural tissue may achieve sensory contrast enhancement. In organisms such as slime mould the internal protoplasmic transport of cellular material could be harnessed to generate the LI mechanism. The sensory contrast enhancement afforded by LI could allow for the enhancement of weak spatial stimuli (such as nutrient location). Conversely, the LA mechanism would amplify weak hazardous stimuli, providing alternate migration paths away from hazardous regions. The relatively slow restoration of baseline activity also allows a temporary memory effect denoting the approximate location of attractant and hazard

stimuli. Because the LI and LA phenomena in this model do not rely on fixed inhibitory connectivity it is particularly suited to systems and organisms which have adaptive architectures and body plans respectively.

In the context of adaptive materials and robotics applications the mechanism illustrates how complex sensory behaviour can be distributed within an unorganised material (or robotic collective) itself. This allows greater freedom from having to pre-specify connectivity to implement sensory contrast enhancement and allows redundancy for individual faulty components. We hope that ongoing research may lead to other unorganised material approximations of complex neural functions seen in brightness perception (including illusory phenomena such as neon colour spreading, illusory contours and brightness assimilation effects), and implementation of other spatial feature detectors (including orientation detection, edge completion, gestalt phenomena, optic flow), and direction discrimination.

Part III

Material Computation in a Multi-agent
Model of *Physarum Polycephalum*:
Mechanisms and Applications

Chapter 6

Modelling Computational Behaviour of *Physarum*

“Any problem can be solved using the materials in the room.”

(Attributed to Edwin Land)

6.1 Introduction

In this part of the book we firstly examine how the multi-agent model reproduces the computational approximations first seen in slime mould which was initiated by the research of Nakagaki [183] who observed that the *Physarum* plasmodium was capable of solving simple maze problems. This initial work was significantly extended in terms of computational breadth, notably by the works of Adamatzky (see [4] for an overview). The first chapter in this section builds upon the simulation of the biological behaviour of *Physarum* given in Chapter 4 and examines how the model plasmodium computes by network formation and adaptation.

In subsequent chapters we use the model plasmodium as a computing substrate itself. We demonstrate means of guiding the material behaviour of the model slime mould (using attractant fields, repellent fields and simulated light irradiation) to implement spatially represented unconventional computation approaches to a number of classical computational problems, including Voronoi diagrams, convex hulls, concave hulls, combinatorial optimisation, data smoothing, spline curves, path planning, simple statistical analysis and estimation. These approaches have in common the fact that they utilise the emergent quasi-physical behaviours in the model (network formation, minimisation and morphological adaptation) to perform an *embodied* computation.

6.2 Maze Solution by Morphological Adaptation

Solution of a maze was the initial experimental finding which attracted the attention of the scientific community to the computational behaviour of

Physarum [70, 183, 184]. The plasmodium solves the maze by morphological adaptation of its transport network after the plasmodium has completely covered the maze. As noted in chapter 2, the plasmodium network is only an approximation of the shortest path, and in the majority of runs variants of the shortest path were found. The representation of the problem (initialising the plasmodium to completely cover all paths, then retracting redundant and longer veins) is also different to classical approaches to maze solving which typically search without knowing the complete maze configuration in advance, using a combination of depth and breath searching [185].

To assess the behaviour of the model plasmodium on maze solving a large virtual plasmodium was placed to completely cover all paths in a maze (Fig. 6.1a, an analogue of the original experimental design in [70]). The size of the virtual plasmodium was reduced over time using the growth and adaptation behaviour to maintain connectivity, and retraction of pseudopodia from dead-ends was observed (Fig. 6.1b-e). Unlike the real organism, however, all possible paths connecting the start to exit persisted. Attempts to ‘force’ the virtual plasmodium to choose the shorter of the paths were performed by removing particles selected at random. This resulted in the plasmodium shrinking to give thinner paths until connectivity was broken. However this method did not guarantee that the shortest path through the maze persisted. Gunji noted that protoplasmic flux in the *Physarum* plasmodium is not as idealised as that represented in the Tero model, noting that flow is irregular, redundant and partially dependent on the shape of the organism itself [123].

How can the shape of the maze affect flux within the virtual plasmodium? The shape of the maze walls affect the tortuosity of the paths and evolution of the virtual plasmodium tends to enhance flux in paths where changes in direction are less frequent, thus favouring ‘easier’ as well as shorter paths. This may be partly due to the fact that the virtual plasmodium is not anchored firmly to the substratum, as in the case of the real plasmodium. The virtual plasmodium attempts to minimise the path choices by shifting the positions of the Steiner points. In an environment without obstacles the Steiner points are free to move and eventually competing paths merge to form a single path. In the maze, however, the walls provide obstacles to free movement of the Steiner points. The competing paths, indicated by their respective Steiner points are indicated in Fig. 6.1g and separated by bounded regions. In the case of region ‘C’ the two paths above and below the point are effectively anchored, whereas the pseudopodium on the left is not anchored and shrinks back into the main vertical flow. The natural shrinkage direction of the Steiner points in regions ‘A’ and ‘B’ is indicated but movement in these directions is prevented by the maze walls. As diffusion does not cross maze walls (chemoattractant is removed from wall regions) the walls ‘pinch’ the path thickness in these areas, reducing the attraction for paths which make significant contact with wall regions. Reducing the population size shrinks the width of the network paths but selection of shorter paths cannot be guaranteed and ‘easier’ (as opposed to shorter) paths were often selected. Reducing the frequency of chemoattractant diffusion

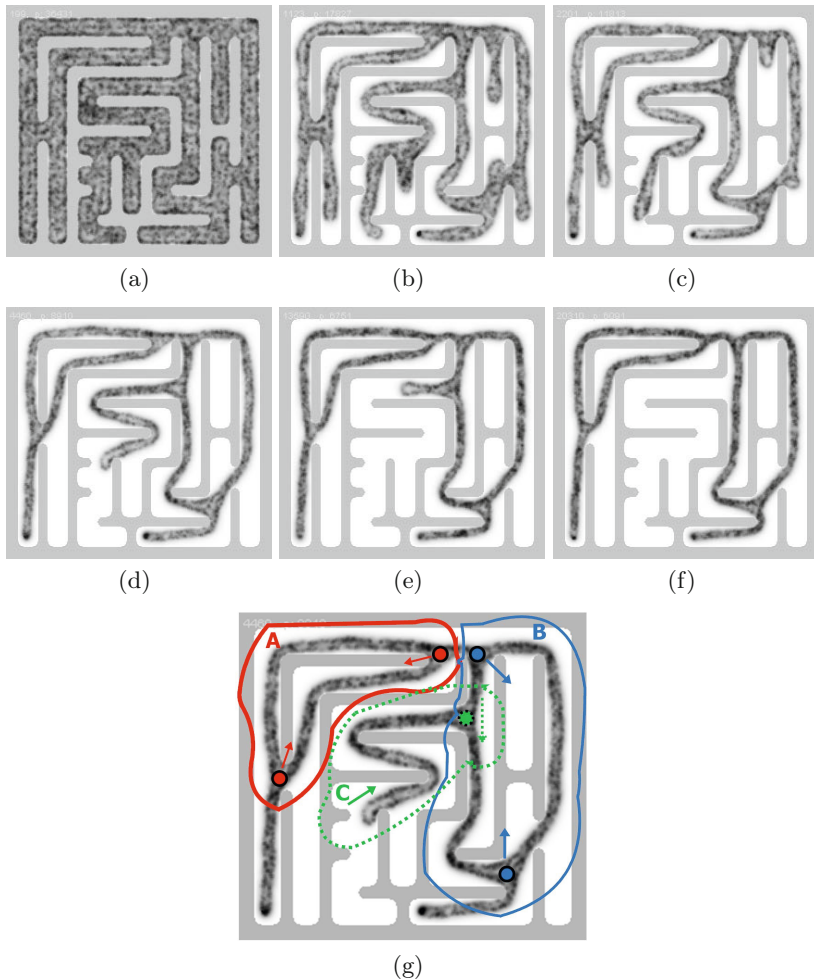


Fig. 6.1 Approximation of maze problem by virtual plasmodium. (a) Population inoculated in entire habitable region of maze and nutrients projected at start and exit points, (b-e) Retraction of virtual pseudopodia, (f) Persistence of path combinations connecting start and exit, (g) Regions of competing path flux.

(for example, to every 50 scheduler steps instead of every step) mimicked a stronger adhesion of the path to the substratum whilst leaving individual particles free to decide path choices but did not reliably increase the path selection.

6.3 Natural Network Formation and Minimisation in *Physarum*

In its natural environment, *Physarum* grows towards and engulfs nearby nutrient sources, forming a protoplasmic network which is used to distribute fragments of nutrients about its amorphous body plan. The properties of some of these networks with small numbers of nodes were studied in [9] who found that the networks were efficient in terms of both network length and resilience to random disconnections. The natural and distributed embodied computation is obviously of benefit to *Physarum* in terms of energy expenditure and its ultimate survival, however these findings also coincided with a growing theoretical and practical interest in complex networks [186]. *Physarum* networks, like those of collective organisms such as ants and fungi [97], [187] are of particular interest because they are constructed without reference to, or knowledge of, the overall distribution of the data nodes (nutrients). The fact that these so-called ‘bottom-up’ networks show good efficiency in terms of length and resilience suggests possible approaches for network minimisation where costs of distance (e.g. costs of fuel or robotic tool path movement time) and resilience (e.g. disruptions in supply chains). Some properties of the multi-agent model plasmodium networks were studied in Chapter 4, along with environmental factors affecting their construction and minimisation. In the next sections we examine the construction and dynamical evolution of multi-agent networks with a view to discovering factors which influence their evolution which may be useful in applying these methods to computing problems.

6.4 Spanning Trees

A spanning tree is a connected undirected graph of edges forming a tree structure connecting all of the nodes in a graph without cycles. Proximity graphs are graphs connecting a set of points whose connectivity is determined by particular definitions of neighbourhood and distance [188, 189]. For example in the construction of the Relative Neighbourhood Graph (RNG), two points p and q are connected only when there is not a third point r that is closer to both p and q than the distance between p and q . Each subsequent member of the Toussaint hierarchy of proximity graphs contains the links of the graphs earlier in the hierarchy, adding extra links to satisfy the different neighbourhood definitions. As the hierarchy increases, so does the number of paths and cycles within the graph.

Adamatzky found that a growing *Physarum* plasmodium approximates spanning trees and the Toussaint hierarchy of proximity graphs, noting that current implementations of Belousov-Zhabotinsky (BZ) chemical processors, although able to perform plane division problems such as Voronoi diagrams, are not able to compute spanning trees. This inability of chemical processors is primarily because of the propagation of the wavefronts in all directions

from target nodes and also because there is no record left in the medium of the front propagation [78, 77, 80].

Physarum, however, can tackle a wider range of problems than simple chemical processors. Recall from chapter 4 that in nutrient-poor environments, the plasmodium grows by extending pseudopodia in the specific direction of nearby chemoattractant sources, whereas in nutrient-rich conditions the plasmodium grows radially in all directions (in a manner more akin to classical BZ propagation). Adamatzky suggested that the *Physarum* plasmodium may utilise an efficient method of environmental interaction to guide its behaviour when foraging: When initialised on an oat flake in nutrient-poor conditions, the plasmodium receives local stimuli in the form of a diffusing chemoattractant gradient [80]. The binding of chemoattractant compounds to receptors in the plasmodium modulates the hardness of the plasmodium membrane. The stimulated region softens, and the hydrostatic pressure within the plasmodium vein network causes cellular material to stream towards the source of chemoattractant in the form of a type of pseudopodium (a *lamellopodium*). The plasmodium thus grows towards a nearby node, engulfing it, and stopping (or at least reducing) the diffusion of chemoattractant from the node. The growing pseudopodium then migrates towards the next source of attractant and a spanning tree is ultimately formed (as in Fig. 4.5). The virtual plasmodium also approximates the construction of spanning trees in nutrient-poor conditions. In the example shown in Fig. 6.2 A small population was initialised on the lower-most node (Fig. 6.2a) and grew by extending pseudopodia to link the remaining nodes to form the spanning tree (Fig. 6.2b-d). Fig. 6.2e-h (and supplementary recording) shows a representation of the changing chemoattractant gradient field as the model migrates towards and engulfs the nutrient sources.

6.5 Construction and Minimisation of Proximity Graphs

When inoculated at a single node *Physarum* was shown to forage to the remaining nodes, approximating a spanning tree. The plasmodium continued its foraging even after the tree was complete, increasing its connectivity to approximate proximity graphs in higher regions of the Toussaint hierarchy (see examples of the hierarchy for simple datasets in Fig. 6.3), most closely approximating the Relative Neighbourhood Graph (RNG) [80]. When the plasmodium inoculated at all nodes simultaneously, the plasmodium approximated higher connectivity members of the proximity graph family, the Gabriel Graph (GG) and Delaunay Triangulation (DTN), however the connections were thicker between edges corresponding to GG compared to thinner tubes representing DTN edges. The author suggested that the growth front of the plasmodium under different environmental conditions corresponded to the neighbourhood definition of different proximity graphs (for example the lune neighbourhood of RNG or the circular neighbourhood

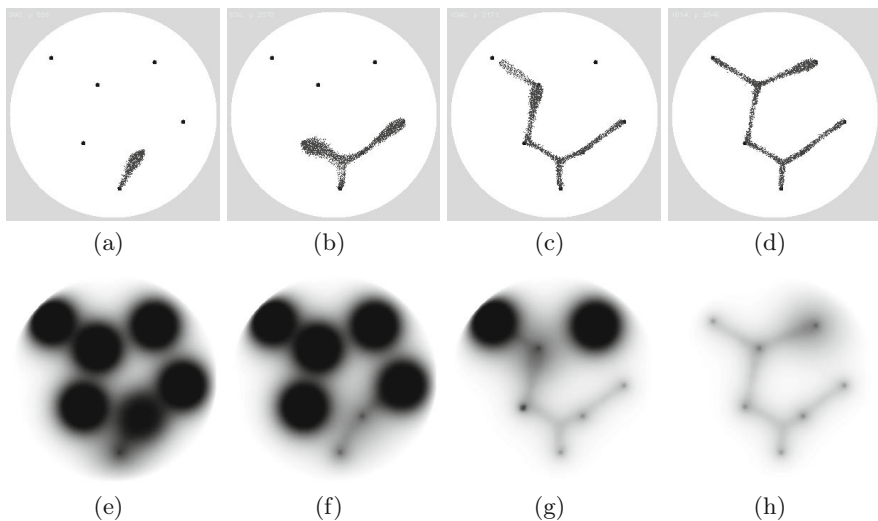


Fig. 6.2 Construction of a spanning tree by the model plasmodium. (a) Small population (particle positions shown) inoculated on lowest node (bottom) growing towards first node and engulfing it, reducing chemoattractant projection, (b-d) Model population grows to nearest sources of chemoattractant completing construction of the spanning tree, (e-h) Visualisation of the changing chemoattractant gradient as the population engulfs and suppresses nutrient diffusion.

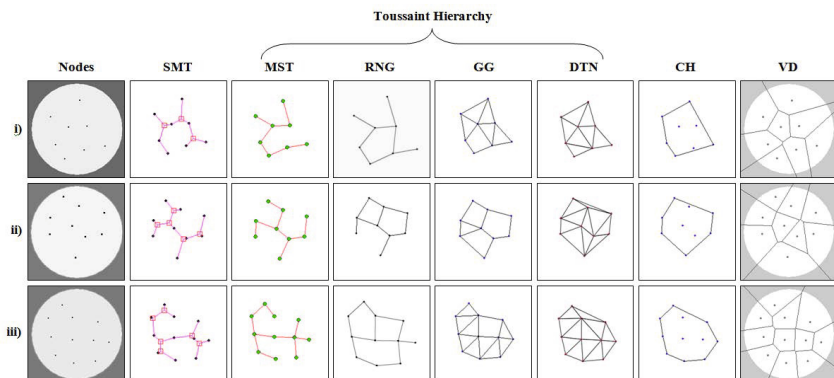


Fig. 6.3 Graphs representing connectivity, proximity, area and tessellation of a set of nodes. Three data sets shown (i-iii), SMT—Steiner Minimum Tree, MST—Minimum Spanning Tree, RNG—Relative Neighbourhood Graph, GG—Gabriel Graph, DTN—Delaunay Triangulation, CH—Convex Hull, VD—Voronoi Diagram.

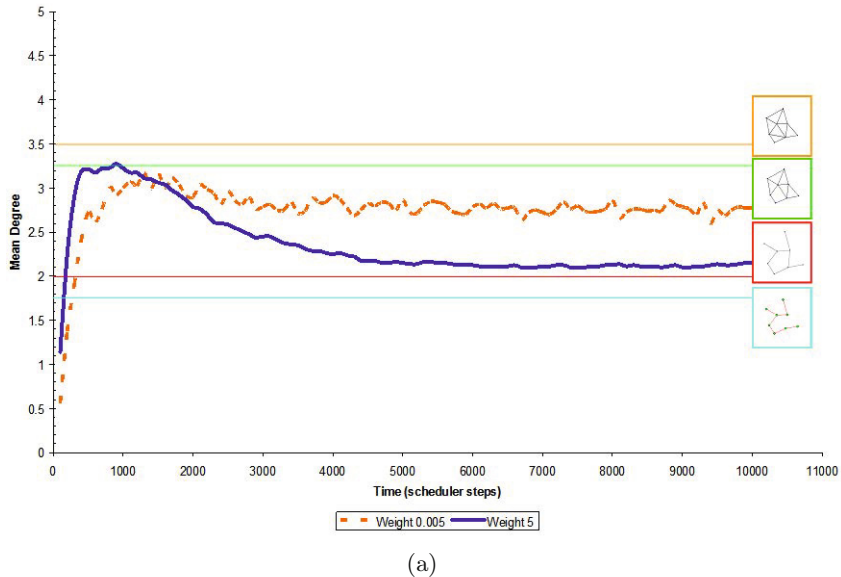
of GG). Therefore nutrient-poor environments would be expected to induce more sparsely connected networks than nutrient-rich environments (for example, a weak stimulus from only one direction would induce a conical foraging pseudopodium shape, whereas multiple strong stimuli would present a radial growth pattern).

To explore the dynamic connectivity of the emergent transport networks during the formation and evolution of the networks a small population ($\%p\ 3$, 1200 particles) was initialised on the arena at both very low ($Proj_d\ 0.005$) and very high ($Proj_d\ 5$) node concentration. Twenty runs at each concentration, for each dataset D1, D2 and D3 in Fig. 6.3, were carried out and each run lasted for 10,000 scheduler steps. Mean degree of connectivity (the mean number of nodes to which a single node was connected) was measured every 100 scheduler steps (using the method described in chapter 8, section 8.2.1) and the results are summarised in Fig. 6.4– 6.6a.

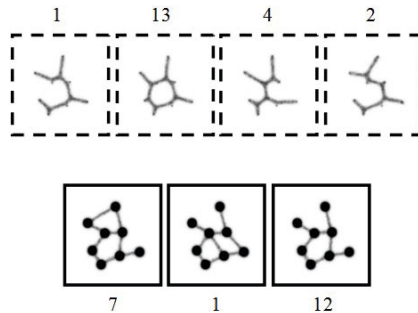
During each experiment the population initially rapidly grew in size and formed a transport network around the nodes. The attraction to the nodes then minimised the transport network configurations. Under high concentration conditions, network connections were strongly attracted to the nodes and the tension pulled the networks to configurations with low mean degree values. Networks with high tension tended to have more cycles than networks with low concentration (low tension). Representative networks from the Toussaint hierarchy are placed to the right of each chart at the vertical positions corresponding to their mean degree. Fig. 6.4– 6.6b illustrate the pattern subtypes of networks found at the end of each experiment from each dataset at the two node concentrations (solid boxes are high concentration and dashed boxes low concentration). It can be seen that the high node concentration subtypes appear to match the proximity graph configurations in the Toussaint hierarchy at correspondingly similar mean degree values.

The results from low concentration conditions differed significantly from their respective examples in the Toussaint hierarchy. Despite having fewer cycles, the networks formed under low concentration conditions had a much higher mean degree of connectivity. This is because the relatively low attraction to the nodes results in pulling of the network from the nodes and the formation of Steiner points. The addition of Steiner points indirectly increases the degree connectivity whilst minimising network length, as shown in Fig. 6.7. The resulting graphs have relatively few cycles and, in most cases, approximate spanning tree structures, but have mean degree values similar to proximity graphs in the RNG and GG range.

Although the low concentration networks result in more tree-like networks there are a number of examples (particularly in the case of the D3 dataset) where the minimisation of network cycles cannot be completed to give the tree structure (Fig. 6.8). The reason that such cyclic networks cannot be minimised is that the arrangement of the network around the nodes results in an arrangement of interior angles which are less than the critical angle at which



(a)



(b)

Fig. 6.4 Evolution of connectivity of virtual plasmodium in 8 node graph. (a) Evolution of mean degree at high ($Proj_d=5$) and low (dashed, $Proj_d=0.005$) nutrient concentration. Positions of related proximity graphs indicated at the right side of chart, (b) Final network subtypes observed at low concentration (top images, small nodes) and high concentration (bottom images, large nodes). Number shows how many examples of subtypes were observed in 20 runs.

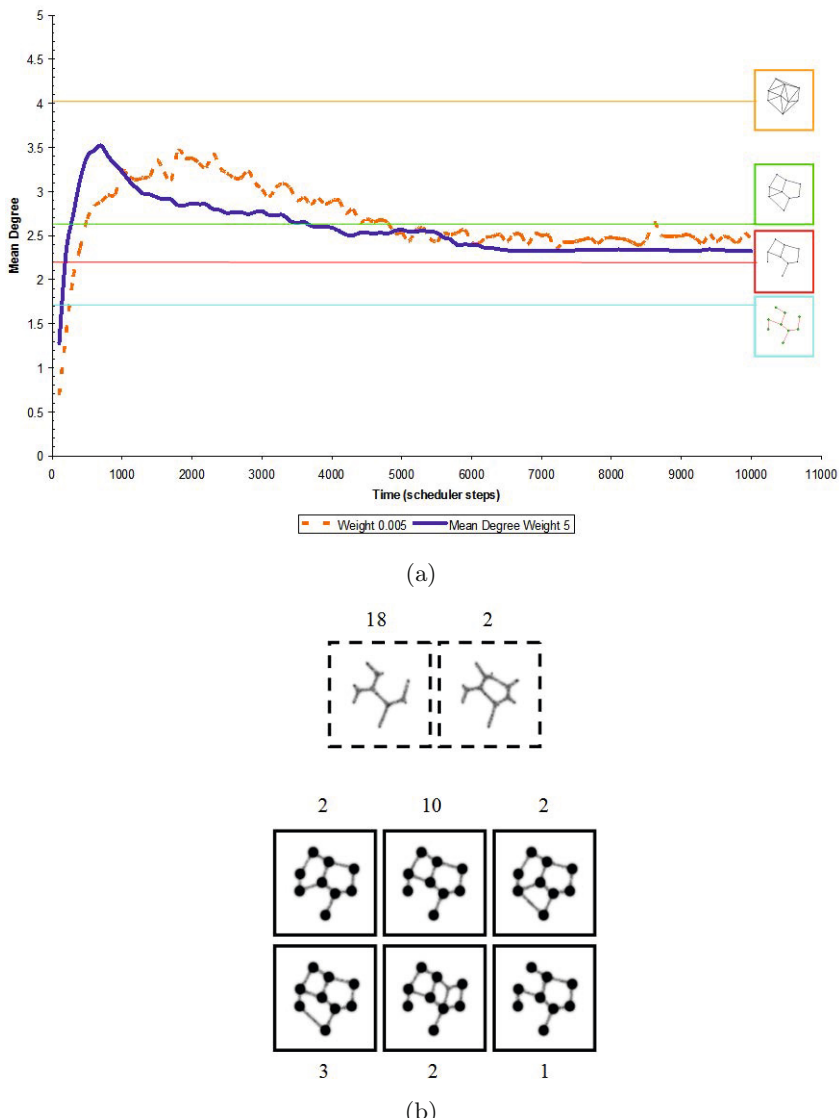


Fig. 6.5 Evolution of connectivity of virtual plasmodium in 9 node graph. (a) Evolution of mean degree at high ($Proj_d=5$) and low (dashed, $Proj_d=0.005$) nutrient concentration. Positions of related proximity graphs indicated at the right side of chart, (b) Final network subtypes observed at low concentration (top images, small nodes) and high concentration (bottom images, large nodes). Number shows how many examples of subtypes were observed in 20 runs.

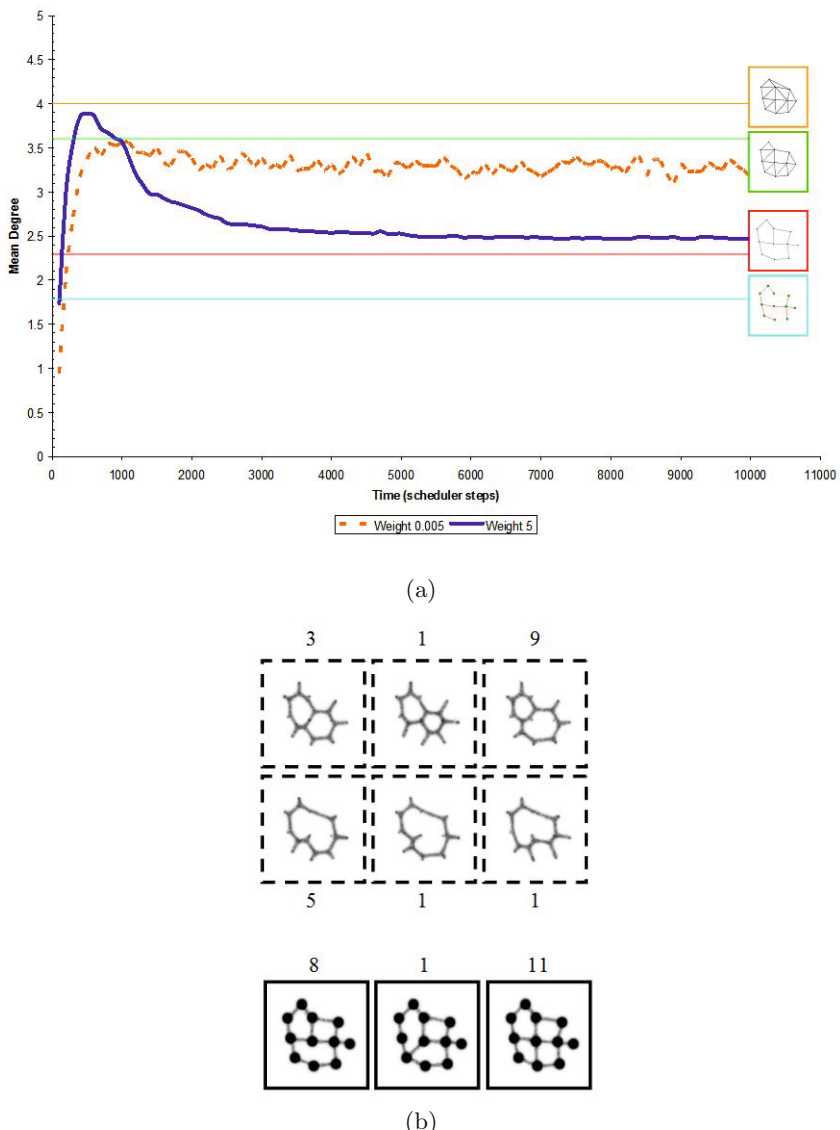


Fig. 6.6 Evolution of connectivity of virtual plasmodium in 11 node graph. (a) Evolution of mean degree at high ($Proj_d=5$) and low (dashed, $Proj_d=0.005$) nutrient concentration. Positions of related proximity graphs indicated at the right side of chart, (b) Final network subtypes observed at low concentration (top images, small nodes) and high concentration (bottom images, large nodes). Number shows how many examples of subtypes were observed in 20 runs.

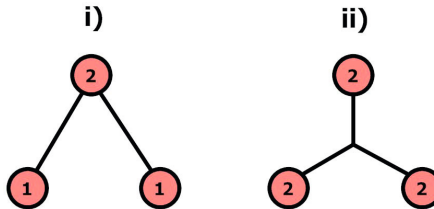


Fig. 6.7 Addition of Steiner point reduces length and indirectly increases degree. i) Minimum Spanning tree connecting two nodes, degree of each node is inside nodes, network has mean degree of 1.33, ii) Addition of Steiner point gives Steiner tree, with an indirect mean degree of 2 and minimum network length.

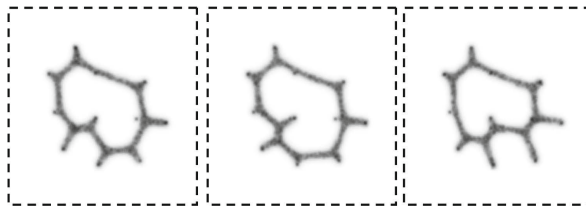


Fig. 6.8 Examples where minimisation cannot be completed because of large interior angles.

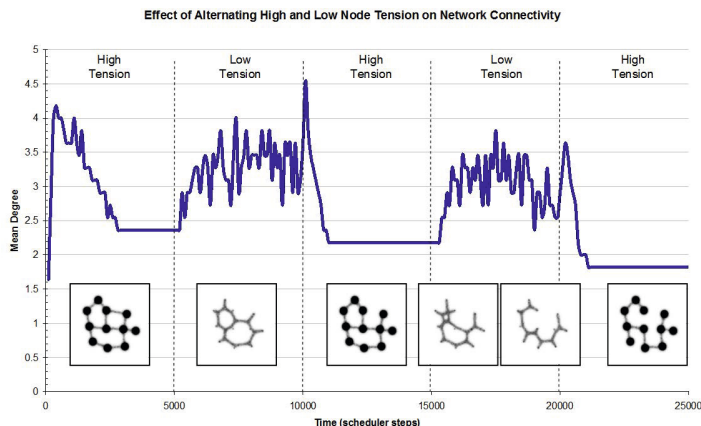


Fig. 6.9 Alternating high and low tension phases to close network cycles. Main plot line shows mean degree of connectivity. Vertical bars indicate phases in tension (via nutrient concentration) at every 5000 steps. Images show exemplar configurations during each stage as cycles are removed from the network.

unzipping can fully occur. One method to overcome the limitation on minimisation is to alternate between high tension nodes (giving cyclic networks) and low tension nodes (reducing the number of cycles). An example of alternating global tension is shown in Fig. 6.9 where the initial phase was high tension and each alternating phase lasted for 5,000 scheduler steps. The chart line shows fluctuations in mean degree during each alternating phase and characteristic network subtypes at the end of each phase (the second low tension phase shows two such images as two cycles were closed during this phase). By repeatedly alternating network tension (via node concentration) the number of cycles in the network is reduced until a tree structure finally emerges. Why does alternating network tension result in the complete closure of network cycles? We believe this occurs partly because of the initial high tension phase which results in a larger number of smaller network cycles (as opposed to one large cycle). The second reason is that the repeated application of high tension phases temporarily reduces the angles between the nodes, allowing minimisation to occur in the subsequent low tension phase. The chart plot indicates the stepwise nature of the minimisation process showing that at each high tension phase the number of cycles is reduced. The pre-selection of nutrient concentration node weights effectively tunes the evolution of the transport network to those with pre-defined characteristics (for example trees or cyclic networks).

Adamatzky noted that *Physarum* continues foraging after the transport network has been constructed [80] and thus does not ‘halt’ in the same way classical algorithms behave. The virtual plasmodium in its non-oscillatory condition will halt when relaxation of the network is complete and no further stimuli are added. However in this ‘halting’ state the collective is actually in a state of dynamic equilibrium: the stable network pattern persists but the pattern itself is composed of the continued activity of its constituent parts. If the network adaptation is performed under oscillatory conditions, the foraging does continue after the initial network minimisation.

6.6 From Area to Distance, Exploration to Exploitation

Instead of adopting strategies to remove cycles from the multi-agent networks, it is possible to avoid this by beginning with a solid structure which does not contain any cycles, i.e. initialise the virtual plasmodium as a solid mass, rather than a network. With a real *Physarum* plasmodium any inoculation as a solid mass (in reality a homogenous paste of plasmodium patterned in a particular shape) will quickly form networks, breaking up the solid structure. This is also the case with the multi-agent model but it is also possible — by reducing the speed of network shrinkage — to reduce the overall area of the initial population without introducing cycles.

Fig 6.10 (top row) shows inoculation as a large square mass covering an regular array of stimulus points. By slowly shrinking the virtual plasmodium

the shrinking mass reduces its area and also conforms to the local stimuli of the array points (this shrinkage can be achieved by simply randomly reducing particles or biasing the growth and shrinkge parameters in favour of gradual shrinkage). As shrinkage continues the remaining population forms a network which approximates the Steiner Minimum Tree (Fig 6.10 top row, right side). There is a self-organised transformation between an efficient area representation in the intial inoculation to an efficient network representation after shrinkage is complete.

One limitation of the shrinkage method is that it shrinks uniformly towards the centre of the material. This may bias the final network somewhat. However we found empirically that by temporarily (by manual intervention) relaxing the shrinkage, then later re-applying the process, it was possible to generate accurate Steiner tree representations for up to 64 nodes (Fig. 6.11). The *Physarum* model of Tero et al. was also used as a starting point to approximate Steiner trees. However, in their approach the meandering network paths formed by their model plasmodium (for up to 16 nodes) were replaced by straight lines before a separate gradient descent method was used to move the positions of the Steiner points to minimise total network distance [190]. As the minimisation behaviour of the multi-agent approach is an emergent property of the ‘material’, no separate minimisation of the Steiner point positions is required. The minimising properties of soap films are a well known mechanism for optimisation (both literal or serving as an inspiration for classical

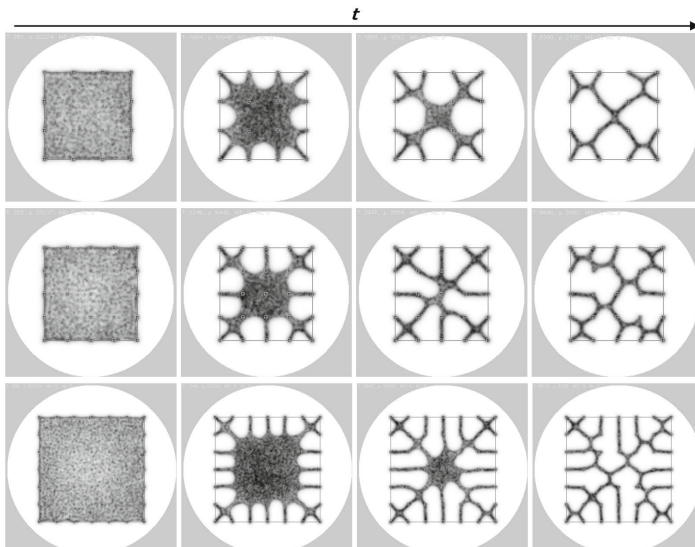


Fig. 6.10 Approximation of Steiner tree by shrinkage of virtual plasmodium. Population initialised as a large sheet within Convex Hull. Shrinkage of sheet yields approximation of Steiner tree in 4x4 (top), 5x5 (middle), and 7x7 node arrays.

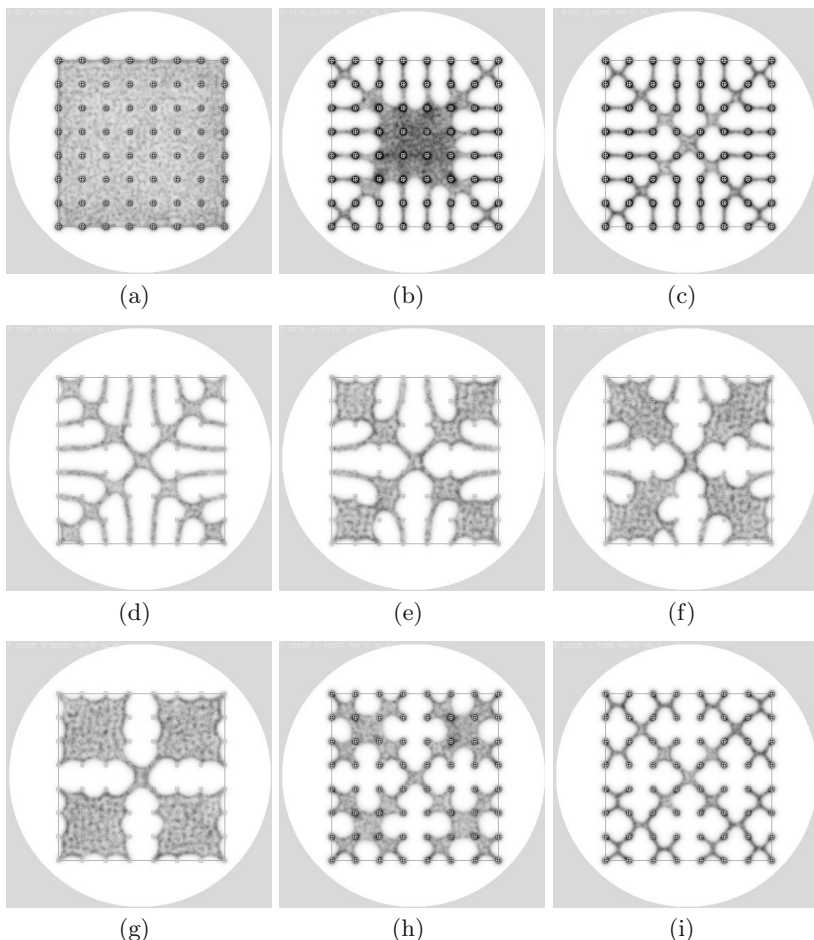


Fig. 6.11 Combined shrinkage and relaxation for 8x8 node array. (a-c) Shrinkage alone yields non-optimal tree, (d-f) ‘Re-inflation’ by manual adjustment of growth/shrinkage parameters, (g-i) Re-shrinkage generates Steiner tree.

approaches (see [191, 192, 193, 165]) and the multi-agent approach suggests a simple spatially represented method by which transformations between area and distance representations may be obtained. Although the manual intervention precludes using approach in concrete applications it is interesting to note that the evolution of the network in different parts of the array appears to be modularised (for example, the structure in Fig. 6.11g). In later Chapters 8 and 9 we describe mechanisms of automating the effects of changing environmental stimuli on the population, towards the development of useful computational geometry applications.

6.7 Summary: Innate Material Approximation of Network Computation

The model plasmodium reproduces the previously reported spatially represented computational behaviour of *Physarum* by utilising the intrinsic pattern formation and minimisation behaviour of the model, combined with growth/shrinkage and the response to attractants and repellents. In the next chapters we examine specific applications which utilise the embodied computation of this spatially represented unconventional computing substrate.

Chapter 7

Approximating Classical Computing Devices with the Multi-agent Model

“Early, before the sun, they struggle off to the gates.”

(David Bowie, 1983)

7.1 Introduction

In the previous chapter we examined how the network formation and adaptation of the model slime mould could be used to approximate computations. Although slime mould computes by means of its spatial propagation and shape adaptation, this is not the way the current dominant form of computation — classical computation — operates. In modern computer systems problems are abstracted into a symbolic representation and implemented by programs which are ultimately executed by microscopic operations involving transformation of input signals by logic gates. In this chapter we build upon previous research into implementing logic gates with slime mould [92] which found that the organism could indeed implement simple gates. We extend these experiments with the model plasmodium and assess their performance, asking if the model slime mould can — and whether it should — implement more complex gates. The design of the composite gates in this chapter was implemented by Andrew Adamatzky and model experiments were performed by the author.

7.2 *Physarum* Gates

Physarum gates constructed in [92] were made of agar gel channels. Presence of a plasmodium in an input channel represents logical input TRUTH ('1') and absence of plasmodium — logical input FALSE ('0'). Values of signal in output channels are encoded similarly. Sources of chemoattractants (glucose) are placed near exits of output channels. The chemoattractants diffusing in

the agar gel channels establish gradients which guide the plasmodia towards closest sources of attractants.

In experiments discussed in [92] plasmodia inoculated in different input channels exhibited an aversion toward each other. They did not merge. If propagating plasmodium p_1 encountered another plasmodium p_2 in a channel p_1 wanted to travel in the plasmodium p_1 chosen another route of propagation. The fact that two ‘colliding’ plasmodia do not merge was also supported by our experiments on constructing Voronoi diagram by plasmodia inoculated on nutrient-rich agar [80, 76]. Approaching wave-fronts of growing plasmodia usually ‘freeze’ for an up to 16 hours, when collide, however later the fronts merge. Outcomes of interaction between two localized (i.e. propagating as wave-fragments) plasmodia depends on many factors, and ‘elastic’ collision is just one amongst many scenarios of the plasmodia interactions.

In the paper by [92] some output channels of *Physarum* gates were considered as buffers. Let us now slightly redesign the gates [92] and interpret all outputs of the gates as Boolean logic values [94].

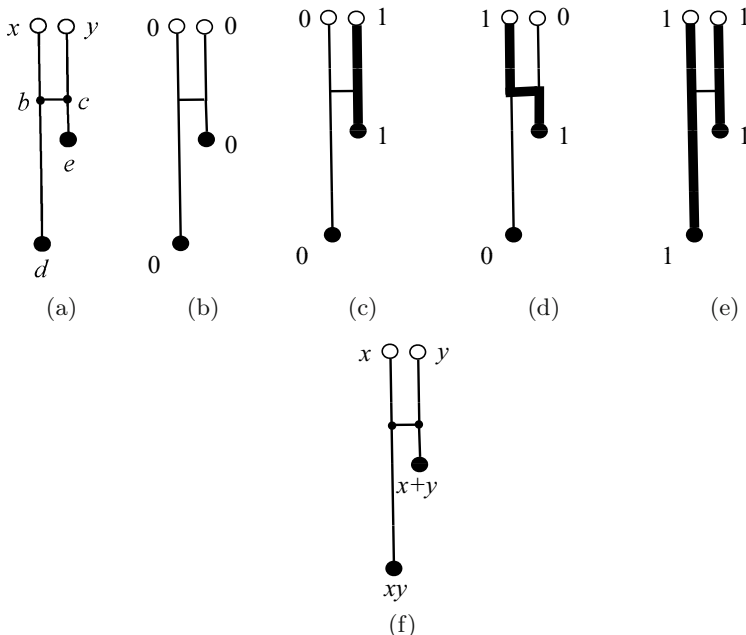


Fig. 7.1 Scheme of G_1 gate: (a) landmark points are shown; (b)–(e) configuration of plasmodia in gates for all combinations of input values — $x = 0, y = 0$ (b), $x = 0, y = 1$ (c), $x = 1, y = 0$ (d), $x = 1, y = 1$ (e), the plasmodia bodies are shown by thick lines; (f) input-output logical function realized by the gate. Chemoattractants are placed in sites marked by solid black discs.

Consider G_1 gate in (Fig 7.1a). Physical structure of the gate satisfies the following constraints $|xb| = |yc|$ and $|bd| > |bc| + |ce|$ (Fig 7.1a). Chemoattractants are placed in sites d and e . We assume strength of attraction to d (e) at point p is proportional to distance $|pd|$ ($|pe|$) (Fig 7.1a).

Situations corresponding to input values $(0, 0)$, $(0, 1)$ and $(1, 0)$ are simple. When no plasmidia are inoculated in x and y nothing appears at outputs d and e (Fig 7.1b). When plasmidium is placed only in site y the plasmidium follows the route $(yc)(ce)$ (Fig 7.1c). If plasmidium inoculated only in site x the plasmidium follows the route $(xb)(bc)(ce)$ (Fig 7.1d).

The main trick of the gate is in how input values $x = 1$ and $y = 1$ are handled. The plasmidia are inoculated in sites x and y (Fig 7.1d). The plasmidium growing from site y follows route $(yc)(ce)$. The plasmidium growing from site x tends to follow route $(xb)(bc)(ce)$, however part of the route (ce) is already occupied by another plasmidium. Therefore the plasmidium, starting in x , grows along the route $(xb)(bd)$ (Fig 7.1d).

A table of transformation $\langle x, y \rangle \rightarrow \langle d, e \rangle$ shows that the gate G_1 (Fig 7.1f) implements logical conjunction and logical disjunctions $\langle x, y \rangle \rightarrow \langle xy, x + y \rangle$ at the same time but on two different outputs.

Geometrical structure of G_2 gate is shown in Fig. 7.2. Chemoattractants are placed in sites c and d and plasmidia can be inoculated in sites x , y and z (Fig. 7.2a). Lengths of channels in the gate satisfy the following conditions: $|xc| < |xd|$, $|ac| < |ad|$, $|bc| < |bd|$, and $|zb| + |bc| < |ya| + |ac|$.

In [92] input channels y and z (Fig. 7.2a) were assigned to constant TRUTH inputs an output channel c to a buffer (unused output to collect ‘excess’ of plasmidium). Let consider scenario when all three input can take values ‘0’ and ‘1’ and both outputs have a meaning.

If plasmidium placed in site z it propagates toward closest attractant-site c (Fig. 7.2c); similarly a plasmidium inoculated in site y propagates towards attractant-site c (Fig. 7.2d). When plasmidia are placed in sites y and z simultaneously, the plasmidium from the site z follows the route $(zb)(bc)$ and thus blocks the way for plasmidium propagating from y (Fig. 7.2e)). Therefore the plasmidium originating in y moves to attractant-site d (Fig. 7.2e). The situations sketched in Fig. 7.2g–j can be described similarly. Considering the transformations $\langle x, y, z \rangle \rightarrow \langle c, d \rangle$ we find that the gate implements the following logical function $\langle x, y \rangle \rightarrow \langle x, xy \rangle$. If y - and z -inputs are constant TRUTH, $y = 1$ and $z = 1$, the gate G_2 is a negation (this how it was initially designed in [92]).

Physarum gates G_1 and G_2 can be cascaded by linking output gel-channels of one gate to input gel-channels of another gate. An example of such cascading in a form of one-bit half adder is shown in Fig. 7.3. Four pieces of plasmidia are fed in input channels as constant TRUTH. The plasmidia representing Boolean variables x and y are multiplied or branched and fed into gate G_1 and two copies of gate G_2 . Output channels of gates G_2 are fed into data channels of another gate G_1 . In addition to results we are looking for — xy and $x \oplus y$ — the circuit (Fig. 7.3) produces several byproducts:

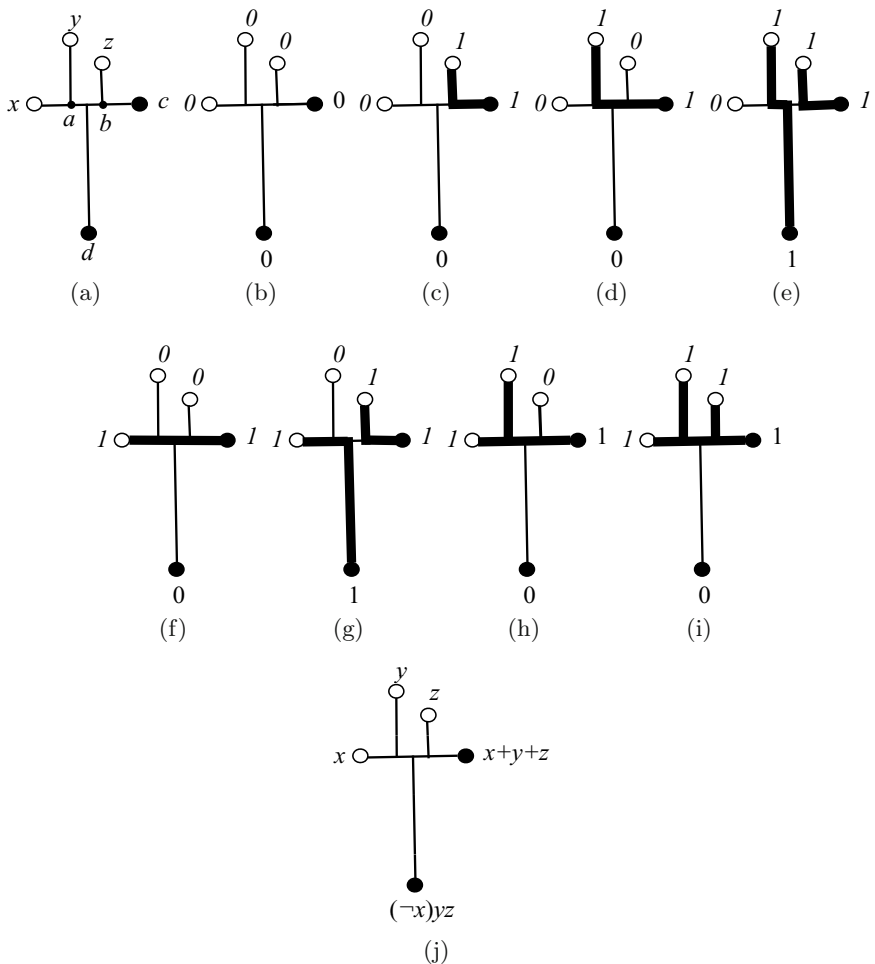


Fig. 7.2 Scheme of G_2 gate. (a) landmark points are shown; (b)–(i) configuration of plasmodia in gates for all values of input tuple $\langle x, y, z \rangle$: (b) $\langle 000 \rangle$, (c) $\langle 001 \rangle$, (d) $\langle 010 \rangle$, (e) $\langle 011 \rangle$, (f) $\langle 100 \rangle$, (g) $\langle 101 \rangle$, (h) $\langle 110 \rangle$, (i) $\langle 111 \rangle$, the plasmodia bodies are shown by thick lines; (j) input-output logical function realized by the gate. Input are marked with circles, outputs with solid discs. Chemoattractants are placed in sites marked by solid black discs.

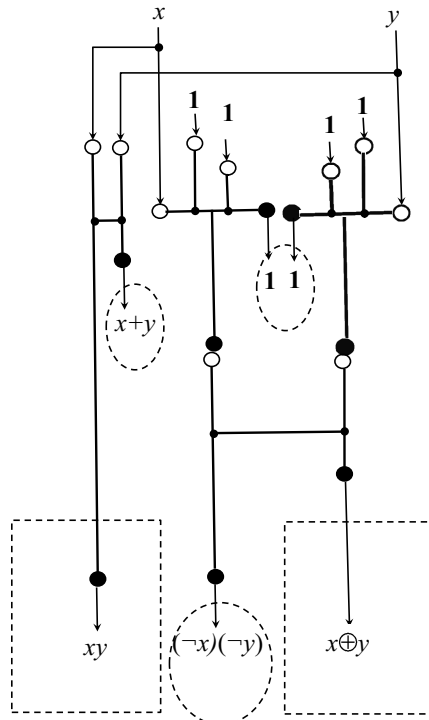


Fig. 7.3 Scheme of *Physarum* one-bit half-adder. Input variables are x and y , 1 on input channels represent constant TRUTH. Carry value xy and sum $x \oplus y$ are highlighted by dotted rectangle, unused outputs $x + y$, 1 and $(\neg x)(\neg y)$ by dotted ellipses.

$x+y$, $(\neg x)(\neg y)$ and two copies of constants TRUTH. These signals can be used further down in the chain of computation or routed in the buffer zones (plasmadium pool). Plasmodia representing constant TRUTH can be also rerouted back to control inputs of gates G_2 .

7.3 Asynchronism

Synchronization of signals is amongst key factors in proper functioning of logical circuits. Architecture of *Physarum* gates allow for a certain degree of asynchronism. Let us evaluate a degree of asynchronism of gates G_1 and G_2 .

Assume outputs of gate G_1 are read in $w \geq |xb| + |bc| + |bd|$ time units after on the plasmodia entered its data channel. Let plasmodia representing logical variables x and y enter their channels at time steps τ_x and τ_y . Let $x = 1$ and $y = 1$. Then x -plasmodium must reach site c of gate G_1 (Fig. 7.1a) after the site c is occupied by y -plasmodium. That is $\tau_x + |xb| \geq \tau_y + |yc|$. Due to

$|xb| = |yc|$ (Fig. 7.1a) we have $\tau_x \geq \tau_y$. If $x = 1$ the x -plasmadium must reach exit of the output channel (xd) before ‘signal reading’ time-window closed. Therefore we have $\tau_y \leq \tau_x \leq \alpha_1 = w - |xd| + |bc|$. The parameter α_1 is a degree of asynchronism of gate G_1 . In the same manner we obtain a constraint on timing τ_x , τ_y and τ_z of signals x , y and z in gate G_2 : $\tau_z \leq \tau_y \leq \tau_x \leq w - |ya| - |ad|$. Thus degree of asynchronism of gate G_2 is $\alpha_2 = w - |ya| - |ad|$.

Architectures of *Physarum* gates G_2 (Fig. 7.2) and G_1 (Fig. 7.1) assume gradients of chemoattractants from output sites (where sources of attractants) are placed to input sites (solid black discs in Figs. 7.2 and 7.1). What will happen if we reverse the gradients and place sources of chemoattractants in input sites of original gates and consider output sites of original gates as inputs of new gates (Fig. 7.4)? We will write gates G_1 and G_2 with reversed gradients and input-outputs as $\overline{G_1}$ and $\overline{G_2}$.

7.4 Outcomes of Reversing Gradients of Chemoattractants

Let us consider gate $\overline{G_1}$. If plasmodium placed in site d (Fig. 7.4a) it propagates towards site b (because it is the only choice) and then follows gradients towards closest source of chemoattractants, site x . Plasmodium inoculated in site e travels along the route $(ec)(cy)$. Two plasmodium placed in sites d and e simultaneously, do not interact. This shows that gate $\overline{G_1} : \langle x, y \rangle \rightarrow \langle x, y \rangle$ acts as a simple conductor of signals when polarity of chemoattractant gradients is reversed (Fig. 7.4b).

In gate $\overline{G_2}$ plasmodium placed in site c always propagates towards closest source of attractants, site z . Plasmodium placed in site x if $|xa| > |zb|$ but the plasmodium propagates to site z if $|xa| < |zb|$ (Fig. 7.4c). The plasmodium placed in c and/or d never reaches site y , therefore output marked ‘ y ’ is

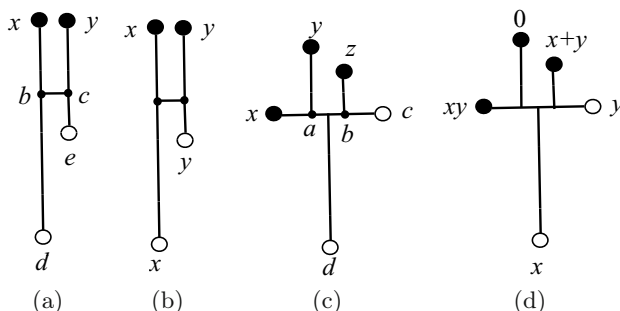


Fig. 7.4 Gates $\overline{G_1}(a)(b)$ and $\overline{G_2}(c)(d)$. Landmarks are shown in (a) and (c), the gates functional schemes in (b) and (d). Inputs are marked with circles, outputs with solid discs. Chemoattractants are placed in sites marked by solid black discs.

always ‘0’. Analysis of all combinations of input signals demonstrate that for $|xa| < |zb|$ we have $\overline{G_2} : \langle x, y \rangle \rightarrow \langle x, y \rangle$, and for $|xa| > |zb|$ we have $\overline{G_2} : \langle x, y \rangle \rightarrow \langle xy, x + y \rangle$ (Fig. 7.4d).

In summary, when gradients of chemoattractants and input-output swapped in gates G_1 and G_2 the gate G_1 becomes a simple conductor and the gate G_2 becomes gate G_1 .

7.5 Computational Modelling of *Physarum* Gate Behaviours

To model the *Physarum* gate behaviours the three physical criteria identified in [92] and utilised in the design of the logic gates need to be implemented. The criteria can be summarised as:

1. *Physarum* grows and moves towards nutrient chemoattractant gradients.
2. If two plasmodium fragments encounter each other, they will avoid contact where other routes exist.
3. If two plasmodium fragments cannot avoid contact, the plasmodia will fuse.

The environment is represented by a greyscale image where different values correspond to different environmental features (for example, habitable areas, inhabitable areas, nutrient sources). The particles move about their environment (a two-dimensional lattice) and sample sensory chemoattractant data from an isomorphic diffusion map. When particles move about their environment they deposit chemoattractant to the same structure. Chemoattractant gradients were represented by projection of chemoattractant to the diffusion map at the locations indicated on the gate schematic illustrations. The projection weight was set at 20 multiplied by the chemoattractant pixel value (255). The weight factor is high as chemoattractant is deemed to be completely absorbed when it encounters the edges of the chamber and a large weight value is necessary to ensure the required propagation distance. The diffusion kernel was a 7×7 window for all experiments. Diffusion was achieved by the mean of the local window at each location in the diffusion map and damped at 10^{-4} (i.e. new value is equal to the mean multiplied by $1-10^{-4}$). We assumed that diffusion of chemoattractant from a nutrient source was suppressed when the source was engulfed by particles. The suppression was implemented by checking each pixel of the food source and reducing the projection value (concentration of chemoattractants) by multiplying it by 10^{-3} if there was a particle within a 9×9 neighbourhood surrounding the pixel. Particle sensor offset was 5 pixels, angle of rotation set to 45 degrees, and sensor angle was 45 degrees.

Growth and shrinkage states are iterated separately for each particle and the results for each particle are indicated by tagging Boolean values to the particles. The growth and shrinkage tests were executed every three scheduler steps and the method employed is specified as follows. If there are

1 to 10 particles in a 9×9 neighbourhood of a particle, and the particle has moved forwards successfully, the particle attempts to divide into two (i.e. a new particle is created) if there is an empty location in the immediate neighbourhood surrounding the particle. If there are 0 to 20 particles in a 5×5 neighbourhood of a particle the particle survives, otherwise it is annihilated.

7.5.1 Modelling Individual Gates

To implement the gates using the model, the schematic illustrations in Fig. 7.1 and Fig. 7.2 were transformed into the spatial representations shown in Fig. 7.5. The spatial pattern and greyscale encoding (boundaries, nutrient sources) is used to configure the diffusive map.

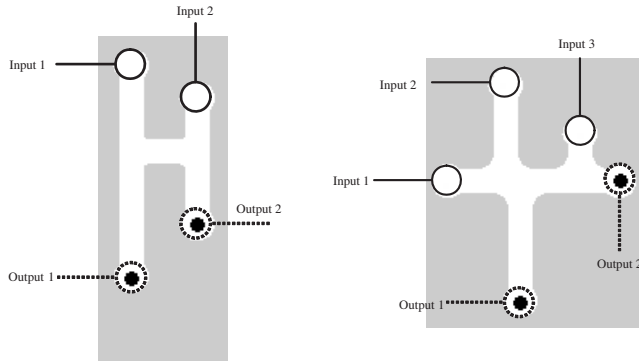


Fig. 7.5 Spatial implementation of logic gates G_1 and G_2 used in the particle model

Particles were introduced (depending on logical input conditions) at the areas indicated by solid circles at the top of the gates. Strong sources of chemoattractant were introduced at the outputs indicated as enclosed by dashed circles. The chemoattractant diffused from the output locations along channels etched into the gate configurations (white areas) and chemoattractant was removed immediately on contact with boundaries of the channels (light grey areas). The particle population was inoculated at identical times at the inputs, sensing, growing and moving towards the propagating diffusion gradients. To ‘anchor’ the growing paths to the start positions a very small amount of chemoattractant was also deposited at the respective start positions (the amount chosen was the lowest level needed to anchor the position without affecting the actual gate computation). Population inoculation and chemoattractant diffusion occurred at the same time and there was little or no directed growth of the population until the chemoattractants reached the source of inoculation.

The operation of the gates occurs due to the complex interactions between the chemoattractant diffusion gradients. Because there is a quantitative aspect to the chemoattractant gradient (i.e. particles sense not only the presence but also the concentration of the diffusion gradient), the gradient concentration is affected by the length and width of the gate channels [194]. The point at which the competing wave fronts meet is a spatial interface which delineates path choices in a similar way to those observed in chemical reaction-diffusion computations [72]. Thus, the environment is partially responsible for the initial selection of path choice. This ‘background processing’ by the environment satisfies the first of the three aforementioned criteria for plasmodium gate construction.

Two more factors add to the complexity of gradient interactions: Firstly when the particle representation of the plasmodium engulfs a food source, the diffusion of chemoattractant from that source is suppressed (reduced by a factor of one thousand). This alters the concentration of the gradient field from the engulfed source and the interface position where competing fronts meet shifts to reflect the new gradient field. Secondly, the collective movement of the particle population also results in local chemoattractant deposition along the path (this deposition is responsible for the local recruitment of particles by positive feedback and also acts to maintain the cohesiveness of the particle swarm). The local deposition of chemoattractant is also subject to the same diffusion as that which affects the food sources (in fact it is represented computationally as the same ‘substance’) and the diffusion away from the particle population also acts to generate a dynamical interface which competes with the food source gradients.

Suppression of food source gradients and local modification of gradients by the particle collective represents a highly dynamical spatial computation in which both local and distant sources of information (food source location, path availability) are integrated by both environmental and collective swarm computation. It can also be seen that the local modification of the gradient by the particle collective indirectly satisfies the second criterion for plasmodium gate construction — attempted avoidance of local plasmodia. The dynamical gradient interface represents a fragile boundary between two separate swarms, two separate food gradients or a combination of both swarm and food gradients. The third criterion — fusion of plasmodia can be represented in the particle model when movement of separate particle paths is limited and perturbation of the dynamic boundary occurs. This can result in fusion of network paths which corresponds to fusion of plasmodia.

The complex evolution of gradient fields can be seen in an example run of G_2 with the inputs 011 in Fig. 7.6. The top row shows the particle positions and the bottom row shows the chemoattractant gradient field enhanced by a local method of dynamic contrast enhancement. The first column shows the propagation of chemoattractant gradient from the two food sources and the interfacial region (dashed arcs). Note that the gradient from the right suppresses the gradient from the bottom source. The second column shows

the effect of suppression of the rightmost food source when engulfed by the particle population which has migrated towards it. Because the bottom food source is not suppressed the gradient from this source is stronger than the right side and the interface boundary shifts to the right of the T-junction. Note that there is also a weaker interface boundary between the diffusion gradient emanating from the bottom food source and the chemoattractant deposition from the particle population in the long vertical column. The third column shows the result of the competition between the food gradient and the population gradient — the food gradient is stronger and the population grows and migrates downwards to the food node.

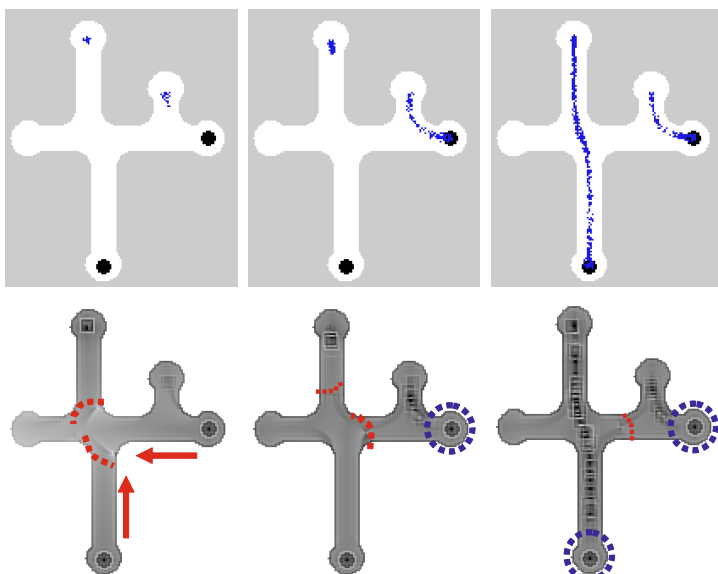


Fig. 7.6 Evolution of ‘plasmodium’ positions and interaction fronts in the particle model for the G_2 gate with inputs 011. Top Row: Particle positions. Bottom Row: Chemoattractant gradient. Arrows indicate propagation of gradient from food sources. Dashed arcs represent boundary regions separating competing gradients. Dashed circles represent diffusion from food sources suppressed by engulfment See text for explanation.

When the bottom node is suppressed the two separate paths remain stable and do not fuse. A fragile interfacial boundary can be seen between the two network paths (dashed arc) and, as long as the particles do not cross the ‘buffer’ space between the two paths, the paths will not fuse.

Results using the particle model for gates G_1 and G_2 are shown in Fig. 7.7 and Fig. 7.8 . The G_1 gate achieved 90% reliability and the G_2 gate achieved 98.57% reliability. The input conditions 0-0 were not included with the results because the output result for these inputs is guaranteed regardless of gate

design. For the G_1 gate we see that the shorter path to the right food source attracts the simulated plasmodium in both 0-1 and 1-0 condition. Note that no branching occurs from the plasmodium to the left nutrient source when the right source is connected. This is because the movement of particles (and their deposition to the diffusion map) creates a local diffusion field around the particle collective. The strength of this locally generated field is enough to suppress the field emanating from the left food source and no branching is observed. If the strength of the local field were less than that of the nutrient source then branching and growth to the left nutrient source would indeed occur.

The errors in the G_1 gate all occurred in the 1-1 input condition. The ‘pattern’ of the error is that the left particle stream did not continue downwards to the food source, but fused with the right side particle stream (indicated by dashed box). Analysis of all of the results found that whenever the growing particle plasmodium encountered a junction in a gate an apparent ‘hesitation’ was seen. The growth tip appeared to be indecisive as to which direction to take. When a direction was eventually chosen the growth speed increased when the growth tip moved past the junction. The hesitation, and indeed some of the gate errors, was caused by disturbances in the diffusion field near the tip of the growing plasmodium. The diffusion gradient emanating from the nutrient sources is relatively uniform whereas the gradient from the plasmodium tip is more intermittent in quality (because the tip growth is non uniform and changeable in form). In contrast the gradient from a moving straight part of the particle plasmodium was more uniform. The fragility of the gradient field at the growth tip was further perturbed by the spatial changes in the environment at the junctions. This, coupled with increased possible choices of directions, led to what we describe as junctional errors. The junctional errors are characterised by failures in searching of the growing plasmodium tip and were responsible for all of the failure instances of the G_1 gate.

The G_2 gate, although more complex in design, was more reliable than G_1 and the only errors which occurred were a single junctional error in the 011 input condition and an error in the 111 input condition. This error was classed as a timing error and was caused by different growth rates from the two left-side inputs. Ideally the two particle streams should meet and fuse but differences in the growth of the two separate streams led to non fusion and errors in output. To illustrate the transient dynamical nature of growth tip hesitation at junctions, junctional and timing errors, please refer to the supplementary video recordings related to this chapter.

7.6 Modelling the Half Adder

To implement the half adder based on gates G_1 and G_2 with the particle model the scheme of the half adder in Fig. 7.3 was slightly modified as shown

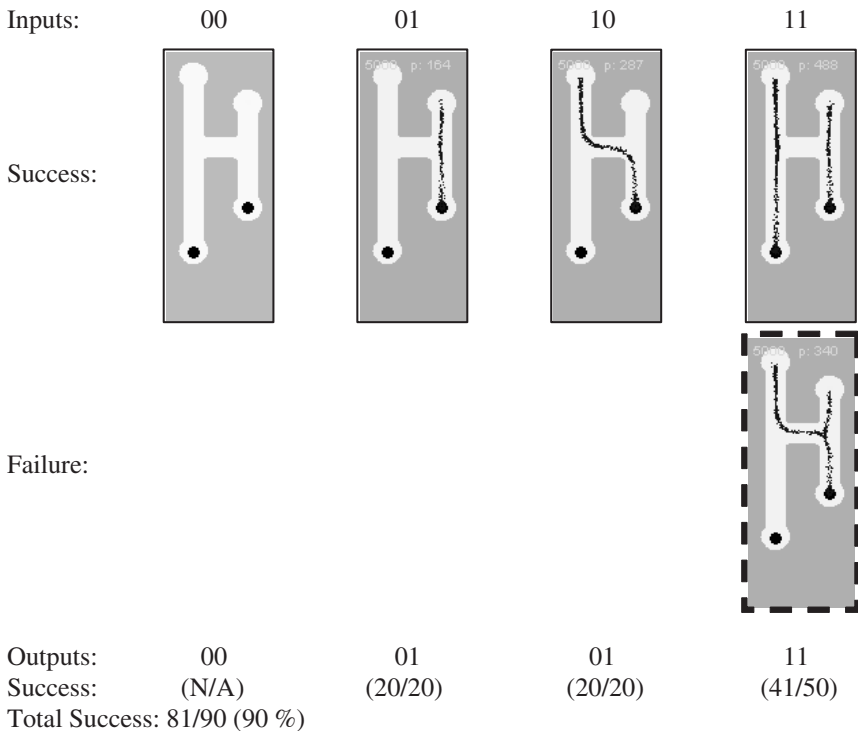


Fig. 7.7 Summary of results for particle approximation of *Physarum* based logic gate G_1

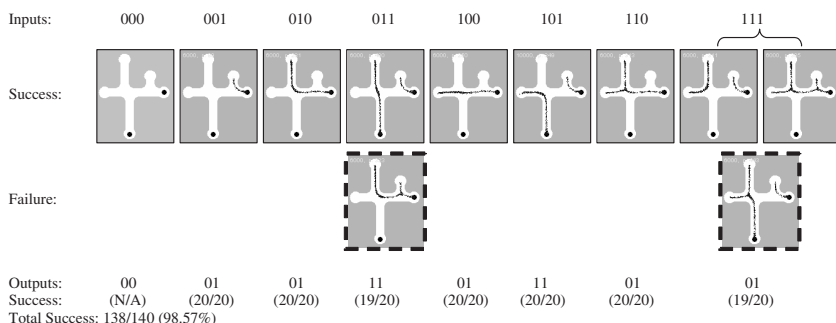


Fig. 7.8 Summary of results for particle approximation of *Physarum* based logic gate G_2

in Fig. 7.9. The G_2 gate combination was simplified by ‘sharing’ the food source between both gates. Constant TRUTH inputs (‘1’) were provided as some of the gate inputs to implement the desired function. The outputs of the combined G_2 gates were fed to act as inputs to the lower G_1 gate. To ensure that the particle population continued to the input positions of the lower gate synthetic chemoattractant stimuli (small dots) were placed to guide any plasmodium along the channel to the input positions. The ‘ $G_2G_2G_1$ ’ triplet combination acted as the XOR (summation) part of the half adder. The AND section of the half adder (carry computation) was implemented as a single G_1 gate (Fig. 7.9, left). In the simulations the branching of initial X and Y signals to provide the inputs to both sections of the half adder was not implemented in an effort to simplify the design and the relevant X and Y inputs were introduced to the gate manually.

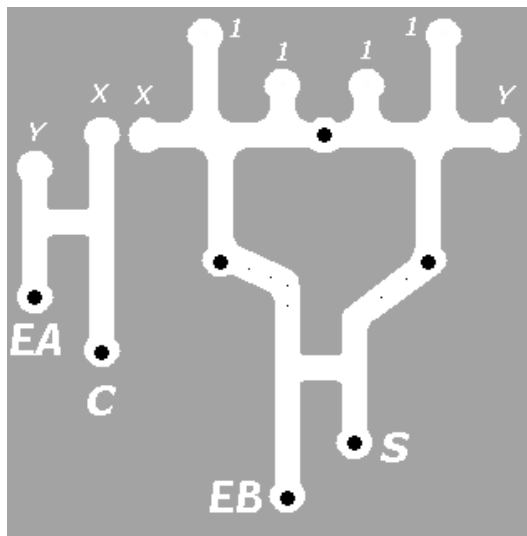


Fig. 7.9 Spatial representation of half adder based on combinations of G_1 and G_2 . X and Y: Inputs to half adder, 1: constant TRUTH signals, S: Sum output, C: Carry output. Solid discs are food sources and small dots are small food sources to feed outputs towards lower gate inputs. EA and EB: Error checking flags (see text)

The use of constant TRUTH inputs to the half adder introduces errors in gate output when inputs are 0-0. This is because the outermost truth signals at the inputs of the G_2G_2 gates travel down through the gates and into the lower G_1 gate. This would result in the ‘no input’ condition actually causing an erroneous output. Apart from redesigning the gate this presents an opportunity to consider possible use of error checking signals in the gate design. One possible error checking signal is the ‘EA’ output in the left side of

the circuit (Fig. 7.9, left). It can be seen that this flag should be set whenever any of the inputs are set to true. It would therefore be possible to use the absence of the EA output to indicate a 0-0 input to the half adder, and thus indicate erroneous output from the constant TRUTH inputs to G_2G_2 . Another possible use of outputs to indicate error conditions is the ‘EB’ output from the left G_1 portion of the $G_2G_2G_1$ triplet (Fig. 7.9, bottom). It can be seen (Fig. 7.10) that the EB flag should never be set unless the 0-0 condition caused by constant TRUTH inputs occurs. This flag could be combined with the lack of EA output to indicate errors. When the EB flag is set without the presence of EA then a fault can be assumed to have occurred within the half adder $G_2G_2G_1$ triplet. Of course the addition paths and mechanisms to make use of these error checking flags adds another layer of complexity to the circuitry which is out of the scope for this research. The results of the half adder approximation can be seen in Fig. 7.10

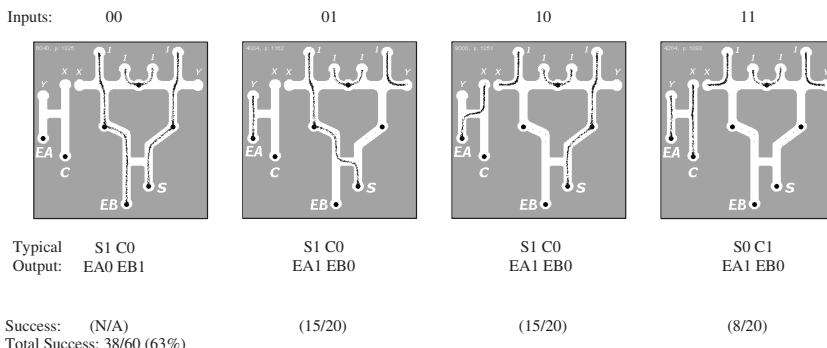


Fig. 7.10 Examples of input and output conditions for the particle approximation of the half adder.

The failure rate for the half adder approximation, even when not including the difficulty posed by the 0-0 configuration, was significantly higher than for the single gates. The majority of the failures were caused by timing errors, which occurred when the outermost inputs to the G_2G_2 combined gate did not fuse correctly with the constant TRUTH inputs and, instead, travelled down towards the lower gate. Junctional errors also occurred three times in the left G_1 gate for the 1-1 input condition.

The combination and extension of the individual gates appeared to compound the errors in the individual gates. Although no definitive answer can be given as to why the unreliability increased, we speculate that the combining of the gates subtly affected the propagation and profile of the chemoattractant gradients.

7.7 Summary: *Physarum*-Based Logic Gates — A Square Peg in a Round Hole?

The results from the computational approximation of *Physarum* support the findings of [92] that the organism can be used to construct simple logic gates, and also the computing schemes within this chapter which explored the creation of more complex combined gates and half adder circuitry. The findings suggest that, although such circuits can indeed be built, the presence of both timing errors and junctorial (search) errors would severely limit the effectiveness and practicality with even more complex circuits.

The matter of errors of the gate operations (timing errors and junctorial errors) requires further consideration. The term ‘error’ depends on the perspective taken. From an experimental viewpoint the occasionally unreliable operation of the gates is erroneous. But the notion of externally applied — by the experimenter — environment conditions and metrics of success cannot be easily applied to the behaviour of a living (or even simulated) collective organism, whose sole imperative is the location and connection of nutrient sources for survival. By following the biological imperative the organism is not actually doing anything ‘wrong’.

Ascribing such obviously successful survival strategies as erroneous behaviour merely because they do not suit the experimenter’s demands seems to do a disservice to the organism. At the risk of further anthropomorphism it seems as if the collective is hampered by a *double-bind* caused by conflicting biological and computational requirements: “Please forage successfully, but not too successfully”.

It appears that this conflict could not easily be resolved from an engineering perspective because, on one hand, we cannot lessen the requirements of digital circuit operation to accept logically incorrect output. Nor is it possible to rein-in the natural foraging ability of the plasmodium. Although it is possible to track the logical errors by using spare signal channels (as noted in the half-adder circuit), acknowledging that there is an internal problem does not actually rectify the problem. Simple logic gates form the basis of complex circuits whose reliability must be total so that they may be considered as ‘black box’ interchangeable components in hardware design. They are designed from the ‘top-down’ to achieve their reliability and unpredictable or emergent results cannot be tolerated using this design approach. *Physarum*-based computing uses the opposite approach — simple low-level interactions generate complex and unpredictable emergent computing abilities from the ‘bottom-up’. Although we cannot guarantee the low-level reliability of the output of foraging in the *Physarum* plasmodium we *can* state that the plasmodium will forage and that the resultant emergent behaviour will be complex and unpredictable. Harnessing this spatial and temporal unpredictability, for example in a manner as suggested by [195], may prove to be a more suitable application of the computational properties of *Physarum*.

Although the use of *Physarum* for classical logical gates indeed makes use of its intrinsic properties (gradient oriented growth, avoidance, fusion), the confinement of this naturally amorphous, dynamic and flexible organism into architectures which require precise timing and predictable path traversal does not utilise the natural advantages which the organism possesses. The increasing failure rate when circuit complexity is scaled upwards may — perhaps fancifully — be interpreted as the embodiment of an internal frustration by the plasmodium at such confinement and control. It appears likely that *Physarum* may be more naturally suited to device implementations which harness its abilities in integrating complex, noisy, unpredictable, spatial and temporal signals. In such devices the concept of rigid control of behaviour will be reduced to an influence on behaviour, where the influence is applied as a +ve or -ve stimuli which affects behaviour. We investigate such implementations in chapter 13.

To conclude, the results in this chapter suggest that it might be better to fit a computation task to the natural spatial behaviour of *Physarum*, rather than the opposite way round. If we are to use the network formation and morphological adaptation of the model plasmodium for useful problems we require a means of controlling — or at least *influencing* — its behaviour. In the next chapter we explore a real-time feedback mechanism aimed at trying to guide the evolution of the virtual plasmodium.

Chapter 8

Dynamical Reconfiguration of Transport Networks Using Feedback Control

“We sleep, but the loom of life never stops, and the pattern which was weaving when the sun went down is weaving when it comes up in the morning.”

(Henry Ward Beecher, 1858)

8.1 Introduction

In previous chapters we have examined how the microscopic particle interactions of the multi-agent model of slime mould generate emergent behaviours which have material-like properties. Because this ‘virtual material’ is naturally adaptive in its shape, and because it can be influenced by external stimuli, it may potentially be classed as a so-called Smart Material. Smart materials are materials which can change their structural and/or functional properties in response to external stimuli [196]. These may produce a change in morphology. For example, a deformed substance made from a shape memory metal alloy [197] will return to a previously ‘programmed’ shape when heated. Alternately, the external stimuli may result in a change of the function of the substrate. Examples include piezoelectric materials [198] which can be used as both sensors (responding to force by producing electrical charge) and actuators (responding to electrical current by producing a mechanical force). Smart materials may also refer to the self-assembly of structures at very small scales, as seen in biological systems [199]. In this method physical phenomena which exhibit self-organisation at small scales are harnessed to provide regularised assembly and patterning of small structures. Examples include the assembly of bulk materials and thin layers [200], with regularly spaced domains [201], or structures which exhibit or utilise complex macroscopic properties, such as hydrophobic patterning [202].

Smart materials suggest novel and advantageous methods of product assembly, device control, and even self-repair yet the technology faces significant difficulties. Aside from the obvious challenges in materials science, one important issue is how to control the behaviour of large aggregates of smart

material substrate to conform them to the desired structural and functional behaviour? Yet natural systems represent an enviable solution to many of the problems faced by smart materials: For example, from a single specifying unit, a fertilised cell, and given the requisite energy and nutrient supply, a fully functioning ‘device’ ultimately emerges from a combination of low-level physical, chemical and genetic interactions (a tiny ‘window’ on these interactions is given in [203]). From a relatively small pool of materials emerges an organism which is capable of growth, movement, sensory functions, environmental interactions, learning, maintenance, and self repair. The goal of biologically inspired smart materials is to harness some of the mechanisms used by natural systems, particularly self assembly and the coupling of low-level physical forces, to develop materials, and ultimately entire devices, whose form and function are reconfigurable.

Physarum plasmodium may be considered as a living spatially represented smart material because it is composed of relatively simple parts yet exhibits complex self assembly and controllable pattern formation. The plasmodium material can act as sensor and actuator [53], and the mechanisms controlling both properties arise from simple interactions and are distributed within un-specialised tissue resulting in fault tolerance and self-repair (for example a plasmodium may be split into two parts, yielding two functional plasmodia, or alternately two plasmodia may fuse to form a single plasmodium). Control of the plasmodium smart material is by attractants (nutrient sources, warmth) which the plasmodium moves towards, and repulsive sources (sodium chloride, light irradiation) which the plasmodium tries to avoid [83]. It is possible to control the spatial patterns of the plasmodium for the direct spatial encoding of problems. Gross control of plasmodium morphology was used in [96] and [83] by manually adding and removing nutrient sources or hazards, but can the desired spatial configurations be achieved automatically?

An interesting hybrid spatial/logical approach to controlling *Physarum* was used by Aono and his colleagues [195] in which a *Physarum* plasmodium was constrained by patterning it as the hub of a circular chamber surrounded by 16 stellate projections. Each projection corresponded to a possible link between nodes in a four node network. By applying an image analysis system and a neural-type feedback mechanism similar to Hopfield-Tank networks [204] they controlled the natural extension of pseudopodia to the projections surrounding the arena by light irradiation. Each arm represented a possible connection between cities in a Travelling Salesman Problem tour and the neural feedback mechanism was used to enforce the avoidance of invalid tours. The method was capable of finding good tours to the problem and the plasmodium spontaneously adapted its morphology between good nearby suboptimal tours, thus avoiding being trapped in local minima conditions.

The paper by Aono et al. shows that by constraining the natural spatial behaviour of the *Physarum* plasmodium it is possible to control its peripheral morphology to represent abstract problem representations. More recently, the same experimental approach, and similar results, was performed with a

different material substrate composed of a population of the protist *Euglena gracilis* experimentally and in simulation [87]. The fundamental difference in the nature of the computing substrates (single-celled vs multi-cellular) suggests that distributed computation may be possible with a wide range of relatively simple materials.

Although the Aono et al. experiments demonstrated the morphological control of the periphery of the plasmodium, the full range of patterning of the migrating and adapting plasmodium was not exploited for computational purposes. Instead, the problem was encoded to fit the constraints of the experimental cell. In this chapter we investigate possible mechanisms for the dynamic *spatial* reconfiguration of smart materials, with the ultimate aim of controlling the behaviour of the material for spatially represented computation. We use the virtual plasmodium model which was shown in previous chapters to adapt its morphology in response to nutrient stimuli, depending upon nutrient concentration. We attempt to dynamically control its morphology in real time using a novel real time network analysis method which is coupled to a feedback mechanism whereby the spatial configuration of the material can be altered by the dynamic adjustment of network node concentration to achieve pre-desired network characteristics. We present some results which illustrate the complex network transitions of the material in response to excitation, inhibition and refractory conditions generated by the feedback system, suggesting that the method and materials may be useful for spatially represented unconventional computation approaches to combinatorial optimisation tasks, including the Euclidean Travelling Salesman Problem. We conclude by discussing some advantages and limitations of the current approach and suggestions for future research.

8.2 Dynamical Reconfiguration of Transport Networks

In chapter 6, Fig. 6.9 we found that by systematically alternating periods of very high node concentration followed by very low node concentration, it was possible to gradually reduce the degree of connectivity of the network. The adjustment of node concentration was performed by adjusting the projection weight of chemoattractant into the diffusive lattice for all nodes simultaneously. This, however, raises the possibility of a more dynamic control of network evolution within a single run: By using a suitable feedback mechanism is it possible to dynamically adjust individual node concentration so that a ‘preferred’ network configuration can be generated? By ‘preferred’ we mean a configuration that satisfies some pre-desired connectivity criterion, such as mean degree of connectivity per node. Both node concentration adjustments and preferred configuration need only be specified in a local fashion. To feed back information to adjust node concentration we require some analysis of the current state of the transport network so we can provide local measures of the network configuration. The method given here uses information about

the degree of node connectivity (i.e. for each node: how many other nodes is it connected to in total, and to which nodes).

8.2.1 Real-Time Analysis of Network Configuration

Analysing the state and connectivity of a spatially represented network is a computationally demanding task when performed at regular time intervals. This workload is in addition to the computation required to generate the transport network behaviour of the virtual material and also the feedback mechanism. This raises an important distinction between the approach used by Aono et al. (which coupled the physical system of the slime mould to a computer controlled sensory/feedback mechanism) and the approach in this chapter where the ‘physical system’ is itself the emergent product of a low-level simulation. The simulation of the physical system therefore demands particularly low cost methods of analysing the current state of the system. Using classical image processing methods requires sampling of current spatial state of the system. This involves smoothing the image, thresholding the image, binarisation, skeletonisation and finally establishing connectivity by tracking from node to node for each node at every network analysis step. To make the approach more computationally tractable we sought to develop a method whereby the network connectivity could be generated from the ‘bottom-up’ by the collective actions of the particles which comprise the transport network, yet still provide an accurate representation of network connectivity. The analysis which provides information about node connectivity is generated in the following way: Before an experiment is started the start positions of the nodes are automatically detected once by standard image processing methods and stored in an array, giving the number of network nodes and their (x, y) co-ordinates. This information is used to construct a two-dimensional array, the node connectivity table. Each entry in the table stores the relative strength of the path between the two nodes referenced at the node table row and column positions. At the start of an experiment all connectivity is reset to zero.

During an experimental run each particle, initialised at a random position, receives a ‘*source_node*’ identifier when it passes the vicinity (specified by *node_radius* parameter, value of 11) of the first node it encounters. When the particle moves about the lattice its position is checked to see if it is in the vicinity of a new node. When the particle encounters a new node the new node is set as the ‘*destination_node*’. The node connectivity table at the two positions (*source_node* and *destination_node*) is incremented by a value (*node_inc*), set to 1 (Fig. 8.1, top row). Finally the particle takes the *destination_node* value as the new *source_node* and clears the *destination_node* value until another new node is encountered. This process is repeated for all of the particles in the lattice and, over time, a collective ‘picture’ of node connectivity emerges as path weights increase in the node connectivity table. The method of using the particles themselves to build

up a measure of connectivity requires some additional complexity in the behaviour of the particles but is efficient in terms of storage (each particle needs only to store the source and destination node) and computational time since typically the adaptive population size quickly settles to <1000 particles. Although a rough approximation, each collective update of the node table thus takes 1000 simple computations (entries to the table) whereas classical image analysis methods are limited mostly in performance by screen area (typically 200×200 for these experiments) and thus each step in the image processing pipeline would require a minimum of 40,000 calculations, and some parts of the pipeline, particularly connectivity tracking, require much greater cost. The collective representation of connectivity has another advantage over classical methods in that the table also contains implicit information about the relative strength of path weights (i.e. how ‘busy’ each path connection is) which would not be achievable using classical tracking methods. This information is utilised during the feedback method and significantly affects the evolution of the network. One objection to this method of connectivity analysis is that it requires more complexity than would be seen in simple particles. This is indeed a valid criticism when applied to material properties of simple molecules and the method used does take the liberty of arbitrarily extending such limitations in the interests of computational tractability. It is of note, however, that similar distributed representations of collective connectivity have been observed in simple insects such as bee [205] and ant [206] colonies.

The collective representation of connectivity established by the particles may be subsequently used by the control system to apply feedback to the population. The degree of connectivity of a node to all other nodes can be assessed by checking the connectivity strengths along its row in the node table (any nodes with a value greater than zero indicates a connection to this node). The node connectivity table is effectively an emergent history, or collective memory, of the connectivity of the emergent transport network. However because the network is highly dynamical with constant changes in connectivity, the information in the table is soon outdated and irrelevant. To reduce the memory time of the node table all of the nodes in the table are decremented at every scheduler step by a value *node_decay*. This ensures that the node table can keep up to date with the changing network topology. Note that the *node_decay* parameter is critical in setting the memory time of the network. If the value is too low the connectivity table information used to control the feedback system will be out of date (e.g. referring to connections which no longer exist). However it is necessary to enforce some slight lag in order for the feedback method to have some tangible effect on the network structure (i.e. it takes some time for the ‘material’ to respond to changes in node concentration). The effects of this parameter will be discussed in more detail in the description of the feedback mechanism.

The result of the dynamical network analysis is a transformation of the actual transport network flux into a real-time dynamic topological representation of network connectivity (Fig. 8.1, bottom row). Although the actual

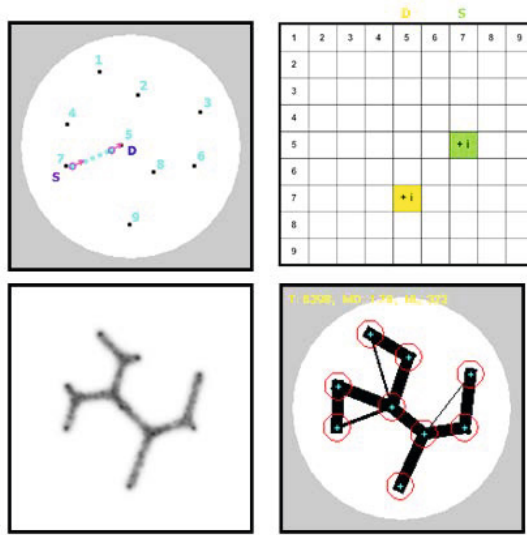


Fig. 8.1 Schematic illustration of real-time analysis of emergent transport networks. Top Left: Node positions (1-8) are stored by automatic detection before experiment begins. Particle source node (s) and destination node (d) are indicated. Top Right: Node connectivity table is updated whenever a particle arrives at a different node. Bottom Left: Actual spatial configuration of emergent transport network. Bottom Right: Topological connectivity of emergent transport network. Crosses indicate node positions and circles indicate radius of the particle node detection vicinity. Thicker lines between indicate stronger connections. See text for explanation of cross lines between nodes.

network and topology are similar, the topological representation shows extra connections (shown as the thin lines between nodes on Fig. 8.1, bottom right). This is because at low node concentration (where node concentration is similar to network path strength) the transport network is partially detached from the nodes to adopt the minimal network shape (the Steiner tree, which has additional junctions in addition to the original node array). In doing so, some of the particles in the network path between three nodes do not actually visit the fixed middle node, instead passing through the Steiner point between the nodes. The topological representation illustrates that a fixed node may be indirectly connected, via a Steiner node, to a nearby node. The relative differences in strength between node connections can be visualised by the differences in thickness of the dynamical representation of network topology.

8.3 Network Feedback Mechanism

The connectivity information in the node table is used during the feedback process to dynamically adjust node concentration and is dependent on certain rules. Different sets of rules may be specified to achieve different connectivity effects. The effect we are seeking in this prototype example is to attain a degree of connectivity for all nodes of exactly 2, thus the aim is to generate a complete network with only one cycle where all nodes have connectivity of 2. Such a path is a possible tour of the Travelling Salesman Problem (TSP, although not necessarily an optimal tour). The feedback rules are summarised in Fig. 8.2.

Degree	Node Status	Desired Action	Mechanism
0	Disconnected from network	Reconnect node to network	Increase node weight. Seed new particles
1	Connected to only one other node	Connect to another node	Increase node weight. Seed new particles towards other single nodes.
2	Connected to two nodes in chain	Reinforce Connectivity	Increase node weight
3	Directly or indirectly connected to three nodes	Reduce Connectivity	Decrease node weight
> 3	Directly or indirectly connected to more than three nodes	Strongly Reduce Connectivity	Strongly decrease node weight

Fig. 8.2 Feedback mechanism rules to enforce degree of 2 connectivity per node

The concentration of the nodes is initially set to a predefined fixed value ‘*start_weight*’ at the start of an experiment because at the early stages of an experimental run a record of the network connectivity is yet to emerge in the node connectivity table. At regular intervals specified by the ‘*feedback_interval*’ parameter (every 10 scheduler steps) the degree of connectivity of each node is analysed and is updated according to the rules in Fig. 8.2. If the degree is < 2 then node concentration is increased by the ‘*weight_inc*’ parameter (set to 0.001). If the degree is < 1 (i.e. no network path passes through the node) the node concentration is incremented by (*weight_inc* * 2). Node concentration is subject to a maximum value, ‘*weight_max*’, typically set to 10. Increasing node concentration attracts nearby network paths to the node due to the increased distance of diffusion of attractant from the node and nearby paths are ‘snagged’ by the node. If a network path is already connected to a node then further increasing the node concentration strengthens the attraction of the path to the node (effectively ‘tightening’ the path and shortening the path distance between nodes).

If the degree of connectivity at a node is > 2 then inhibition of the node is achieved by decreasing node concentration by the ‘*weight_dec*’ parameter (set to 0.0001). If the degree is > 3 then node concentration is decreased by

($weight_dec * 2$). Decreasing node concentration reduces the attraction of network paths to a node. The minimum value of node concentration is zero. At low node concentration the network detaches from the node as its attraction to the network is less than the flow within the network path. To further reduce the attraction to an overpopulated node, network trails nodes in such nodes are decremented by ‘*path_decrease*’ which is calculated by the number of particles within a 5×5 window of the node position multiplied by 0.1.

The advantage of decreasing network paths from nodes is that much stronger changes in network connectivity can be obtained by temporarily decoupling paths from nodes. However, an issue which arises is how to re-establish contact with a node which has little contact with the remainder of the network (degree 1, i.e. the node is at the end of a path of connected nodes), or has been completely detached from the network due to low node concentration. To re-establish contact and increase connectivity to the node new network particles are seeded around the isolated node, preferentially in the direction of other isolated nodes but at a random angle otherwise. The distance at which new particles were seeded was set to a random value between zero pixels and the ‘*scatter_distance*’ parameter (typically 10-20 pixels). The re-seeding mechanism would be very difficult (if not impossible) to implement with molecular materials but it may be possible to implement such a feature in other methods of physical computation such as gas discharge plasmas used in [59] for optimal path planning. It could also be argued that the re-seeding method also adds a mode of global control to an otherwise bottom-up approach, however, the reattachment of nodes is merely used to satisfy minimal constraints of network connectivity. A similar method was applied (but under more strict constraining conditions) in the original Hopfield-Tank approach to enforce a correct solution “syntax” [204], but although the re-seeding mechanism does allow large changes in network connectivity, it is not part of a global method to enforce solutions and thus does not detract from the bottom-up mode of network evolution.

The changes in node concentration (via increases or decreases in node projection strength) combined with the limited memory storage of the connection weight array (caused by a lag due to the decay factor) combine to generate a neural network-like feedback behaviour. The increase in node concentration and subsequent attraction of the network paths corresponds to excitation. Conversely the reduction in node concentration and the subsequent reduction in influence of the nodes on network paths correspond to inhibition. The neural network analogy can be extended if we consider the arrival of particles at the nodes as spiking stimuli which are integrated at regular intervals as feedback excitation or feedback inhibition. The persistence of the collective memory of network structure generates a lag period during which concentration at inhibited nodes is not increased. The lag (between actual network configuration and the collective memory of configuration) and low concentration at inhibited nodes allows the network structure to adapt and reconfigure. When inhibition is present (due to degree >2 connectivity), the inhibition

combined with the delay lag can be considered as a refractory period. The refractory period is not programmed into the feedback mechanism but is an emergent property of the feedback lag and can be utilised to ensure that network adaptation can occur, without the network responding too quickly to changes in topology. The cycle of feedback behaviours can be summarised by Fig. 8.3 showing the relationship between actual network connectivity, the collective memory of logical connectivity, the feedback mechanism, and the subsequent effect on node concentration.

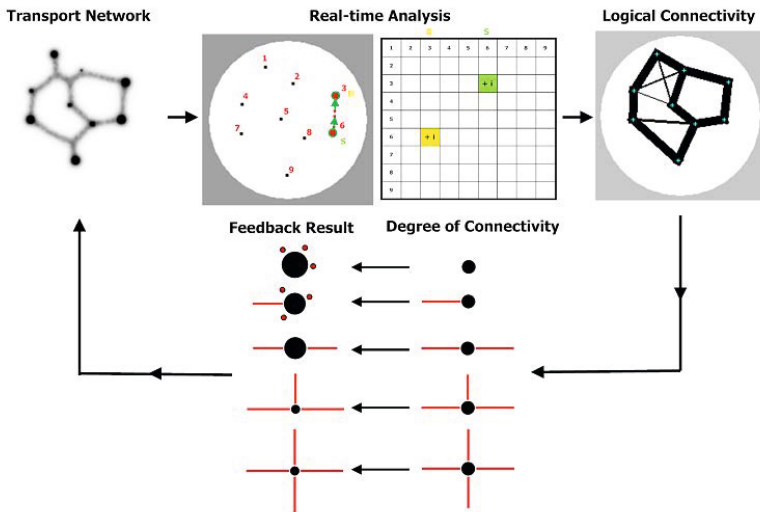


Fig. 8.3 Relationship between network behaviour, analysis and feedback mechanisms in adaptive reconfiguration of emergent transport networks.

8.4 Results

We began with simple images with regularly spaced node arrangements to examine the behaviour of the network in response to dynamic adjustment of node concentration. Fig. 8.4 shows a simple image with six nodes and the results of five separate experiments at different node projection weights. At the highest setting (5) there is little reduction in network length as the nodes exert a very strong attraction to the network, preventing the network paths from direct interaction. As node concentration decreases the influences of the nodes decrease and network paths come into contact with other paths resulting in minimisation until, at the lowest concentration, the network evolves to its minimum shape to form the Steiner tree. The varying network patterns at different node concentration suggests that dynamical reconfiguration of node weights (i.e. dynamically varying weights over time) would yield a wider variety of network connectivity and thus complex network evolution.

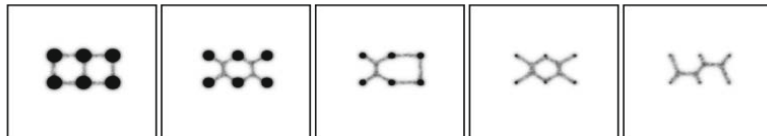


Fig. 8.4 Results from separate experiments with fixed node concentration. Left to right: Node concentration 5, 1, 0.1, 0.01, 0.005.

When dynamic reconfiguration (DR) is activated the network evolution begins in the regular manner but then undergoes a very complex transformation as each network node concentration is individually adjusted in response to connectivity feedback (Fig. 8.5). The complex evolution can be seen more fully in the supplementary video recordings. The two nodes (indicated in (a), circled) are of degree three and so their projection weight is progressively weakened by the feedback mechanism. When the concentration of the two inner nodes is sufficiently weak their ‘hold’ on the network is removed and the network detaches from the node and contracts, moving upper and lower network paths towards each other (b). When the upper and lower paths contact their flows merge and the 4 way junction is minimised (c), resulting in both network cycles being pulled to the outer nodes of the shape (d). Because the two vacant nodes (seen in (e), circled) are no longer visited by particles, their inhibition is reduced as the cumulative ‘memory’ of the prior connectivity at each node is gradually erased. When this occurs, the node concentration is progressively increased until the lower node attracts the network path by seeding new network trails at random positions close to the lower node (f). The upper node reattaches itself to the network in a similar way (g). Although it is not apparent in the static images, there is considerable interplay between the current network pattern evolution and previous network history. This is due to the lag caused by the cumulative record of network connectivity, combined with the refractory period caused by the inhibition of low node concentration. This refractory period causes temporary detachment of nodes from the network (h). The network evolution continues (i-j) until all nodes are of degree two and the network then remains in this stable configuration. It is notable that the DR approach is successful in generating a minimal tour around the nodes, even though the ‘search’ performed by the feedback mechanism is effectively blind.

When a pattern of 12 nodes arranged in a cross-like fashion is presented to the network we saw that the outermost nodes were minimised to degree two before the effects of the DR procedure had any influence on inhibiting the node concentration ((Fig. 8.6)a-c). When the concentration of the inner nodes (degree 4) was reduced the network was pulled to the outer nodes (d-e). On removal of inhibition, and as the inner node concentration increased, the nodes attracted the network paths from the outer nodes and a minimal tour

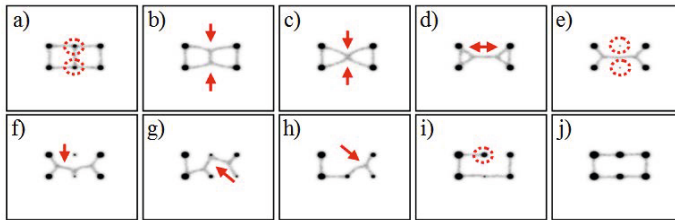


Fig. 8.5 Dynamical reconfiguration of six node network, see text for details

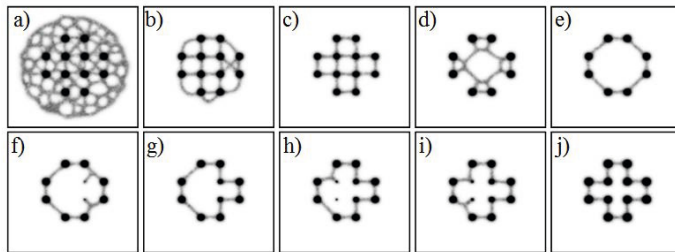


Fig. 8.6 External node fixation as a stabilising factor in network minimisation

was again generated to form a stable state. The anchoring of the network to outer nodes is a common motif and appears to stabilise the evolution of the network, ensuring that changes in configuration in one area do not impinge on the structure of the network too greatly at other locations.

Particular spatial patterns in the transitions between network configurations are regularly seen. Some of these motifs are relatively simple, relating directly to the feedback mechanism, including the passive attachment (of ‘snagging’) of nearby paths by attraction to the nodes, the minimisation of path length between two nodes (‘tightening’), the releasing (‘detaching’) of network paths from nodes at very low node concentration, and the active re-connection (‘grabbing’) of isolated nodes to the network by seeding new particles around the isolated nodes. Other motifs are more complex and cannot simply be reduced to the feedback options at a single node. For example, interactions with nearby nodes selectively weaken certain nodes and can guide network evolution away from deadlock conditions. This allows a network path edge to shift position (‘sliding’) between nearby nodes, leaving nearby connectivity relatively unaffected and thus subtly adjusting network structure. The network evolution motifs newly observed in the DR method complement the constraining of paths by nodes and the ‘zipping’ and ‘unzipping’ of network paths previously observed in the virtual material.

When examining the evolution of the DR network there are transition periods as the network responds to changes in node concentration. These are followed by relatively stable periods as the new network configuration has an effect on the collective record in the feedback system (as new configurations are reinforced and the ‘memory’ of older configurations fades). Each stable period of connectivity may be considered as the spatial equivalent of a high-level computational output arising from low-level functionality: The function ‘output’ is a new (relatively) stable configuration and the low-level function, or procedure, is the sequence of atomic interactions where network paths are altered by changes in local attraction by the amplification and inhibition of node concentration. As an example of the relationship between high-level and low-level spatial activity, consider the sequence of temporarily stable configurations in Fig. 8.7 from an experiment with a 4×3 regular network of nodes.

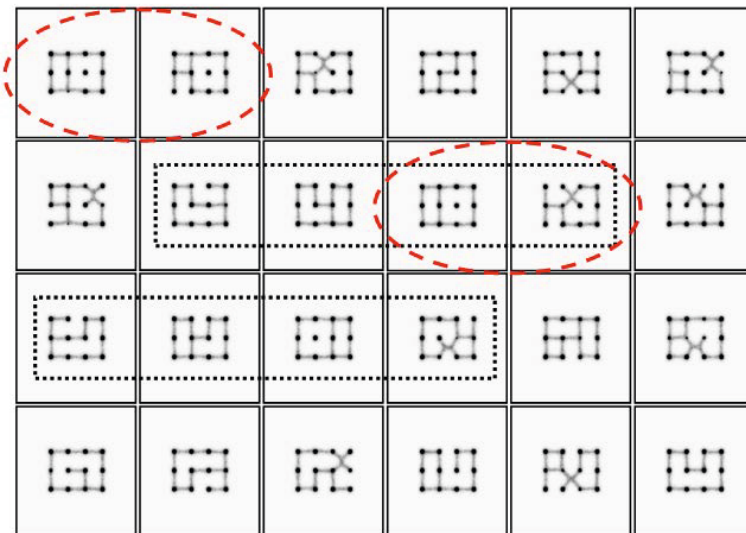


Fig. 8.7 Temporarily stable configurations after reconfiguration transitions

The sequence shows 23 transitions until the final pattern, corresponding to a minimal tour, stabilises the network. Although the minimal tour is found the blind nature of the search ensures that the search is not optimal. In a number of cases a pattern very close to that of the final tour is found, only to be lost in the next reconfiguration. A number of patterns are unique but occasionally identical individual patterns and identical transitions between

patterns are seen. For example, the two sequences of patterns surrounded by dashed rectangles in Fig. 8.7 are identical (albeit mirror images of each other) and undergo two identical transitions before differing only in the output pattern of the third transition. To find the cause of the different transition outputs we must examine the low-level interactions which generate the relatively stable high-level patterns. The transitions examined are those indicated by dashed ellipses in Fig. 8.7 because the first images in each transition pattern are identical and not simply mirror images, making the low-level transitions simpler to follow. The low-level transformations of the identical pattern that result in differing outputs are shown in Fig. 8.8.

Although the connectivity of the two initial patterns (i) and (ii) is identical, the connection weights at the nodes are not exactly the same. In (i)a there is only one ‘weakened’ node (circled) whereas in (ii)a there are two nodes (circled) which are influenced by the feedback mechanism. This difference is responsible for the different pattern in the stable output result because transition (i)b-f only involves the lower nodes in the network whereas in transition (ii)b-g both lower and upper nodes are incorporated into the network evolution (direction of network path movement is indicated by arrows and newly reactivated nodes are circled). This result illustrates both the sensitivity of the mechanism to small changes in connectivity and also the effect of previous network connectivity history on future evolution of the network.

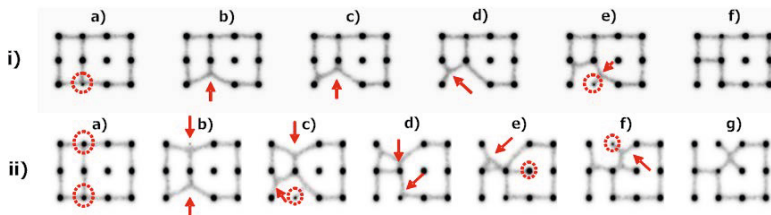


Fig. 8.8 Different low-level interactions cause differing transitions between patterns

The examples of the DR mechanism shown previously have used regular spaced nodes. This results in relatively simple transformations with only a narrow range of angles in the networks (typically 90° or 45°). How does the DR mechanism respond to more complex arrangements of nodes, with irregular placement in terms of distance between nodes and node angle?

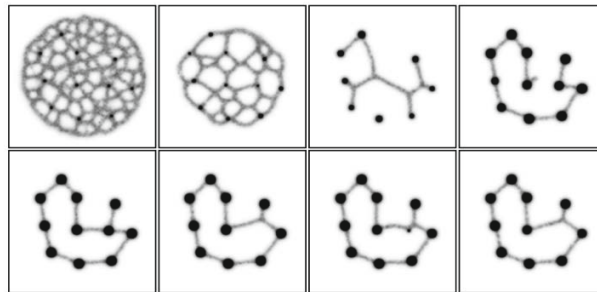


Fig. 8.9 Dynamical reconfiguration showing evolution of more complex node arrangements

Fig. 8.9 shows the evolution of one network which follows a similar evolution to those with regular node arrays: A ‘backbone’ of outer nodes is the first to stabilise and then the configuration of inner nodes is incorporated into the network structure. Unlike the regular arrays, however, the network configuration never fully stabilises. Certain configurations are generated (for example those shown on the bottom row of Fig. 8.9), only to be remodelled (because one or more nodes has mean degree of 3). This pattern of evolution was found to be very repetitive with the network oscillating between semi stable states.

Fig. 8.10a illustrates the effect of the DR method on the mean degree of node connectivity throughout an experimental run. The mean degree fluctuates as the network configuration changes in response to the dynamical adjustment of node concentration. The images above the plot (dashed boxes) show configurations at the time of increasing mean degree (i.e. sub-optimal networks at the crests of the plot). These configurations are typically transient and occur during major shifts of network patterns. The lower images below the plot (solid boxes) coincide with local minima of mean degree. Note that although these local minima have mean degree close to the desired specification (2), the patterns are not stable (due to isolated nodes or occasional degree of 3) and the network soon transforms into another configuration. The evolution of the network only halts when stability of configuration has been achieved. Also shown in Fig. 8.10b is an illustration of the changing node concentration for each of the 11 nodes throughout the same experiment (time direction is arrowed). The highest point on each node ‘lane’ corresponds to maximal node concentration (10, no inhibition of node weight at all) and the lowest point corresponds to the minimum concentration (zero, maximum inhibition of node weight, i.e. no projection of attractants). The pattern of node concentration shows the independent nature of the node weight adjustment by the feedback mechanism, and it is only when the network stabilises into the final pattern that the node weights are synchronised.

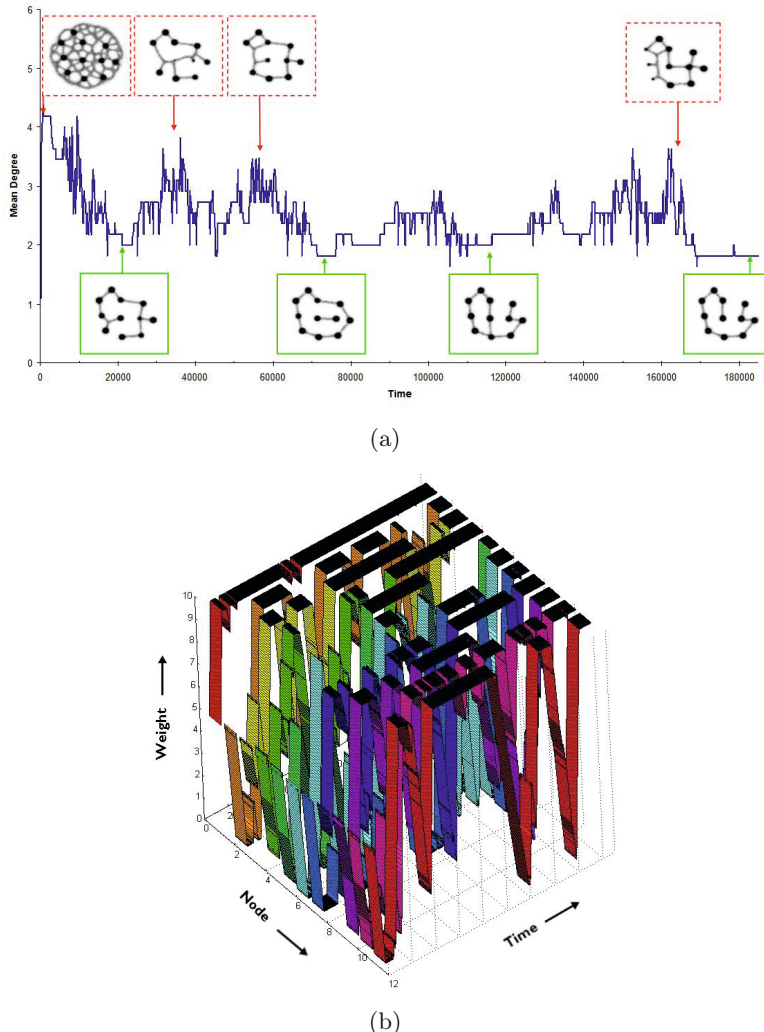


Fig. 8.10 Oscillations in mean degree during dynamic reconfiguration caused by changing node concentration. (a) Plot of mean degree with indicative network structures, (b) 3D plot of node weight concentration throughout the experiment.

8.5 Characteristics, Limitations and Interpretations of Results

We characterise the behaviour of the DR method using examples in which the method is able to evolve stable networks of degree 2 connectivity which correspond to valid TSP solutions alongside examples in which TSP tours are either transient or incomplete. In examples with rectilinear and regularly spaced nodes complete TSP tour solutions were found for examples of up to 12 nodes (cities). This compares favourably with the original slime mould research of Aono et al. [85, 195] which contained a 4 city problem and has since been expanded to 8 cities. Of course both this approach and the original slime mould methods are mainly concerned with understanding the complex dynamics within their respective materials and have some way to progress before matching current state-of-the-art classical approaches capable of solving many thousands of city instances.

In problems with irregularly placed cities the performance of the DR method was more variable (Fig. 8.9 to Fig. 8.12) and the causes of the variation are worthy of further consideration. On some runs a complete circuit was not found at all and the connectivity pattern instead approximated a Hamiltonian path (a network where each node is visited once only). The results in Fig. 8.11 show the similarities between the DR networks and the optimum Euclidean TSP tours (column 2, calculated by Simulated Annealing method) for three different sets of points. The general network shape (column 3) appears to approximate the TSP tour but some of the nodes are not visible as they are inhibited by the feedback system. The connectivity diagram (column 4) shows the ‘problem areas’ in the dynamical network (lighter coloured circles) which prevent complete optimisation of the network. For the first two sets of points (top and middle row) the correct optimisation is prevented because the network cannot remain attached around a node which is relatively far away from other nodes (column 3, dashed circles). Instead the network detaches from this node and forms a Steiner point between the three surrounding nodes. The detachment from this node was observed even when stronger maximum node concentration was used. In the case of the bottom row set of points it appears that the network cannot stabilise due to the very acute angle between two nodes (column 2, dashed circle) which causes paths to merge and detach from the node. In this case the network cannot stabilise and oscillates between nearby configurations (as in Fig. 8.9, bottom row). This appears to be very similar behaviour to that discussed in the original slime mould research in which oscillation between nearby tours was also observed [85]. The final column shows Hamiltonian paths for two of the data sets (the middle row dataset never converged to form the path). In these cases the paths did not connect to form a TSP tour because either the distance between the nodes was too great (top example) or the angles between the nodes was too acute (seeded particles were quickly absorbed into nearby network paths instead of spanning the two nodes).

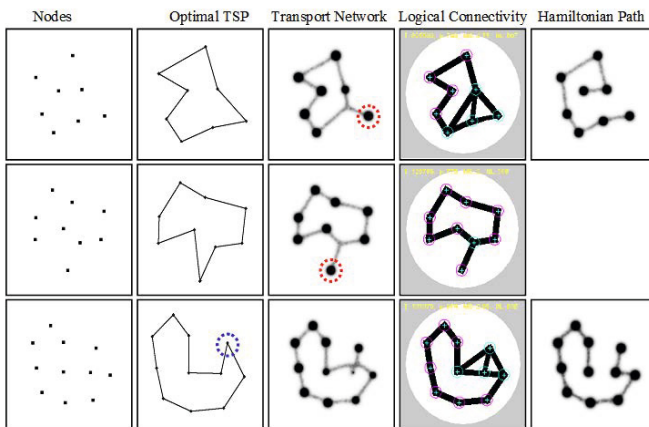


Fig. 8.11 Relationship of dynamical networks, TSP tours and Hamiltonian paths

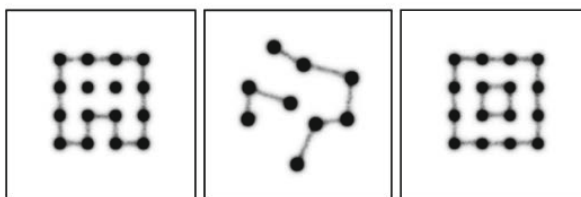


Fig. 8.12 Incomplete or invalid tours generated by the Dynamical Reconfiguration method show limitations of the analysis and feedback mechanisms

It is possible that these partial or incomplete solutions may be amenable to further modification or refinement to provide complete TSP solutions. Such an approach was used by Tero et al. to refine partial solutions to the Steiner problem using a computational model of *Physarum* [190]. Other limitations of the prototype mechanism are concerned with the feedback rules. For example, Fig. 8.12 (first two images) shows some instances where the network is not fully connected and a complete cycle is not found. These examples were caused by setting a very low value to the scatter_distance parameter. Although this can be solved simply by increasing the parameter it represents a limitation when we consider networks where we do not know in advance the distances between the nodes.

The final image shows a network which has mean degree of 2 yet does not form a single cycle. Both sources of error (incomplete tours and multiple cycle tours) are due to limitations in the control mechanism arising from the motivation to keep the prototype mechanism as simple as possible, and to employ only local node information about the network structure. We envisage that additional global tests of network connectivity (for example to check

that a tour is valid by checking if a connected path between all nodes exists), and an enforcement of correct tour “syntax” (as referred to in the original Hopfield-Tank control method [204] could be added to future versions of the analysis/feedback control mechanism.

8.6 Summary: Dynamical Networks — Direct Control or Guided Influence?

We have presented a prototype mechanism to explore the problem of dynamic reconfiguration of transport networks. The mechanism is used to modify the complex collective behaviour of a virtual material, inspired by the true slime mould *Physarum*, whose ‘default’ behaviour demonstrates network minimisation. The dynamical reconfiguration mechanism utilises real-time pattern analysis to attain a collective record of network connectivity of the virtual material as it adapts around the spatial configuration of nutrient node stimuli projecting attractants into the environment. This record is used to measure the degree of connectivity at each node and this information is then fed back to the nodes, enhancing the node concentration for low connectivity ($<=2$) and suppressing the node concentration at high connectivity (≥ 3). A seeding method (creation of new particles near the local area of disconnected nodes) is utilised to re-establish network connections at fully or partially disconnected nodes (≤ 1).

The feedback mechanism alters the attraction of the nodes to the network and the network automatically reconfigures its shape in response to the changing stimuli. An emergent refractory period is effected by controlling the length of time in which the ‘memory’ of the current configuration is retained. This refractory period is necessary to avoid spatial deadlock situations in which the network evolution is trapped between two similar configurations by nearby competing nodes. The DR mechanism generated very complex network transitions which, when analysed, demonstrated apparently high-level stable spatial structures from the low-level ‘atomic’ and indirect actions of changing node concentration. The transitions were composed from characteristic spatial motifs including so-called snagging, tightening, detaching, grabbing and sliding actions.

The method demonstrates a potential approach for the spatially represented unconventional computation of computational geometry and combinatorial optimisation problems. In many cases of bio-inspired computation inspired by living systems (for example ant algorithms or genetic algorithms) the complex spatial behaviour and underlying mechanisms of the living systems are abstracted into conventional symbolic computer instructions and the computation is performed only by analogy with the living system. For example in the Ant Colony Algorithm approach, no actual deposition of pheromone trail, or its subsequent propagation by evaporation and diffusion, is used. Conversely, unconventional computation schemes seek to utilise

the spatial properties of physical and living systems directly in the computational process, for example the propagation of information by diffusion in chemical computation, or growth and adaptation of the *Physarum* plasmodium itself. Utilising the direct physical processes for computation provides a very rich set of behaviours, some of which have been investigated in chapter 6. However, as this chapter demonstrates, the complex behaviour also comes at some cost: namely that of trying to control or govern the very complex evolution of the network and ‘tune’ the analysis and feedback mechanism. The computational ‘richness’ afforded by the spatial computation may be instead interpreted more simply as ‘difficulty’ and akin to the idiom of “nailing jelly to a tree”. However, even the prototype analysis and blind feedback mechanisms developed in this report were shown to approximate TSP tours and Hamiltonian paths in relatively complex spatially represented datasets, suggesting that approach may be worth further investigation.

But why investigate and wrestle with the control of complex spatial behaviour at all? Although we can indeed avoid the computational complexity of spatial systems by resorting to symbolic abstraction in conventional computing devices, it will not be possible to do this in future physical embodiments of smart materials which exist outside the simple and controllable confines of classical computation, in spatially complex and noisy environments. It is hoped that by attempting to ‘tame’ the complex network evolution in the restricted form of a virtually represented spatial system, we may be able to generate interesting and useful approaches and solutions to computational problems which may also be applicable to physical instances of smart materials.

Even with the limited complexity of the analysis and feedback systems introduced in this chapter, we have revealed a rich, and surprising, set of transition behaviours emerging from very simple low-level interactions. We speculate that this is only a small possible subset of behaviours which may exist in alternative analysis and feedback schemes, and that ‘mining’ these behaviours may prove useful for the control of smart materials. To this end we could potentially improve these method in the near future: Firstly, by increasing the sophistication of the pattern analysis method whilst maintaining computational tractability. Secondly we could use a more complex feedback system which will tailor the evolution of the reinforcement and inhibition to more successfully reward more optimal patterns, weaken the memory of less optimal patterns, and remove invalid patterns. This approach may prove a useful method in the dynamical control of the behaviour of smart materials.

The difficulties in trying to control the behaviour of the virtual material may also lead us in search of simpler methods of implementing computation with its innate adaptation properties. In the following chapter we return to the TSP and devise a simple method by which its approximation can be performed by the virtual plasmodium.

Chapter 9

Material Approximation of Combinatorial Optimisation

“There’s a city in my mind,
Come along and take that ride ”

(David Byrne, 1985)

9.1 Introduction

The Travelling Salesman Problem (TSP) is a combinatorial optimisation problem well studied in computer science, operations research and mathematics. In the most famous variant of the problem a hypothetical salesman has to visit a number of cities, visiting each city only once, before ending the journey at the original starting city. The shortest path, or tour, of cities, amongst all possible tours is the solution to the problem. The problem is of particular interest since the number of candidate solutions increases greatly as n , the number of cities, increases. The number of possible tours can be stated as $(n-1)!/2$ which, for large numbers of n , renders assessment of every possible candidate tour computationally intractable. Besides being of theoretical interest, efficient solutions to the TSP have practical applications such as in vehicle routing, tool path length minimisation, and efficient warehouse storage and retrieval.

The intractable nature of the TSP has led to the development of a number of heuristic approaches which can produce very short — but not guaranteed minimal — tours. A number of heuristic approaches are inspired by mechanisms seen in natural and biological systems. These methods attempt to efficiently traverse the candidate search space whilst avoiding only locally minimal solutions and include neural network approaches (most famously in [204]), evolutionary algorithms [207], simulated annealing methods [208], the elastic network approaches prompted in [209], ant colony optimisation [206], living [195] and virtual [210] slime mould based approaches, and bumblebee foraging [205].

Human performance on the TSP has also been studied in both naive and tutored subjects (see, for example, [211]). This is of particular interest because, unlike many nature inspired approaches, the human computation of TSP is by an individual and not based on population methods which evaluate a number of candidate solutions. Human performance on the TSP is also, for a limited number of cities at least, comparable in performance with heuristic approaches [212], [213]. Although there are a number of competing theories as to how exactly humans approximate the TSP [214],[212], [215], discovery of the methods employed may be useful as an insight into the mechanisms underlying complex perceptual and cognitive processes and potentially as an aid for the development of computational algorithms.

In this chapter we adopt a material-based, minimum complexity approach. We show how a spatially represented non-classical, or unconventional, computational mechanism can be used to approximate the TSP. Taking inspiration from the non-neural, material-based computational behaviour of slime mould, we employ a sheet, or ‘blob’ of virtual material which is placed over a spatial map of cities. By shrinking this blob over time, it conforms and adapts to the arrangement of cities and a tour of the TSP is formed. We give an overview of the inspiration for the method in Section 9.2. The shrinking blob method is described in Section 9.3. Examples of the performance of the method compared to exact solutions generated by a TSP solver are given in Section 9.4, along with an analysis of the underlying mechanism and factors affecting the performance of the approach. We conclude in Section 9.5 by summarising the approach and its contribution in terms of simplicity. We examine similarities between the underlying mechanism of the shrinking blob method and proposed models of TSP tour perception and construction in studies of human performance on the TSP. We suggest further research aimed at improving the method.

9.2 Can Slime Mould Directly Compute the TSP?

Although *Physarum* has been previously been used in the approximation of TSP [195], this was achieved by an indirect encoding of the problem representation to enable it to be presented to a confined plasmodium in a controlled environment. In the work by Aono et. al. it was shown that the morphology of the plasmodium confined in a stellate chamber could be dynamically controlled by light irradiation of its boundary. When coupled to an elegant feedback mechanism using an analysis method (to assess the presence of plasmodium at the extremities of the chamber), combined with Hopfield-Tank type neural network rules [204], the plasmodium was used to generate candidate solutions to simple instances of the TSP [85, 86]. In its natural propagative state, however, *Physarum* does not approximate area representations of a set of points, including the Convex Hull, Concave Hull [81] and the TSP. This is because the material comprising the plasmodium spontaneously

forms networks spanning the nutrient sources. Even when the plasmodium is arranged initially as a solid sheet of material, the sheet is soon transformed into a network structure by competitive flux of material within the sheet [9]. It is physically impractical to force a freely foraging plasmodium to conform to a TSP network structure during its nutrient foraging, as shown in Fig. 9.1.

Nevertheless, the material computation embodied within *Physarum* presents interesting possibilities towards generating novel spatially represented methods of unconventional computation. The feedback control of network evolution demonstrated in Chapter 8 resulted in extremely complex transitions of network dynamics and only partial success in constructing TSP tours. In the approach outlined in this chapter we attempt a simpler approach which utilises a larger aggregate mass of the same multi-agent collective which behaves as a morphologically adaptive cohesive ‘blob’ of virtual material.

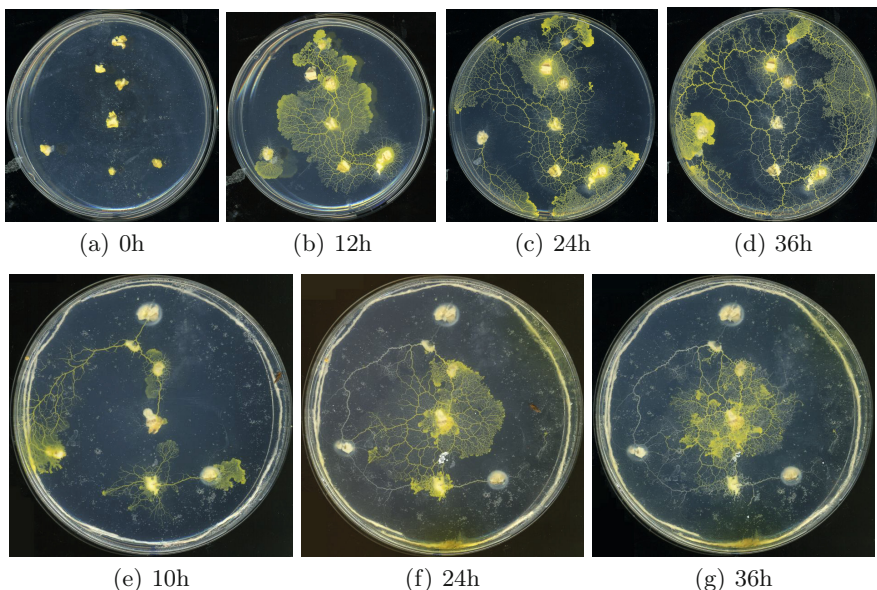


Fig. 9.1 Foraging plasmodium of *Physarum* does not approximate the TSP in both unconstrained and constrained environments. (a) *Physarum* plasmodia are inoculated at oat flakes on non-nutritive agar, (b) individual plasmodia extend from oat flakes and fuse, (c-d) the plasmodium continues to forage and the shape of the TSP is not represented. (e) foraging of plasmodium is constrained by placing a ring of saline soaked thread (1g NaCl / 100g water) at the periphery of the arena, (f) as the salt diffuses into the agar the shape of the plasmodium is confined, (g) the pattern of the plasmodium at 36h is confined but is disconnected from outer nodes (note empty tube remnants) and does not approximate the TSP. Images from [216].

9.3 Material Approximation of the TSP by a Shrinking Blob

In the shrinking blob method we use a piece, or ‘blob’ of a virtual plasmodium material to approximate the TSP. In this application we use a relatively large population of particles which collectively behaves as a sheet of deformable virtual material. An overview of the method follows.

9.3.1 Shrinkage Process

We initialise a sheet of the virtual material around a set of data points corresponding to TSP city nodes (Fig. 9.2a). Chemoattractant is projected into the diffusive lattice at node locations, however, projection is reduced at regions which are covered by the blob sheet. The initial shape of the sheet corresponds to the Convex Hull of the data points. We then shrink the material by systematically removing some of its constituent particle components. The city nodes act as attractants to the material, effectively ‘snagging’ the material at the locations of uncovered nodes and affecting its subsequent morphological adaptation. As the material continues to shrink its innate minimising properties conform to the locations of the city nodes and the area occupied by the material is reduced, becoming a concave area covering the nodes (Fig. 9.2b-e). The shrinkage is stopped when all of the nodes are partially uncovered by the sheet (Fig. 9.2f). The reader is encouraged to view the supplementary video recordings of the shrinkage process as described in the Appendix. The adaptation of the blob to the data stimuli is not entirely smooth, the video recordings show that the blob sheet adapts to the changing stimuli as data nodes are temporarily uncovered and re-covered by the blob. When the shrinkage is halted the area of the sheet corresponds to the area enclosed by a tour of the Euclidean Travelling Salesman Problem. The exact tour formed by the blob can be elucidated by tracking along the perimeter of the blob, adding a city to the tour list when it is first encountered. The tour is complete when the start city is re-encountered. The approach is simple, making use of the innate adaptive emergent properties of the material. Despite being completely unguided and containing no population based heuristic optimisation strategies the approach yields efficient tours. The separate stages of the approach will now be described in detail.

9.3.2 Halting the Computation

It is important to halt the shrinkage of the blob at the right time. If the shrinking is stopped too early an incomplete tour will be formed (i.e. only a partial subset of the nodes will be included in the tour if not all of the nodes are uncovered). Unlike guided heuristic methods a set of candidate tours is not initially formed and subsequently modified. Only a single tour

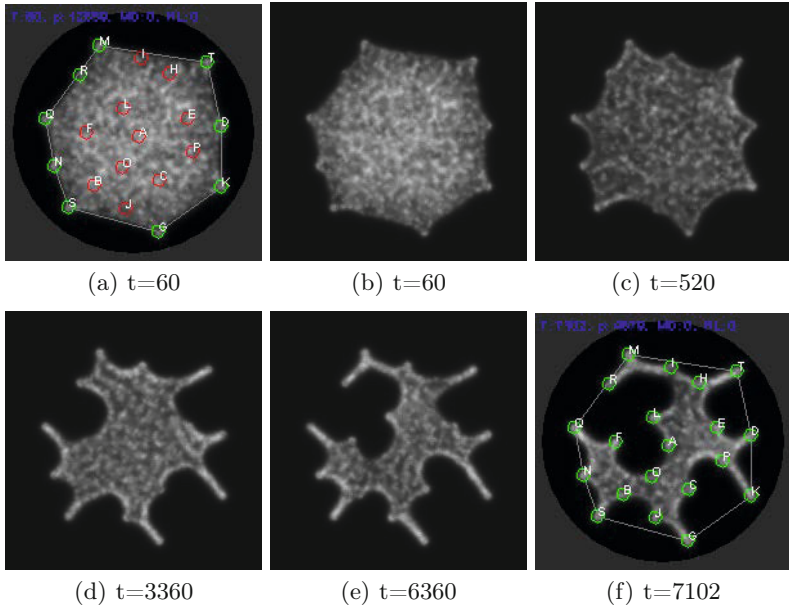


Fig. 9.2 Visualisation of the shrinking blob method. (a) sheet of virtual material initialised within the confines of the convex hull (grey polygon) of a set of points. Node positions are indicated by circles. Outer partially uncovered nodes are light grey, inner nodes covered by the sheet are in dark grey, (b-e) sheet morphology during shrinkage at time 60, 520, 3360, 6360 respectively, (f) shrinkage is stopped automatically when all nodes are partially uncovered at time 7102.

is formed and the shrinking blob approach is akin to the ‘instance machines’ (as opposed to universal machines) proposed by Zauner and Conrad [61]. To automatically halt the computation we use a so-called ‘traffic light’ system. At the start of the method the sheet covers the entire set of nodes. Only the outer nodes are partially covered by the blob. To measure whether a node is covered by the sheet we assess the number of particles in a 5×5 window around each node. If the number of particles is < 15 then the node is classified as uncovered and the node indicator is set to green. Otherwise the node is classified as covered and the node indicator is set to red. At each scheduler step the indicators of all nodes are checked. When all nodes are set to green, all nodes underneath the blob are partially uncovered and the shrinkage is stopped.

9.3.3 Reading the Result of the Computation

To trace the path of cities in the tour discovered by the blob a manual process is used. The collection of partially uncovered nodes and blob shape may

be interpreted as an island shape with the nodes representing cities on the coastline of the island (Fig. 9.3). We begin by selecting the city at the top of the arena. If more than one city is at this y location the left-most city at this y location is selected. This city is the start city of the tour and is added to the tour list \mathbf{T} . Moving in a clockwise direction we trace the perimeter of the blob (walking around the shore of the island ...). Each time we encounter a city, it is added to \mathbf{T} . If a city is subsequently re-encountered (as in the case of narrow peninsula structures as described below) it is ignored. When the path reaches the starting city the tour is complete and the list in \mathbf{T} represents the tour of the TSP found by the shrinking blob.

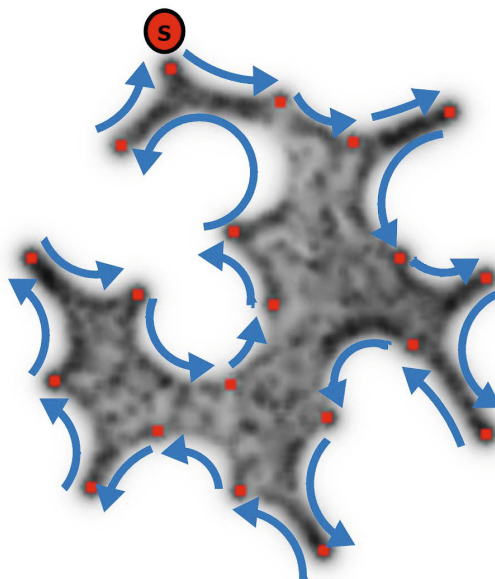


Fig. 9.3 Reading the TSP tour formed by the shrinking blob by perimeter tracking.
(a) Tracking is initialised at the top most node. Perimeter of blob is traced in a clockwise direction. Each time a node is encountered for the first time it is added to the tour. The tour is completed when the start node is re-encountered.

Some special cases in the tracking process must be noted in the case where a city lies on a narrow ‘peninsula’ of the blob as indicated in Fig. 9.4. In Fig. 9.4a the city nearest position x in the path lies close to one side of a narrow peninsula. However the side at which the city is located can be deduced by a small convex bulge on the left side of the blob. In this case the city is not added until it is encountered on the left side of the peninsula. In the case of Fig. 9.4b, however, the city at x is located exactly in the middle of a peninsula and its closest side cannot be discerned. In this instance two interpretations are possible and the subsequent differences in possible tour paths are indicated

by the dotted lines in Fig. 9.4b, i) and ii). In interpretation i) the city is added to \mathbf{T} immediately and in ii) it is not added until it is encountered on its opposite side. If this situation occurs during the tracking process we add the city to \mathbf{T} when it is first encountered.

9.4 Results

We assessed the shrinking blob method by generating 20 datasets, each consisting of 20 randomly generated nodes within a circular arena in a 200×200 lattice. To aid the manual tracking process we added the condition that points must have a separation distance of at least 25 pixels. For each run a population of particles was generated and initialised within the confines of the convex hull (algorithmically generated) of the point set. Any particles migrating out of the convex hull area were removed. As the shrinkage process started the cohesion of the blob emerged and, as shrinkage progressed, the blob adapted to the shape of the city nodes. Ten experimental runs were performed on each dataset and the resulting blob shape was recorded and tracked by the manual tracking process to reveal the tour. The best, worst and mean performance over 10 runs for each 20 datasets was recorded and these results are shown in Fig. 9.5. Results of the shrinking blob method (Fig. 9.5, circles with standard deviation bars) are compared to the shortest exact tour (Fig. 9.5, diamonds) computed by the Concorde TSP solver [217].

Over the 20 datasets tested, the mean tour lengths found by the shrinking blob method was 6.41% longer than the exact minimum TSP tours. The mean best performance over all datasets was 4.27% longer than the exact tours and the mean worst performance was 9.22% longer than the minimum tours. There is significant variation in the performance of the blob method on different datasets. In some instances the minimum blob tour length is very close (0.45% longer) to the minimum tour whereas in other cases it is significantly more (20.13% longer). As indicated in Fig. 9.5 there are also significant differences between the *variations* in performance on the same dataset. Datasets 3 and 16 gave identical tours over their ten runs (1.84% and 0.45% longer than the minimum tour respectively), whereas the performance on dataset 7 ranged from between 7.72% and 20% longer than the minimal tour.

9.4.1 Tour Construction by Concavity Insertion

Although the final tour list is read off by tracking the perimeter of the shrunken blob, the construction of the tour actually occurs by an insertion process as the blob shrinks. The blob is initially patterned with the shape of the convex hull. This is only a partial tour, since only the peripheral nodes which are part of the Convex Hull are included. By recording the stages by which nodes are uncovered and added during the shrinkage process, the

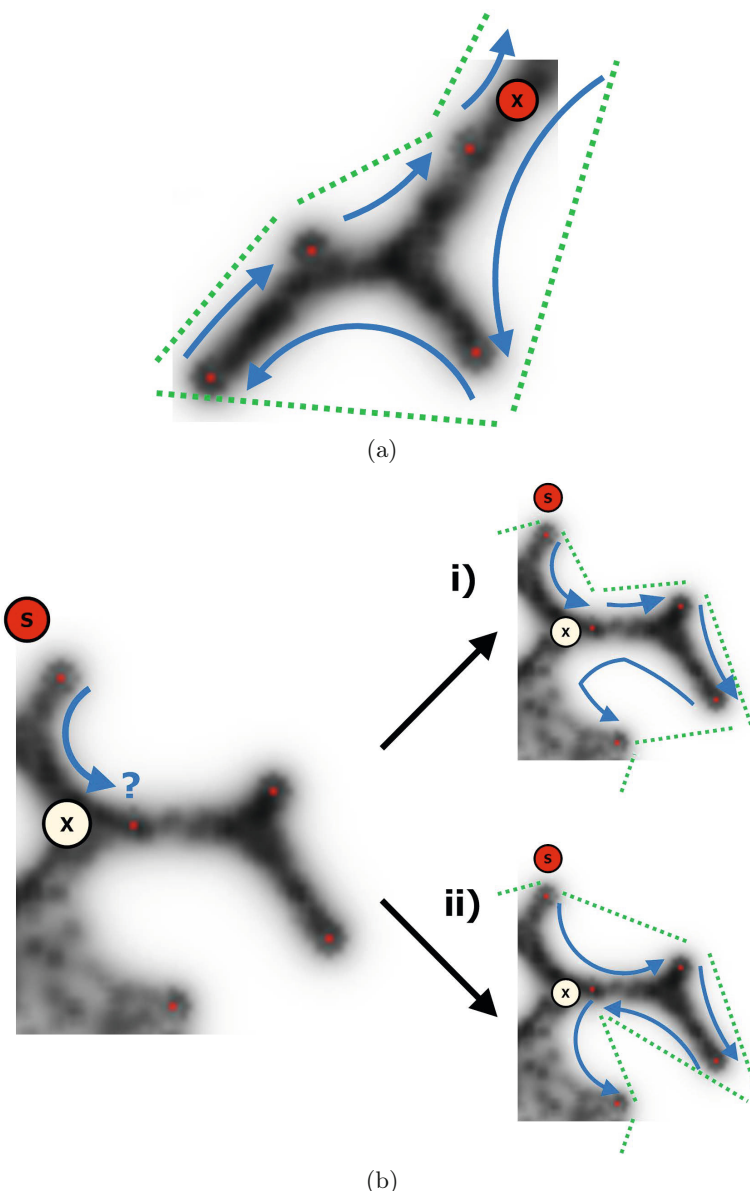


Fig. 9.4 Special cases of when nodes are located on a narrow peninsula, close, or equidistant from either side of the ‘land’. (a) The node at ‘x’ is close to the middle of a narrow portion of the blob. The slight convex bulge in the blob indicates that it is closest to the left side and the node is not added to the tour until it is encountered on the left side. (b) The node at ‘x’ is directly in the middle of a narrow portion of the blob. Two potential tours are possible, shown in i) and ii) with their respective tours as dotted lines. If this case occurs, the node is added to the tour the first time it is encountered, as in i).

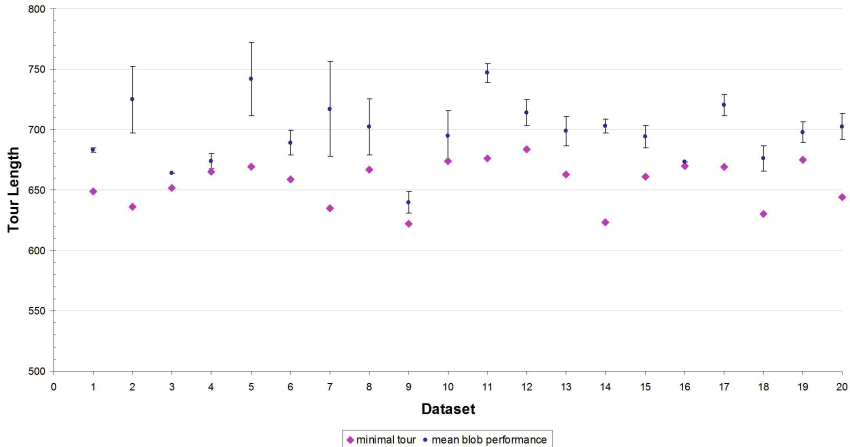


Fig. 9.5 Results of shrinking blob method over 10 runs on each of 20 randomly generated datasets of 20 points compared to exact results from the Concorde TSP solver. Mean tour length indicated by dark circles, standard deviation indicated by error bars, minimal TSP tour by lighter diamonds.

method of construction can be elucidated. Fig. 9.8 shows the visual deformation of the Convex Hull structure as the blob shrinks and new city nodes are added to the list. Note that the blob shrinks simultaneously from all directions and the order of insertion is related to both the proximity of the point from the periphery of the blob and the distance between two outer stimuli at the current periphery of the blob where a concavity forms (discussed further in Section 9.4.3). The actual order of insertion of cities in this example is given in Fig. 9.9.

As the blob shrinks, concavities form in the periphery of the blob which move inwards to the centre of the blob shape. The concave deformation is a transformation of the Convex Hull (**CH**) into a Concave Hull (**OH**). The Concave Hull, the area occupied by — or the ‘shape’ of — a set of points is not as simple to define as its convex hull. It is commonly used in Geographical Information Systems (GIS) as the minimum region (or footprint [218]) occupied by a set of points, which cannot, in some cases, be represented correctly by the convex hull [219]. The Concave Hull is related to the structures known as α -shapes [220]. The α -shape of a set of points, P , is an intersection of the complement of all closed discs of radius $1/\alpha$ that includes no points of P . An α -shape is a convex hull when $\alpha \rightarrow \infty$. When decreasing α , the shapes may shrink, develop holes and become disconnected, collapsing to P when $\alpha \rightarrow 0$. A concave hull is non-convex polygon representing area occupied by P and the concave hull is a connected α -shape without holes. In contrast to α -shapes, the blob (more specifically, the set of points which it covers) does not become disconnected as it shrinks. As the blob adapts its

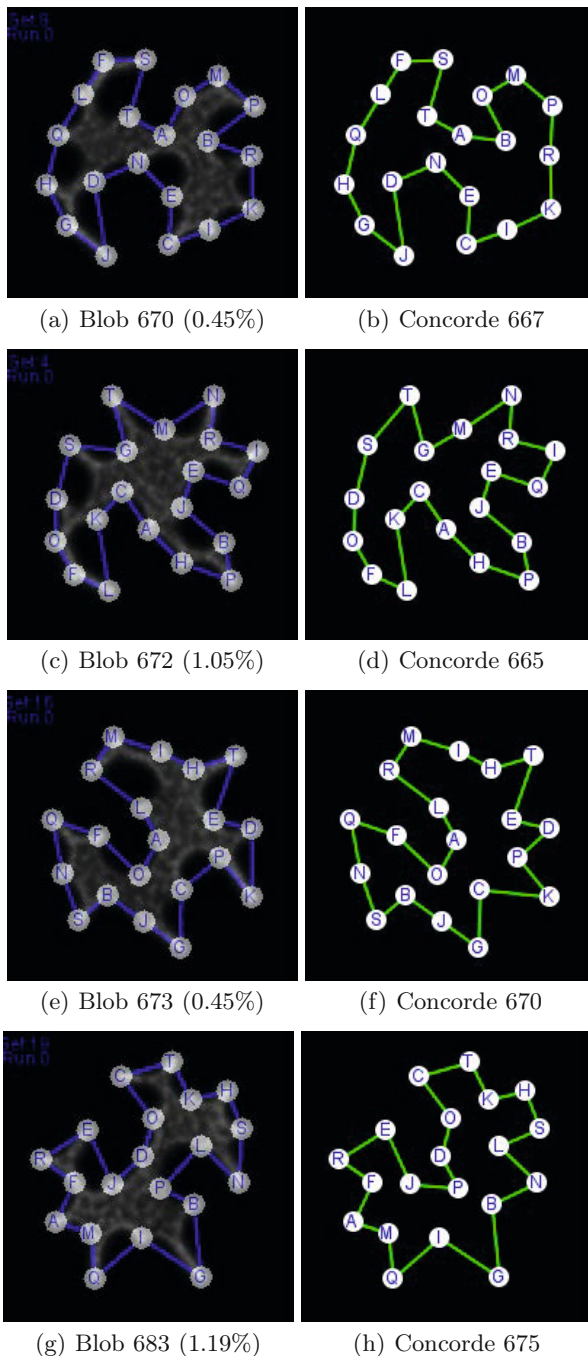


Fig. 9.6 Examples of good performance by the shrinking blob method. (a,c,e,g) Final blob shape with TSP tour overlaid, tour length and percentage greater than exact tour in parentheses, (b,d,f,h) Minimum exact tour found by the Concorde TSP solver.

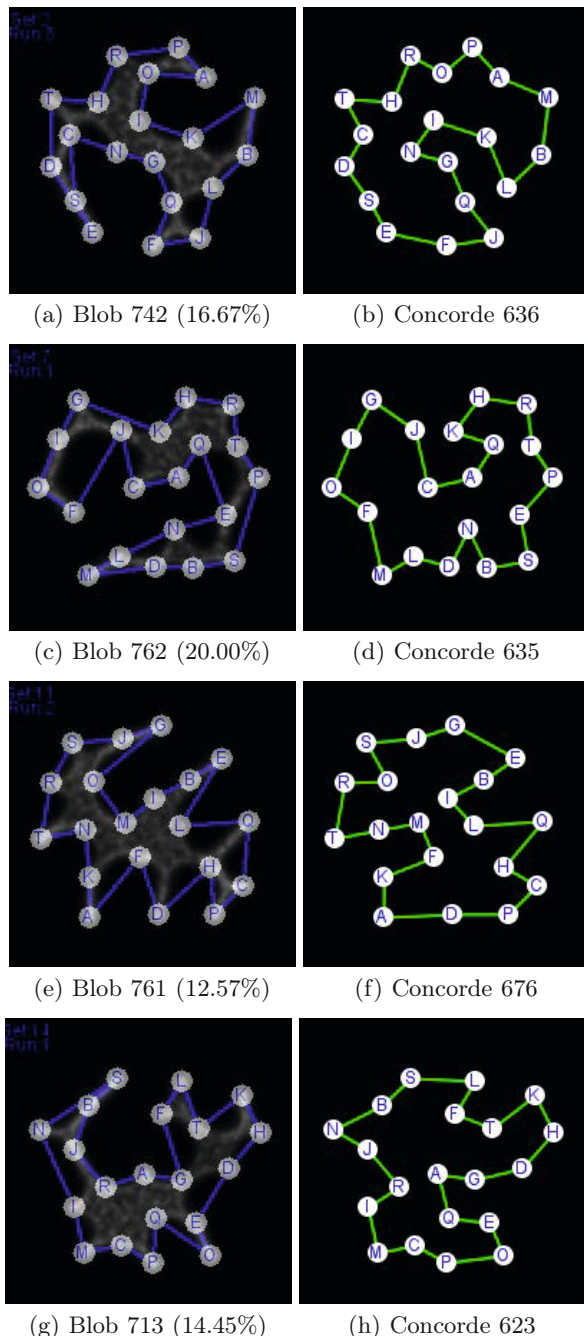


Fig. 9.7 Examples of relatively poor performance by the shrinking blob method. (a,c,e,g) Final blob shape with TSP tour overlaid, tour length and percentage greater than exact tour in parentheses, (b,d,f,h) Minimum exact tour found by the Concorde TSP solver.

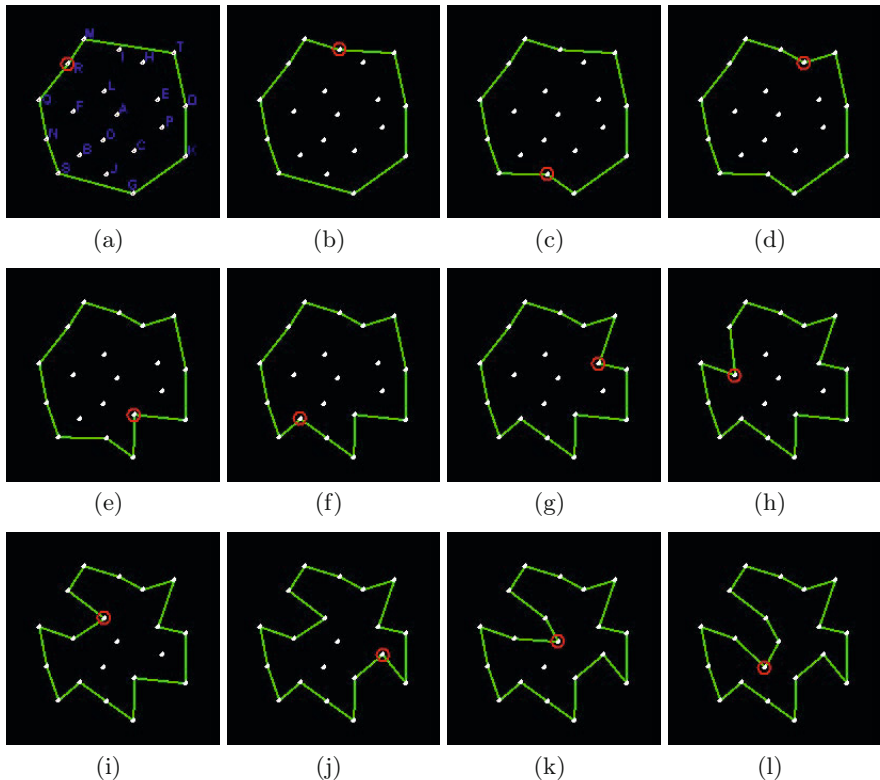


Fig. 9.8 Construction of TSP tour by shrinking blob includes the transformation between Convex Hull and Concave Hull. (a) Initial Convex Hull of dataset 16 (shown by points connected by path) is deformed to a concave shape by the shrinking blob. The stepwise construction of the tour is indicated by adding a circled point as each new city is discovered, (b-k) As the blob continues to shrink new points are included (circled) further reducing the area of the Concave Hull, (l) when shrinkage stops the set of encompassed points is a tour of the TSP.

morphology from Convex Hull to TSP is demonstrates increased concavity with decreased area. Although the shrinkage process is automatically stopped when a TSP tour is formed, the process could indeed continue past the TSP. If shrinkage continues then the blob (now adopting a network shape) will approximate the Steiner minimum tree (SMT), the minimum path between all nodes. As demonstrated in [221] the additional Steiner nodes in the SMT may be removed by increasing the attractant projection from the data nodes. The material adapts to the increased attractant concentration by removing the Steiner nodes to approximate the Minimum Spanning Tree (MST).

<i>M</i>	<i>T</i>	<i>D K</i>	<i>G</i>	<i>S N Q</i>	
<i>M</i>	<i>T</i>	<i>D K</i>	<i>G</i>	<i>S N Q</i>	R
<i>M I</i>	<i>T</i>	<i>D K</i>	<i>G</i>	<i>S N Q</i>	<i>R</i>
<i>M I</i>	<i>T</i>	<i>D K</i>	G J	<i>S N Q</i>	<i>R</i>
<i>M I H T</i>	<i>D K</i>		<i>G J</i>	<i>S N Q</i>	<i>R</i>
<i>M I H T</i>	<i>D K</i>	C G J		<i>S N Q</i>	<i>R</i>
<i>M I H T</i>	<i>D K</i>	<i>C G J</i>	B	<i>S N Q</i>	<i>R</i>
<i>M I H T E D K</i>		<i>C G J B S N Q</i>			<i>R</i>
<i>M I H T E D K</i>		<i>C G J B S N Q F</i>			L R
<i>M I H T E D K P C G J B S N Q F</i>					<i>L R</i>
<i>M I H T E D K P C G J B S N Q F</i>				A	<i>L R</i>
<i>M I H T E D K P C G J B S N Q F O A L R</i>					

Fig. 9.9 Gradual construction of tour by city insertion during shrinkage process in dataset 16, as visualised in Fig. 9.8. Top row shows initial configuration of blob as convex hull. Each row inserts a new city (bold) into the tour as indicated in Fig. 9.8.

9.4.2 Blob TSP Tour is a Waypoint from Convex Hull to Spanning Tree

The insertion process of adding nodes to the Convex Hull reveals an orderly transition to the TSP which continues after further shrinkage, leading to the following finding.

The evolution of the blob shape by morphological adaptation is a transition from **CH** to **OH** to **TSP** to **MST** to **SMT**.

We do not explicitly include α -shapes in this transition since α -shapes can include holes and disconnected structures, which do not form in a defect-free shrinking blob. This transition is based on increasing concavity and decreasing area, and encompasses the a blob TSP tour **bTSP** as part of the hierarchy. Note that the blob tour **bTSP** is only one instance of the set of possible TSP tours **TSP** and is not guaranteed to be the minimal tour. The blob TSP tour is only a transient structure — a waypoint — in the natural shrinkage process (we halt the computation at this point merely because we are interested for the purposes of this report).

It is known from Toussaint that there is a hierarchy of proximity graphs (graphs where edges between points are linked depending on measures of neighbourhood and closeness) [188]. Each member of the hierarchy adds edges and subsumes the edges of lower stages in the hierarchy, and some common graphs (see Fig. 9.10a-e) include the Delaunay triangulation **DTN** to Gabriel Graph **GG** to Relative Neighbourhood Graph **RNG** to Minimum Spanning Tree **MST**. Also shown is the shortest possible tree between all nodes formed by adding extra Steiner nodes (Fig. 9.10f). It was found in [80] that *Physarum* approximates the Toussaint hierarchy of proximity graphs as it constructs

transport networks during its foraging and it was demonstrated in [221] that multi-agent transport networks mimicking the behaviour of *Physarum* also minimise these proximity graphs by following this hierarchy in its downwards direction. From a biological perspective traversing the Toussaint hierarchy suggests a mechanism by which *Physarum* can exploit the trade-off between foraging efficiency (many network links) and transport efficiency (fewer but fault tolerant transport links). This mechanism, may also be present in terms of maximising foraging area searched (exploration) and minimising area for efficient transport (exploitation), as suggested in [123]. We suggest that the hierarchy we observed in the shrinking blob from **CH** to **OH** to **TSP** to **MST** to **SMT** may encompass such an area-based exploration-exploitation mechanism (Fig. 9.10g-l). It is notable that there is some overlap between the Toussaint hierarchy and the shrinking blob hierarchy where deepening concavities in the blob hierarchy appear to correspond to the deletion of outer edges in the Toussaint hierarchy, suggesting that there may be some formal relationship between the two. This possible relationship may suggest further studies.

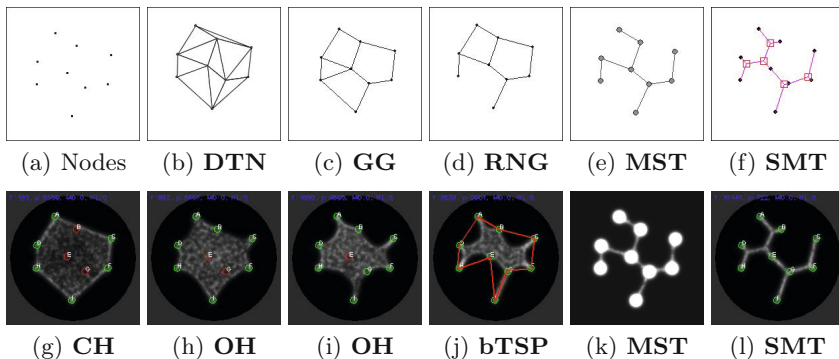


Fig. 9.10 Comparison of the Toussaint Hierarchy (top row) and Shrinking Blob Hierarchy (bottom row). (a) Initial source nodes, (b) Delaunay Triangulation (DTN), (c) Gabriel Graph (GG), (d) Relative Neighbourhood Graph (RNG), (e) Minimum Spanning Tree (MST), (f) Steiner Minimum Tree (SMT), (g) Initial blob is patterned as a Convex Hull (CH), (h-i) as the blob shrinks it adopts the Concave Hull, (j) after uncovering the last node a TSP tour is formed, (k) blob can be forced to adopt MST by increasing node concentration, (l) the ‘natural’ end point of blob shrinkage is the SMT.

9.4.3 Variations in Performance

The results of the shrinking blob method show variations in performance from very good approximations of close-to-minimum tours (Fig. 9.6) to less successful tours (Fig. 9.7). What is the reason for the disparity in performance

on these datasets? If we examine the tour paths we can glean some clues as to the difference in performance. In the ‘good’ results examples the major concave regions of the tour formed by the blob closely match the concavities in the exact computed TSP tour (e.g. Fig. 9.6a and b). However in the ‘poor’ approximation results we can see that the major concave regions of the blob tour do not match the major concavities in the respective exact computed tours (e.g. Fig. 9.7a and b). Given that these concave regions are formed from the deformation of the initial Convex Hull we can see that the concavities in the blob tour appear to be formed, and deepened where there are larger distances between the cities on the initial Convex Hull.

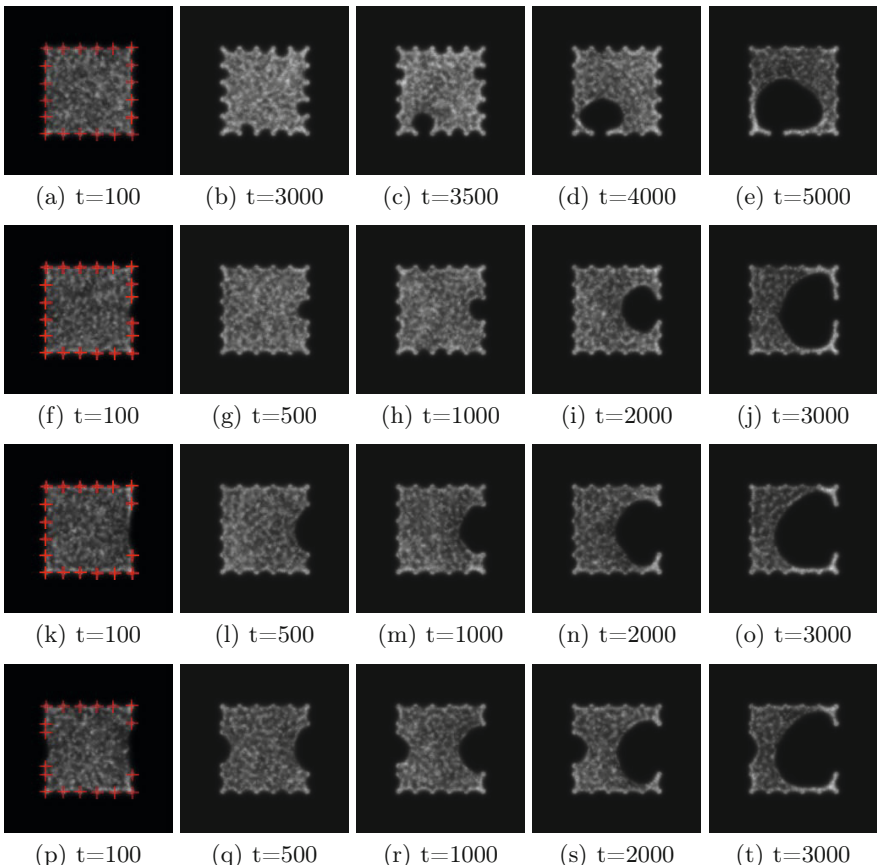


Fig. 9.11 Distance between nodes affects position and speed of concavity formation in shrinking blob. Nodes arranged in the border of square (indicated by crosses on leftmost images). (a-e) all nodes have identical distance of 20 pixels, (f-j) right side has node gap of 30 pixels, (k-o) right side node gap 60 pixels, (p-t) left side node gap 40 pixels, right side node gap 60 pixels.

To explore the role of distance on concavity formation we patterned a blob into a square shape by placing regularly placed stimuli around the border of a square (Fig. 9.11a, stimuli positions, 20 pixels apart, indicated by crosses). When shrinkage of the blob was initiated there is no difference between the stimuli distances. All regions between stimuli initially show small concavities (the ‘perforations’ in Fig. 9.11b) until one gradually predominates and extends inwards. Also of note is the fact that when one concave region predominates, the other concavities shrink (Fig. 9.11c-e). The position of the initial dominating concavity is different in each run (presumably due to stochastic influences on the collective material properties of the blob) and this may explain the small differences in performance on separate runs using the same dataset.

When there is a larger gap between stimulus points the predominating concavity forms more quickly and is larger. This is shown in Fig. 9.11f-j which has a gap of only 30 pixels between neighbouring stimulus points on the right side of the square and in Fig. 9.11k-o which has a gap of 60 pixels between neighbouring stimulus points. The shorter distance between points in (f-j) generates more tension in the sheet, prevent its deformation. The larger distance between stimuli in (k-o) results in less tension in the sheet at this region and the sheet deforms to generate the concavity.

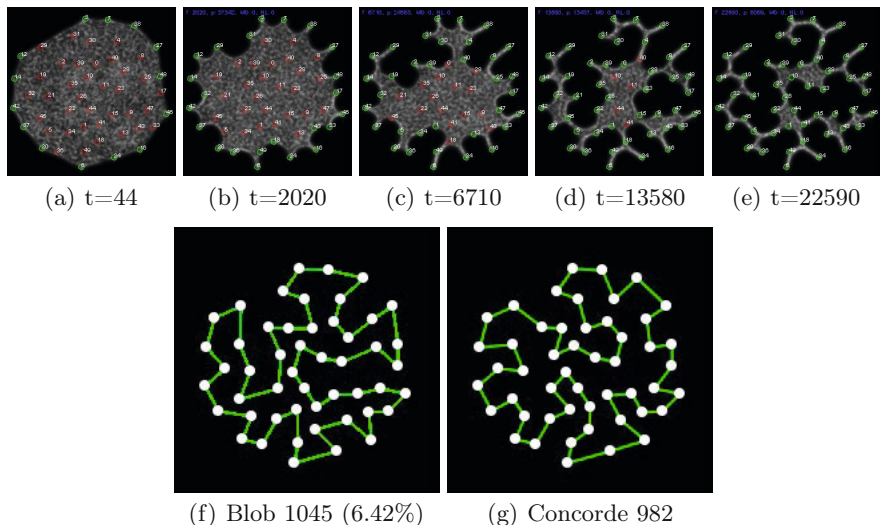


Fig. 9.12 The performance of the shrinking blob method on a larger dataset. (a-e) evolution of the shrinking blob on 50 node dataset, (f) tour formed by shrinking blob and percentage longer than optimal tour shown in parentheses, (g) exact minimum tour by Concorde solver.

When there are multiple instances of large distances between stimuli there is competition between the concave regions and the larger region predominates. This is demonstrated in Fig. 9.11p-t which has a distance gap of 40 pixels on the left side of the square and 60 pixels on the right side. Although two concave regions are formed, the larger deepens whilst the smaller concave region actually shrinks as the blob adapts its shape.

The synthetic examples illustrate the influence of city distance on concavity formation and evolution and these effects are more complex when irregular arrangements of city nodes are used. This is because arrangements of cities present stimuli to the blob sheet when partially uncovered, acting to anchor the blob at these regions, and the morphological adaptation of the blob is thus dynamically affected by the changing spatial configuration of uncovered city nodes. In the examples of relatively poor approximation of the minimum tour (Fig. 9.7) the initial incorrect selection of concavities are subsequently deepened by the shrinking process, resulting in tours which differ significantly in both their visual shape and in the city order from the optimum tour. In the examples of good comparative performance with the exact solver the blob tours differ only in a small number of nodes.

Although outright performance is not the focus of this report, we tested the blob method on a randomly generated dataset of 50 nodes in a preliminary assessment of scalability. We found that over 10 runs the blob method's best result was 6.42% longer than the exact minimum tour computed by the TSP solver. The worst result was 9.88% longer than optimal and the mean result was 7.57% longer than optimal (see Fig. 9.12 for an example). These preliminary results suggest that the method may scale well, however the scalability of the approach requires further investigation. It is worth noting that, in comparison to the shrinking blob approach, previous results using material computation with *Physarum* have been limited to 4 and 8 cities so, even at this early stage, the results obtained by the shrinking blob method — although not optimal — are promising, and may prove amenable to further improvement.

9.5 Summary

We have presented a simple material-based approach to the computation of the Travelling Salesman Problem using a shrinking blob. The method utilises the emergent morphological adaptation properties of a virtual material arising from local interactions within a multi-agent particle system. We shrink this material over time and its deformation and adaptation to the projected data points yields a tour of the TSP. We should again emphasise that the method is notable for its simplicity and novelty rather than its performance. Indeed the performance, when compared to exact TSP solvers or leading heuristic methods, compares relatively unfavourably in terms of absolute tour distance. The method does, however, contain a number of properties that are

intriguing. Firstly, unlike many other nature inspired approaches, the method is not population based and the blob only computes a single instance of a TSP tour. In addition, no attempt is made to modify or optimise the tour. The benefits of population based approaches are that very large search spaces in combinatorial optimisation problems can be traversed and candidate solutions can be compared in some way. This allows the efficient pooling of good solutions, generation of new candidate solutions and avoids local minima. The blob method does not contain any of these beneficial features.

How then, can a shrinking blob naturally generate a good quality (albeit non optimal) TSP tour? The intrinsic performance of the blob is based on its (virtual) material properties which exhibit innate minimisation behaviour. Previous research has demonstrated the network minimisation properties of the material approach, reproducing phenomena seen in soap film evolution [221] and lipid nanotube networks [111]. The maintenance of uniform shape during blob shrinkage also allows no crossing over of paths and it is known from [222] that crossing paths produce non-optimal tours. More specifically, the tour is constructed by insertion of cities into the list as concave regions are formed in the initial Convex Hull pattern and subsequently deepened. This is similar to algorithmic heuristics which, beginning with a Convex Hull, add cities to the list based on certain cost criteria [223], [224]. In the case of the blob, however, there is no explicit consideration of cost when adding cities to the tour. The mechanism of insertion selection in the blob (by deepening concavities) is intrinsic to its quasi-mechanical properties of the ‘material’ which are influenced by the depth of the city to the Convex Hull boundary and the span distance between boundary stimuli.

Although the blob approach differs from population based nature-inspired heuristics it is reminiscent, in character if not in direct operation, with other analogue based methods. In the Elastic Net algorithm, introduced by Durbin and Willshaw, a circular band is initialised at the approximate centre of a pattern of source TSP nodes. The band is expanded iteratively whilst two forces are applied to points on the band which attempt to minimise distances between cities on the band and the overall length of the band itself [209]. In the conceptually opposite approach of [225] the band is initialised on the Convex Hull and the two forces attempt to constrict the band whilst attracting the band towards a city. The tour formed by the band is then subject to a second ‘non-deterministic improvement’ algorithm to escape local minima. The main difference between the blob method and these ‘band’ approaches is that the material properties of the blob method are an emergent property of, and are distributed within, local interactions between components of the material. The computation is thus an embodied property of the material itself.

Can the mechanism underlying the simple material approximation of the TSP in the blob approach contribute to the question of human performance on the TSP? MacGregor and Ormerod noted that humans produced efficient results on the TSP [226] and this finding stimulated further research into

human performance on the problem and possible perceptual and cognitive mechanisms. In their analysis of experimental findings using human subjects Ormerod and Chronicle noted that global perceptual influences appear to play a role in human approximation of the TSP [227]. MacGregor et al. suggested a model based on insertion of cities into the Convex Hull [214]. This model is similar to the shrinking blob mechanism except that in the blob approach the addition of cities occurs in parallel whereas in the MacGregor et al. model it is a sequential process. The blob method also exhibits another property found in optimal tours, that boundary points in the original convex hull are connected in sequence (the sequence may, of course, be interrupted by interior points). Other competing models to explain human TSP performance exist, including variants of hierarchical pyramid models [212], [215] and the global-local model proposed by Best [228]. Merits, problems, biological plausibility and the role of local vs. global perceptual processes of the competing models have been the subject of lively debate and an assessment is beyond the scope of this chapter, but see the review in [211] for an overview. In this review MacGregor states that, despite the growing interest in research into the human performance on the TSP, and combinatorial optimisation problems in general: “As yet, no algorithms have been put forward to explain performance on the MSTP [Minimum Spanning Tree Problem] and the GSTP [Generalised Steiner Tree Problem]...”. It is notable that the shrinking blob method incorporates approximations of all three problems and executes a natural transition from global to local ‘perception’ using material properties which emerge from very simple low-level and bottom-up interactions. Whether this natural computation employed by the blob is of interest, or utility, to human combinatorial optimisation problems is, however, an open question.

Limitations of the approach, as it stands, include its noted relatively modest performance and the reliance of a manual method to interpret the result of the blob computation. Manual interpretation of the blob tour is, of course, open to experimenter bias and for this reason a methodical process must be followed, as described in section 9.3.3. An automated method of tracking the perimeter and ‘reading’ the result of the blob tour would, nevertheless, be of benefit. The shrinkage process is an innate and emergent phenomenon generated by the particle interactions and is not itself affected by the number of data points in the lattice. However, the performance of the underlying system generating the material behaviour is slowed by increases in area and in particle population size. Although the shrinkage process does indeed innately approximate TSP tours the manual reading of the tour path incurs some (human) computational demands. It is difficult to quantify these demands in terms of classical computational complexity metrics. Providing that the result reading procedure is followed correctly any increase in problem scale should — in theory — show a linear increase in readout time. However this may be hampered by the increasing likelihood of mistakes caused by increasing path tortuosity, fatigue and even the repetitive and somewhat tedious nature of

the procedure. Again, the development of a suitably accurate automated of reading the result would aid the assessment of scalability and performance in future research.

Further work, including a comprehensive evaluation of model parameters affecting the material properties of the blob may suggest methods by which the basic features of the shrinking blob approach may be adapted, or improved, to improve the performance in comparison with leading heuristic methods. The material properties and computation of the blob emerge from a population of simple multi-agent particles and it would be satisfying if this virtual material could be implemented and embodied in a real physical substrate with the desired physical (for example visco-elastic, free energy minimisation) properties. Alternately it may be possible to translate the material operation of the unconventional computation blob method into a classical algorithmic method.

Chapter 10

Voronoi Diagrams and Their Variants with Attractant and Repulsion Fields

“Without contraries is no progression. Attraction and repulsion, reason and energy, love and hate, are necessary to human existence.”

(William Blake, 1793)

10.1 Introduction

The Voronoi diagram of a set of n points in the plane is the subdivision of the plane into n cells so that every location within each cell is closest to the generating point within that cell. Conversely the bisectors forming the diagram are equidistant from the points between them. Voronoi diagrams are useful constructs historically applied in diverse fields as computational geometry, biology, epidemiology, telecommunication networks and materials science. Efficient computation of the Voronoi diagram may be achieved with a number of classical algorithms [229, 230] and are also amongst prototypical applications solved by chemical reaction-diffusion non-classical computing devices [231, 58]. Non-classical approaches are typically based upon the intuitive notion of uniform propagation speed within a medium, emanating from the source nodes. The bisectors of the diagram are formed where the propagating fronts meet, visualised, for example in chemical processors, by the lack of precipitation where the fronts merge [58]. Voronoi diagrams can be generated in other physical systems by generalising the propagation mechanism and visualisation of the bisectors and have been implemented in a number of different media including reaction-diffusion chemical processors [231, 58], planar silicon [232], crystalline phase change materials [233], and gas discharge systems [65]. In living systems approximation of Voronoi diagrams may be achieved by inoculating a chosen organism or cell type at the source points on a suitable substrate. Outward growth from the inoculation site corresponds to the propagative mechanism and regions where the colonies or cells meet correspond to bisectors of the diagram.

Physarum has also been shown to approximate the Voronoi diagram by two different methods, based on its interactions with environments containing repellents [75] and attractants [4]. In this chapter we examine the use of attraction and repulsion fields in spatially represented unconventional computation. In section 10.2 we describe in more detail the different methods of utilising *Physarum* for constructing Voronoi diagrams. A computational perspective on the role of attractants and repellents is given in section 10.3 which is used to inform modelling approaches. Model parameters and Voronoi source data representation are described in Section 10.4. In section 10.5 we examine how different inoculation arrangements and the response to repulsion fields affect the patterning of the model. We explore the effects of repellent size and concentration on Voronoi diagram construction and show hybrid diagram constructs which take advantage of the model's innate minimising behaviour with a simultaneous response to repulsion fields. In section 10.6 we summarise the repertoire of spatial combination of Voronoi diagrams using the field approach and suggest some computational tasks which may be amenable to this approach.

10.2 Approximation of Voronoi Diagram by *Physarum Polycephalum*

10.2.1 *Physarum Represents Voronoi Bisectors*

The method of using *Physarum* to approximate Voronoi diagrams by avoidance of chemorepellents was described in [76, 75]. In this method a fully grown large plasmodium was first formed in a circular arena. Then repellent sources were introduced onto the plasmodium. The circular border of the arena was surrounded by attractants to maintain connectivity of the plasmodium network. The plasmodium then adapted its transport network to avoid the repellents whilst remain connected to the outer attractants, approximating the Voronoi diagram.

10.2.2 *Absence of Physarum Represents Bisectors*

Computation of Voronoi diagram may also be achieved by non-repellent methods. This method is proposed in [4] where plasmodia of *Physarum* are inoculated at node sites on a nutrient-rich agar substrate. Attracted by the surrounding stimuli the plasmodia grow outwards in a radial pattern but when two or more plasmodia meet they do not immediately fuse. There is a period where the growth is inhibited (presumably via some component of the plasmodium membrane or slime capsule) and the substrate at these positions is not occupied, approximating the Voronoi diagram. The position of the growth fronts remains stable before complete fusion eventually occurs.

10.3 Computational Perspectives on Slime Mould Computation

Physarum may be considered as a living form of material computation, i.e. a material whose deformation and adaptation in response to environmental stimuli approximates a range of spatially represented computational geometry problems. Its behaviour results in maximising the area explored, using minimal connectivity (the exploration vs exploitation trade-off [123]). *Physarum* does not provide exact solutions to these problems and its behaviour is somewhat unpredictable. It does not exhibit the predictable material evolution seen in, for example, soap films, since the organism is concerned merely with survival, rather than solving externally applied problems.

By interpreting the innate spatial behaviour of slime mould and its environmental interactions from a computational perspective it may be possible to gain some clues as to the development of future morphological computation substrates and means of externally influencing their behaviour.

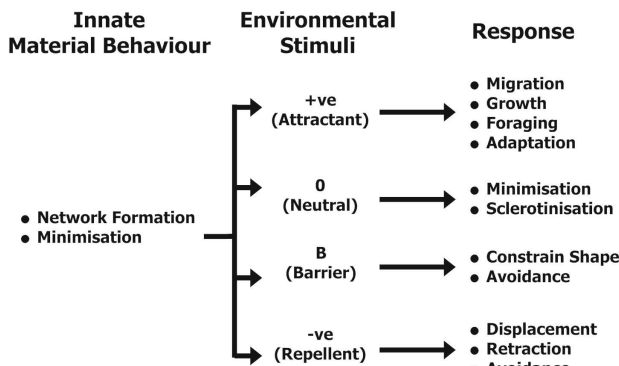


Fig. 10.1 Computational perspective of innate *Physarum* behaviour and response to attractant, neutral and repellent stimuli

External environmental stimuli may be attractive (+ve), neutral (0ve), or repulsive (-ve) to the plasmodial network. If we assume neutral stimuli have no effect on the network (other than the gradual reduction in size due to lack of nutrients) we may consider attractant and repellent stimuli in isolation.

Chemoattractant gradients diffusing from +ve stimuli invoke growth of the plasmodium towards the stimuli. Depending on the strength of the gradient the extension is via pseudopodium-like processes (weak stimuli) or via a fan-like front (stronger stimuli). A special case exists if the plasmodium is surrounded by very high concentration stimuli. In this case the growth will be outward in all directions, generating a radial pattern. It is important to note that the radial outward growth of the plasmodium in this instance is

not due to repulsion at the inoculation site. The plasmodium is instead *pulled* outwards by the surrounding stimuli.

In terms of -ve stimuli it may be difficult to state if the cause of the response is due to preferential avoidance of the stimulus, for example by migrating away from it, or whether the stimulus has a less subtle effect, such as destroying the plasmodium in regions where it touches the stimulus. Nevertheless, it can be said that the general response to -ve stimuli is to move away from the stimulus. Special cases exist where the environment presents unfavourable conditions, rather than actual an actual repellent stimulus. For example a migrating plasmodium will preferentially avoid dry regions placed on agar substrate (e.g. acetate film). In this case the stimulus acts as a barrier or obstacle, even though no -ve stimulus diffuses from the source, and can be used to constrain movement of the organism [70] or guide its migration.

The interaction between *Physarum* and its environment is a complex modification of the innate patterning of the organism. We may interpret *Physarum* as a deformable material which can be deformed towards +ve attractant stimuli and away from -ve repellent stimuli. As it is difficult to control *Physarum* precisely using these methods we must turn to modelling to investigate the effects of combining both +ve and -ve stimuli.

10.4 Model Parameters and Problem Representation

We utilised the growth and shrinkage parameters of the multi-agent as follows. If there are 1 to 10 particles in a 9×9 neighbourhood of a particle, and the particle has moved forwards successfully, the particle attempts to divide into two if there is an empty location in the immediate 3×3 neighbourhood surrounding the particle. If there are 0 to 24 particles in a 5×5 neighbourhood of a particle the particle survives, otherwise it is annihilated. The frequency at which the growth/shrinkage of the population is executed determines a turnover rate for the particles. For these experiments we used a high turnover rate (every three scheduler steps) to ensure a resilient network structure in response to changing presence and concentrations of +ve and -ve stimuli.

Particles were inoculated at the border of planar shapes in the arena (white regions). Particle sensor offset (SO) was 5 pixels except where explicitly stated. Angle of rotation (RA) and sensor angle (SA) were both set to 60 degrees in all experiments. Agent forward displacement was 1 pixel per step and particles moving forwards successfully deposited 1 units into the diffusive lattice, resulting in a temporary storage of agent movement history in the diffusion map. The emergent transport networks corresponding to Voronoi diagrams are represented in the results by the configuration of the particle collective, shown as a spatial map of particle positions.

The spatial configuration of Voronoi source data is represented by a greyscale coded image isomorphic to the 2D lattice (Fig. 10.2a). Particular greyscale values represent uninhabitable boundaries, vacant areas (within which the population can grow, move and adapt the collective morphology) and locations of nutrients. Both attractant and repellent sources are represented by sources of chemoattractant concentration in the same diffusive lattice. Attractant sources are denoted by those which have a positive (> 0) value and repellent sources are represented by values < 0 . The resulting profile of chemoattractant gradients may be interpreted as a 3D stimulus landscape (Fig. 10.2b)

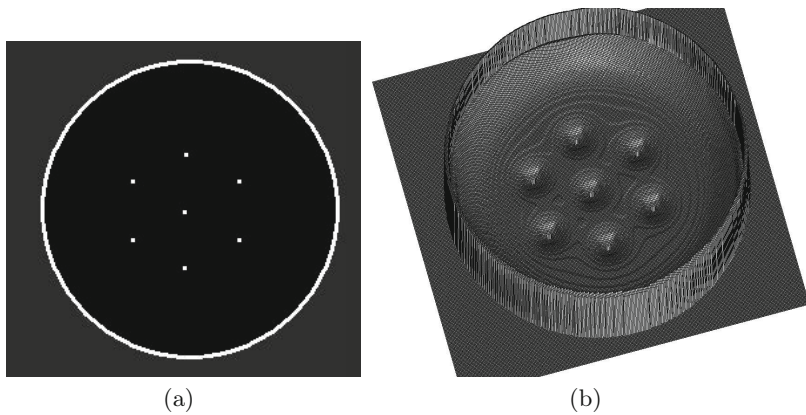


Fig. 10.2 Representation of Voronoi source data configuration as attractant and repellent gradient field. (a) Configuration of model arena showing circular attractant boundary and repellent sources, (b) 3D visualisation of concentration gradient field.

10.5 Results

10.5.1 *Interactions between Attractant and Repellent Fields*

Fig. 10.3 shows the effect of -ve stimuli on path direction. A transport network attached by two +ve stimuli at each end (Fig. 10.3a, attractants circled) is deflected by the nearby placement of -ve stimuli (Fig. 10.3b, c). When the -ve stimuli are removed the path returns to its original configuration. Path deflection may also be cumulative if successive -ve stimuli are added to the arena (Fig. 10.4).

As with attractants, the concentration of -ve stimuli affects their influence on nearby particle networks as the stimuli diffuse into the gradient field. Fig. 10.5 illustrates the effect of concentration level as a circular minimising path (formed by self-assembly of particles introduced at random in the arena) is

constrained by the repellent stimuli emanating from the central node. As the concentration increases, the -ve stimuli diffuse further from the source and the circular path is deformed outwards (Fig. 10.5a-d). If the concentration is subsequently reduced, the network path again contracts, limited by the diffusion distance from the source. Fig. 10.5e plots the increasing distance (circle radius) from the diffusion source as the -ve stimulus concentration increases. Separate plots for increasing values of particle sensor offset (SO) distances are given.

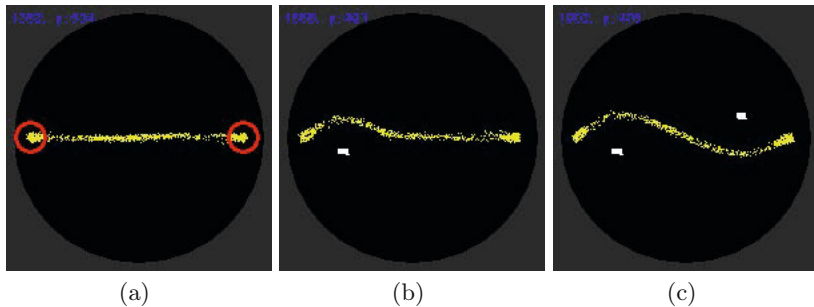


Fig. 10.3 Transport network path deflection by placement of repellent sources. (a) Transport network (yellow) in circular arena between two attractants (circled), (b) repellent source introduced below path distorts path away from repellent, (c) diffusion from second repellent source above the path deflects the path downwards.

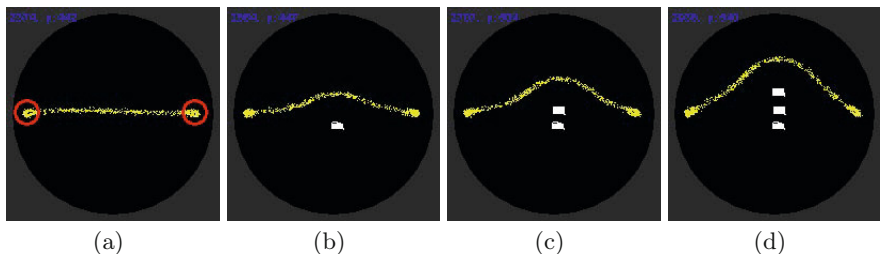


Fig. 10.4 Summation of transport network deflection by placement of repellent sources. (a) Transport network (yellow) in circular arena between two attractants (circled), (b-d) addition of repellent sources deflects path upwards, causing steeper deflection as more repellents are added.

10.5.2 Approximation of Voronoi Diagram Using Repulsion Method

A population of particles was introduced into a circular arena. The interior of the arena was patterned with seven repellent sources and the border of the

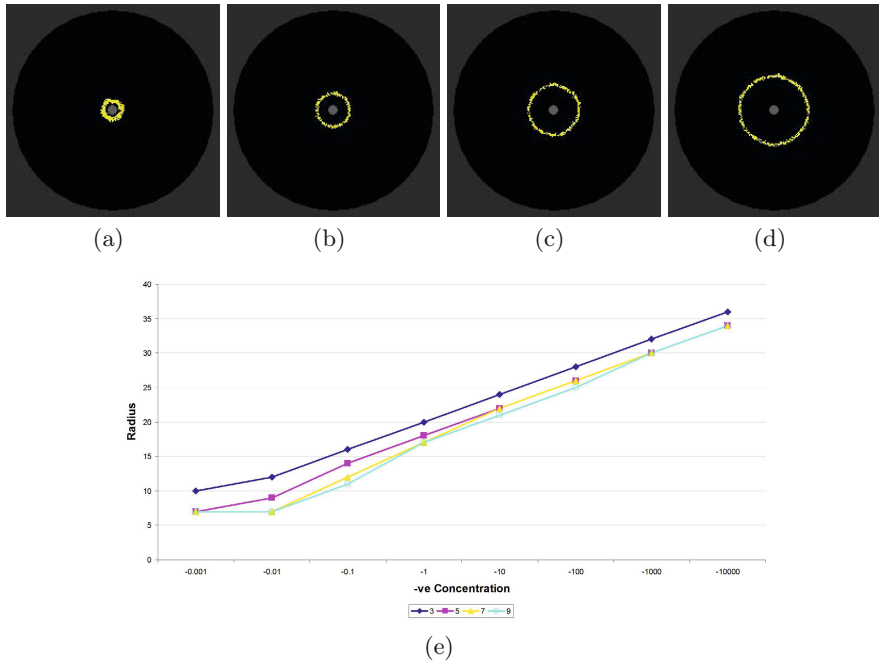


Fig. 10.5 Effect of repellent concentration on contraction of transport network. (a) Model initialised in circular arena with central repellent and network (yellow) contracts around central point, (b-d) as repellent concentration increases the collective is repelled by the diffusion front from the circle, (e) plot of increasing radius from centre as repellent concentration increases. Four experiments shown with different SO distance.

arena was patterned with attractant sources, reproducing the experimental pattern used in [75]. The uniform distribution of particles was repelled by the field emanating from the repellents and attracted by the sources at the border (Fig. 10.6), approximating the Voronoi diagram of the repellent sources.

10.5.3 Approximation of Voronoi Diagram Using Merging Method

To approximate the Voronoi by the merging method in [4] a small population of particles were initialised at locations on a simulated nutrient rich background substrate corresponding to Voronoi source nodes (Fig. 10.7a). The strong stimulation from the high-concentration background generated radial growth (Fig. 10.7b-e) and the Voronoi Diagram is approximated in the model at regions where the separate growth fronts fuse. Note that the model does not explicitly incorporate the inhibition at the touching growth fronts.

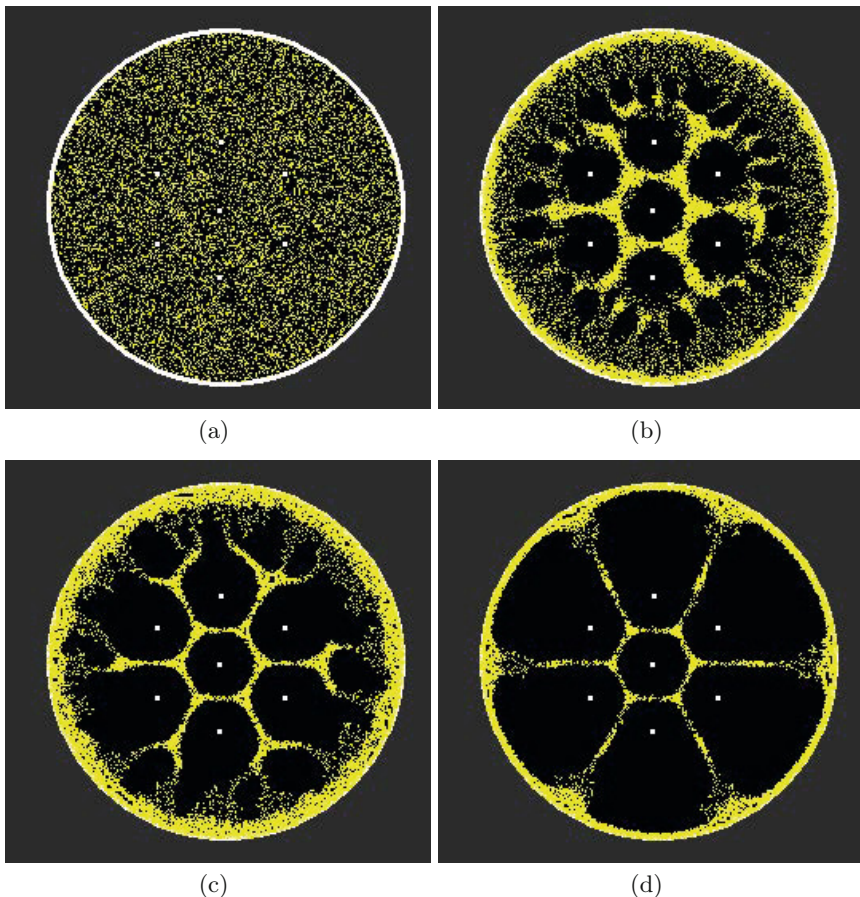


Fig. 10.6 Approximation of Voronoi diagram by model in response to repulsive field. (a) Initial distribution of particles (yellow) representing a uniform mass of plasmodium, (b-c) particles respond to repulsive field by moving away from repellents, (d) final network connects outer attractant and bisectors correspond to Voronoi diagram.

In this case the Voronoi bisector position is instead indicated by the model by the increase in network density at the bisector position (Fig. 10.7e). This approximation is not satisfactory from a computational perspective since it requires subjective visual evaluation and interpretation and the Voronoi bisectors fade after continued adaptation (Fig. 10.7f).

10.5.4 Approximation of Voronoi Diagram Using Combined Repulsion and Merging Method

Can we combine the repulsion and merging methods to compute the Voronoi diagram? To test this question we use a more challenging problem where the sources for the bisectors are planar shapes or curves instead of single point sources, requiring the use of algebraic curves in classical algorithms. Chemical reaction diffusion processors are, however, capable of approximating the Voronoi diagram of complex shapes [234]. To see if the model plasmodium can approximate planar shape Voronoi diagrams and to see if the repulsion and merging methods can be used simultaneously, a population of model particles was initialised at the borders of repellent planar shapes in a simulated arena. The circular arena border was also configured as a repellent source and the remainder of the arena was configured to simulate a nutrient-rich background substrate (light grey regions) which was consumed on contact with the model population, Fig.10.8a.

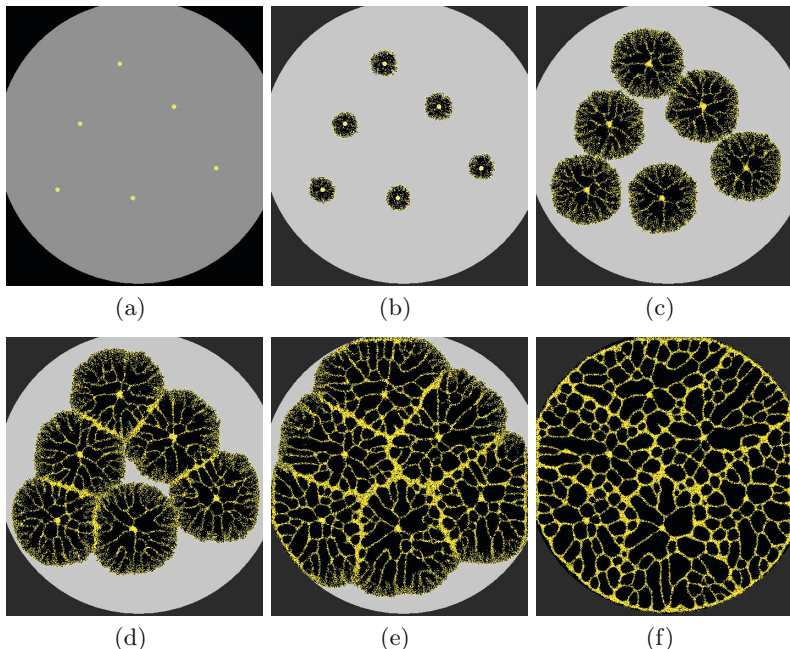


Fig. 10.7 Approximation of Voronoi diagram by merging method. (a) inoculation of separate model plasmodia (yellow) on simulated oat flakes on nutrient-rich background (grey), b-c) Radial expansive growth of model plasmodium, d-e) Growth is temporarily inhibited at regions where other model plasmodia are occupied, These dense regions indicates bisectors of Voronoi diagram, f) Voronoi bisectors fade with continued adaptation.

The model plasmodium simultaneously grows outwards (drawn outwards by the surrounding attractant substrate) and is repelled from behind by the diffusion of the repellent field (Fig. 10.8b,c). The Voronoi bisectors are initially coarsely approximated by the meeting growth fronts (Fig. 10.8d) and the bisectors are then refined as the minimising network formed by the particle population avoids the repellent field from the planar shapes (Fig. 10.8,e-f).

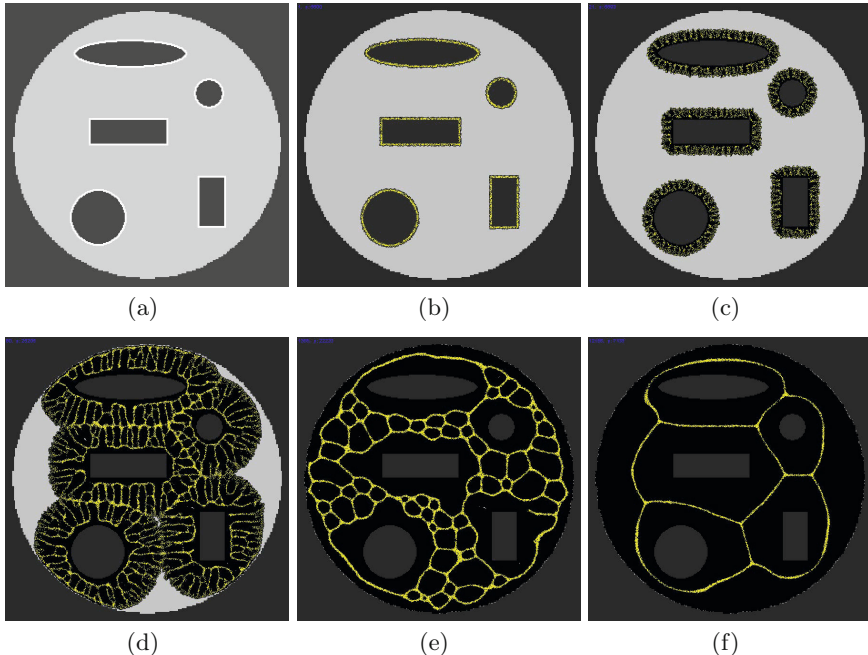


Fig. 10.8 Approximation of planar Voronoi diagram of complex shapes using combined repulsion and merging. (a) Configuration of arena showing inoculation borders of shapes (white), background substrate (light grey) and repulsive regions (dark grey), (b) model (yellow) is initialised at edges of shapes $t=1$, (c) model population extends outwards into arena attracted by gradient of nutrient substrate (light grey) $t=21$, (d) merging growth fronts represent coarse position of Voronoi Diagram $t=80$, (e) and (f) model network adapts to repulsive field from data sources and arena wall to form final approximation of Voronoi Diagram $t=1388$ and $t=12188$.

10.5.5 Towards Hybrid Voronoi Diagrams

The results in Figs. 10.6–10.8 demonstrate that the model can reproduce the approximation of the Voronoi diagram using both the repulsion method in [76] and the merging fronts method in [4]. The results also demonstrate approximation of the Voronoi diagram for more complex 2D shapes and the simultaneous use of attractant and repulsion fields for the computation.

Transport networks formed under the influence of only attractant stimuli take the form of minimising proximity graphs, specifically reproducing the range of graphs in the Toussaint hierarchy (see [188] and also [80] for the same behaviour implemented by *Physarum*). At low nutrient concentration the graphs formed by the model minimise their initial configuration by self-organisation to approximate the Steiner tree and Minimum Spanning Tree, whereas at higher concentration the networks approximate Relative Neighbourhood Graphs and Gabriel graphs (as demonstrated in [221]). How does the relative concentration of repellents affect the innate minimising behaviour of the networks?

An example of how differences in -ve concentration affect network structure is shown in Fig. 10.9. In this example the minimising particle network adapts to the presence and concentration of the repulsive field surrounding the planar shapes. In the first image the -ve stimuli overwhelms the contractile properties of the particle network and a planar Voronoi diagram is formed (Fig. 10.9a). As the concentration of -ve stimuli emanating from the shapes is reduced, however, the contractile behaviour of the particle network exerts its influence, shrinking the network around the shapes (Fig. 10.9b,c). At the lowest repellent concentration, the shapes are wrapped tightly by the ‘band’ of particles (Fig. 10.9d). Note that the internal network does not adopt the bisectors of the Voronoi Diagram, but instead adopts straight lines which form a Steiner point (S) at the location equidistant between the three sources (circled) connecting to the point.

The results in Fig. 10.9 illustrate the effects of a reduction in repellent concentration on Voronoi patterning as contractile forces begin to exert an effect. What is the response in the opposite situation where initially predominating contractile forces become outweighed by repellent concentration? Fig. 10.10 illustrates the situation where a set of point sources are individually surrounded by small contractile bands of particles. At very low concentration, the pattern simply corresponds to the pattern of data sources (Fig. 10.10a). As the repellent concentration increases, however, the expansive force predominates and the cells expand (Fig. 10.10b) and merge with close neighbours forming clusters of neighbouring cells (Fig. 10.10c,d,e) until a single cluster of cells is formed.

The cellular tessellation resembles, but does not perfectly match the Voronoi diagram. Fig. 10.11 illustrates differences between the cellular Voronoi diagram (Fig. 10.11a) and the ‘full’ Voronoi diagram (overlaid). The circled areas indicate regions where the bisector of the cellular diagram does not match the full diagram. The cause of this distortion can be seen in Fig. 10.11b which shows a map of the diffusion field including the contractile network trail (light shaded bisectors) and the gradients emanating from the point sources. It can be seen that in the areas corresponding to the circled regions

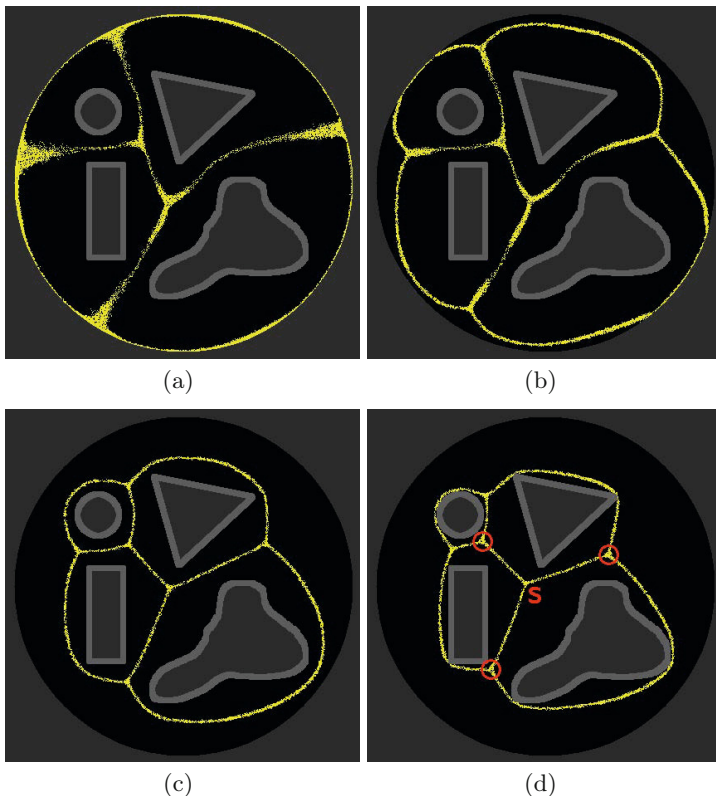


Fig. 10.9 Reducing repellent concentration allows minimising behaviour to exert its influence, inducing formation of hybrid Voronoi diagram. (a) at high concentration the repellent gradient forces the contractile network (yellow) to conform to the position of curved Voronoi bisectors between planar shapes, (b-d) reduction in repellent concentration allows contractile effects of transport network, minimising the connectivity between cells.

in Fig. 10.11a, the contractile force of the network is stronger than the repellent diffusion sources and the bisectors are pulled from the Voronoi bisectors (overlaid). Why is the network pulled away from the outer points? This is partially due to the general nature of the contraction force (the tension forces ensure an inward bias) and partially due to the fact that smaller cells in minimising networks tend to shrink, whilst larger cells tend to grow. It is only at very high repellent concentration that the contractile force is overwhelmed by the repellent force and the Voronoi diagram is correctly approximated (Fig. 10.11c). Weighted Voronoi diagrams are generated in classical

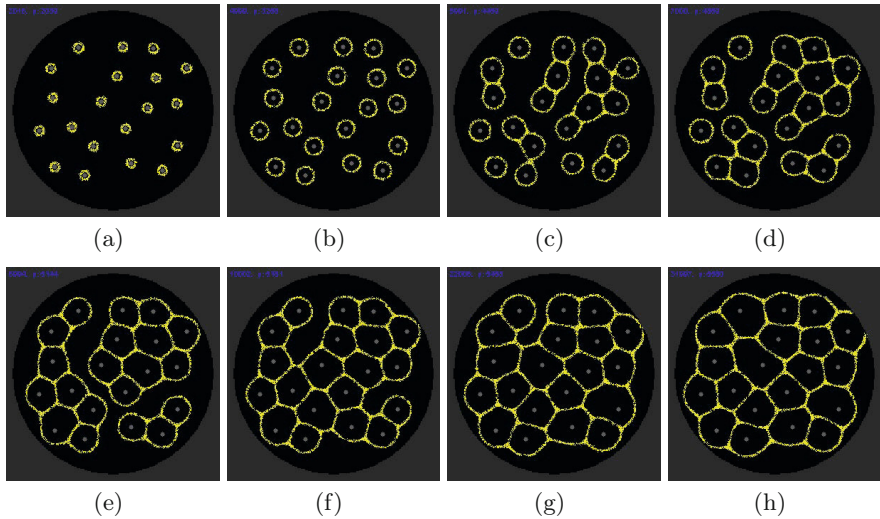


Fig. 10.10 Increasing repellent concentration forms an hybrid ‘cellular’ Voronoi diagram. (a) contractile networks (yellow) initialised around 20 nodes with -ve stimuli emanating from nodes of weight 0.005, (b)-(h) increasing -ve stimuli strength expands networks and cell borders fuse, forming a hybrid ‘cellular’ Voronoi diagram. Node concentration 0.025, 0.05, 0.075, 0.125, 0.15, 0.45, 0.7 respectively.

methods by modifying the distance measure during its computation (for example multiplying the distance by a weighting factor). This weighting may be approximated in the model by varying the relative size of the data points. This affects the amount of chemoattractant projected into the lattice and distorts the diagram to reflect the relative size of the data points within each cell (Fig. 10.11c)).

The combination of contractile particle networks with repulsive stimuli may be used as an unconventional approximation of geometry problems. In the paper by Kim et al. [235] the problem of generating a Voronoi diagram of circles within a bounding circle was addressed using a multi-step process based on constructing a classical Voronoi diagram, generating a seed topology to represent the outer bounding circle, and generation of the exact edge locations. Can the exact solution described in [235] and shown in Fig. 10.12a be approximated in an unconventional computation method? When initialised at random locations in the arena the contractile particle population self-assembled into a network surrounding the circles which represented the repellent sources (Fig. 10.12b). We found that the innate material behaviour was able to approximate closely (but not exactly) the multi-stage result obtained by Kim et al. Further reductions in repellent concentration

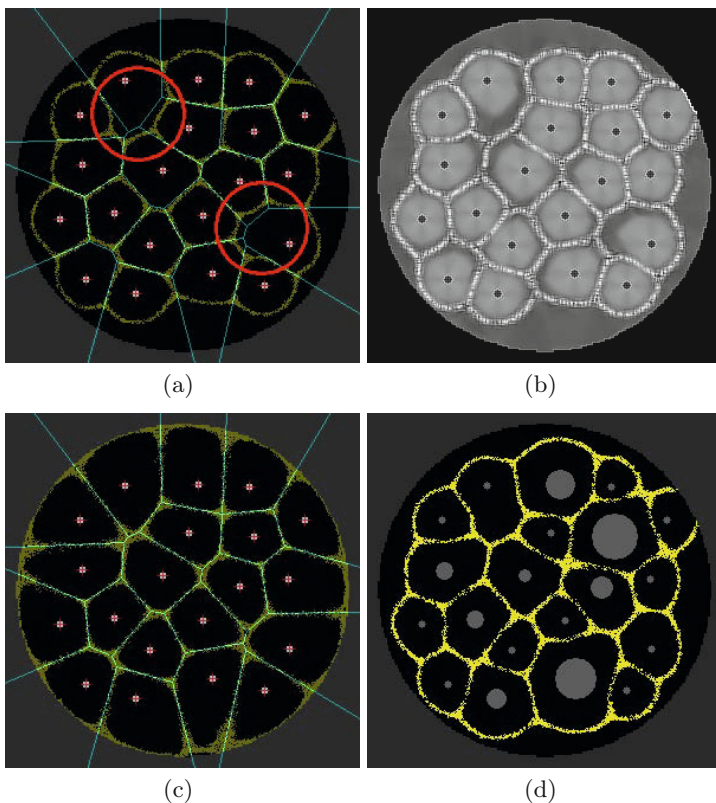


Fig. 10.11 Differences between ‘cellular’ and ‘full’ Voronoi diagram and approximation of weighted Voronoi diagram. (a) ‘cellular’ Voronoi diagram (yellow) formed by method in Fig. 10.10 showing differences (circled in red) between ‘full’ diagram (overlaid in blue), (b) visualisation of contractile network field and repellent field shows shaded regions where contractile network forces overcome repellent forces (see text), (c) particle network (yellow) perfectly matches full Voronoi diagram (blue) only at very high -ve stimuli node concentration (Voronoi diagram by classical method is overlaid), (d) Weighted diagram is approximated by varying size of source data points.

maintained the separate partitioning of the circles whilst reducing the internal distance of the network (Fig. 10.12c). At very low repellent concentrations the circles exerted very little repellent force and merely became obstacles to the minimisation of the particle network, constraining its evolution. The final network encompasses all of the original nodes but appears to minimise the connectivity between the nodes (Fig. 10.12d).

When repellent stimuli are added to a plasmodial network already containing attractants (Fig. 10.13a), the plasmodium abandons its occupation

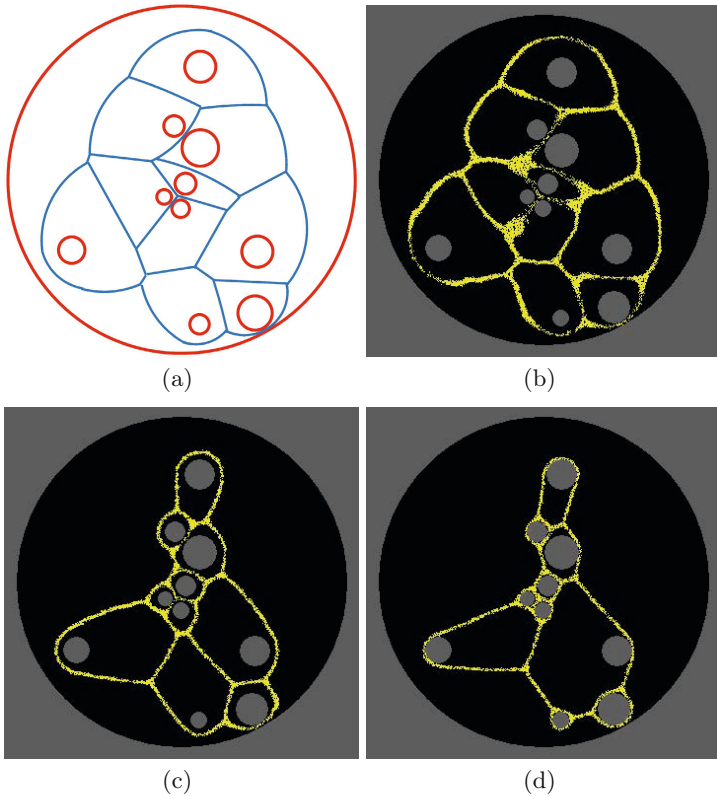


Fig. 10.12 Approximation of the circle Voronoi Diagram problem and its subsequent minimisation using unconventional computation approach. (a) Circle Voronoi diagram as proposed in [235], generating circles shown in red and Voronoi diagram in blue (b) approximation of the circle Voronoi diagram in model plasmodium (yellow) at high repellent concentration, (c-d) reducing repellent concentration maintains partition of shapes whilst reducing network connectivity.

of repellent regions as the repellent diffuses into the surrounding agar. The resulting network avoids the repellents whilst maintaining connectivity between the nutrient sources (Fig. 10.13b). When a model network is also presented with the addition of repellents, the connectivity between the attractant nodes is maintained and the network course adapts to avoid the repellent sources (Fig. 10.13c,d).

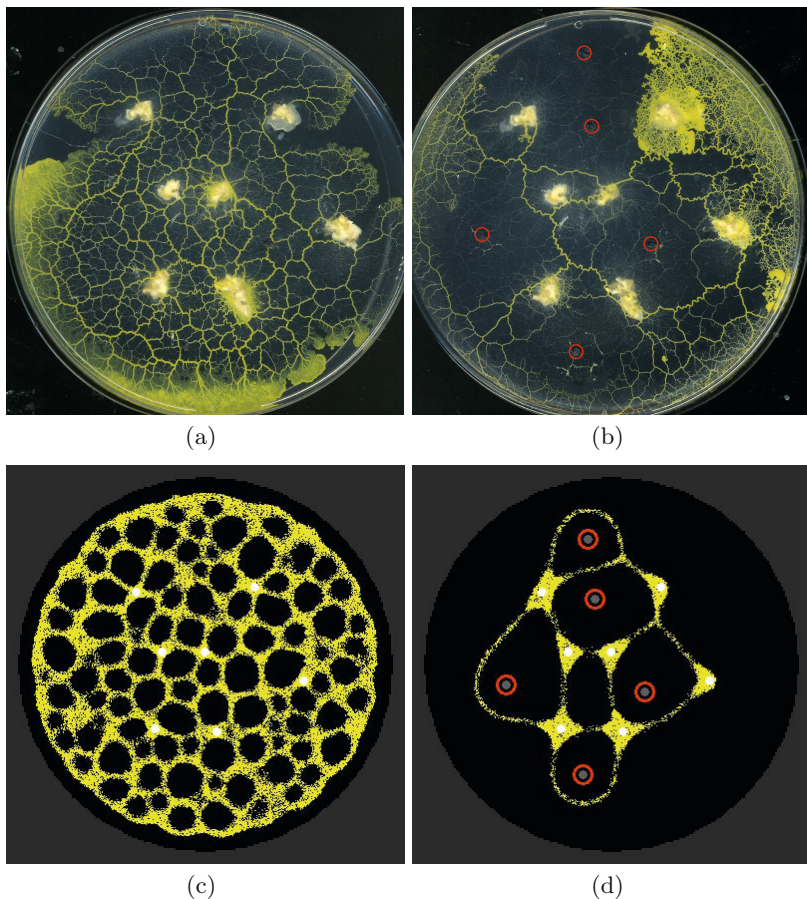


Fig. 10.13 Addition of repellents to attractants forms hybrid of Voronoi diagram and proximity graph. (a) protoplasmic network formed in the presence of nutrient oat flakes, (b) addition of repellent (salt crystals, circled in red) causes plasmodium to abandon repellent areas whilst maintaining connectivity with nutrients after 12h (images a) and b) from [236]), (c) initial simulated protoplasmic network in model (yellow), (d) response of model to the presence of repellents connects the attractants (white) and avoids repellents (circled in red).

10.6 Summary: Environmentally Mediated Plane Division and Minimisation

We have examined the influences of repellent fields on the innate minimising behaviour of synthetic transport networks in the approximation of Voronoi diagrams in unconventional computation systems. Voronoi diagrams are the prototypical applications of unconventional computing architectures which

utilise phenomena of parallel propagation of information to perform useful computation. In this chapter we used the multi-agent model to demonstrate how the synthetic particle networks can reproduce the experimentally observed approximation of Voronoi diagrams using *Physarum* using the repulsion method of [76], and the merging fronts method of [4].

By combining the innate minimising behaviour of the particle networks with repellent diffusion sources we were able to approximate a range of hybrid Voronoi diagrams. The network patterns were dependent on the shape and concentration of the repellent stimuli. High concentration stimuli reproduced Voronoi diagrams in both simple point sources, circular sources, growing cellular sources, and for complex planar shapes. Weighted Voronoi diagrams were approximated by varying the relative size of the data sources. Low concentration repellent stimuli reduced the propagation distance of the repulsive field and allowed the innate contraction behaviour of the particle model to exert an influence on network connectivity. The resulting hybrid networks encompassed the repellent sources, retaining their separate partitioning and minimising the internal network distance between the sources. The combination of separate partitioning of objects in the plane and the minimisation of the distance between the grouped objects may prove useful in a range of geometry problems, including packing, wiring and bundling problems, path planning and robotic guidance. When presented with a combination of attractant and repellent stimuli, the model reproduced the behaviour of the *Physarum* plasmodium by maintaining connectivity of the attractants whilst avoiding the repellent stimuli.

Can the response of synthetic particle networks to +ve and -ve stimuli be rationalised in terms of the behaviour of the organism itself? For attractant stimuli the benefits of minimal network connectivity are obvious and well documented [9], [80]. For repellent stimuli the avoidance of hazards in the environment are also advantageous [76], [75], [84], [82]. By combining the minimal connectivity to (for example) nutrients whilst avoiding hazards in the environment the plasmodium can increase its chances of obtaining energy whilst minimising risk of damage. It is notable that the organism's trade-off between reward and risk in its environment is 'computed' by the response of the very material of which it is composed. This has the advantage of not requiring any neural integration of separate +ve and -ve stimuli. The complexity of slime mould's response, and the rich variety of partitioning and network connectivity in the synthetic particle model to similar stimuli, may suggest ways in which artificial computing schemes can take advantage of opposing signalling cues by means of innate material responses.

Chapter 11

Material Representation of Area and Shape: Convex Hull, Concave Hull and Skeleton

“Lost my shape - Trying to act casual.
Can’t stop - I might end up in the hospital.
I’m changing my shape - I feel like an accident.”

(David Byrne, 1980.)

11.1 Introduction

Computational geometry problems tackle the grouping or partitioning of points in the plane or in higher dimensions. Because of the lack of supportive tissue, the plasmodium typically extends along the space of the surface on which it lives, and hence, *Physarum* may be considered as a 2D organism. We have already examined the network formation properties of the virtual plasmodium multi-agent model in biological (Chapter 4) and computational (Chapter 6) terms and found that nutrient sources can be considered as a coarse representation of points on the plane. Conversely, the networks formed by growth and adaptation of the model can be considered as edges in the plane. The ‘natural’ behaviour of the model networks is to construct and minimise proximity graphs in the plane which link together the nutrient nodes in the diffusive lattice. The exact properties of these proximity graphs depend on model parameters (biased in favour of either dynamical or minimising networks) and based on the concentration of the projected simulated nutrients into the lattice.

The efficiency of proximity graphs formed by *Physarum* and the model is a trade-off between minimum distance (or minimum amount of material) and resilience to random disconnections. However, although the networks connect all of the nutrient sources, they do not group them, or provide a representation of the space or shape in which they reside. In this Chapter we examine potential mechanisms in which we can use the model to represent area and shape.

11.2 Convex Hull by Material Shrinkage around Attractants

The Convex Hull of a set of points is the smallest convex polygon enclosing the set, where all points are on the boundary or interior of the polygon (Fig. 11.1a). Classical algorithms to generate Convex Hulls are often inspired by intuitively inspired methods, such as shrink wrapping an elastic band around the set of points, or rotating calipers around the set of points [237, 238]. Is it possible to approximate the Convex Hull using emergent transport networks by mimicking a physically inspired method? To achieve this we initialise a circular ring of virtual plasmodium *outside* the set of points (Fig. 11.1b). Because of the innate minimising behaviour of the particle networks the population thus represents a ring of deformable elastic material.

This bounding ‘band’ then automatically shrinks to encompass the outer region of the set of points. The minimising properties of the paths ensure that the edges of the Hull are straight and convex. There are some practical limitations of this approach. Firstly, the bounds of the set of points must be known in advance, which is not always the case in certain Convex Hull problems. Secondly, points which are inside the final Hull, but close to the ‘band’ (for example near the top edge in Fig. 11.1c) may, via diffusion of their projected attractant, attract the band inwards, forming a concavity. This possibility may be avoided by restricting the nodes to project stimuli only when they have been directly contacted by particles comprising the shrinking band. One benefit of this is that the nodes which are actually part of the final Hull are highlighted (Fig. 11.1e, the larger nodes).

11.3 Convex Hull by Material Shrinkage around Repellents

Alternatively, to avoid the potential of attraction to nodes within the Hull boundary, it is possible to have the ‘band’ shrink around the array of points which are actually *repulsive* to the particles comprising the band. This is achieved by projecting a repellent stimulus (for example, a negative value into the lattice) at the nutrient node locations. The band will still shrink to envelope the nodes but — because of the repulsion effect — will not actually contact the nodes. This generates a Convex Hull which encompasses the nodes but does not directly touch them (Fig. 11.2) and results in a Hull which slightly overlaps the original dataset.

11.4 Convex Hull by Self-organisation

If the boundary of the Hull points is not known in advance then it is possible to utilise a method which employs both self-organisation and repulsion to

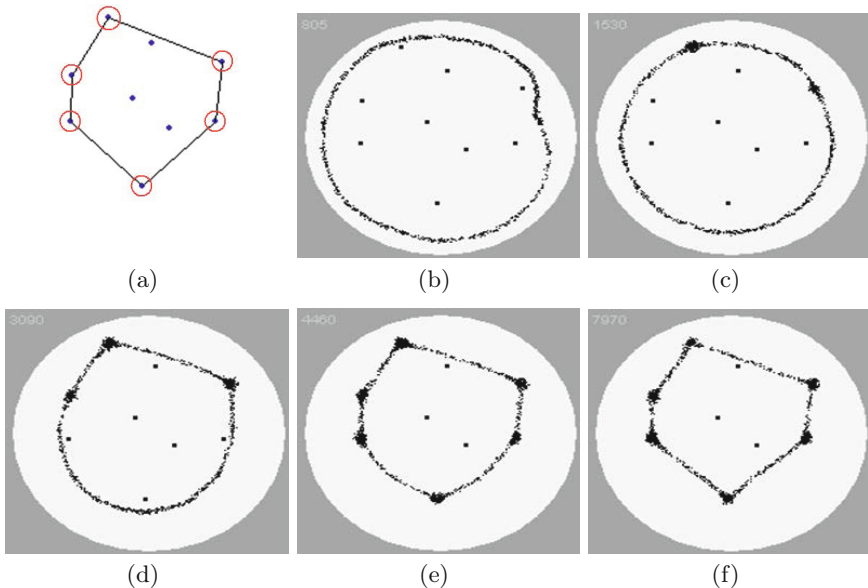


Fig. 11.1 Approximation of Convex Hull by shrinking band of virtual plasmodium. a) original data set with Convex Hull (edges). Nodes which are part of the Convex Hull are circled, b-e) A circular band of virtual plasmodium initialised outside the region of points and shrinks. In this example nodes only emanate nutrients when touched by virtual plasmodia (see text), f) bounding points of final Convex Hull are indicated by larger nodes.

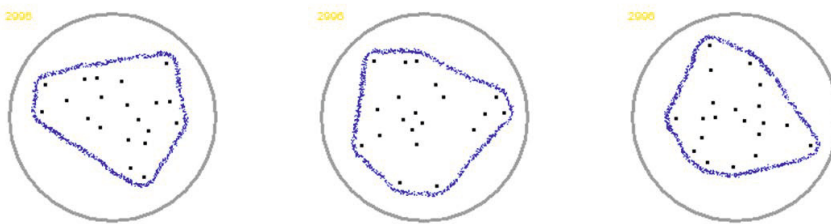


Fig. 11.2 Convex Hull via shrinkage around repellent stimuli. Three separate examples are shown. A band of virtual plasmodium shrinks around the set of points to approximate the Convex Hull. Note a small peripheral region is indicated because of the repulsive region.

approximate the Hull, as shown in Fig. 11.3. In this approach the particle population is initialised at random locations within the lattice (both outside and inside the set of points). The particles are repelled by the repellent nodes and move away from these regions. If a particle touches a node it is annihilated and randomly initialised to a new blank part of the lattice. Over time, the inner region of the lattice becomes depleted of particles, but in contrast the region outside the set of point (which is further away from the repulsive nodes) becomes more populous. The increasing strength of the emerging Convex Hull trail outside the dataset attracts particles from inside the dataset (because the deposited ‘ring’ of flux is higher in concentration than the inner region, due to the increased number of particles) and the particles are drawn out into this ring. The natural contraction of the outer ring approximates the final Convex Hull.

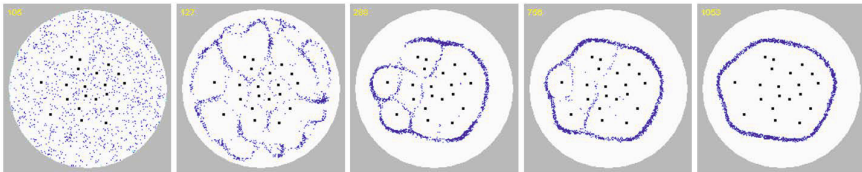


Fig. 11.3 Convex Hull via self-organisation within repulsive field. Particle population is initialised randomly in the arena and is repulsed by nodes. Convex Hull emerges at the border and internal connections gradually weaken.

11.5 Representing the Shape of a Set of Points

The area occupied by, or the ‘shape’ of, a set of points is not as simple to define as its Convex Hull. It is commonly defined in Geographical Information Systems (GIS) as the Concave Hull, the minimum region (or *footprint* [218]) occupied by a set of points, which cannot, in some cases, be represented correctly by the Convex Hull [219]. For example, a set of points arranged to form the capital letter ‘C’ would not be correctly represented by the Convex Hull because the gap in the letter would be closed (see Fig. 11.5a).

Attempts to formalise concave bounding representations of a point set were suggested by Edelsbrunner et al. in the definition of α -shapes [220]. The α -shape of a set of points, P , is an intersection of the complement of all closed discs of radius $1/\alpha$ that includes no points of P . An α -shape is a Convex Hull when $\alpha \rightarrow \infty$ (Fig. 11.4a). When decreasing α , the shapes may shrink, develop holes and become disconnected (Fig. 11.4b-d), collapsing to P when $\alpha \rightarrow 0$. A Concave Hull is non-convex polygon representing area occupied by P . A Concave Hull is a connected α -shape without holes.

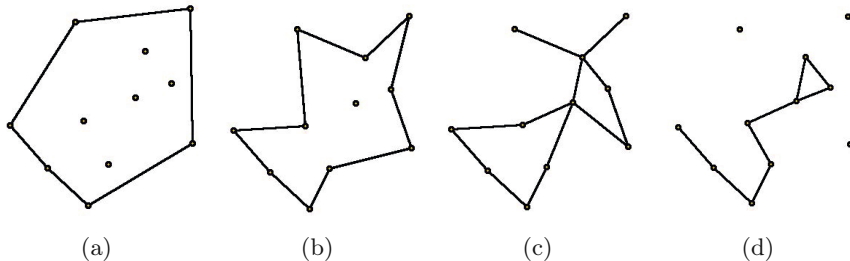


Fig. 11.4 Examples of α -shape of a set of points as α decreases. Note the limitations of this approach as the shapes can contain cycles (c) or become disconnected from the data points (d).

11.6 Approximation of the Concave Hull by Shrinkage

The virtual plasmodium approximates the Concave Hull via its innate morphological adaptation as the population size is slowly reduced. A slow reduction in population size prevents hole defects forming in the material which would result in cyclic networks instead of the desired solid shape. The reduction in population size may be implemented by either randomly reducing particles at a low probability rate or by adjusting the growth and shrinkage parameters to bias adaptation towards shrinkage whilst maintaining network connectivity.

In the examples shown below the virtual plasmodium is initialised as a large population (a solid mass) within the confines of a Convex Hull (calculated using the classical algorithmic method) of a set of points (Fig. 11.5b). By slowly reducing the population size (by biasing the parameters towards shrinkage), the virtual plasmodium adapts its shape as it shrinks. Retention of the mass of particles to the nodes is ensured by chemoattractant projection and as the the population continues to reduce, the shape outlined by the population becomes increasingly concave (Fig. 11.5c-f).

The graph of changing population size as the virtual plasmodium adapts (Fig. 11.6) shows that the population stabilises as the concave shape is adopted. If varying degrees of concavity are required, the current population size as a fraction of the original size, or alternatively the rate of population decline, could possibly be used as a simple parameter to tune the desired concavity.

If the shrinkage of the initial Convex Hull were to continue beyond the Concave Hull the area would shrink until a network representation (approximating the Steiner tree) is formed. The shrinkage of the agent population thus represents the transition between area coverage and network distance.

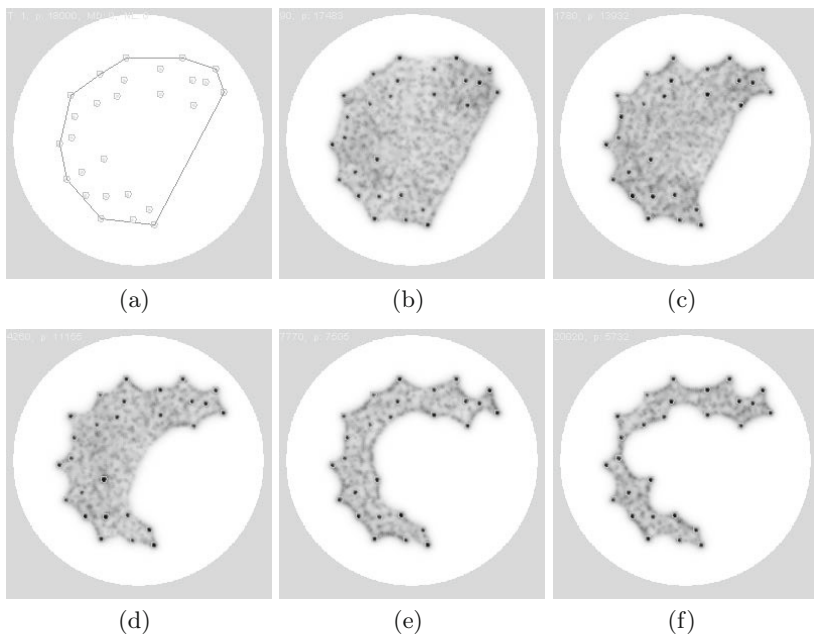


Fig. 11.5 Concave Hull by uniform shrinkage of the virtual plasmodium. (a) Set of points approximating the shape of letter ‘C’ cannot be intuitively represented by Convex Hull, (b-f) Approximation of concave hull by gradual shrinkage of the virtual plasmodium, $p=18,000$, $SA\ 60^\circ$, $RA\ 60^\circ$, $SO\ 7$.

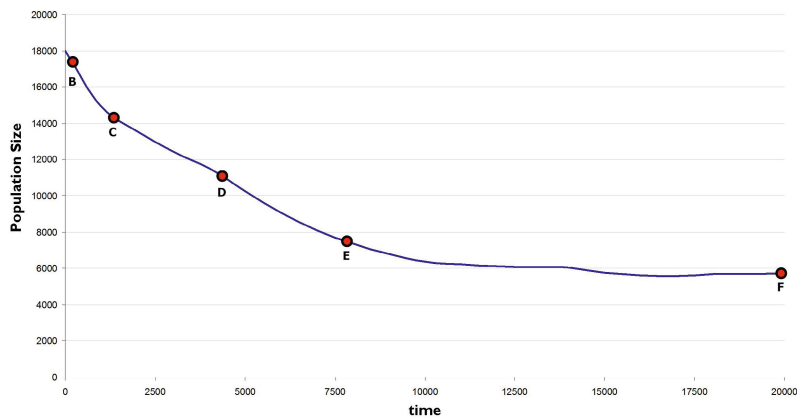


Fig. 11.6 Decrease in population size as concave shape formed from a Convex Hull of the point set in Fig. 11.5a. Plot shows population size over time. Letters and circles B-E represent population levels in the corresponding images of Fig. 11.5(b-e).

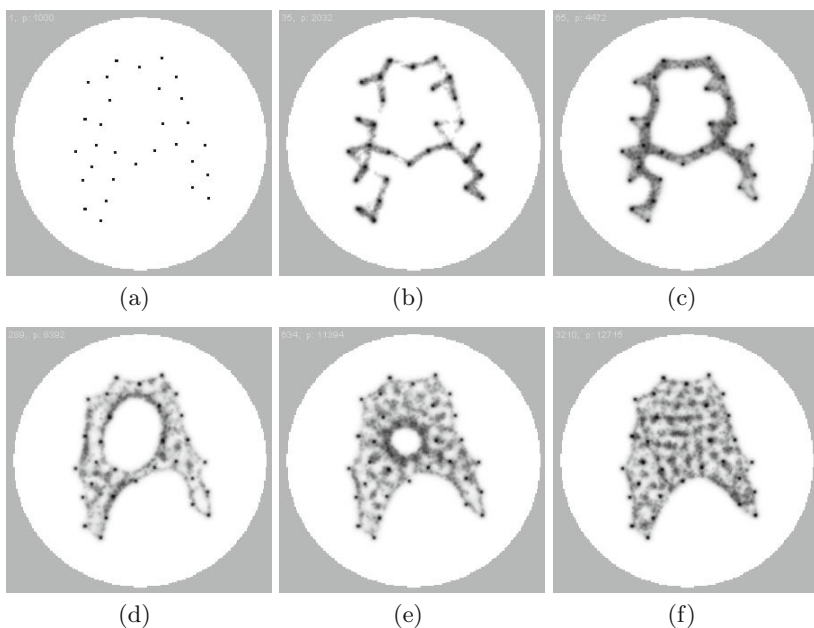


Fig. 11.7 Alternate method of generating α -shape and Concave Hull by merging regions

11.7 Approximating the Concave Hull by Growth

The shrinkage of a solid mass of virtual plasmodium cannot construct α -shapes, shapes with vacant regions within them, for example as with the letter ‘A’. However, by initialising the a smaller population size at the node sites themselves, the individual fragments of ‘plasmodium’ grow and fuse together when each fragment senses the attractant deposited by a neighbouring fragment, eventually recovering the general shape of the letter (Fig. 11.7,a-d). Further increasing the population size (manually or by biasing growth/shrinkage parameters) results in removal of the internal space and transition from an α -shape to a solid Concave Hull (Fig. 11.7,e-f).

One limitation with this approach is that we cannot guarantee that all sites will fuse. For example, if one node is a significant distance from all other sites it will not sense the stimulus from more distant sites. This node will thus not fuse with the remaining masses, resulting in two separate shapes. We can overcome this limitation by ensuring that the initial inoculation sites are connected in some way. A suitable candidate pattern is the Minimum Spanning Tree (MST) structure of the data points (Fig. 11.8a and b). This structure guarantees connectivity between all points and also does not possess any cyclic regions. By inoculating the model plasmodium on the MST pattern and biasing the growth/shrinkage parameters towards growth, the model then

'inflates' the MST (Fig. 11.8c-i) and automatically halts its growth (maintaining a constant population size) as a Concave Hull is approximated (Fig. 11.9). To visualise the classical Concave Hull edges from this pattern we can use the approach described in [216] and traverse the perimeter, constructing the Concave Hull by adding nodes which are located on the periphery of the shape, yielding the classical (straight lines) structure of the Concave Hull (Fig. 11.8i, edges).

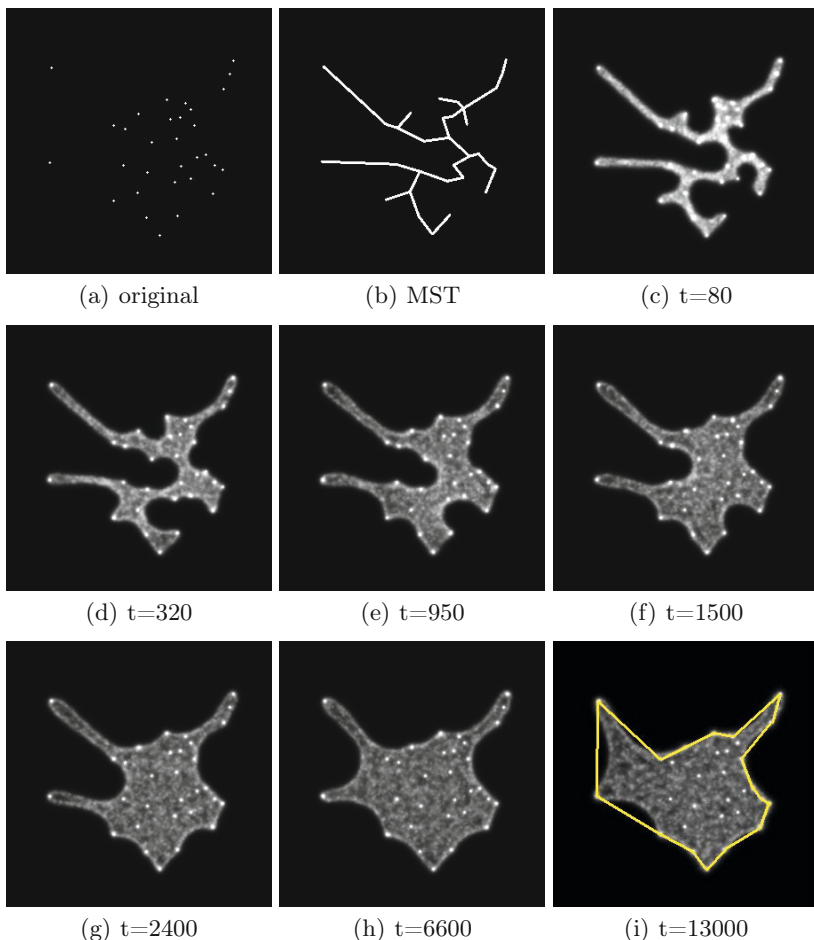


Fig. 11.8 Growth of Concave Hull from Minimum Spanning Tree. a) points representing the locations of major cities in People's Republic of China, b) Minimum Spanning Tree of points connects all points without cycles, c-i) after inoculating the virtual plasmodium on the Minimum Spanning Tree the virtual plasmodium grows to approximate the Concave Hull, stabilising its growth automatically (overlaid edges show classical Concave Hull).

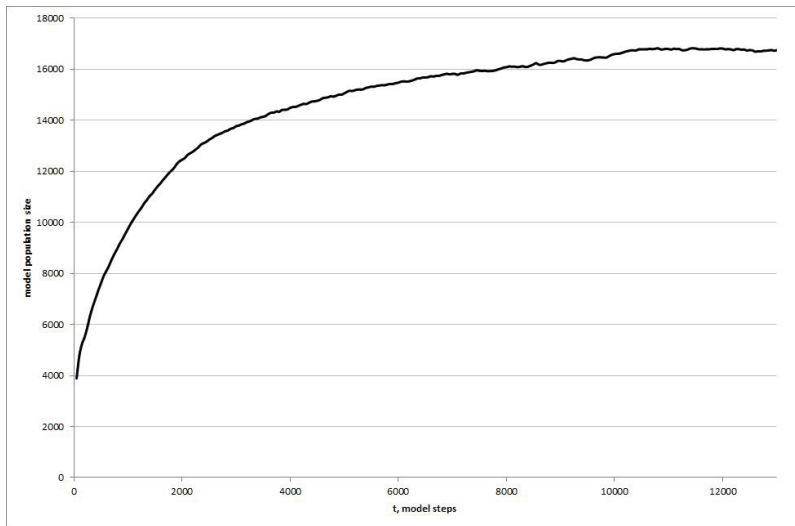


Fig. 11.9 Increase and stabilisation of population size as concave hull grows from inoculation of the model plasmodium on the MST. Plot shows population size over time.

11.8 Transformation between Convex and Concave Hull

By growing the population from the MST a representation of the Concave Hull is generated. Can we ‘tune’ the shape of the final pattern? In Fig. 11.10 we assess this on a simple test structure, a set of points arranged in a square. After inoculation on the MST the population grows and at 5000 steps the blob fills the region between the bounding points (in this square pattern the Concave Hull is the same as the Convex Hull). By adjusting the value of the G_{max} growth parameter it was found that the concavity of the blob could be adjusted. Fig. 11.11 shows the effect of different values of G_{max} in five different experiments. As G_{max} increased, the concavity reduced until at $G_{max}=25$ the final blob was fully convex. At higher G_{max} values the growth was not constrained by the stimuli from the point sources, causing uncontrolled growth patterns (Fig. 11.11e).

11.9 Internal Representation of a Shape - Skeletonisation

Image skeletonisation (or line thinning) is a transformation to recover an efficient and minimal shape descriptor [239]. It is widely used in image pre-processing and as a stage in the image analysis pipeline. Although a huge number of skeletonisation algorithms exist, nature inspired approaches were

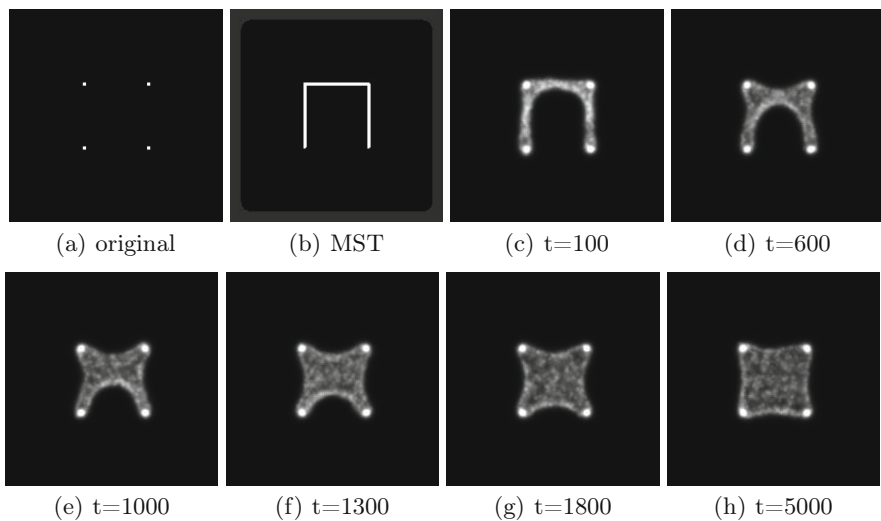


Fig. 11.10 Tuning concavity of growth from Minimum Spanning Tree. a) 4 points arranged in square pattern, b) Minimum Spanning Tree of square points used as inoculation sites, c-h) after inoculation on the Minimum Spanning Tree the virtual plasmodium grows to approximate the Concave Hull.

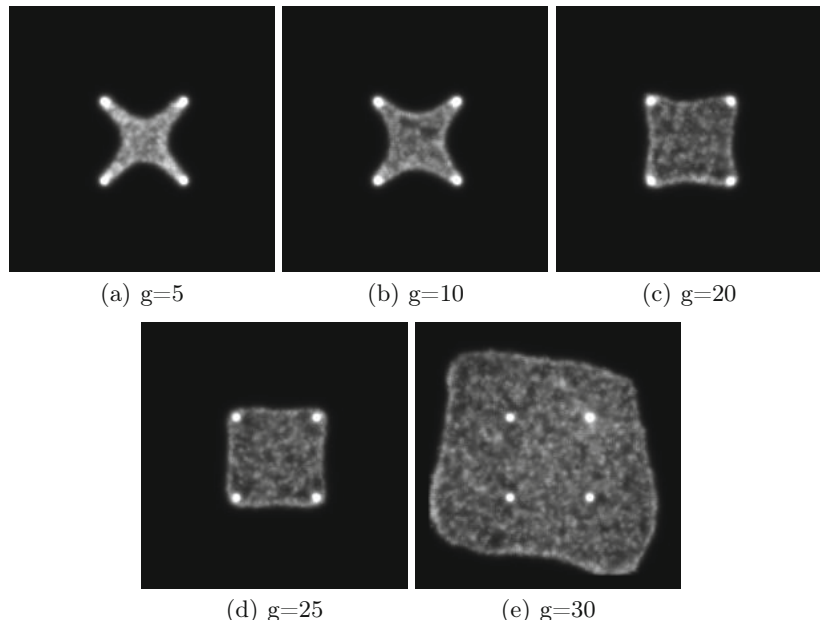


Fig. 11.11 Increasing G_{max} growth parameter reduces blob concavity. Separate experiments run for 5000 steps, except in the case of ‘e’ which was halted at 3000 steps due to unconstrained growth. a) $G_{max} = 5$, b) $G_{max} = 10$, c) $G_{max} = 20$, d) $G_{max} = 25$, e) $G_{max} = 30$.

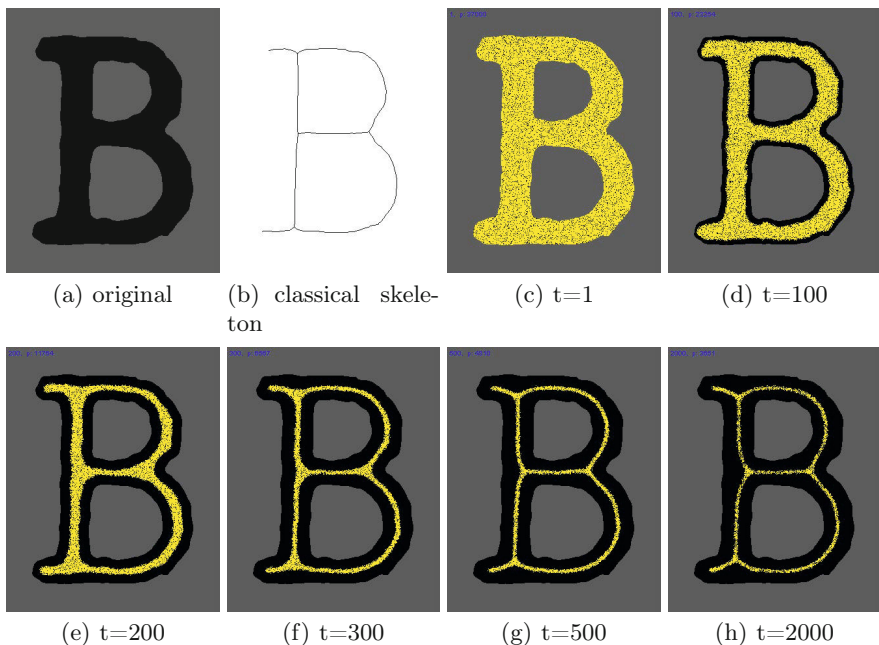


Fig. 11.12 Approximating the skeleton of a shape by shrinkage. a) original binary ‘B’ shape, b) classical skeleton computation, c) initialisation of model plasmodium inside the shape whose borders (grey) project a repulsive field, d-h) Shrinkage of model plasmodium thins the shape, approximating the skeleton.

first devised by Blum in his ‘grassfire’ approach, utilising propagating fronts (hypothetical flames in a fire) emerging from the borders of shapes. The quench points where the fronts meet correspond to the medial axis — or skeleton — of the shape [240]. Other alternative substrates have been developed which are based on the same propagation approach including chemical computers [241], crystallisation [233] and in simulation [194].

To explore skeletonisation in the model we combine the front propagation approach with the innate shape relaxation behaviour of the model. In Fig. 11.12 the model plasmodium is initialised within the confines of a letter ‘B’ shape. A repulsive is projected from outer regions of the shape (grey areas). The population size shrinks over time to form a thin network (Fig. 11.12h). Complete relaxation of the virtual plasmodium is prevented by the repellent field. Classical skeletonisation algorithms (for example, as found in the image analysis toolkit ImageJ [168]) also compute the skeleton of this shape (Fig. 11.12b) but these often generate spurious spur like branches when the initial shape is noisy or jagged.

In Fig. 11.13 the same source letter ‘B’ shape is contaminated by border defects, resulting in a ragged outline. The classical algorithm shows a large

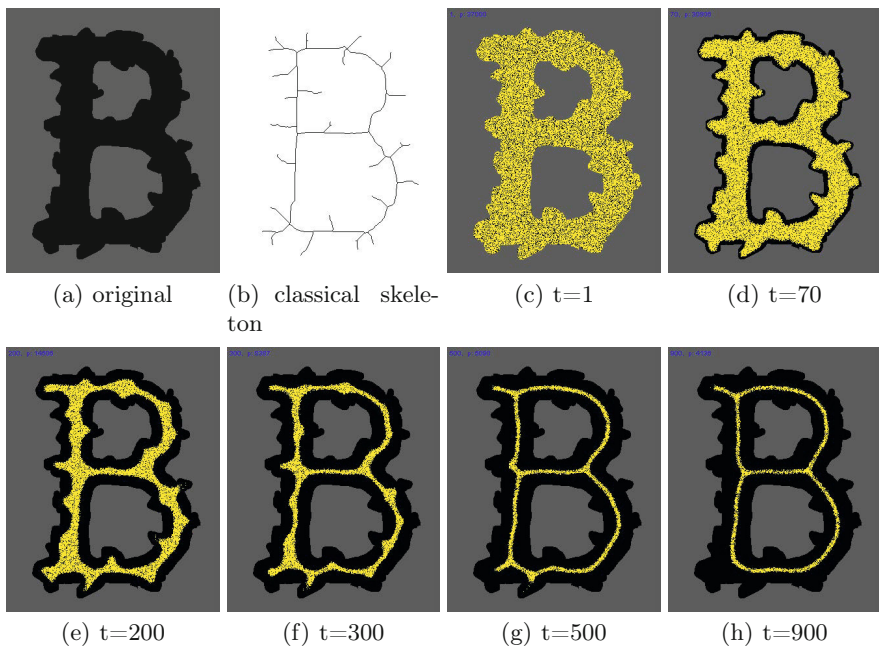


Fig. 11.13 Approximating the skeleton of a ragged shape by shrinkage. a) original binary ‘B’ shape with ragged defects, b) classical skeleton computation results in spur line artifacts, c) initialisation of model plasmodium inside the shape whose borders project a repulsive field, d-h) Shrinkage of model plasmodium thins the shape, approximating the skeleton without spurs.

number of spurs (Fig. 11.13b). The presence of spurs would necessitate a further processing of the output image to ensure their removal. When the model plasmodium is presented with this ragged shape, the defects are smoothed and eventually removed during the shrinkage process (Fig. 11.13c-h), leaving a simple thin descriptor line.

In the case of planar shapes classical skeletonisation algorithms can result in spur defects even when the original image does not contain any large defects ((Fig. 11.14a and b)). The model plasmodium shrinks inwards to generate a skeleton which does not contain spurs. Although this method generates good performance, it is not perfect. Note that the edges of the final agent ‘skeleton’ ((Fig. 11.14h)) at the lizards left feet are slightly thicker (caused by the narrowing of the stimulus shape) and the plasmodium has retracted slightly from the end point of the Lizard head. Nevertheless these results demonstrate that the propagating front method can be combined with the minimisation behaviour of the material to yield novel new approaches.

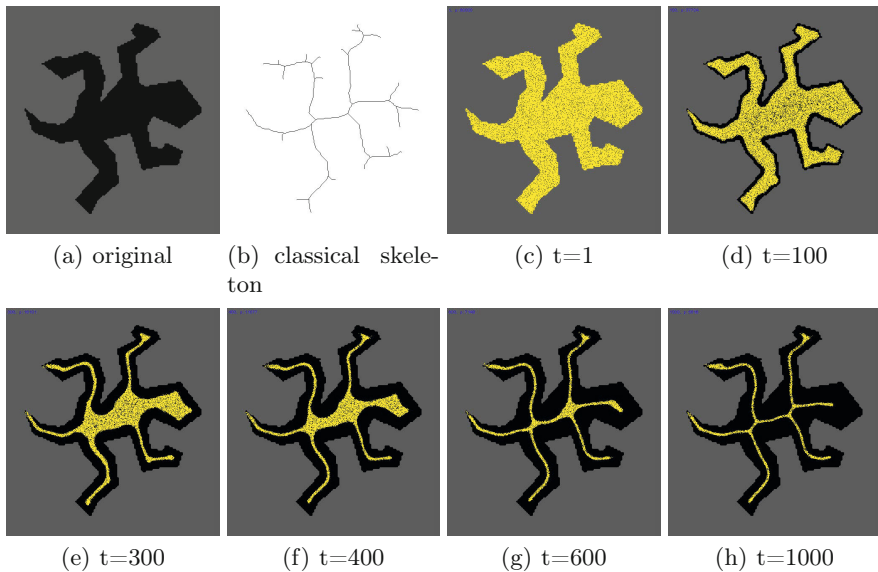


Fig. 11.14 Approximating the skeleton of a planar shape. a) original binary ‘Lizard’ shape, b) classical skeleton computation results in spur line artifacts, c) initialisation of model plasmodium inside the shape whose borders project a repulsive field, d-h) Shrinkage of model plasmodium thins the shape, approximating the Lizard skeleton without spurs.

11.10 Summary: Representing Area and Shape

The results in this Chapter demonstrate that the multi-agent approach can approximate kinaesthetically inspired approaches to problems in which a representation of shape is needed. This is not seen in the behaviour of *Physarum* itself, due to the spontaneous formation of networks. However it is possible to bias the pattern formation mechanisms of the model to generate different shrinkage behaviours. In the case of the Convex Hull we approximated the intuitive ‘band’ method but were also able to generate novel methods based on repulsion and self-organisation. The Concave Hull was approximated by shrinkage from the Convex Hull and also by growth. Growth-based approximation of the Concave Hull was initially performed by fusion of individual virtual plasmodia inoculated on point sources but this can generate disconnected shapes. By inoculating the population on the MST it was possible to grow fully connected Concave Hulls and indeed tune the evolution of the Hull concavity by adjusting a growth parameter. The combination of repulsive field propagation and material shrinkage enabled the approximation of interior skeletons of shapes without spur artifacts.

These results show that the innate behaviour of the model is suitable for spatially represented problems relating to the definition of shapes (their borders, their areas and their minimal internal descriptors). We continue to explore the potential of shape relaxation and minimisation on smoothing problems in the next chapter.

Chapter 12

Material Computation of Data Smoothing and Spline Curves

“My life is one long curve, full of turning points.”

(Attributed to Pierre Trudeau)

12.1 Computational Limitations of Slime Mould

Although *Physarum* slime mould has desirable computational properties, it also has some practical limitations. Although relatively simple and inexpensive to culture, its computation is slow, taking many hours — or even days — during which time it must be maintained within strict environmental parameters of temperature, light exposure and humidity. *Physarum* may also be relatively unpredictable in its behaviour which, although useful in wild conditions, is a hindrance when repeatability is concerned.

The protoplasmic transport networks formed by the plasmodium are not as precise as those constructed using classical approaches. The network paths meander and branch between the nutrient nodes (Fig. 12.1, a) and do not necessarily pass directly through the nodes (Fig. 12.1, b), giving an imprecise result. A growing plasmodium also produces a slime capsule surrounding the organism which anchors the plasmodium to its substrate, limiting the scope for further adaptation and minimisation of the tube network (greater network adaptation can be seen when growing the organism on a water substrate [113] but this is impractical for most purposes). *Physarum* responds to the adhesion by either spawning new tube growth from existing tubes, or abandoning unused tubes. However, the remnants of the old tubes still remain (Fig. 12.1, c), and influence future movement choices of the plasmodium [242]. The presence of imprecise network paths, old tube remnants, extraneous tubes, or tortuous tube paths, can prevent a clear result from being displayed. Finally, in classical computation, problems and their solutions may be represented symbolically. However, in *Physarum* computing the problem, and solution, must be given a direct spatial representation. Although this is not a limitation *Per*

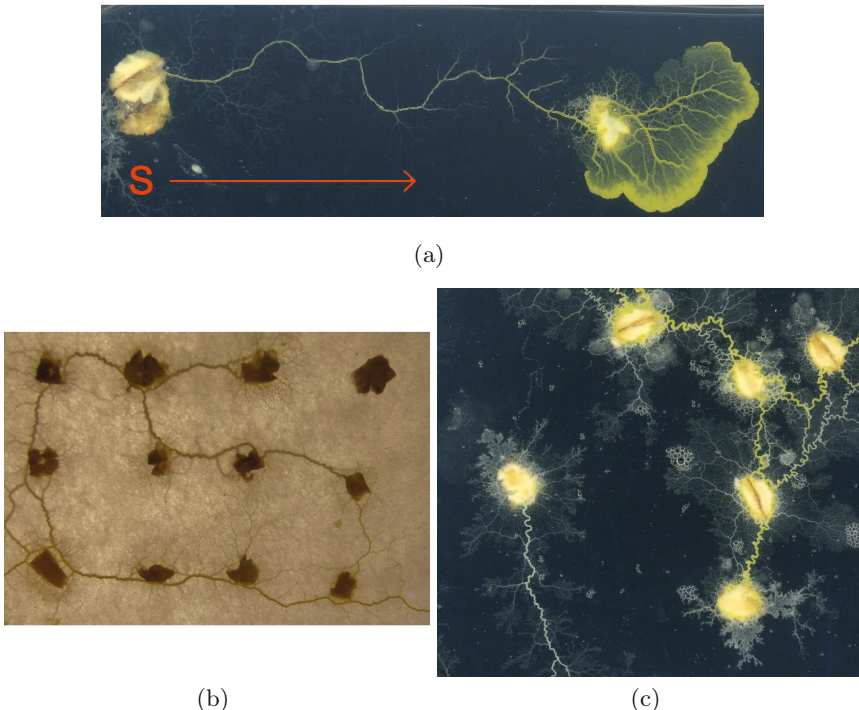


Fig. 12.1 *Physarum* tube networks networks and features which restrict computational functionality. a) *Physarum* plasmodium on plain agar inoculated on the left oat flake (S) grows towards the flake on the right, forming a protoplasmic tube connecting the nutrients, b) protoplasmic tube network connecting multiple nutrient oat flakes (damp filter paper substrate, backlit illumination), c) slime capsule and remnants of previous vacant tubes (paler paths) act to constrain network adaptation and path choice. Images from [243].

se, it does require (perhaps unfamiliar) techniques of representing problems in space to exploit the distributed and parallel computational properties of the organism.

12.2 Towards Modelling Morphological Adaptation in Slime Mould

Due to the practical and computational limitation of slime mould we require a synthetic analogue of the organism to explore possibilities of spatially represented computation. One technique available is computer modelling, where we attempt to reproduce the complex patterning of slime mould along with the complex interactions it has with its environment. However, we are not simply trying to extract the features of slime mould for classical algorithms.

Such an approach may indeed prove useful for certain tasks, but would not inform us in any way about the distributed emergent behaviour and control of the organism. Instead we wish to construct a virtual material using the same principles of slime mould. Namely, simple component parts and local interactions. The aim is to generate collective emergent behaviour utilising self-organisation to yield an embodied form of material computation which can reproduce the wide range of complex patterning and environmental responses seen in slime mould, without some of the drawbacks caused by the particular living and physical properties of the organism itself.

12.3 Overview of Morphological Adaptation Approach

In this chapter we utilise the morphological adaptation inherent in the model to explore the effect of complete adaptation of a virtual material to spatial datasets. Specifically we explore the approximation of data smoothing functions and spline curves. We use model parameter settings which ensure strong adaptation of a pre-existing network which are described in Section 12.7.3. In Section 12.4 we examine the properties of the material adaptation in response to high and low frequency data variations and give examples showing the potential to summarise simple statistical properties of data in 1D space for smoothing functions, including moving average and low pass filtering. In Section 12.5 we explore 2D datasets and approximate the formation and evolution of spline curves, including B-splines (approximating splines), both unclamped and clamped, in open and closed curves of differing curve degree. Some quasi-mechanical properties of material-based spline curves are noted in Section 12.6, along with some practical limitations of the approach. In Section 12.7 we examine the problem of approximating interpolating spline curves using the model and find that interpolating splines are not directly possible due to the presence of narrow vertex angles which cause additional nodes to form in the network. Pre-processing of the original dataset polyline was attempted to resolve this limitation. Pre-processing the original polyline into a rectilinear configuration is explored in Section 12.7.1 and a simpler method of pre-processing is described in 12.7.2 in which the polyline is transformed into a wider tube in which the virtual material is then initialised and contained. In Section 12.8 we summarise the material approach noting some of its useful properties, some limitations and suggest scope for further research and potential applications. Due to the dynamical behaviour of the material adaptation the reader is encouraged to refer to the supplementary video recordings described in the Appendix.

12.4 Data Smoothing and Filtering

Smoothing and filtering of datasets plays an important factor in all aspects of information technology and signal processing in general. The methods

can be as simple as those achieved with a small number of simple analogue electrical components to remove certain aspects of a signal. At the other extreme are complex digital algorithms to enhance certain trends within complex datasets. Can the innate morphological adaptation behaviour of the *Physarum* model be used for data smoothing applications? To test this idea we represented a 1D signal as a sequence of Y-axis data values along a time-line represented by X-axis values (Fig. 12.2a). The virtual material was patterned in this initial shape and was initially held in place by projecting attractants in the shape of the original pattern (Fig. 12.2b). We examined the effect of completely removing the attractant stimulus, and the effect of reducing the stimulus strength. When the attractant stimulus was removed the material relaxes and adapts into a profile which smooths the data, matching the moving average of the original data. The moving average is computed conventionally by a kernel computing the mean of the current data point and its left and right data points of window size $w/2$. The moving average filter has non-periodic boundary conditions and subsequently the moving average line narrows as the kernel window size increases (to prevent the window exceeding the bounds of the data). The amount of smoothing by the material deformation (i.e. corresponding to the kernel window size of the moving average) is dependent on the length of time that the material adapts for (Fig. 12.2c-h). Note that the width of the material also shrinks over time, mirroring the narrowing of the moving average line as the kernel window increases.

Instead of completely removing the original data stimuli it is possible to try and use the original stimuli to constrain the adaptation of the model. This is achieved by projecting a weaker representation of the original data stimuli. The effect of maintaining a weakened stimulus strength was subtly different to the moving average and appeared to partially filter the data. Specifically, the material tended to adhere in areas of the data that were relatively unchanging, whilst detaching from regions that underwent large changes in direction (Fig. 12.3). This behaviour corresponds to that of an iterative low-pass filtering process where high frequency signal components are removed whilst low frequency components remain. Note that by maintaining a weak stimulus, the width of the material spanning the dataset is not significantly reduced, in contrast to the material approximation of the moving average.

In both of these examples the material appears to adapt more strongly to sudden changes in stimuli. To assess this behaviour we initialised the virtual material with the pattern of sine waves and square waves of identical amplitude but different frequencies. Fig. 12.4 shows snapshots taken which indicate that relaxation occurs more strongly with high frequency changes, for example when comparing Fig. 12.4 c) and e). The presence of weak stimuli in pattern of the original configuration data appears to act as a brake on the relaxation process. The adhesion of the virtual material to attractant regions results in less curved paths (Fig. 12.4 d,f) when compared to the smoother paths when no stimulus was present (Fig. 12.4 c,e).

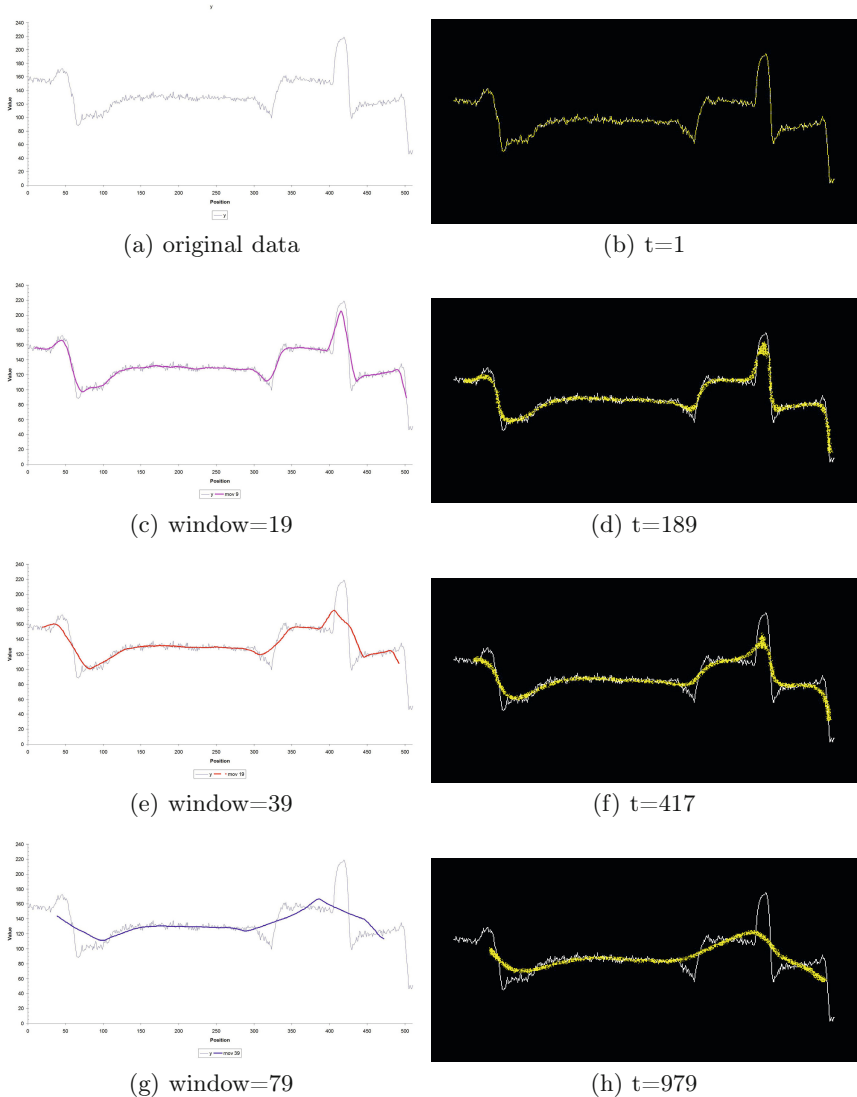


Fig. 12.2 Relaxation of virtual material approximates the moving average. (a,c,e,g) original data (thin line) and overlaid moving average filtered data (thick line) with 1D kernel of size 19, 39 and 79 respectively, (b,d,f,h) initialisation of virtual material on original data followed by snapshots at increasing time intervals.

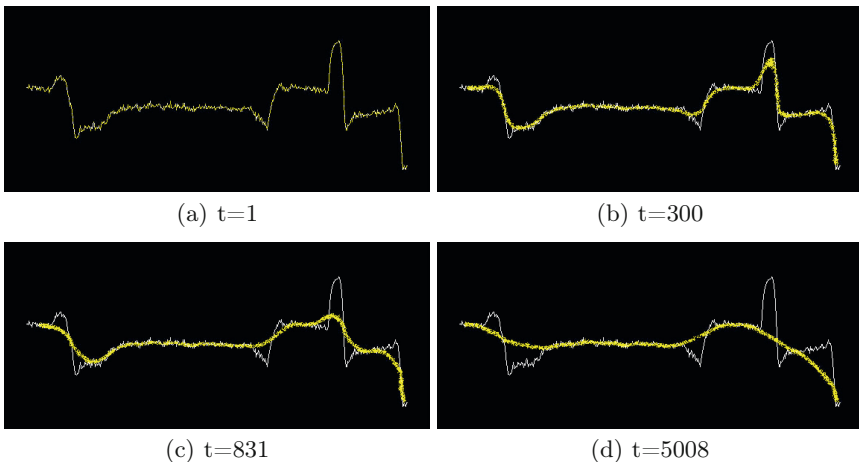


Fig. 12.3 Weak background stimulus constrains adaptation of the virtual material approximating a low pass filter. a) Initialisation of virtual material on original data weakly projected into the lattice at concentration of 0.255 units, b-d) snapshots at increasing time intervals showing removal of sharp peaks and troughs in the data.

12.5 Approximating Spline Curves by Morphological Adaptation

Splines are mathematical functions constructed piecewise from polynomial functions. Spline functions connect separate data points with a smooth continuous curvature where the individual functions join (at regions called *Óñots* [244],[245]). Spline functions are useful for curve fitting problems (*approximating splines*, where the spline smooths the path between data points) [246]. They may also be used in interpolation problems (*interpolating splines*, where the spline curve passes through all of the data points) [247]. Due to the natural curvature enabled by spline curves, and rapid development in computer aided design systems, they have proven popular in design and architecture [248]. The term spline apparently refers to the use of flexible strips formerly used in the shipbuilding and motor-vehicle industries to allow the shaping of wood and metal shapes into smooth forms by deforming them at selected points using weighted metal objects known as ducks. Thus, there is an inherent mechanical nature to the operation and interpretation of spline curves. The mechanical properties have been used as an inspiration for deformable models and templates, initiated by [249], primarily for image segmentation, and subsequently extended to 3D application [250], [251]. To assess the potential for collective and emergent material shrinkage using the model of *Physarum* we use simpler datasets in these examples.

It is known that B-splines (approximating splines) are contained within the Convex-Hull of their original polyline. For this reason it may be a good

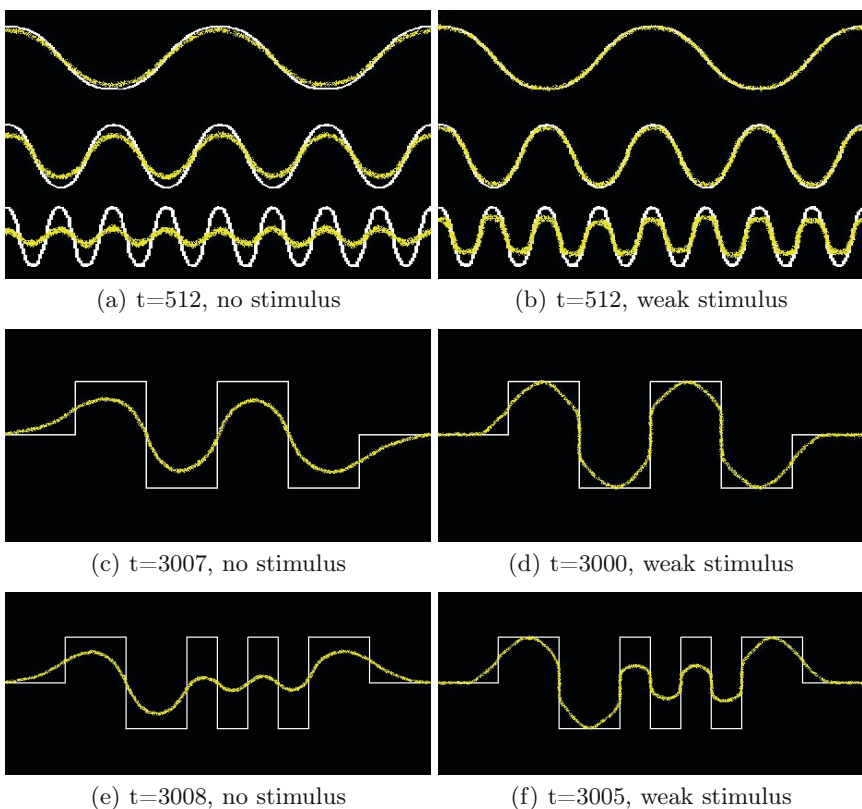


Fig. 12.4 Differences in relaxation in response to frequency changes and background pattern stimulus. a) original sine wave pattern and relaxation with no stimulus, b) original sine wave pattern and relaxation pattern with weak background stimulus, c) square wave pattern with no stimulus, d) square wave pattern with weak stimulus, e) high frequency square wave with no stimulus, f) high frequency square wave with weak stimulus.

candidate for approximation by a collective material shrinkage mechanism, since it has previously been shown (for the purposes of combinatorial optimisation) that a large blob of virtual material patterned in the shape of the Convex-Hull adapts and shrinks over time to smaller representations lying within the Convex Hull [216]. We assessed the behaviour of the material under a range of different stimuli conditions to see if it could approximate B-spline curves. In the first case an unclamped quadratic B-spline curve of different degrees is calculated by numerical methods (Fig. 12.5, a-d). The blob of virtual material was initialised in the pattern of the original polyline connecting the points. During adaptation and shrinkage of the blob without any node stimuli, the pattern approximates the unclamped B-spline. As time

progresses the blob adapts the shape of the B-spline of increasing degree (Fig. 12.5, e-h). Ultimately the blob shrinks to a small point which appears to approximate the centroid position of the original shape. Further investigation of this apparent statistical computation (computation of centroid) is the subject of current research (in preparation).

In the second case a clamped quadratic B-spline curve of different degrees is calculated by numerical methods (Fig. 12.5, i-l). The virtual material was initialised in the pattern of the original polyline connecting the points and the clamping of the material was enforced by projecting attractant at the location of the two end points. During adaptation and shrinkage of the clamped blob, the pattern approximates the clamped B-spline. As time progresses the blob adapts the shape of the B-spline of increasing degree (Fig. 12.5, m-p). Adaptation of the unclamped blob occurs more quickly than when the blob is clamped at the control points. The clamped condition shows a non-linear time course and the relationship between curve degree and relaxation time is explored in Section 12.6.2.

Relaxation of the virtual material may also approximate B-spline curves in more complex configurations, as shown in Fig. 12.6 in which a set of 20 points is used to generate a B-spline curve of degree 2 and 5. The virtual material, again initialised in the path of the original polyline, relaxes over time when most of the initial attractant stimulus is removed (except for the two end points to clamp the relaxing population). Increasing relaxation time period again corresponds to increasing degree of the original spline curve (Fig. 12.6 c,d).

Closed shapes may be represented by clamped spline curves by repeating the same start data points. For unclamped open shapes, overlapping the first and last three points generates a smooth open curve (Fig. 12.7,a). For clamped open shapes the first point is overlapped by the end point (Fig. 12.7,b). For the material approximation of open spline curves the material is simply patterned with the closed polyline (Fig. 12.7,c) and if a clamping point is required this is represented by attractant projection at the desired clamping site (Fig. 12.7,d).

12.6 Properties and Limitations of Material-Based Spline Curves

12.6.1 Quasi-Mechanical Properties

Two unusual properties of the material adaptation approach to spline curves are of note, both relating to the innate mechanical nature of the material adaptation. The first of these effects can be seen by comparing material curves with the classical quadratic B-spline curves of differing degrees. These spline curves retain the proximity of the knots to their respective polylines used in their generation (Fig. 12.8). The curve formed by the particle population on a similar configuration, however, has no explicit representation of knots as the

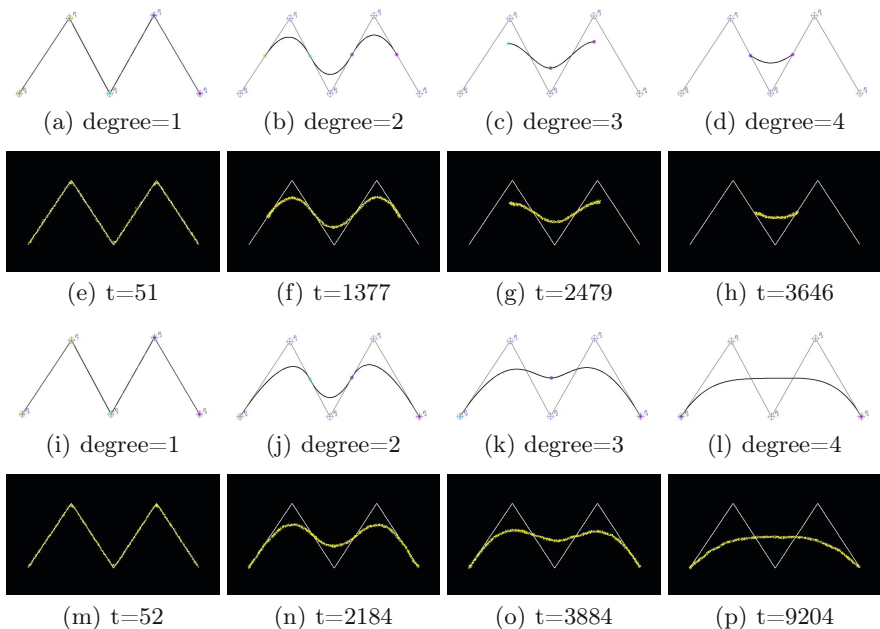


Fig. 12.5 Approximation of B-spline by material adaptation on ‘M’ shape configuration. Each experiment summarised on a single row. a) unclamped B-spline (5 points connected by polyline) of degree 1, (b-d) same configuration B-splines of degrees 2, 3 and 4 respectively, (e-h) evolution of material adaptation approximates the unclamped B-spline of different degrees, i) clamped B-spline of degree 1 (same configuration as above with start and end points clamped), (j-l) clamped B-spline of degree 2, 3 and 4 respectively, (m-p) evolution of material adaptation approximates the clamped B-spline of different degrees, material is clamped by attractants at end points.

emergent curvature is an emergent property of the particle interactions. The pattern of the material is thus not constrained by the original configuration pattern, except for the start and end points which are clamped by attractant projection. The spiral curve not only becomes more rounded (Fig. 12.9, d), but the adaptation and shrinkage proceeds to completely ‘unwind’ the spiral shape, until a single line connects the start and end points (Fig. 12.9, i).

The second property relates to the behaviour of the material curve in response to a weak background stimulus, patterned in the shape of the original polyline. Curvature is still dependent on relaxation time but the weak attraction constrains the evolution of the material curve, preferentially detaching from regions with sharp angular changes, whilst remaining attached to longer lines and lines connected by only small changes in angle (This phenomenon can be seen in Fig. 12.10, and its related online supplementary recording

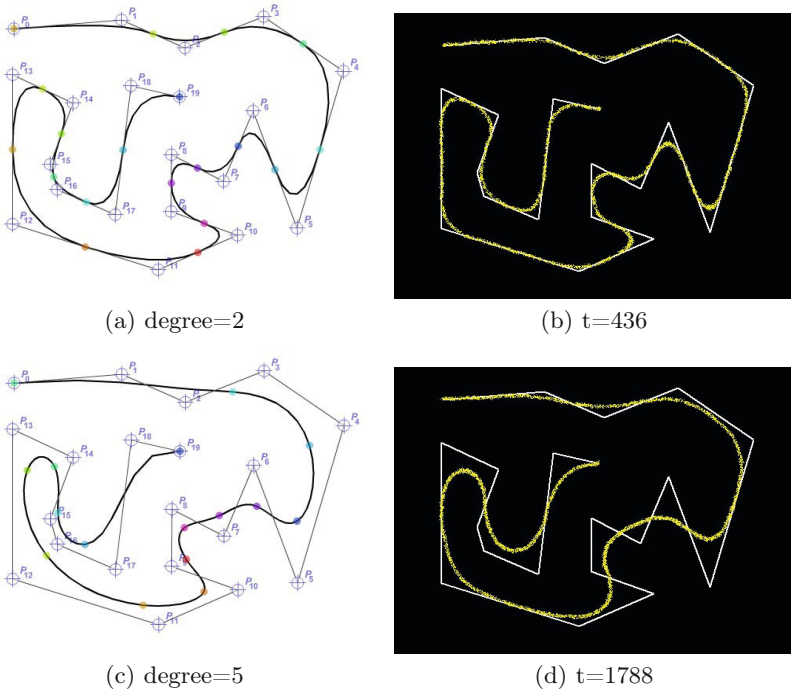


Fig. 12.6 Clamped B-spline of complex shape and approximation by virtual material. Left: B-spline at differing degrees, composed of 20 points, clamped at start and end points. Points shown as labelled hollow circles connected by faint lines, knots shown as solid circles on thicker spline curve. Right: Approximation of spline curve by relaxation of virtual material, clamped at start and end points.

“Fig. 12.10: Preferential adhesion to straight paths”). The material appears to slowly ‘peel away’ from the corner regions whilst adhering to straight edges.

12.6.2 Computational Properties and Limitations

Comparing the performance of the material computation by the model to classical methods of computing spline curves is somewhat difficult. Classical computation time of spline curves is mainly determined by the number of data points, and thus the number of basis functions to form the curve between the points (see [248] for more details). Computation time in the model (due to the spatial implementation of diffusion within the lattice) is mainly influenced by the area of the lattice containing the original polyline. The number of points does not impact upon the computation time since the entire band of ‘material’ is considered, instead of discrete points along the polyline. The curve degree does, however, impact the computation time, since degree in the model is

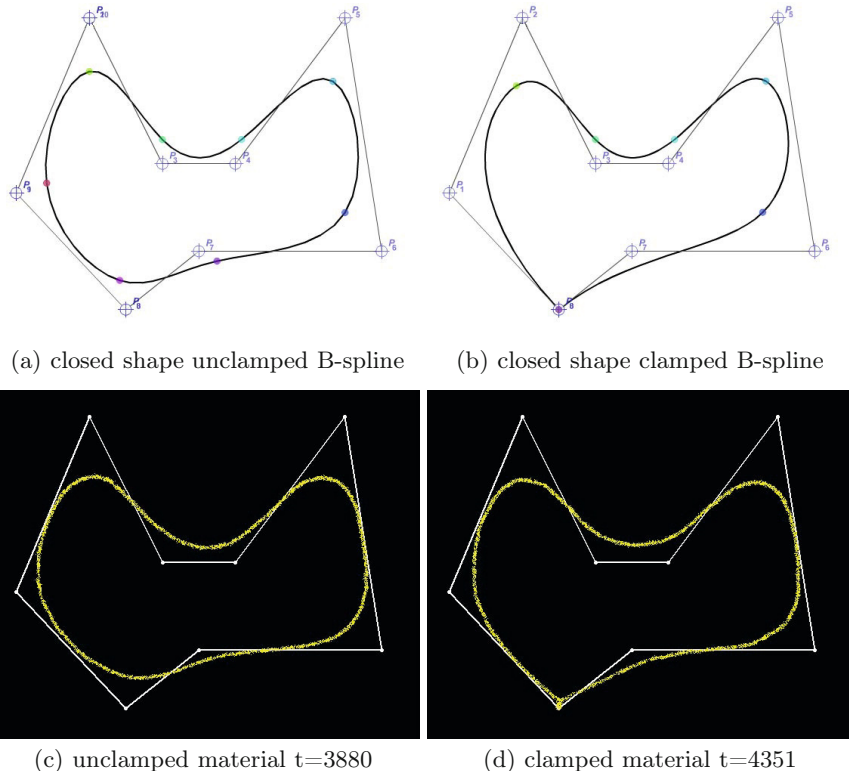


Fig. 12.7 Approximation of B-spline curves in closed cyclic shapes. a) closed shape with no clamping points, b) closed shape clamped at point 8, c) material approximation of unclamped shape, d) material approximation of clamped shape by projecting attractant at data point 8.

related to relaxation time. Fig. 12.11 shows the relationship between material relaxation and time for a simple triangular shape. The chart plots the distance of the material from the baseline where the material is clamped at each end (Fig. 12.11, inset images). The circled points in the chart correspond to times when the configuration of the material matches increasing degrees of the approximated spline curve. Note that the time course becomes increasingly non-linear as relaxation progresses. However, for practical approximation of spline curves, the adaptation occurs well before (< 5000 steps) complete material relaxation is required.

A limitation to the approach is that, due to its direct spatial implementation (as opposed to the abstract mathematical representation traditionally used), the material cannot approximate curves with crossing data. In Fig. 12.12 we show the example of a B-spline curve where the polyline used to

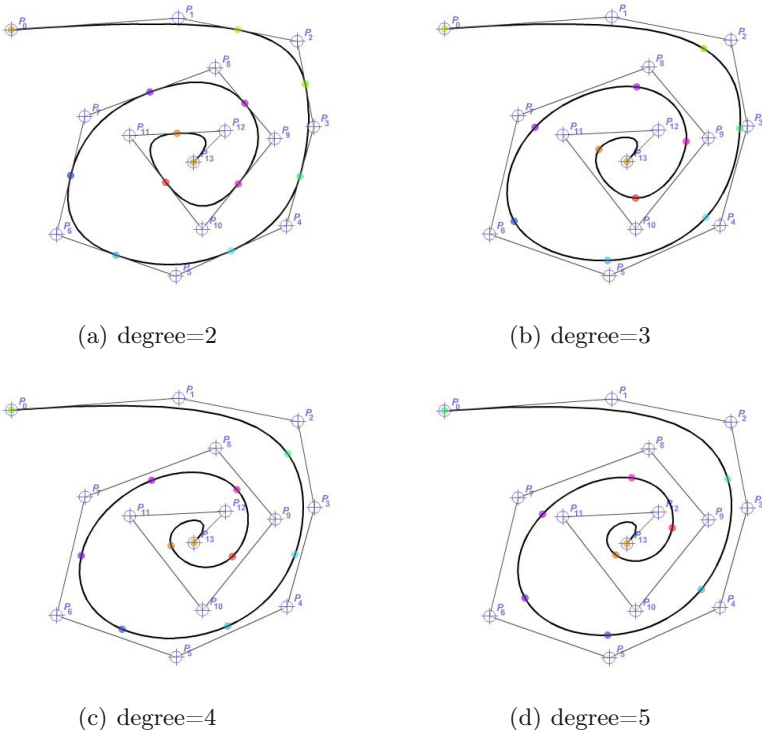


Fig. 12.8 Clamped B-spline of differing degrees, composed of 14 points, clamped at start and end points. Points shown as labelled hollow circles connected by faint lines, knots shown as solid circles on thicker spline curve.

generate the curve crosses its own path (Fig. 12.12,a), which results in spline curves with crossings (curves of different degree are shown in Fig. 12.12,b-e). When the virtual material is initialised on the same polyline (Fig. 12.12,f) the resulting material evolution shows an elongation of the crossing point, splitting the curve into separate regions which relax separately before later merging again. As can be seen from Fig. 12.12,g-j this poorly approximates spline curves of increasing degree. This limitation, however, would not apply to 1D temporal datasets (where it is not possible to ‘loop backwards’ to previous data) and may not be commonly encountered in 3D datasets (for example for applications of 3D image surface smoothing). This extension of the 2D agent model to a 3D habitat is a logical extension and the subject of ongoing research. Preliminary results suggest that the minimisation and relaxation seen in 2D data also occurs in 3D surfaces.

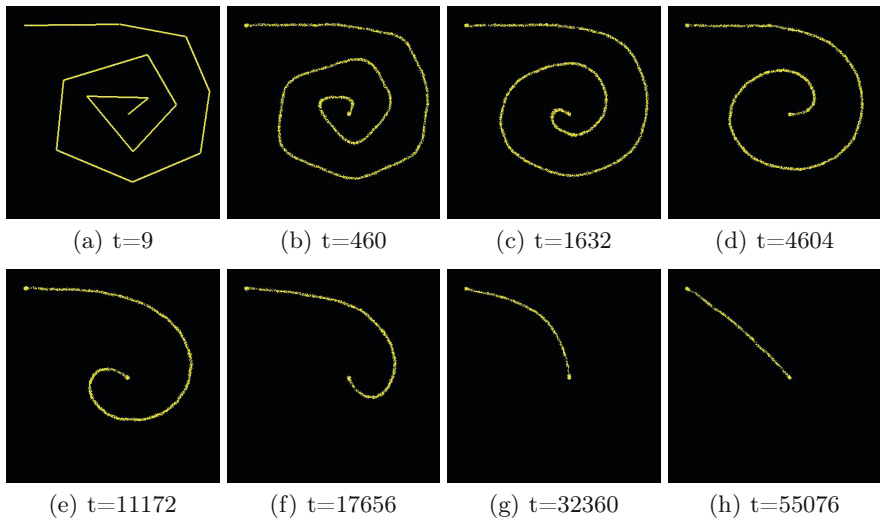


Fig. 12.9 Formation and mechanical evolution of virtual material on spiral configuration. a) material patterned in the original configuration before adaptation, (b-h) evolution of material adaptation clamped at the start and end points by attractant projection.

12.7 Interpolating Spline Curves

Interpolating splines are curves which pass through each data point in the curve. The virtual material method cannot directly approximate interpolating splines when the data points act as attractant projection sites (Fig. 12.13, a-c, data stimuli indicated at red dots). This is due to the innate minimising behaviour of the virtual material. When the material forms an acute angle where two edges meet (for example the tops of the ‘M’ shape, Fig. 12.13, a), the material forms additional points, Steiner nodes, at the vertices where the edges meet (Fig. 12.13, b). These points move as the material continues to adapt, eventually approximating the Steiner tree (Fig. 12.13, c), the network connecting all the points which has the minimum distance. Although this is a useful construct for other applications, it is not desirable for the task of approximating spline curves.

12.7.1 *Interpolating Splines via Rectilinear Pre-processing*

Steiner points only form when the vertex angle is below a certain threshold. This suggests that if the initial stimuli graph could be transformed to give non-acute angles it may be possible for the material to relax and form a curve that

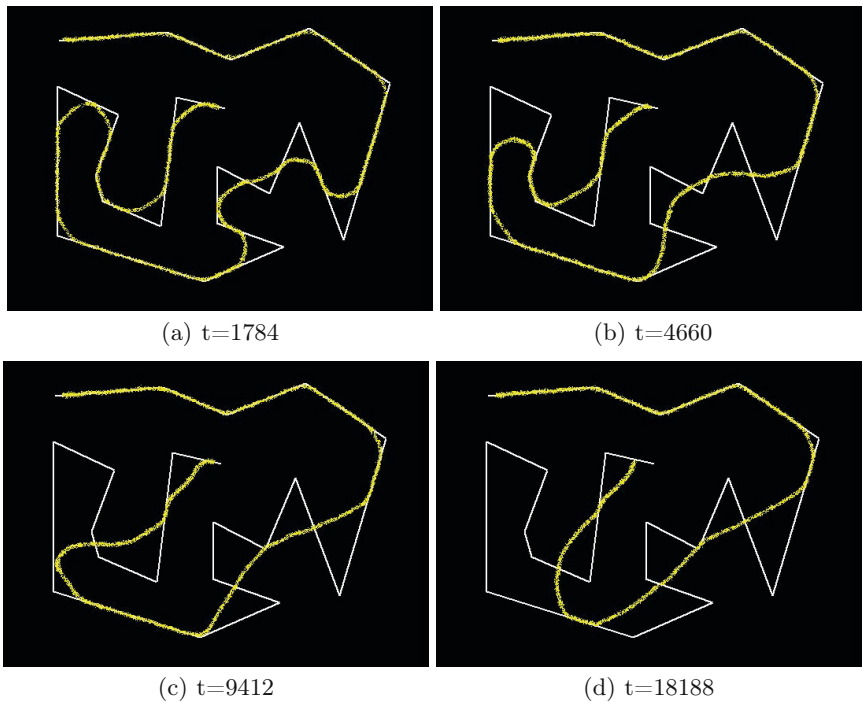


Fig. 12.10 Constraining the material spline via adhesion to weak attractant. A weak attractant signal is projected in the pattern of the white polyline, constraining the evolution of the virtual material. Relaxation constrained by longer lines with shallow angles and more pronounced at short lines and large changes in angle. The material appears to ‘peel away’ from the original polyline, predominantly at angular regions.

passes through all the data points. In Fig. 12.13, e the initial edges are transformed into rectilinear paths that pass through the nodes. This is achieved via a simple step function where each step occurs midway between the current node and the next node. This ensures that Steiner points will not (initially, at least) be formed at vertices where edges meet. Note that the position of the nodes is not changed at all. When the material is initialised on this rectilinear path and the path stimuli subsequently removed (leaving only the original nodes as stimuli), the material relaxes to approximate an interpolating spline curve. It is important to note, however, that eventually the material will relax to a configuration where the angle at the vertex is sufficiently acute to allow Steiner points to form. Thus, the interpolating spline curve is a transient state in the configuration of the material. Another limitation with the pre-processing approach is the calculation of the rectilinear paths through the nodes. This is trivial to achieve with a 1D dataset (which simplifies the position and direction of the step) but more difficult with 2D datasets.

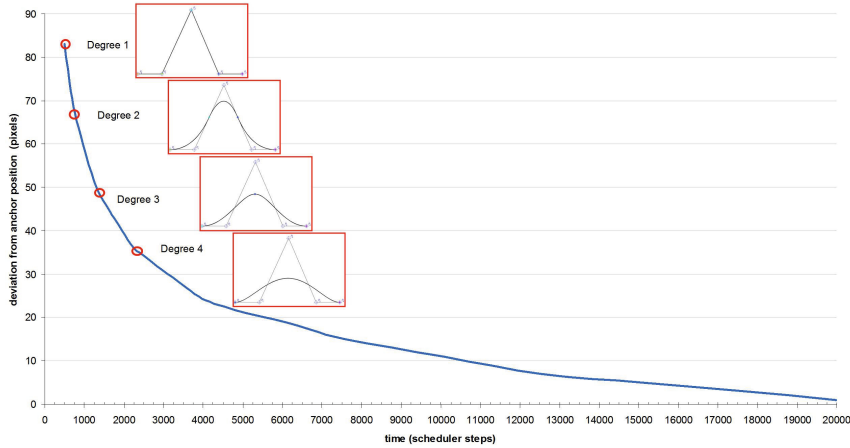


Fig. 12.11 Relationship between virtual material relaxation time and spline curve degree. Chart shows deviation distance of virtual material from the top of a triangle to its base as it relaxes over time (material is clamped at the two end points). Equivalent degree of B-spline curve is indicated by circle positions and inset figures.

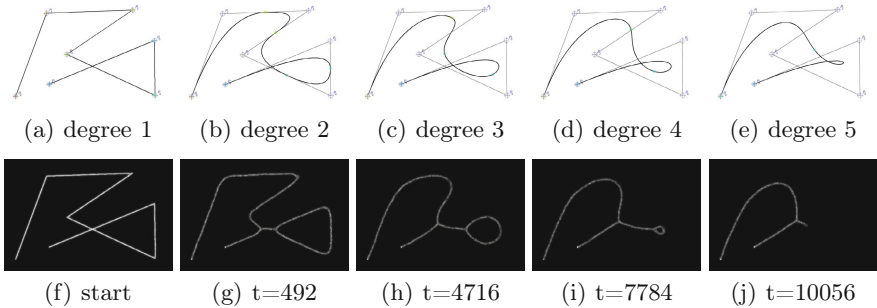


Fig. 12.12 Material approximation of spline curves is confused by crossing paths. a) original data points and polyline showing crossed paths, b-e) B-spline curves of increasing degree, f) material initialised on original polyline with crossed path, f) separation of loop and curve where paths crossed, h-j) closure of loop and shrinkage of the material poorly approximates spline curves of increasing degree.

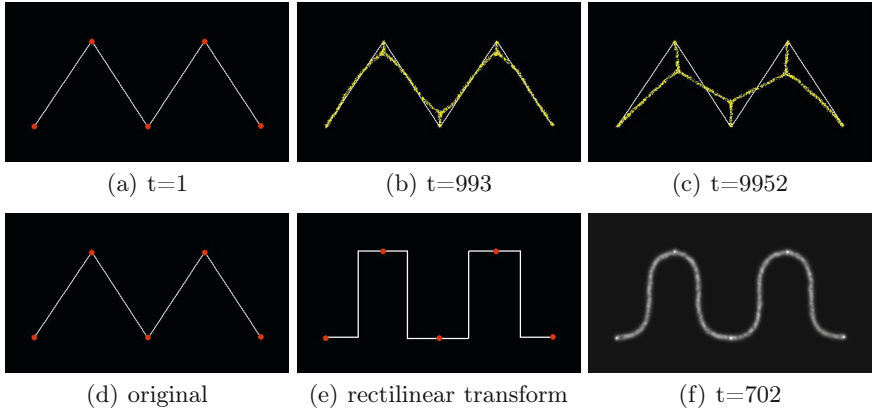


Fig. 12.13 Approximation of interpolating splines by pre-processing the initial configuration stimuli. a) initial M shape stimuli showing source node projection sites (red dots) connected by lines, b) interpolating splines cannot be directly approximated because Steiner points form at the vertices where edges meet, c) the material continues to relax, approximating the Steiner tree, d) original configuration, e) pre-processing of (d) using a simple step function to give rectilinear path through original nodes, f) relaxation of material initialised on rectilinear path approximates an interpolating spline curve.

12.7.2 Interpolating Splines via Interior Containment

The challenge for interpolating splines using a material approach is to allow the material to relax and adapt its shape whilst still forcing the material to pass through the required data points. This can be achieved by initialising the material *inside* the polyline connecting the data points and relaxing within the confines of this shape. The shape is then analogous to a wide pipe containing the material which is anchored at each end. This pipe may be generated from the original polyline by a very simple dilation morphological processing operator to make the polyline thicker (Fig. 12.14, a and b) and the original data points are represented by the apices of the pipe. The material is initialised within this pipe and anchored at each end point by attractant projection (Fig. 12.14, c). The material relaxes and shrinks, forming a shorter and smoother path between the two end points and interpolating between the remaining data points (Fig. 12.14, d).

12.7.3 Model Parameters and Problem Data Representation

The spatially implemented computation requires that the data configuration be contained within the 2D lattice containing the particle population. Data configurations are loaded as greyscale image files and this data is interpreted by the scheduler and projected into the diffusive lattice as a virtual chemoattractant to attract the particle population. For 1D data smoothing the Y-axis represents the actual data values and the X-axis represents the time series. Comparison data smoothing curves (moving average and low-pass filter) were numerically generated using manual construction of filter kernels of increasing width using Microsoft Excel.

For 2D curve approximation B-spline curves and interpolating spline curves were generated using the interactive software method by Foretník [252], allowing the user to specify points. The software then generated the respective

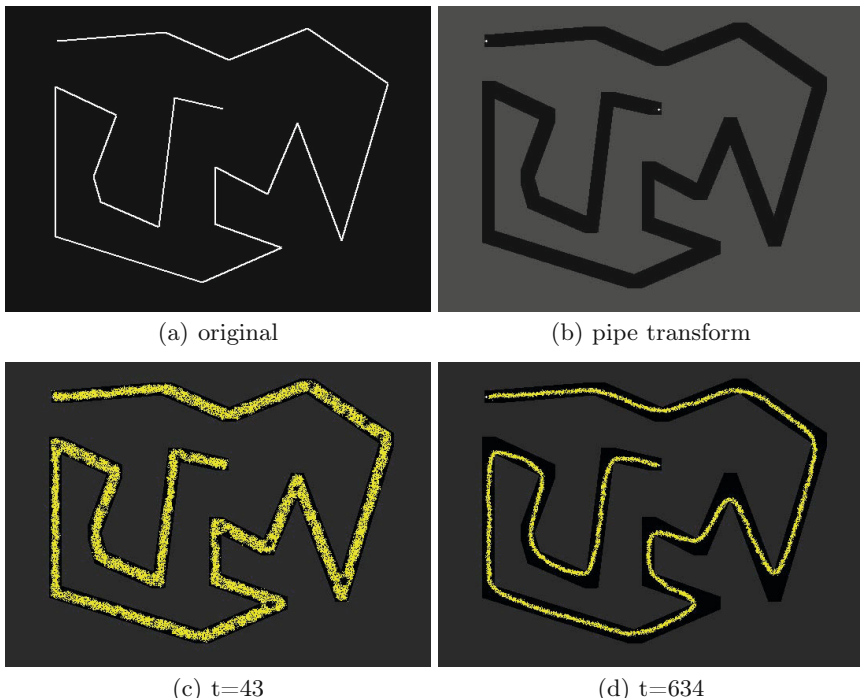


Fig. 12.14 Approximating interpolating splines by interior containment. a) Original polyline connecting data points, b) expansion of original line into wide pipe by simple dilation morphological operator, c) initialisation of material into pipe, d) relaxation, adaptation and shrinkage to form interpolating spline within the confining pipe.

polylines and curves with specifiable degree and clamping options. For the material approximation the polylines connecting the data points were projected into the lattice at a value of 2.55 units per data pixel. This projection causes the particle population to be attracted to the data configuration, initially preventing adaptation of the population. The particle population was initialised on the 1D data line or 2D polyline respectively and particle movement was halted for short time (20 scheduler steps) to allow attraction to the initial data stimuli. To initiate complete relaxation the source data was removed from the lattice and any clamping points represented by projection of discrete data points at 2.55 units per pixel. To initiate partial relaxation due to weakened attractant stimuli the data projection was weakened to 0.255 units per data pixel, allowing relaxation, but constraining the relaxation along straighter paths. Variations in both *SA* and *RA* parameters have been shown to generate a wide range of reaction-diffusion patterns (see Fig. 3.13) and for these particular experiments we used *SA* 90° and *RA* 45° which results in stronger and more rapid adaptation of the virtual material.

12.7.4 Material Shrinkage Mechanism

Relaxation and adaptation of the virtual material is implemented via tests executed at regular intervals as follows. If there are 1 to 10 particles in a 9×9 neighbourhood of a particle, and the particle has moved forwards successfully, the particle attempts to divide into two if there is a space available at a randomly selected empty location in the immediate 3×3 neighbourhood surrounding the particle. If there are 0 to 24 particles in a 5×5 neighbourhood of a particle the particle survives, otherwise it is deleted. Deletion of a particle leaves a vacant space at this location which is filled by nearby particles, causing the collective to shrink slightly. As the process continues the material shrinks and adapts its morphology to the stimuli provided by the polyline or clamping points. If no external stimuli are present the material will eventually adapt to a minimal circular shape and shrink down to a small cluster of points in size. The frequency at which the growth and shrinkage of the population is executed determines a turnover rate for the particles. The frequency of testing for particle division and particle removal was every 2 scheduler steps. This relatively high frequency (compared to other applications using the virtual material approach, e.g. [216]) is due to the strong shrinkage invoked by the particular *SA/RA* combination used, necessitating a high adaptation frequency to maintain connectivity of the band of material as it adapts and shrinks.

12.8 Summary: Exploiting Material Relaxation Phenomena for Data Smoothing

True slime mould *Physarum polycephalum* is known to approximate complex spatially represented computation despite it lacking any organised nervous system. The distributed nature of its computation suggests practical applications for self-organised computing collectives. In this article we consider some limitations to spatially implemented unconventional computing by morphological adaptation in slime mould *Physarum polycephalum*, specifically those caused by its adhesion to its substrate. We used a previous particle model of *Physarum* which exhibits deformable network adaptation to try answer the question of ‘what would happen if such adhesion was not an obstacle to adaptation?’ The results suggest that distributed computation by simple entities may be useful for data smoothing and image processing applications.

By patterning 1D datasets as variations in the Y-axis along a time path represented by X-axis positions we initialised the particle model along example datasets. The datasets were presented to the model as projected nutrient ‘chemoattractant’ and we then examined the material evolution under different stimuli conditions. We found that the material approximated the moving average when the stimulus was completely removed and the low-pass filter when stimuli was partially removed.

By directly patterning the shape of 2D datasets (data points connected by polylines) into the model lattice we found that the adaptation of the material approximated spline curves under clamped and unclamped conditions. The degree parameter of spline curves corresponded to the time evolution of the material. B-splines (a type of approximating spline curve) were reproduced by removal or weakening of the original stimulus polyline. Interpolating splines (curves which pass through the data points) were found to be a more difficult problem due to the tendency of the model to form Steiner points at the vertices where acute edges met. Pre-processing of the original dataset was necessary and approximation by internal confinement was the simpler of the two approaches considered. The emergent mechanical properties of the model resulted in some unusual additional features (a mechanical ‘unwinding’ of the curve to its control points, and a preferential adhesion to longer, straighter paths under weak stimuli).

It should be acknowledged that there are already many methods in signal processing which are either inspired by (or directly model by numerical methods) physical processes, including anisotropic diffusion [253], deformable templates [249], and — of course — spline curves themselves. The specific contribution of the approach outlined in this article is that the quasi-physical properties of the virtual material (relaxation, adaptation and shape minimisation) emerge from the very simple particle interactions and the adaptation properties are — as with real slime mould — distributed within the ‘material’ itself. The material behaviour can be influenced by very simple point

attractant stimuli (e.g. clamping points) and edge attractant stimuli (adhesion edges). The method may thus be seen as a minimal complexity example of physically inspired data processing.

There is also possible scope for influence by repellent stimuli: in [236] repellent stimuli have been used to deform Voronoi cell boundaries to generate hybrid Voronoi diagram constructs in which the innate contractile nature of the minimising networks were constrained by the diffusion gradient emanating from the repellent stimuli. This suggests possible future methods of dynamic control of smoothing functions. However, the flip side of distributed control is that previously simply specifiable parameters may be transformed into a more nebulous method of control. A good example is the degree of B-spline curvature which is dependent on the amount of relaxation time of the model. Although this is intuitively simple to understand (material left to relax for a longer time will relax to a greater degree) it may be less easy to directly relate (in terms of simple parameters) curvature to relaxation time.

To conclude we have shown that, by considering particular physical limitations of adaptation in slime mould *Physarum polycephalum*, we can explore speculative ‘what if?’ questions by utilising a particle model of *Physarum* that shares properties of having simple component parts, local interactions and distributed emergent behaviour. Using this model we spatially approximated complex data smoothing and spline curve functions by means of morphological adaptation. This generates both a baseline minimal specification for computation via physical processes and also expands the computational repertoire of unconventional computing devices. Further work could be carried out towards extending the approach into robust deformable template models (for example with contour completion and size adaptation), 3D surface smoothing functions and examining the potential of the approach for related data analysis, combinatorial optimisation and constraint satisfaction problems.

Chapter 13

Tracking Statistical Properties and Changing Data via Morphological Adaptation

“Things change, people change, hairstyles change, interest rates fluctuate.”

(Hillary Flammond, 1984)

13.1 Sclerotinisation as an Inspiration for Centroid Computation

The sclerotium stage is a part of the life cycle of *Physarum*, whose entry is provoked by adverse environmental conditions, particularly by a gradual reduction in humidity. In prolonged dry conditions the mass of plasmodium aggregates together, abandoning its protoplasmic tube network to form a compact, typically circular or elliptical, toughened mass [254]. Sclerotinisation protects the organism from environmental damage and the slime mould can survive for many months — or even years — in this dormant stage, re-entering the plasmodium stage when moist conditions return. Biologically, the sclerotium stage may be interpreted as a primitive survival strategy and it has been interpreted computationally as a biological equivalent of freezing or halting a computation [96] in spatially represented biological computing schemes.

Does the position of the sclerotium in *Physarum* exhibit any regular properties? And, if so, can the phenomenon of sclerotinisation in *Physarum* serve as an inspiration for a mechanism of geometric material computation? In this chapter we continue to explore the computing properties of relatively large aggregate blobs of the multi-agent collectives by examining whether it is possible to extract global statistical properties of datasets via indirect means using only local interactions within the multi-agent population. In section 13.1 we take the phenomenon of sclerotium formation in *Physarum* as an inspiration to develop a spatially represented unconventional computing mechanism based upon material cohesion, shrinkage and adaptation. Using this mechanism we extract geometric properties, specifically the centroid, of 2D datasets

via shrinkage and adaptation of the agent population. In Section 13.2 we examine the performance of the shrinkage method on spatial arrangements of 1D numerical datasets in extracting the arithmetic mean. The ability of the collective to cope with dynamically changing stimuli is assessed in Section 13.3 in which we attempt to use the blob to track the position of a simulated mobile target in the presence of noise-free and noise-contaminated stimuli, and using different stimulus types. The mechanisms of cohesion, shrinkage and shape adaptation by which the material computation is performed is described in Section 13.4, including some limitations and drawbacks of the approach. We conclude in Section 13.5 by examining the properties that enable these bulk collectives to extract global information and suggest further potential applications in statistics and robotics. Due to the dynamical nature of the material adaptation the reader is encouraged to refer to the supplementary video recordings described in the Appendix. A description of the model parameters for these experiments is given in Section 13.4.1.

To assess sclerotium position a set of oat flakes was patterned in the location of 23 most populous cities of the Iberian peninsula and inoculated the plasmodium in the Madrid region (Fig. 13.1a). The plasmodium colonised all the oat flakes within 58 hours and sclerotium formation was then initiated by gradual desiccation. An example of a sclerotium is shown in Fig. 13.1b. The positions of sclerotium formation over 20 experiments are superimposed in Fig. 13.1h. The sclerotia adopt a variety of different area coverage patterns in approximately circular or elliptical shapes [255]. Dense areas, representing more frequent sclerotium positions, can be seen in the Madrid region (occurring in 50% of experiments) and also in more southerly regions in 80% of experiments (Fig. 13.1h). These patterns, although *suggestive* of some regularity in aggregation, obviously show too much variability to claim that the plasmodium approximates any computation in the formation of the sclerotium position. Possible reasons why regular sclerotium position was not formed include the variations in the current active zone of the plasmodium immediately before sclerotinisation, variations in protoplasmic transport, and the layout of the tube network and slime capsule before sclerotium formation (*Physarum* has recently been shown to be sensitive to its previous locations, as recorded by its slime capsule [242]). It is also not fully understood how environmental factors affect sclerotium formation. Do influences such as the drying agar substrate influence the plasmodium? For example, if outer regions of the agar dry more quickly and harden before inner regions, the differences in substrate hardness may influence plasmodium movement [124].

The above factors, coupled with the innate network formation behaviour of the organism, render it infeasible to uniformly shrink the organism under controllable conditions. The process of sclerotium formation must therefore be interpreted as an inspiration for spatially represented computational mechanisms, rather than as a computation in itself. To investigate computation by shrinkage and aggregation mechanisms we use the particle model which can uniformly respond and adapt to changes in synthetically imposed

environmental conditions. We must approximate the environmental conditions which provoke sclerotium formation. We do this by simulating the removal of all stimuli, thus allowing the virtual plasmodium to adapt and shrink in time. The coarse results presented in Fig. 13.1h suggest that the plasmodium may approximate the centroid of the distribution of nutrients. The geometric centroid is a weighted mean of all the X and Y co-ordinates of a shape. For a two-dimensional shape with uniform thickness the centroid can be considered as the centre of mass of the shape and, for certain complex shapes, the centre of mass may lie outside the shape itself. Can the virtual plasmodium shed any light on any computation — or otherwise — by the *Physarum* plasmodium?

As an initial assessment we patterned the virtual material into the entire shape of the Iberian peninsula Fig. 13.1i (the white area represents the initial pattern of the blob of virtual material). The coverage of the entire shape simulates a completely uniform transport network and eliminates any bias by a pre-selected network configuration. The blob is held in place for a short period (50 scheduler steps) by projecting attractant in the original pattern, before all attractant is removed. The blob then adapts its shape, using its innate relaxation behaviour to adopt a minimal circular shape. The blob is reduced in size by randomly removing particles from the mass ($p = 0.0005$ removal, per particle, per scheduler step) and the initial shape of the collective adapts and shrinks to a small mass (Fig. 13.1c-g) mimicking sclerotium formation. The final centre position of the blob was recorded over ten runs and is shown in Fig. 13.1i as an aggregation of blue dots, compared to the exact centroid position indicated by the red cross. Surprisingly, despite the stochastic influences on the model, the mean absolute error in position of the blob ‘sclerotium’ compared to the exact centroid position was only 3.39 pixels with a standard deviation of 1.35. Although it must be emphasised that the shrinkage and adaptation of the virtual blob is a very simple approximation of sclerotium formation this does suggest, in a wider computational sense, that the physical adaptation over time (via shape minimisation and shrinkage) may abstract some computationally (and perhaps biologically...) useful information about the original configuration. These preliminary results led us to further investigate methods and results in the approximation of statistical properties of complex datasets by morphological adaptation.

To assess different morphological adaptation methods and to see how well the adaptation approximates the centroid we initiated a large mass of virtual material in the pattern of a number of shapes. The shapes selected have different properties, such as solid, containing holes, concave, and convex. The material was held in the initial pattern by projecting attractants into the lattice corresponding to the original pattern for 50 scheduler steps. The centroid of each of the original patterns was computed conventionally by the mean value of all points within the pattern (for example Fig. 13.2a, circled). Since the particle population was initially configured as the original pattern the centroid of the population obviously initially matched the centroid of

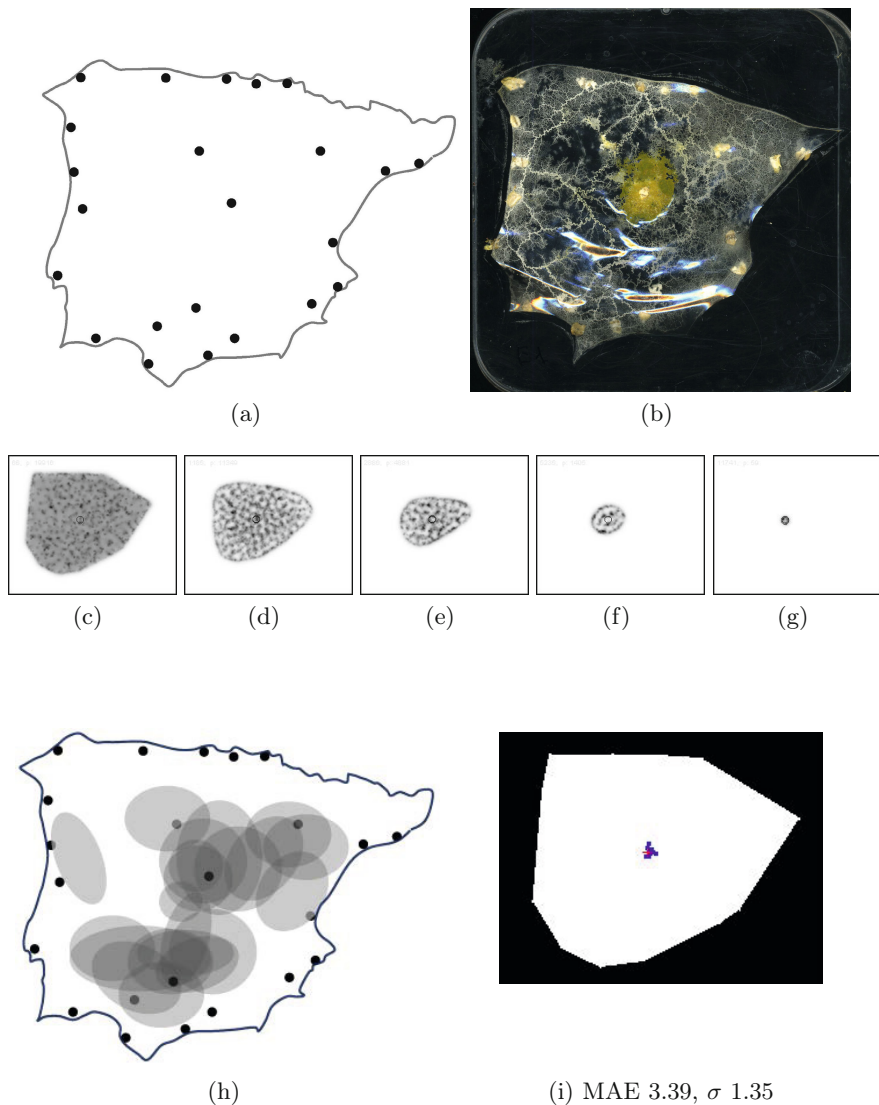


Fig. 13.1 Sclerotinisation as an approximation of the computation of centroid. a) Distribution of 23 most populous cities on the mainland Iberian peninsula, b) example showing sclerotinisation of *Physarum* and remnants of protoplasmic tubes, c-g) a shrinking blob of virtual material initialised in the Convex Hull of the cities approximates the centroid as it shrinks, h) overlay of final sclerotium positions over 20 separate experiments, i) virtual blob inoculated on the Convex Hull of the Iberian dataset showing actual centroid (red cross) and superimposed final blob position (blue squares). Images from [255] and [256]

the original. The attractant stimuli was then completely removed from the lattice and the material underwent morphological adaptation via its emergent relaxation behaviour. Two morphological adaptation mechanisms were investigated. In the first method shape adaptation was separate from shrinkage and the blob was allowed to adapt its shape whilst retaining the same number of particles. Shrinkage was delayed for 5000 scheduler steps and only shape adaptation was initially used. After the material has recovered an approximately circular shape (at 5000 scheduler steps) the population was then reduced in size by randomly removing particles from the blob (at probability $p = 0.0005$). As particles were removed the blob automatically shrunk in size, the shrinkage of the blob allowing a visual result of the centroid position (Fig. 13.2a-f). In the second method the shrinkage was implemented immediately after the stimulus was removed and occurred simultaneously with the shape adaptation (Fig. 13.2g-l). During both methods the centroid of the virtual material is computed conventionally by averaging the co-ordinates of all particles within the blob and compared to the centroid of the original pattern and the experiments were halted when the population size became < 50 . The Euclidean distance between the original centroid and blob centroid (the mean absolute error, MAE) over ten runs is shown in the graphs for delayed shrinkage (Fig. 13.2m) and immediate shrinkage (Fig. 13.2n) respectively.

The results for the lizard shape indicate that as the material adapts to the removal of stimuli and the shrinkage process, it is able to approximate and maintain the same centroid position as the original shape to within - on average - two pixels accuracy. For the delayed method (MAE 3.39, σ 1.52), the centroid is tracked most accurately during the initial adaptation phase (< 5000 steps) and the error then increases slightly during the shrinkage process (Fig. 13.2m). The error increases towards the end of the shrinkage process (> 12000 steps) because the reduced number of particles in the blob allows random perturbations within the collective to be amplified. For the immediate shrinkage method the error accumulates more quickly then stabilises after 6000 steps (MAE 2.09, σ 1.36).

Results for the variety of shapes using the immediate shrinkage method are shown in Fig.13.3. Each sub-figure shows the centroid position of the original shape (marked by a red cross) and the distribution of blob centroids (the final position of the blob after adaptation and shrinkage) over ten runs, marked as a distribution blue dots. The results show better performance at tracking the centroid of convex shapes, including those with holes (Fig.13.3a-c). As shapes become increasingly concave, the error begins to increase. The worst performance is on shapes with strongly concave features where the centroid lies outside the boundary of the original shape (Fig.13.3e-f).

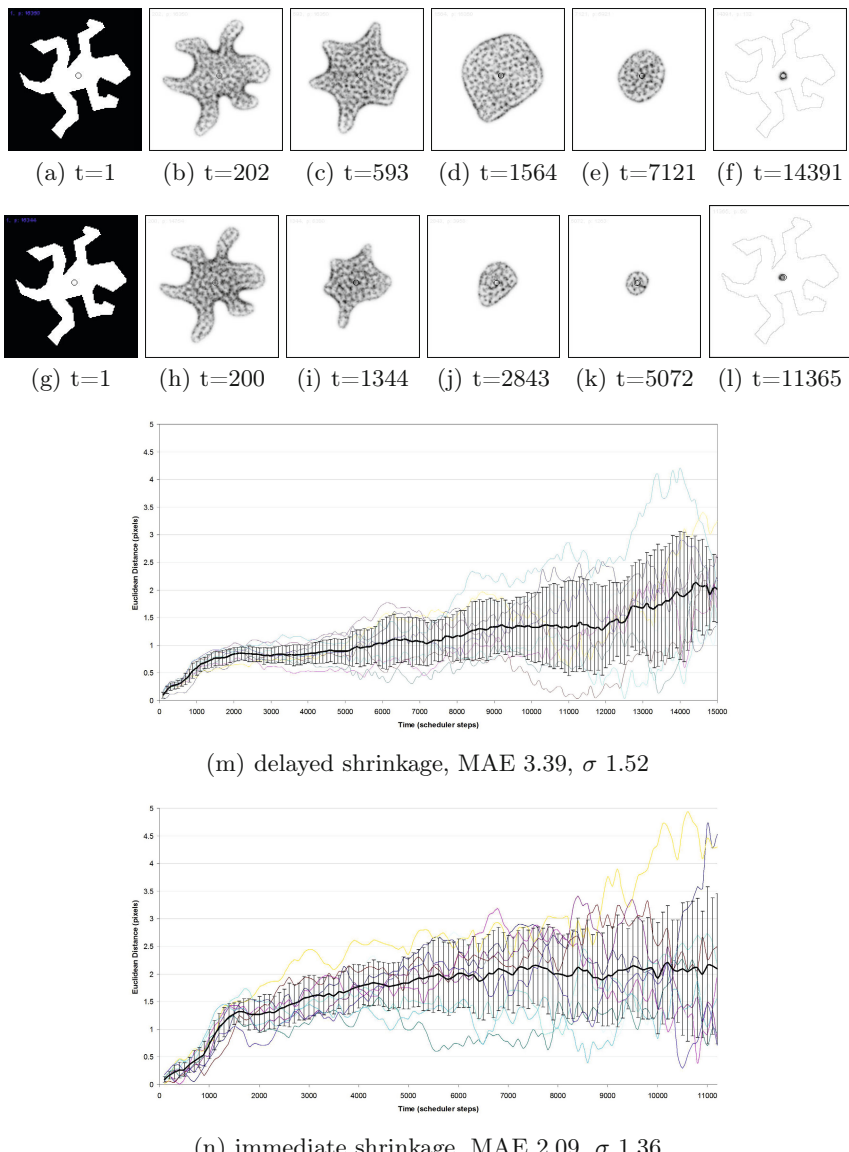


Fig. 13.2 Approximating the centroid by morphological adaptation and shrinkage. a) initial lizard shape with centroid indicated (circle), b-d) After initialisation in the original pattern the material undergoes adaptation, relaxing to approximate a circular shape, e-f) material reduces in size when particles are removed, g-l) adaptation with simultaneous shrinkage, m-n) charts plotting mean absolute error of blob centroid from original image centroid during adaptation then shrinkage (m) and adaptation with simultaneous shrinkage (n). 10 runs are shown overlaid (faint lines) with mean (thick line) and standard deviation error bars.

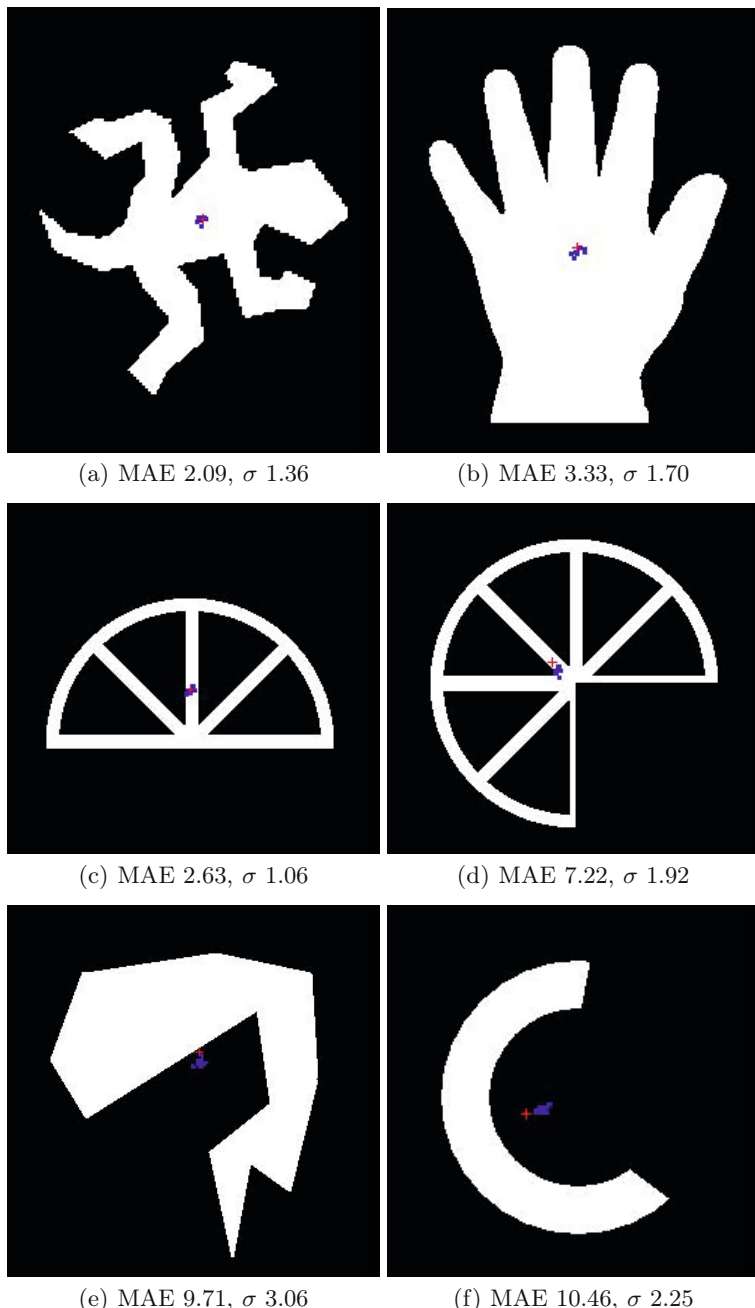


Fig. 13.3 Illustration of difference between blob approximation of centroid and image centroid. a-f) original image with centroid position (red cross shape) and distribution of blob positions over 10 runs (blue dots) with mean absolute error (MAE) and standard deviation (σ) indicated in labels.

13.2 Approximating Arithmetic Statistics by Morphological Adaptation

Instead of aggregating the geometric properties of a shape in two dimensions can we utilise the shrinkage method to summarise arithmetic properties of a spatially represented numerical dataset? To assess this possibility we randomly generated 20 numbers from the range of 0 to 100 and used these values as Y axis positions. The generated data values were sampled from a uniform distribution but had a wide range of variance across all experiments (σ of between 542 and 1293 for the sorted data experiments and σ between 462 and 1159 for the unsorted data experiments). X axis positions were generated using regular spacing of 20 pixels between the data points and we then connected these data points to give a shaped path on which to initialise the virtual material. The method was assessed over 50 randomly generated datasets for both unsorted lists of data (Fig. 13.4a,c,e,g,i,k) and for data points pre-sorted by value (Fig. 13.4b,d,f,h,j,l). During each run the virtual material was initially held in place by attractant projection for 20 steps of the model (Fig. 13.4a) and the attractant was then removed, causing the adaptive population to smooth and shrink the original shape. For unsorted data values the initial behaviour was to shrink away from sharp peaks and troughs connecting the data points (Fig. 13.4c) until an approximately smooth line was formed (Fig. 13.4e). This band of material then shrunk horizontally from each end (Fig. 13.4g,i). Each experiment was halted when the population size of the blob was < 50 and the final Y-axis position of the centre of the remaining population was compared to the arithmetic mean of the original data (Fig. 13.4k). In the case of the pre-sorted data values the smoothing of the line was much more short lived and the line began shrinking from both ends almost immediately. For the unsorted data points the mean error of the final blob position when compared to the numerically calculated arithmetic mean was 5.90 pixels (σ 3.7) and for the pre-sorted population the mean error was 2.23 pixels (σ 1.72). We did not find any strong correlation between the standard deviation of the randomly generated data points and performance (error) of the final position of the blob (Pearson correlation coefficient of $\rho = -0.07$ for sorted data and $\rho = 0.09$ for unsorted data).

How is the material shrinkage mechanism affected by skewed data distributions? To assess this we altered that random number generation procedure to generate skewed data distributions by the following method: For each of the 20 numbers generated we selected from the range of 80—100 with $p = 0.9$ and from the range 0—20 with $p = 0.1$, thus generating a list of numbers that was heavily biased towards higher numbers. We ran 25 experiments for both unsorted and sorted datasets. For unsorted skewed data (Fig. 13.5a,c,e,g,i, note that the Y-axis is inverted and larger values are lower) the error was 5.69 pixels (σ 4.07), similar to the results obtained for the uniformly distributed data. For the pre-sorted skewed data, however, the error increased to 10.57 (σ 3.04) and the final value of the blob was found to be higher than

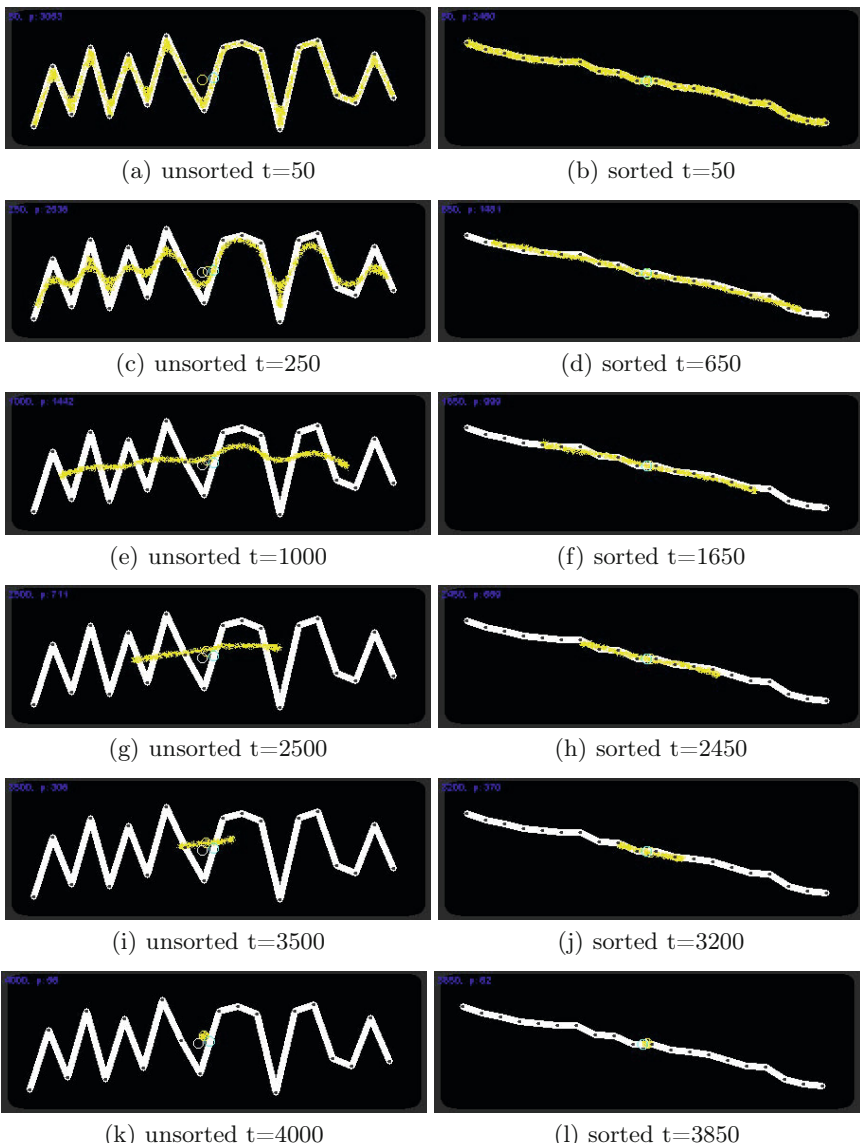


Fig. 13.4 Approximation of arithmetic mean of 1D data by morphological adaptation. Left column shows adaptation of unsorted data points, right column shows sorted data points. Individual data points indicated on inverted Y-axis by dark dots on connected line, adaptive population shown as coarse shrinking blob.

the arithmetic mean in every case (Fig. 13.5b,d,f,h,j). This difference from the arithmetic mean and other simple variants of the mean (such as the harmonic mean or geometric mean which are both lower than the arithmetic mean) suggests that the final blob position was influenced, or *weighted* in

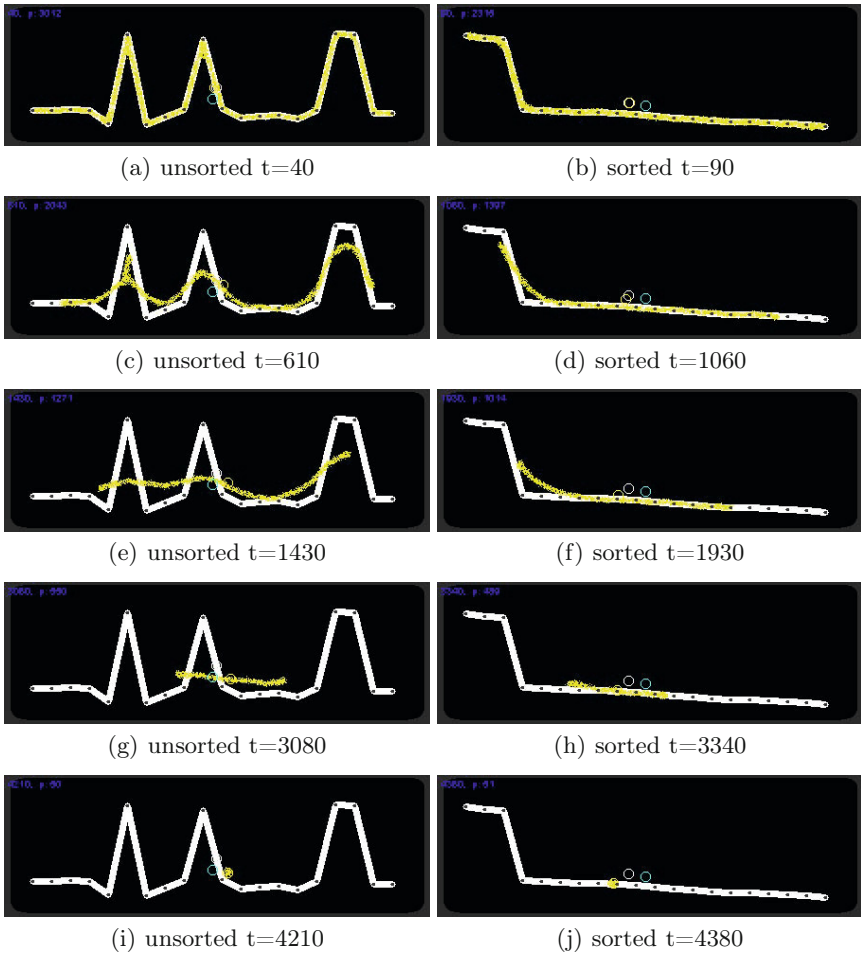


Fig. 13.5 Approximation of arithmetic mean of skewed 1D data distribution. Left column shows adaptation of unsorted data points, right column shows sorted data points. Individual data points indicated on inverted Y-axis by dark dots on connected line, adaptive population shown as coarse shrinking blob.

some way, by the greater number of larger data values. These results suggest that using morphological adaptation as a spatially implemented means of unconventional computation can — at least coarsely — approximate the arithmetic mean of a set of numbers.

13.3 Spatial Approximation of Data Tracking

Estimation functions seek to provide accurate information (output) about certain properties of a physical system using inputs which are corrupted or unreliable in some way. Estimation may be by simple statistical summation of previous inputs, or can be aided by construction of a model of the system or recursive knowledge about previous estimation errors [257]. An example application is the tracking of the actual position of a vehicle [258] given inputs (for example image snapshots or GPS co-ordinates) which are corrupted with noise, thus providing incorrect information about the position of the vehicle at any single positional update. The model of vehicle behaviour may have certain assumptions about normal vehicle movement. For example, vehicles typically move forwards or backwards and steer to the left or to the right or their current position. This simple model information suggests, for example, that sudden crab-like movement sideways without moving forwards is unusual and likely to be caused by erroneous position data.

Organisms such as *Physarum* slime mould live in an environment which is extremely noisy, from a signals perspective. Moreover *Physarum* does not possess any special senses or neural systems which are necessary in higher creatures to determine the presence of nutrients or threats. Yet *Physarum* has been shown to be capable of complex choices in terms of optimal path selection [70], nutrient quality [12] and nutrient composition [14]. The organism is able to integrate complex spatial and temporal information in a distributed manner throughout its amorphous body plan. Behavioural selection based on the sensorial fusion of disparate input stimuli is via changes in streaming and overall movement direction. Chemotaxis gradients (both attractant and repellent) coming into contact with the plasmodium affect the properties of the membrane, in terms of membrane softening or changes in local oscillation frequencies, ultimately causing changes in streaming behaviour towards attractants and away from repellents.

Can such simple material deformation mechanism be employed synthetically to provide coarse estimation functions? To assess this possibility we employed oscillatory ‘blobs’ of the virtual material to try to dynamically track the position of a moving stimulus whose exact position p is corrupted by Gaussian noise. In the oscillatory mode of behaviour the individual particles comprising the collective may exhibit transient resistance to obstructions in movement. These regions of transient resistance interact locally with regions containing vacant spaces, resulting in interacting and competing travelling waves and emergent amoeboid movement [259], [260]. Under normal non-oscillatory conditions any particles whose movement is obstructed simply select a random new direction, resulting in smooth morphological adaptation (initiation of oscillatory behaviour is discussed more fully in Chapters 15 and 16). The oscillatory movement conditions were used for the noisy estimation approximation because they allow faster morphological adaptation

in the face of rapidly changing environmental stimuli and a blob of oscillating virtual material also exhibits directional persistence towards more recent stimuli. This directional persistence acts as a very simple approximation and model of vehicular directional persistence.

We examined noisy estimation of object tracking in 2D environments using attractant (+ve) stimuli, repellent (−ve) stimuli and a fusion of both attractant and repellent (\pm ve) stimuli. 2D environments were represented by placing the blob in the middle of a square lattice, tracking movement of a simulated vehicle moving on the X-Y plane. Attractant stimuli were represented by the temporary projection of point attractant at stimulus locations into the lattice for a 10 scheduler steps. Attractant stimuli near the periphery of the blob caused the blob to stream towards the stimulus. Repellent stimuli were represented by simulated illumination of the environment. The Area inside a square region surrounding the stimulus location (50×50 pixels wide, corresponding to the approximate size of the blob area) was masked off and all regions outside this square were exposed to temporary projection (for 10 scheduler steps) of simulated illumination. Illumination was simulated by the following method: If an agent is located within an illuminated region the value of sensed chemoattractant is reduced by multiplying it by a weighting factor of 0.1, thus reducing the value of sensed chemoattractant in the illuminated region. The illumination causes exposed areas of the blob to migrate away from exposed regions. For combined +ve and −ve stimuli the scheduler alternated between +ve and −ve stimuli every 10 steps.

We represented the movement of the original vehicle movement position p by an outward spiral movement initiated in the centre of the arena. We recorded tracking of the moving signal by the blob in both noise-free and noise contaminated conditions. For the noise contaminated signals the original X-axis and Y-axis position of the vehicle p was recorded and each axis position was contaminated with Gaussian noise of $\sigma = 20$ to give the noisy stimulus n . The noisy stimulus n was projected to the blob by a temporary projection of point attractant stimulus or masked repellent region. The aggregate position of the blob was recorded by the centroid of all particles comprising the blob b . The position of the moving stimulus was updated every 25 steps. As the distance from the start position increased, the displacement of the simulated vehicle at each movement update became larger. The positions of p , n and b were recorded along with the absolute error (in pixels) of the position of the noisy stimulus n compared to original stimulus p and the error of the position of the original stimulus p compared to the blob centre b .

A typical example of the tracking behaviour of the blob under different stimuli types in noise-free conditions is shown in Fig. 13.6. At the start of the experiment 1500 particles comprising the blob are initialised at random positions within an 80×80 window at the centre of the arena and after approximately 250 steps the particles coalesce into an amorphous blob shape. In Fig. 13.6a-c the original trajectory of the moving target is indicated by the pale trace spiral and the actual path taken by the blob is indicated by

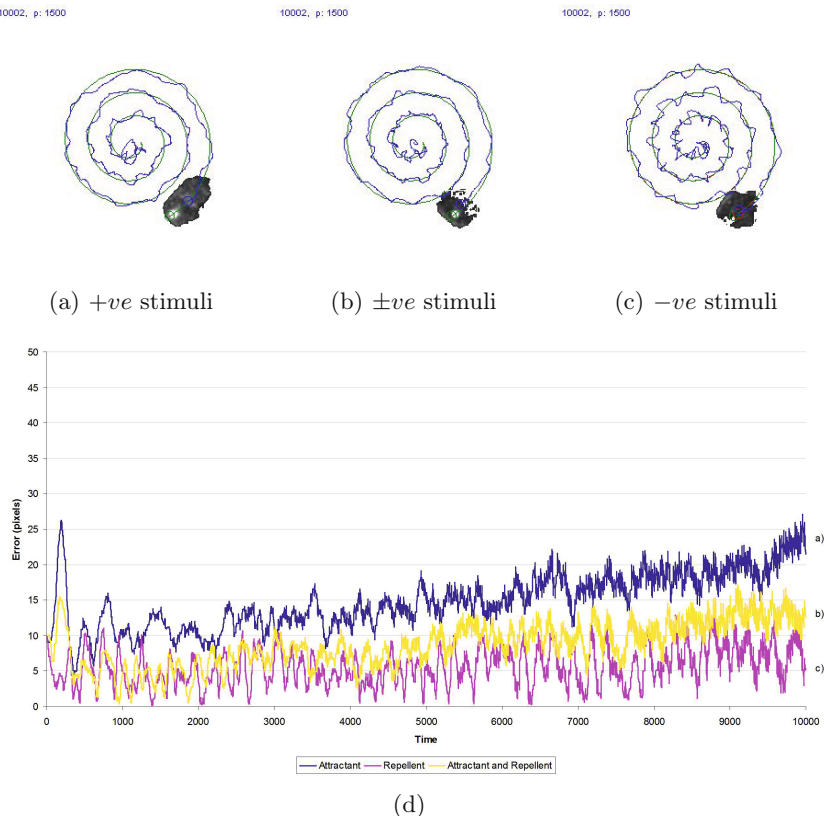


Fig. 13.6 Tracking a moving target via material adaptation and amoeboid movement under noise-free conditions. Original target path shown as light traces, blob path shown as dark traces and blob final position shown as grey mass. a) +ve attractant stimuli only, b) ±ve stimuli, c) -ve repellent stimuli only, d) plot of tracking error over time for methods a-c respectively.

the darker trace path. On initial inspection it would appear that the +ve (Fig. 13.6a) or ±ve (Fig. 13.6b) stimuli give the most accurate tracking. However the plot of distance error between p and b indicate that the +ve (attractant) stimuli results in the most error, which increases over time as the displacement of the vehicle per step increases. Although the traced blob paths in Fig. 13.6a and b are smoother than in Fig. 13.6c there is significant time lag between the current blob position and the actual target position to cause a larger overall error. The combined ±ve stimuli condition performs slightly better than +ve stimuli alone but the best performance in tracking is attained by the -ve (repellent only) stimulus condition (Fig. 13.6c).

When both the X and Y position of the moving target is contaminated with Gaussian noise of $\sigma = 20$, both the $+ve$ and $\pm ve$ conditions lose track of the target as its displacement increases (Fig. 13.7a and b, and the two corresponding plots in Fig. 13.7g). Only the $-ve$ repellent stimulus alone is able to track the target, although its error also increases over time (Fig. 13.7c and corresponding plot in Fig. 13.7g). The effect of corrupting the stimuli signal with noise in both axes is indicated in Fig. 13.7d-f which shows the history of noise corrupted signals superimposed on the original signal and blob position. In all three stimulus types the plots (both noise free and noise contaminated) show oscillations in the accuracy of tracking the original target. This is due to the lag time of the blob in adjusting its position (i.e. shifting its mass of particles) in response to the moving target.

13.4 Mechanisms of Data Tracking by Morphological Adaptation

The results demonstrate that it is possible to use very simple material-based shrinkage and adaptation behaviour to indirectly reveal and summarise properties of geometric and arithmetic datasets. The actual computational mechanism is very simple: The mechanism transforms and shrinks the original shape into a minimal configuration. For a 2D shape this minimisation first withdraws external projections, then approximates a circle which, if reduced in size, will reduce to a point location. The method approximates the centroid of objects containing holes and also (although to a lesser degree of accuracy) concave objects whose centroid lies outside the shape itself. The adaptation occurs at the periphery of the mass of particles, initially withdrawing any projections into the main mass. The cohesion of the blob then pulls outward regions of the collective together and even away from the original starting shape area (in the case of concave shapes) to approximate the centroid (Fig. 13.3e-f and supplementary recordings). It is notable that the shrinkage of narrow projections occurs more quickly than in shapes which have a larger curve radius.

A similar effect is seen in the approximation of 1D arithmetic statistics. For an unsorted ‘string’ of 1D numbers the material first flattens out the peaks and troughs between the linked numbers in the material before shrinking down to a point. In the case of a sorted list of numbers the string of numbers is already almost straight and the accuracy (compared to the unsorted case) is improved because both ends of the material shrink at almost identical rates. Again, it is notable that steeper peaks and troughs are flattened out more quickly than curves with smaller gradients. Indeed, it has recently been shown that the method described in this report filters high-frequency changes in information more quickly than low-frequency changes and thus be used in data smoothing applications [243]. This data-dependent difference in behaviour may be responsible for the apparent weighting of the final position of the blob in the case of pre-sorted data with a skewed distribution.

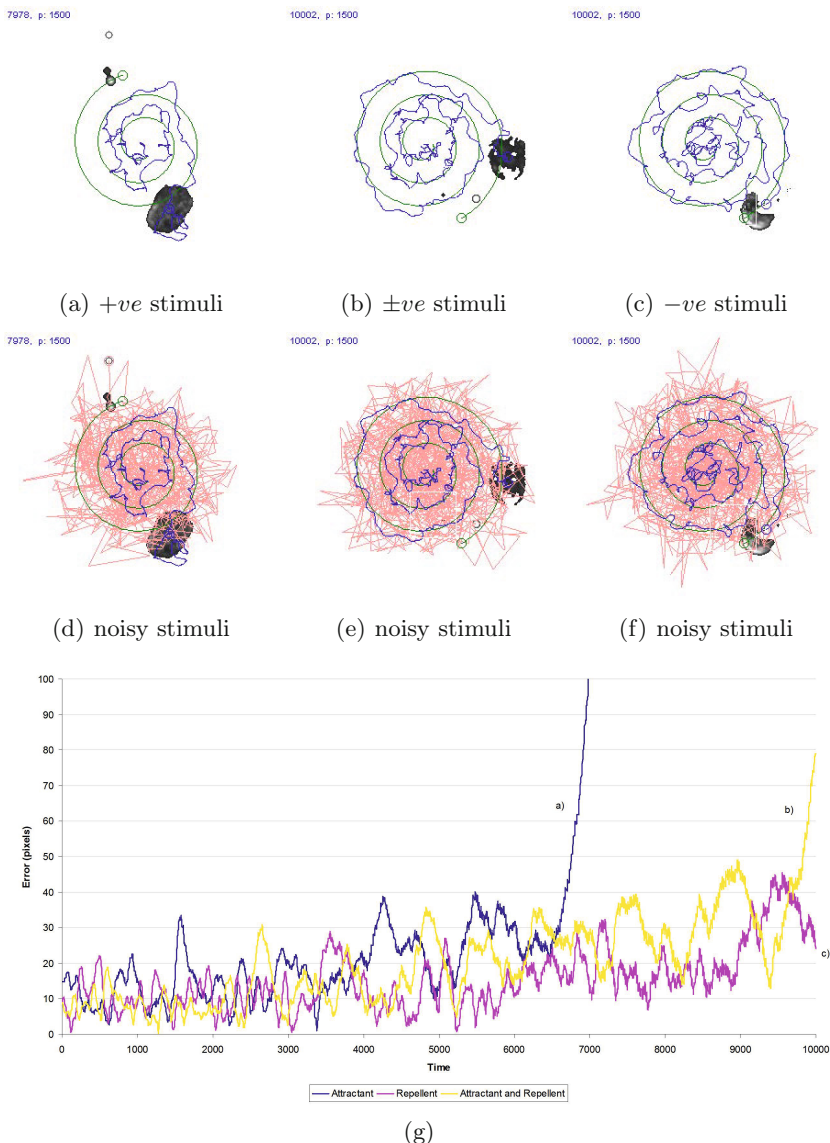


Fig. 13.7 Tracking a moving target via material adaptation and amoeboid movement under noisy stimulus conditions. Original moving target path shown as light trace, blob path tracking noisy signal shown as dark trace and blob final position shown as grey mass. a) +ve attractant stimuli only, b) ±ve stimuli, c) -ve repellent stimuli only, d) noise contaminated stimuli for +ve condition e) noise contaminated stimuli for combined ±ve conditions, f) noise contaminated stimuli for -ve condition, g) plot of tracking error over time for methods a-c respectively.

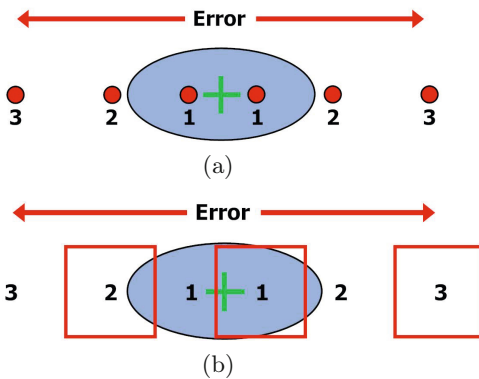


Fig. 13.8 Effect of increasingly erroneous signals on blob tracking response for attractant and repellent stimuli. Blob indicated by blue oval, actual target location indicated by green cross, erroneous +ve location stimuli as red circles, erroneous -ve location stimuli as red squares. Larger numbers indicate increasingly large errors of position. Top: position of erroneous +ve point attractant stimuli, Bottom: position of erroneous -ve stimuli mask zones.

The ability of the self-oscillating amoeboid blob of material to track the noise contaminated target is, in part, due to the innate cohesion of the blob and in part due to the relatively large area of the blob. Although the blob streams towards (or away from, in the case of -ve stimuli) potentially incorrect locations, the continuous update of (albeit noisy) positions ensures that the blob is not influenced too strongly by any one particular data point. Furthermore, any particularly erroneous data point stimulus actually has less of an effect on the blob than smaller errors. For +ve stimuli with a very small error margin from the true location (e.g. code 1 in Fig. 13.8, top) this will cause regions on both sides of the blob to move towards the stimulus site. For moderately large errors (code 2 in Fig. 13.8, top) the blob will stream outwards towards the erroneous stimuli but the cohesion of the remainder of the blob will give a resistant force against deformation. A large erroneous stimulus (code 3 in Fig. 13.8, top) is less likely to influence the blob at all, since the blob is attracted more strongly to closer stimuli.

A similar situation occurs with -ve stimuli where areas outside the masking square are exposed to repellent stimuli. Small deviations from the true signal (e.g. code 1 in Fig. 13.8, bottom) result in areas on both sides of the square migrating inside the mask, but this region is already occupied by a large proportion of unexposed particles which prevent large shifts in blob position. Larger errors (code 2 in Fig. 13.8, bottom) cause an influx into the masking zone which is resisted partly by the presence of unexposed particles inside the masking zone and partly due to the relatively large migration distance. For very large errors (code 3 in Fig. 13.8, bottom) the entire blob is

exposed to the repellent stimuli and thus the overall position of the blob does not shift significantly. This ability to integrate and absorb a large number of noisy inputs allows the blob to track the original target despite the large noise component contaminating the signal.

The representation of numerical data in classical algorithms is efficient and inexpensive, in terms of computer resources. The transformation to a spatial unconventional computing representation requires significant spatial resources in terms of image area. It is not possible to reduce the representation of a single data point lower than a certain size because the emergent material effects are exerted only above a certain particle sensor size (≥ 3 pixels). Furthermore, the speed of the model framework is mostly dependent on image area size (the diffusion of the environment at each scheduler step requires a convolution operation at each site) and partially dependent on population size. The time taken for the material to relax to a state where the result can be ‘read’ is also dependent on the size range of the data involved which also limits the practicality of the method as it currently stands. However it may be possible in future work to improve the spatial encoding of the numerical data used in the model to a more compact and efficient scheme.

13.4.1 Environment and Problem Data Representation

For the experiments in this section we used a sensor offset (*SO*) value of 9. Variations in both *SA* and *RA* parameters have been shown to generate a wide range of reaction-diffusion patterns (see Fig. 3.13) and for these experiments we used *SA* 90° and *RA* 45° which results in stronger and more rapid adaptation and cohesion of the virtual material.

For the object tracking experiments we require a means of moving the position of the blob in response to the changing data. This is implemented by exploiting the self-organised amoeboid movement of the blob under oscillatory conditions. Instead of randomly selecting a new direction if a move forward is blocked, the particle increments separate internal co-ordinates until the nearest cell directly in front of the particle is free. When a cell becomes free, the particle occupies this new cell and deposits chemoattractant into the lattice at the new site. The effect of this behaviour is to remove the fluidity of the default movement of the population. The result is a surging, resistant pattern of movement. The strength of the resistance effect can be damped by a parameter *pID* which determines the probability of a particle resetting its internal position co-ordinates, lower values providing stronger inertial movement. For these experiments we use a *pID* value of 0.05 which provides enough internal oscillations within the blob to generate amoeboid movement.

Diffusion in the lattice was implemented at each scheduler step and at every site in the lattice via a simple mean filter of kernel size 3×3 . Damping of the diffusion distance, which limits the distance of chemoattractant gradient diffusion, was achieved by multiplying the mean kernel value by 0.9 per

scheduler step for centroid and arithmetic mean experiments, and by 0.93 for object tracking experiments (the oscillatory conditions require less damping to ensure blob cohesion in this case). The spatially implemented computation in the model requires that the data configuration be represented as a pattern within the 2D lattice. Data configurations for centroid approximation are loaded as greyscale image files and the shapes within these images are used as locations to initialise the particle population and to project virtual attractant into the diffusive lattice to initially confine the particle population. For the arithmetic mean experiments the data series were generated using pseudo-random number generators (generating numbers with a uniform distribution) and these numbers were spatially represented by marking the lattice pixel sites corresponding to these numbers in order to initialise the material at these locations. Neighbouring sites were linked by straight lines six pixels wide in order to provide a continuous path on which to inoculate the virtual plasmodium.

13.4.2 Material Shrinkage Mechanism

For the centroid approximation material shrinkage was implemented by deleting a particle with probability $p = 0.0005$ at each scheduler step. When particles are removed the cohesion of the blob causes the particles to move inwards, filling the spaces and thus shrinking the blob. This simple method is sufficient when the particles comprise a large blob. For the arithmetic mean approximation, however, the thinner band of material is susceptible to breakage during shrinkage so a different method is required to ensure continuity of the material and this was implemented as follows: If there are between 1 and 10 particles (including the current particle) in a 9×9 neighbourhood of a particle, and the particle has moved forwards successfully, a new particle is created if there is a space available at a randomly selected empty location in the immediate 3×3 neighbourhood surrounding the particle. If there are between 0 and 24 particles (including the current particle) in a 5×5 neighbourhood of a particle the particle survives, otherwise it is deleted. This parameter effectively controls the speed of blob shrinkage. Deletion of a particle leaves a vacant space at this location which is filled by nearby particles, causing the collective to shrink. After a particle is deleted, the filling in of the vacant area occurs as a stochastic consequence of the particles' sensory and motor methods and no bias is introduced into the material structure. The frequency at which the growth and shrinkage of the population is executed determines a turnover rate for the particles. The frequency of testing for particle division and particle removal was every 2 scheduler steps. This relatively high frequency (compared to other applications using the virtual material approach, e.g. [216]) is due to the strong shrinkage invoked by the particular *SA/RA* combination used, necessitating a high adaptation frequency to maintain connectivity of the material as it adapts and shrinks.

13.5 Summary: Towards Harnessing Material Relaxation for Statistics

Motivated by the complex computation performed by the single-celled organism slime mould *Physarum polycephalum*, we have demonstrated experiments that explore whether morphological adaptation in a distributed collective of very simple mobile-agent particles can be used to extract salient statistical properties of complex datasets. The mechanism is based upon the innate emergent properties of cohesion and shape relaxation within the population which behaves as a deformable virtual material. We found that by patterning the population inside a two-dimensional shape, a shrinking population can approximate the geometric centroid of a 2D dataset at the final site of shrinkage. This result appears to mimic — at least superficially — the process of sclerotium formation in slime mould in the presence of sustained adverse environmental conditions. By abstracting this idea to numerical 1D datasets (albeit represented in 2D space) we found that the final position of the shrinking population approximated the arithmetic mean of the datasets (more accurately in the case of pre-sorted datasets). Finally we demonstrated that a self-oscillatory ‘blob’ of the model slime mould which has previously been shown to be capable of self-organised amoeboid movement [260] can track the position of moving targets via attractant or repellent stimuli, or a fusion of both stimulus types. This tracking of the target was found to be resilient in the presence of uncertain or noisy information about the exact current position of the target.

The results in this chapter demonstrate that the collective bulk mechanical properties which emerge from, and are embodied within, low-level local interactions, such as cohesion, minimisation and shape adaptation, can be harnessed to extract statistical properties of complex 1D, 2D and noisy dynamical datasets. The impetus behind this research is not to discover the ‘best’ method of calculating these functions, since numerical methods of doing so are already well understood and indeed more accurate. Instead the purpose is to try to understand what are the *minimal* requirements for discovering such information within these datasets. Future robotic devices will hopefully be able to access such embodied material computation to gain information about features of their environment which would otherwise require external or off-line processing. Mechanical analogies are also a useful method to explain and understand complex algorithms in computational geometry [237] and in statistics more generally [261]. We speculate that material computation methods may in future provide both practical methods for the distributed solution of statistical problems and also potentially generate novel statistical metrics based on collective material properties. More generally, this may provide a greater understanding of how simple organisms with limited computational abilities can approximate complex problems.

Chapter 14

Morphological Adaptation Approaches to Path Planning

“The lights outside tonight are far from home.”

(Kurt Wagner, 2000.)

14.1 Path Planning: Unconventional Computing Approaches

Path planning (or motion planning) is a common application of computer science and robotics where a path has to be found between points (typically two points, source and destination point) within an arena. The representation of the arena may already be known or may be discovered by localisation and mapping methods (in this chapter we consider examples where the arena layout is known in advance). The resultant path should be short, minimising distance between the points. Other constraints may also apply, such as requiring paths of sufficient width, avoiding walls, avoiding obstacles, or minimising the number of turns.

Unconventional computing seeks to utilise the computing potential of natural physical systems to solve useful problems. Since these systems are localised in space, they typically use different mechanisms to classical approaches. In recent years physical propagation through space in chemical substrates has been used as a search strategy. Babloyantz first suggested that travelling wave-fronts from chemical reactions in excitable media could be used to approximate spatial problems [262]. Wave propagation in the Belousov-Zhabotinsky (BZ) chemical reaction was subsequently used to discover the path through a maze [72]. In this research a trigger wave was initiated at the bottom left corner of a maze and its propagating wave front recorded by time-lapse photography. Direction of wave propagation was calculated from the collective time-lapse information to give vectors which indicated the direction of the travelling wave. The path from any point on the maze to the

exit (the source of the diffusion) was followed by tracking backwards (using the vector information) to the source.

Wave-front propagation generates a solution from any (and indeed *every*) point in the arena. Branching paths (for example around obstacles) are searched in parallel and the solution time is dependent on the spatial size (in terms of maximum path length) of the arena and the wave-front propagation speed. Although computationally efficient, a direct spatial encoding of the problem (arena, desired start and end points) must be stored, as opposed to a more compact graph or grid encoding in classical approaches.

Reading the output of the parallel calculations is not a simple approach using chemical substrates. Although the propagating wave solves the shortest path for all points in the arena, finding and tracking the desired path from start to end point requires separate processes. Different approaches have been attempted including image processing [263], using two wave-fronts in both directions [264], and hybrid chemical and cellular automata approaches [171]. More recently, a direct visual solution to path planning was devised in which an oil droplet (exploiting convection currents and surface tension effects) migrated along a pH gradient formed within a maze to track the shortest path through the maze [71].

In this chapter we continue the exploration of material computation by morphological adaptation seen in [216] and [243] and examine its application to path planning. Taking inspiration from the behaviour of slime mould, we use a large sheet, or ‘blob’ of virtual slime mould which is located within an arena in which a path between two points (represented by attractants) must be found. By shrinking this blob over time, it withdraws from the confines of the arena boundary and adapts its shape to connect the start and end points of the path. Examples of the shrinkage method are given in Section 14.2, along with more challenging additions to the problem such as multiple-path options, collision-free paths and obstacle avoidance. We conclude in Section 14.3 by summarising the approach and its contribution to unconventional computing methods of path planning in terms of its simplicity.

14.2 Morphological Adaptation in the Model Slime Mould

We placed a large population of particles within the confines of a 2D arena (Fig. 14.1a), so that the virtual plasmodium completely filled the arena (Fig. 14.1b). Start and end points of the path were represented by projection of attractant into the arena at their respective locations. The virtual plasmodium was attracted to these start and end points. The population size was reduced by adjusting the parameters governing the growth and shrinkage in favour of shrinkage. The collective ‘blob’ began to shrink and, as it did so, adapted its shape to maintain connectivity to the start and end points and conform to the borders of the arena (Fig. 14.1c-e). Any extraneous

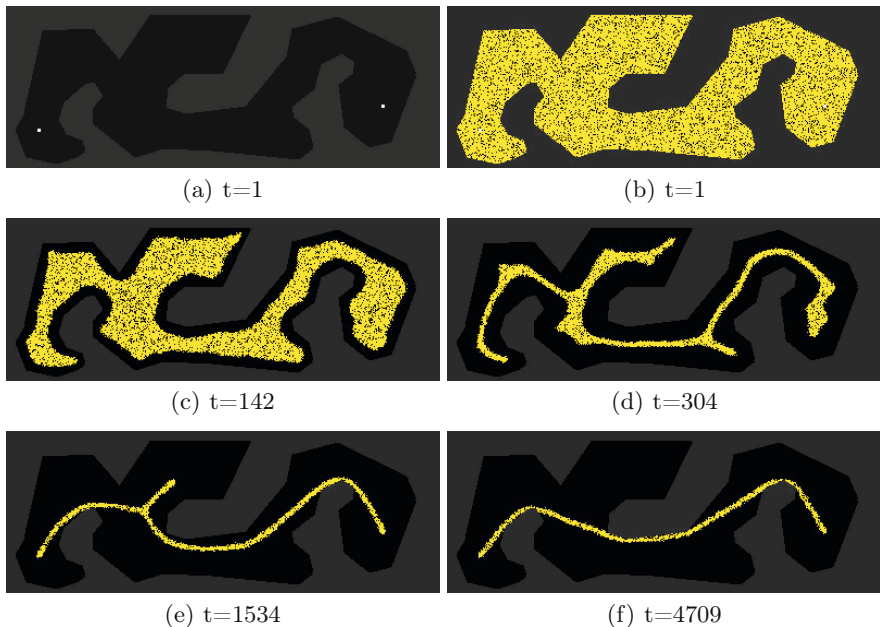


Fig. 14.1 Approximation of shortest path between two points by morphological adaptation in a virtual slime mould. a) 2D Arena defined by borders (grey), habitable regions (black) and start and end points (white), b) initialisation of virtual plasmodium in habitable region, c-f) shrinkage of blob causes adaptation of shape and attraction to points, ultimately forming the shortest path between the points.

pseudopodium-like appendages were withdrawn until only a single path connected the start and end points, forming the shortest path between the two points (Fig. 14.1f). This path was composed of a thin band of particles.

14.2.1 Multiple Paths and Many-to-One Path Selection

Most applications for path planning involve finding a path between two points. However it may be necessary to calculate a connecting path between multiple points. This can be achieved in the morphological adaptation approach by having multiple nutrient attractant sources. When a large blob is placed within a polygon arena containing multiple sources, it retains its connection to all points as it shrinks (Fig. 14.2). The final network path (Fig. 14.2d) indirectly connects all source points. Note that the connections between the sources are not simple edges to and from each point. This is not possible because straight edges would pass through the protruding arena boundaries. Instead there is a core curved path running between the outermost points (1 and 4) with pseudopodium-like extensions protruding from this path to connect the inner points (2 and 3). Note that this core path

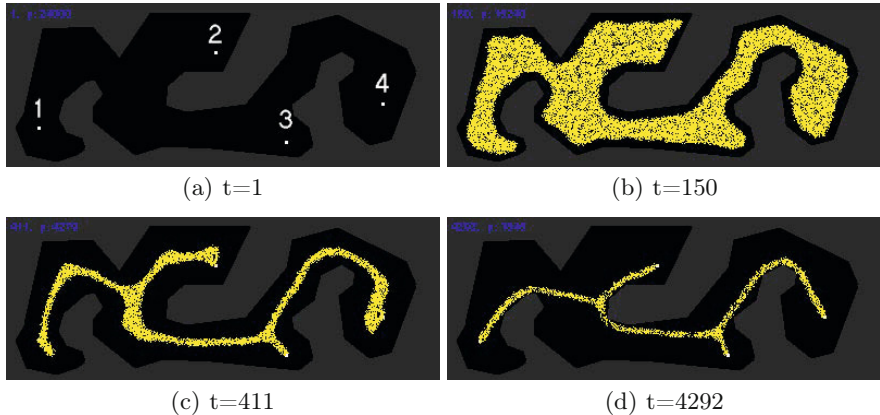


Fig. 14.2 Multiple source path planning by morphological adaptation. a) arena with four locations (numbered white points), b-d) shrinkage of virtual plasmodium yields a network with a core path extending from the outermost points with extensions connecting the inner points.

passing between four points differs from that of Fig. 14.1f which passes between only two outer points. The connection between the core path and the two inner points (2 and 3) distorts the core path in the direction of the inner points.

Given this path connecting all four points, how does the morphological adaptation method respond to the removal of certain path options? In Figs. 14.3 and 14.4 we demonstrate the effect of removing different path options. Beginning with the path connecting four points (Fig. 14.3a) we remove points 2 and 3 by deleting the attractant sources at these locations from the lattice. The pseudopodium-like projections connecting these branches to the core path both retract into the core path due to the lack of attractant from these sources (Fig. 14.3b,c). The retracting projections merge with the main flow of particles in the core path. When retraction of these branches is complete the core path connecting points 1 and 4 continues its adaptation to adopt a minimal path between the outer points following the contours of the arena boundary (Fig. 14.3d).

If we remove different source points from the same starting configuration, the adaptation takes a different course. Fig. 14.4 shows the results of a different experiment with the same four points initially connected (Fig. 14.4a). When source points 2 and 4 are removed from the lattice the pseudopodium withdrawal again commences (Fig. 14.4b,c) and the final remaining path adopts a minimal connection between points 1 and 3 (Fig. 14.4d).

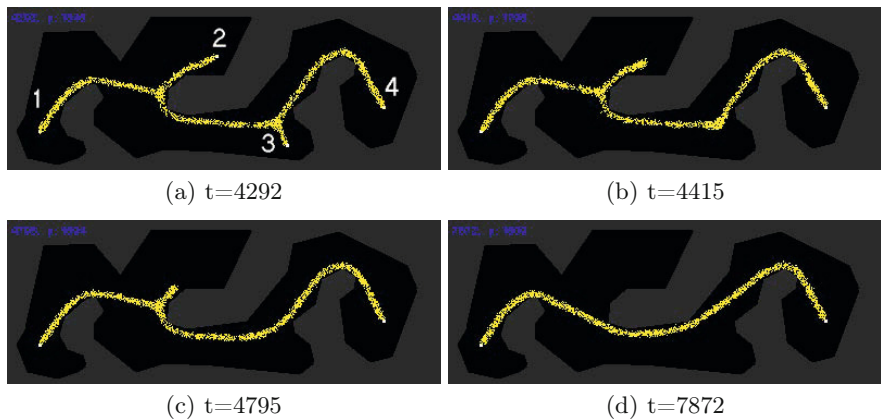


Fig. 14.3 From multiple paths to single path by morphological adaptation. a) multiple paths connecting four attractants (numbered), b-d) removal of attractant source from nodes 2 and 3 causes withdrawal of pseudopodia from previous sources and ultimately a single path formed between nodes 1 and 4.

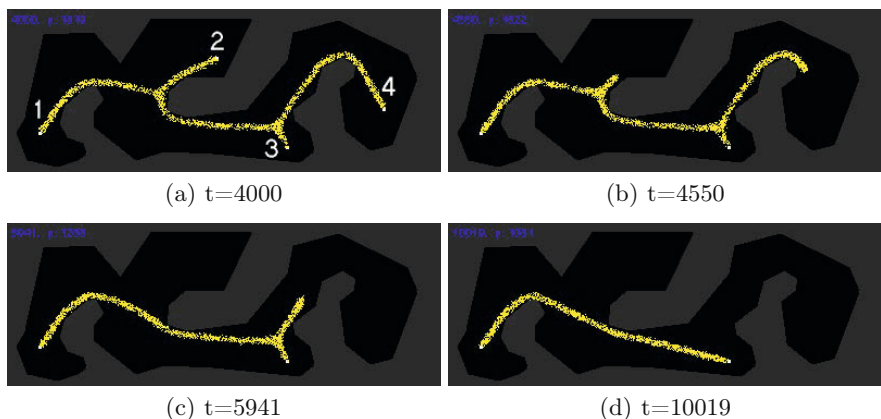


Fig. 14.4 From multiple paths to single path by morphological adaptation. a) multiple paths connecting four attractants (numbered), b-d) removal of attractant source from nodes 2 and 4 causes withdrawal of pseudopodia from previous sources and ultimately a single path formed between nodes 1 and 3.

14.2.2 Collision-Free Paths

In many applications a collision-free path may be required, for example if the desired path has to avoid close proximity to walls. To achieve this method by morphological adaptation we represented the walls of the arena as repellent sources (repellent sources project negatively weighted values into the diffusive lattice). We used the same arena as in earlier experiments, but with different start and end points (Fig. 14.5a,b). As the blob shrunk it formed the shortest path (following the walls) when repellent diffusion was not activated (Fig. 14.5c-f). When repellent diffusion from the arena walls was activated the virtual plasmodium still maintained its connectivity to the start and end points but also avoided the diffusing repellent values projecting from the walls of the arena (Fig. 14.5g). Further increasing the concentration of the repellent source increased the distance of the path from the walls (Fig. 14.5h).

14.2.3 Avoiding Obstacles and Preventing Multiple Paths

The response of the morphological adaptation in the presence of obstacles is shown in Fig. 14.6. Again the model is initialised within the habitable region of the arena. When the virtual plasmodium shrinks and adapts its shape in the presence of obstacles we see that multiple paths are formed around the obstacles which connect the start and end points (Fig. 14.6f). Even if we projected repellents from these obstacles, the effect would only be to widen the distance of the multiple paths from these obstacles, and not to form a single path.

The final shrunken multiple paths connecting the nutrient sources are observed because they actually already existed upon initialisation, as the blob was initialised around the obstacles (see Fig. 14.6b). To ensure only a single path is generated we devised a two-part repulsion mechanism. The first part of the mechanism occurs by initialising the blob to cover the *entire* arena (including the obstacles). This part in isolation would not solve the problem of multiple paths, however: If the obstacles repelled the blob immediately then the virtual plasmodium would simply flee the obstacle regions from all directions and multiple paths would still be retained. The second part of the mechanism ensures that only a single path is retained. The shrinkage process is performed more slowly and we generate repellent fields only from obstacles (more specifically, exposed *fragments* of large obstacles) that have been partially uncovered by the shrinkage of the blob.

The mass of the blob is thus shifted away from obstacles by their emergent repulsion field. Because the blob shrinks slowly inwards from the outside of the arena obstacles are slowly uncovered and the repulsion field further pushes the blob inwards until a single path connecting the source attractants is formed. The shrinkage and repulsion mechanism is illustrated in Fig. 14.7 where the arena (including obstacles) is completely covered by a large mass

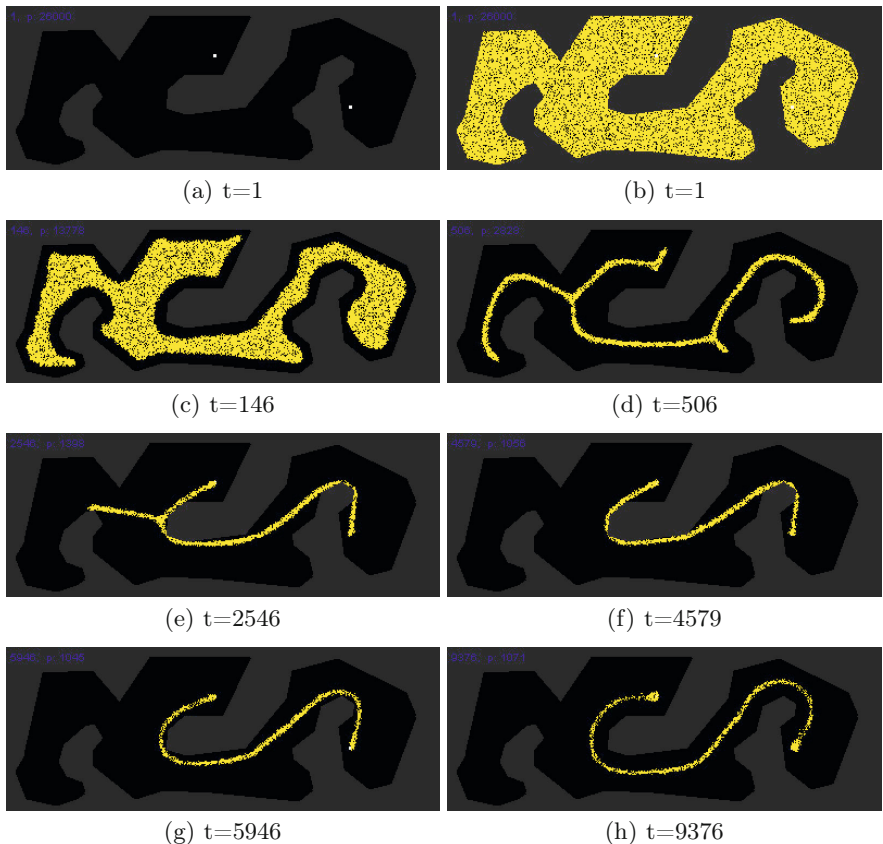


Fig. 14.5 Approximation of collision-free shortest path by morphological adaptation and repulsion. a) 2D Arena defined by borders (grey), habitable regions (black) and start and end points (white), b) initialisation of virtual plasmodium in habitable region, c-f) shrinkage of blob causes adaptation of shape and attraction to points, forming the shortest path between the points, g) repulsion field emitted from arena walls causes virtual plasmodium to avoid wall regions, forming a collision-free path, h) increasing concentration of repulsion field causes further adaptation of the virtual plasmodium away from walls.

of particles comprising the virtual plasmodium (Fig. 14.7b). The blob shrinks inwards as the periphery of the blob is drawn inwards (Fig. 14.7c). When an obstacle is partially uncovered repellent is projected into the diffusive lattice at exposed obstacle fragments (Fig. 14.7d, arrowed). The blob at these regions is repelled and moves away from the exposed obstacle fragment. The shrinkage process continues and when a larger obstacle is partially exposed the repellent projected into the lattice again causes the blob to move away

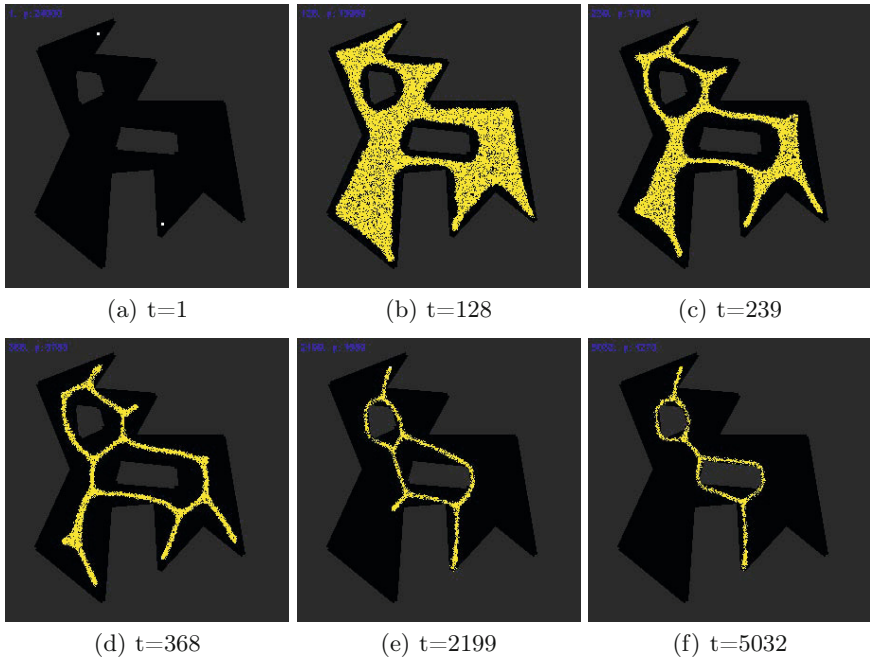


Fig. 14.6 Addition of obstacles results in multiple paths connecting start and end points. a) 2D Arena defined by borders and obstacles (grey), habitable regions (black) and start and end points (white), b-e) shrinkage of virtual plasmodium within habitable region, f) shrinkage of virtual plasmodium around obstacles causes multiple paths around obstacles on the path between start and end points.

from this region (Fig. 14.7f, arrowed). Further exposure of this large lower obstacle causes the blob to continue to be repelled away (Fig. 14.7g) until eventually only a single path remains which connects the source attractants and threads between the obstacles (Fig. 14.7h).

In the presence of a large number of obstacles, the repulsion field emanating from newly-exposed obstacles acts to deform the shrinkage of the virtual plasmodium. The mass of particles is deformed both by the attractant stimuli from the start and end points of the path (Fig. 14.8d) and the gradual exposure of the obstacles as the blob shrinks. Fig. 14.8 shows the deformation of the blob and also the changing concentration gradient field as the shrinkage continues, until only a collision-free path between the obstacles remains.

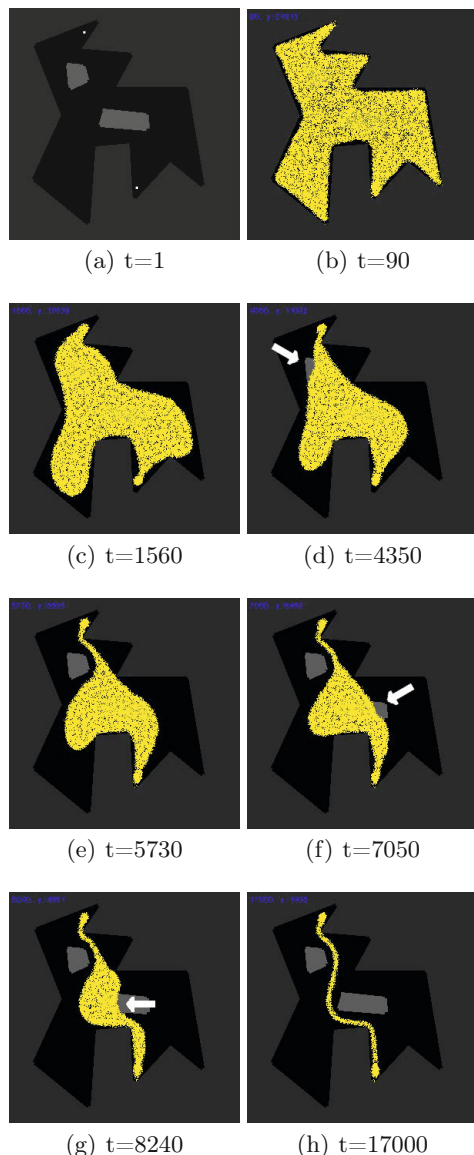


Fig. 14.7 Mechanism of shrinkage combined with repulsion at exposed obstacle fragments generates a single path. a) arena with habitable areas (black), inhabitant areas (dark grey), obstacles light grey and path source locations (white). b) blob initialised on entire arena, including obstacles, c) gradual shrinkage of blob, d) exposure of obstacle fragment generates repellent field at exposed areas (arrow), e) blob moves away from repellent field of obstacle, f) lower obstacle is exposed causing repellent field at these locations (arrow), g) further exposure causes migration of blob away from these regions (arrow), h) final single path connects source points whilst avoiding obstacles.

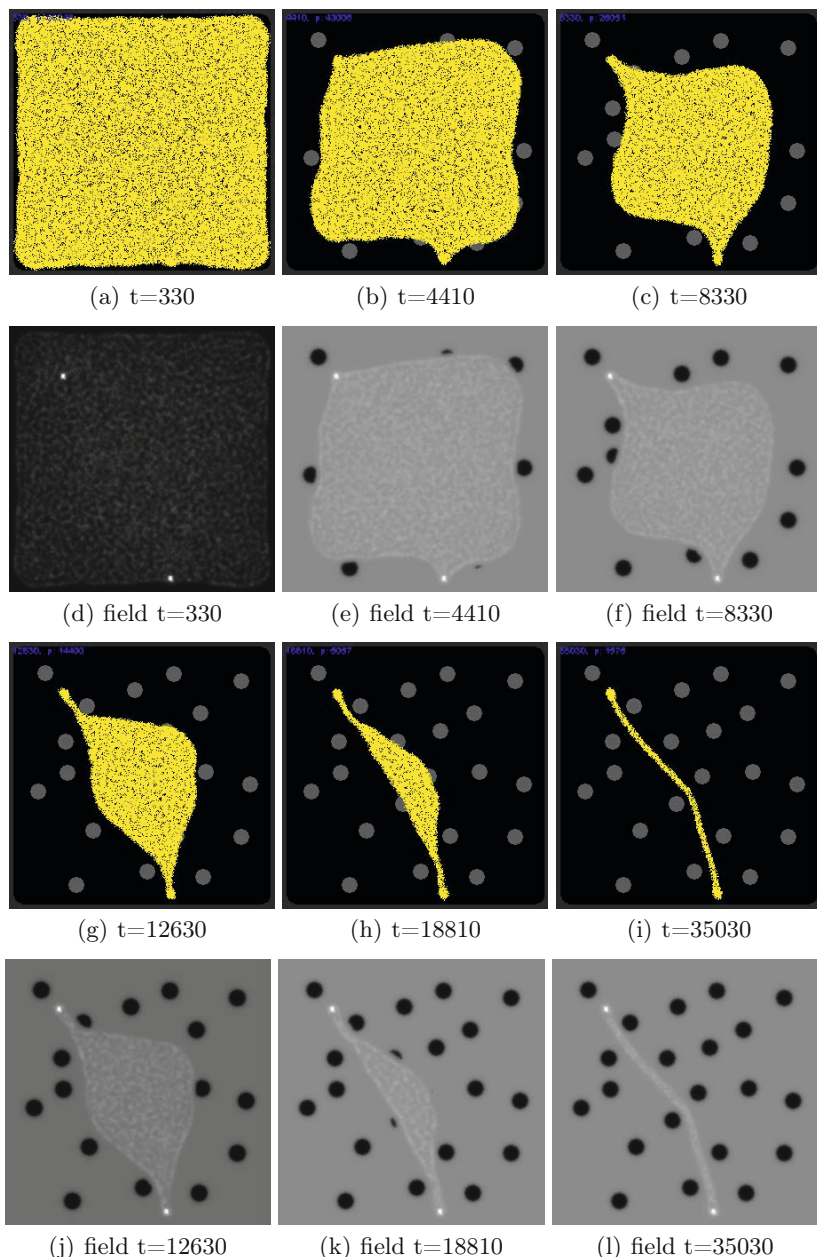


Fig. 14.8 Shrinkage and exposed repulsion method in complex obstacle field. (a-c) and (g-i) uniform shrinkage of blob is distorted by attraction to start and end stimuli and repulsion from exposed obstacles, (d-f) and (j-l) visualisation of gradient field showing attractants at start and end stimuli (bright spots), blob (mid-grey mass) and repulsion field from exposed obstacles (dark circles). Greyscale gradient field images transformed by gamma correction ($\gamma = 0.6$) to improve clarity.

14.2.4 Model Parameters and Problem Representation

Path start and end points were represented by projection of chemo-attractant to the diffusive lattice at their positions indicated by white pixels on the source configuration images. Lattice size varied with each particular arena but varied from 150 pixels minimum size to 416 pixels maximum size. The attractant projection concentration was 6.375 units per scheduler step. Projection of repellent sources from arena boundaries (used in collision-free planning experiments) was implemented by negatively valued projection (-6.375 units) into the lattice at arena boundary locations causing repulsion of the blob from these regions. Uncovering of obstacles by the shrinking blob acted to project repellent into the lattice (-6.375 units) at exposed areas of obstacles, causing the blob to be repelled from these regions. Each pixel comprising the obstacle was deemed to be uncovered if there were any agent particles within an 11×11 window of the pixel. If an obstacle was covered by particles the repellent projection was suppressed by reducing the projection of repellent to -0.006375 units. This ensured that repulsion from obstacles only occurred when a significant part of the obstacle had been uncovered by the shrinking blob. Diffusion in the lattice was implemented at each scheduler step and at every site in the lattice via a simple mean filter of kernel size 3×3 . Damping of the diffusion distance, which limits the distance of chemo-attractant gradient diffusion, was achieved by multiplying the mean kernel value by 0.9 per scheduler step.

The blob was initialised by creating a population of particles and inoculating the population within the habitable regions of the arena. The exact population size differed depending on the size of the arena (and habitable area) initial blob was typically composed of between 24000 and 70000 particles. Particles were given random initial positions within the habitable area and also random initial orientations. Particle sensor offset distance (SO) was 7 pixels. Angle of rotation (RA) was set to 45° and sensor angle (SA) was set to 90° . Agent forward displacement was 1 pixel per scheduler step and particles moving forwards successfully deposited 5 units of chemo-attractant into the diffusive lattice. This value is slightly less than the attractant projection value, causing the particles to be anchored to projection sites and ultimately constraining the shape of the shrinking blob. Both data projection stimuli and agent particle trails were represented by the same chemo-attractant ensuring that the particles were attracted to both data stimuli and other agents' trails. The collective behaviour of the particle population was cohesion, minimisation, and morphological adaptation to the configuration of stimuli.

14.2.5 Shrinkage Mechanism

Adaptation of the blob size was implemented via tests at regular intervals. Growth of the population was implemented as follows: If there were between 1 and 10 particles in a 9×9 neighbourhood of a particle, and the particle had

moved forward successfully, the particle attempted to divide into two if there was a space available at a randomly selected empty location in the immediate 3×3 neighbourhood surrounding the particle. Shrinkage of the population was implemented as follows: If there were between 0 to 79 particles in a 9×9 neighbourhood of a particle the particle survived, otherwise it was deleted. Deletion of a particle left a vacant space at this location which was filled by nearby particles (due to the emergent cohesion effects), thus causing the blob to shrink slightly. As the process continued the blob shrunk further and adapted its shape to the stimuli provided by the configuration of path source points, arena boundaries and repellent obstacles. The frequency at which the growth and shrinkage of the population was executed determined the turnover rate for the population. The frequency of testing for particle division was every 10 scheduler steps and the frequency for testing for particle removal was every 2 scheduler steps. Since the shrinking blob method is only concerned with the reduction in size of the population it might be asked as to why there were tests for particle division at all. The particle division mechanism was present to ensure that the adaptation of the blob was uniform across the sheet to prevent ‘tears’ or holes forming within the blob sheet, particularly at the start of an experiment before flux within the blob was initially stabilised.

14.3 Summary: Shaping a Material to Find a Path

We have demonstrated how unconventional computation of path planning problems may be performed directly in 2D space by morphological adaptation in a virtual material inspired by the adaptation of slime mould *Physarum polycephalum*. Unlike previous implementations of path planning problems in chemical substrates the method does not rely on a two-stage computation (one stage to perform the computation, another stage to highlight the path). The method computes a simple path with only two attractant sources. Multiple paths were represented by having more than two attractant sources and a single path was selected between two of these sources by removal of redundant sources. Collision-free paths were discovered by the simultaneous addition of repellent sources at arena boundaries. Obstacle avoiding paths were discovered using a mechanism whereby obstacles were represented by a gradual exposure of repellent sources. The contribution of this method is in the simplicity of the approach: the behaviour of the shrinking blob is distributed within the material itself and emerges from the simple and local interactions between the particles which comprise the blob. The path finding process is governed, to a large extent, by the spatial configuration of the arena and the obstacles within the arena. Since the blob initially occupies all of the space within the arena the path finding method may be described as subtractive — all redundant or inefficient paths are removed during the shrinkage process. This is achieved by withdrawal of pseudopodia (for example from dead-ends in the arena) and also by displacement of the blob by the repellent

fields emitted from the gradually exposed obstacles. Unlike chemical-based approaches the method is not initiated at either the path start or end points but is initialised by shrinkage from the arena boundary. Diffusion from the source points still occurs but is merely used to anchor the blob material at these points and does not require propagation of the diffusion front throughout the entire arena. Likewise, repellent diffusion occurs from the boundary (for collision-free paths) and from obstacles (for obstacle-avoiding paths) but this diffusion also is only local and does not require propagation throughout the entire arena.

In this and previous chapters we have examined the network adaptation behaviour of the multi-agent model. The relative predictability of the model adaptation is due to the smooth particle flow that occurs when particle collisions occur under the default motor behaviour. In the *Physarum* plasmodium the protoplasmic flux is not as uniform or predictable. Differences in protoplasmic transport cause temporary blockages, changes in pressure, surging transport of material and oscillating thickness of the plasmodium, and network adaptation is typically more complex and unpredictable. Chapters 15 and 16 demonstrate how such oscillatory phenomena emerge (and can be usefully utilised) in the virtual plasmodium when smooth particle flux is de-activated.

Part IV

**From Emergent Oscillations
to Collective Transport
and Amoeboid Movement**

Chapter 15

Emergence and Transitions of Spatio-temporal Oscillations

“Shake, baby, shake, you know I can fit you in my arms.
Brake, baby, brake, taking me in with all your charms.”

(Emma Anderson, 1996.)

15.1 Introduction

In this chapter we experimentally investigate the re-generation and synchronisation of oscillation patterns in *Physarum*, and use the virtual plasmodium model to replicates the process. This chapter mainly consists of two parts: First we present experimental observation of oscillatory behaviour in the *Physarum* slime mould, and then present modelling results of oscillatory patterns, pattern transitions and synchronisation behaviour. Experimental work and data analysis using plasmodium of *Physarum* in sections 15.2 and 15.3 was performed by Dr. Soichiro Tsuda [259].

15.2 Oscillatory Behavior in the *Physarum* Plasmodium

15.2.1 Experimental Setup

Physarum cells were cultured on 1.5 % agar gel in the thermostatic chamber and fed with oat flakes once a day. They were starved at least for 12 hours prior to experiments.

To observe the regeneration process of the cell, a tubular structure of a fully-developed *Physarum* cell culture is cut with a sharp scalpel. Liquid protoplasm draining from the cut is collected by tweezers and transferred in a well of a mask on a 1.5 % agar gel and smoothed so that the whole well is filled with the cell (Fig. 15.1a). The liquid protoplasm gels soon

after it is transferred to the dish and starts the body restructuring process in order to become a single plasmodial cell. The dish is covered with a lid to prevent the cell from drying out, placed under a microscope (Leica Zoom 2000, Germany) and illuminated from underneath with monochromatic light of wavelength 600 nm (Fig. 15.1b). The *Physarum* plasmodium is known to be insensitive to the wavelength of light in terms of the cellular oscillation activity [265]. A microscope camera image was taken every 3 seconds for over 5 hours. As the brightness level of a pixel in an image is inversely proportional to the thickness of the cell, the relative thickness oscillation can be calculated by image analysis.

We tested five different well diameter: 1.5, 3.0, 4.5, 6.0, and 7.5 mm. The wells were made from polycarbonate, printed by a 3D printer (Fused Deposition Modelling (FDM) Titan). By changing the well size, the cell size can be controlled because the plasmodium stays inside a well throughout the experiment because it prefers wet areas (i.e. agar) and does not grow on the mask.

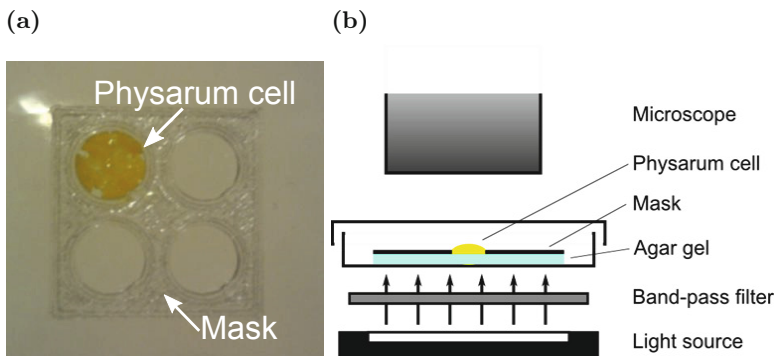


Fig. 15.1 Experimental setup for *Physarum* cell oscillation. (a) a piece of *Physarum* plasmodium is placed inside a hole of a mask on 1.5 % agar gel (invisible in the figure). (b) A schematic illustration of the setup. The cell in a Petri dish. The cell thickness oscillation is recorded under a microscope with back lighting through a band-pass filter.

15.2.2 Image Analysis

Recorded images are processed for analysis on a PC with following steps: (1) Each image is converted from RGB to greyscale image. (2) Subtract an image taken at t from an image at $t - \Delta t_1$. By this process thickness change of the *Physarum* plasmodium can be extracted because thickness is inversely proportional to the brightness of an image (i.e. the backlight transmitted through the cell). In this research, $\Delta t_1 = 15$ was chosen empirically. (3) Apply a moving average filter spatially over 21×21 pixels and temporally over 7 images on each pixel of the subtracted image. This is an image

smoothing filter in order to reduce camera noise in the image. (4) Rescale the image into 5 greyscale levels according to the maximum and minimum of the subtracted image.

15.2.3 Phase Synchronisation Analysis Using Hilbert Transform

In order to estimate the time for a whole cell to be synchronised, we define a measure based on phase difference of signals [266]. Given a periodically oscillating signal $s(t)$, the Hilbert Transform of the signal $s_H(t)$ is defined as follows:

$$s_H(t) = \frac{1}{\pi} \text{P.V.} \int_{-\infty}^{\infty} \frac{s(\tau)}{t - \tau} d\tau \quad (15.1)$$

where P.V. means that the integral is calculated in the sense of the Cauchy principal value. Based on this, the analytic representation of the signal (in short, analytic signal) $\zeta(t)$ can be defined as :

$$\zeta(t) = s(t) + is_H(t) = A(t)e^{i\phi(t)} \quad (15.2)$$

where $A(t)$ and $\phi(t)$ are *instantaneous amplitude* and *instantaneous phase* of the signal at time t . This is a concept originally introduced by [267] and widely used as a mathematical representation of an arbitrary signal [268, 269]. From Equation 15.2, the instantaneous phase $\phi(t)$ is $\phi(t) = \tan^{-1}(s_H(t)/s(t))$. Given two signals $s_1(t)$ and $s_2(t)$, a phase difference between them can be calculated as:

$$\phi_1(t) - \phi_2(t) = \tan^{-1} \frac{s_{H,1}(t)s_2(t) - s_1(t)s_{H,2}(t)}{s_1(t)s_2(t) + s_{H,1}(t)s_{H,2}(t)} \quad (15.3)$$

where $\phi_1(t)$ and $\phi_2(t)$ are instantaneous phases of signals s_1 and s_2 . If the phase difference becomes constant over time, this means the two signals are synchronised in terms of the phase.

This method is developed by [270] in order to study the synchronisation of chaotic oscillators, in which the amplitudes of signals can be uncorrelated but the phases can be synchronised. Thickness changes of the *Physarum* slime mould also show chaotic oscillations.

We focus on temporal thickness oscillations at 69 points (7×7 grid points and additional 20 points around the grid) of recorded images, which cover the most of the cell in the image. Using one of the 69 points as a base point, phase differences $\Phi_i(t)$ between oscillations at the base point and one of other 68 points were calculated by Equation 15.3:

$$\Phi_i(t) = \phi_i(t) - \phi_1(t) \quad (i = 2, \dots, 68) \quad (15.4)$$

Finally, the synchronisation index $S(t)$ at each time step is defined as follows:

$$S(t) = \text{Var}(\langle \Phi_i(t + \Delta t_2) - \Phi_i(t) \rangle) \quad (15.5)$$

where $\text{Var}()$ is a function to calculate the variance and $\Delta t_2 = 40$. There are two possible cases when the cell is synchronised: Oscillation at the base point is (1) synchronised with other points. (2) not synchronised but oscillations between other points are synchronised. In the former case $\Phi_i(t + \Delta t_2) - \Phi_i(t)$ (slope of phase difference curve) becomes nearly zero because $\Phi_i(t)$ for all i is constant. Accordingly the synchronisation index $S(t)$ becomes small. In the latter case, slopes $\Phi_i(t + \Delta t_2) - \Phi_i(t)$ are non-zero, but they take similar values due to the synchronisation between other points. As a result, the variance of slopes becomes small, and $S(t)$ also becomes small.

From preliminary experiments, we defined that the cell is fully synchronised when $S(t)$ goes below 1. In other words, we define the length of time from the start of an experiment to the point when the synchronisation index goes below 1 as the time required for a whole cell to become synchronised (hereafter referred as “synchronisation time”). We ignored the first 30 min because, during this period, the *Physarum* cell does not move or oscillate at all but $S(t)$ can be below 1 even though the cell is not synchronised.

15.3 Experimental Results

15.3.1 Oscillation Patterns of Body-Restructuring *Physarum* Cell

When observed under the microscope, a cell of *Physarum* plasmodium just transferred to a well does not look uniform because of gentle mixing. It consists of small dark granules and transparent parts. Granules are considered to contain organelles and transparent parts are endoplasm, liquid part of plasmodial protoplasm. A cell in a larger well contained more granules in it.

A typical time course of the cell reconstruction was as follows: Within 10 minutes, the plasmodial cell starts contractile oscillation. At this stage, each granule independently contracts and the oscillation rhythms are unsynchronised to oscillations of other granules (Fig. 15.2a). Gradually small granules start to merge together with neighbouring granules, and areas that show a synchronised oscillation become larger and larger along with the fusion of granules (Fig. 15.2b). As a result, an area within which a synchronised oscillation is observed extends over time until the whole cell in a well shows a synchronised oscillation (Fig. 15.2c).

To illustrate this, *Physarum* thickness change of each image on a line (a grey arrow in Fig. 15.2c) is plotted against time as in Fig. 15.2d. The total length of the plot is about 1 hour. This space-time plot shows how a globally synchronised pattern emerges in the plasmodium. As mentioned above, small granules oscillate independently at an early stage of the experiment.

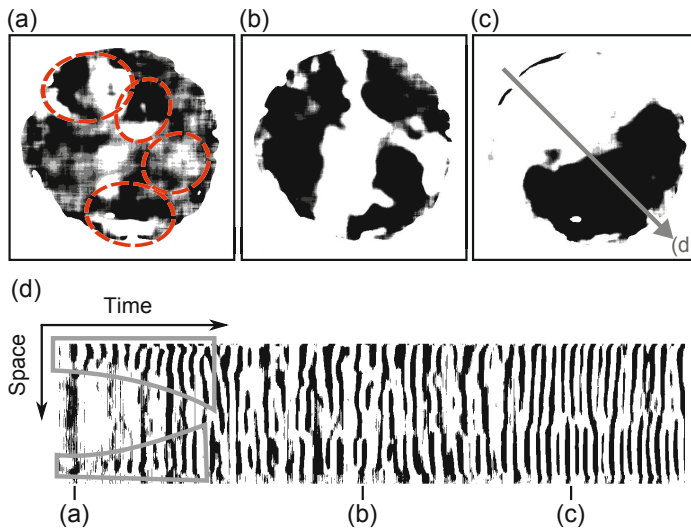


Fig. 15.2 (a) An example of plasmodial oscillation pattern in 1.5 mm well at an early stage. Black regions indicate thickness is increasing whereas white ones is decreasing. Synchronised areas are indicated by dotted circles. (b)(c) Snapshot images taken after 30 and 50 minutes, respectively. (d) space-time plot of *Physarum* oscillation along an arrow in (c). First 1.2 hours from the start is plotted. (a-c) in the plot corresponds to the above snapshots of *Physarum* thickness oscillation (a-c).

There are two oscillating granules on the line, one in the upper part and another small one in the bottom part of the plot, which are indicated by grey rectangles in Fig. 15.2d. These two parts become larger and larger over time. This means the area exhibiting synchronous oscillation is gradually expanding. After approximately 30 minutes the spatio-temporal pattern becomes somewhat chaotic (the period around (b)). Various types of complex oscillating patterns can be observed in this period and there are a few areas where synchronised oscillation can be observed (In the case of Fig. 15.2b, roughly 3 synchronised areas can be found). Those areas eventually synchronise together. At this stage, the whole cell shows a fully synchronised oscillation and patterns in Fig. 15.2d was periodic (the period around (c)).

After the cell reached this phase, there were mainly two types of oscillation patterns observed: bilateral oscillation (anti-phase oscillation between two halves of a well as in Fig. 15.3a) and rotating wave pattern (clockwise or anti-clockwise, Fig. 15.3bc). In some rare cases a convective wave pattern (two rotating waves colliding at the centre of a well) was observed, but it did not persist for a long period. These oscillation patterns were constantly switching between one another after a couple of cycles. Fig. 15.3d illustrates such frequently changing patterns. This is a spatio-temporal thickness oscillation plot along a circle indicated in Fig. 15.3bc. In this case, it shows a

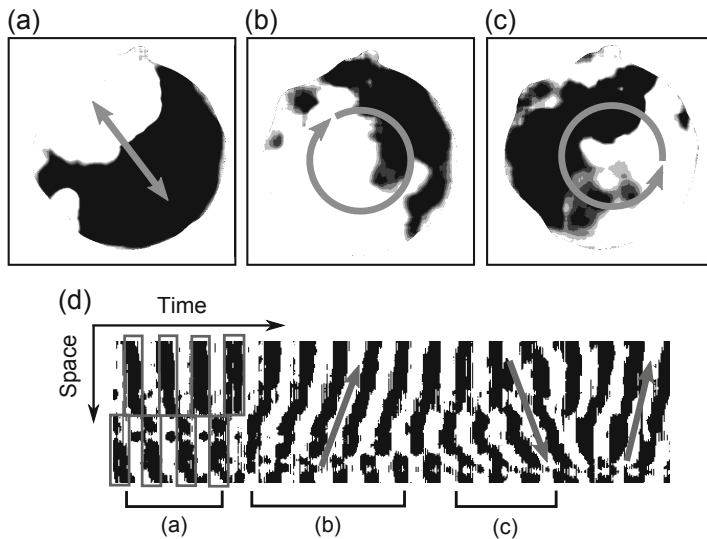


Fig. 15.3 (a) space-time plot in (e) is plotted along the grey arrow, 360 points. (b) Bilateral oscillation (c) clockwise oscillation (d) anti-clockwise oscillation of a *Physarum* plasmodium in 4.5 mm well. (e) space-time plot of *Physarum* oscillation. (b-d) in the plot corresponds to the period when above oscillation patterns were observed.

bilateral oscillation at first, represented as checkerboard-like patterns where upper and lower halves show alternating stripe patterns (grey squares in Fig. 15.3d). The pattern soon switches to a clockwise rotating wave (upward grey arrow), followed by switching to an anti-clockwise rotating wave (downward grey arrow). It comes back to a clock-wise rotation pattern in the very end of the plot.

The same time development of oscillation regeneration as described above was observed in all of the five well sizes investigated. In all cases independently oscillating granules gradually fuse together, eventually forming one single cell, showing a synchronised oscillation. After complete fusion occurred oscillation patterns observed were mostly bilateral oscillation or rotating wave patterns in all sizes. The larger the cell becomes, the bigger the size of travelling waves in the cell becomes accordingly. This would suggest that the *Physarum* plasmodium has no fixed-size “unit” for generating oscillation, and may be related to the size-independent behaviour of the slime mould. It is known that the cell develops a phase gradient within the body when exposed to non-uniform environmental stimuli [37]. This works as a positional information field [129], which affects the migration direction of the plasmodium (for example when approaching a nutrient source). In principle, the positional information can be formed independent of the size: If the cell size becomes larger, the field (phase gradient) becomes larger. Thus, whatever the cell size is, the

plasmodium is able to react to external stimuli in the same manner. What we observed here appears to be one of the size-independent behaviours of the plasmodium. The cell is able to develop a fully synchronised oscillatory pattern and the types of patterns were similar whatever the cell size was. In the following section, we focus on the synchronisation time for a whole cell to be fully synchronised, using the synchronisation index defined in Section 15.2.3.

15.3.2 Phase Synchronisation Analysis

Fig. 15.4a,c,e show time development of phase differences $\Phi_i(t)$ for 1.5, 4.5, and 7.5 mm wells, respectively. Fig. 15.4b,d,f are corresponding synchronisation index $S(t)$. Results of the analysis of the first 15000 s (250 min) recording data are plotted.

These examples represent different types of time course evolution of the synchronisation index. Fig. 15.4a and b show that the cell oscillation becomes synchronised from 5500 to 7500 s. Please note that the phase difference curves (Fig. 15.4a) are not flat but constantly increasing, while the synchronisation index (Fig. 15.4b) is small. This indicates that the base point for phase difference calculation is not synchronised with other points, but other points are synchronised. The phase difference curves then become unstable for approximately 4500 s, as represented by the increase in synchronisation index. This is because the synchronised cell showed various complex pattern changes (as discussed in Fig. 15.3, but more frequent). The synchronisation index $S(t)$ is not a good measure if the cell shows frequent oscillation pattern changes because when it changes from one oscillation pattern to another, the phase difference between two points changes. This makes the phase difference curve noisier, but it does not mean there are several independent oscillation waves in the cell. Only one single travelling wave can be found there, but with more frequent pattern changes. At the end of the plot, the phase difference curves become constant and accordingly the synchronisation index comes back to a lower level.

Fig. 15.4c and d are a normal case of cell synchronisation. The *Physarum* cell reaches a fully synchronised phase around at 3600 s and after this point the synchronisation index remains low throughout the experiment. This means the cell remains to be synchronised and did not go through frequent pattern changes.

In the last case, Fig. 15.4e and f, the curves become flat around at 4500 s, as in the previous two cases. However, in the latter half of the plot, the synchronisation index demonstrated larger values. This was caused by small mushroom-shaped blob structures growing vertically from the cell. In most cases cells developed many of such structures in the cell because horizontal growth was restricted by the wall of the well and therefore it was only allowed to grow in the vertical direction. If they were small, they did not affect the synchronisation index. However, in Fig. 15.4e and f, the vertical growth was very large and it affected phase relationships between local points.

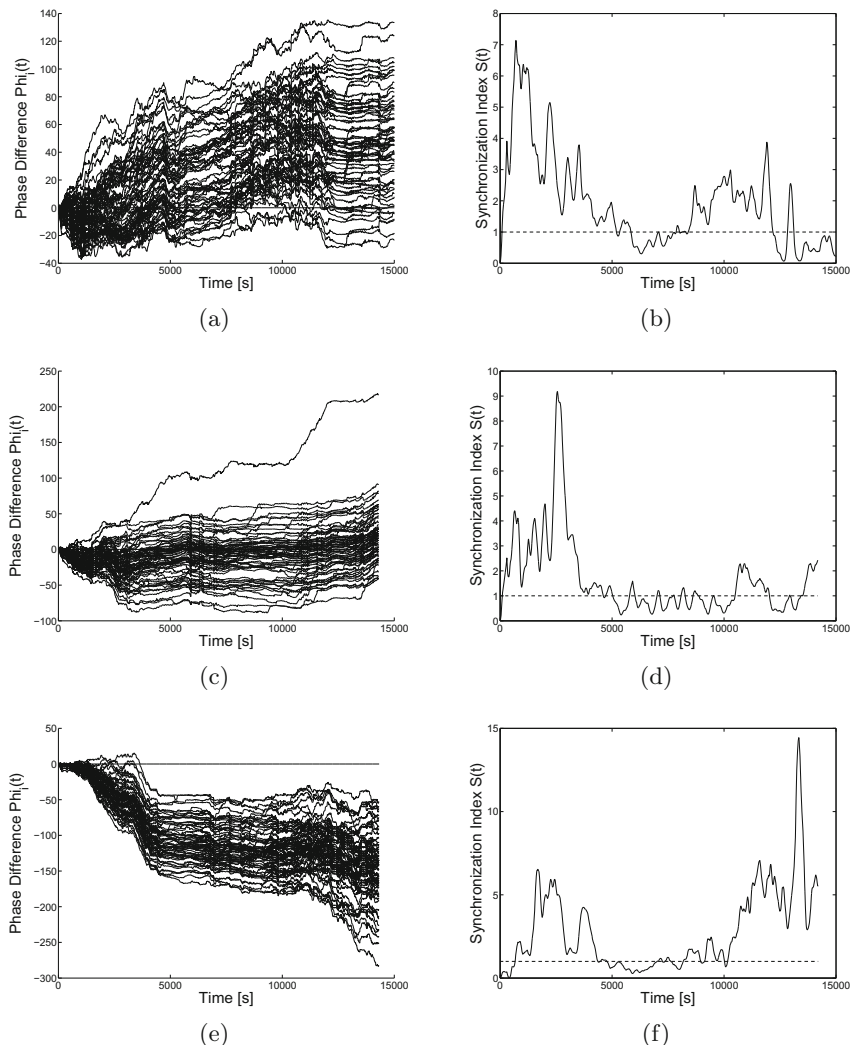


Fig. 15.4 Time development of phase difference and corresponding synchronization index $S(t)$ for 1.5 mm well ((a) and (b)), 4.5 mm well ((c) and (d)), and 7.5 mm well ((e) and (f)). Dotted lines in (d-f) indicate the threshold ($= 1$). First 15000 s data were plotted.

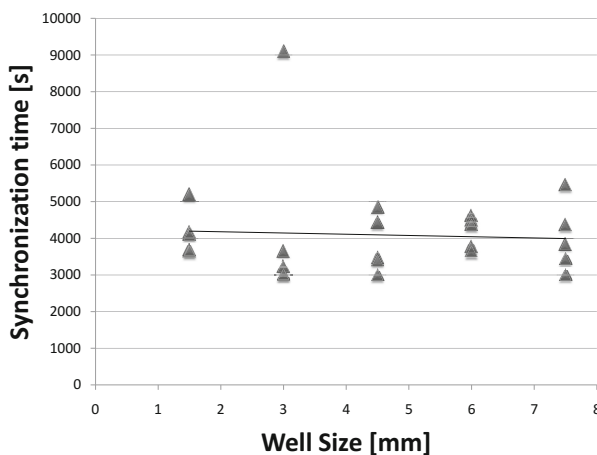


Fig. 15.5 A scatter plot of synchronisation time against well size. Synchronisation time remains constant over the well sizes.

Fig. 15.5 is a plot of synchronisation time (i.e. the length from the start of experiment to the point when the synchronisation index $S(t)$ goes below 1 for the first time) against each well size. Five repeat experiments were performed for each well size. Although there is one exception in the 3.0 mm well experiment, in all the cases they take about 4000 s for a cell to be fully synchronised. This means that a plasmodium whose diameter is smaller than 7.5 mm is able to regain a synchronised contractile oscillation in 1 hour or so. In raw videos of the experiment, it was observed that cells fully synchronised in 1 hour (3600 s) or so.

15.4 Oscillatory Behaviour in the Particle Model

Although the particle model is able to reproduce many of the network based behaviours seen in the *Physarum* plasmodium such as spontaneous network formation, shuttle streaming and network minimization, the default behaviour does not exhibit oscillatory phenomena and inertial surging movement, as seen in the organism. This is because the default action when a particle is blocked (i.e. when the chosen site is already occupied) is to randomly select a new orientation, resulting in very fluid network evolution. As demonstrated in Chapter 3 the networks exhibit minimising properties, Plateau angles and adhere to von Neumann's law. In this respect they resemble the evolution of soap films and the lipid nanotube networks seen in [111].

The oscillatory phenomena seen in the plasmodium are thought to be linked to the spontaneous assembly/disassembly and contraction of actomyosin fibres within the plasmodium which generate contractile forces on the protoplasm. In the immobile gel phase the fibres contract, exerting a

force on the protoplasmic sol. In the mobile sol phase the liquid material is transported within the protoplasmic tube network. Reproducing this pattern of changing transport resistance in the particle model requires only a simple change to the motor stage. Instead of randomly selecting a new direction if a move forward is blocked, the particle increments separate internal coordinates until the nearest cell directly in front of the particle is free. When a cell becomes free, the particle occupies this new cell and deposits chemoattractant into the lattice. The effect of this behaviour is to remove the fluidity of the default movement of the population. The result is a surging, inertial pattern of movement, dependent on population density (the population density specifies the initial amount of free movement within the population). The strength of the inertial effect can be damped by the parameter (pID , set to 0.05 for all experiments) which sets the probability of a particle resetting its internal position coordinates, lower values providing stronger inertial movement.

15.4.1 *Emergence of Oscillatory Activity in the Model Plasmodium*

When this simple change in motor behaviour is initiated surging movements are seen and oscillatory domains of chemoattractant flux spontaneously appear within the virtual plasmodium showing characteristic behaviours: temporary blockages of particles (gel phase) collapse into sudden localized movement (solation) and vice versa. The oscillatory domains themselves undergo complex evolution including competition, phase changes and entrainment. We utilize these dynamics below to reproduce the oscillatory patterns seen in the *Physarum* plasmodium at different well sizes.

The particle lattice was configured to reflect the environment of a single well containing and confining the plasmodium. Movement was prevented outside this region (specifically, if the border region was encountered, a random change in direction was made). The population size p was fixed at 90% of the well size, leaving 10% of the free space available for movement. No growth/shrinkage rules were implemented for these experiments. The results show patterns of the concentration of chemoattractant flux within the population. Areas of greater flux are shown as darker regions. Since deposition of chemoattractant only occurs when movement is successful the concentration relates to the amount of active transport caused by oscillations in plasmodium thickness. This is indirectly related to thickness changes of the plasmodium detected in laboratory conditions and there is a reciprocal relationship between contraction of the plasmodium in a local region and subsequent transport of material from that region, as noted by [42].

The reciprocal relationship can be visualised in the model in a simple experiment where the arena (150×50 pixels) was patterned into the shape of a dumbbell consisting of a narrow central channel connecting two opposite circular wells. Square 20×20 pixel regions within each end were sampled

from the trail lattice at every 5 scheduler steps (Fig. 15.6a). The particle population (2250 particles) was inoculated within the arena with parameters $SA\ 22^\circ$, $RA\ 22^\circ$, $SO\ 7$) and oscillatory movement was initiated. After a short period reciprocal oscillations of particle trail flux were seen each end of the dumbbell (Fig. 15.6b) which exhibited anti-phase oscillations (see plots in Fig. 15.6g and h).

The validating observation emergence of regular oscillatory activity in the dumbbell arena enabled the exploration of oscillation patterns within single well structures (due to the complex evolution of the patterns the reader is encouraged to refer to the supplementary recordings). The output of the model is represented by snapshots of the lattice, an 8-bit greyscale image sampled at every ten scheduler steps. Since both the experimental and model output is in the same format (a digitized image), the spatial and temporal filtering and analysis of the model output is identical to the experimental output. The sampling rate is sufficient to capture the oscillation pattern transitions. However, for the phase synchronisation analysis the sampling rate was increased to record an image every scheduler step.

Initial experiments with the sensory parameters SA and RA showed that a wide range of values yielded complex oscillatory patterns in single well arenas (see supplementary video recordings for chapter 15). The differences in base pattern type at different SA/RA combinations were caused by differences between sensor arm angle and rotation angle. Whichever SA/RA was used there was a common evolution to all experiments. There was an initial period where multiple foci of oscillating flux appeared. These small regions gradually exerted an influence upon each other and entrainment of patterns was seen. The size of the entrained regions depended upon both the SO parameter (sensory radius) and the well size. We selected a small sample from the parameter ranges (specifically $SA\ 22.5^\circ$ and $RA\ 45^\circ$) in an attempt to explore the complex experimentally observed phase transitions. These SA/RA settings were used because, when considering the transport networks, they generated foraging-like behaviour. Greyscale output images from the model were saved every 10 iterations and a spatio-temporal moving average and thickness extraction for space-time plots were calculated as per the experimental method above.

15.4.2 Consistent Oscillation Pattern with Fixed Scale

When a fixed value was used for the Sensor Offset (SO) scale parameter, there was an initial period of chaotic interactions until a stable type of oscillatory pattern predominated. Occasionally the oscillatory behaviour was interrupted, however variations on this pattern were then observed throughout the time course of the simulation (Fig. 15.7). Although the fixed SO parameter was able to successfully generate emergent oscillatory behaviours, there was no predictable transition between the pattern types observed experimentally. When higher values of SO were used (with identical SA/RA)

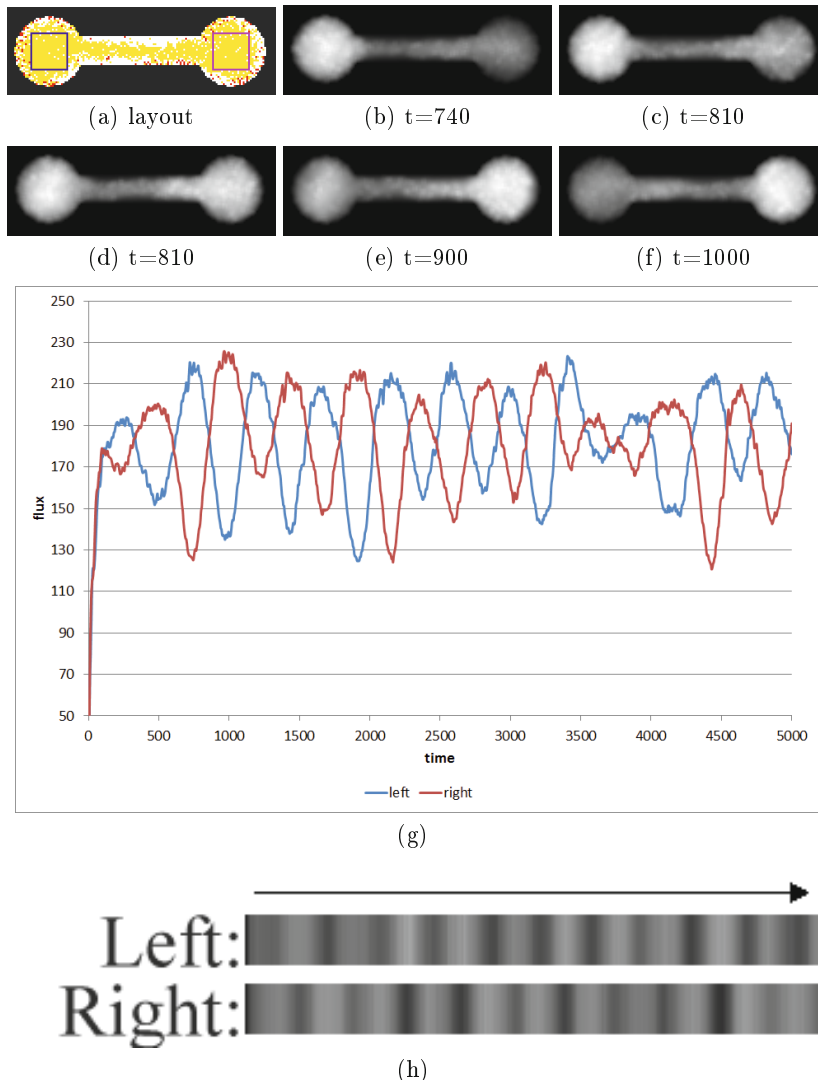


Fig. 15.6 Emergence of reciprocal oscillations in a dumbbell-shaped arena. a) arena with square sampling areas (cyan and pink) and particle population (yellow), b-f) oscillation of flux from left chamber to right chamber (brighter regions indicate greater flux), g) plot of anti-phase oscillations in left and right chambers, h) phase plot visualisation of reciprocal oscillations between left and right chambers (separate experiment),

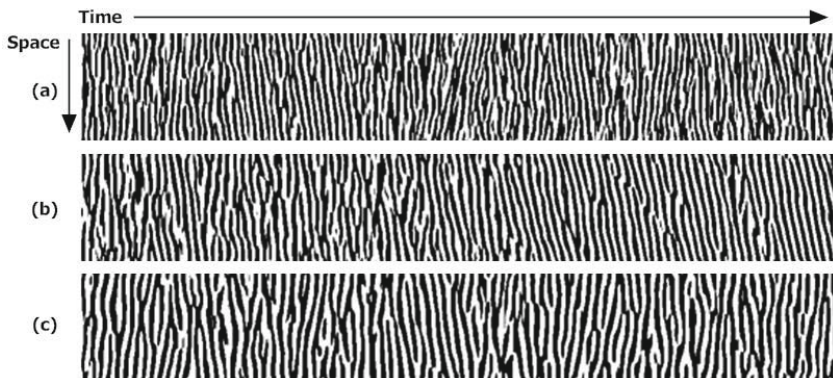


Fig. 15.7 A constant SO parameter during an experimental run results in no significant changes in pattern type. Experiment iterated for 10,000 steps. Plots were sampled from a circular pattern within the well at half the well radius (as indicated by arrow in Fig.15.9a). Well size were all 200 pixels, SO for each run: (a) 9 pixels, (b) 21 pixels, (c) 41 pixels.

fewer independent foci of oscillations were seen. When the SO parameter increased significantly the type of oscillation pattern changed. This supports the idea that the independent domains in the plasmodium interact over an increasingly large scale.

15.4.3 Pattern Transitions with Increasing Scale

To reproduce the experimental observation of the growth and fusion of oscillatory domains, and resultant change in pattern type, we gradually increased the SO parameter during the experiment. Beginning with an SO value of 3 pixels, the SO parameter for all particles was increased by 3 pixels every 500 iterations of the model. This resulted in a larger local sensory radius for each particle, causing the behaviour to be influenced by local particles at larger distances. An entrainment of movement was observed as the collective sensory coupling increased. The results showed clear transitions between different pattern types which were observed visually and in terms of the space-time plots (Fig. 15.8). The order of pattern transition tended to be: (1) Chaotic behaviour, (2) Interacting domains, (3) Rotational pattern, (4) Lateral type patterns, and (5) Pulsatile annular pattern. However, as with the experimental plasmodium, some reversion to earlier patterns was also observed. The observation of these pattern types matches those found experimentally with the plasmodium fragments in this report and from the patterns which emerged from protoplasmic droplets presented in [28]. The term *Lateral type patterns* requires further explanation as it not only refers to the bilateral patterns described in this report and in [28] but also to the lateral patterns

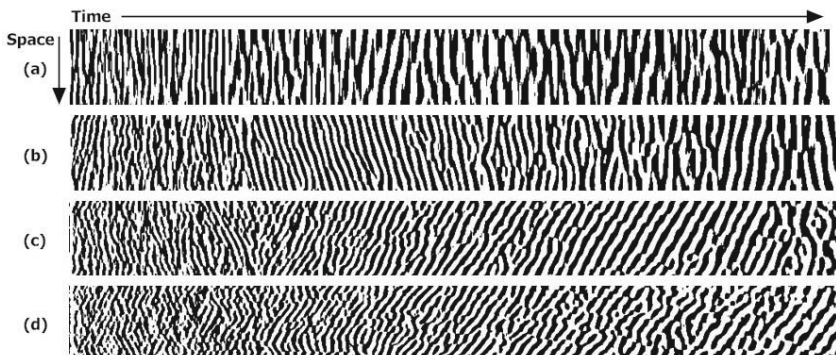


Fig. 15.8 When increasing SO parameter during an experiment, well diameter affects pattern types, transitions and timing of transitions. Experiment iterated for 10,000 steps. Plots were sampled from a circular pattern within the well at half the well radius (as indicated by arrow in Fig. 15.9a). Well sizes: (a) 100 pixels, (b) 200 pixels, (c) 300 pixels, (d) 400 pixels.

observed in veinless plasmodia in [271], described by the authors as upward or opposite zonal waves and splitting patterns. We may speculate that the different lateral type patterns observed are actually all the same pattern type which may differ because of the locations at which they are initiated.

15.4.4 Discriminating between Pattern Types

At the smallest well size (100 pixels) entrainment of the entire particle collective occurred relatively quickly (Fig. 15.8a). The rotation patterns within this small well were simply two rotating regions of light and dark areas. Larger wells produced propeller-like rotational patterns (e.g. Fig. 15.9a), with increasing numbers of ‘propellor’ vanes as the well sizes increased. Synchronous oscillations (both bilateral and later with a pulsatile annular pattern) were observed some time after the rotational patterns. When larger well sizes were used, there was a longer time period before transition between pattern types. This can be seen from the phase plots in Fig. 15.8b and c, which show increasing delays before the onset of rotational patterns. The effect of the larger well size is also evidenced by the rather fragmented aspect to the phase plots which indicate a weaker initial coupling between different regions (Fig. 15.8d). Although the model was able to replicate the oscillatory patterns and transitions, there appeared to be some limitation on the maximum well size for entrainment of the particle population to completely occur. With the largest well size (400 pixels), the phase plots indicate the regions stay independent for much longer periods. When SO was very large (greater than 80 pixels) the large scale oscillations became frozen and the only flux of particles was

along narrow domains within the collective. Whether this behaviour is a feature of the real plasmodium, or merely a modelling artifact, requires further investigation.

The phase plots of the regular periods of oscillation patterns seen with SA 22.5° and RA 45° (rotation, bilateral and annular synchronisation) can be seen in Fig. 15.9. Animated video recordings of the entire well phase patterns and transitions can be seen in the supplementary material. Experiments using other SA/RA settings produced other oscillatory patterns, including the convective oscillatory patterns seen in the larger well experiments. Experiments with the particle model suggest that the causes of the changes in oscillatory regimes (and the reversion to previous patterns) may be the gradual increase in sensory influence. As the SO parameter increases, previously separated oscillators begin to interact and some begin to predominate. The increase in sensory influence also appears to reduce the freedom of movement of the oscillatory patterns. The initially separate oscillatory bodies adopt spiral and circular paths. These independent circular paths then fuse into a single circumferential path (rotation pattern). The scope for movement is further reduced by the emergence of synchronous oscillations (movement is limited by the diameter of the well in bilateral oscillations, and to a radius distance with annular oscillations). This observation is difficult to quantify, however, and does not simply explain the reversion to previous patterns which possess greater freedom of movement. It is plausible that, just as there appears to be a mechanism within the plasmodium for increasing influence over distance, there may be another opposing mechanism which decreases influence over distance. The polymerisation/depolymerisation of actin filaments within the plasmodium could be one possible mechanism of increasing/decreasing the region of influence.

15.4.5 Phase Synchronisation with Increasing Scale

Phase synchronisation analysis was also performed on the model output. When the SO parameter was fixed at 19 pixels (which is large enough to generate a stable rotational oscillation pattern) a plateau in the phase difference curve similar to that observed experimentally was observed after 1000 scheduler steps (Fig. 15.10a). This plateau coincided with the establishment of the regular oscillation pattern and a corresponding reduction in the synchronisation index was also seen (Fig. 15.10b). The flattening of the phase difference curve persisted until after 4000 steps when the phase curve again increased. The cause of this increase is a partial collapse of the pattern in the centre of the well caused by interacting fragments (although the pattern, taken as a whole, does persist). To assess the effect of pattern transitions on phase synchronisation the SO parameter was set to 10 and increased every 2000 steps by 10 pixels. This rather large step increase and long time duration between increments was chosen to maximize the time between transitions

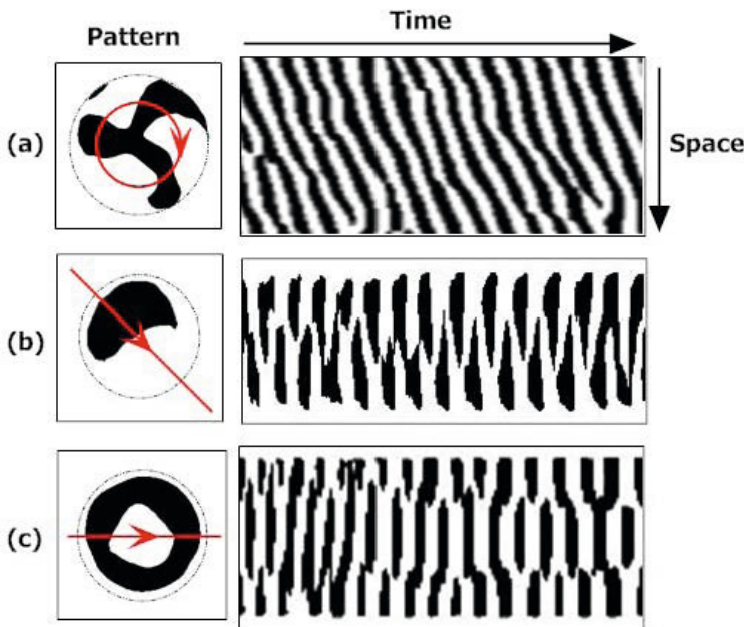


Fig. 15.9 Characteristic oscillation patterns observed within the particle model. Left side indicates pattern type and sample through virtual plasmodium. Right side indicates space-time plot. (a) Rotating pattern observed in 200 pixel well, (b) Bilateral oscillation observed in 100 pixel well, (c) Synchronous annular pattern observed in 100 pixel well.

so that any phase synchronisation would be discernible, and to ensure pattern transitions at each increment. Even so, the effect of transitions reduces the clarity of the phase synchronisation analysis. The phase difference curve shows that the pattern transitions (from disorganized, to rotational, lateral ('zonal' type) and annular) reduce the apparent flattening of the difference curve. When the SO parameter is increased above 40 the phase difference increases significantly (Fig. 15.10c and d). The plot of synchronisation index shows that after each increase in SO (every 2000 steps) there is an increase in index which reduces as the new oscillation pattern stabilizes. This pattern continues with each change of SO until the index starts to increase greatly as SO is increased above 40. As with the experimental results we found that the pattern transitions significantly affect the phase synchronisation of the separate regions of the well. The limitations caused by the frequent pattern transitions prevented us from analysing the effect of well size on phase synchronisation to a sufficient degree of accuracy.

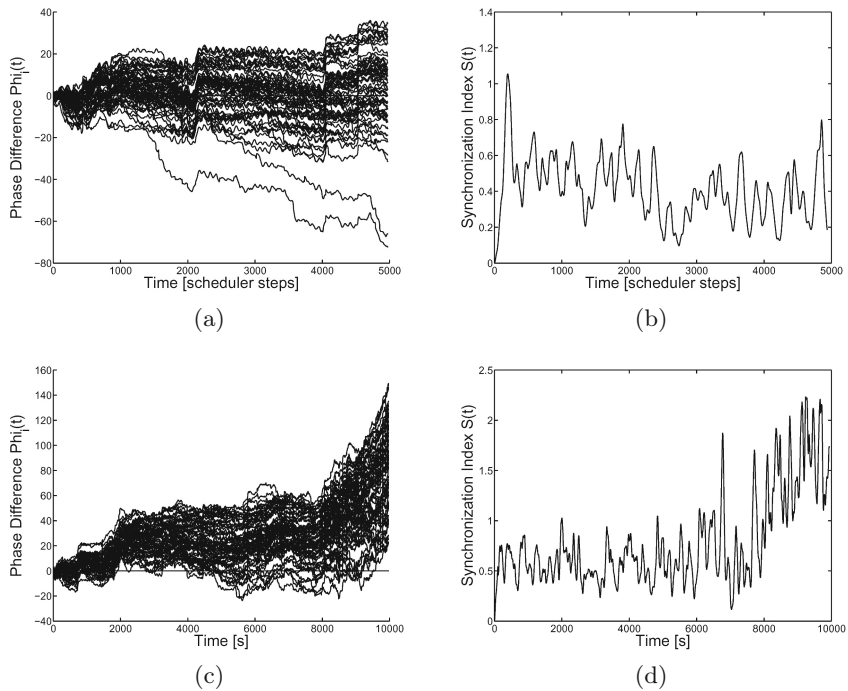


Fig. 15.10 Time development of phase difference and synchronisation index in model with 200 pixel well $S(t)$ for fixed SO 19 ((a) and (b), run for 5000 steps), and increasing SO , starting at 10 and increasing every 2000 steps by 10 ((c) and (d)), run for 10000 steps.

15.5 Summary: The Emergence of Synchronous Oscillations

We experimentally investigated the regeneration process of the *Physarum* plasmodium in a well and computationally modelled oscillation patterns of the cell observed in the experiments using a particle model. In experiments with real *Physarum* cells, it has been found that cells exhibited similar time course of oscillation regeneration independent of the well size. A granule-like cell serves as an oscillator unit at first and by the fusion of granules the cell eventually reaches a state in which all the parts in the cell are synchronised. [28] observed oscillation patterns of unbounded *Physarum* cells (approximately 1.5 mm diameter) during the regeneration of contractile oscillation and identified 4 distinctive patterns: standing wave, drifting spirals, stable spirals, and synchronous oscillation. Although their condition is similar to ours, in particular the case of the 1.5 mm well, our experiments did not confirm all the patterns they reported. This is possibly because of the boundary for the cell. In their experiments, cells were placed simply on a plain agar

gel and able to move freely after they completed the reconstruction of the body plan. On the other hand, in our setup cells are constrained to move only within a well. This may well have affected the way a plasmodium oscillates, as it is empirically known that the *Physarum* plasmodium shows a stable and sustained oscillation pattern when it is free to move and grow. This would partly explain the frequent pattern change we observed. Because of the surrounding walls, the movement of the plasmodium is constantly blocked and it may have led to more frequent pattern changes in the fully synchronised phase.

Although the physiological mechanism of cell synchronisation is yet to be investigated further, physiological findings of the cell suggest that there are two factors involved in the oscillation synchronisation [272]: Ectoplasmic local contraction and endoplasmic flow. The ectoplasm (gel phase) of the *Physarum* protoplasm contains actin in filamentous form (F-actin). This molecule is periodically polymerized and fragmented, which creates cell contraction and relaxation rhythm in a local part of the cell. The endoplasm (sol phase) flow generated by the contraction rhythm mediates the oscillation synchronisation between local parts, otherwise local rhythms do not synchronise at all [273]. In the experiments with real plasmodium cells, we observed that small granular cells showing independent oscillations in the beginning were gradually synchronised with time. Given the previous physiological findings above, our observation can be considered as a process of the endoplasmic flow network development, which coordinates the synchronisation between granular cells. Phase synchronisation analysis showed that cells in all the well sizes tested here are able to become synchronised in 4000 s or so (Fig. 15.5). This result would suggest that the *Physarum* plasmodium is able to develop an endoplasmic flow network within a fixed time, as long as the cell is smaller than 7.5 mm. It should be noted, however, that the largest well tested was 5 times bigger than the smallest one and nevertheless cell oscillations became synchronised within the same period of time. This could be considered as another example of the size-independent properties of the organism.

The particle based simulation demonstrated the emergence of oscillatory behaviour from simple coupled particle interactions. With fixed particle coupling values of the *SO* parameter we found that patterns of oscillations emerged whose particular characteristics were dependant on the local interaction distance (*SO* parameter size). In our simulation, we also observed that the particle model replicates the transition between oscillation patterns well when the Sensor Offset (*SO*) parameter was gradually increased. Accordingly the whole system with large *SO* value acquired an (amorphous) interaction network, which effectively corresponds to the endoplasmic flow network in the plasmodium cell. The *SO* parameter effectively works as the coupling strength with neighbouring particles. As the *SO* parameter increased local competing oscillation patterns merged to form new pattern types. These pattern types were generally more restricted in their movement as *SO* increased.

It appears that the increasing interaction distance limits the degree of freedom of the oscillatory movement within the well, almost as if the pattern is forced to adapt to fit within the particular confines of the well shape.

Phase synchronisation analysis of the evolution of oscillation patterns in the particle model was also demonstrated. When a fixed *SO* value was used the phase difference analysis showed a flattening of the phase curve, indicating that independent regions of the well were synchronised in phase, a fact supported by the reduction in the synchronisation index during this period. For experiments with increasing interaction distance, however, the phase difference did not show significant or persistent flattening of phase differences due to the transition in oscillation patterns, although the synchronisation index appeared to indicate a gradual reduction in phase variance after the transition to a new pattern.

The emergence of complex oscillatory phenomena from the interactions between the simple and identical particles within the collective raises the question of how these oscillatory phenomena arise. The cause is due to transient interruption of particle motion created by the small modification to the motor behaviour when compared to the default (non-oscillatory) motor behaviour. In the default behaviour there is a generally uniform flux within the particle collective and any interruptions in flux (caused by blockages in highly populated areas) are quickly dissipated within the aggregate mass of particles as particles select new random directions when blocked. In the modified (oscillatory) motor behaviour, however, a blocked particle will maintain the same direction and thus blocked regions do not dissipate quickly and the mass of particles is separated into regions where movement is possible (regions containing some free space) or is not possible (static occupied regions). Since particles only deposit chemoattractant after successful forward movement the congestion free regions will accumulate more chemoattractant than congested regions. The increased difference of chemoattractant deposition in turn affects the particles' choice of direction (since particles are attracted towards regions of higher flux). A gradual entrainment of particle direction towards regions with higher concentration ensues, however these regions themselves become more likely to be congested due to the influx of particles. Moreover previously congested regions subsequently become less congested as the particles near this region were attracted to relatively vacant regions. An oscillation pattern thus emerges as particles move towards regions of higher flux. A complete 'gridlock' situation is avoided because the distribution of chemoattractant within the mass of particles is mediated by localised diffusion of the chemoattractant which causes a lag between the particles' motor and sensory coupling.

Although the collective behaviour of the particle population can generate emergent oscillatory behaviour very similar to that seen in *Physarum*, does it relate in any way to the actual physical interactions occurring within the plasmodium? The collective particle behaviour may be explained in terms of the *Physarum* plasmodium by relating it to the internal phenomena of

plasmodium contraction and subsequent protoplasm transport as a result of the contraction. Particle motion represents the spontaneous contraction and change in thickness of regions of the plasmodium, and the changes in local chemoattractant flux caused by particle motion represent the protoplasmic transport. It is known that when placed in a constrained architecture (for example a dumbbell shape) there is a reciprocal relationship between protoplasmic transport and plasmodium thickness [42]. In dumbbell configurations with a suitably wide connecting channel the contraction of one oscillator (one side of the dumbbell) results in flux towards the other side and the activity then reciprocates in the opposite direction and so on. We suggest that the particle interactions collectively mimic this behaviour in terms of freedom to move (vacancy) and lack of freedom to move (congestion). The emergence of large domains of vacancy and congestion arise from microscopic differences in movement which undergo amplification (due to the local positive feedback nature of the chemoattractant deposition and attraction), and the subsequent entrainment and competition between oscillators as the *SO* parameter is increased.

An important factor to consider is that all of the complex spatio-temporal oscillatory patterns (in both experimental and simulation findings) emerged from bottom-up local interactions between simple and identical components. That such complex oscillatory behaviour can emerge from simple interactions suggests further investigation into the role of relatively simple physical influences on adaptive behaviour. The amorphous nature of the *Physarum* plasmodium presents attractive possibilities from structural, computational and robotics perspectives. The plasmodium may be considered, on one hand, as a programmable material whose morphology may be specified and altered by +ve (chemoattractants, warmth) and -ve (chemorepellents, light etc.) stimuli. On the other hand, the material itself displays impressive and well documented computational properties which are also, to some degree, subject to external control. The computational possibilities of even small fragments of *Physarum* plasmodium arise from the same simple interactions and are distributed throughout the material, placing it in the category of programmable and functional bio-materials. Although there are numerous difficulties in trying to persuade the plasmodium to adopt and indeed maintain the required structural and functional patterns, the simple low-level interactions which generate the emergent behaviours suggest that it may be possible to develop *Physarum* inspired programmable-functional materials for computation and robotics. In the next chapter we explore how the oscillatory phenomena may be used to generate controllable collective transport and amoeboid movement.

Chapter 16

Modelling Collective Transport and Amoeboid Movement

“Be aware of the contact between your feet and the Earth. Walk as if you are kissing the Earth with your feet.”

(Thich Nhat Hanh, 1991)

16.1 Collective Transport — Introduction

In this chapter we examine how the oscillatory phenomena described in the previous chapter may be patterned and harnessed to generate regular travelling waves which may be used to transport material within the virtual plasmodium, or to transport the virtual plasmodium itself by a cohesive amoeboid movement. The emergence of oscillatory behaviour in the model corresponds to differences in distribution of protoplasm within the plasmodium and subsequent changes in thickness of the plasmodium. In a real *Physarum* plasmodium the changes in thickness of the plasmodium membrane are used to provide impetus (pumping of material through the vein network, or bulk movement of the plasmodium). There is a known relationship between the spontaneous contraction of the plasmodium and the subsequent transport of protoplasm away from that region [42]. The region undergoing contraction becomes thinner (allowing more light to pass through when illuminated) and regions away from the contraction become thicker as more protoplasm is present (allowing less light to pass through). In the computational model the transport of particles represents the free flux of protoplasm within the material and the increase in flux (mass particle movement) is indicated in the supplementary video recordings by an increase in greyscale brightness. A decrease in the bulk movement of particles represents congestion and a lack of transport and is indicated by a decrease in greyscale brightness (since deposition of chemoattractant factor only occurs in the event of successful forward movement). For clarity in the static images, the greyscale images are inverted (dark areas indicate greater flux).

The particle population's environment is a 2D lattice, represented by a digitised image configured to represent the habitat of the experimental plasmodium. We designed simple shapes in which the particle collective, which composes the virtual material, is confined. The particle population is free to move within unconfined areas. The shapes are composed of 'wall' regions where movement cannot occur, 'vacant' regions where movement was possible and (where relevant) 'stimulus' regions which provide attraction stimuli, or repulsion stimuli, to the particle population. At the start of each experiment the particle population is randomly distributed through the vacant space in the experimental arena and all particles have random initial orientations. A fixed population size was used. The total amount of free possible particle movement is dependent on the population size as a fraction of vacant space. In these results we use a 90% occupancy rate unless otherwise specified, i.e. 90% of all vacant areas are occupied by particles. In all of the experiments there is an initial period where oscillatory behaviour is not initially 'switched on' and this results in self-organised regular domains (the so-called 'vacancy islands' noted in chapter 3). When oscillatory motor behaviour is activated these regular domains collapse and the emergence of small domains of regular oscillatory patterns begins. Over time these domains coalesce and compete, causing entrainment of the population into regular oscillation patterns, influenced by both the particle sensory parameters and also by the shape of the experimental arenas.

We use the arena shape to constrain the oscillatory behaviour to ascertain the possibility of utilising the oscillatory behaviours to provide useful 'engine-like' output. By this we mean that the oscillation patterns should be periodic, regular and reliable, in the same way that mechanical engines provide regularly and reliably timed patterns of impetus.

16.1.1 *Data Analysis*

We sampled regular frames from the emergent chemoattractant flux patterns and analysed the differences in particle flux by comparing the greyscale levels in different regions of the arena. We were particularly concerned with the reliable initiation of oscillatory behaviour and the characteristics of the behaviour (e.g. the period, the intensity and any coupling effects). Initiation of oscillatory activity and the emergence of travelling oscillatory waves is best illustrated by referring to the relevant supplementary recordings.

16.2 Results

We have previously shown in chapter 15 that the particle population successfully reproduces the behaviour of the plasmodium when confined within a circular well, resulting in the spontaneous emergence of oscillation patterns. The type of pattern produced depends on the sensory parameters of each

particle (*SA* and *RA* parameters) and the *SO* parameter which, when increased, causes a transition to a different pattern. In a circular well the patterns most frequently observed were rotational patterns. When *SO* interaction distance was further increased lateral oscillations were observed, followed by an annular pattern. There appears to be a relationship between the circular confining shape of the arena and the type of pattern produced.

We speculate that the reason for the change in pattern type (which, over time, is also observed in the real plasmodium) is that the scale of interactions between the oscillatory regions becomes too large for the circular well, the interactions are constrained and a new pattern is formed which can ‘fit’ within the confines of the well. This suggests that the intrinsic oscillations which spontaneously emerge can be shaped in some way by architectural changes to the environment. To further explore this relationship between oscillation pattern type and the environment shape we explored different methods of patterning the virtual arena in order to assess differences in oscillation pattern type and pattern evolution.

16.2.1 Transport Motion in Open Ended Arenas

We patterned the environment with a simple tube shape whose horizontal ends were looped around at the edge of the environment by invoking periodic boundary conditions for the particles. The vertical wall boundaries confined the population to the tube. Snapshots and a space-time plot are shown in Fig. 16.1. The space time plot is recorded by sampling every pixel along the width of the image at exactly halfway down the tube section and assembling an image based upon these sampled values (pixel brightness is related to chemoattractant trail concentration). After a short period where the non-oscillatory motor condition was used (see top of space-time plot in Fig. 16.1d) the oscillatory motor behaviour was initiated. Small oscillatory domains representing different concentrations of chemoattractant flux appeared (Fig. 16.1a), travelling in different directions. Over time these domains competed and became fewer in number (Fig. 16.1b) until the tube was evenly divided into regular domains of high flux (regions of free movement) and low flux (regions of obstructed movement). These self-organised domains travelled in a single direction (the actual direction, left or right, differed between experiments) in a regular manner (Fig. 16.1c and lower section of space-time plot) and are an example of a phase transition into ordered movement patterns as first described for ‘off-lattice’ particles in [109].

The travelling waves arising from the collective particle behaviour actually travel in the opposite direction to the bulk particle motion. In the example shown in Fig. 16.2 the direction of the travelling wave (Fig. 16.2b, solid arrow) is right-to-left, whereas the actual movement of the particles (Fig. 16.2a, dashed arrow) tends to move from left-to-right. Since particles can only move when a space in the lattice becomes available the vacant spaces appear to move in the opposite direction of the particles and the particles themselves

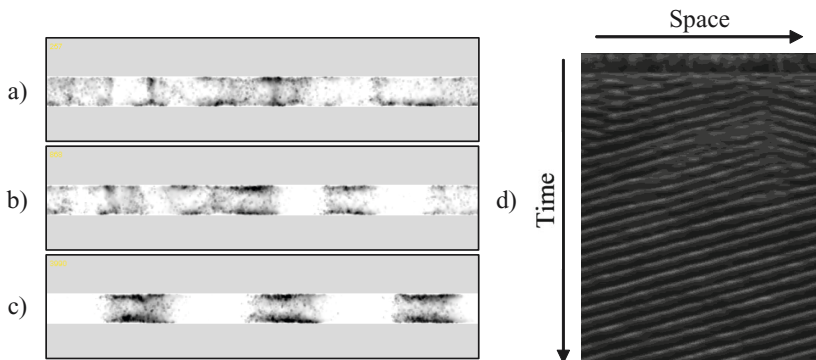


Fig. 16.1 Emergence of travelling wave transport in a tube shaped environment. Left: Snapshots taken at (a) 257, (b) 868 and (c) 3990 scheduler steps, Right: Space time plot showing emergence of regular transport.

show a greater probability of moving when a region of relatively vacant space is near (Fig. 16.2c and enlarged inset d). Also note that particle movement tends to occur in the darker regions (lighter regions in the video recordings), which are regions with more vacant space and greater chemoattractant flux). The spaces themselves appear to move backwards because a particle moving from its current position to occupy a vacant space subsequently leaves a new vacant space at its previous position. Because chemoattractant is only deposited by the particles after a successful movement, the chemoattractant flux will be patterned by the distribution of vacant spaces and the wavefront thus moves in the opposite direction to the particles. The bulk movement of the particles is also much slower than the travelling waves, as indicated by Fig. 16.2, which shows that a single particle takes approximately 8000 scheduler steps to traverse the width of the arena, whereas the travelling wave crosses the arena in approximately 400 steps, a 20:1 difference (although the particle's progress is hindered somewhat by the resistance caused by the low numbers of vacant spaces and changes in direction on contact with wall boundaries). The opposite direction of the self-organised travelling wave with respect to particle movement is reminiscent of the characteristic backwards propagation seen, for example, in traffic jams [274].

Further analysis of the directional alignment of the particles revealed some unexpected properties of the particle population in relation to the travelling wave. At the start of an experiment the distribution and alignment of the particle population is randomly chosen (Fig. 16.3a) and the ratio of particles facing left and those facing right is typically equal at 50:50 (we consider particle alignment as being 'left facing' or 'right facing', depending on whether their actual orientation angle falls into either category). When the travelling wave has emerged and stabilised the distribution of the particles is such

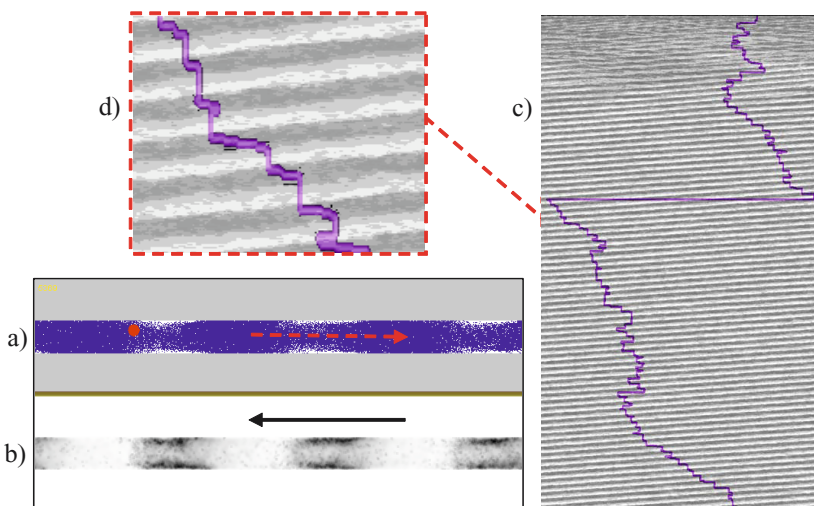


Fig. 16.2 Collective particle drift is opposite to the direction of wave propagation. (a) Particle positions and direction of tracer particle (circled), (b) Chemoattractant wave propagation, (c) Space-time plot overlaid with tracer particle position, (d) Enlarged portion showing tracer particle movement (horizontal movement) tends to occur in areas with greater vacancies (high chemoattractant flux).

that they are grouped in regions (Fig. 16.3b) which are similar, but slightly offset, to the regions of high and low chemoattractant concentration seen in the travelling wave (Fig. 16.3c). The particles in each region share the same general alignment and the different regions alternate with respect to the alignment of the particles within them (i.e. regions are LEFT, RIGHT, LEFT, RIGHT, and so on). The final alignment ratio at the end of an experiment was typically 53:47 (rounded average of ratios over ten runs), with the majority of particles facing in the direction of the travelling wave. The particles change their directional alignment at the same speed as the oncoming travelling wave. The actual movement of the particles, as previously noted, is much slower and in the opposite direction to the wave.

Contractile waves travelling along *Physarum* protoplasmic tubes (Fig. 16.3) can be used to pump liquid substances, nutrient components and fine-grained granular substances within its body plan [275]. By patterning the environment to remove all wall boundaries and ensure periodic boundary conditions the emergent oscillatory patterns self-organised into travelling waves (Fig. 16.4). However there was a much greater length of time needed for the competition between the wave patterns to complete and form synchronous travelling waves. The increase in time before synchronous waves emerge can be explained by the greater initial freedom of movement afforded by the lack of movement constraints from the environment.

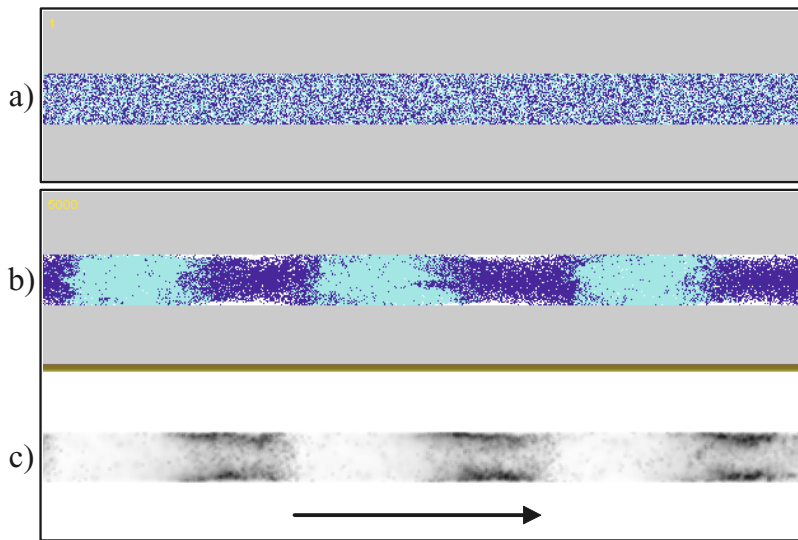


Fig. 16.3 Collective particle alignment and the travelling wave. (a) Initial random distribution of particles and their alignments, (b) When the stable travelling wave occurs particles are distributed into groups sharing similar directional alignment: lighter regions are oriented to face right and darker regions are oriented leftwards, (c) Chemoattractant flux in travelling wave moving to the right.

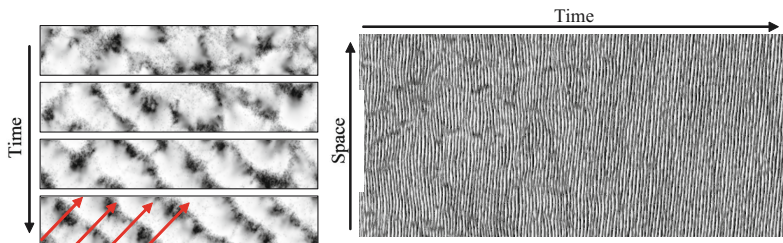


Fig. 16.4 Helical transport in non-patterned environment with periodic boundary conditions. Left: Snapshots of competition and entrainment of wavefronts with final helical-type movement arrowed, Right: Space-time plot showing long period before regular transport occurs.

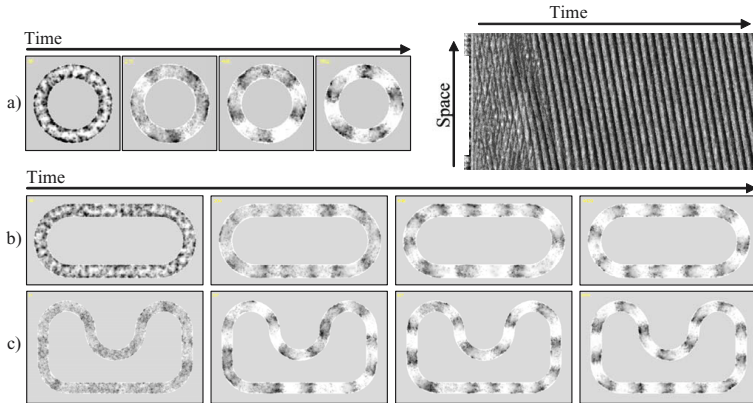


Fig. 16.5 Emergence of rotary motion oscillations. (a) Emergence of rotary motion and visualisation of space-time plot showing regular motor pulses. Space time plot was created by recording 360 points inside the vacant track of the circle, (b) Tracked rotary movement from a combination of circular and straight regions, (c) Conveyor type motion from a more tortuous looped path.

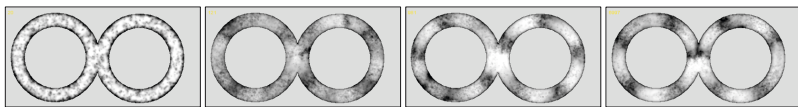


Fig. 16.6 Emergence of gear-like coupling in an overlapping two rotor pattern. Snapshots taken at 20, 121, 981 and 6997 scheduler steps.

By removing the movement at the boundaries and instead patterning the vacant space into looped structures rotary motion of the travelling waves was achieved (Fig. 16.5). The competition period before synchronisation was relatively brief (Fig. 16.5a, space-time plot), again because the environmental barriers reduce initial freedom of movement. The looped structures also enabled travelling wave motion even when the environment added non-circular elements, and more tortuous paths (Fig. 16.5b and c). The successful initiation of rotary motion suggests the possibility of generating reliable distributed wave based conveyor transport, as per the method suggested by [276].

By combining two circular patterns and introducing a region which overlapped and exposed to two separate wavefronts it was possible to achieve entrainment, after 5000 scheduler steps, of the pulses from one rotary ‘motor’ to another, mimicking the transmission and synchronisation of movement to another ring by an apparent fluidic coupling effect (Fig. 16.6). Like a conventional gear transmission, the rotation of two facing rings was in opposite directions. However, unlike conventional gear trains, the ‘teeth’ (wavefront peaks) did not overlap.

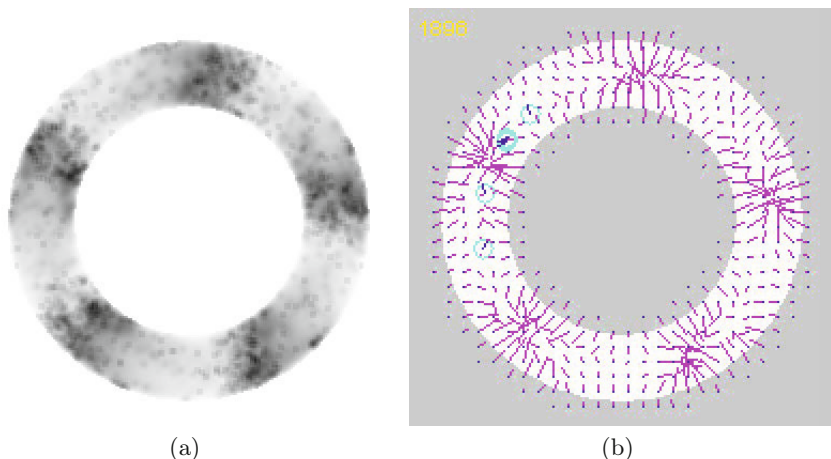


Fig. 16.7 Simulating passive transport of substances using information from travelling waves. (a) Spatial representation of snapshot of emergent travelling waves. (b) Computed vector field based upon direction and gradient of travelling waves is used to move passive objects (circular shapes).

To simulate the transport of substances using the emergent travelling waves of the model we computed a vector field based at every scheduler step on instantaneous snapshots of the wave activity (Fig. 16.7a). The vector field was computed by dividing the habitable areas of the lattice into 15×15 pixel regions. Each vector value was located at the centre of a region and was computed from the difference of chemoattractant flux at extreme borders of each region. The difference between left and right borders giving the dx value and the difference between top and bottom borders giving the dy value. These values were converted to polar coordinates to provide the angle of the strongest local concentration (direction) and the force given to the transported substances. The values within the computed vector field were used to move passive substances, whose locations are represented by the circular areas (Fig. 16.7b). The supplementary video recording illustrates how information within the travelling wave patterns can be translated into motive force to transport the passive substances in a cilia-like fashion. The recording of the vector field also shows the direction and size of the inputs to the transported substances.

16.2.2 Transport in Closed Path Patterns

The transport motion in open ended looped patterns stabilises because the bulk particle drift eventually synchronises with the travelling waves. The distribution of the particle population becomes relatively evenly distributed

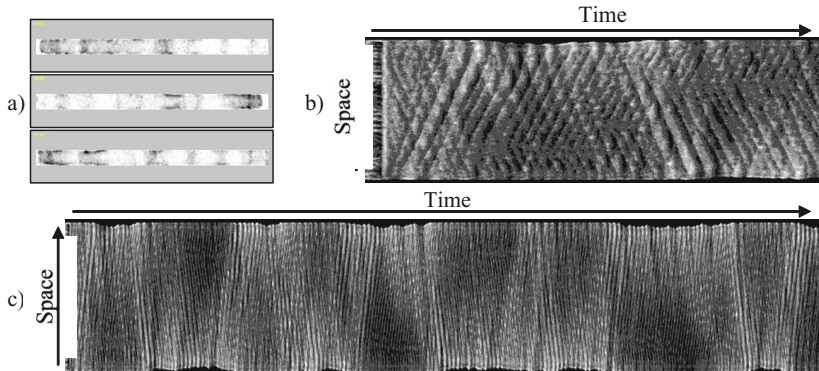


Fig. 16.8 Complex second-order oscillations caused by bulk drift in closed path environments. (a) Pulsatile oscillations at different sides of a closed chamber, (b) Initial phase of space-time plot showing initiation of oscillatory behaviour and competition between oscillatory domains, (c) long term (20,000 steps) space-time plot showing second order oscillations as bulk particle positions oscillate from one side of the chamber to the other. Dark regions at either side of plot indicate periods of second-order oscillations.

within the path, punctuated by regularly spaced changes of particle occupation density. When closed path patterns were used, however, the uniform distribution cannot occur because separate ends of the path cannot communicate the transport of particles. Thus, over time, the drift of particles results in a tendency for the particle population density to become greater at one end of the chamber. Once there is an imbalance at one end the number of vacant spaces at that end falls and the particles are then attracted to the opposite side of the chamber where more vacant areas exist (areas which have greater likelihood of particle flux). Short term oscillatory transport and competition within the chamber still occurs (Fig. 16.8a and b), as with looped patterns, but this is mediated by a second order of oscillations, which occurs over a much longer time scale since it is caused by the slower bulk drift of particles (Fig. 16.8c). The effect is regular changes in direction of transport direction within the tube, suggestive of shuttle streaming of material in *Physarum* between two nutrient sources in a protoplasmic tube. From a robotics perspective this behaviour also suggests a possible mechanism of how changes in direction in open-ended looped systems could be achieved. By temporarily introducing a blockage in a looped path a build up of particles eventually results in a lack of vacancies and movement in the current direction. The imbalance of population size and freedom of movement will cause in a reversal of direction.

16.2.3 Transport Within ‘Pinned’ Sheets of Virtual Plasmodium

Another method to confine the collective to a region is by using strong sources of attractant to effectively ‘pin down’ the collective in place instead of confining it physically within a region by its boundaries. Attractant sources are represented by projecting regularly spaced simulated nutrients at every scheduler step into the chemoattractant diffusion field. These sources diffuse and attract the individual particles of the collective. By spacing the placement of attractants the collective is retained in place in a sheet-like fashion by the attraction of the particles to the sources and the mutual attraction of particles to their own deposition of chemoattractant into the diffusion field (Fig. 16.9a).

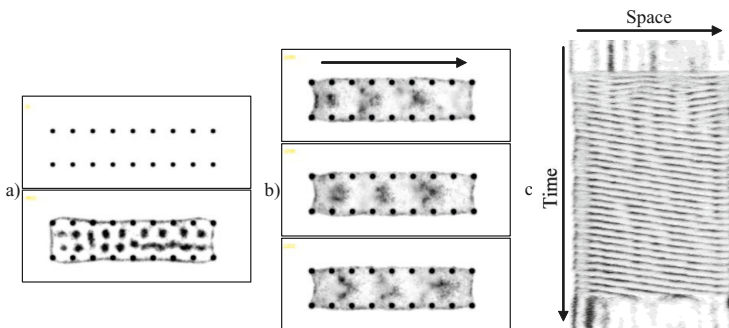


Fig. 16.9 Confinement by attractant projection and the emergence of travelling waves. (a) Regularly spaced projection of chemoattractant sources (top) confines position of collective (bottom), (b) When oscillatory motor behaviour is activated a travelling wave emerges across the confined collective, (c) Space-time plot of the emergence of travelling waves in a pinned collective.

When oscillatory motor behaviour is activated travelling waves of chemoattractant movement emerge in different directions (Fig. 16.9b). These waves compete for a short time before one direction predominates (Fig. 16.9c).

16.3 Amoeboid Movement — Introduction

This section is motivated by reproducing the amoeboid movement for robotics purposes, as exhibited during the growth and foraging behaviour of *Physarum*, however it takes a different approach to generating amoeboid movement from that of Umedachi et al. [114]. Instead of trying to build an amoeboid robot by coupling pre-existing oscillatory components, we take a more literal approach to robotic control, as espoused by [277], and investigate how oscillatory behaviour may emerge from the local interactions between simple component

parts to generate self-organised amoeboid movement. In the previous section we examined how large confined populations could be used to generate travelling waves within the material. In this section we utilise the oscillatory phenomena within *unconfined* populations of virtual material to produce collective, amorphous and controllable amoeboid movement, and demonstrate mechanisms for external control of the material by simulated chemoattraction and repulsion by light hazards.

16.4 Emergence of Collective Amoeboid Movement

Physarum utilises internal protoplasmic transport to migrate towards nutrient sources and away from hazardous sources [161], and adapts its gross body plan to changing environments [9, 163, 11]. Small plasmodia can shift the entire plasmodium away from unfavourable conditions such as bacterial or fungal contamination. The plasmodium is also notable for its ability to survive physical damage; fragments of plasmodium excised can survive independently and individual plasmodia may be fused to form a single organism. To utilise a vehicular analogy, *Physarum* not only represents the internal mechanicals (motive force mechanism, transmission coupling), but also the moving vehicle itself, and is a vehicle which can survive the removal of parts, the introduction of new foreign parts and the repair of damaged parts.

We set out to explore the behaviour of the particle collective to assess its behaviour when compared to a fragment of *Physarum* plasmodium. When oscillatory motor behaviour is not used the particle collective condenses into a uniform circular shape, or blob, as the initial transport network condenses (Fig. 16.10a). The non-oscillatory blob shows regular vacancy domains (dark areas) and the fluid particle motion afforded by the non-oscillatory motor condition ensures that the blob is cohesive and takes a minimal shape. The non-oscillatory blob is also resilient to external perturbation. When excited by an externally applied source of chemoattractant (Fig. 16.10a, mouse position in fourth image), the deformation of the collective induced by the stimulus as it is attracted to the stimuli is repaired when the stimulus is removed, the collective returning to its minimal shape.

When oscillatory motor behaviour is initialised at pID 0.05 the regular domains collapse as the particle motion becomes less fluid (Fig. 16.10b) and oscillations emerge and travel through the collective. Because the small collective is not constrained by any externally applied pattern the oscillations distort the shape of the collective. When the pID parameter is further reduced to 0.01 there is even greater restriction on the fluidity of individual particle movement and the oscillations become stronger and distort the collective's boundary significantly (Fig. 16.10c). The large shift of a mass of particles causes the collective to move across its environment. The cohesion of the collective is maintained but other SA/RA parameter settings, combined with lower sensor interaction (SO) distance, can result in the fragmentation of the

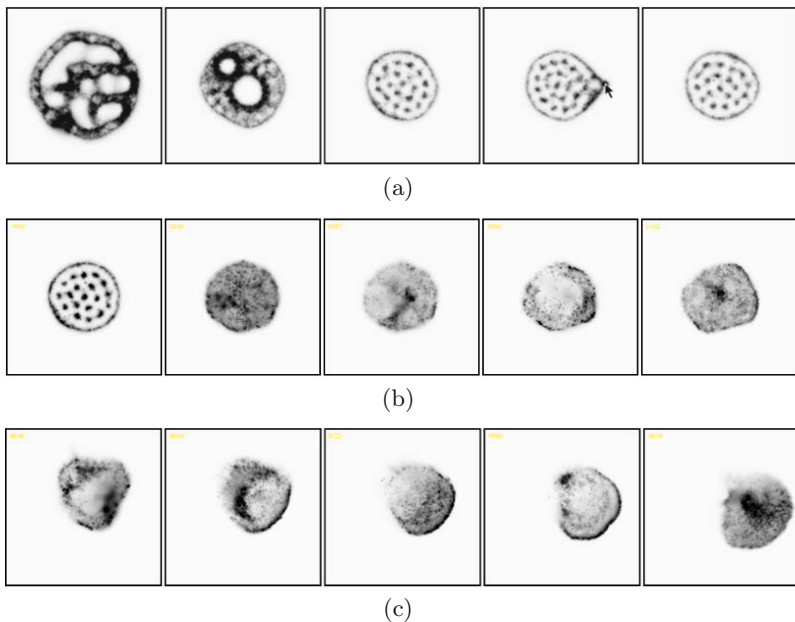


Fig. 16.10 Initiation of oscillatory behaviour and amoeboid movement in model plasmodium. (a) Condensation of blob material in non-oscillatory behaviour shows vacancy domains and resilience to deformation. Collective of 9380 particles, $SA = 90^\circ$, $RA = 45^\circ$, $SO = 15$, (b) Initial non-oscillatory collective with regular vacancy domains (left) and onset of oscillatory behaviour at 1950, 2039, 2057, 2086 and 2122 scheduler steps. pID set to 0.05, (c) Further reduction of pID to 0.01 results in stronger oscillations and amoeboid movement at 4648, 4684, 4720, 4768 and 4836 scheduler steps.

collective (see supplementary material for examples of oscillation patterns using different SA/RA combinations).

16.5 Persistent Movement in a Small Blob Fragment

The amoeboid movement seen in Fig. 16.10 occurs because the oscillation waves distort the boundary of the collective whilst it is still able to maintain a cohesive whole. Because the population maintains its cohesion, any distortion of the boundary on one side must result in a shift in population distribution from the opposite side (since the collective is non-compressible and occupies a fixed area). The diameter of the collective (a function of the number of pixel sized particles comprising it) must be large enough for oscillations to emerge and to confine an oscillation pattern within it.

When the collective is comprised of only a relatively small number of particles, the distortion of the boundary forms an approximately semicircular

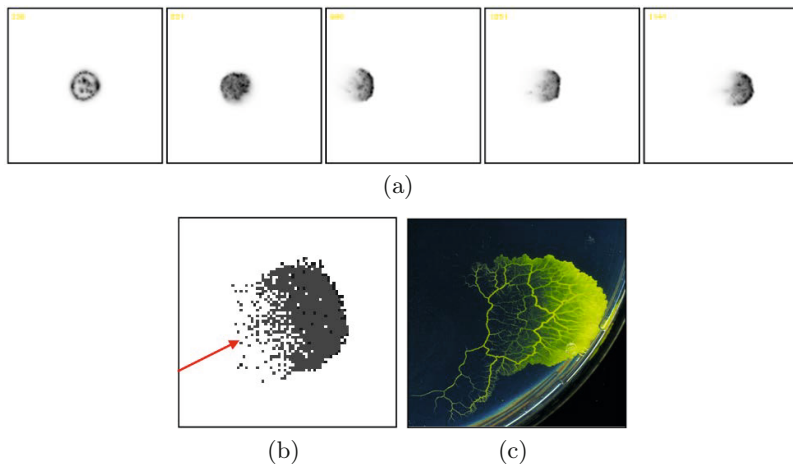


Fig. 16.11 Persistent forward movement of blob fragments. (a) Non-oscillatory condition, initiation of oscillatory behaviour and (final 3 images) self-perpetuating transport of blob fragment. Chemoattractant concentration is greatest at the front of the dome shape, (b) Enlargement showing composition of blob fragment, the persistent shape is maintained despite turnover of component parts. Population size 900 particles, $SA\ 90^\circ$, $RA\ 45^\circ$, $SO\ 9$, $pID\ 0.001$, (c) Independently moving fragment of *Physarum* (Image courtesy of Andrew Adamatzky, [4]).

domed shape and the small number of particles ensures that the collective cannot maintain a fully circular shape. However the persistence of forward movement generated by the oscillatory motor behaviour at low pID values causes the dome shape itself to be maintained over time, and the small fragment of virtual plasmodium propagates forwards (Fig. 16.11a). Movement of the fragment is relatively smooth and different from the pulsatile motion observed in larger collectives. Particles move towards the front of the domed profile (Fig. 16.11b, dark pixels) and then, over time, move to the side. Particles at the sides of the fragment ultimately fall behind only to re-enter the dome at the centre. Higher pID values result in more frequent changes of direction of the fragment as the dome shaped front profile cannot be maintained. If the population size is increased, the single sided dome shape cannot be maintained and the resultant motion becomes pulsatile and chaotic. The movement of small blob fragments in the particle collective mimics amoeboid motion observed in *Physarum* on a non-nutrient substrate (Fig. 16.11c) which has been shown to be equivalent to the propagation of wave fragments in sub-excitable media [79, 78]. Both artificial blobs and real *Physarum* blobs exhibit reflection (reversal of direction) when encountering the boundary of their environment and can both be directionally guided by the placement of attractants and repellents [82].

16.6 External Control of Collective Amoeboïd Movement

Movement of the *Physarum* plasmodium is strongly affected by local environmental conditions. Attractant sources (such as increasing temperature gradients and chemoattractant nutrients) cause the plasmodium to move and grow towards the attractants whereas repulsive sources (salts, dry regions) cause the plasmodium to try to avoid such regions [161]. The plasmodium is able to integrate many separate localised inputs to compute its response to the environment. One method in which this is achieved is by the modulation of local oscillation patterns in response to attractants or hazards. Attractants tend to increase localised oscillation strength and hazards decrease oscillation strength. We set out to see if a localised response to external influences could be used to govern the collective movement of the particle population.

Attractant sources were previously used as a method to confine the collective to a region by pinning it down. By externally presenting an attractant source (effectively a simulated nutrient source) near to a cohesive blob of virtual material (circle in Fig. 16.12a) a concentration gradient emerged from the source (Fig. 16.12b, left). When the diffusion gradient reached the sensors of the closest particles at the front of the collective it provoked local movement towards the source. The cohesion within the collective resulted in a pseudopodium-like extension of the border region which extended towards the source (Fig. 16.12b, middle), ultimately engulfing it. Travelling waves spontaneously emerged within the collective, caused by vacancies as particles at the leading edge moved forwards towards the attractant source. The travelling waves caused the collective to shift its position towards the source (Fig. 16.12b, right). Consumption of the source was simulated by simply decrementing the value projected to the diffusion field when the source was covered by a particle. When the source was consumed by the population, the collective regained its previous approximately circular shape.

To approximate the repulsion of the collective to hazardous sources such as the simulated response to irradiation by visible light we added a condition to the sensory stage of the algorithm to the effect that if any particles of the collective were in a region (L_w , a square window centred about each agent) exposed to ‘light’ (a defined area within the arena), those particles would have their sensitivity to chemoattractant diminished whilst they remained in this region (achieved by multiplying the sampled sensor values with the damping factor L_d , lower values generating a stronger response to irradiation). The effect of exposing regions of the collective to simulated light damage was that the collective immediately started to move away from the irradiated region (Fig. 16.13a). Specifically, oscillation waves moved from the irradiated region towards the unexposed regions. The shift of particles from the irradiated region eventually moved the collective away from the stimulus. The cause of movement away from the light can be found at the interface between irradiated and unexposed areas. Before irradiation (Fig. 16.13b) all regions of the

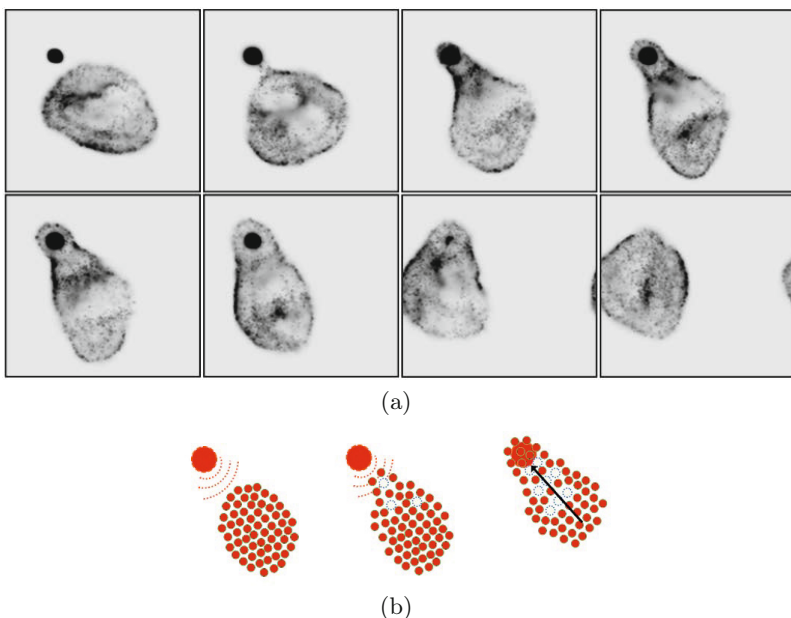


Fig. 16.12 Control of amoeboid movement by chemoattraction. (a) Chemoattractant source is projected into diffusion field, provoking extension of the collective. Collective engulfs the source via travelling waves moving toward the source. Collective re-adopts its original shape when nutrients are exhausted, (b) Illustration of chemoattraction to the nutrient source (left), Migration of leading particles towards source (middle), Emergence of travelling waves pull the collective, engulfing the source (right).

collective are equally mutually attractive to the particles (subject to fluctuations caused by discrepancies in particle movement and intrinsic oscillations within the collective). There is a strong coupling between the particles in the collective caused by the offset sensor distance. Some of the particles at the interface of the irradiated region will receive input from the unexposed region and will be attracted to that area because the chemoattractant concentration in unexposed areas is perceived as greater due to the sensory damping in irradiated regions (Fig. 16.13c). The movement of particles near the interface towards unexposed regions causes both new vacant spaces (Fig. 16.13d) and also an increase in chemoattractant concentration (because only mobile particles deposit chemoattractant). This results in the emergence of travelling waves away from the irradiated region until eventually the entire collective has migrated from the hazard.

16.7 Cleavage and Fusion of the Collective

The previous results demonstrated that the collective changes its shape during self-oscillatory behaviour and also in response to simulated attractants and hazards. The collective retains its typically circular shape due to the cohesion of the individual particles making up the population. When the morphology of the collective is disturbed by its movement towards, or away from, externally applied stimuli it can reform the original shape when the stimulus is removed. An adaptive morphology is a very desirable property in robotic devices since it imbues the robot with great flexibility of size and movement, enabling it to traverse environments which traditionally are difficult to navigate (for example narrow spaces, gratings etc.). This feature is only possible because the properties of the movement and guidance of the collective are distributed throughout the collective and not located in fixed sized and inflexible units as is the case with conventional robotic systems. This is also the case with the *Physarum* plasmodium which adapts its shape and growth patterns in response to its environment. One of the most remarkable properties of the plasmodium is the ability to survive external damage beyond simple attraction and repulsion. A piece of plasmodium excised from the growing tip can survive, and indeed continue to move and grow as an independent entity. Furthermore two independent plasmodia can fuse to form a single plasmodium when placed in close proximity. These phenomena are not only desirable from a robotics perspective in terms of resilience and damage repair, but offer new and as yet little explored opportunities in robotic movement and control.

We set out to find if the particle collective could also replicate these highly desirable features as seen in the real plasmodium. We took a large single oscillating collective (5000 particles) and applied a narrow band of hazardous simulated light irradiation through its centre (Fig. 16.14a, dashed box represents irradiated area). Particles immediately began to surge away from the irradiated region on both sides and the collective narrowed in diameter and became further pinched in shape until the collective was cleaved into two independently controllable blobs. Under normal circumstances the cohesion of the blob would prevent cleavage, however the irradiated region reduces cohesion in this area, allowing the blob to split in two. The cleavage mechanism can be applied in different ways. For example both resulting blobs can be of equal size and have similar oscillatory properties. Alternately it is possible to cleave the collective in such a way to have one large stationary blob and one smaller mobile blob (recall that a blob which is small enough will be able to move spontaneously in a persistent direction).

It is possible to guide each blob independently using either a pulling type mechanism (externally applied attractants) or a pushing type mechanism (simulated irradiation). In Fig. 16.14b we guide the lower right blob (arrowed) towards the larger blob by pushing it from its opposite side with simulated irradiated light. As the blobs become closer (specifically, to a

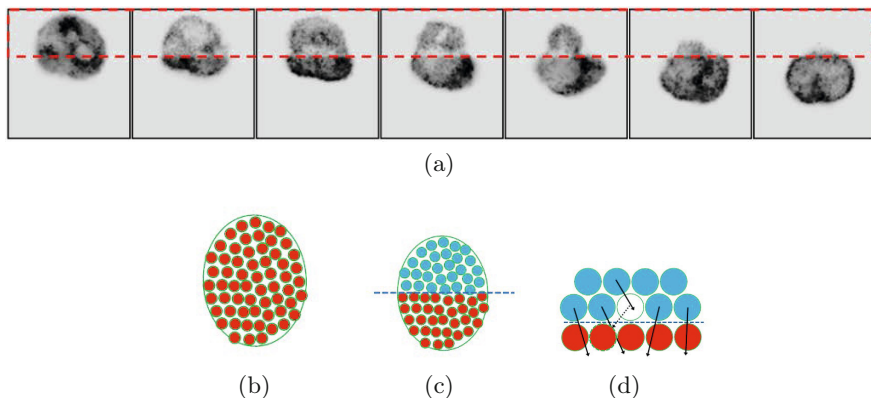


Fig. 16.13 Avoidance of simulated light irradiation by particle collective. (a) Area within dashed box is stimulated with simulated light irradiation. Particle collective oscillates sending travelling waves towards unexposed region, moving the collective away from the irradiated region, (b) Condition before irradiation — equal concentration of chemoattractant, (c) Irradiated areas (top) perceived as weaker concentration, (d) Particles at irradiation interface are more attracted to unexposed areas. Migration across interface causes chemoattractant deposition and further attraction to the region.

separation distance which is sufficient for the border particles in each blob to sense the chemoattractant flux in the other blob) the closest border regions of each blob surge towards each other and a single larger collective is formed by the fusion. Cleavage and guidance of the particle collective by simulated hazards reproduces the control of *Physarum* plasmodial migration (Fig. 16.14c) by light irradiation and repellents [84, 82].

16.8 Morphological Adaptation of the Collective

As an example of the robotic flexibility endowed by the adaptive morphology of the collective, and the guidance mechanisms enabled by its external control, we show in Fig. 16.15 three examples of how a blob can be guided externally (in this case a repulsive pushing by simulated irradiation) in order to traverse narrow, separated or tortuous paths where the path may be much narrower than the diameter of the collective itself. In Fig. 16.15a, the blob has a diameter of approximately 52 pixels and is guided through a channel of width 30 pixels by automatically reconfiguring its morphology. In Fig. 16.15b, the blob is split into two parts by irradiating a rectangular region at the entrance of the channel. The two separated blobs may be guided separately by simulated radiation and are re-fused near the exit of the channels. Finally, in Fig. 16.15c, the blob automatically separates its structure in response to the different obstacles and re-forms its shape by mutual attraction and cohesion

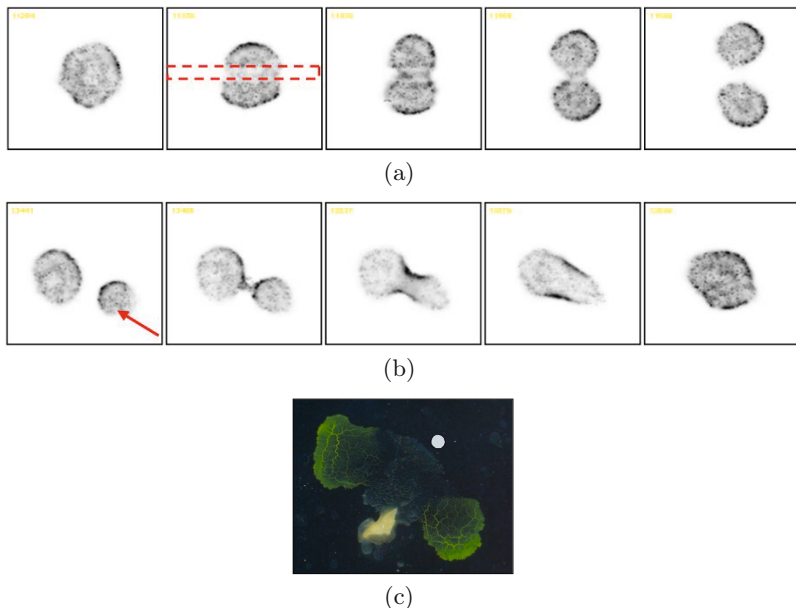


Fig. 16.14 Controlling blob morphology by splitting and fusion. (a) 'Blob' of aggregate particles is split by applying simulated light irradiation (dashed box), disrupting particle flux in that region. The single blob separates into two smaller blobs, each capable of individual oscillation and external control, (b) Fusion of two independent particle aggregates. The blob on the lower right is guided diagonally upwards in the direction of the arrow towards the larger blob. The two independent blobs fuse forming a single aggregate, (c) Cleavage of plasmodium of *Physarum*. Fragment of plasmodium initialised at triangular region. Crystal of potassium chloride placed at circular region. Diffusion of potassium chloride cleaves the plasmodium into two independent fragments, Image courtesy of Andrew Adamatzky, [82].

of the particles. No fine control of the individual components, nor complex pre-determinism of path choice, is necessary; the collective is guided by adaptation of its shape to the environment (for example, the walls of the narrow tunnels) and avoidance of the simulated irradiation (the irradiation location is not shown, but follows the previous examples of simply exposing the rearward part of the collective to push it forwards). When clear of the obstacles, the original circular shape is reformed. If the blob is returned backwards through the obstacle path again the path chosen can be somewhat different to the original path with the same result.

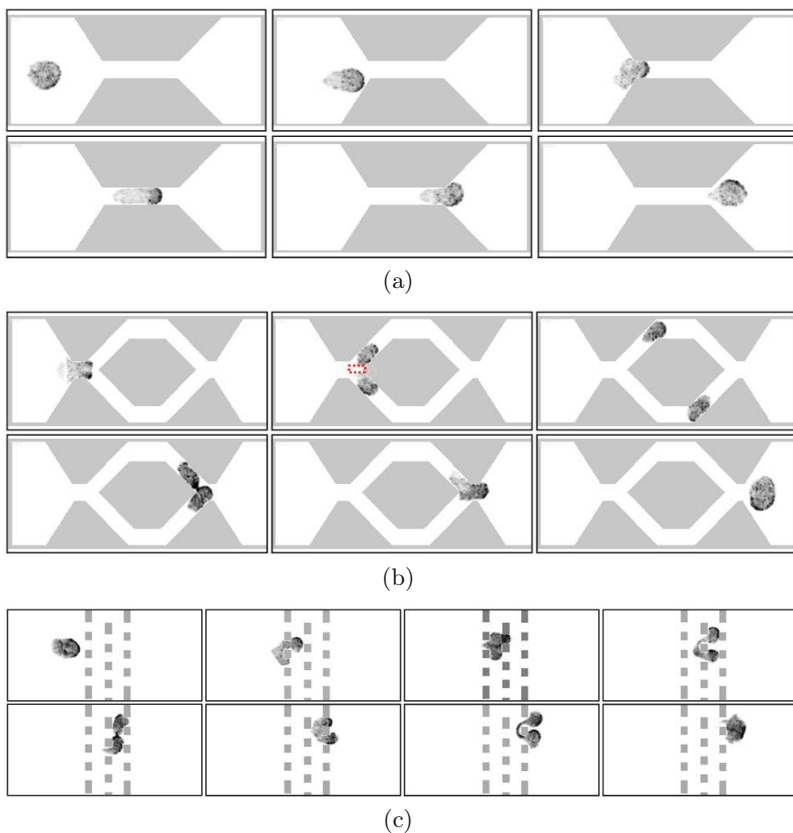


Fig. 16.15 Exploiting the adaptive morphology of the collective. (a) Large aggregate moves through a channel narrower than the aggregate diameter, (b) Aggregate is cleaved by hazard irradiation (boxed) and guided separately before being refused into original size, (c) Aggregate is pushed through tortuous narrow grating and reforms original aggregate shape.

16.9 Summary: Towards Distributed Soft-Bodied Robotics

Inspired by internal transport within the *Physarum* plasmodium, we explored how the distributed transport within the organism could be reproduced for synthetic distributed transport. By patterning a densely packed particle population into different shapes we were able to simulate reliable and regular oscillatory movement as emergent travelling waves which were fashioned into rotary, reciprocal, helical, and coupled transport mechanisms. The waves, consisting of peaks and troughs of simulated chemoattractant flux, were found to travel at opposite directions, and with much greater velocity, than the un-

derlying particle drift motion which generated the waves. By computing a simple vector field from the wave motion it was possible to simulate motive forces to transport substances within the environment.

We generated collective amoeboid movement in the virtual plasmodium using self-organization between simple non-oscillatory component parts. *Physarum* is attractive because it satisfies many physical and computational properties which are desirable in robotics applications (self-oscillatory, simple components, distributed sensory and motor control, integration of multiple sensory stimuli, amorphous and adaptive shape, amenable to external influence, resilience to damage, self repair) and can be regarded as a living example of a so-called smart material because of the way in which it combines robotic and control functions in a distributed manner throughout its constituent material.

How can such complex behaviour emerge from the interactions between simple component parts? Answering this question may provide insights into the development of non-living smart materials which would have the advantages demonstrated by the *Physarum* plasmodium, but without some of its limitations, such as slow speed, fragility and unpredictability. Because of its simple components and structure, any search for a ‘secret source’ of the plasmodium’s complexity would be fruitless. Instead we set about answering the question by posing in reverse: rather than try to find out how the organism produces such complex behaviour from simple parts, is it possible to artificially generate similarly complex behaviour from simple parts and interactions?

Condensation of the collective in its virtual environment resulted in cohesive blob-like sheets of virtual material which exhibited spontaneous internal oscillations. The oscillations were composed of regular spatial domains of mobile particles and temporarily restricted particles. The wave-like propagation of the oscillatory domains resulted in a collective amoeboid movement as the perimeter of the particle collective was deformed by the internal oscillations. External control of the blob sheets was achieved by stimulating the collective with simulated attractants (pulling the collective towards the source) and repellents (‘pushing’ the collective away from simulated light irradiation). We were also able to reproduce the resilience of the *Physarum* plasmodium to damage by cleaving the collective into two separate and independent blobs and fusing two independent blobs to form a single functional blob. Finally the adaptive morphology of the collective was demonstrated by guiding the collective through an obstacle field narrower than the diameter of the collective itself. The flexible modularity and morphology seen in this approach builds upon previous work on the external influence and control of robotic devices [278, 279] by enabling separate and functional modules of arbitrary size to be created and re-formed from a single collective.

The results demonstrate how very simple and local low-level interactions within a simple material can generate complex and emergent behaviour which appear, at first glance, to transcend the capabilities of the simple ‘matter’ of

which they are composed. As noted by previous swarm approaches, there need not be anything magical or special about the properties of these materials; the complexity emerges merely from their interactions [107, 106, 109]. This complex behaviour is harnessed effortlessly by organisms such as *Physarum* as part of a parsimonious survival strategy, enabling their persistence in unpredictable, changeable and hazardous environmental conditions. By understanding the generative mechanisms underlying the complex behaviour it may be possible to incorporate these features within real physical materials for small scale robotic devices. By utilising the robotic substrate material itself for distributed computation, transport and movement it may be possible to reduce the number of specialised components, thus further simplifying the production of the devices.

Part V
Conclusions and Beyond
Physarum Models

Chapter 17

Summary of the Approach and Modelling beyond *Physarum*

“Where can the horizon lie?”

(David Bowie, 1970)

17.1 Overview

This book investigated the complex biological and computational behaviour of the true slime mould *Physarum Polycephalum*. The aim was to answer the question of how a simple single-celled organism, without any supposed requisites for intelligent behaviour, is capable of such complex feats of distributed and emergent computation. A model of the *Physarum* plasmodium was implemented using a material based multi-agent approach. This modelling approach was chosen in an attempt to provide a natural complement to the plasmodium itself: the model is composed of very simple components; material flux is inherent in the approach; spontaneous formation and evolution of transport networks occurs; distributed response to environmental stimuli is observed; emergent oscillatory patterns and transitions are generated; collective transport and amoeboid movement are obtained. Perhaps most significantly, the complex behaviour of the multi-agent approach is, like the plasmodium, distributed within the uniform ‘material’ itself and not reliant on specific or unique components, ensuring that dynamic and flexible responses to environmental stimuli (growth, shrinkage, foraging, guidance by stimuli and hazards, response to excision, cleavage and fusion) were also reproduced.

17.2 Main Research Findings

In this chapter we summarise the individual findings of the multi-agent approach to modelling *Physarum* and assess the overall contribution of the

research in terms of its originality and significance to the field. We note limitations of the research and suggest possible methods of addressing the limitations and extending the research in further work. We conclude by suggesting some possible applications of the modelling approach to other domains.

17.2.1 Model

The model is inspired and based on a virtual material approach using a multi-agent based reaction-diffusion pattern formation mechanism. Unlike the model proposed by Tero et al. [163, 121] which abstracted the flux within the plasmodium into classical numerical algorithms, we chose to take a non-classical, or unconventional computation, modelling approach. This was partly motivated by our interest in spatially represented non-classical approaches, but mainly because we considered that more could be discovered about the distributed properties of the behaviour of plasmodium by adopting a similarly low-level approach. We utilised simple individual multi-agent behaviour divided into sensory and motor functions. The collective *pattern* of mobile and immobile agent particles represented the structure (gel phase) of the plasmodium network and the collective *movement* of the population represented flux (sol phase) within the plasmodium network. A persistent representation of flux was provided by the agents' deposition of a generic chemoattractant which diffused within a discrete lattice. Diffusion was via a very simple mean filter kernel, adjustable to provide damping of the signal (and thus control of diffusion distance).

In the sensory stage of the agent algorithm the agents' offset sensors sampled the diffusive lattice, generating an indirect coupling of the particles. This represents the initial disordered array of overlapping actomyosin fibres within the plasmodium. The energetics responsible for the actomyosin contraction forces within the plasmodium are not considered within the model. This is a limitation which is necessary partly for biological simplicity and partly for computational tractability. Individual particles, therefore, are provided at each scheduler step with a given movement distance. However, because only particles which are able to move into a vacant site can actually move, certain phenomena observed within the plasmodium are accurately approximated, such as the softening of the plasmodial mass at the membrane region and flux along network paths.

17.2.2 Pattern Formation and Adaptation

The feedback provided by the coupling of agent movement to their own (and neighbours) previous activity, via the diffusive lattice, generated an auto-catalytic LALI (Local Activation, Lateral Inhibition) type reaction-diffusion pattern formation mechanism, specifically utilising a substrate

depletion LALI mechanism, as opposed to explicit encoding of lateral inhibition. The formation of an initial plasmodial network from a uniform ‘sheet’ of particles was observed, as was the selection of a shorter path choice, supporting the theory that material flux is responsible for network formation within the plasmodium. Initially disordered arrangements of particles spontaneously formed emergent transport networks composed of the mobile particles. During parametric evaluation the networks were found to exhibit a complex range of pattern formation. Minimisation of the transport networks was observed with quasi-material properties, resembling the evolution of soap film networks and lipid nanotube networks. The bulk behaviour of the particle collective reduced anisotropic artifact effects caused by the regular square diffusion lattice. The use of a hexagonal diffusion lattice architecture would be expected to remove any anisotropy from the network structure, however this was explicitly *not* chosen because the use of a hexagonal lattice might erroneously suggest that the minimisation behaviour and subsequent second-order emergent phenomena (the demonstration of von Neumann’s law and Plateau angles) was merely due to the biasing effect of a hexagonal lattice.

17.2.3 Biological Behaviour of the Virtual Plasmodium

The addition of behaviour to encode growth and shrinkage enables the utilisation of the base model behaviour to represent the complex interaction of *Physarum* with its environment. The specific behaviours, although appearing rather arbitrary, are similar to those encountered historically in Cellular Automata growth rules [280] and indeed in CA-like models of *Physarum* itself [124, 123]. Such rules are based loosely on notions of space availability and overcrowding. The growth and shrinkage used in the multi-agent model are also based upon these concepts and uncontrolled growth is prevented by ensuring that only particles that have moved forwards successfully can be considered for growth. Nevertheless, as with the ‘perpetual’ motor behaviour of the particles, elucidation and consideration of real biological energetic mechanisms would be advantageous in future extensions to this work.

Even with the relatively simple growth and shrinkage behaviour, the model is collectively able to respond to the complex environmental cues presented by the environment under both idealised and noisy conditions. Extension of pseudopodia in the direction of external nutrients and subsequent retraction when the nutrients are removed or consumed was observed. Connectivity of the network, in terms of network distance and number of network cycles, was influenced by nutrient concentration. Growth patterns approximated those of the *Physarum* plasmodium itself; florid radial growth in nutrient-rich conditions and dendritic growth in nutrient-poor conditions. Network connectivity of the virtual plasmodium, in terms of degree and junction angle, was found to match that seen in *Physarum* plasmodia [167]. Growth of the virtual plasmodium was found to be dependent on nutrient distance, size,

concentration, and substrate properties, reproducing previous experimental results with *Physarum* [163, 9, 11, 12, 14].

17.2.4 Reproduction of Neural Phenomena in Unorganised Non-neural Systems

A fascinating aspect of *Physarum* is how it can achieve its complex behaviour without it possessing any neural tissue (and indeed organised musculature, vasculature or skeleton). We demonstrated in Chapter 4 that *Physarum* may use diffusion in the environment in an efficient two-way interaction to ‘offload’ (or outsource) some computation. There are some neural mechanisms, such as Lateral Inhibition (LI), which are well conserved in a number of different organisms. We examined whether it is possible to approximate the local contrast enhancement effect of LI using unorganised non-neural approaches, namely flux within the model plasmodium. We found that material flux in response to local stimuli is indeed capable of contrast enhancement responses. This local response also resulted, over a longer period of time, in a global redistribution of the model plasmodium body plan which corresponded to a collective representation of the presented stimulus pattern. These results demonstrate that the neural model of computation is only one mechanism which can yield complex behaviour in living organisms. The unorganised aspect of this approach is enticing as it removes the requirement for complex excitatory and inhibitory wiring and could potentially simplify the development of artificial sensors and also suggests potential embedded alternatives to the separation of control systems and motor systems in soft bodied robotic systems.

17.2.5 Computational Behaviour of the Virtual Plasmodium

The virtual plasmodium was assessed to see if it could be used to reproduce the computational feats of *Physarum*. In maze problems, the model reproduced the shrinkage and retraction of pseudopodia from maze dead ends to leave only paths connecting the start and exit. However, alternate path choices were maintained and, if the size of the virtual plasmodium was further reduced, the shortest path could not be guaranteed, contrary to the results using the model in more simple path choice experiments. This variability in performance was also seen in the real plasmodium [70]. However the classically encoded *Physarum* model of Tero et al. is able to find the absolute shortest path [120]. Gunji noted that protoplasmic flux in the *Physarum* plasmodium is not as idealised as that represented in the Tero model, noting that flow is irregular, redundant and partially dependent on the shape of the organism itself [123]. This may explain the discrepancy between the numerical

model and the spatial implementation of flux in the virtual plasmodium and *Physarum* plasmodium.

The model plasmodium constructed spanning trees and proximity graphs. When initialised at a single node, the model constructed graphs in a similar manner to the *Physarum* plasmodium, giving weight to the suggestion by Adamatzky that *Physarum* modulates the environmental stimuli presented by nutrients by engulfing them [80]. When initialised at random locations on the arena, the model plasmodium formed networks corresponding to higher regions in the Toussaint hierarchy of proximity graphs comparable to Relative Neighbourhood Graphs and Gabriel Graphs. At low nutrient concentration Steiner points were formed between nodes and although the graphs resembled those of spanning tree structures in the lower regions of the Toussaint hierarchy, the extra connectivity afforded by the Steiner points resulted in higher connectivity. This demonstrates that the model, like the *Physarum* plasmodium, is able to construct networks with relatively low material requirements (short length) yet which yield relatively high connectivity. A comparison of the multi-agent model with the approach used by Tero et al. (for example, [120, 104]) was performed by Becker who suggested that the agent approach more closely approximated the networks of *Physarum* [281]. A shrinkage method was used to avoid the formation of cycles in the virtual plasmodium networks (which can prevent complete minimisation). A solid mass of virtual plasmodium covering a set of points was reduced in size, adapting its shape automatically to the stimuli to form approximations of Steiner trees, effectively demonstrating how the material could be used to transform area into distance, maintaining connectivity whilst minimising distance.

17.2.6 Modelling *Physarum*-Based Logic Circuits

We demonstrated that the model plasmodium can be used to construct more complex combined logic gates and half adder circuitry. However, the findings suggest that the presence of both timing errors and junctional (search) errors would severely limit the effectiveness and practicality with even more complex circuits. It is more likely that the natural computational behaviour of the model (which exploit morphological adaptation phenomena and environmentally mediated control) are better suited to spatially represented unconventional computing schemes, rather than classical approaches.

17.2.7 Dynamical Control of Emergent Transport Networks

Experiments on dynamically guiding or controlling the behaviour of plasmodium using external stimuli were made by Adamatzky [84, 96] and Aono [85]. We sought to find if the emergent minimising behaviour of the virtual plasmodium could also be dynamically controlled by modulating the

concentration of attractant stimuli nodes based on feedback information of current network connectivity, the goal being to generate tours of the Travelling Salesman Problem (TSP). We found extremely complex transformations of network dynamics and structures and discovered particular emergent low-level transition motifs which interacted to generate more stable long-term structures. The mechanism made use of emergent excitatory and inhibitory dynamics and, despite the blind nature of the search process, a number of good TSP tours were found for the datasets used. The results in this chapter suggest that the goal of external field feedback control of a physical system [2] is possible, yet is a very difficult task. However the extremely complex emergent behaviours (e.g. complex transitions, metastable states) discovered in these preliminary experiments trying to control such a material may merit interest and further research in themselves.

17.2.8 Material Computation for Combinatorial Optimisation

The shrinking blob method of approximating the Travelling Salesman Problem (TSP) is intriguing because of its simplicity. A very simple material computation process was used (simple shrinkage), along with a simple automatic halting mechanism. Only one instance of a candidate tour was used (compared to, for example, population approaches such as genetic algorithms). Furthermore, no modification of the path is made as the tour is constructed. It is surprising that such single-instance mechanical computation of the TSP yielded relatively good results. Another unusual property of the spatial implementation of the TSP is that the final blob pattern also generated a visual representation of the tour result. The similarity to the tour construction process to manual human construction of TSP tours is also intriguing in terms of developing kinaesthetic solutions to computational geometry problems.

17.2.9 Voronoi Diagrams and Variants, Using Attractant and Repellent Stimuli

The model reproduced the construction of Voronoi diagrams by the merging method, using growth from nutrient sources on a nutrient-rich substrate. Repulsive nodes were used to more accurately delineate the boundary between Voronoi regions. Weighted Voronoi diagrams were constructed by varying the size of individual nutrient nodes. Variants of Voronoi diagrams were constructed by utilising repulsive nodes combined with the contractile particle networks. By adjusting the respective repulsion and contraction forces a transition from area representation (Voronoi polygons) to connectivity representation (proximity graphs) was obtained.

17.2.10 Material Representation of Area and Shape: Convex Hull, Concave Hull and Skeleton

Convex Hulls were constructed using three different kinaesthetically inspired methods: contraction of a ‘band’ of virtual plasmodium initialised outside the field of attractant nodes, contraction around repulsive nodes, and a method based on self-organisation within a field of repulsive nodes.

The mechanism used by *Physarum* to move from exploration to exploitation [123], or the transformation of area to distance, was used in the model to obtain constructs which represented the area covered by a set of points (classically represented by Concave Hulls, or α -shapes). A uniform sheet of virtual plasmodium was initialised in a Convex Hull surrounding a set of nodes and the virtual plasmodium was reduced in size by removing particles. The shrinking collective adapted its morphology to conform to the set of nodes, effectively ‘shrink wrapping’ the virtual plasmodium around the nodes and forming the Concave Hull. For shapes with holes which cannot be described by Concave Hulls, α shapes were constructed by initialising small populations at the set of points which grew and merged to form a single representation of the shape.

The results in Chapters 6 and 9 suggest a continuum of minimisation phenomena, from Convex Hulls (maximum area, with minimum perimeter), to Concave Hulls, through the family of proximity graphs, until a Steiner Minimum Tree (minimum network material) is formed. It would be desirable to have a simple parameter which could generate shapes along this continuum. However it is not easy to reconcile the reduction of area with a simultaneous reduction in perimeter (the response of the *Physarum* plasmodium is to fragment a solid mass into networks, converting the problem into a distance measure). We found that by adjusting the one model growth parameter it was possible to ‘grow’ Concave Hulls from Minimum Spanning Trees and effectively tune the resulting shape between Concave Hull-type patterns towards Convex Hull Patterns.

Approximations of internal skeletons were also generated by shrinking the virtual plasmodium when inoculated as a binary shape whose border presented a very strong repulsion field. The preliminary results suggest that the innate relaxation and minimisation behaviour could be used as a strategy to avoid the spur-like artifacts often seen in classical skeletonisation algorithms.

17.2.11 Data Smoothing and Spline Curves

By harnessing the innate relaxation behaviour of the model it was possible to approximate data smoothing functions (moving average and low pass filters). When these are computed numerically they are implemented by a local kernel which compares the neighbouring values. In the model plasmodium the smoothing effect emerges as the virtual material relaxes. By exploiting the fact that large changes in angle relaxed more quickly than gradual changes

it was possible to encode the numerical data values as a spatial pattern. We implemented B-spline curves using a similar approach by patterning the plasmodium as a polygonal line and then relaxing this polyline by removing the initial stimulus. This application is a natural fit for the innate behaviour of the model and it may be possible to build upon these results by tackling different problems such as regression and clustering problems.

17.2.12 Material Approximation of Simple Statistical Analysis and Estimation

Data smoothing by the model demonstrated that it was possible to approximate simple filtering problems using the model. We extended this approach to consider the 2D geometry problem of computation of centroid by patterning the model plasmodium with the desired shape and examining its behaviour as it reduced in size. The final position of the population approximated the centroid closely, although the error increased with strongly concave shapes. We also found that the shrinkage behaviour was also able to approximate global statistical properties of numerical datasets. These results (along with the data smoothing and spline curve approximation) suggest that the interactions between independent components comprising a material are able to transmit some information about its global properties as its natural material behaviour (in this case, relaxation) changes over time. In classical computing devices data and the program operations which process the data are stored separately. In using the model to approximate these smoothing and statistical problems we are merging the separate notions of data and program.

17.2.13 Path Planning by Morphological Adaptation

The first application of *Physarum* computing was an attempt at solving mazes [183]. In this chapter we examined the behaviour of the model in more open arenas, the aim being to form a path between source and destination nodes. By the application of attractants and repellents we were able to approximate the shortest path and collision-free paths. To avoid multiple paths around obstacles an approach was devised whereby repellents were projected only from areas which had been uncovered by the shrinking model plasmodium. These emergent repellent fields acted to guide the paths around the obstacle field. Path planning is a canonical example of unconventional computing substrates (notably in chemical processors [171]) and the fact that *Physarum* and the model plasmodium can solve these problems helps clarify their computational equivalence to other unconventional substrates.

17.2.14 Oscillatory Phenomena and Pattern Transitions

The smooth evolution of emergent transport networks using the default non-oscillatory motor behaviour enables predictable behaviour in network minimisation. This is because interruptions in particle flow are only transient, ensuring smooth network evolution in the event of particle collisions. Removing the default collision behaviour (where obstructions cause changes in particle direction) generates oscillatory motor behaviour as interruptions in flux build-up within the virtual material. The obstructions cause spatial and temporal changes in the distribution of particle flux and the collective behaviour of the particles exhibits surging movement with greater directional persistence. Rhythmic reciprocal oscillations were generated in a simple dumbbell shaped arena. In circular wells we found that oscillations were initialised as multiple small foci which interacted to generate competition and entrainment. Characteristic patterns of oscillation demonstrated initially by Takagi and Ueda were reproduced [28]. Increasing the sensor offset parameter reflected the transitions between oscillation patterns, and the gradual synchronisation of the plasmodium. The reproduction of oscillatory phenomena in the model, along with the network formation and minimisation phenomena, helps validate the multi-agent modelling approach and also renders the approach amenable for performing research into distributed soft-bodied robotics.

17.2.15 Collective Transport and Amoeboid Movement

The oscillatory phenomena observed in the virtual plasmodium were harnessed to generate (after a period of competition and entrainment) regular trains of oscillations as travelling waves in densely packed patterned environments, resulting in peristaltic, helical, rotary, and coupled transport mechanisms. A simple proof-of-concept method was shown, illustrating how the travelling waves could be used to effect the passive transport of simple cargo particles, thus reproducing the transport of particles within the *Physarum* plasmodium [83]. Isolated sheet-like ‘blobs’ of the virtual plasmodium exhibited internal oscillations which shifted the position of the material giving amoeboid movement. The mobile blobs demonstrated movement to attractant stimuli and avoidance of simulated light hazard stimuli. Because the motive force and co-ordination of movement is distributed throughout the virtual material the blobs can be guided via external fields through narrow or tortuous passages and even survive excision and cleavage: the separate blobs each being functional and controllable robots which may be refused to re-form the original blob.

17.3 Contribution, Limitations and Scope for Further Work

In terms of originality, this approach to approximating *Physarum* behaviour is, to our best knowledge, the first to utilise a multi-agent approach to generate quasi-material, second order behaviours (specifically network minimisation via emergent T1 and T2 topological relaxation processes), and the emergence of spatio-temporal oscillatory dynamics.

The utilisation of the environment as a parallel computational mechanism has been previously noted and exploited by prototype reaction-diffusion unconventional computing devices [264, 241]. The results in chapter 4 on growth and adaptation suggest that the *Physarum* plasmodium may also exploit this background environmental computation, but in a more complex manner than a passive propagation: by engulfing and suppressing the diffusion of nutrients the plasmodium engages in a dynamical modulation of the chemoattractant gradient field. This results in the observation of apparently ‘intelligent’ computational behaviour from the simple plasmodium material: The collective extends pseudopodium-like processes towards nearby nutrient sources and retracts them away from depleted nutrients, restoring a minimal shape. Thus, the virtual plasmodium on one hand is simply adopting its morphological plan in response to the growth and shrinkage cues from the changing environment. On the other hand, however, the engulfment and consumption of nutrients modulates the information in the environment in a much more complex way than passive approaches, suggesting a parsimonious survival strategy for *Physarum* without requiring specialised neural tissue.

Although *Physarum* generates complex transport networks which statistically show efficient properties, it is relatively difficult to predict the exact network pattern which will be formed in any single example. In the interests of repeatability, the interruptions of the flux within the ‘default’ virtual plasmodium are very short lived and the collective behaviour is a relatively predictable and smooth minimisation process approximating soap film minimisation. Although this is sufficient to reliably reproduce the minimisation behaviour of the plasmodium, the flux of protoplasm within the real plasmodium is subject to much less idealised conditions. Flux within real protoplasmic veins and indeed gel/sol transformations within the plasmodium itself are much less predictable, and the persistence of the external slime capsule in the environment also affects subsequent protoplasmic flux in these areas. The results presented in chapter 15, concerning the emergence and evolution of oscillatory dynamics, suggest that it is the locally coupled interactions between independent oscillatory bodies, and the ensuing competition and entrainment between them, which is responsible for the complex collective oscillatory behaviour (pattern transition, synchronisation, travelling wave propagation and amoeboid movement).

By reproducing the flexibility of the plasmodium, for example by cleaving the collective to yield two independently controllable fragments, we also unequivocally demonstrated that the complex adaptive response of the plasmodium is distributed within the plasmodium and need not be located in any particular, or particularly special, components. This renders the search for a particular ‘pacemaker’ or ‘trigger’ of the oscillatory behaviour redundant. Soft-bodied robotics is a growing field which seeks to exploit self-organised, self-oscillatory, and distributed movement as seen in living systems for controllable robotic devices which currently rely on specialised components, centralised control and which lack morphological adaptability [282]. The unique properties of *Physarum* have already inspired work in this field [4, 283] and the results in chapters 15 and 16 may make a further contribution.

With any computational model, the multi-agent approach must make certain assumptions to render it computationally tractable. The main assumptions taken with this model is that we do not explicitly include the complex biochemical transformations responsible for the initial generation of the ectoplasmic contractile force — we take this force as a ‘given’. The model is set at a level, or grain, which explores how the flux of material within the plasmodium (caused by the force) can self-organise to form and evolve protoplasmic networks. The mechanism to implement adaptive growth and shrinkage of the particle population is also relatively simple and does not explicitly model the energetic requirements to produce new plasmodial constituents. However, the growth and adaptation mechanisms, although simple, do still adapt in a de-centralised and distributed manner to the presence and concentration of nutrients and repellents.

The apparent irony at the use of classical computing devices (simply put, PC programs) to generate a virtual material for use in the study of unconventional computing substrates must also be noted. Can classical computing devices ever be used as the basis for the direct study of (as opposed to merely configuring, logging, providing interaction etc.) non-classical computation? In defence we could cite the very simple, local nature of the components, the emergent and distributed nature of the material properties and the complex second-order behaviour of the virtual plasmodium and so on. However the validity of the approach may be a matter of personal interpretation, even dogma, and such objections may also be raised at studies using low-level methods, such as CA or lattice gas approaches. It is hoped that the richness of behaviours, described in this book, from such simple interactions may at least slightly placate such objections.

From a theoretical perspective the research makes a contribution to the field of pattern formation where previously studies have been dominated by numerical models or cellular automata. We have demonstrated that a wide range of reaction-diffusion patterning is possible using a multi-agent approach

which is very simple when compared to numerical approaches to generating reaction-diffusion patterns. The model yields a rich variety of patterning which does not rely on two-stage reactions in order to generate certain pattern types, as necessary in other approaches [132, 133]. An analysis of the self-organised pattern formation in the multi-agent approach was performed in [284] who interpreted the patterning in terms of transient patterns and re-organising patterns. In this book we considered a virtual material comprised of only a single particle type, with a single architecture. It is notable that particles with identical shapes but opposite behaviour of those considered in this book (where particles are *repelled* by chemoattractant) also show very complex pattern formation and evolution [179]. We must also consider the possibility of complex patterning by agents with completely different shapes (e.g. particles with fewer, or more, sensors, arranged in different architectures), suggesting that the simple agent based method of dynamical pattern formation described within this book may generate interesting behaviours, or applications, to be explored in further research. Preliminary research in these areas is described in the following pages and show that the model is capable of approximating phase separation and interfacial mixing patterns (both using a combination of two opposite agent types).

In Chapter 3 the material properties of the model were explored in the context of the formation of transport networks from initially homogeneous arrangements of virtual plasmodium. In many materials, altering the environment or properties of the material (for example growing boundaries or shrinking materials in drying conditions) place stresses on materials which respond by adapting their patterns [285]. Preliminary experiments with the model reproduce the material response to changing boundaries by forming septate patterns or fragmentation into droplets, suggesting a possible application in the modelling of these processes. Most examples in this book use simple point-like sources of chemoattractant to attract or anchor the virtual material. More complex chemoattractant gradients would also be expected to expand the patterning repertoire of the multi-agent approach and preliminary experiments have demonstrated the formation of a range of complex and self-organised phyllotaxis-like spiral patterns. Extending the model into three-dimensional space may also extend the 2D area minimisation capabilities of the model towards volumetric surface area minimisation problems. Examples of these initial experiments into more generalised patterning with the multi-agent approach can be found in the supplementary video recordings.

17.4 Extending and Generalising Multi-agent Pattern Formation

The multi-agent model presented in this thesis is designed to approximate the behaviour of *Physarum Polycephalum* using a virtual material approach. The aim was to reproduce the behaviour of *P. Polycephalum* using similarly

simple microscopic component parts to elicit emergent, and quasi-physical, macroscopic behaviour. The specific patterning is determined by the morphological structure of the particle (designed to mimic the phenomena of actin assembly/disassembly and branching), the sensory and motor behaviour, and also by adjustment of the sensory parameters of the agent particles. We should bear in mind, however, that the agent morphology and behaviour described in this book is only one possible architecture and that many more combinations exist. The examples in this chapter explore some possible variations on the architecture and behaviour of the agent particles. These variations are presented to illustrate that the virtual material approach may have other applications beyond the model of *P. Polycephalum* with the aim of stimulating future research using this or similar approaches.

17.4.1 Variations of Deposition and Stimuli Projection

The default behaviour of the base agent particle is an attraction based behaviour in which the particle deposits a source of chemoattractant as it moves forward. The particle is attracted to nutrients projected into the diffusion field. It is also possible, however to vary the particle deposition behaviour to include deposition of negative values into the diffusion field, and to have no deposition on forward movement. Alternately the projection of stimuli may also take negative values (chemorepellents) or be absent (no projection). The composite image in Fig.17.1 shows the results of patterning in combinations of positive, negative and absent stimuli projection and deposition behaviour in attraction based agents. In (i) the particles do not form a pattern but are repelled from the vicinity of the nodes by the -ve projection. In (ii) there is no stimuli projection or deposition by the agent particles and no stable pattern is formed. In (iii) the particles are attracted to the stimuli at the nodes but the -ve deposition results in no stable pattern. The pattern in (iv) approximates the Voronoi diagram as the agent particles have only a passive response (no deposition) to the -ve projections. No patterning is seen in (v) as there is no projection, nor coupling between agent particles. In (vi) the passive agents merely migrate to the stimuli points. The bottom row consists of particles with the standard +ve deposition behaviour. In (vii) the +ve deposition of the particles forms transport networks but the condensation of the networks cannot continue due to the repulsive field around the nodes, forming a hybrid Voronoi/Proximity graph noded in Chapter 6. A ‘basic’ condensing transport network is seen in (viii), taking the form of a contracting circle due to the lack of node stimuli. Finally, in (ix) the transport network forms and is constrained by the attraction to the nodes, minimising the shape to a proximity graph.

17.4.2 Variations in Particle Speed

If we have an agent population where one half of the population moves more slowly than the other half (with otherwise identical agent parameters) we can see the effects of the difference on the shape of the population. The initially uniformly mixed mass (Fig. 17.2a) is distorted by the forces created by the different movement speeds (Fig. 17.2b-d). The different speeds cause the particles to migrate to different parts of the mass (Fig. 17.2e-g) until a clear distinction is seen between anterior and posterior regions of the mass (Fig. 17.2h).

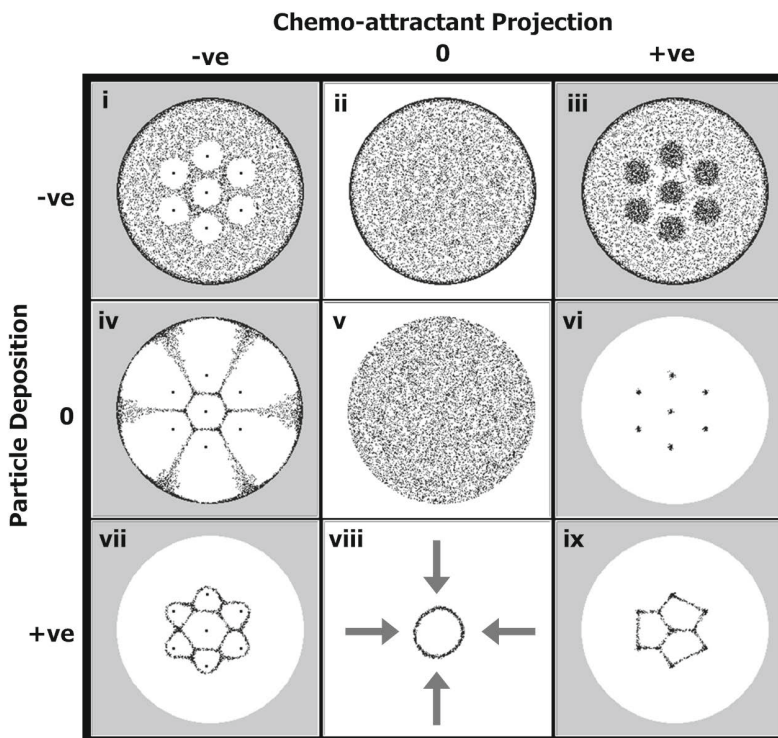


Fig. 17.1 Combinations of agent deposition and stimuli projection. Agent population with attraction behaviour within circular arena. Stimuli are hexagonal array of nodes with additional central node. -ve = negative stimuli/deposition, 0 = no stimuli/deposition, +ve = positive stimuli/deposition. See text for details of i-ix.

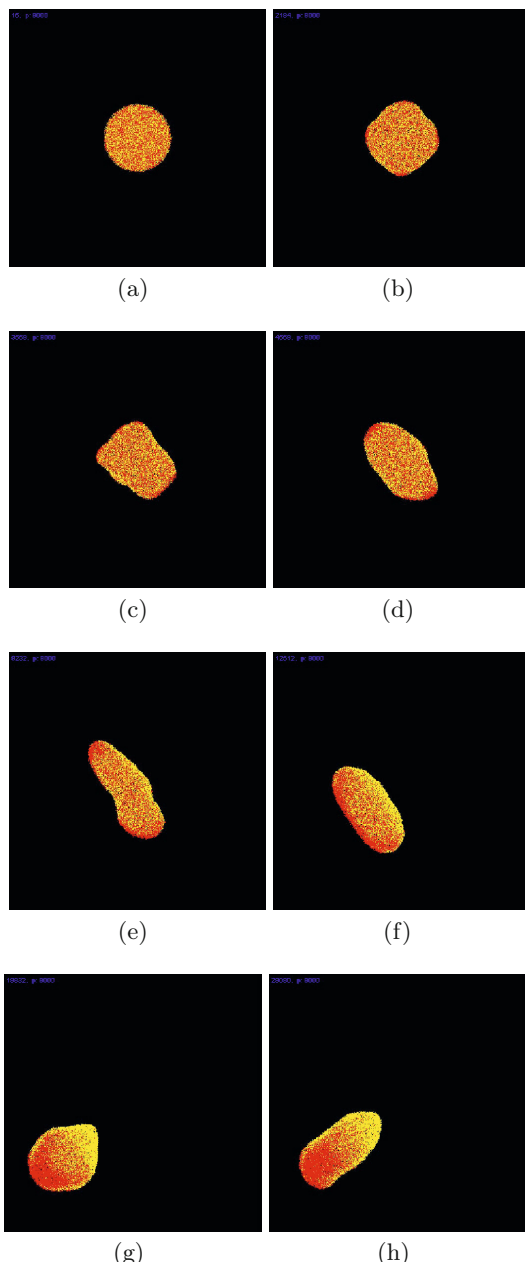


Fig. 17.2 Differences in movement speed in two halves of a population results in a regular anterior-posterior ordering from a mixed mass. a) mass of agents of a single attraction type but two different movement speeds yellow particles move 0.5 units per step, red particles move 1 unit per step. b-h) differences in speed cause distortions in the mass until the mass becomes ordered into two anterior-posterior regions.

17.4.3 Behavioural Variations: Repulsive Behaviour

The default behaviour of the agent particles is to orient in the direction of, and move towards, the strongest local source of chemoattractant. This results in the formation and evolution of minimising emergent transport networks. If the behaviour of the agent particles is reversed, that is if the agents are repulsed by (try to move away from) the chemoattractant which they deposit, a different type of patterning is produced. Instead of diffusive patterns (patterns caused by attraction to diffusion gradients), a range of dissipative patterns are produced. Fig. 17.3 shows periodic patterns which are typical of classical Turing structures. The transitions between pattern types occur as *SA* and *RA* values are adjusted - depending on agent position within the lattice - within a single experiment.

As with the attraction based agents, patterning is dependent on population density (since deposition only occurs after successful movement and successful movement itself depends on free space availability). Fig. 17.4 illustrates the transition in patterning when movement is limited at a population density of %p70. In this instance the flux is greater (dark regions) where movement is not limited. The lighter regions indicate areas where agents are clumped together and cannot move. Note the repetition of patterning as both *SA* and *RA* increase past 180°.

The algorithm for chemorepulsive patterning is conceptually the exact opposite of the algorithm specified in Fig. 3.2b in Chapter 3. Agent particles still deposit chemoattractant when they move forwards. However, instead of orienting towards the strongest source of chemoattractant, the agent orients itself away from the source. For some parameter settings (e.g. *RA* 45°, *SA* 45°) the formation of regularly spaced periodic circular structures is observed. The regular spacing is caused by agents attempting to move away from the source of the chemoattractant that they are depositing. The evolution of the circular structures is complex and highlighted in more detail in Fig. 17.5, top row.

The circular (approximately honeycomb tiling) domains initially emerge as tight circular flows of agents. Typically a circular flow is surrounded by six weaker regions, conceptually similar to the layout of the cartridge chambers in a revolver-type pistol. The concentration of agents from the inner circle is gradually distributed to these outer chambers as the flow of agents is balanced. Over a longer time period, the stable domains within the global lattice begin to exert a larger influence and the regular patterning is slowly enforced and propagated (see supplementary video recordings). On very large lattices the evolution of regular patterning proceeds simultaneously in different regions (Fig. 17.8, left). The regions are connected by irregular ‘paths’ composed of unstable flow. The patterning within the competing domains may be slightly offset in position or angle (Interface between domains is indicated in overlay in Fig. 17.8, right). Larger domains tend to dominate,

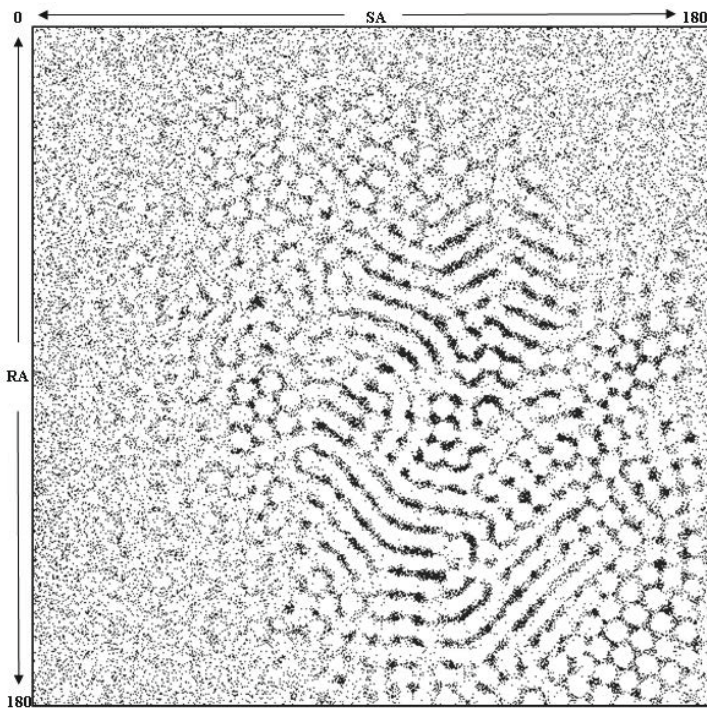


Fig. 17.3 Transitions between patterns with chemorepulsion behaviours formed by varying SA and RA from zero to 180° . 540×540 pixel lattice, $\%p$ 15, SO 15, run for 500 steps

shrinking the size of smaller domains until the entire lattice is covered by a single pattern.

Similar behaviours are observed for the emergence of regular striped domains (Fig. 17.5, bottom row). Initially stripes formed in a number of different directions but one particular direction begins to predominate, transforming neighbouring striped regions to the dominant orientation, ultimately resulting in a regularly distributed striped field. Unlike the pattern formation caused by chemoattraction, which are stable at sensor scales of SO 3, or above, the dissipative patterns are only stable at higher SO settings (typically $SO > 11$). This is because there is no auto-catalytic reinforcement of the dissipative patterns. Persistence of the patterns is caused by the eventual even distribution of particles throughout the lattice. Too much local movement disrupts the pattern (since particles are trying to avoid regions with higher concentration of chemoattractant). Increasing SO scale increases the size and distance between repeating pattern regions (Fig. 17.6) and larger scale patterns stabilise more quickly than those at smaller scales.

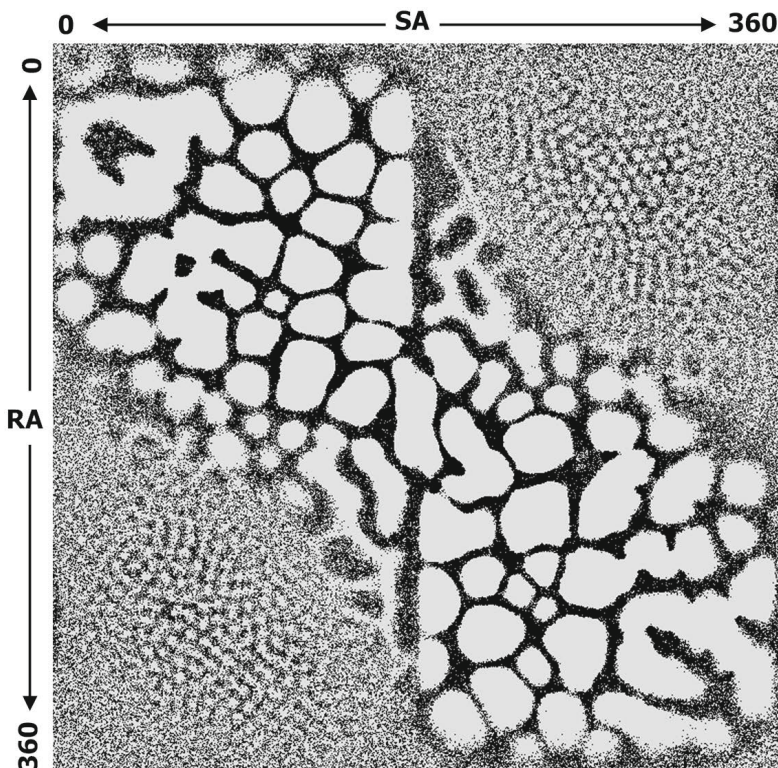


Fig. 17.4 Chemorepulsion pattern transitions at high population density. Patterns formed by varying SA and RA from zero to 360° , 720×720 pixel lattice, $\%p = 70$, $SO = 11$, run for 500 steps. Note that increasing SA and RA beyond 180° mirrors the type of patterning.

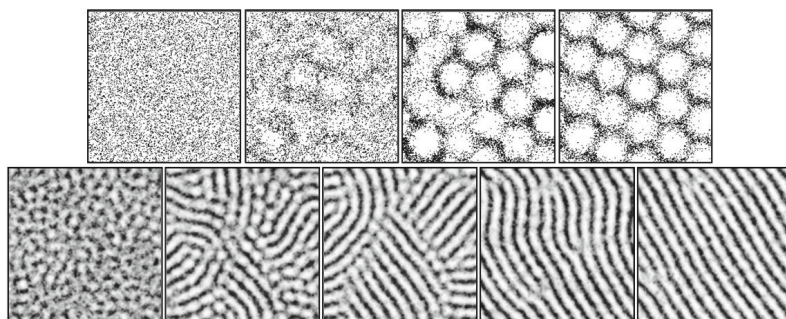


Fig. 17.5 Evolution of dissipative patterns with repulsive agent behaviour. (Top Row) 200×200 lattice, $\%p = 20$, $RA = 45^\circ$, $SA = 45^\circ$, $SO = 40$, (Bottom Row) 200×200 lattice $\%p = 20$, $RA = 67.5^\circ$, $SA = 112.5^\circ$, $SO = 13$

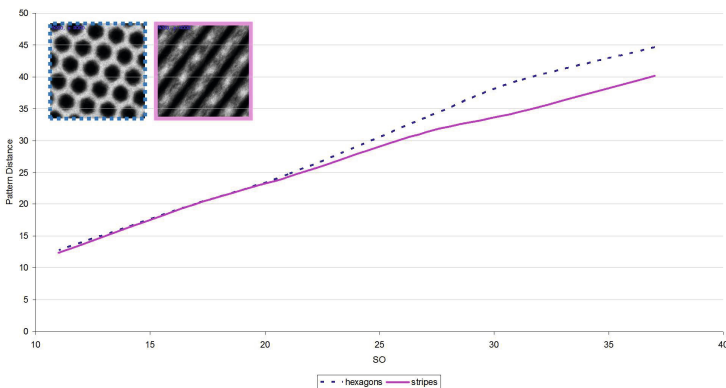


Fig. 17.6 Effect of sensor scale on repulsive pattern period distance. Graph shows increasing distance between patterns as SO increases. Distance measured at border of adjacent hexagons (dashed, $SA 45^\circ$, $RA 45^\circ$) or stripes (solid, $SA 90^\circ$, $RA 90^\circ$). Inset images show example repulsive patterns at SO 37 for hexagons and stripes.

The formation of dissipative patterns can be affected by external stimuli. In Fig. 17.7 the self-organised patterns differ when the boundary shape (projecting an attractant stimulus) is altered. The particles are repelled by the attractant stimuli (and by the stimuli which they themselves deposit) and Fig. 17.7a-e shows the effect of a circular boundary, with a hierarchy of concentric rings forming. The first rings to form are closest to the boundary edge and new inner rings form when the outer ring stabilises. If a different shaped boundary is used, the inner patterns reflect the original boundary (Fig. 17.7f-k).

Experiments were carried out to assess the effect of damage to the established patterns formed by chemorepulsion patterning. The creation of a synthetic ‘wound’ was achieved by the instantaneous removal of agents within a square region. The agents that were removed were replaced at random locations in the undamaged area to maintain the same population size. During the agent replacement period no agents were allowed to cross the wound boundary. When the number of agents was the same as before the damage was inflicted the agents were allowed to migrate into the wound area. Fig. 17.9 shows the effect of chemorepulsion agents during the initial patterning process and in response to damage infliction. The figure shows the uniform flux of agents into the wound area and the closure of the wound. The initial pattern is re-established under the influence of the undamaged areas surrounding the wound site. The final ‘healed’ pattern is identical to the pattern before the damage was inflicted.

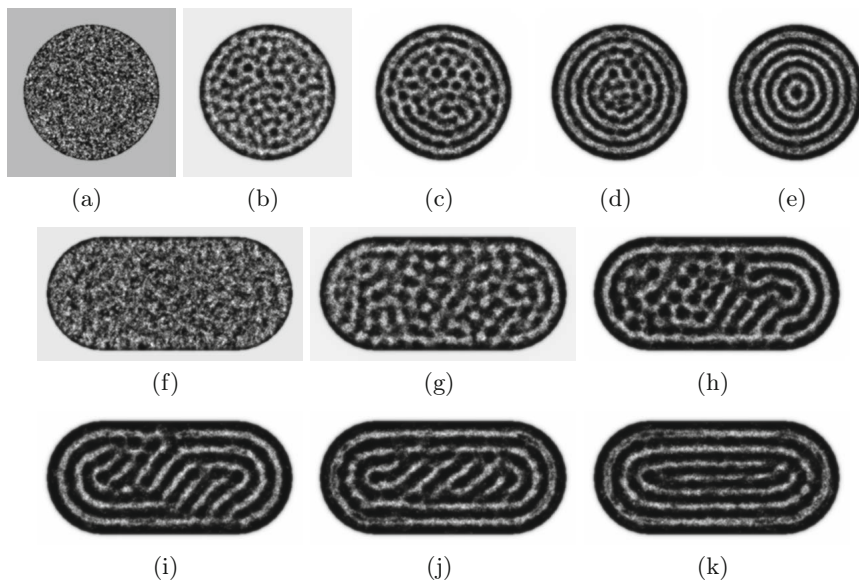


Fig. 17.7 Boundary stimulus effect on internal patterning. Boundary pattern projects attractant stimulus into arena, causing particles to move to and avoid stimuli, a-e) circular boundary causes formation of self-organised concentric circles, f-k) oval boundary generates internal concentric ovals.

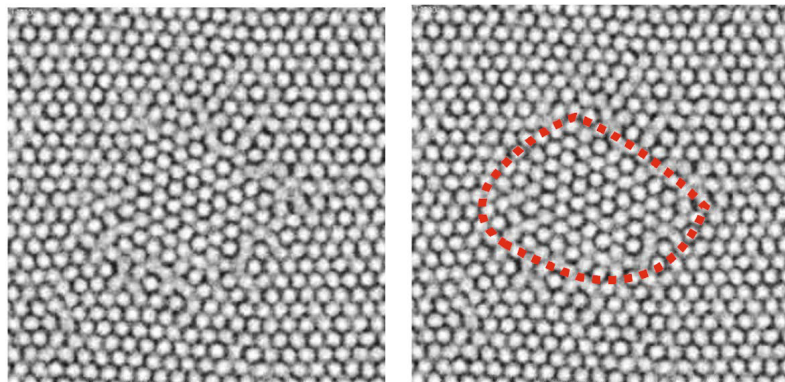


Fig. 17.8 Separate competing domains within repulsive lattice. Left: lattice containing two regular domains separated by unstable interface. Right: overlay of interface which shrinks over time as the outer pattern predominates and stabilises.

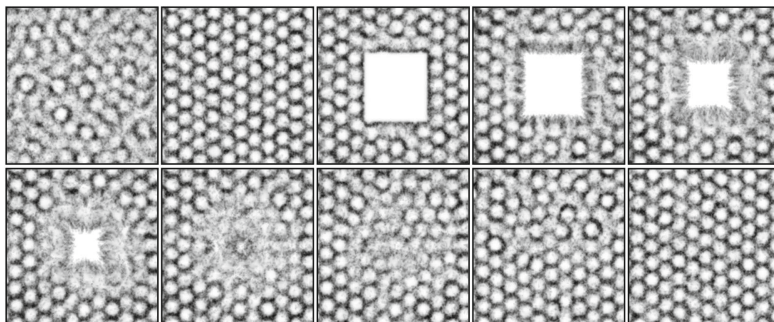


Fig. 17.9 Recovery of pattern after damage. Top Row: initial pattern formation, regular hexagonal pattern, damage to central area, and migration of agents towards the wound area, Bottom Row: Completion of migration closes the damaged area (1-2), re-organisation of the wound area re-establishes the initial pattern. Lattice 300×300 lattice, $RA 45^\circ$, $SA 45^\circ$, $SO 27$, $\%p 10$

17.4.4 Behavioural Variations: Combinations of Different Particle Types

The patterning demonstrated in the model has been generated by a single agent type (attraction based or repulsion based). In physical and living systems, however, there are obviously many more ‘cell’ types, with different behaviours for each. The combination of agents with different behaviours would thus reasonably be expected to result in more complex patterning. In this section we present simple examples of the results of mixing different behavioural types. We consider binary opposite behaviours: a combination of attraction based patterning with repulsion based patterning.

When both particle types are initialised at random positions within the same arena we observe the self-organised patterns characteristic of phase separation (Fig. 17.10) where labyrinthine patterns are formed (Fig. 17.10b,c) due to the local effects of the opposite behaviours of the particles. These initial patterns then grow and coarsen as the two phases continue to separate (Fig. 17.10d-f).

When the particles are initialised at separate sides of an arena, the interface becomes distorted by local perturbations in flux at the interface. These distortions are locally amplified, resulting in an eventual mixing between the two compartments. The mixing pattern depends upon particular deposition patterns and examples are shown of encapsulation type patterns (Fig. 17.11) and interdigitating interfacial patterns (Fig. 17.12).

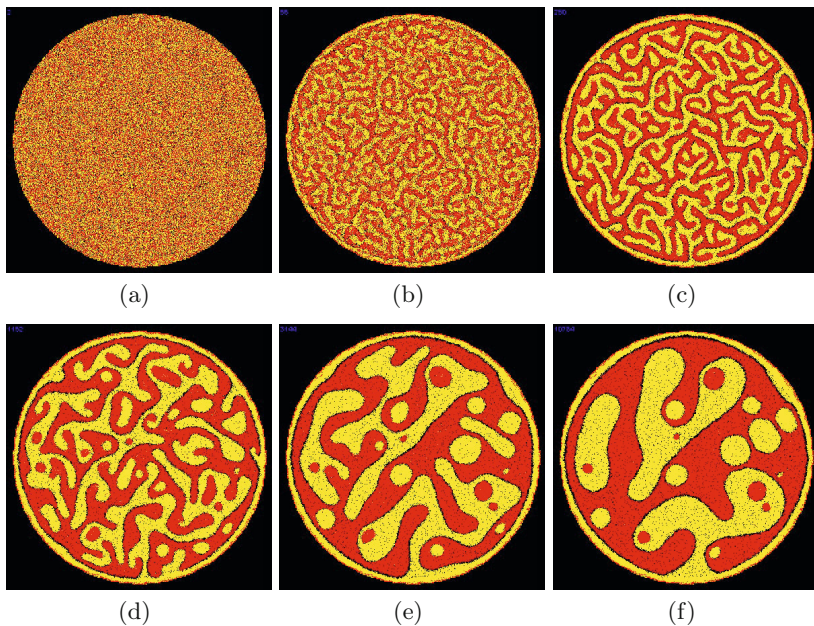


Fig. 17.10 Phase separation behaviour in combined attraction and repulsion agents. a) initially random distribution of attraction (yellow) and repulsion (red) agents, b,c) initial formation of labyrinthine patterns, d-f) separation of both agent types as different phase domains grow.

The patterns formed by two opposite particle types, Attraction and Repulsion, are dependent on the relative deposition of the two particle types. A parametric evaluation of the effect of deposition is shown in Fig. 17.13. The results include a complete lack of patterning (Fig. 17.13i and v), partial patterning (Fig. 17.13ii and iv), patterns arranged into bundles (iii, vi and vii) and phase separation patterns (viii and ix).

Patterning in combinations of opposite particle types is still affected by variations in the *SA* and *RA* parameters. This can result in patterns which are surprisingly unintuitive. For example Fig. 17.14 shows the spontaneous self-organisation of striped dynamical networks. Each network path is composed of alternating domains of attraction and repulsion particles. Attraction particles (yellow) in this instance excavate chemoattractant trail by -5 units per step whilst repulsion particles deposit attractant at 5 units per step.

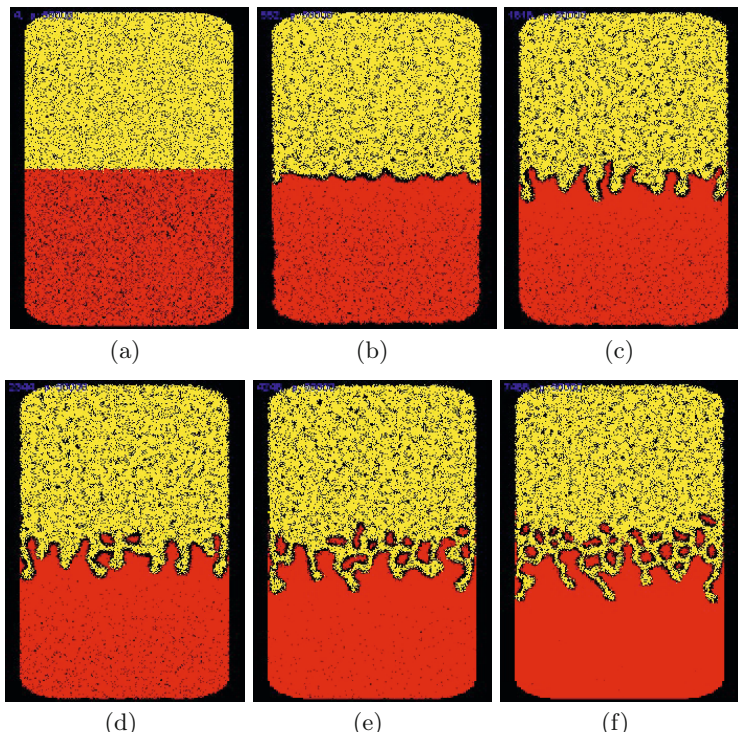


Fig. 17.11 Interfacial mixing with encapsulation patterning. a) an arena containing a separated mixture of attraction (yellow) and repulsion (red) particles, b) distortion of interface as particles interact, c-f) interfacial mixing generates encapsulated regions where repulsion particles are enclosed by yellow particles.

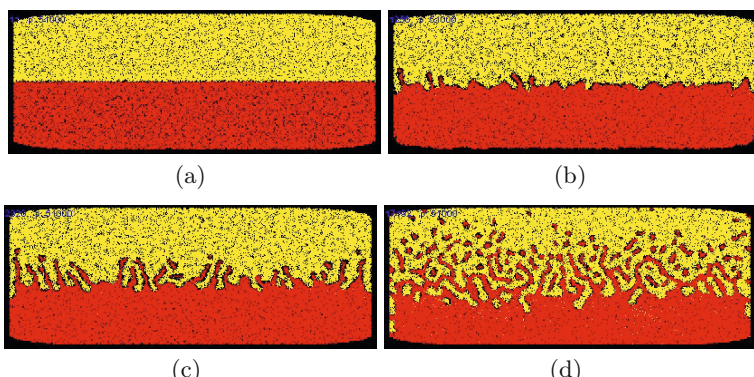


Fig. 17.12 Interfacial mixing with interdigitate patterns. a) an arena containing a separated mixture of attraction (yellow) and repulsion (red) particles, b) distortion of interface as particles interact, c-f) interfacial mixing generates interdigitate patterns where both particle types are enclosed by finger-like projections.

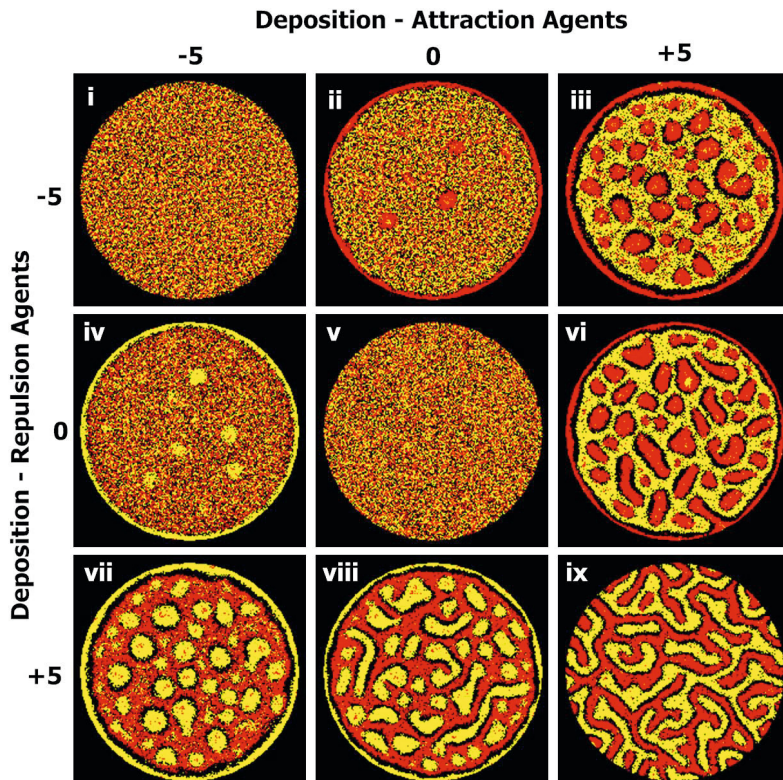


Fig. 17.13 Effect of +ve and -ve deposition in mixed agent types. $\%p=20$, SA 60° , RA 60° , all experiments run for 200 steps.

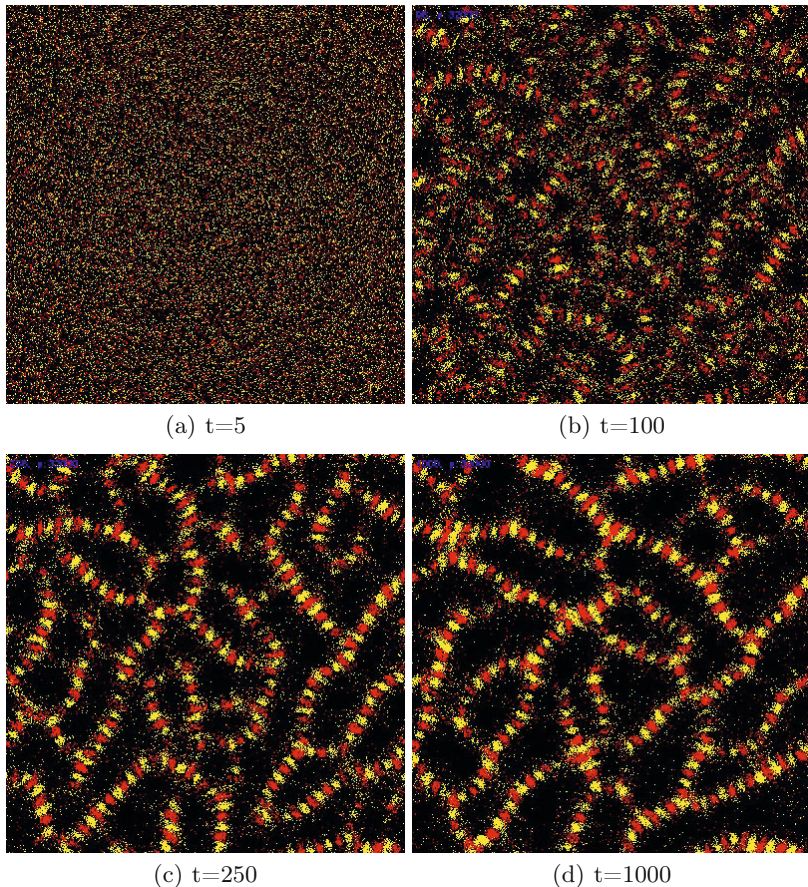


Fig. 17.14 Self-organised formation of striped networks. Attraction and repulsion agents interact to produce networks whose paths are composed of alternating domains of attraction and repulsion particles. Lattice 400x400 pixels, $\%p=20$, $SA 45^\circ$, $RA 90^\circ$, $SO 15$, Attr $depT=-5$, Rep $depT=-5$

17.4.5 Effects of Boundary Conditions and Pre-existing Gradients

Previous examples of patterning in the multi-agent model was typically produced with simple boundary conditions (fixed or periodic) and on a blank diffusive lattice. Pattern formation in physical systems, and in living systems, may be strongly influenced by pre-existing information gradients (for example chemoattractant or traction gradients), noisy or uneven gradients, changing physical conditions (as in drying materials, [286]) or more complex boundary conditions, such as changing boundaries in growing environments. We present

some preliminary results which illustrate the effects of boundary conditions and pre-existing gradients on patterning using the multi-agent approach.

In Fig. 17.15 the effect on patterning of a growing environment is illustrated in the agent model. Such patterning is caused by the changing stimulus due to the physical changes which occur (for example leaf venation patterns have been modelled within a growing tensor field in [29]). A fixed sized population of attraction particles was initialised within a rectangular arena with non-periodic boundary conditions, where the particles were attracted to stimulus projected at the arena boundary. Over time the vertical height of the arena was gradually increased whilst the number of particles remained the same. The growth of the arena produced strains in the ‘material’, resulting in small defects forming (Fig. 17.15) which gradually increased in size. Minimisation within the material ultimately resulted in vertical bamboo-like septate patterns.

In all the examples shown so far in this book the particles are directly coupled to the diffusive lattice, i.e. they both sense the concentration of chemoattractant in the lattice and also *deposit* chemoattractant into the lattice. However, this coupling does not have to be direct. In Fig. 17.16 we see complex patterning even when agent particles do not deposit values into the lattice. In this experiment a mixture of attractant and repulsion based agents are initialised with random positions in a circular arena which has a single source of attractant projected into the lattice at its centre. The attractant particles (yellow) try to move towards the attractant source whilst the repulsion particles (red) try to move away from the source. Because of the crowded lattice, the different types of particles collide, blocking the flow of the particles. This results in the growth of a layered structure to the arena, initiated at the centre, which resembles a phyllotaxis-type rose-petal pattern (Fig. 17.16d).

Complex patterns can also be observed when only a single agent particle type is used. In Fig. 17.17 a population of attractant particles is randomly initialised on an arena with a linear chemoattractant gradient which increases towards the centre (In Fig. 17.17a). The particles attempt to migrate towards the centre of the arena but instead of depositing chemoattractant into the lattice, they excavate attractant from the lattice. The resulting patterns resemble spirals in, for example, sunflower heads (Fig. 17.17c). If, however, the attractant particles deposit attractant into the lattice (instead of excavating from the lattice) a different kind of pattern is produced, resembling Lichtenberg figures (Fig. 17.17d) [287].

If the agent particles are initialised from the outside rim of the arena, the patterns grow from the outside in towards the increasing gradient at the centre of the arena. Fig. 17.18 demonstrates the patterning (by attractant agents, depositing attractant) as the iris-like growth front converges on the centre of the arena.

Alternately, self-organised spiral patterns emerge when repulsion particles are inoculated at the very centre of the arena. In Fig. 17.19 and Fig. 17.20 the

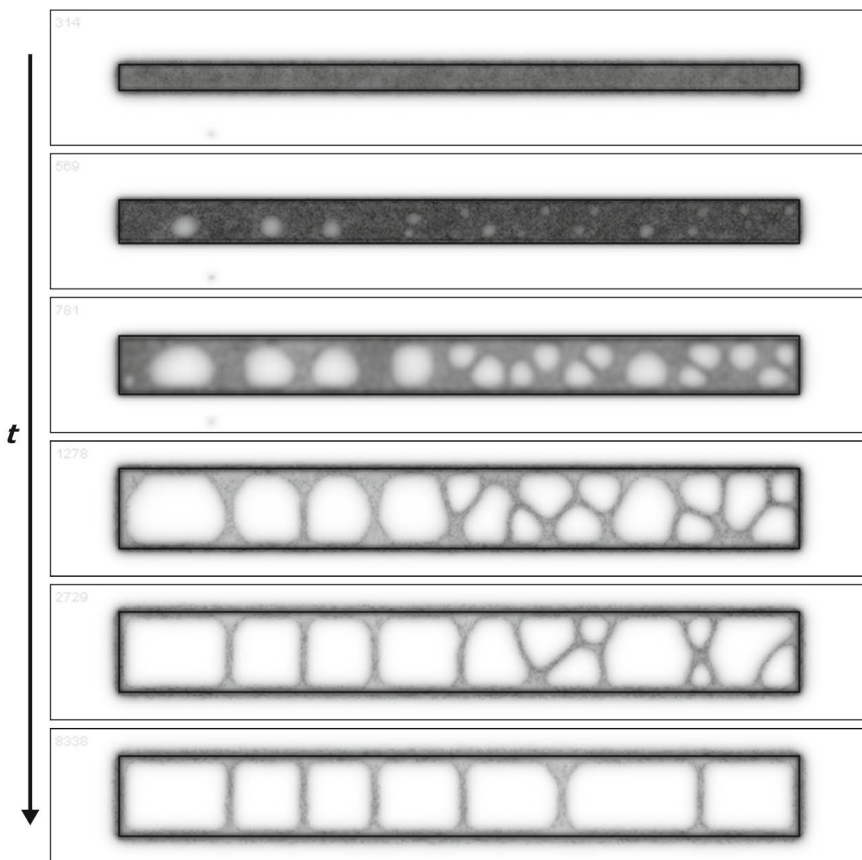


Fig. 17.15 Septate patterning in a growing environment. Fixed population is initialised as a sheet within a rectangular environment. Boundary projects attractant and the growing boundary deforms and tears the sheet, resulting in septate patterning (time proceeds downwards).

repulsion particles attempt to move away from the chemoattractant which they deposit as they move. In the presence of a linear gradient increasing towards the centre of the arena (not shown) the particles form multi-arm rotating spirals as they migrate to the outside of the arena (Fig. 17.19).

If no initial gradient is present in the arena, the rotating pattern still forms but is much more sparse in appearance and takes approximately ten times longer to stabilise (Fig. 17.20).

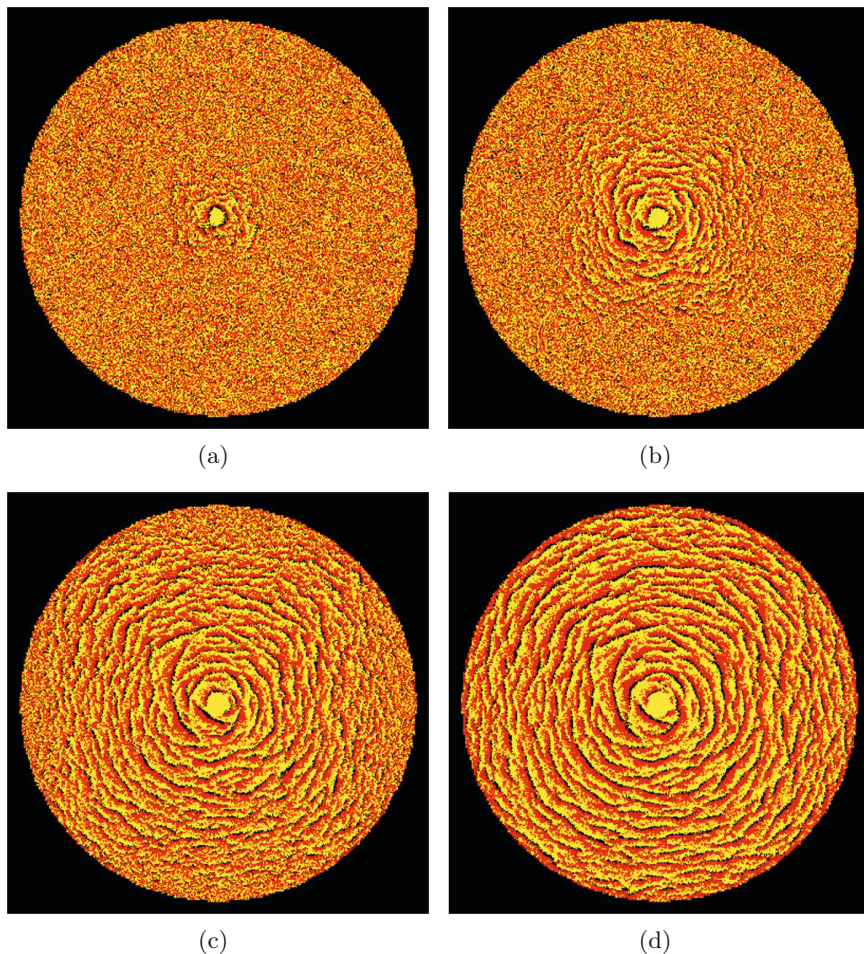


Fig. 17.16 Mechanical interactions between opposite behaviours result in ‘rose-petal’ patterning. Attraction (lighter) and repulsion (darker) agents interact within a circular arena with an attractive stimuli at the centre. Opposite moving agents result in blockages initiated around the central position which ultimately take on a distinctive phyllotaxis-like pattern.

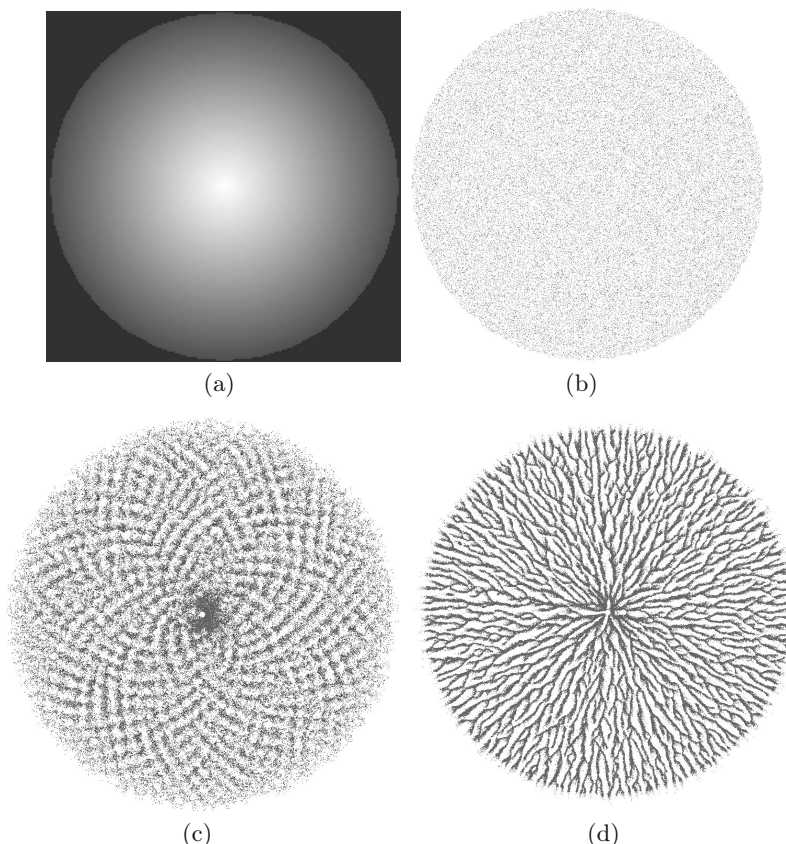


Fig. 17.17 Complex patterning in reaction to central concentration gradient. (a) Initial attraction gradient within circular arena - intensity corresponds to stimulus concentration, (b) Initial random placement of attractant agent particles within arena, (c) formation of phyllotaxis-type double spiral pattern caused by obstruction as excavating agents migrate to the central area, d) if particles deposit attractant then patterns reminiscent of Lichtenberg figures are produced.

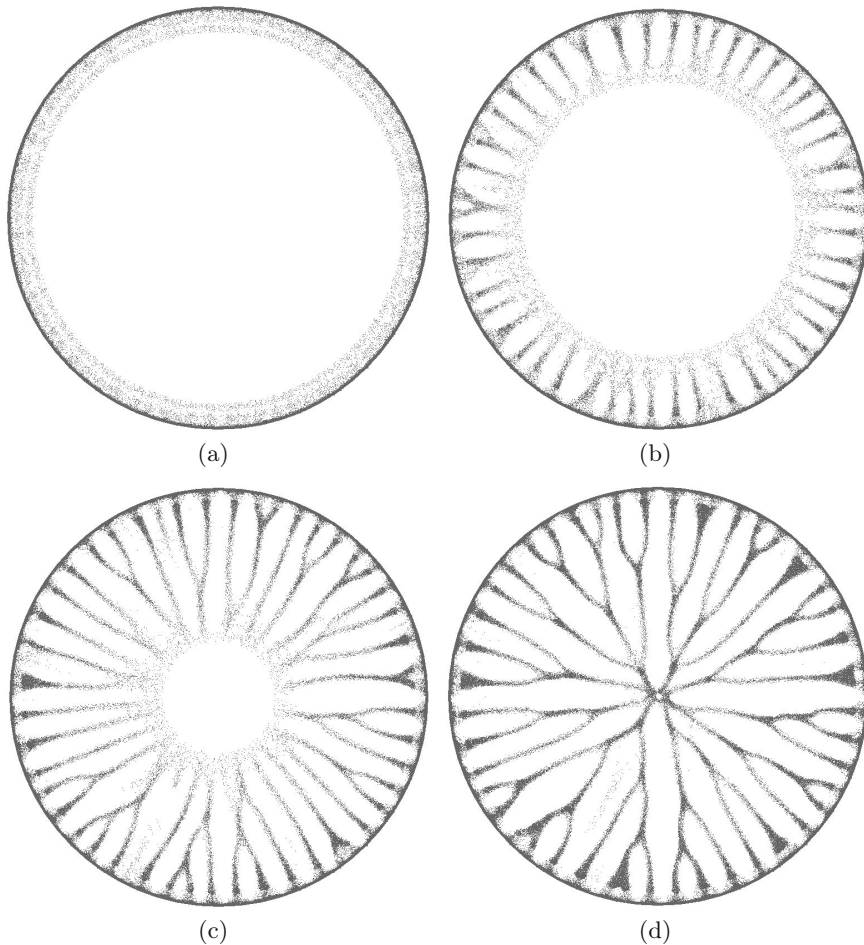


Fig. 17.18 Inoculation at the rim of the arena (containing the initial gradient in Fig. 17.17a) generates an iris-like growth front as the agent particles migrate towards the centre of the arena.

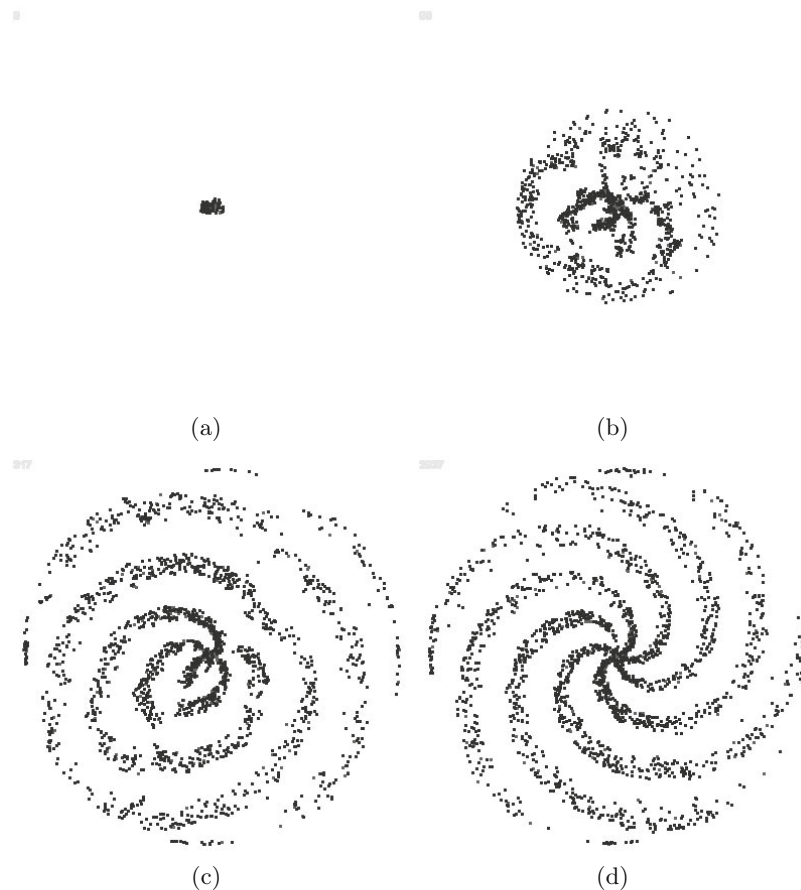


Fig. 17.19 Formation of rotating multi-arm patterns. Spiral arms formed by repulsion type agents initiated at the centre of the arena containing a linear stimulus gradient and migrating away from their own trail deposition.

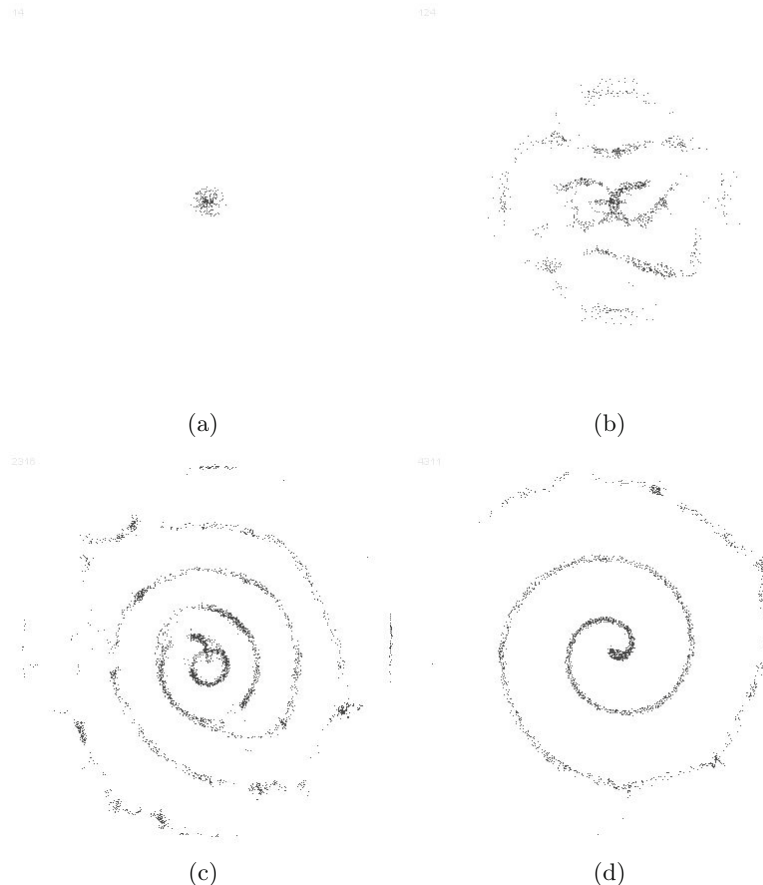


Fig. 17.20 Sparse single-arm spiral patterns. Spiral pattern formed by repulsion type agents initiated at the centre of the arena (without a stimulus gradient) and migrating away from their own trail deposition.

17.4.6 Towards Three Dimensional Models

Physarum can be interpreted as a planar 2D organism due to the fact that it flows over its environment and possesses no structural support system. However it is possible to extend the scope of the multi-agent model to explore patterning in three dimensional environments. Since the behaviour of the 2D model reproduces many features of soap film edge evolution, it might reasonably be expected that extending the model into three dimensions may reproduce the surface area minimisation properties seen in soap films [193].

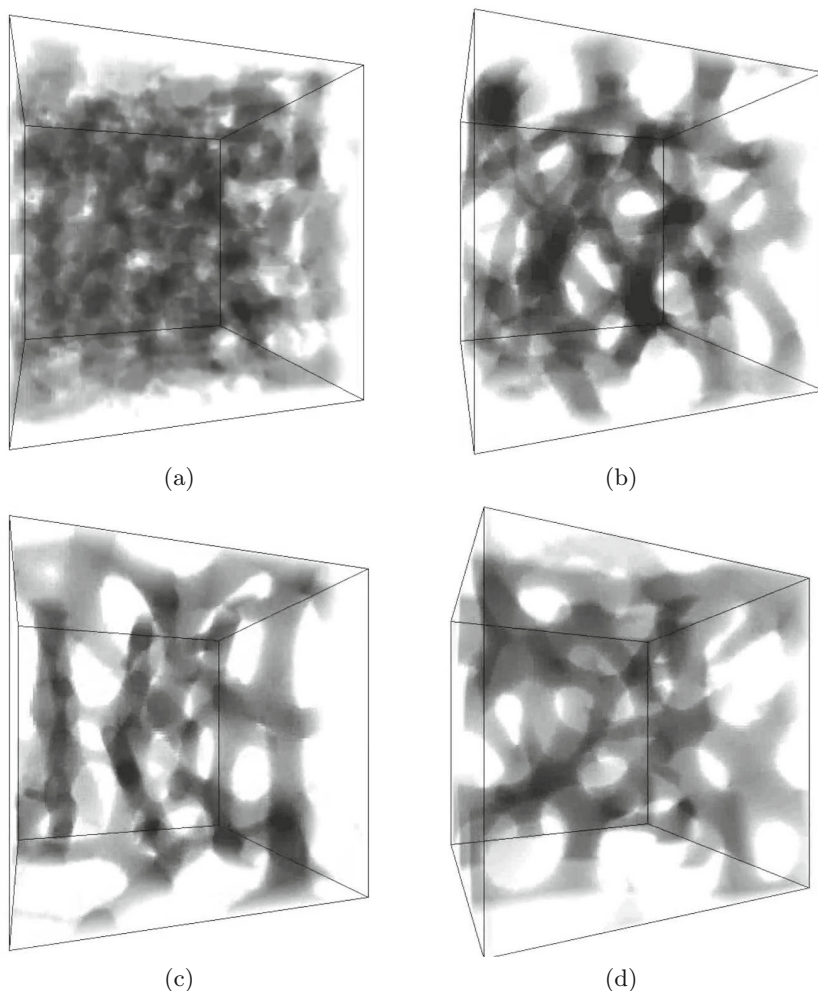


Fig. 17.21 3D Branching transport networks. $SA 22.5^\circ$, $RA 45^\circ$, $SO 7$

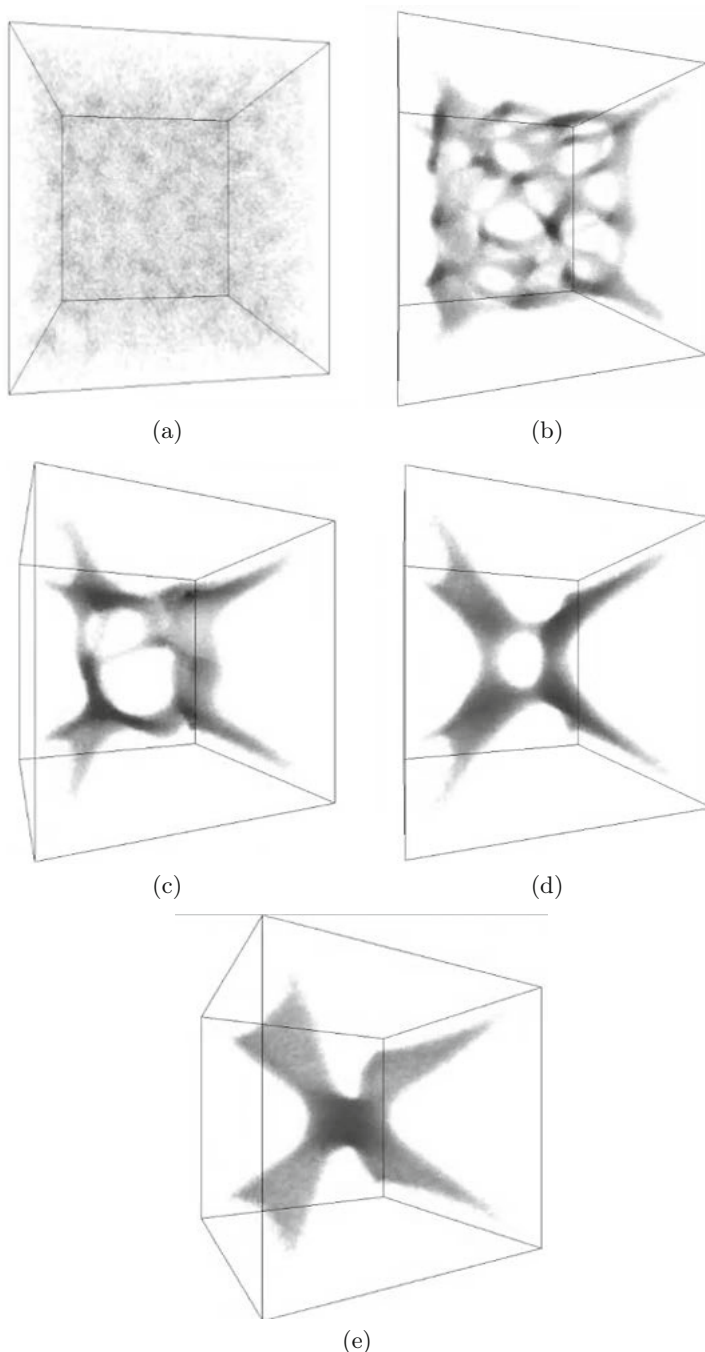


Fig. 17.22 3D Minimising transport networks. $SA\ 22.5^\circ$, $RA\ 45^\circ$, $SO\ 7$. Data points representing the corner locations of a cube are projected into the lattice.

One difficulty with the extension into three dimensions is how to represent the extra inputs to the offset sensors. This is achieved by including two extra sensors to include the Front-Forward and Front-Backward sensors, in addition to the pre-existing Front, Front-Left and Front-Right sensors (the transformation between 2D and 3D sensors may be mentally visualised as moving from a planar anchor shape to a 3D ‘grappling hook’ shape). The sensory algorithm must also be modified to include the input from the new sensors, however the general behaviour is the same: orient to face the strongest local source of chemoattractant. The behaviour of the virtual material in three dimensions reproduces the dynamical branching patterns of the 2D model (Fig.17.21) when SA 22.5° and RA 45° . The model demonstrates surface minimisation behaviour seen in soap films (Fig.17.22) when nutrient data points representing the corners of a cube are projected into the lattice. The population assembles sheet-like structures connecting the points and the shape of the structures evolves to reduce the surface area Fig.17.22d).

17.4.7 Summary: *Physarum* and Beyond

The brief examples demonstrated in this chapter suggest a wider application of the multi-agent material approach for the more general study of pattern formation phenomena. Despite the simple particle behaviour and diffusion method, a wide range of patterning can be approximated, including reaction-diffusion, dissipative, interfacial, phase separation, mechanical and phyllotactic patterns. The importance of physical forces on biological pattern formation was first described in detail by Thompson [288] however it is fair to say that this influence was temporarily abandoned in the excitement of the discovery and subsequent advances in genetic influences on biological systems. The influence of physical forces and chemotactic cues on patterning during embryogenesis, maintenance of the body plan, and tumorigenesis is now becoming more widely accepted (for example see [203, 137, 289]) and such patterning is characteristically dynamical rather than fixed. We hope that the multi-agent approach developed to model the dynamical and emergent behaviour of *Physarum* may provide a small contribution to the study of pattern formation phenomena in other chemical, physical and biological systems.

Appendix A

Supplementary Material

This Appendix lists the supplementary material related to this book. The supplementary material can be viewed online at: <http://uncomp.uwe.ac.uk/jeff/book/material.htm>.

A.1 Supplementary Video Recordings

The video recordings are recordings of experiments using the virtual plasma model. The recordings are divided into folders, corresponding to the relevant chapter and named to correspond to the relevant section or figure.

A.2 Interactive Multi-agent Model

A simple version of the multi-agent model used to develop the virtual plasma model is included. The model is written using the Processing language.

A.3 Source Code

The source code shows simplified version of the model, coded using the Processing language. The source code demonstrates the base behaviour of the model in a simply laid out way and is commented to give relevant information for those wishing to extend or adapt the model.

References

- [1] Langton, C.G., Shimohara, K.: Artificial Life 5, vol. 5. The MIT Press (1997)
- [2] Stepney, S.: The neglected pillar of material computation. *Physica D: Non-linear Phenomena* 237(9), 1157–1164 (2008)
- [3] Holland, J.H.: *Emergence: From Chaos to Order*. Oxford University Press (2000)
- [4] Adamatzky, A.: *Physarum Machines: Computers from Slime Mould*, vol. 74. World Scientific Pub. Co. Inc. (2010)
- [5] Stephenson, S.L., Stempen, H., Hall, I.: *Myxomycetes: a handbook of slime molds*. Timber Press Portland, Oregon (1994)
- [6] Wohlfarth-Bottermann, K.E.: Biological aspects of motility. *NATO Advanced Science Institutes Series: Series A: Life Sciences* 106 (1986)
- [7] Wohlfarth-Bottermann, K.E.: Oscillating contractions in protoplasmic strands of *Physarum*: simultaneous tensiometry of longitudinal and radial rhythms, periodicity analysis and temperature dependence. *Journal of Experimental Biology* 67, 49–59 (1977)
- [8] Kamiya, N., Kuroda, K.: Studies on the velocity distribution of the protoplasmic streaming in the myxomycete plasmodium. *Protoplasma* 49(1), 1–4 (1958)
- [9] Nakagaki, T., Kobayashi, R., Nishiura, Y., Ueda, T.: Obtaining multiple separate food sources: behavioural intelligence in the *Physarum* plasmodium. *R. Soc. Proc.: Biol. Sci.* 271(1554), 2305–2310 (2004)
- [10] Nakagaki, T., Guy, R.D.: Intelligent behaviors of amoeboid movement based on complex dynamics of soft matter. *Soft Matter* 4(1), 57–67 (2007)
- [11] Nakagaki, T., Saigusa, T., Tero, A., Kobayashi, R.: Effects of amount of food on path selection in the transport network of an amoeboid organism. In: *Proceedings of the International Symposium on Topological Aspects of Critical Systems and Networks*. World Scientific (2007)
- [12] Latty, T., Beekman, M.: Food quality affects search strategy in the acellular slime mould, *Physarum polycephalum*. *Behavioral Ecology* 20(6), 1160 (2009)
- [13] Latty, T., Beekman, M.: Food quality and the risk of light exposure affect patch-choice decisions in the slime mold *Physarum polycephalum*. *Ecology* 91(1), 22–27 (2010)

- [14] Dussutour, A., Latty, T., Beekman, M., Simpson, S.J.: Amoeboid organism solves complex nutritional challenges. *Proceedings of the National Academy of Sciences* 107(10), 4607 (2010)
- [15] Achenbach, F., Naib-Majani, W., Wohlfarth-Bottermann, K.E.: Plasmalemma invaginations of *Physarum* dependent on the nutritional content of the plasmodial environment. *Journal of Cell Science* 36(1), 355 (1979)
- [16] Ueda, T., Terayama, K., Kurihara, K., Kobatake, Y.: Threshold phenomena in chemoreception and taxis in slime mold *Physarum polycephalum*. *The Journal of General Physiology* 65(2), 223–234 (1975)
- [17] Matsumoto, K., Ueda, T., Kobatake, Y.: Propagation of phase wave in relation to tactic responses by the plasmodium of *Physarum polycephalum*. *Journal of Theoretical Biology* 122, 339–345 (1986)
- [18] Hejnowicz, Z., Wohlfarth-Bottermann, K.E.: Propagated waves induced by gradients of physiological factors within plasmodia of *Physarum polycephalum*. *Planta* 150, 144–152 (1980)
- [19] Ridgway, E.B., Durham, A.C.: Oscillations of calcium ion concentrations in *Physarum polycephalum*. *The Journal of Cell Biology* 69(1), 223–226 (1976)
- [20] Ueda, T., Matsumoto, K., Kobatake, Y.: Spatial and temporal organization of intracellular adenine nucleotides and cyclic nucleotides in relation to rhythmic motility in *Physarum* plasmodium. *Experimental Cell Research* 162(2), 486–494 (1986)
- [21] Yoshimoto, Y., Matsumura, F., Kamiya, N.: Simultaneous oscillations of Ca^{2+} efflux and tension generation in the permeabilized plasmodial strand of *Physarum*. *Cell Motility* 1(4), 433–443 (1981)
- [22] Ueda, T., Götz, O.K., Wohlfarth-Bottermann, K.E.: Reaction of the contractile apparatus in *Physarum* to injected Ca^{++} , ATP, ADP and 5'AMP. *Cytobiologie* 18(1), 76 (1978)
- [23] Hatano, S., Oosawa, F.: Isolation and characterization of plasmodium actin. *Biochimica et Biophysica Acta (BBA)-General Subjects* 127(2), 488–498 (1966)
- [24] Isenberg, G., Wohlfarth-Bottermann, K.E.: Transformation of cytoplasmic actin: Importance for the organization of the contractile gel reticulum and the contraction-relaxation cycle of cytoplasmic actomyosin. *Cell and Tissue Research* 173, 495–528 (1976)
- [25] Ishigami, M.: Dynamic aspects of the contractile system in *Physarum* plasmodium: I. changes in spatial organization of the cytoplasmic fibrils according to the contraction-relaxation cycle. *Cell Motility and the Cytoskeleton* 6(5), 439–447 (1986)
- [26] Wohlfarth-Bottermann, K.E.: Oscillatory contraction activity in *Physarum*. *The Journal of Experimental Biology* 81, 15–32 (1979)
- [27] Kamiya, N.: The protoplasmic flow in the myxomycete plasmodium as revealed by a volumetric analysis. *Protoplasma* 39(3), 344–357 (1950)
- [28] Takagi, S., Ueda, T.: Emergence and transitions of dynamic patterns of thickness oscillation of the plasmodium of the true slime mold *Physarum polycephalum*. *Physica D* 237, 420–427 (2008)
- [29] Couder, Y., Pauchard, L., Allain, C., Adda-Bedia, M., Douady, S.: The leaf venation as formed in a tensorial field. *The European Physical Journal B-Condensed Matter and Complex Systems* 28(2), 135–138 (2002)

- [30] Mitchison, G.J., Hanke, D.E., Sheldrake, A.R.: The polar transport of auxin and vein patterns in plants [and discussion]. *Philosophical Transactions of the Royal Society of London. B, Biological Sciences* 295(1078), 461–471 (1981)
- [31] Scheres, B., Xu, J.: Polar auxin transport and patterning: grow with the flow. *Genes & Development* 20(8), 922 (2006)
- [32] Kamiya, N.: Physical and chemical basis of cytoplasmic streaming. *Ann. Rev. Plant Physiol.* 32, 205–236 (1981)
- [33] Oster, G.F., Odell, G.M.: Mechanics of cytogels I: oscillations in *Physarum*. *Cell Motility* 4(6), 469–503 (1984)
- [34] Mackey, M.C., Glass, L.: Oscillation and chaos in physiological control systems. *Science* 197(4300) (1977)
- [35] Hooper, S.L.: Central pattern generators. In: *Encyclopedia of Life Sciences*. John Wiley and Sons (2001)
- [36] Kuo, A.D.: The relative roles of feedforward and feedback in the control of rhythmic movements. *Motor Control* 6, 129–145 (2002)
- [37] Miyake, Y., Tabata, S., Murakami, H., Yano, M., Shimizu, H.: Environmental-dependent self-organization of positional information field in chemotaxis of *Physarum* plasmodium. *Journal of Theoretical Biology* 178, 341–353 (1996)
- [38] Tanaka, J., Miyake, Y.: Modulation of intracellular rhythm and behavior of *Physarum* plasmodium under the condition of mutual entrainment. In: *Proceedings of the SICE 2000 Conf.*, p. 212-A4. The Society of Instrument and Control Engineers (2000)
- [39] Miura, H., Yano, M.: A model of organization of size invariant positional information in taxis of *Physarum* plasmodium. *Prog. Theor. Phys.* 100(2), 235–251 (1998)
- [40] Takahashi, K., Uchida, G., Hu, Z.S., Tsuchiya, Y.: Entrainment of the self-sustained oscillation in a *Physarum polycephalum* strand as a one-dimensionally coupled oscillator system. *Journal of Theoretical Biology* 184, 105–110 (1997)
- [41] Takamatsu, A., Fujii, T.: Time delay effect in a living coupled oscillator system with the plasmodium of *Physarum polycephalum*. *Phys. Rev. Lett.* 85, 2026–2029 (2000)
- [42] Takamatsu, A., Fujii, T., Endo, I.: Control of interaction strength in a network of the true slime mold by a microfabricated structure. *BioSystems* 55, 33–38 (2000)
- [43] Takamatsu, A., Fujii, T., Yokota, H., Hosokawa, K., Higuchi, T., Endo, I.: Controlling the geometry and the coupling strength of the oscillator system in plasmodium of *Physarum polycephalum* by microfabricated structure. *Protoplasma* 210, 164–171 (2000)
- [44] Takamatsu, A., Tanaka, R., Yamada, H., Nakagaki, T., Fujii, T., Endo, I.: Spatiotemporal symmetry in rings of coupled biological oscillators of *Physarum* plasmodial slime mold. *Physical Review Letters* 87(7), 78102 (2001)
- [45] Takamatsu, A.: Spontaneous switching among multiple spatio-temporal patterns in three-oscillator systems constructed with oscillatory cells of true slime mold. *Physica D: Nonlinear Phenomena* 223(2), 180–188 (2006)
- [46] Golubitsky, M., Schaeffer, D.G., Stewart, I.: Singularities and groups in bifurcation theory, vol. 2. Springer (1988)

- [47] Fricker, M.D., Tlalka, M., Bebber, D., Tagaki, S., Watkinson, S.C., Darrah, P.R.: Fourier-based spatial mapping of oscillatory phenomena in fungi. *Fungal Genetics and Biology* 44(11), 1077–1084 (2007)
- [48] Matsumoto, K., Ueda, T., Kobatake, Y.: Reversal of thermotaxis with oscillatory stimulation in the plasmodium of *Physarum polycephalum*. *Journal of Theoretical Biology* 131, 175–182 (1988)
- [49] Takamatsu, A., Takahashi, K., Nagao, M., Tsuchiya, Y.: Frequency coupling model for dynamics of responses to stimuli in plasmodium of *Physarum polycephalum*. *Journal of Physical Society of Japan* 66, 1638–1646 (1997)
- [50] Nakagaki, T., Ueda, T.: Phase switching of rhythmic contraction in relation to regulation of amoeboid behavior by the plasmodium of *Physarum polycephalum*. *Journal of Theoretical Biology* 179, 261–267 (1996)
- [51] Saigusa, T., Tero, A., Nakagaki, T., Kuramoto, Y.: Amoebae anticipate periodic events. *Physical Review Letters* 100(1), 18101 (2008)
- [52] Takagi, S., Ueda, T.: Annihilation and creation of rotating waves by a local light pulse in a protoplasmic droplet of the *Physarum* plasmodium. *Physica D: Nonlinear Phenomena* 239(11), 873–878 (2010)
- [53] Tsuda, S., Zauner, K.P., Gunji, Y.P.: Robot control with biological cells. *BioSystems* 87(2-3), 215–223 (2007)
- [54] Davidenko, J.M., Pertsov, A.V., Salomonsz, R., Baxter, W., Jalife, J., et al.: Stationary and drifting spiral waves of excitation in isolated cardiac muscle. *Nature* 355(6358), 349 (1992)
- [55] Huang, X., Troy, W.C., Yang, Q., Ma, H., Laing, C.R., Schiff, S.J., Wu, J.Y.: Spiral waves in disinhibited mammalian neocortex. *The Journal of Neuroscience* 24(44), 9897–9902 (2004)
- [56] Ronald, E.M.A., Sipper, M., Capcarrère, M.S.: Design, observation, surprise! a test of emergence. *Artificial Life* 5(3), 225–239 (1999)
- [57] Boschetti, F., Gray, R.: A turing test for emergence. In: *Advances in Applied Self-Organizing Systems*, pp. 349–364 (2008)
- [58] de Lacy Costello, B., Ratcliffe, N., Adamatzky, A., Zanin, A.L., Liehr, A.W., Purwins, H.G.: The formation of voronoi diagrams in chemical and physical systems: experimental findings and theoretical models. *International Journal of Bifurcation and Chaos in Applied Sciences and Engineering* 14(7), 2187–2210 (2004)
- [59] Reyes, D.R., Ghanem, M.M., Whitesides, G.M., Manz, A.: Glow discharge in microfluidic chips for visible analog computing. *Lab Chip* 2(2), 113–116 (2002)
- [60] Dubinov, A.E., Maksimov, A.N., Mironenko, M.S., Pylayev, N.A., Selemir, V.D.: Glow discharge based device for solving mazes. *Physics of Plasmas* (1994-present) 21(9), 093503 (2014)
- [61] Zauner, K.P., Conrad, M.: Parallel computing with dna: toward the anti-universal machine. In: Ebeling, W., Rechenberg, I., Voigt, H.-M., Schwefel, H.-P. (eds.) *PPSN 1996. LNCS*, vol. 1141, pp. 696–705. Springer, Heidelberg (1996)
- [62] Salomaa, A., Paun, G., Rozenberg, G.: DNA computing: New computing paradigms. *Texts in Theoretical Computer Science*. Springer (1998)
- [63] Amos, M., Păun, G., Rozenberg, G., Salomaa, A.: Topics in the theory of DNA computing. *Theoretical Computer Science* 287(1), 3–38 (2002)

- [64] Privman, V., Arugula, M.A., Halámek, J., Pita, M., Katz, E.: Network analysis of biochemical logic for noise reduction and stability: A system of three coupled enzymatic and gates. *The Journal of Physical Chemistry B* 113(15), 5301–5310 (2009)
- [65] Zanin, A.L., Liehr, A.W., Moskalenko, A.S., Purwins, H.G.: Voronoi diagrams in barrier gas discharge. *Applied Physics Letters* 81, 3338 (2002)
- [66] Mitchell, M.: An introduction to genetic algorithms. MIT Press, Cambridge (1996)
- [67] Koza, J., Poli, R.: Genetic programming. In: *Search Methodologies*, pp. 127–164 (2005)
- [68] Kennedy, J., Eberhart, R.: Particle swarm optimization. In: *Proceedings of the IEEE International Conference on Neural Networks*, vol. 4, pp. 1942–1948. IEEE (1995)
- [69] Dorigo, M., Stutzle, T.: Ant colony optimization. MIT Press (2004)
- [70] Nakagaki, T., Yamada, H., Toth, A.: Intelligence: Maze-solving by an amoeboid organism. *Nature* 407, 470 (2000)
- [71] Lagzi, I., Soh, S., Wesson, P.J., Browne, K.P., Grzybowski, B.A.: Maze solving by chemotactic droplets. *Journal of the American Chemical Society* 132(4), 1198–1199 (2010)
- [72] Steinbock, O., Tóth, Á., Showalter, K.: Navigating complex labyrinths: optimal paths from chemical waves. *Science* 267(5199), 868 (1995)
- [73] Jones, J.: An emergent pattern formation approach to dynamic spatial problems via quantitative front propagation and particle chemotaxis. *International Journal of Unconventional Computing* 4(4), 1–34 (2008)
- [74] Adamatzky, A.: Slime mold solves maze in one pass, assisted by gradient of chemo-attractants. *IEEE Transactions on NanoBioscience* 11(2), 131–134 (2012)
- [75] Shirakawa, T., Gunji, Y.-P.: Computation of Voronoi diagram and collision-free path using the Plasmodium of *Physarum polycephalum*. *Int. J. Unconventional Computing* 6(2), 79–88 (2010)
- [76] Shirakawa, T., Adamatzky, A., Gunji, Y.-P., Miyake, Y.: On simultaneous construction of voronoi diagram and delaunay triangulation by *Physarum polycephalum*. *International Journal of Bifurcation and Chaos* 19(9), 3109–3117 (2009)
- [77] Adamatzky, A.: *Physarum* machines: encapsulating reaction-diffusion to compute spanning tree. *Naturwissenschaften* 94(12), 975–980 (2007)
- [78] Adamatzky, A.: If BZ medium did spanning trees these would be the same trees as *Physarum* built. *Physics Letters A* 373(10), 952–956 (2009)
- [79] Adamatzky, A., de Lacy Costello, B., Shirakawa, T.: Universal computation with limited resources: Belousov-zhabotinsky and *Physarum* computers. *International Journal of Bifurcation and Chaos* 18(8), 2373–2389 (2008)
- [80] Adamatzky, A.: Developing proximity graphs by *Physarum polycephalum*: does the plasmodium follow the toussaint hierarchy. *Parallel Processing Letters* 19, 105–127 (2008)
- [81] Adamatzky, A.: Slime mould computes planar shapes. *International Journal of Bio-Inspired Computation* 4(3), 149–154 (2012)
- [82] Adamatzky, A.: Routing *Physarum* with repellents. *The European Physical Journal E: Soft Matter and Biological Physics* 31(4), 403–410 (2010)

- [83] Adamatzky, A.: Manipulating substances with *Physarum polycephalum*. Materials Science & Engineering C 38(8), 1211–1220 (2010)
- [84] Adamatzky, A.: Steering plasmodium with light: Dynamical programming of *Physarum* machine. Arxiv preprint arXiv:0908.0850 (2009)
- [85] Aono, M., Hara, M.: Amoeba-based nonequilibrium neurocomputer utilizing fluctuations and instability. In: Akl, S.G., Calude, C.S., Dinneen, M.J., Rozenberg, G., Wareham, H.T. (eds.) UC 2007. LNCS, vol. 4618, pp. 41–54. Springer, Heidelberg (2007)
- [86] Aono, M., Hara, M.: Spontaneous deadlock breaking on amoeba-based neurocomputer. BioSystems 91(1), 83–93 (2008)
- [87] Ozasa, K., Aono, M., Maeda, M., Hara, M.: Simulation of neurocomputing based on the photophobic reactions of *Euglena* with optical feedback stimulation. BioSystems 100(2), 101–107 (2010)
- [88] Adamatzky, A.: Simulating strange attraction of acellular slime mould *Physarum polycephalum* to herbal tablets. Mathematical and Computer Modelling (2011)
- [89] Conrad, M.: Information processing in molecular systems. Currents in Modern Biology (now BioSystems) 5, 1–14 (1972)
- [90] Margolus, N.: Physics-like models of computation. Physica D 10, 81–95 (1982)
- [91] Roselló-Merino, M., Bechmann, M., Sebald, A., Stepney, S.: Classical computing in nuclear magnetic resonance. Int. Journal of Unconventional Comput. 6(3-4), 163–195 (2010)
- [92] Tsuda, S., Aono, M., Gunji, Y.-P.: Robust and emergent *Physarum* logical computing. BioSystems 73, 45–55 (2004)
- [93] Adamatzky, A.: Slime mould logical gates: exploring ballistic approach. Arxiv preprint arXiv:1005.2301 (2010)
- [94] Jones, J., Adamatzky, A.: Towards *Physarum* binary adders. Biosystems 101(1), 51–58 (2010)
- [95] Adamatzky, A.: *Physarum Machine*: Implementation of a Kolmogorov-Uspensky machine on a biological substrate. Parallel Processing Letters 17(4), 455–467 (2007)
- [96] Adamatzky, A., Jones, J.: Programmable reconfiguration of *Physarum* machines. Natural Computing 9(1), 219–237 (2010)
- [97] Bebber, D.P., Hynes, J., Darrah, P.R., Boddy, L., Fricker, M.D.: Biological solutions to transport network design. Proceedings of the Royal Society B: Biological Sciences 274(1623), 2307–2315 (2007)
- [98] Fricker, M., Boddy, L., Nakagaki, T., Bebber, D.: Adaptive biological networks. In: Adaptive Networks, pp. 51–70 (2009)
- [99] Latty, T., Ramsch, K., Ito, K., Nakagaki, T., Sumpter, D.J.T., Middendorf, M., Beekman, M.: Structure and formation of ant transportation networks. Journal of The Royal Society Interface 8(62), 1298–1306 (2011)
- [100] Helbing, D., Molnar, P., Farkas, I.J., Bolay, K.: Self-organizing pedestrian movement. Environment and Planning B 28(3), 361–384 (2001)
- [101] Adamatzky, A., Jones, J.: Road planning with slime mould: If *Physarum* built motorways it would route M6/M74 through newcastle. International Journal of Bifurcation and Chaos 20(10), 3065–3084 (2010)

- [102] Adamatzky, A., Akl, S., Alonso-Sanz, R., Van Dessel, W., Ibrahim, Z., Ilachinski, A., Jones, J., Kayem, A., Martínez, G.J., De Oliveira, P., et al.: Are motorways rational from slime mould's point of view? *International Journal of Parallel, Emergent and Distributed Systems* 28(3), 230–248 (2013)
- [103] Strano, E., Adamatzky, A., Jones, J.: *Physarum* itinerae: Evolution of roman roads with slime mould. *International Journal of Nanotechnology and Molecular Computation (IJNMC)* 3(2), 31–55 (2011)
- [104] Tero, A., Takagi, S., Saigusa, T., Ito, K., Bebber, D.P., Fricker, M.D., Yumiki, K., Kobayashi, R., Nakagaki, T.: Rules for biologically inspired adaptive network design. *Science* 327(5964), 439–442 (2010)
- [105] Helbing, D.: Traffic and related self-driven many-particle systems. *Reviews of Modern Physics* 73(4), 1067 (2001)
- [106] Reynolds, C.W.: Flocks, herds and schools: A distributed behavioral model. In: ACM SIGGRAPH Computer Graphics, vol. 21, pp. 25–34. ACM (1987)
- [107] Buhl, J., Sumpter, D.J.T., Couzin, I.D., Hale, J.J., Despland, E., Miller, E.R., Simpson, S.J.: From disorder to order in marching locusts. *Science* 312(5778), 1402 (2006)
- [108] Matsushita, M., Wakita, J., Itoh, H., Watanabe, K., Arai, T., Matsuyama, T., Sakaguchi, H., Mimura, M.: Formation of colony patterns by a bacterial cell population. *Physica A: Statistical Mechanics and its Applications* 274(1), 190–199 (1999)
- [109] Vicsek, T., Czirók, A., Ben-Jacob, E., Cohen, I., Shochet, O.: Novel type of phase transition in a system of self-driven particles. *Physical Review Letters* 75(6), 1226–1229 (1995)
- [110] Zhang, S.: Fabrication of novel biomaterials through molecular self-assembly. *Nature Biotechnology* 21(10), 1171–1178 (2003)
- [111] Lobovkina, T., Dommersnes, P.G., Tiourine, S., Joanny, J.F., Orwar, O.: Shape optimization in lipid nanotube networks. *The European Physical Journal E: Soft Matter and Biological Physics* 26(3), 295–300 (2008)
- [112] Lobovkina, T., Gozen, I., Erkan, Y., Olofsson, J., Weber, S.G., Orwar, O.: Protrusive growth and periodic contractile motion in surface-adhered vesicles induced by Ca^{2+} gradients. *Soft Matter* 6(2), 268–272 (2010)
- [113] Adamatzky, A., Jones, J.: Towards *Physarum* robots: computing and manipulating on water surface. *Journal of Bionic Engineering* 5(4), 348–357 (2008)
- [114] Umedachi, T., Kitamura, T., Takeda, K., Nakagaki, T., Kobayashi, R., Ishiguro, A.: A modular robot driven by protoplasmic streaming. *Distributed Autonomous Robotic Systems* 8, 193–202 (2009)
- [115] Teplov, V.A., Romanovsky, Y.M., Latushkin, O.A.: A continuum model of contraction waves and protoplasm streaming in strands of *Physarum* plasmodium. *Biosystems* 24(4), 269–289 (1991)
- [116] Pershin, Y.V., La Fontaine, S., Di Ventra, M.: Memristive model of amoeba learning. *Physical Review E* 80(2), 021926 (2009)
- [117] Sherratt, J.A., Lewis, J.: Stress-induced alignment of actin filaments and the mechanics of cytogel. *Bulletin of Mathematical Biology* 55(3), 637–654 (1993)
- [118] Radszuweit, M., Engel, H., Bär, M.: A model for oscillations and pattern formation in protoplasmic droplets of *Physarum polycephalum*. *The European Physical Journal-Special Topics* 191(1), 159–172 (2010)

- [119] Tero, A., Kobayashi, R., Nakagaki, T.: A coupled-oscillator model with a conservation law for the rhythmic amoeboid movements of plasmodial slime molds. *Physica D: Nonlinear Phenomena* 205(1), 125–135 (2005)
- [120] Tero, A., Kobayashi, R., Nakagaki, T.: *Physarum* solver: A biologically inspired method of road-network navigation. *Physica A: Statistical Mechanics and its Applications* 363(1), 115–119 (2006)
- [121] Tero, A., Yumiki, K., Kobayashi, R., Saigusa, T., Nakagaki, T.: Flow-network adaptation in *Physarum* amoebae. Theory in Biosciences 127(2), 89–94 (2008)
- [122] Gunji, Y.-P., Shirakawa, T., Niizato, T., Haruna, T.: Minimal model of a cell connecting amoebic motion and adaptive transport networks. *Journal of Theoretical Biology* 253(4), 659–667 (2008)
- [123] Gunji, Y.-P., Shirakawa, T., Niizato, T., Yamachiyo, M., Tani, I.: An adaptive and robust biological network based on the vacant-particle transportation model. *Journal of Theoretical Biology* 272(1), 187–200 (2011)
- [124] Takamatsu, A., Takaba, E., Takizawa, G.: Environment-dependent morphology in plasmodium of true slime mold *Physarum polycephalum* and a network growth model. *Journal of Theoretical Biology* 256(1), 29–44 (2009)
- [125] Sawa, K., Balaž, I., Shirakawa, T.: Cell motility viewed as softness. *International Journal of Artificial Life Research (IJALR)* 3(1), 1–9 (2012)
- [126] Hickey, D.S., Noriega, L.A.: Relationship between structure and information processing in *Physarum polycephalum*. *International Journal of Modelling, Identification and Control* 4(4), 348–356 (2008)
- [127] Turing, A.M.: The chemical basis of morphogenesis. *Philosophical Transactions of the Royal Society of London. Series B, Biological Sciences* 237(641), 37–72 (1952)
- [128] Koch, A.J., Meinhardt, H.: Biological pattern formation: from basic mechanisms to complex structures. *Reviews of Modern Physics* 66(4), 1481–1507 (1994)
- [129] Gierer, A., Meinhardt, H.: Theory of biological pattern formation. *Kybernetik* 12, 30–39 (1972)
- [130] Murray, J.D.: How the leopard gets its spots. *Scientific American* 258(3), 80–87 (1988)
- [131] Liu, R.T., Liaw, S.S., Maini, P.K.: Two-stage turing model for generating pigment patterns on the leopard and the jaguar. *Physical Review E* 74(1), 011914–1 (2006)
- [132] Murray, J.D.: On pattern formation mechanisms for lepidopteran wing patterns and mammalian coat markings. *Philosophical Transactions of the Royal Society of London. B, Biological Sciences* 295(1078), 473–496 (1981)
- [133] Turk, G.: Generating textures on arbitrary surfaces using reaction-diffusion. *Computer Graphics* 25(4), 289–298 (1991)
- [134] de Kepper, P., Castets, V., Dulos, E., Boissonade, J.: Turing-type chemical patterns in the chlorite-iodide-malonic acid reaction. *Physica D: Nonlinear Phenomena* 49(1-2), 161–169 (1991)
- [135] Ouyang, Q., Swinney, H.L.: Transition from a uniform state to hexagonal and striped turing patterns. *Nature* 352(6336), 610–612 (1991)
- [136] Murray, J.D., Oster, G.F.: Cell traction models for generating pattern and form in morphogenesis. *Journal of Mathematical Biology* 19(3), 265–279 (1984)

- [137] Serini, G., Ambrosi, D., Giraudo, E., Gamba, A., Preziosi, L., Bussolino, F.: Modeling the early stages of vascular network assembly. *The EMBO Journal* 22(8), 1771–1779 (2003)
- [138] Ambrosi, D., Bussolino, F., Preziosi, L.: A review of vasculogenesis models. *Journal of Theoretical Medicine* 6(1), 1–19 (2005)
- [139] Manoussaki, D.: A mechanochemical model of angiogenesis and vasculogenesis. *ESAIM: Mathematical Modelling and Numerical Analysis* 37(04), 581–599 (2003)
- [140] Tosin, A., Ambrosi, D., Preziosi, L.: Mechanics and chemotaxis in the morphogenesis of vascular networks. *Bulletin of Mathematical Biology* 68(7), 1819–1836 (2006)
- [141] Oster, G.F.: Lateral inhibition models of developmental processes. *Mathematical Biosciences* 90(1-2), 265–286 (1988)
- [142] Meinhardt, H., Gierer, A., et al.: Pattern formation by local self-activation and lateral inhibition. *Bioessays* 22(8), 753–760 (2000)
- [143] Hartline, H.K., Ratliff, F.: Inhibitory interaction of receptor units in the eye of *Limulus*. *The Journal of General Physiology* 40(3), 357–376 (1957)
- [144] Bonabeau, E.: From classical models of morphogenesis to agent-based models of pattern formation. *Artificial Life* 3(3), 191–211 (1997)
- [145] Bizon, C., Shattuck, M.D., Swift, J.B., McCormick, W.D., Swinney, H.L.: Patterns in 3d vertically oscillated granular layers: simulation and experiment. *Physical Review Letters* 80(1), 57–60 (1998)
- [146] Kessler, M.A., Werner, B.T.: Self-organization of sorted patterned ground. *Science* 299(5605), 380–383 (2003)
- [147] Matsushita, M., Wakita, J., Itoh, H., Rafols, I., Matsuyama, T., Sakaguchi, H., Mimura, M.: Interface growth and pattern formation in bacterial colonies. *Physica A: Statistical Mechanics and its Applications* 249(1), 517–524 (1998)
- [148] Ben-Jacob, E.: Bacterial self-organization: co-enhancement of complexification and adaptability in a dynamic environment. *Philosophical Transactions of the Royal Society of London. Series A: Mathematical, Physical and Engineering Sciences* 361(1807), 1283–1312 (2003)
- [149] Deneubourg, J.L., Aron, S., Goss, S., Pasteels, J.M.: The self-organizing exploratory pattern of the argentine ant. *Journal of Insect Behavior* 3(2), 159–168 (1990)
- [150] Bonabeau, E., Theraulaz, G., Deneubourg, J., Franks, N.R., Rafelsberger, O., Joly, J., Blanco, S.: A model for the emergence of pillars, walls and royal chambers in termite nests. *Philosophical Transactions of the Royal Society of London. Series B: Biological Sciences* 353(1375), 1561–1576 (1998)
- [151] Burstedde, C., Klauck, K., Schadschneider, A., Zittartz, J.: Simulation of pedestrian dynamics using a two-dimensional cellular automaton. *Physica A: Statistical Mechanics and its Applications* 295(3), 507–525 (2001)
- [152] Jarrett, T.C., Ashton, D.J., Fricker, M., Johnson, N.F.: Interplay between function and structure in complex networks. *Physical Review E* 74(2), 026116 (2006)
- [153] Bohn, S., Douady, S., Couder, Y.: Four sided domains in hierarchical space dividing patterns. *Physical Review Letters* 94(5), 54503 (2005)
- [154] Dufresne, E.R., Stark, D.J., Greenblatt, N.A., Cheng, J.X., Hutchinson, J.W., Mahadevan, L., Weitz, D.A.: Dynamics of fracture in drying suspensions. *Langmuir* 22(17), 7144–7147 (2006)

- [155] Niemeyer, L., Pietronero, L., Wiesmann, H.J.: Fractal dimension of dielectric breakdown. *Physical Review Letters* 52(12), 1033–1036 (1984)
- [156] Nase, J., Lindner, A., Creton, C.: Pattern formation during deformation of a confined viscoelastic layer: From a viscous liquid to a soft elastic solid. *Physical Review Letters* 101(7), 74503 (2008)
- [157] Glazier, J.A., Gross, S.P., Stavans, J.: Dynamics of two-dimensional soap froths. *Physical Review A* 36(1), 306 (1987)
- [158] Isenberg, C.: Problem solving with soap films: Part i. *Physics Education* 10, 452 (1975)
- [159] Helbing, D., Johansson, A.: Pedestrian, crowd and evacuation dynamics. Swiss Federal Institute of Technology (2009)
- [160] Streiff, M., Mlot, N., Shinotsuka, S., Alexeev, A., Hu, D.: Ants as fluids: Physics-inspired biology. Arxiv preprint arXiv:1010.3256 (2010)
- [161] Durham, A.C.H., Ridgway, E.B.: Control of chemotaxis in *Physarum polycephalum*. *The Journal of Cell Biology* 69, 218–223 (1976)
- [162] Nakagaki, T., Yamada, H., Ueda, T.: Modulation of cellular rhythm and photoavoidance by oscillatory irradiation in the *Physarum* plasmodium. *Biophysical Chemistry* 82(1), 23–28 (1999)
- [163] Nakagaki, T., Iima, M., Ueda, T., Nishiura, Y., Saigusa, T., Tero, A., Kobayashi, R., Showalter, K.: Minimum-risk path finding by an adaptive amoebal network. *Physical Review Letters* 99(6), 68104 (2007)
- [164] Harun, A., Holm, E.A., Clode, M.P., Miodownik, M.A.: On computer simulation methods to model zener pinning. *Acta Materialia* 54(12), 3261–3273 (2006)
- [165] Dutta, P., Khastgir, S.P., Roy, A.: Steiner trees and spanning trees in six-pin soap films. *American Journal of Physics* 78, 215 (2010)
- [166] Deneubourg, J.L., Goss, S.: Collective patterns and decision-making. *Ethol. Ecol. Evol.* 1, 295–311 (1989)
- [167] Baumgarten, W., Hauser, M.J.B.: Detection, extraction, and analysis of the vein network. *Journal of Computational Interdisciplinary Sciences* 1(3), 241–249 (2010)
- [168] Rasband, W.S.: Imagej, us national institutes of health, bethesda, maryland, usa (1997)
- [169] Arganda-Carreras, I., Fernández-González, R., Muñoz-Barrutia, A., Ortiz-De-Solorzano, C.: 3d reconstruction of histological sections: Application to mammary gland tissue. *Microscopy Research and Technique* 73(11), 1019–1029 (2010)
- [170] Mukundan, R.: Binary vision algorithms in Java. Internal technical report (1999)
- [171] Adamatzky, A., de Lacy Costello, B.: Reaction-diffusion path planning in a hybrid chemical and cellular-automaton processor. *Chaos, Solitons & Fractals* 16(5), 727–736 (2003)
- [172] Theraulaz, G., Bonabeau, E.: A brief history of stigmergy. *Artificial Life* 5(2), 97–116 (1999)
- [173] Houtgast, T.: Psychophysical evidence for lateral inhibition in hearing. *The Journal of the Acoustical Society of America* 51(6B), 1885–1894 (1972)
- [174] Serino, A., Haggard, P.: Touch and the body. *Neuroscience & Biobehavioral Reviews* 34(2), 224–236 (2010)

- [175] Urban, N.N.: Lateral inhibition in the olfactory bulb and in olfaction. *Physiology & Behavior* 77(4), 607–612 (2002)
- [176] Hartline, H.K., Ratliff, F.: Inhibitory interaction in the retina of limulus. In: *Physiology of Photoreceptor Organs*, pp. 381–447. Springer (1972)
- [177] Macknik, S.L., Martinez-Conde, S.: The spatial and temporal effects of lateral inhibitory networks and their relevance to the visibility of spatiotemporal edges. *Neurocomputing* 58, 775–782 (2004)
- [178] Kandel, E.R., Schwartz, J.H., Jessell, T.M.: *Principles of neural science*, vol. 4. McGraw-Hill, New York (2000)
- [179] Jones, J.: Characteristics of pattern formation and evolution in approximations of *Physarum* transport networks. *Artificial Life* 16(2), 127–153 (2010)
- [180] Peromaa, T.L., Laurinen, P.I.: Separation of edge detection and brightness perception. *Vision Research* 44(16), 1919–1925 (2004)
- [181] Pessoa, L., Mingolla, E., Neumann, H.: A contrast-and luminance-driven multiscale network model of brightness perception. *Vision Research* 35(15), 2201–2223 (1995)
- [182] Blakeslee, B., McCourt, M.E.: A unified theory of brightness contrast and assimilation incorporating oriented multiscale spatial filtering and contrast normalization. *Vision Research* 44(21), 2483–2503 (2004)
- [183] Nakagaki, T., Yamada, H., Toth, A.: Path finding by tube morphogenesis in an amoeboid organism. *Biophysical Chemistry* 92(1-2), 47–52 (2001)
- [184] Nakagaki, T.: Smart behavior of true slime mold in a labyrinth. *Research in Microbiology* 152(9), 767–770 (2001)
- [185] Lumelsky, V.J.: A comparative study on the path length performance of maze-searching and robot motion planning algorithms. *IEEE Transactions on Robotics and Automation* 7(1), 57–66 (1991)
- [186] Watts, D.J., Strogatz, S.H.: Collective dynamics of ‘small-world’ networks. *Nature* 393(6684), 440–442 (1998)
- [187] Fricker, M., Boddy, L., Bebbert, D.: Network organisation of mycelial fungi. In: *Biology of the Fungal Cell*, pp. 309–330. Springer (2007)
- [188] Toussaint, G.T.: The relative neighbourhood graph of a finite planar set. *Pattern Recognition* 12(4), 261–268 (1980)
- [189] Jaromczyk, J.W., Toussaint, G.T.: Relative neighborhood graphs and their relatives. *Proceedings of the IEEE* 80(9), 1502–1517 (1992)
- [190] Tero, A., Nakagaki, T., Toyabe, K., Yumiki, K., Kobayashi, R.: A method inspired by *Physarum* for solving the steiner problem. *International Journal of Unconventional Computing* 6, 109–123 (2010)
- [191] Miehle, W.: Link-length minimization in networks. *Operations Research*, 232–243 (1958)
- [192] Šaltenis, V.: Simulation of wet film evolution and the euclidean steiner problem. *Informatica* 10(4), 457–466 (1999)
- [193] Courant, R., Robbins, H., Stewart, I.: *What is Mathematics?: an elementary approach to ideas and methods*. Oxford University Press, USA (1996)
- [194] Jones, J.: Passive vs active approaches in particle approximations of reaction-diffusion computing. *Int. J. Nanotechnol. Mol. Comput.* 1(3), 37–63 (2009)
- [195] Aono, M., Hirata, Y., Hara, M., Aihara, K.: Amoeba-based chaotic neuro-computing: Combinatorial optimization by coupled biological oscillators. *New Generation Computing* 27(2), 129–157 (2009)

- [196] Gandhi, M.V., Thompson, B.S.: Smart materials and structures. Springer US (1992)
- [197] Otsuka, K., Wayman, C.M., et al.: Shape memory materials. Cambridge Univ. Pr. (1999)
- [198] Chopra, I.: Review of state of art of smart structures and integrated systems. *AIAA Journal* 40(11), 2145–2187 (2002)
- [199] Stupp, S.I.: Self-assembly and biomaterials. *Nano Letters* (2010)
- [200] Ariga, K., Hill, J.P., Lee, M.V., Vinu, A., Charvet, R., Acharya, S.: Challenges and breakthroughs in recent research on self-assembly. *Science and Technology of Advanced Materials* 9, 014109 (2008)
- [201] Darling, S.B.: Directing the self-assembly of block copolymers. *Progress in Polymer Science* 32(10), 1152–1204 (2007)
- [202] Chandler, D.: Interfaces and the driving force of hydrophobic assembly. *Nature* 437(7059), 640–647 (2005)
- [203] Hayashi, T., Carthew, R.W.: Surface mechanics mediate pattern formation in the developing retina. *Nature* 431(7009), 647–652 (2004)
- [204] Hopfield, J.J., Tank, D.W.: Computing with neural circuits: A model. *Science* 233(4764), 625 (1986)
- [205] Lihoreau, M., Chittka, L., Raine, N.E.: Travel optimization by foraging bumblebees through readjustments of traplines after discovery of new feeding locations. *The American Naturalist* 176(6), 744–757 (2010)
- [206] Dorigo, M., Bonabeau, E., Theraulaz, G.: Ant algorithms and stigmergy. *Future Generation Computer Systems* 16(8), 851–871 (2000)
- [207] Larranaga, P., Kuijpers, C.M.H., Murga, R.H., Inza, I., Dizdarevic, S.: Genetic algorithms for the travelling salesman problem: A review of representations and operators. *Artificial Intelligence Review* 13(2), 129–170 (1999)
- [208] Hasegawa, M.: Verification and rectification of the physical analogy of simulated annealing for the solution of the traveling salesman problem. *Physical Review E* 83(3), 036708 (2011)
- [209] Durbin, R., Willshaw, D.: An analogue approach to the travelling salesman problem using an elastic net method. *Nature* 326(6114), 689–691 (1987)
- [210] Jones, J.: Towards programmable smart materials: Dynamical reconfiguration of emergent transport networks. *Int. Journal of Unconventional Comput.* 7(6), 423–447 (2011)
- [211] MacGregor, J.N., Chu, Y.: Human performance on the traveling salesman and related problems: A review. *The Journal of Problem Solving* 3(2), 2 (2011)
- [212] Graham, S.M., Joshi, A., Pizlo, Z.: The traveling salesman problem: A hierarchical model. *Memory & Cognition* 28(7), 1191–1204 (2000)
- [213] Dry, M., Lee, M.D., Vickers, D., Hughes, P.R.: Human performance on visually presented traveling salesperson problems with varying numbers of nodes. *The Journal of Problem Solving* 1(1), 4 (2006)
- [214] MacGregor, J.N., Ormerod, T.C., Chronicle, E.P.: A model of human performance on the traveling salesperson problem. *Memory & Cognition* 28(7), 1183–1190 (2000)
- [215] Pizlo, Z., Stefanov, E., Saalwechter, J., Li, Z., Haxhimusa, Y., Kropatsch, W.G.: Traveling salesman problem: A foveating pyramid model. *The Journal of Problem Solving* 1(1), 8 (2006)
- [216] Jones, J., Adamatzky, A.: Computation of the travelling salesman problem by a shrinking blob. *Natural Computing* 13(1), 1–16 (2014)

- [217] Applegate, D., Bixby, R., Chvatal, V., Cook, W.: Concorde tsp solver (2006), <http://www.tsp.gatech.edu/concorde>
- [218] Galton, A., Duckham, M.: What is the region occupied by a set of points? In: Raubal, M., Miller, H.J., Frank, A.U., Goodchild, M.F. (eds.) GIScience 2006. LNCS, vol. 4197, pp. 81–98. Springer, Heidelberg (2006)
- [219] Duckham, M., Kulik, L., Worboys, M., Galton, A.: Efficient generation of simple polygons for characterizing the shape of a set of points in the plane. *Pattern Recognition* 41(10), 3224–3236 (2008)
- [220] Edelsbrunner, H., Kirkpatrick, D., Seidel, R.: On the shape of a set of points in the plane. *IEEE Transactions on Information Theory* 29(4), 551–559 (1983)
- [221] Jones, J.: Influences on the formation and evolution of *Physarum polycephalum* inspired emergent transport networks. *Natural Computing* 10(4), 1345–1369 (2011)
- [222] Flood, M.M.: The traveling-salesman problem. *Operations Research* 4(1), 61–75 (1956)
- [223] Golden, B., Bodin, L., Doyle, T., Stewart, W.: Approximate traveling salesman algorithms. *Operations Research* 28(3-Part-II), 694–711 (1980)
- [224] Kurz, M.E.: Heuristics for the traveling salesman problem. Wiley Encyclopedia of Operations Research and Management Science (2011)
- [225] Al-Mulhem, M., Al-Maghribi, T.: Efficient convex-elastic net algorithm to solve the euclidean traveling salesman problem. *IEEE Transactions on Systems, Man, and Cybernetics, Part B: Cybernetics* 28(4), 618–620 (1998)
- [226] MacGregor, J.N., Ormerod, T.: Human performance on the traveling salesman problem. *Attention, Perception, & Psychophysics* 58(4), 527–539 (1996)
- [227] Ormerod, T.C., Chronicle, E.P.: Global perceptual processing in problem solving: The case of the traveling salesperson. *Attention, Perception, & Psychophysics* 61(6), 1227–1238 (1999)
- [228] Best, B.J.: A model of fast human performance on a computationally hard problem. In: Proceedings of the 27th Annual Conference of the Cognitive Science Society, pp. 256–262 (2005)
- [229] Fortune, S.: A sweepline algorithm for voronoi diagrams. *Algorithmica* 2(1), 153–174 (1987)
- [230] De Berg, M., Cheong, O., Van Kreveld, M.: Computational geometry: algorithms and applications. Springer-Verlag New York Inc. (2008)
- [231] Tolmachiev, D., Adamatzky, A.: Chemical processor for computation of voronoi diagram. *Advanced Materials for Optics and Electronics* 6(4), 191–196 (1996)
- [232] Asai, T., De-Lacy Costello, B., Adamatzky, A.: Silicon implementation of a chemical reaction-diffusion processor for computation of voronoi diagram. *International Journal of Bifurcation and Chaos* 15(10), 3307–3320 (2005)
- [233] Adamatzky, A.: Hot ice computer. *Physics Letters A* 374(2), 264–271 (2009)
- [234] Adamatzky, A., de Lacy Costello, B.: On some limitations of reaction-diffusion chemical computers in relation to voronoi diagram and its inversion. *Physics Letters A* 309(5-6), 397–406 (2003)
- [235] Kim, D., Kim, D.S., Sugihara, K.: Euclidean voronoi diagram for circles in a circle. *International Journal of Computational Geometry & Applications* 15(02), 209–228 (2005)
- [236] Jones, J., Adamatzky, A.: Slime mould inspired generalised voronoi diagrams with repulsive fields. *Int. J. Bifurcation and Chaos* (2013) (in press)

- [237] Sellares, J.A., Toussaint, G.: On the role of kinesthetic thinking in computational geometry. *International Journal of Mathematical Education in Science and Technology* 34(2), 219–237 (2003)
- [238] Jarvis, R.A.: On the identification of the convex hull of a finite set of points in the plane. *Information Processing Letters* 2(1), 18–21 (1973)
- [239] Saeed, K., Tabędzki, M., Rybnik, M., Adamski, M.: K3m: A universal algorithm for image skeletonization and a review of thinning techniques. *International Journal of Applied Mathematics and Computer Science* 20(2), 317–335 (2010)
- [240] Blum, H.: A transformation for extracting new descriptors of shape. *Models for the Perception of Speech and Visual Form* 19(5), 362–380 (1967)
- [241] Adamatzky, A., Tolmachiev, D.: Chemical processor for computation of skeleton of planar shape. *Advanced Materials for Optics and Electronics* 7(3), 135–139 (1997)
- [242] Reid, C.R., Latty, T., Dussutour, A., Beekman, M.: Slime mold uses an externalized spatial ‘memory’ to navigate in complex environments. *Proceedings of the National Academy of Sciences* 109(43), 17490–17494 (2012)
- [243] Jones, J., Adamatzky, A.: Material approximation of data smoothing and spline curves inspired by slime mould. *Bioinspiration and Biomimetics* 9(3), 036016 (2014)
- [244] Reinsch, C.H.: Smoothing by spline functions. *Numerische Mathematik* 10(3), 177–183 (1967)
- [245] De Boor, C.: A practical guide to splines, vol. 27. Springer-Verlag New York (1978)
- [246] Eilers, P.H.C., Marx, B.D.: Flexible smoothing with b-splines and penalties. *Statistical Science*, 89–102 (1996)
- [247] Hou, H., Andrews, H.: Cubic splines for image interpolation and digital filtering. *IEEE Transactions on Acoustics, Speech and Signal Processing* 26(6), 508–517 (1978)
- [248] Foretník, J.: Architektura, geometrie a výpočetní technika. PhD thesis (2010)
- [249] Kass, M., Witkin, A., Terzopoulos, D.: Snakes: Active contour models. *International Journal of Computer Vision* 1(4), 321–331 (1988)
- [250] Cohen, L.D.: On active contour models and balloons. *CVGIP: Image Understanding* 53(2), 211–218 (1991)
- [251] Heimann, T., Meinzer, H.-P.: Statistical shape models for 3d medical image segmentation: A review. *Medical Image Analysis* 13(4), 543–563 (2009)
- [252] Foretník, J.: Interactive Nurbs Demonstration,
<http://geometrie.foretnik.net/files/NURBS-en.swf>
(accessed: September 20, 2013)
- [253] Perona, P., Shiota, T., Malik, J.: Anisotropic diffusion. In: *Geometry-Driven Diffusion in Computer Vision*, pp. 73–92. Springer (1994)
- [254] Junc, J.A.: Studies on sclerotization in *Physarum polycephalum*. *American Journal of Botany*, 561–567 (1954)
- [255] Adamatzky, A., Alonso-Sanz, R.: Rebuilding iberian motorways with slime mould. *Biosystems* 105(1), 89–100 (2011)
- [256] Jones, J., Adamatzky, A.: Approximation of statistical analysis and estimation by morphological adaptation in a model of slime mould. *Int. Journal of Unconventional Comput.* (2014) (in press)

- [257] Grewal, M.S., Andrews, A.P.: Kalman filtering: theory and practice using MATLAB. Wiley.com (2011)
- [258] Yilmaz, A., Javed, O., Shah, M.: Object tracking: A survey. *Acm Computing Surveys (CSUR)* 38(4), 13 (2006)
- [259] Tsuda, S., Jones, J.: The emergence of synchronization behavior in *Physarum polycephalum* and its particle approximation. *Biosystems* 103, 331–341 (2010)
- [260] Jones, J., Adamatzky, A.: Emergence of self-organized amoeboid movement in a multi-agent approximation of *Physarum polycephalum*. *Bioinspiration and Biomimetics* 7(1), 016009 (2012)
- [261] Farebrother, R.W.: Visualizing statistical models and concepts, vol. 166. CRC Press (2002)
- [262] Babloyantz, A., Sepulchre, J.A.: Front propagation into unstable media: a computational tool. In: *Nonlinear Wave Processes in Excitable Media*, pp. 343–350. Springer (1991)
- [263] Rambidi, N.G.: Biologically inspired information processing technologies: Reaction-diffusion paradigm. *Int. J. Unconventional Comput.* 1(2), 101–121 (2005)
- [264] Agladze, K., Magome, N., Aliev, R., Yamaguchi, T., Yoshikawa, K.: Finding the optimal path with the aid of chemical wave. *Physica D: Nonlinear Phenomena* 106(3-4), 247–254 (1997)
- [265] Nakagaki, T., Uemura, S., Kakiuchi, Y., Ueda, T.: Action spectrum for sporulation and photoavoidance in the plasmodium of *Physarum polycephalum*, as modified differentially by temperature and starvation. *Photochem. Photobiol.* 64(5), 859–862 (1996)
- [266] Pikovsky, A., Rosenblum, M., Kurths, J.: Synchronization: A universal concept in nonlinear sciences. Cambridge Nonlinear Science Series, vol. 12. Cambridge (2001)
- [267] Gabor, D.: Theory of communication. *J. IEE (London)* 93(3), 429–457 (1946)
- [268] Panter, P.: Modulation, Noise, and Spectral Analysis. McGraw-Hill, New York (1965)
- [269] Smith, M.J.T., Mersereau, R.M.: Introduction to Digital Signal Processing. A Computer Laboratory Textbook. Wiley, New York (1992)
- [270] Rosenblum, M., Kurths, J.: Analysing synchronization phenomena from bivariate data by means of the hilbert transform. In: *Nonlinear Analysis of Physiological Data*, pp. 91–99. Springer (1998)
- [271] Nakagaki, T., Yamada, H., Ueda, T.: Interaction between cell shape and contraction pattern in the *Physarum* plasmodium. *Biophysical Chemistry* 84(3), 195–204 (2000)
- [272] Kessler, D.: Plasmodial structure and motility. In: *Cell Biology of *Physarum* and *Didymium**, vol. 1, ch. 5. Academic Press (1982)
- [273] Yoshimoto, Y., Kamiya, N.: Studies on contraction rhythm of the plasmodial strand iii. role of endoplasmic streaming in synchronization of local rhythms. *Protoplasma* 95, 111–121 (1978)
- [274] Flynn, M.R., Kasimov, A.R., Nave, J.C., Rosales, R.R., Seibold, B.: Self-sustained nonlinear waves in traffic flow. *Physical Review E* 79(5), 56113 (2009)
- [275] Cifarelli, A., Dimonte, A., Berzina, T., Erokhin, V.: On the loading of slime mold *Physarum polycephalum* with microparticles for unconventional computing application. *BioNanoScience* 4(1), 92–96 (2014)

- [276] Adamatzky, A., de Lacy Costello, B., Skachek, S., Melhuish, C.: Manipulating objects with chemical waves: Open loop case of experimental belousov-zhabotinsky medium coupled with simulated actuator array. Physics Letters A 350(3-4), 201–209 (2006)
- [277] Ishiguro, A., Shimizu, M., Kawakatsu, T.: Don't try to control everything!: An emergent morphology control of a modular robot. In: Proceedings of 2004 IEEE/RSJ Int. Conf. on Intelligent Robots and Systems, Sendai, Japan, September 28–October 2, pp. 981–985 (2004)
- [278] Bojinov, H., Casal, A., Hogg, T.: Multiagent control of self-reconfigurable robots. In: Proceedings of the Fourth International Conference on MultiAgent Systems, pp. 143–150. IEEE (2000)
- [279] Salemi, B., Shen, W.M., Will, P.: Hormone-controlled metamorphic robots. In: Proceedings of the 2001 IEEE International Conference on Robotics and Automation, ICRA, vol. 4, pp. 4194–4199. IEEE (2001)
- [280] Gardner, M.: Mathematical games: The fantastic combinations of John Conway's new solitaire game Life. Scientific American 223(4), 120–123 (1970)
- [281] Becker, M.: Design of fault tolerant networks with agent-based simulation of *Physarum* polycephalum. In: 2011 IEEE Congress on Evolutionary Computation (CEC), pp. 285–291. IEEE (2011)
- [282] Trivedi, D., Rahn, C.D., Kier, W.M., Walker, I.D.: Soft robotics: Biological inspiration, state of the art, and future research. Applied Bionics and Biomechanics 5(3), 99–117 (2008)
- [283] Umedachi, T., Takeda, K., Nakagaki, T., Kobayashi, R., Ishiguro, A.: Fully decentralized control of a soft-bodied robot inspired by true slime mold. Biological Cybernetics 102(3), 261–269 (2010)
- [284] Hamann, H., Schmickl, T., Crailsheim, K.: Self-organized pattern formation in a swarm system as a transient phenomenon of non-linear dynamics. Mathematical and Computer Modelling of Dynamical Systems 18(1), 39–50 (2012)
- [285] Boudaoud, A., Chaïeb, S.: Mechanical phase diagram of shrinking cylindrical gels. Physical Review E 68(2), 021801 (2003)
- [286] Pauchard, L., Adda-Bedia, M., Allain, C., Couder, Y.: Morphologies resulting from the directional propagation of fractures. Physical Review E 67(2), 027103 (2003)
- [287] Ficker, T.: Electrostatic discharges and multifractal analysis of their lichtenberg figures. Journal of Physics D: Applied Physics 32(3), 219 (1999)
- [288] Thompson, D.W.: On Growth and Form. Cambridge University Press (1917)
- [289] Bauer, A.L., Jackson, T.L., Jiang, Y.: A cell-based model exhibiting branching and anastomosis during tumor-induced angiogenesis. Biophysical Journal 92(9), 3105–3121 (2007)

Index

- α -shape 202
- amoeboid movement 298
 - adaptive response to environmental obstacles 305
 - cleaving a blob of virtual plasmodium 304
 - externally influencing movement 302
 - attractant sources 302
 - repellent sources 302
 - fusing separate virtual blobs 304
 - initiation of travelling waves 299
 - moving blob fragments 300
 - reformation of shape 304
- arithmetic mean 240
- skewed data distributions 240
- centroid computation 233
 - hollow and concave shapes 237
 - in multi-agent model 235
 - in slime mould 234
- Chevreul staircase illusion 101
- collective transport 289
 - circular arenas 293
 - closed arenas 296
 - gear train 295
 - helical transport 293
 - open ended arenas 291
 - particle drift 292
 - second-order oscillations 297
 - transporting substances 295
 - travelling waves 291
- within constrained sheets of virtual plasmodium 298
- concave hull 202
 - by growth and fusion 205
 - by shrinkage 203
 - transformation via growth parameter 207
- convex hull 200
 - by self organisation 200
 - by shrinking band 200
 - by shrinking band - repellent version 200
 - transformation via growth parameter 207
- data smoothing 215
 - high frequency preference 216
 - low pass filter 216
 - moving average 216
- data tracking 242
 - attractant stimuli 244
 - noise contaminated data 245
 - repellent stimuli 245
 - self-oscillatory blob 243
 - tracking mechanism 246
- dynamical reconfiguration of transport networks 143
 - approximating the TSP 156
 - feedback mechanism 147
 - guided influence 158
 - high-level transition motifs 151
 - limitations of approach 156
 - network evolution 149
 - network stabilisation 154

- node attraction 147
- node suppression 147
- re-seeding disconnected nodes 148
- real-time analysis 144
- topological connectivity 145

- lateral inhibition, *see* neural mechanisms
- logic gates 125
 - asynchronism 129
 - attractant gradient interactions 132
 - compounding errors 138
 - half adder 135
 - individual gate models 132
 - junction hesitation 135
 - multi agent approach 131
 - reversing gradients 130
 - suitability of spatial implementation 139
 - timing errors 135

- maze solving
 - chemical wave 22
 - droplets 21
 - multi-agent model 109
 - slime mould 21
- morphological adaptation
 - arithmetic statistics 240
 - centroid computation 235
 - data smoothing 215
 - estimation functions 243
 - mechanisms of material computation 246
 - spline curves 218
 - towards material computation for statistics 251
- multi-agent model 33
 - adaptive population size 40
 - approximating substrate differences 84
 - approximating the illumination response 42
 - avoidance of illuminated regions 70
 - avoiding repellents 71
 - building blocks of model 37
 - collective perception 97
 - construction of spanning tree 65
 - consumption of nutrients 43, 82

- continuum of patterning 34
- contraction after growth 68
- dendritic growth 64
- diffusion mechanism 42
- engulfment of nutrients 43
- environment representation 41
- environmental noise effects 81
- environmentally mediated complexity 86
- generalising the model 324
- lateral activation 94
- lateral inhibition 94
- maze adaptation 109
- maze tortuosity 110
- motivations 33
- motor behaviour 38
 - oscillatory condition 39
- network connectivity 71
 - dynamical evolution of 74
- network fromation from solid sheet 61
- nutrient distance effects 79
- nutrient size and concentration effects 80
- oscillation patterns 282
- overview 36
- particle structure 38
- presentation of attractants 41
- presentation of repellents 42
- proximity graphs 113
- pseudopodium extension and retraction 75
- pseudopodium withdrawal 62
- radial growth 66
- reciprocal oscillations 280
- repulsive behaviour 328
- selection of shorter path 62
- sensory behaviour 38
- spanning trees 112
- Steiner trees 120
- variations in particle speed 326

- neural mechanisms 91
 - collective perception 97
 - lateral activation by hazards 94
 - lateral inhibition 91
 - lateral inhibition by attractants 94
 - non-neural approximations 93

- simultaneous brightness
 contrast 100
- staircase illusion 97
- non-classical computation, *see*
 unconventional computation
- nutrient concentration
 effect of network evolution 115
 effect on growth 80
- mixed concentration background
 substrates 70
- nutrient-rich background
 substrates 66
- poor quality background
 substrates 64
- oscillatory behaviour 269
 image analysis 270
 model 277
 emergence 278
 fixed scale 279
 increasing scale 281
 pattern types 282
 phase synchronisation 283
 reciprocal oscillations 278
- pattern types 273
 phase synchronisation analysis 271
 results 275
 regeneration of patterns 272
- path planning 253
 collision-free paths 258
 front propagation methods 253
 morphological adaptation
 approach 254
 multiple path removal 256
 multiple paths 255
 obstacle avoidance 258
- pattern formation 16
 boundary conditions and pre-existing
 gradients 337
- cohesion 49
- combining particle types 333
- dissipative islands 47
- external influence 54
- interfacial patterns 333
- iris-like patterns 342
- LALI models 27
- Lichtenberg figure-type
 patterns 341
- network minimisation 55
 node angle 55
 Plateau angles 58
 von Neumann's law 58
- network motifs 44
- network self-assembly 44
- parametric mapping 53
- phase separation patterning 333
- phyllotaxis patterns
 rose petal 338
 sunflower-type spirals 338
- planar sheet structures 47
- population density 48
- repulsive boundary effects 329
- repulsive multi-agent model 328
 honeycomb tiling 328
- pattern damage and restoration
 331
- striped domains 329
- scaling effects 47
- septate patterning 338
- shuttle streaming effect 46
- spiral patterns 343
- striped network formation 334
- three dimensional patterns 345
- Turing-type patterns 53
- Physarum polycephalum 13
 computation by 22
 computational models 25
 intelligence 21
 life cycle 13
 maze solving 21
 oscillation patterns 269
 oscillatory dynamics 18
 oscillatory phenomena 17
 oscillatory rhythm 18
 reciprocal oscillations 18
 robotics 23
- proximity graphs 113
 area to distance transformation
 120
- closure of cycles 115
 evolution of connectivity 115
- sclerotium stage
 inspiration for centroid
 computation 233
- life cycle 14

- Simultaneous Brightness Contrast
 (SBC) illusion 103
- skeletonisation 207
 by relaxation 209
 planar shapes 210
 spur defects 209
- smart materials 141
- spline curves 218
 clamped 220
 closed shapes 220
 crossed lines 223
 interpolating splines 225
 interior containment 228
 rectilinear pre-processing 225
- mechanical history 218
- properties and limitations of
 adaptation approach 222
 quasi-mechanical evolution 220
 retaining weak background
 stimulus 221
 unclamped 219
- Steiner trees, *see* multi-agent model
- Travelling Salesman Problem 161
 shrinking blob method 164
 halting procedure 164
 performance variation 174
 reading the output 165
 relation to Toussaint hierarchy
 173
 shrinkage process 164
 tour construction mechanism 167
- spatially implemented problem
 solving 177
- travelling waves, *see* collective transport
- unconventional computation 19
 advantages 20
 chemical computation 22
 emergence in 19
 limitations 20
 self-organisation 20
 self-organisation in 20
 substrate implementations 20
- universal machine 19
- Voronoi diagram 181
 approximation by slime mould 181
 merging fronts method 182
 repellent method 182
 circles within circles problem 193
 environmental stimuli 183
 environmentally mediated plane
 division 196
 interactions between attractants and
 repellents 185
 multi-agent model
 expanding cells method 191
 hybrid diagrams 190
 merging fronts method 187
 modification using repellents 194
 planar shapes 189
 repellent method 186
 weighted Voronoi diagram 192